

TECHNICAL DIGEST

1 9 9 6

ADAPTIVE OPTICS

STATEMENT BY STATEMENT A

Approved for public release;
Distribution Unlimited

JULY 8-12, 1996

MAUI, HAWAII

1996 TECHNICAL DIGEST SERIES

VOLUME 13



SPONSORED AND MANAGED BY
OPTICAL SOCIETY OF AMERICA

DO NOT QUALITY INSPECTOR



September 16, 1996

Major William Arrasmith
AFOSR/NE
110 Duncan Ave. Ste. B115
Bolling AFB, DC 20332-8080

RE: Organization of the 1996 Adaptive Optics Topical Meeting
Grant # F49620-96-1-0278

Dear Major Arrasmith:

Thank you for your support for the Adaptive Optics Topical meeting. Thanks to your support, we had very successful meetings and were able to provide travel support to speakers who would not otherwise had been able to attend.

In response to the grant terms, I am enclosing three copies of the Special Final Report for the Adaptive Optics Topical Meeting. As described in the grant contracts, the Special Final Report consists of a Technical Digest and an Attendance List.

Thanks again for your support.

Sincerely,

A handwritten signature in black ink, appearing to read "Naomi Chavez".

Naomi Chavez
Conference Services Manager

Approved for public release;
distribution unlimited.

AIR FORCE OF SCIENTIFIC RESEARCH (AFSC)
NOTICE OF TRANSMITTAL TO DTIC
This technical paper has been reviewed and is
approved for public release IAW AFR 190-12
Distribution is unlimited.
Joan Boggs
STINFO Program Manager

REPORT DOCUMENTATION PAGE

AFRL-SR-BL-TR-98-

Public reporting burden for this collection of information is estimated to average 1 hour per response, including the gathering and maintaining the data needed, and completing and reviewing the collection of information. Send comments regarding this burden estimate or any other aspect of this collection of information, including suggestions for reducing this burden, to Washington Headquarters Services, Directorate for Information Operations and Reports, 1215 Jefferson Davis Highway, Suite 1204, Arlington, VA 22202-4302, and to the Office of Management and Budget, Paperwork Reduction Project (0704-0182), Washington, DC 20503.

0589

1. AGENCY USE ONLY (Leave blank)		2. REPORT DATE March 14, 1997		3. REPORT TYPE AND DATES COVERED Final 06/01/96-05/31/97	
4. TITLE AND SUBTITLE Organization of the 1997 Adaptive Optics Topical Meeting				5. FUNDING NUMBERS F49620-96-1-0278	
6. AUTHOR(S) David W. Hennage					
7. PERFORMING ORGANIZATION NAME(S) AND ADDRESS(ES) Optical Society of America 2010 Massachusetts Ave. NW Washington, DC 20036				8. PERFORMING ORGANIZATION REPORT NUMBER	
9. SPONSORING/MONITORING AGENCY NAME(S) AND ADDRESS(ES)				10. SPONSORING/MONITORING AGENCY REPORT NUMBER	
11. SUPPLEMENTARY NOTES					
12a. DISTRIBUTION/AVAILABILITY STATEMENT Approved for public release Distribution unlimited				12b. DISTRIBUTION CODE	
13. ABSTRACT (Maximum 200 words) The adaptive optics topical meeting provided an international forum for discussion on adaptive optics for atmospheric turbulence compensation. Its approach centered on three types of sessions: reviews of techniques and technologies by experts in the field; poster sessions, including one minute oral presentation, providing detailed information on individual systems, techniques, etc; and interactive sessions allowing people working on similar problems to raise and discuss their concerns and solutions.					
14. SUBJECT TERMS				15. NUMBER OF PAGES	
				16. PRICE CODE	
17. SECURITY CLASSIFICATION OF REPORT Unclassified		18. SECURITY CLASSIFICATION OF THIS PAGE Unclassified		19. SECURITY CLASSIFICATION OF ABSTRACT Unclassified	
				20. LIMITATION OF ABSTRACT UL	

CONFERENCE EDITION

*Summaries of the papers
presented at the topical meeting*

ADAPTIVE OPTICS

July 8-12, 1996
Maui, Hawaii

1996 Technical Digest Series
Volume 13

SPONSORED AND MANAGED BY
Optical Society of America



Optical Society of America
2010 Massachusetts Avenue NW
Washington DC 20011-1023

19980824 170

DTIC QUALITY INSPECTED 1

Articles in this publication may be cited in other publications. To facilitate access to the original publication source, the following form for the citation is suggested:

Name of Author(s), "Title of Paper," in *Adaptive Optics*, Vol. 13, 1996 OSA Technical Digest Series (Optical Society of America, Washington DC, 1996), pp. xx-xx.

Optical Society of America

ISBN

Conference Edition	1-55752-450-5
Postconference Edition	1-55752-451-3
(Note: Postconference Edition includes postdeadline papers.)	
1996 Technical Digest Series	1-55752-417-3

Library of Congress Catalog Card Number

Conference Edition	95-72771
Postconference Edition	95-72772

Copyright © 1996, Optical Society of America

Individual readers of this digest and libraries acting for them are permitted to make fair use of the material in it, such as to copy an article for use in teaching or research, without payment of fee, provided that such copies are not sold. Copying for sale is subject to payment of copying fees. The code 1-55752-417-3/96/\$6.00 gives the per-article copying fee for each copy of the article made beyond the free copying permitted under Sections 107 and 108 of the U.S. Copyright Law. The fee should be paid through the Copyright Clearance Center, Inc., 21 Congress Street, Salem, MA 01970.

Permission is granted to quote excerpts from articles in this digest in scientific works with the customary acknowledgment of the source, including the author's name and the name of the digest, page, year, and name of the Society. Reproduction of figures and tables is likewise permitted in other articles and books provided that the same information is printed with them and notification is given to the Optical Society of America. In addition, the Optical Society may require that permission also be obtained from one of the authors. Address inquiries and notices to Director of Publications, Optical Society of America, 2010 Massachusetts Avenue, NW, Washington, DC 20036-1023. In the case of articles whose authors are employees of the United States Government or its contractors or grantees, the Optical Society of America recognizes the right of the United States Government to retain a nonexclusive, royalty free license to use the author's copyrighted article for United States Government purposes.

Printed in the U.S.A.

Contents

Agenda of Sessions	v
AMA Adaptive Optics Systems	1
AMB Poster Previews: 1	7
AMC Laser Technology and Laser Guide Stars	89
ATuA Real Implementation Problems and Issues	107
ATuB Astronomical Science and Techniques	111
AWA Post-Processing of Adaptive Optics Corrected Imagery	129
AWB Additional Adaptive Optics Applications	143
AWC Atmospheric and Adaptive Optics Performance Characterization	149
AWD Poster Previews: 2	165
AThA Wavefront Sensing Techniques and Detectors	215
AThB Adaptive Optics Control Optimization	229
AThC Poster Previews: 3	239
AFA Wave-front Correctors	301
Key to Authors and Presiders	315

**1996 ADAPTIVE OPTICS
TECHNICAL PROGRAM COMMITTEE**

Peter Wizinowich, *W. M. Keck Observatory, USA, Chair*

Byron Welsh, *Air Force Institute of Technology, USA, Chair*

Brent Ellerbroek, *Phillips Laboratory, USA, Chair*

Domenico Bonaccini, *European Southern Observatory, Germany*

Janet Fender, *Phillips Laboratory, USA*

Masanori Iye, *National Astronomical Observatory, Japan*

Gerard Lelievre, *Observatoire de Paris, France*

Michael Lloyd-Hart, *University of Arizona, USA*

Vladimir P. Lukin, *Institute of Atmospheric Optics, Russia*

Richard Myers, *University of Durham, U.K.*

Robert Tyson, *W. J. Shafer Associates, Inc., USA*

PIKAKE ROOM

7:45am-8:00am

Welcome

Peter Wizinowich, *W. M. Keck Observatory*
Byron Welsh, *Air Force Institute of Technology*

8:00am-9:45am

AMA • Adaptive Optics Systems

Masanori Iye, *National Astronomical Observatory, Japan* and
Richard M. Myers, *University of Durham, U.K., Presiders*

8:00am (Invited)

AMA1 • Review of large telescope adaptive optics systems, David Sandler, *Thermo Trex Corp. and Steward Observatory*. Adaptive optics promises to provide dramatic increase in the scientific capabilities of the new generation of large telescopes. This paper presents an overview of systems under development or planned for new telescopes with diameter $D \geq 6.5$ m. (p. 2)

8:45am (Invited)

AMA2 • Review of astronomical adaptive optics systems on medium-sized (1.5-5 m) telescopes, François Rigaut, *Canada-France-Hawaii Telescope*. We present an exhaustive review of adaptive optics systems with a vocation for astronomy. After a brief historical introduction, we review the different technological approaches and the results. (p. 5)

9:15am (Invited)

AMA3 • Review of non-astronomical active AO technologies, Janet Fender, Russell K. Botts, *U.S. Air Force Phillips Laboratory*. Abstract not available. (p. 6)

PIKAKE ROOM

9:45am-10:15am

AMB • Poster Previews: 1

Masanori Iye, *National Astronomical Observatory, Japan* and
Richard M. Myers, *University of Durham, U.K., Presiders*

9:45am

AMB1 • W. M. Keck Observatory adaptive optics facility, P. Wizinowich, D. S. Acton, A. Gleckler, T. Gregory, P. Stomski, W. M. Keck Observatory; K. Avicola, J. Brase, H. Friedman, D. Gavel, C. Max, *Lawrence Livermore National Laboratory*. A natural and laser guide star adaptive optics facility is being designed for the Keck telescope. An overview of program, facility, and subsystems is presented. (p. 8)

9:46am

AMB2 • Keck adaptive optics: optical bench subsystem, T. Gregory, P. Wizinowich, D. S. Acton, P. Stomski, J. Maute, M. Sirota, W. M. Keck Observatory; A. Gleckler, *Kaman Aerospace*; S. Radau, *ROM Engineering*. The optical and optomechanical design of the optical bench subsystem for the Keck adaptive optics system is reviewed. (p. 11)

9:47am

AMB3 • Keck adaptive optics: user interface and supervisory control subsystem, P. Stomski, P. Wizinowich, D. S. Acton, W. Lupton, J. Gathright, A. Conrad, H. Lewis, T. Gregory, W. M. Keck Observatory. The subsystem is defined in terms of required functionality, computer hardware, and software architectures. Details of some system and process control components are provided. (p. 14)

9:48am

AMB4 • Keck adaptive optics: wavefront controller subsystem, J. Brase, J. An, K. A. Avicola, D. Gavel, C. Max, S. Olivier, K. Waltjen, J. Watson, *Lawrence Livermore National Laboratory*; P. Wizinowich, S. Acton, A. Gleckler, T. Gregory, P. Stomski, W. M. Keck Observatory. The wave-front control subsystem of the Keck adaptive optics (AO) system carries out the wave-front sensing and high-speed control required for atmospheric turbulence correction. We describe the wave-front sensing, computer system, and correction hardware and its overall functions and capabilities. (p. 17)

9:49am

AMB5 • Performance of Keck adaptive optics with sodium laser guide stars, Don Gavel, Scot Olivier, Jim Brase, *Lawrence Livermore National Laboratory*. Abstract not available. (p. 21)

9:50am

AMB6 • Adaptive optics specification for a 10-m telescope on the ORM, Nicholas Devaney, *Instituto de Astrofísica de Canarias, Spain*. We summarize work being carried out to specify the adaptive optics requirements for the planned 10-m telescope for the Observatorio del Roque de los Muchachos, La Palma. Model and real data on turbulence profiles in La Palma are used in simulations to predict system performance. (p. 24)

9:51am

AMB7 • Subaru adaptive optics program, Hideki Takami, Masanori Iye, Naruhisa Takato, *National Astronomical Observatory, Japan*; Masashi Otsubo, *The Graduate University for Advanced Studies, Japan*; Koji Nakashima, *Univ. Tokyo, Japan*. An adaptive optics program for the Cassegrain focus of SUBARU 8.2-m telescope under construction atop Mauna Kea is presented. (p. 25)

9:52am

AMB8 • Progress toward the 6.5-m MMT infrared adaptive optics system, M. Lloyd-Hart, J. R. P. Angel, D. G. Sandler, *Univ. Arizona*; P. Salinari, *Osservatorio Astrofisico di Arcetri, Italy*; D. Bruns, T. K. Barrett, *ThermoTrex Corp.* We report on progress made toward the infrared-optimized adaptive optics system, based on an adaptive secondary mirror, being constructed for the 6.5-m telescope. (p. 28)

9:53am

AMB9 • Sodium laser guide star observations with FASTTRAC II, T. D. Groesbeck, M. Lloyd-Hart, J. R. P. Angel, D. W. McCarthy, Jr., G. Brusa, P. M. Gray, B. A. McLeod, S. Mohanty, T. Martinez, B. Jacobsen, D. M. Wittman, P. T. Ryan, *Univ. Arizona*; D. G. Bruns, D. G. Sandler, *ThermoTrex Corp.* We present astronomical and engineering results from FASTTRAC II, a sodium laser guide star adaptive optics system for the MMT that uses a dye laser producing >3 W of cw output power. (p. 31)

9:54am

AMB10 • Lick Observatory laser guide star adaptive optics system commissioning, Scot S. Olivier, Jong An, Kenneth Avicola, Horst D. Bissinger, James M. Brase, Herbert W. Friedman, Donald T. Gavel, Bruce Macintosh, Claire E. Max, Kenneth E. Waltjen, *Lawrence Livermore National Laboratory*. A sodium-layer laser guide star adaptive optics system has been developed at Lawrence Livermore National Laboratory for use on the 3-m Shane Telescope at Lick Observatory located on Mount Hamilton, near San Jose, California. (p. 34)

9:55am

AMB11 • Conceptional design for a user-friendly adaptive optics system at the Lick Observatory, Horst D. Bissinger, Scot S. Olivier, Claire E. Max, *Lawrence Livermore National Laboratory*. This versatile design concept is for a permanently installed adaptive optics system on the 3-m Shane Telescope at Lick Observatory. (p. 37)

9:56am

AMB12 • The Palomar adaptive optics system, Richard Dekany, *Jet Propulsion Laboratory*. The Palomar Adaptive Optics System is a Cass-mounted IR astronomy instrument, currently under construction at JPL, incorporating active laser metrology to minimize the effects of mechanical flexure. (p. 40)

9:57am

AMB13 • Results from the Cassegrain adaptive optics system of the Mount Wilson 100-in telescope, J. C. Shelton, S. L. Baliunas, *Mount Wilson Observatory*; T. G. Schneider, *Schneider Engineering*; D. McKenna, *Canada France Hawaii Telescope*. Images are presented from the cassegrain AO system of the 100-in telescope showing a resolution of 0.068 arcsec and the ability to see faint companions. (p. 43)

9:58am

AMB14 • First results of the CFHT adaptive optics bonnette on the telescope, François Rigaut, Derrick Salmon, Robin Arsenault, Scot McArthur, Jim Thomas, *Canada-France-Hawaii Telescope*; Olivier Lai, Daniel Rouan, Pierre Gigan, Jean-Pierre Veran, *Observatoire de Paris-Meudon, France*; David Crampton, Murray Fletcher, Jim Stilburn, Brian Leckie, Scot Roberts, Robert Woof, *Dominion Astronomical Observatory, Canada*; Corinne Boyer, Pascal Jagourel, Jean-Paul Gaffard, *CILAS, France*. The CFHT adaptive optics bonnette is a general user instrument for astronomical applications. The results of the first technical and scientific runs at the telescope are presented. (p. 46)

9:59am

AMB15 • Future directions for the University of Hawaii adaptive optics program, J. Elon Graves, Malcolm Northcott, *Univ. Hawaii*. The highly successful AO program at the UH is now planning to expand the curvature technology into higher order correction systems. The new instrument will be optimized for polarmetric, coronagraphic, and planetary science. (p. 49)

10:00am

AMB16 • Adaptive optics for a 70-cm solar telescope, D. Soltau, Th. Kentischer, M. Roser, W. Schmidt, M. Stix, *Kiepenheuer-Institut für Sonnenphysik, Germany*; D. S. Acton, *W. M. Keck Observatory*. Based on measurements and experiences with the Lockheed 19 segment deformable mirror, we present design considerations that could lead to significant performance improvements of our 70-cm solar telescope on Tenerife. (p. 53)

10:01am

AMB17 • Optimization of the Starfire Optical Range 3.5-m adaptive optics for astronomical imaging, Donald J. Link, Russell G. Vernon, *Science Applications International Corp.* SAIC's atmospheric compensation simulation code is used to optimize imaging performance for the SOR 3.5-m telescope using natural, sodium, and hybrid guidestar adaptive optics. (p. 56)

10:02am

AMB18 • Status of the advanced electro-optical system (AEOS) adaptive optics, John R. Kenemuth, James J. McNally, James R. Passaro, *USAF Phillips Laboratory/LII*; Paul J. Berger, *MIT Lincoln Laboratory*; Carlo La Fiandra, Rene Abreu, *Hughes Danbury Optical Systems*. A status report is presented on the development of the 941-actuator adaptive optics system for the Air Force's 3.6-m telescope being installed on Haleakala, Maui, Hawaii. (p. 58)

10:03am

AMB19 • Mechanically induced line-of-sight jitter in the Starfire Optical Range 1.5-m telescope, James M. Brown II, *USAF Phillips Laboratory/LIG*; James C. Goodding, *CSA Engineering Inc.* An evaluation of line-of-sight jitter is presented. The source of the jitter is dominated by mechanical vibrations resulting from resonant modes in mirror-metering structures. (p. 60)

10:04am

AMB20 • Five-order adaptive optics for meter-class telescopes, Donald G. Bruns, *Stellar Products*. A lens-based adaptive optics system for visual astronomical telescopes is designed, built, and tested. Atmospheric aberrations up to defocus and astigmatism are corrected. (p. 63)

10:05am

AMB21 • Natural guide-star adaptive optics for the 4.2-m William Herschel Telescope, David Buscher, Peter Doel, Ron Humphreys, Richard Myers, *Univ. Durham, UK*; Martyn Wells, *Univ. Edinburgh, UK*; Andy Longmore, *Royal Observatory Edinburgh, UK*; Bruce Gentles, Gareth Jones, Sue Worswick, *Royal Greenwich Observatory, UK*. A staged development to provide a natural guide star AO system for the WHT based on the Durham University segmented DM ELECTRA system is described. (p. 66)

10:06am

AMB22 • The next generation space telescope, Bernard D. Seery, John C. Mather, John Campbell, Keith Kalinowski, *NASA/Goddard Space Flight Center*; James W. Billbro, *NASA Marshall Space Flight Center*; Peter Stockman, Pierre Bely, *Space Telescope Science Institute*. NASA is currently planning a successor to the Hubble Space Telescope and the Space Infrared Telescope Facility that marries a large aperture with infrared detectors to study the origin and growth of the first galaxies. (p. 67)

10:07am

AMB23 • A low cost, high performance, self-scanning correlating white light fringe tracker system, Jeffrey T. Baker, *Rockwell Power Systems Co.*; Isabelle Percheron, Darryl Sanchez, *USAF Phillips Laboratory*. An inexpensive, high-performance self-scanning correlating white light fringe tracker system is developed for use in broadband very long baseline stellar interferometry experiments. (p. 69)

10:08am

AMB24 • Current status of the Oxford scalable sodium laser guide star system, G. P. Hogan, H. Booth, L. Montandon-Varoda, C. E. Webb, *Clarendon Laboratory, UK*. Our sodium laser guide star system is designed to be scalable, using pulse interleaving to increase average power without intensity. Current status is presented. (p. 71)

MONDAY

JULY 8, 1996

10:09am

AMB25 • A solid-state Raman laser for sodium D_2 line resonant excitation, E. C. Cheung, J. G. Ho, H. Injeyan, M. M. Valley, J. G. Berg, *TRW*; R. L. Byer, Y. Huang, *Stanford Univ.* Modelocked pulses from a Nd:YAG laser are Raman shifted to 1178 nm in a CaWO_4 crystal and intracavity doubled to 589 nm in a synchronous pumped resonator configuration. (p. 74)

10:10am

AMB26 • Nd:YAG laser beam pointing stability and artificial guide star generation, Vadim A. Parfenov, Sergei N. Rodin, S. I. Vavilov *State Optical Institute, Russia*. The problem of laser beam pointing instability at guide star generation is discussed. Results of experimental study of beams angular position stability of Nd:YAG lasers are reported. (p. 77)

10:11am

AMB27 • First results of a polychromatic artificial sodium star for the correction of tilt, Herbert Friedman, *Lawrence Livermore National Laboratory*; Renaud Foy, Michel Tallon, *Centre de Recherche en Astronomie de Lyon, France*; Arnold Migus, *École Polytechnique-ENSTA, France*. The first results of the return signals from a polychromatic artificial sodium star (PASS) are presented and agree with atomic physics models of the interaction. (p. 78)

10:12am

AMB28 • Design of an infrared camera-based aircraft detection system for laser guide star installations, Herbert Friedman, Bruce Macintosh, *Lawrence Livermore National Laboratory*. The characteristics of infrared cameras are discussed in relation to an aircraft detection system for laser guide star installations on ground-based telescopes. (p. 81)

10:13am

AMB29 • Focal anisoplanatism effect affecting techniques for laser guide star absolute tilt measurements, A. Riccardi, R. Ragazzoni, S. Esposito, *Osservatorio Astrofisico di Arcetri, Italy*. We present calculations aimed at establishing the error resulting from the anisoplanatism effect when two auxiliary telescopes are used to obtain the overall backward wave-front tilt from a laser guide star. (p. 84)

10:14am

AMB30 • Analysis of sodium layer scattering physics, Peter W. Milonni, *Los Alamos National Laboratory*; John M. Telle, *USAF Phillips Laboratory*. Detailed calculations of sodium guide star brightness are described with emphasis on two types of laser pulse train excitation phase-modulated long pulses and coherent short pulses. (p. 85)

10:15am-10:45am

Coffee Break

SOUTH PACIFIC BALLROOM

10:45am-11:45am; 1:00pm-2:00pm

AMB • Poster Session: 1

11:45am-1:00pm

Lunch

PIKAKE ROOM

2:00pm-4:10pm

AMC • Laser Technology and Laser Guide Stars

Michael Lloyd-Hart, *University of Arizona, Presider*

2:00pm (Invited)

AMC1 • Review of laser technology and status, Robert Q. Fugate, *Starfire Optical Range*. This paper reviews the status of laser technology for the generation of artificial laser guide stars. (p. 90)

2:30pm

AMC2 • Laser systems for the generation of sodium layer guide stars, H. Friedman, G. Erbert, T. Kuklo, T. Salmon, G. Thompson, N. Wong, J. Malik, *Lawrence Livermore National Laboratory*. The design and installation of several laser systems for the generation of sodium layer guide stars is presented. (p. 93)

2:50pm (Invited)

AMC3 • Characterization of the mesospheric sodium layer, George C. Papen, Chester S. Gardner, Jirong Yu, *Univ. Illinois*. The spatial and temporal characteristics of the mesospheric Na layer are important to understanding optimizing active adaptive optical telescopes. We present recent results on characterizing the Na layer at 40° N and over Hawaii. (p. 96)

3:20pm

AMC4 • Exploring high altitude beacon concepts other than sodium, John M. Telle, *USAF Phillips Laboratory*. The most prominent high altitude species are nitrogen and oxygen. Techniques for exciting these species are discussed. Molecular properties are reviewed. (p. 100)

3:40pm (Invited)

AMC5 • Review of tilt correction methods for laser guide star adaptive optics, Domenico Bonaccini, *European Southern Observatory, Germany*. Abstract not available. (p. 103)

PIKAKE ROOM

7:45am-11:30am

ATuA • Real Implementation Problems and IssuesPeter L. Wizinowich, *W. M. Keck Observatory, Presider*

7:45am-8:00am

IntroductionPeter Wizinowich, *W. M. Keck Observatory*

8:00am-9:30am

Panel Discussion: System Engineering Issues**Topics:** error budget, design requirements, interfacing with science instruments, risk control, LGS vs. NGS ao.**Panel members:**Peter Wizinowich, *W. M. Keck Observatory*Bob Fugate, *Starfire Optical Range*David Sandler, *Thermo Trex Corp.*Richard Myers, *University of Durham, U.K.***ATuA1 • Keck adaptive optics: error budget**, Peter Wizinowich, *W. M. Keck Observatory*. An error budget, with performance predictions, is provided for the Keck adaptive optics facility. This is a useful tool for evaluating engineering and observing trade-offs. (p. 108)

9:30am-10:00am

Coffee Break

10:00am-11:30am

Panel Discussion: Technical Issues**Topics:** dichroics, detectors, focus sensing with LGS, atmospheric dispersion correction, WFS calibration**Panel members:**Domenico Bonaccini, *European Southern Observatory*Martyn Wells, *University of Edinburgh, U.K.*Chris Shelton, *Mt. Wilson Observatory*Buzz Graves, *University of Hawaii*

11:30am-1:00pm

Lunch

PIKAKE ROOM

1:00pm-3:20pm

ATuB • Astronomical Science and TechniquesGerard Lelievre, *Observatoire de Paris, France*

1:00pm (Invited)

ATuB1 • Bubbles, disks, and planets: science with the University of Hawaii AO system, Laird M. Close, Francois Roddier, Claude Roddier, Malcolm Northcott, J. Elon (Buzz) Graves, *Univ. Hawaii*. We review recent UH AO scientific results and techniques. In particular detections of expanding bipolar bubbles and possible circumstellar disk fragmentation are found in 0.15" IR images of the young star HL Tau. (p. 112)

1:30pm

ATuB2 • Observing with adaptive optics, M. J. Northcott, *University of Hawaii*. We now routinely use the UH adaptive optics system for astronomical observations. Procedures that we have developed to ensure good quality data will be described. (p. 115)

1:50pm

ATuB3 • Halo properties and their influence on companion searches at the Starfire Optical Range, P. T. Ryan, J. R. P. Angel, D. W. McCarthy, L. M. Close, S. Mohanty, *Univ. Arizona*; R. Fugate, *USAF Phillips Lab Kirtland AFB*; D. G. Sandler, *ThermoTrex Corp.* Abstract not available. (p. 118)

2:10pm (Invited)

ATuB4 • AO based spectroscopy: prospects and pitfalls, Guy Monnet, *European Southern Observatory, Germany*. Abstract not available. (p. 121)

2:40pm

ATuB5 • An optical ultrahigh resolution spectrograph for use with adaptive optics, J. Ge, B. Jacobsen, J. R. P. Angel, N. Woolf, J. H. Black, M. Lloyd-Hart, P. Gray, *University of Arizona*; R. Q. Fugate, *USAF Phillips Lab*. A prototype ultrahigh resolution spectrograph has been built with an adaptive optics telescope. It provides 250,000 resolving power, 300 Å wavelength coverage, and 0.8% efficiency. (p. 122)

3:00pm

ATuB6 • Phase diversity imaging: report of experiments and simulations, Robert A. Gonsalves, Steven M. Ebstein, Peter Nisenson, *Lexitek, Inc*; Chris Shelton, *Mount Wilson Institute*. Phase diversity imaging processes degraded images that are recorded simultaneously, but in diverse channels. Experiments conducted at Lexitek's laboratory and at Mt. Wilson are reported. (p. 125)

PIKAKE ROOM

8:00am–10:00am

AWA • Post-Processing of Adaptive Optics Corrected ImageryByron M. Welsh, *Air Force Institute of Technology, Presider*

8:00am (Invited)

AWA1 • Post-processing of adaptive optics images: Blind deconvolution analysis, Julian C. Christou, *USAF Phillips Laboratory*; E. Keith Hege, *University of Arizona*; Stuart M. Jefferies, *National Solar Observatory*. Because of nonstationary behavior of adaptive optics compensation, blind deconvolution is used to extract both object and point spread function from observations. (p. 130)

8:30am (Invited)

AWA2 • Fourier phase spectrum estimation using deconvolution from wave-front sensing and bispectrum reconstruction, Michael C. Roggemann, Byron M. Welsh, *Air Force Institute of Technology*; Cynthia A. Hyde, *Univ. Dayton*. The Fourier phase spectrum estimate obtained from DWFS is shown to be superior to that obtained from the bispectrum when good SNR wave-front measurements can be made. (p. 133)

9:00am (Invited)

AWA3 • Roles for phase diversity in compensated imaging, Richard G. Paxman, *Environmental Research Institute of Michigan*. Phase diversity can be used for post-detection correction of compensated images or as a wave-front sensor in support of a compensated imaging system. (p. 136)

9:30am (Invited)

AWA4 • Speckle techniques for adaptive optics in the partial correction regime, E. Tessier, *Royal Greenwich Observatory, UK*; C. Perrier, *Observatoire de Grenoble, France*. We show the advantages of using speckle techniques when adaptive optics work in the partial correction regime. (p. 139)

10:00am–10:30am

Coffee Break

PIKAKE ROOM

10:30am–11:30am

AWB • Additional Adaptive Optics ApplicationsJanet S. Fender, *USAF Phillips Laboratory, Presider*

10:30am (Invited)

AWB1 • Review of industrial applications, Fritz Merkle, *European Southern Observatory, Germany*. Abstract not available. (p. 144)

11:00am (Invited)

AWB2 • Adaptive optics for the human eye, David R. Williams, Junzhong Liang, Donald T. Miller, *Univ. Rochester*. Adaptive correction of the eye's aberrations provides unprecedented optical quality, offering a new tool to probe the limits of vision and image the retina. (p. 145)

11:30am–1:15pm

Lunch

PIKAKE ROOM

1:15pm–3:05pm

AWC • Atmospheric and Adaptive Optics Performance CharacterizationVladimir Lukin, *Institute of Atmospheric Optics, Russia, Presider*

1:15pm (Invited)

AWC1 • Models and measurements of atmospheric turbulence characteristics and their impact on AO design, Vladimir P. Lukin, *Institute of Atmospheric Optics, Russia*. The asymptotic and numerical analysis of characteristics for telescopes and stellar interferometers is performed based on the development of models of atmospheric turbulence. The influence of the outer scale of turbulence is under study. (p. 150)

1:45pm

AWC2 • A new method for separating atmospheric layers using a Shack–Hartmann curvature sensor, Andreas Glindemann, Thomas Berkefeld, *Max-Planck-Institut für Astronomie, Germany*. Use of a Shack–Hartmann sensor for measuring the wave-front gradient and wave-front curvature by integrating over the subapertures allows separation of the influence of atmospheric layers. (p. 153)

2:05pm

AWC3 • Focal anisoplanatism and conjugation of the correcting surface to turbulence, Martyn Wells, *Univ. Edinburgh, UK*; Vince Klückers, Miles Adcock, *Imperial College, UK*. The benefits of conjugating the correcting mirror in a LGS AO system to a turbulent layer and the optics required to achieve this are described. (p. 156)

2:25pm

AWC4 • Second-order statistics of the performance of the Starfire Optical Range adaptive optics system, Dustin C. Johnston, James M. Brown II, Julian C. Christou, Brent L. Ellerbroek, Robert Q. Fugate, *Starfire Optical Range*; Michael D. Olier, James M. Spinhirne, *USAF Phillips Laboratory/LIG*. We present results of an experiment designed to measure the performance of the Starfire Optical Range adaptive optics system at high sample rates. (p. 158)

2:45pm

AWC5 • Temporal characteristics and modeling of atmospherically distorted wave-front slopes, Donald McGaughey, George J. M. Aitken, *Queen's Univ., Canada*. Temporal predictability found in Kolmogorov wave-front slopes is the result of spatial filtering by the observing aperture and can be modeled by linear filtering. (p. 161)

3:05pm–3:15pm

Coffee Break

PIKAKE ROOM

3:15pm–3:45pm

AWD • Poster Previews: 2Byron M. Welsh, *Air Force Institute of Technology, Presider*

3:15pm

AWD1 • Adaptive optics at MPE: astronomical results and future plans, A. Quirrenbach, *Max-Planck-Institut für Extraterrestrische Physik, Germany*. AO observations of the stellar clusters 30 Doradus and NGC3603, and of H₂ in T Tauri are presented. The status of ALFA (AO with LGS) is described. (p. 166)

3:16pm

AWD2 • Coronagraphic spectrometer, Masanori Iye, Kouji Murakawa, Youichi Ito, Noboru Ebizuka, Motohide Tamura, *National Astronomical Observatory, Japan*. The scientific objectives, design concept, and expected performance of a coronagraphic spectrometer planned for 8-m Subaru telescope are described. (p. 168)

3:17pm

AWD3 • Adaptive optics long exposure point spread function retrieval from wave-front sensor measurements: tests on real data, Jean-Pierre Véran, Daniel Rouan, *Observatoire de Paris, France*; François Rigaut, *Canada-France-Hawaii Telescope*; Henri Maitre, *Télécom Paris, France*. We have tested our point spread function retrieval method on real adaptive optics data. Accuracy of the results is discussed in an image restoration perspective. (p. 171)

3:18pm

AWD4 • Phase diversity wave-front sensing and image reconstruction on the MDI Instrument at L1, T. D. Tarbell, Z. A. Frank, *Stanford-Lockheed Institute for Space Research*; D. S. Acton, W. M. Keck Observatory. Phase diversity techniques are applied to images of solar granulation taken with the Michelson doppler imager at the first Lagrangian point. (p. 174)

3:19pm

AWD5 • Intensity peak tracking in extended-object astronomical imaging, David W. Tyler, W. J. Schafer Associates. Analysis comparing intensity peak tracking and centroid tracking is presented, along with results using telescope data. A morphology-dependent metric to specify an appropriate algorithm is derived. (p. 177)

3:20pm

AWD6 • Simultaneous short exposure measurements of anisoplanatism using compensated images at optical and near-infrared wavelengths, Julian C. Christou, Brent L. Ellerbroek, Timothy L. Pennington, James F. Riker, J. Timothy Roark, Earl J. Spillar, *USAF Phillips Laboratory*. We discuss simulations and experimental measurements of anisoplanatism using binary star images obtained with laser guide star compensation at the Starfire Optical Range 1.5-m telescope. (p. 180)

3:21pm

AWD7 • Paper withdrawn. (see paper ATuB6)

3:22pm

AWD8 • Simulation of adaptive optics improvement on laser communication link performance, Brian Rosenberg, Pierre R. Barbier, *Univ. Maryland*. We simulate the performance of a terrestrial laser communication link in saturated turbulence and assess the improvement provided by adaptive optics. (p. 184)

3:23pm

AWD9 • Combined intracavity and outer cavity adaptive correction of aberrations in a solid-state laser, Vladimir I. Polejaev, *Utah State Univ.*; Alexander V. Koryabin, Victor I. Shmalhausen, *Moscow State Univ., Russia*. This report presents the results of experimental investigations of a combined intracavity and outer-cavity adaptive correction of pulsed solid-state laser radiation. (p. 187)

3:24pm

AWD10 • Variances of optical transfer functions of the turbulent atmosphere, Igor P. Lukin, *Institute of Atmospheric Optics, Russia*. The variances of optical transfer functions of the optical system "Turbulent Atmosphere—Telescope" are investigated theoretically by two methods of posterior processing (Labeyrie and Knox-Tompson) of the astronomical images. These characteristics are approximated the phase variances of intensity spectrum of the images. (p. 190)

3:25pm

AWD11 • Spatial spikes of intensity of the atmospherically distorted images, Igor P. Lukin, *Institute of Atmospheric Optics, Russia*. Statistics of the random field of spatial spikes of intensity of the stellar speckle image are investigated. It is shown that the astronomical image consists of randomly located diffraction images, the intensity of which is determined by the average value of the intensity of whole image. (p. 191)

3:26pm

AWD12 • "1001" correlations in random wave fields, Isaac Freund, *Bar-Ilan Univ., Israel*. The sampling theorem requires that most parameters of "random" fields be correlated. Topological constraints underlie these correlations. Quantitative measurements of Gaussian fields yield "1001" different correlations. (p. 194)

3:27pm

AWD13 • Atmospheric characterization for adaptive optics at the Keck telescope, Gary Chanan, Romana Crnkovic, Frank Dekens, *Univ. California-Irvine*. Atmospheric characterization measurements at the Keck telescope consistently yield an outer scale of turbulence of 200 m or less. We discuss the implications for adaptive optics. (p. 197)

3:28pm

AWD14 • Evaluation and development of SCIDAR with the aid of a three-dimensional propagation code, Miles J. Adcock, Vincent A. Klückers, Nicholas J. Wooder, Christopher Dainty, *Imperial College of Science, Technology, and Medicine, UK*. The technique of scintillation distance and ranging (SCIDAR) is investigated and developed, aided by a three-dimensional simulation of light propagation through the atmosphere. (p. 200)

3:29pm

AWD15 • Measurement of a non-Kolmogorov structure function, Tom Nicholls, Nicholas J. Wooder, Christopher Dainty, *Imperial College of Science, Technology, and Medicine, UK*. The Kolmogorov model for the structure function of atmospheric phase fluctuations is tested using simple Shack-Hartmann centroid measurements. (p. 203)

3:30pm

AWD16 • Measurements of the isoplanatic angle of the wave-front tilt, Thomas Berkefeld, Andreas Glindemann, *Max-Planck-Institut für Astronomie, Germany*. Investigating the tilt correlation as a function of separation angle, exposure time, and aperture, the maximum angular distance between the object and the tip-tilt guide star is determined. This distance can be increased by multiple guide stars. (p. 206)

WEDNESDAY

JULY 10, 1996

3:31pm

AWD17 • Focal spot in the presence of phase dislocations, V. A. Tartakovski, N. N. Mayer, *Institute of Atmospheric Optics, Russia*. The focal spot size, structure, and motion by intensification of turbulence and by appearance of the phase dislocations are investigated. (p. 209)

3:32pm

AWD18 • Phasing of elements of a primary mirror of AST-10, V. Lukin, B. Fortes, *Institute of Atmospheric Optics, Russia*. Application of adaptive optics effects for correction dephasing elements of segmented primary mirror and distortions relevant with turbulence are considered. We received the requirements for the spatial resolution of secondary adaptive mirror as applied to the AST-10 project. (p. 211)

LUAU GARDENS

7:30pm-9:00pm

Conference Reception

PIKAKE ROOM

8:00am-10:10am

ATHA • Wavefront Sensing Techniques and DetectorsBrent L. Ellerbroek, *USAF Phillips Laboratory* and Robert Q. Fugate, *USAF Phillips Laboratory, Presiders*

8:00am (Invited)

ATHA1 • Review of CCDs and controllers: status and prospects,James W. Beletic, *European Southern Observatory, Germany*. Wavefront sensor CCDs and controller electronics are reviewed, including functional systems and those in development. All major programs and manufacturers are presented and compared. (p. 216)

8:30am

ATHA2 • Aluminum gallium arsenide/gallium arsenide photon counting cameras for very low light level wave-front sensing, Gary C. Loos, *USAF Phillips Laboratory*; Timothy W. Sinor, *Litton Electro-Optical Systems*; J. M. Abraham, *Ball Aerospace*. We compare the performance of photon counting cameras with Generation III photocathodes to charge coupled devices for very low light level adaptive optics wave-front sensing. (p. 217)

8:50am (Invited)

ATHA3 • Comparison of adaptive optics technologies for large astronomical telescopes, Brent L. Ellerbroek, *USAF Phillips Laboratory*; Malcolm J. Northcott, *Univ. Hawaii*; François Rigaut, *Canada-France-Hawaii Telescope*; Doug Simons, *International Gemini Project Office*. We present the results of independent numerical simulations of adaptive-optics systems for 8-m astronomical telescopes using both Shack-Hartmann and curvature wave-front sensors. (p. 220)

9:20am (Invited)

ATHA4 • Applications of neural networks in adaptive optics, George J. M. Aitken, *Queen's Univ., Canada*. This paper reviews applications of neural networks to wave-front sensing and prediction, centroiding, estimation of atmospheric parameters, and other complex nonlinear problems in adaptive optics. (p. 223)

9:50am

ATHA5 • Prediction of wave-front sensor slope measurements using artificial neural networks, Dennis A. Montera, Byron M. Welsh, Michael C. Roggemann, Dennis W. Ruck, *Air Force Institute of Technology*. Neural networks are compared with statistical predictors to determine WFS slope measurements. Solutions that operate over broad ranges of seeing conditions are investigated. (p. 226)

10:10am-10:30am

Coffee Break

PIKAKE ROOM

10:30am-11:40am

ATHB • Adaptive Optics Control OptimizationBrent L. Ellerbroek, *USAF Phillips Laboratory* and Robert Q. Fugate, *USAF Phillips Laboratory, Presiders*

10:30am (Invited)

ATHB1 • Optimal estimators for astronomical adaptive optics, Walter J. Wild, *Univ. Chicago*. We review the theoretical basis and use of optimal estimators for zonal astronomical adaptive optics systems that incorporate servo control and atmospheric characteristics. Experimental results are discussed. (p. 230)

11:00am

ATHB2 • Optimization of closed-loop adaptive-optics control algorithms using measured performance data: experimental results, Brent L. Ellerbroek, *USAF Phillips Laboratory*; Troy A. Rhoadarmer, *University of Arizona*. We describe a method for optimizing wave-front control algorithms using closed-loop performance data and present experimental results combining laser and natural guidestar wave-front sensing. (p. 233)

11:20am

ATHB3 • Adaptive correction of phase-distorted extended source images: experimental results, D. V. Pruidze, *New Mexico State Univ.*; J. C. Ricklin, *Army Research Laboratory*; D. G. Voelz, *USAF Phillips Laboratory*; M. A. Vorontsov, *New Mexico State Univ. and Army Research Laboratory*. Experimental results for a nine-electrode deformable mirror adaptive imaging system are presented. Image quality criteria based on statistical analysis of the speckle field are used. (p. 236)

PIKAKE ROOM

11:40am-12:15pm

ATHC • Poster Previews: 3Peter L. Wizinowich, *W. M. Keck Observatory, Presider*

11:40am

ATHC1 • Fast CCD imaging systems for tilt-tip and wave-front sensing applications, Craig D. Mackay, *Institute of Astronomy and AstroCam Ltd., UK*. New generations of fast, low-noise CCDs and their controllers are achieving the read-out noise and high frame rates that are critical to the successful completion of true adaptive optics systems. We describe the performance achieved for a variety of systems from those on COAST, the site evaluation program on the William Herschel Telescope on La Palma, and the results from the latest fast CCDs and new generation of CCD controllers. (p. 240)

11:41am

ATHC2 • Scan-Hartmann wave-front sensor, Valeri A. Tartakovski, Vladimir P. Lukin, *Institute of Atmospheric Optics, Russia*. Measurements of many Hartmann spot displacements are replaced by tracking only one focal spot that is scanned on the field from its parts with higher intensity. (p. 241)

11:42am

ATHC3 • Combined wave-front sensor with internal reference source: experimental study, Vladimir I. Podoba, Vadim A. Parfenov, Alexander G. Seregin, *S. I. Vavilov State Optical Institute, Russia*. A new wave-front sensor combining autocollimation-point and interferometric channels and hologram structure on the controllable mirror is presented. The results of measurements of the hologram aberrations and limit angles of the mirror inclinations are discussed. (p. 243)

11:43am

ATHC4 • Discrete-zonal method for widening field of view of adaptive telescope, V. I. Podoba, B. E. Bonshtedt, S. N. Koreshev, V. B. Lakhtikov, G. I. Lebedeva, A. G. Seregin, D. N. Yeskov, *S. I. Vavilov State Optical Institute, Russia*. Possibilities of widening field of view of astronomical telescopes built on two-stage optics concept is discussed. A new method for correcting the image quality over discrete annular zones by control of the effective asphericity of mirrors is analyzed. (p. 244)

11:44am

ATHC5 • Focault-like wave-front sensor, A. Riccardi, S. Esposito, R. Ragazzoni, L. Fini, P. Ranfagni, *Observatorio Astrofisico di Arcetri, Italy*. We present first laboratory results for a focault-like wave-front sensor suitable for adaptive optics systems based on a squared-based refractive pyramid. (p. 246)

11:45am

ATHC6 • Experimental comparison of two approaches for solar wave-front sensing, Thomas R. Rimele, *National Solar Observatory*; Richard R. Radick, *USAF Phillips Laboratory*. We describe experiments performed recently at the National Solar Observatory/Sacramento Peak to compare two wave-front sensing approaches for solar imaging. (p. 247)

11:46am

ATHC7 • Use of artificial neural networks for Hartmann sensor lenslet centroid estimation, Dennis A. Montera, Byron M. Welsh, Michael C. Roggemann, Dennis W. Ruck, *Air Force Institute of Technology*. Neural networks are used to improve Hartmann wave-front sensor lenslet centroid estimation. A turbulent atmosphere, read noise, and shot noise are considered. (p. 250)

11:47am

ATHC8 • Simple neural networks as wave-front slope predictors: training and performance issues, Peter J. Gallant, George J. M. Aitken, *Queen's Univ., Canada*. Accelerated gradient descent-based neural network training for a wave-front slope predictor is improved by addition of a second time series point as a training target. (p. 253)

11:48am

ATHC9 • Sparse aperture phasing with phase diversity: experimental results, Rick Kendrick, Ray Bell, Alan Duncan, *Lockheed-Martin Advanced Technology Center*. Phasing of a 12-aperture sparse array has been demonstrated in the laboratory with use of phase diversity to determine piston and tilt errors on the subapertures. (p. 256)

11:49am

ATHC10 • Optimization of adaptive optics digital imagery systems by design of experiments, Robert T. Brigantic, Michael C. Roggemann, Kenneth W. Bauer, Byron M. Welsh, *Air Force Institute of Technology*. We present results of research aimed at selecting adaptive optics system control parameters to yield optimal images under widely varying seeing conditions. (p. 258)

11:50am

ATHC11 • Tip-tilt control loop optimization, L. Fini, S. Esposito, *Observatorio Astrofisico di Arcetri, Italy*. We address problems of control loop parameters optimization for a tip-tilt correction system based on the approach followed for the T. N. G. tracking system. (p. 261)

11:51am

ATHC12 • Optimized adaptive optics design for low light level, optical-wavelength imaging interferometer arrays, David W. Tyler, W. J. Schafer Associates. Expressions for optimal AO actuator spacing and control loop bandwidth are derived. Simulations are used to predict two-telescope fringe visibilities by use of the optimal designs. (p. 262)

11:52am

ATHC13 • Optimization of bimorph mirror electrode pattern for Subaru AO system, Masashi Otsubo, *The Graduate Univ. Advanced Studies, Japan*; Hideki Takami, Masanori Iye, *National Astronomical Observatory, Japan*. Design of electrode pattern for 36-element bimorph mirror for Subaru AO system was evaluated considering atmospheric turbulence, pure tilt, residual error, and stroke. (p. 265)

11:53am

ATHC14 • Wavefront control optimization using adaptive filters, M. Lloyd-Hart, T. Rhoadarmer, *Univ. Arizona*. Data from the SOR adaptive optics system have been used to explore optimal wavefront control using digital filters which are continually updated to reflect prevailing values of statistical atmospheric parameters. (p. 268)

11:54am

ATHC15 • Principles of action of segmented corrector, Alexander P. Smirnov, Vladimir V. Reznichenko, *S. I. Vavilov State Optical Institute, Russia*. Determination of misalignment contributions of the optical system induced by individual elements errors and optimization of "coarse" and "fine" corrections are the main purposes of the present paper. (p. 271)

11:55am

ATHC16 • Fast steering mirror performance, D. Bruns, *ThermoTrex Corp.*; S. Esposito, *Observatorio Astrofisico di Arcetri, Italy*; J. Farinato, *Univ. Padova, Italy*; R. Ragazzoni, *Astronomical Observatory of Padova, Italy*. A fast steering mirror actuated with electro-magnetic voice coils has been designed and built. (p. 272)

11:56am

ATHC17 • Status of the design of an adaptive secondary for the 6.5-m conversion of the MMT telescope, Guido Brusa, Peter Gray, *University of Arizona*; Ciro Del Vecchio, Piero Salinari, *Osservatorio Astrofisico di Arcetri, Italy*; Walter Gallieni, *ADS Italia S.r.l. Sistemi Avanzati, Italy*. Mechanical and thermal design studies for an adaptive secondary mirror to be used for the 6.5-m conversion of the multiple mirror telescope (MMT), together with a 36 actuator, spherical shape prototype of the adaptive mirror are presented. Emphasis is on the design of the electro-magnetic force actuator and on the three-layer structure of the unit (i.e., thin deformable shell, thick reference plate, actuator support, and heat sink plate). (p. 273)

11:57am

ATHC18 • CHARM: A tip-tilt tertiary system for the Calar Alto 3.5-m telescope, Andreas Glindemann, Mark J. McCaughrean, Stefan Hippler, Karl Wagner, Ralf-Rainer Rohloff, *Max-Planck-Institut für Astronomie, Germany*. We present a tip-tilt tertiary mirror system for the Calar Alto 3.5-m telescope that reduces the rapid image motion from typically 0"2 to <0"03 rms. (p. 275)

11:58pm

ATHC19 • Active and adaptive bimorph optics: mirrors, technology and design principles, Andrey G. Safronov, *TURN Ltd., Russia*. The present paper is concerned with existing deformable bimorph mirrors. An effective technology of their construction is proposed providing a significant increase of the mirrors sensitivity as well as their controllable aperture. (p. 278)

11:59am

ATHC20 • High-resolution adaptive system with a phase knife in the optical feedback loop, A. V. Larichev, I. P. Nikolaev, *Moscow State Univ., Russia*; P. Violino, *Univ. Turin, Italy*. An adaptive optical system with a liquid crystal light valve as a wave-front corrector is investigated. Significant reduction of the variance of the output radiation phase is demonstrated. (p. 279)

12:00m

ATHC21 • Liquid crystal spatial modulators with segmented mirror for adaptive optics, Vladimir V. Reznichenko, Vladislav V. Nicitin, *Peterlab, Russia*; Arkadi P. Onokhov, Michail V. Isaev, Natalia L. Ivanova, *S. I. Vavilov State Optical Institute, Russia*; Leonid A. Beresnev, Wolfgang Haase, *Tecynische Hochschule, Germany*. We develop efficient optically controlled liquid-crystal optically addressed spatial light modulators that possess modulation parameters for reflected light. (p. 282)

12:01pm

ATHC22 • Design of optical wave-front corrector based on liquid crystal concept, Vladimir V. Reznichenko, Vladislav V. Nicitin, *Peterlab, Russia*; Arkadi P. Onokhov, Michail V. Isaev, Natalia L. Ivanova, *S. I. Vavilov State Optical Institute, Russia*. A mack-up of a nematic liquid crystal (LC) phase corrector is developed for applications in adaptive optical systems. Optical surface processing technology is investigated for preparation of the modulator individual components. (p. 283)

12:02pm

ATHC23 • Liquid crystal glasses with local modulation, Maxim G. Tomilin, Arkadi P. Onokhov, Michail V. Isaev, *S. I. Vavilov State Optical Institute, Russia*; Vladimir V. Reznichenko, *Peterlab, Russia*; Vladimir I. Kogan, *Industry Construction Bank, Russia*. A mack-up of nematic liquid crystal (LC) glasses with local modulation is developed for wide application. The processing technology is investigated for preparation of a new principle of local modulation. (p. 284)

12:03pm

ATHC24 • Liquid crystal displays as programmable adaptive optical elements, Don A. Gregory, John L. McClain Jr., *Univ. Alabama-Huntsville*; Tracy D. Hudson, *U.S. Army Missile Command*. A liquid crystal television has been programmed to operate as a cylindrical or spherical Fresnel lens. This concept may be used to perform adaptive beam steering. (p. 285)

12:04pm

ATHC25 • Polarization-insensitive 127-segment liquid crystal wave-front corrector, Gordon D. Love, Sergio R. Restaino, Richard C. Carreras, Gary C. Loos, *USAF Phillips Laboratory*; Rob. V. Morrison, Tom Baur, Greg Kopp, *Meadowlark Optics Inc.* We describe an improved 127-segment liquid crystal spatial light modulator that operates with unpolarized light for wave-front control and correction. (p. 288)

12:05pm

ATHC26 • Digital filtering techniques and centroid predictors in AO servo-systems, D. Gallieni, D. Bonaccini, *European Southern Observatory, Germany*. We present our results on digital filtering studies in adaptive optics systems, as well as the application of linear prediction techniques applied to WFS centroid motions. The cases of avalanche photodiode and CCD-based WFS are considered. Closed loop simulations with actual data are presented. (p. 291)

12:06pm

ATHC27 • Report on the optical quality of ADONIS' DM and relay optics: Is the mirror aging?, R. Tighe, E. Prieto, *European Southern Observatory, Chile*. We present results of measurements on ADONIS' deformable mirror, in order to try to record the evolution of its surface quality, if any. (p. 294)

12:07pm

ATHC28 • Adaptive optics servo-system performance estimator: practical implementation, E. Prieto, D. Bonaccini, H. Geoffray, P. Prado, *European Southern Observatory, Germany*; L. Demailly, *Observatoire de Paris-Meudon, France*. We present results obtained with the ESO 3.6 m telescope Adaptive Optics Near Infrared System (ADONIS), on the performance estimation of science image quality. We compared actual results from the science IR cameras with results from algorithms using wavefront sensor residuals. (p. 297)

12:08pm

ATHC29 • Searching for brown dwarfs and extra-solar planets from the ground using adaptive optics, David Sandler, *Univ. Arizona and ThermoTrex Corp.*; Steven Stahl, *ThermoTrex Corp.*; Roger Angel, *Univ. Arizona*. The adaptive optics system under development for the new 6.5 m MMT, using an adaptive secondary mirror, will allow direct detection of cool brown dwarfs much closer in than Gliese 229B. An advanced system with 10,000 actuators will allow direct detection of Jupiter-like planets around bright stars within 10 pc. Requirements and detection limits will be discussed. (p. 300)

12:15pm-1:30pm

Lunch Break

SOUTH PACIFIC BALLROOM

1:30pm-3:30pm

Poster Session: 2

PUA KENIKENI ROOM ONE

3:30pm-5:30pm

The Development and Applications of CCDs for Wavefront Sensing: Panel Discussion

We will discuss the present state of the art of small-format, low-noise CCDs for wavefront sensing for astronomical adaptive optics. A small panel of experts in CCD technology and the needs of adaptive optics systems will be present to open the discussion with summaries in their respective areas. All those interested in learning the latest developments and identifying possible future directions for exploration are invited to attend.

Panel Members:

Peter Wizinowich, *W. M. Keck Observatory (Keck AO System)*
 Michael Lloyd-Hart, *Center for Astronomical Adaptive Optics*
 (Requirements for the 6.5 m MMT)
 Robert Fugate, *Starfire Optical Range (Current State of Lincoln Lab CCD Development)*
 Jim Beletic, *ESO (CCD Development for ESO/VLT)*
 Craig Mackay, *AstroCam, (High speed controllers)*

FRIDAY

JULY 12, 1996

PIKAKE ROOM

8:00am-9:20am

AFA • Wave-front Correctors

Robert K. Tyson, *W. J. Schafer Associates Inc., President*

8:00am

AFA1 • Adaptive secondary development, Donald Bruns, Todd Barrett, *ThermoTrex Corp.*; Guido Brusa, *University of Arizona*; Roberto Biasi, Daniele Gallieni, *Politecnico di Milano, Italy*. The MMT will be converted to a single 6.5-m primary mirror in 1997. The new telescope will be equipped with adaptive optics for high-resolution infrared astronomy at wavelengths between 1.6 and 5 μm . (p. 302)

8:20am

AFA2 • Keck adaptive optics: test of a deformable mirror in a freezing environment, D. S. Acton, P. Stomski, P. Wizinowich, J. Maute, T. Gregory, *W. M. Keck Observatory*; M. Ealey, T. Price, *Xinetics Inc.* Hysteresis curves and drift measurements are presented for a Xinetics 37-actuator PMN deformable mirror at 1 °C and 21 °C. (p. 305)

8:40am

AFA3 • Wave-front estimation by phase diversity and compensation with a liquid crystal wave-front corrector, Gordon D. Love, Sergio R. Restaino, Richard C. Carreras, *USAF Phillips Laboratory*; Steven M. Ebstein, Robert A. Gonsalves, Peter Nisenson, *Lexitek Inc.*; William Junor, *Rockwell Power Systems*. Laboratory-induced aberrating wave-fronts were estimated from phase diversity images. Non-real-time compensation with a liquid crystal adaptive optic yielded a Strehl increase of about 2.7. (p. 308)

9:00am

AFA4 • All-optical adaptive systems: nonlinear optics approach for phase distortion suppression, M. A. Vorontsov, *Army Research Laboratory and New Mexico State Univ.* We discuss a new adaptive optics technique that uses nonlinear two-dimensional optical feedback systems with Kerr or photorefractive-type nonlinearity for temporally varying phase distortion suppression. (p. 312)

Monday, July 8, 1996

Adaptive Optics Systems

AMA 8:00 am-9:45 am
Pikake Room

Presiders:
Masanori Iye, *National Astronomical Observatory, Japan*
Richard M. Myers, *University of Durham, U.K.*

Review of Large Telescope Adaptive Optics Systems

David Sandler

*ThermoTrex Corporation, 9550 Distribution Ave., San Diego, CA 92121
and*

*Center for Astronomical Adaptive Optics, Steward Observatory,
University of Arizona, Tucson, AZ 85721*

Tel: 619.578-5885; Fax: 619.578.1419; email: dsandler@cts.com

Introduction

The new generation of large telescopes begins a truly exciting new era for ground-based astronomy. By the end of the decade, nearly a dozen new telescopes with diameter $D \geq 6.5$ m will be in operation. Equipped with adaptive optics, these telescopes will provide unprecedented resolution from the ground. The rapid increase in our knowledge of the atmosphere, the refinement of adaptive optics components, and the steady increase in confidence arising from the experience of numerous groups around the world are all coming together at the right time for adaptive optics to fulfill its promise for astronomy.

When measured against the cost and technical challenges, the greatest benefit of adaptive optics for astronomy will be realized on the new large telescopes. The combination of increased light gathering power and sharper diffraction limit produces a potential D^4 improvement in light concentration over smaller telescopes, and larger apertures lead to increased sky coverage for natural stars, through both wider isoplanatic fields and capability of sensing fainter stars. The use of laser guide stars is also optimized for large telescopes, since the required power scales as the subaperture size used for wavefront sensing. Based on field measurements of focus anisoplanatism, a single sodium beacon will provide accurate correction for imaging at $\lambda \geq 2.2 \mu\text{m}$, for $D \geq 8$ m. Thus, sodium lasers of several watts will allow diffraction-limited imaging at the K-band diffraction limit of 0.05 arcseconds, meeting the Hubble optical resolution from the ground.¹

The purpose of this paper is to present an overview of adaptive systems under development or planned for new large telescopes. Atmospheric data from several groups which support the feasibility of AO at large aperture will be presented. Individual projects will be reviewed, laying out the scientific goals for each and the timetable for expected completion. The adaptive optics method for each telescope will be summarized, including type of wavefront sensing and choices of detector and deformable mirror, and projected operating parameters will be given. An attempt will be made to compare the expected performance of the systems on an equal footing, appealing to phenomenological treatment of AO error sources.

Large telescope AO projects

Laser guide star systems. Adaptive optics for the Nasmyth platform of the 10 m Keck II telescope²

is currently under development by the Keck Observatory and Lawrence Livermore National Laboratory (LLNL). The Multiple Mirror Telescope (MMT) will be converted to a single 6.5 m primary mirror in 1997, and an adaptive system for the f/15 Cassegrain focus of the new MMT³ is under development at Steward Observatory and ThermoTrex Corporation. Both the new MMT and Keck telescopes will use a sodium laser beacon, of ~ 10 th magnitude, to correct high-order wavefront errors. The Keck will use a photon-counting APD quad cell for natural-star tilt sensing; the MMT will use an infrared quad cell to sense tilt at $\lambda \approx 1.6 \mu\text{m}$. The limiting sky coverage will be discussed for these two options.

The Keck system will use a commercial 349- actuator pupil-plane deformable mirror, with extensive crossing of wavefront sensor subapertures across boundaries of the 36 primary mirror segments. The Arizona-ThermoTrex group is developing an adaptive secondary mirror for the MMT, with the goals of simplifying the adaptive optics beamtrain and achieving low emissivity in the thermal infrared. The baseline design for MMT adaptive optics will be carried over to the Large Binocular Telescope (LBT), consisting of two $D=8.4$ m mirrors co-mounted with a 14 m separation between centers. Because of the Keck and MMT systems are already in the stage of development and scheduled for completion in 1997, these systems will be discussed in considerable detail during the paper.

Natural guide star systems. Three telescope projects are planning natural guide star AO systems. The 8.2 m SUBARU telescope will develop a Cassegrain system⁴ using a 36-actuator bimorph mirror controlled using curvature sensing with an array of APD modules. A prototype system is currently under development for testing at 1.6 m aperture in Japan. The GEMINI 8 m telescope on Mauna Kea, which will be optimized for performance in the thermal infrared, will be equipped with adaptive optics⁵, with a goal of maintaining low emissivity. The first generation system will use natural guide stars, with the capability of a straightforward upgrade to a sodium beacon. A unique feature of the GEMINI design is the use of a deformable mirror conjugate to the median altitude of turbulence, about 6 km altitude above the site. Design calculations indicate that substantial gains in the isoplanatic patch and sky coverage may result. The ESO VLT will employ adaptive optics⁶ beginning with a first generation system (NAOS) for the Nasmyth focus of the first VLT unit. The development program is an offspring of the ESO Come-On-Plus and ADONIS systems at the ESO 3.6 m telescope. NAOS will use a conventional deformable mirror with ~ 250 actuators; optimal modal control will be used, as demonstrated at the 3.6 m telescope, to adjust control spatio-temporal bandwidths according to the brightness and off-axis separation of the field star.

Critical issues and challenges

While detailed designs are complete, and the fundamental hardware components are nearly at hand for large telescope adaptive optics, many challenges remain for fully optimized and routine operation. In addition, critical issues remain, especially in light of the fact that closed-loop wavefront control with a sodium beacon has yet to be demonstrated to produce the factors of ~ 10 improvement in image sharpness in the near infrared. These factors will be discussed, and key milestones on the path of reliable AO for large telescopes will be suggested.

References

1. D. Sandler, S. Stahl, J.R.P. Angel, M. Lloyd-Hart, D. McCarthy, Adaptive optics for diffraction-limited infrared imaging with 8 m telescopes, *JOSA A* 11, 925 (1994).
2. A. Gleckler and P. Wizinowich, W.M. Keck Observatory adaptive optics program, *Proc. SPIE* 2534, 386 (1995).
3. D. Sandler, M. Lloyd-Hart, T. Martinez, P. Gray, J.R.P. Angel, T. Barrett, D. Bruns, S. Stahl, 6.5 m MMT infrared adaptive optics system: detailed design and progress report, *Proc. SPIE* 2534, 372 (1995).
4. H. Takami, M. Iye, N. Takato, Y. Hayano, M. Otsubo, K. Nakashima, SUBARU adaptive optics program, proceedings of the Topical Meeting on Adaptive Optics, Garching, Oct. 2-6 (1995).
5. R. Racine, The GEMINI Adaptive Optics System, proceedings of the Topical Meeting on Adaptive Optics, Garching, Oct. 2-6 (1995).
6. N. Hubin, The ESO VLT adaptive optics program, proceedings of the Topical Meeting on Adaptive Optics, Garching, Oct. 2-6 (1995).

Review of astronomical adaptive optics systems on medium size (1.5-5m) telescopes

François Rigaut

Canada-France-Hawaii Telescope,

65-1238 Mamalahoa Hwy, Kamuela, HI-96743

We present an exhaustive review of adaptive optics systems with a vocation for astronomy. After a brief historical introduction, we review the different technological approaches and the results.

Review of Non Astronomical Active and Adaptive Optics Technologies

Janet S. Fender
Optical Sensing Division
Phillips Laboratory
PL/LIM Kirtland AFB, NM 87117
(505) 846-4014 phone
(505) 846-4039 fax

Russell R. Butts
Airborne Laser Technology Division
Phillips Laboratory
PL/LIA Kirtland AFB, NM 87117
(505) 846-0357 phone
(505) 846-0473 fax

Active and adaptive optics developed by the defense and industrial communities for high performance optical telescopes and laser propagation are reviewed in this paper.

Monday, July 8, 1996

Poster Previews: 1

AMB 9:45 am-10:15 am
Pikake Room

Presiders:

Masanori Iye, *National Astronomical Observatory, Japan*
Richard M. Myers, *University of Durham, U.K.*

W.M. Keck Observatory Adaptive Optics Facility

P. Wizinowich, D.S. Acton, A. Gleckler, T. Gregory, P. Stomski
W.M. Keck Observatory, 65-1120 Mamalahoa Highway, Kamuela, HI 96743, U.S.A.
Tel: 808 885-7887; Fax: 808 885-4464; email: peterw@keck.hawaii.edu

K. Avicola, J. Brase, H. Friedman, D. Gavel, C. Max
Lawrence Livermore National Laboratory, P.O. Box 808, Livermore, CA 94550

Introduction

The W.M. Keck Observatory, in collaboration with Lawrence Livermore National Laboratory (LLNL), is currently in the critical design phase of a natural guide star (NGS) and single laser guide star (LGS) adaptive optics (AO) user facility for the Nasmyth platform of the Keck II 10-m telescope.¹ Two science instruments will accompany the AO facility: a near infrared camera (NIRC-2) being built at Caltech, and a near infrared spectrometer (NIRSPEC) being built at UCLA. NASA is planning to fund an interferometer between the Keck telescopes which will require a second NGS AO facility on Keck I.

The preliminary design review for the NGS facility was held in November 1995, and the laser review will be held in March 1996. The critical design reviews will be held this summer. The facility is scheduled to be installed on the telescope in 1997, and to be operational near the end of 1998.

Design requirements for the facilities are described in reference 2, and the error budget in reference 3. Briefly, the facilities will be optimized for science wavelengths between 1.0 and 2.3 μm using faint NGS, or a single LGS (~ 10 mag) with a NGS (> 19 mag) for tip/tilt sensing; and be operational from 0.8 to 5.0 μm (or to > 10 μm for interferometry).

System Architecture and Subsystem Designs

The AO facility is divided into four main subsystems for the purpose of fabrication: user interface and supervisory control⁴, optics bench⁵, wavefront controller⁶, and the laser subsystem⁷. The first two subsystems are being fabricated at the Observatory and the second two at LLNL. With the exception of the laser subsystem, most of the hardware, including the science instruments, will be located in an enclosure on the Nasmyth platform, as shown in Figure 1.

The user interface and supervisory control subsystem provides a graphical user interface with single station control and coordination of the entire AO facility through an EPICS (Experimental Physics and Industrial Control System) environment. The controllers for each subsystem are located in VME crates connected via a private ethernet link.

The optics bench consists of an image rotator, an off-axis parabola to collimate the f/15 input beam and to reimaged the telescope pupil on the deformable mirror (DM), and a second off-axis parabola to reproduce the f/15 beam and telescope exit pupil. The light to the science instrument passes through a visible/infrared dichroic and an infrared atmospheric dispersion corrector (ADC). The

visible light reflected from the dichroic passes through a visible ADC to the wavefront sensor, the tip/tilt sensor, and an acquisition camera. The tip/tilt sensor is fed with a 589-nm transmissive/visible reflecting dichroic. Stars are acquired within the 2 arcmin diameter tip/tilt field by translating the sensor; and within the 1 arcmin diameter wavefront sensor field by steering a pair of mirrors to simultaneously maintaining the DM to lenslet registration. The entire wavefront sensor including the pupil relay optics must be translated as the LGS focal plane varies as a function of the distance to the sodium layer.

There is another layer to the optics bench which includes the alignment, calibration and diagnostic tools including a telescope simulator in front of the image rotator, a diagnostics camera after the IR ADC, an interferometer monitoring the DM, and a camera looking at a target in the science instrument to monitor its alignment to the optics bench.

The wavefront controller subsystem consists of the closed-loop control components from the wavefront and tip/tilt sensor cameras to the DM and fast steering mirror. An existing Georgia Tech. fabricated camera, based on a 64x64 pixel MIT/LL CCD with 11 electrons read noise at 2 MHz frame rate, will be used for wavefront sensing. The tip/tilt sensor will use 4 EG&G photon counting avalanche photodiodes; we also intend to use this quadrant array, with astigmatism introduced in the beam, to sense the telescope focus^{1,5}. A 349-actuator DM will be used; we are currently testing a 37-actuator Xinetics DM in the dome environment⁸. The reconstructor computer will be based on a 16 i860 Mercury board. The effects of changing illumination on the wavefront sensor due to rotation of the non-circular Keck pupil will be compensated by cycling through a set of reconstructor matrices and centroid offsets.

The laser will be a Nd:YAG pumped, 30 kHz pulsed, 3-stage dye laser developed by LLNL, with an anticipated output of 20 W. The YAGs and dye master oscillator will be located in a room on the dome floor; two phase modulators will be used to spread the narrow dye output across the mesospheric sodium profile. The dye preamplifier and amplifier stages (pumped by fibers from the laser room), along with the 50-cm projection telescope, and an alignment and diagnostics table will be located on the side of the Keck telescope.

Risk Control

There are many new features to this system which will challenge both the technology and the implementation. These include the 10-m segmented primary, a rotating hexagonal pupil, off-axis wavefront and tip/tilt sensing, 3x3 pixels/subaperture wavefront sensing, a focus sensor and wavefront sensor translation stages to correct for the sodium layer distance variations, and 0.02 arcsec (15 μ m) diameter images.

Our approach will, therefore, be to start simple (i.e., a 9-m circular aperture, on-axis NGS, and 4x4 pixels/subaperture) with a good set of alignment, calibration and diagnostic tools, and phase in the additional features in order to meet the requirements; and to draw upon the expertise of the AO and astronomy communities. The result should be impressive science from the start.

References

1. A. Gleckler and P. Wizinowich, "W.M. Keck Observatory adaptive optics program," SPIE Proc. 2534, San Diego (July 1995).
2. Keck Adaptive Optics Science Team, Adaptive Optics for the Keck Observatory, Keck Observatory Report No. 208 (revised January 1996).
3. P. Wizinowich, "Keck AO: error budget," these proceedings.
4. P. Stomski et al., "Keck AO: user interface and supervisory control," these proceedings.
5. T. Gregory et al., "Keck AO: optics bench," these proceedings.
6. J. Brase et al., "Keck AO: wavefront controller subsystem," these proceedings.
7. H. Friedman et al., "Keck AO: laser subsystem," these proceedings.
8. S. Acton et al., "Keck AO: DM testing," these proceedings.
9. G. Chanan et al., "Keck AO: atmospheric characterization," these proceedings.

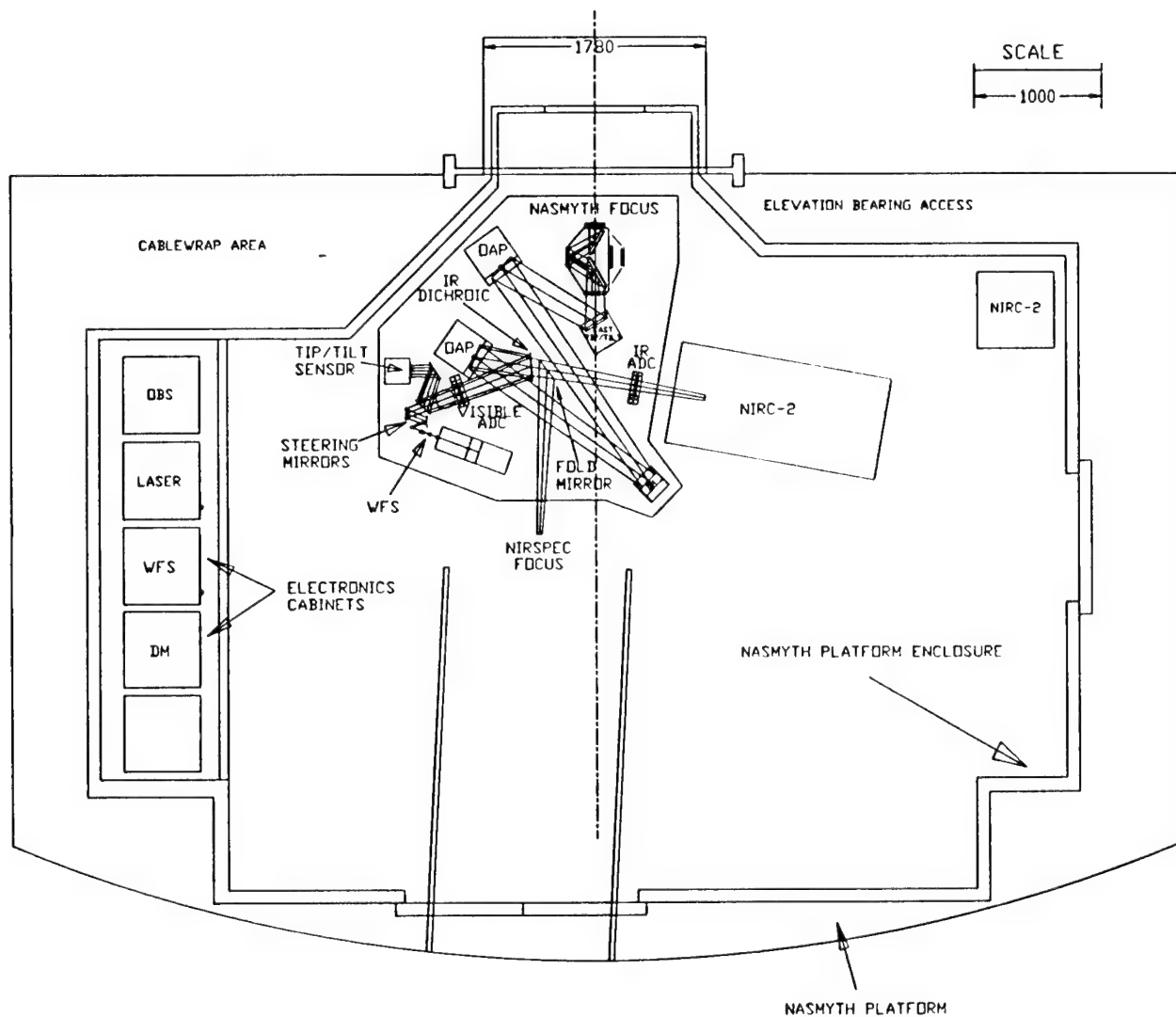


Figure 1.

Keck Adaptive Optics: Optical Bench Subsystem

T. Gregory¹, P. Wizinowich¹, D. S. Acton¹, A. Gleckler², P. Stomski¹, S. Radau³, J. Maute¹, M. Sirota¹

¹W. M. Keck Observatory, 65-1120 Mamalahoa Highway, Kamuela, HI 96743
Tel. 808/885-7887, Fax. 808/885-4464, email tgregory@keck.hawaii.edu

²Kaman Aerospace, 3480 E. Britannia Drive, Tucson, AZ, 85706

³ROM Engineering, Box 65170, Tucson, AZ, 85718

Introduction

The W. M. Keck Observatory and Lawrence Livermore National Labs are currently developing an adaptive optics (AO) system for use on the 10-meter Keck II telescope. This paper will review the Optical Bench Subsystem, placing emphasis on the requirements that led to the current design.

Requirements

Many requirements and specifications have been set forth for the Keck AO system. Those that have most significantly affected the design of the Optics Bench Subsystem are listed below:

1. The beam to the science instrumentation must have the same $f\#$ and pupil location as that of the telescope beam ($f/15$, pupil at 19.96 meters).
2. The science instrumentation will be centered on the telescope axis, with a 1-arcminute field of view (maximum), and no restrictions on the position and orientation of the object. Therefore, the wavefront and tip/tilt sensors must be movable to different field positions. The wavefront sensor (WFS) must span a 1-arcminute field of view, and the tip/tilt sensor must span a 2-arcminute field of view.
3. The AO system must support both natural guide stars and a laser guide star.
4. Wavefront sensing (tip/tilt and higher-order aberrations) from 0.4 to 1.0 microns.
5. Science instrumentation wavelengths optimized over 1.0 to 2.3 microns, allowing wavelengths from 0.8 through 5 microns (10 microns for interferometry).
6. Atmospheric dispersion must be compensated.
7. The emissivity contribution from the Optics Bench must be < 0.25 .
8. Throughput to the science instrumentation must be $> 70\%$ at science wavelengths, and the throughput to the wavefront sensor must be $> 45\%$.
9. Field dependent errors in the AO system must be kept to a minimum.
10. Must provide a camera for acquisition over the 2-arcminute field of view.
11. Image rotation on the science instrumentation must not degrade a long-exposure.
12. The alignment between the AO Bench and NIRC2 must remain stable to within $5\ \mu\text{m}$ while exposing.
13. The corrected beam must be directed to one of the two science instruments or the interferometer path.
14. The WFS must have an adjustable field stop as well as an adjustable plate scale.

In the remainder of this summary, we briefly describe the components on the Optical Bench, (see the figure at the end) emphasizing how the above requirements led to their design. Details will be given in the poster presentation.

Image Rotator

The AO system will be mounted on the left Nasmyth platform at the $f/15$ bent Cassegrain focus. An image rotator is provided to compensate for field rotation as the telescope tracks the object across the sky. This rotator will consist of three mirrors that are fixed with respect to each other, and are made to rotate about the optical axis. Mirrors were chosen over prisms because of the broad spectral and low emissivity requirements. The mirrors in the rotator will have low-emissivity coatings, as will all mirrors in the AO system. In order to keep from distorting the image in a long exposure, the image rotator must align to within about 10 arcseconds, and the rotational accuracy of the image rotator needs to be about 5 arcseconds.

Reimaging Optics

After passing through the image rotator, the beam reflects off of a tip-tilt mirror and an off axis parabola (OAP) which collimates the beam and reimages the telescope primary onto a deformable mirror (DM). The tip-tilt mirror and the DM are part of the Wavefront Controller Subsystem. The beam is then sent to an identical off-axis parabola, which approximately cancels the aberrations introduced by the first OAP and produces an output beam identical to that of the telescope's.

Dichroic Beamsplitters

The science wavelengths are, by specification, different from those used in the wavefront sensing. In order to meet the transmission requirements, an IR/visible dichroic beamsplitter is used to separate the spectrum for the two paths. The dichroic reflects light below 1 micron, so it can be used for wavefront sensing. Light between 1 and 5 microns is transmitted for the science path. An IR transmitting beamsplitter was chosen because it was more technically feasible.

When using an artificial guide star, it is necessary to make wavefront tip/tilt measurements from a nearby natural guide star. The fraction of the sky that can be corrected by the AO system will depend on the sensitivity of the tip/tilt sensor. To increase the light to the tip/tilt sensor, the visible light beam is split into two paths with a sodium line (589 nm)/visible reflecting dichroic beamsplitter. When operating the AO system with a natural guide star, the sodium/visible dichroic beamsplitter can be removed.

Atmospheric Dispersion Correction

All of the imaging paths may suffer from atmospheric dispersion. If not corrected, the dispersion would degrade the performance of the AO system at angles away from the zenith. Ideally, we would like to place a single Atmospheric Dispersion Corrector (ADC) at the front of the Optical Bench. However, an ADC design that functions simultaneously over the 0.4 - 2.5 microns band does not currently exist.

A visible ADC will be placed in the path of the reflected beam from the IR/visible dichroic beamsplitter. This ADC will correct the dispersion in the tip/tilt, wavefront sensor, and acquisition paths. An IR ADC will be placed in the beam path just before the science instrumentation. This ADC will be mechanically removable for wavelengths above 2.5 microns.

Tilt and focus sensing path

This sensor--part of the Wavefront Controller Subsystem--is designed to measure the tip/tilt terms and the time-averaged focus term in the wavefront. This sensor will be mounted on a precision encoded X-Y-Z translation stage so it can acquire a natural star anywhere within the 2-arcminute field of view.

Wavefront sensing path

Perhaps the most stringent requirement of the Optical Bench is the off-axis operation of the wavefront sensor. This requires that different parts of the field be steered to a field stop in the wavefront sensor, without translating the wavefront sensor with respect to the DM. To accomplish this, we settled on the use of two field selection mirrors, placed just before the beam comes to a focus at the WFS. The field selection mirrors will allow a star anywhere within a 1-arcminute diameter circle to be sent through the WFS. Because of the registration requirements between the DM and the wavefront sensor, the field selection mirrors must be accurate to within a few arcseconds (on the mirrors).

At the entrance to the WFS, an adjustable field stop is employed in order to cut down on background light that would otherwise enter the WFS. The pupil on the deformable mirror is reimaged onto a sheet of microlens arrays. This sheet contains several arrays of microlenses--each with different focal lengths. (This way, the focal length of the microlens array can be optimized for a given set of seeing conditions.) The sheet of arrays is mounted on a precision encoded XY translation stage, so that the optimal array can be inserted automatically. The images from the microlens array are relayed to a CCD camera. Since each array has a different characteristic focal length, the CCD camera is mounted on a translation stage which is moved to the correct focus for each lenslet group.

The entire WFS moves along a translation stage to compensate for the finite distance to the sodium layer, when using an artificial laser guide star. As the position along this focus stage changes, a lens moves on another translation stage in order to keep the pupil correctly imaged on the microlens array.

NIRC2 Alignment Monitor

One of the science instruments that will be used with the AO system is the Near-Infrared Camera II (NIRC2). Since this camera is mounted separately (inside a cryogenic dewar) from the AO optical bench, there exists the potential for the relative alignment between the two instruments to drift during a long exposure, lowering the Strehl ratio of the corrected image.

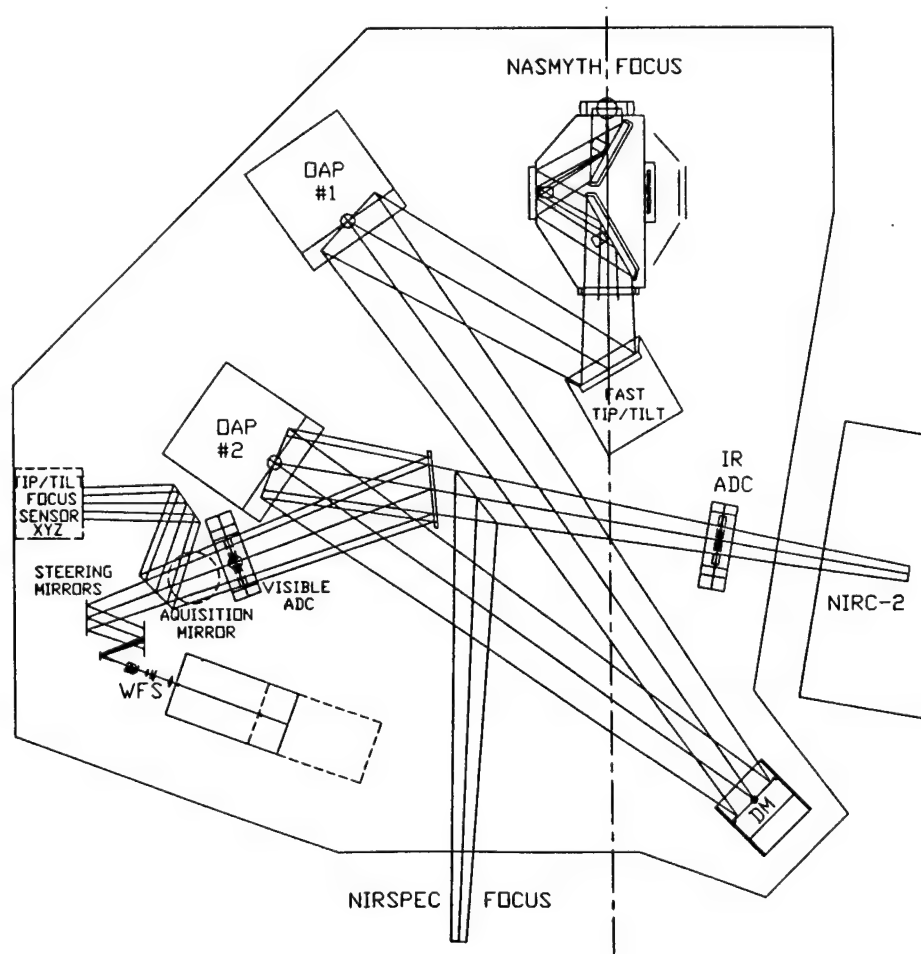
We plan to insert an alignment target on the optical bench inside of NIRC2. A small window in the front of NIRC2 will allow the target to be monitored by a camera on the AO bench. By applying cross correlation algorithms to the digitized images, we can determine the relative X-Y shift and focus change of NIRC2.

Acquisition, Calibration and Diagnostics.

The AO system will be responsible for acquiring the natural and artificial guide stars. A 1024 X 1024 pixel visible CCD camera will be used for this purpose. This camera needs to benefit from the field-correcting aspects of the twin parabolas, and be corrected for atmospheric dispersion by the visible ADC. During acquisition, the beam will be directed to the acquisition camera by inserting a mirror or beamsplitter in the beam just after the visible ADC.

A diagnostics camera can be inserted into the science path with a movable fold mirror. We are considering a visible camera with a large format, and a small infrared camera. This camera will allow us to record corrected images while in the lab or at the observatory, for diagnostic purposes.

A telescope simulator can be inserted into the beam path with a movable fold mirror. The telescope simulator produces a white-light image with the same f-ratio and pupil location as the telescope. The image formed by the telescope simulator can be placed anywhere within the 2-arcminute field of view. The telescope simulator will also have laser sources for alignment of the Optics Bench and to simulate operation with a laser guide star.



Keck Adaptive Optics: User Interface and Supervisory Control Subsystem

P. Stomski, P. Wizinowich, D. S. Acton, W. Lupton, J. Gathright, A. Conrad, H. Lewis, T. Gregory,
W. M. Keck Observatory, 65-1120 Mamalahoa Highway, Kamuela, HI 96743, U.S.A.
Tel: 808 885-7887; Fax: 808 885-4464; email: pstomski@keck.hawaii.edu

Introduction

The user interface and supervisory control subsystem (UISC) of the W. M. Keck Observatory Adaptive Optics (AO) system serves three main purposes. First, it is the single point of control for the AO system, the wavefront controller subsystem, the optics bench subsystem and the laser subsystem. Second, it manages the coordination and supervision of the AO subsystems to provide a user-friendly facility with a high degree of automation. Third, it interacts with the other observatory systems as needed. The UISC is primarily a software system. The critical design of this subsystem is currently under way.

As the single point of control for the AO system, the UISC must provide a user with a graphical interface with the following capability:

- Start/stop the system (including self tests and safety shut down)
- Run alignment procedures
- Initiate calibration of system components
- Diagnose and recover from system faults
- Acquire science objects and guide stars
- Initiate closed loop operation
- Monitor system performance
- Support new and existing observing techniques (including nodding)
- Track non-sidereal objects
- Perform atmospheric characterization and system optimization
- Automate repetitive tasks using scripts

In its role as coordinating supervisor of AO subsystems, the UISC must perform several functions:

- Communicate with the wavefront controller subsystem, optics bench subsystem and laser subsystem. This communication takes the form of sending commands to the subsystems and receiving status and vital statistics back from the subsystems.
- In response to user actions, initiate high level coordination sequences involving the AO subsystems and telescope control subsystems. These coordination sequences control the progression and timing of operations across subsystems.
- Manage system state transitions.

In addition to interacting with other AO subsystems, the UISC is also responsible for communication with other observatory and telescope systems. Specifically, the UISC manages external interfaces with the following:

- The telescope primary mirror Active Control System (ACS)
- The telescope Drive Control System (DCS)
- Science instruments

Hardware Architecture

The computer hardware for the UISC consists of a SUN workstation in the telescope control room and a VME CPU in a crate on the Keck II telescope Nasmyth platform. As illustrated in the figure at the end of this summary, these two computer systems, as well as the VME computers of the other subsystems, are

connected via a private AO Ethernet. The SUN workstation is also connected to the observatory environment via a site-wide local area network (LAN).

The VME CPU is currently specified as being Motorola 68040 based, but an upgrade to a more powerful processor is expected. The UISC design will be done for a generic CPU, so that an upgrade will not require major subsystem changes.

Software Architecture

The software architecture of the UISC is based on the Experimental Physics and Industrial Control System (EPICS). EPICS is a distributed process control system made up of several powerful tools including a data archiver, alarm handler, sequencer, and a communications protocol called Channel Access. EPICS has also been integrated with a graphical programming tool called Capfast. These tools are used to create databases and manage dependencies. The VME CPU for the UISC will run EPICS under the VxWorks operating system. The SUN will run EPICS under the Solaris operating system.

The GUI will be developed using a package called DataViews. This package is already used in other Keck telescope systems and science instruments. DataViews is a powerful tool for building graphical user interfaces. We plan on using HTML to build our on-line documentation, help, diagnostic and troubleshooting facilities. We can then run an HTML browser such as Mosaic or Netscape to give the user access to hyper-text documentation.

System Control

Many control loops will be active when the Keck AO system is running. Some of these loops are managed by the wavefront controller subsystem and others are managed by the UISC.

The wavefront controller will manage the following real-time control loops:

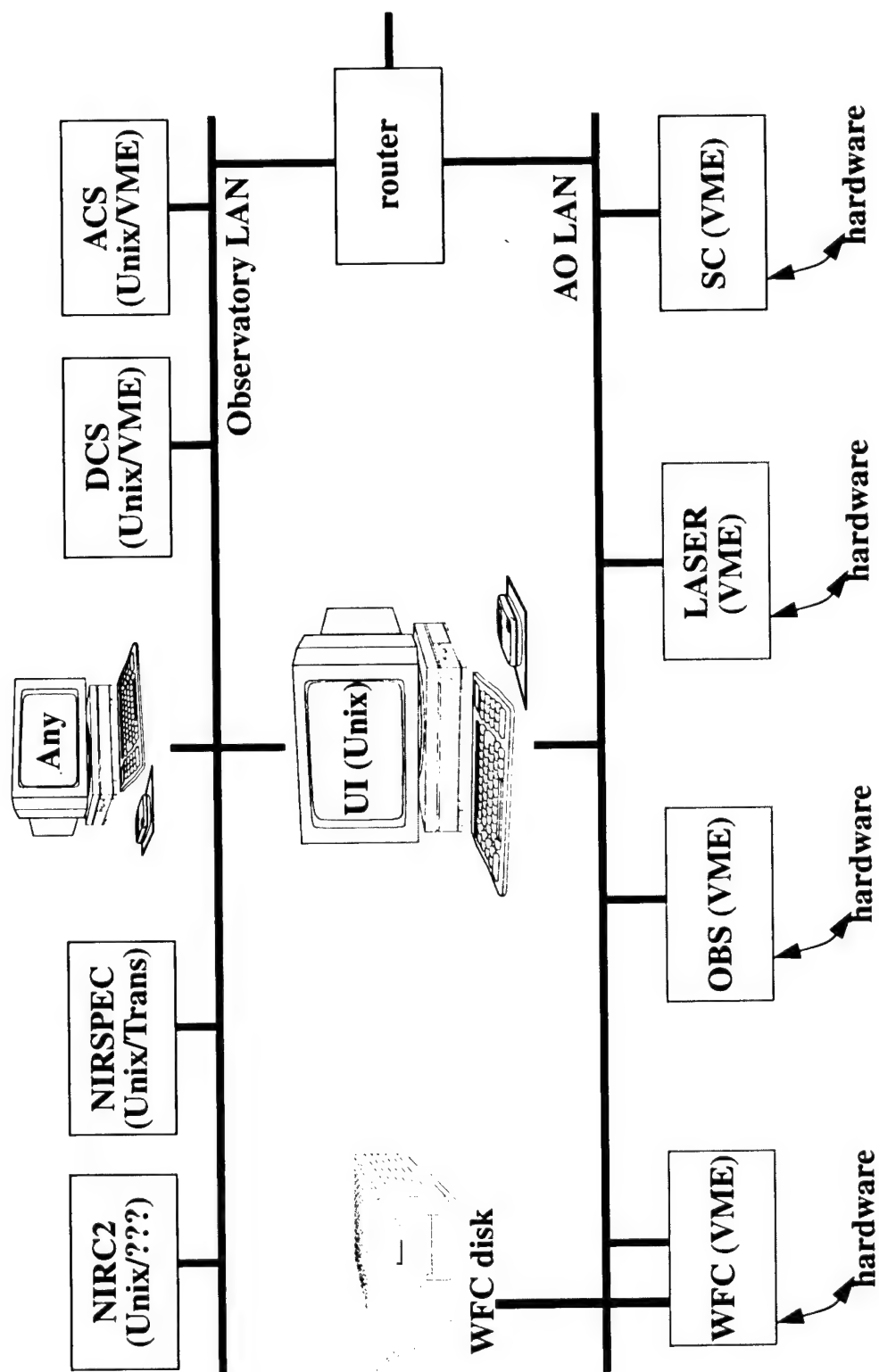
1. Wavefront sensor - deformable mirror loop
2. Tip/Tilt sensor - tip/tilt mirror loop (laser guide star operation)
3. Wavefront sensor - tip/tilt mirror loop (Natural guide star operation)
4. Wavefront sensor - laser pointing control loop

The UISC will manage the following control loops and open loop compensations:

1. Tip/Tilt mirror position - telescope pointing loop
2. Deformable mirror focus term - telescope secondary mirror piston control loop
3. Deformable mirror coma term - telescope secondary mirror tilt control loop
4. Deformable mirror coma term - telescope primary mirror tilt control loop
5. Focus sensor - wavefront sensor focus stage position loop
6. Pupil rotation compensation
7. IR Atmospheric Dispersion Corrector beam deviation compensation
8. Visible Atmospheric Dispersion Corrector beam deviation compensation
9. Science instrument alignment shift compensation
10. Focus sensor field dependence compensation

More details on each of the areas mentioned will be given in the poster session of these proceedings.

Hardware Architecture



Keck Adaptive Optics: Wavefront Control Subsystem

J. Brase, J. An, K.A. Avicola, D. Gavel, C. Max, S. Olivier, K. Waltjen, J. Watson

Lawrence Livermore National Laboratory
P.O. Box 808, L-437
Livermore, CA 94550

P. Wizinowich, S. Acton, A. Gleckler, T. Gregory, P. Stomski

California Association for Research in Astronomy
W.M. Keck Observatory
65-1120 Mamalahoa Highway
Kamuela, HI 96743

Introduction to adaptive optics at Keck

Adaptive optics on the Keck 10 meter telescope will provide an unprecedented level of capability in highresolution ground-based astronomical imaging [1,2]. The system is designed to provide near diffraction limited imaging performance with Strehl > 0.3 median Keck seeing of $r_0 = 25$ cm, $t_0 = 10$ msec at 500 nm wavelength. The system will be equipped with a 20 watt sodium laser guide star to provide nearly full sky coverage.

The wavefront control subsystem is responsible for wavefront sensing and the control of the tip-tilt and deformable mirrors which actively correct atmospheric turbulence. The spatial sampling interval for the wavefront sensor and deformable mirror is $d = 0.56$ meters which gives us 349 actuators and 244 subapertures.

The wavefront control design is based on the adaptive optics system operating at Lick Observatory [3]. It uses commercial off the shelf components for wavefront sensing, computer-based control, and for the deformable mirror. The tip-tilt sensor and mirror are custom LLNL designs. In Section 2 we will summarize the wavefront control system design. Section 3 will briefly discuss some of the particular issues in designing a wavefront controller for the Keck Telescope.

The wavefront control design

A block diagram of the Keck wavefront control subsystem is shown in Figure 1. The host computer is a Force SPARC 5 single board based system. Its principal functions are to receive commands from the user interface or supervisory control subsystems [4], to coordinate the actions of the realtime control systems based on these commands, and to transmit telemetry and diagnostic information back to the user interface or supervisory control subsystems.

The two realtime controllers communicate with the SPARC host through the VME-64 bus. On the left in Figure 1 is the tip-tilt control system which is based on a single 68040 processor. On the right is the deformable mirror control system which uses 16 Intel i860 processors to control the 349 actuators.

In laser guide star operations the wavefront tip-tilt from a nearby natural star is sensed with an avalanche photodiode (APD) quadcell. The quadcell is formed by a four lenslet array which is fiber optic coupled to the four EG&G APD photon counting detectors. In natural guidestar operations the tip-tilt is sent to the controller from the wavefront sensor via VME shared memory. Accumulated photon counts or wavefront sensor tip-tilt values are processed by the MVME162 68040-based processor at sample rates up to 1 KHz. The tip-tilt mirror is a 20 cm lightweight silicon carbide mirror.

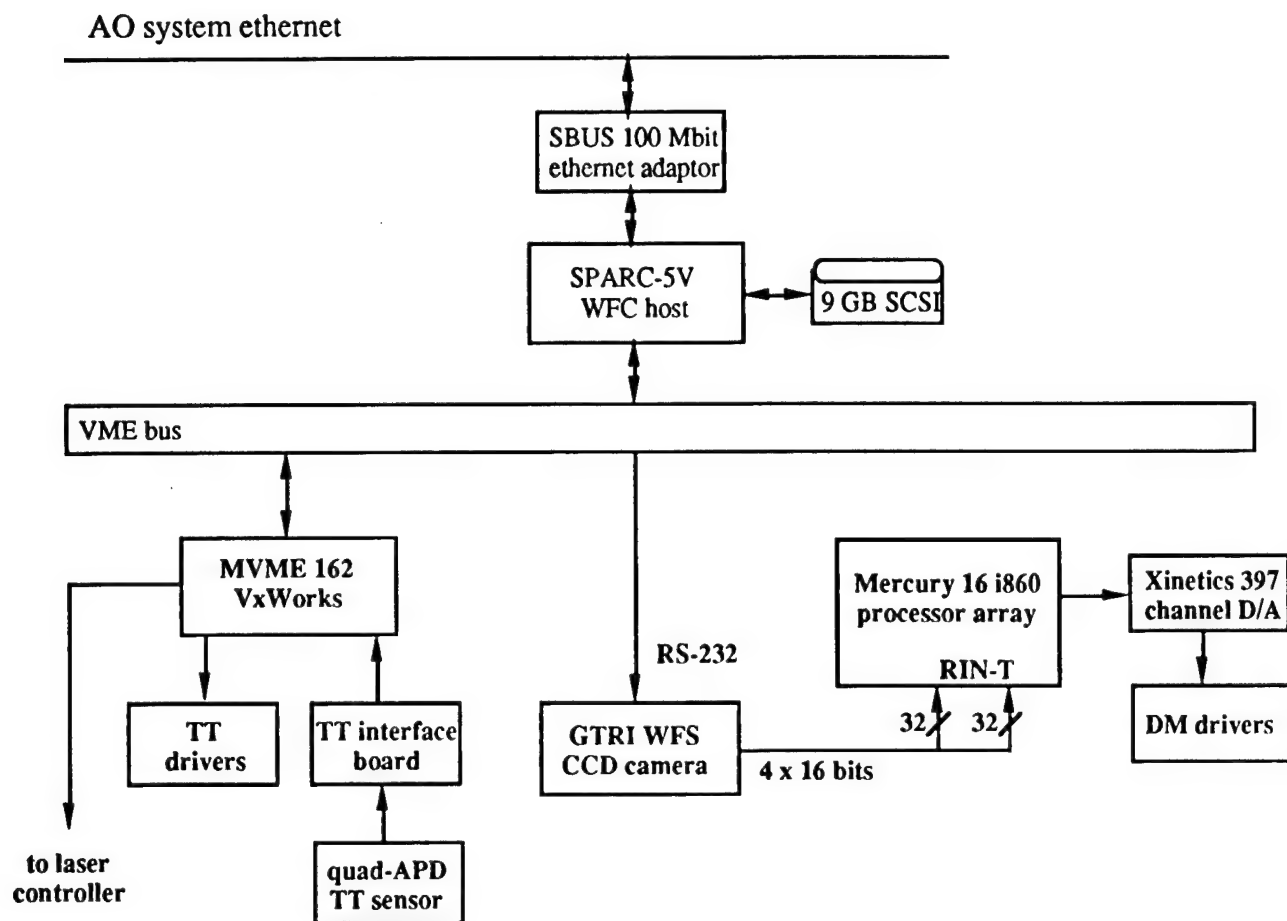


Figure 1. Block diagram of the Keck wavefront control subsystem. The system host and interface to the rest of the adaptive optics system is at the top; the tip-tilt controller and DM controller connect to the host through the VME bus.

High order wavefront errors are measured with a 244 subaperture Hartmann sensor. The wavefront sensor camera was developed by GTRI based on a Lincoln Laboratory 64 x 64 four-port CCD. The CCD has 12 e⁻ read noise at a maximum rate of 2000 frames per second. Realtime control of the deformable mirror is based on a Mercury Computer Systems board set with 16 Intel i860 processors connected through a six port high speed crossbar network. The system provides a peak computational rate of up to 1.28 Gflops. The processor array computes image centroids to estimate the wavefront slope,

reconstructs the slopes to give the error wavefront, and performs integral control of the deformable mirror actuators. The total time delay for data transfer and computation is approximately one msec. The Xinetics deformable mirror has a total of 349 PMN actuators. The actuator-subaperture-telescope aperture mapping is shown in Figure 2.

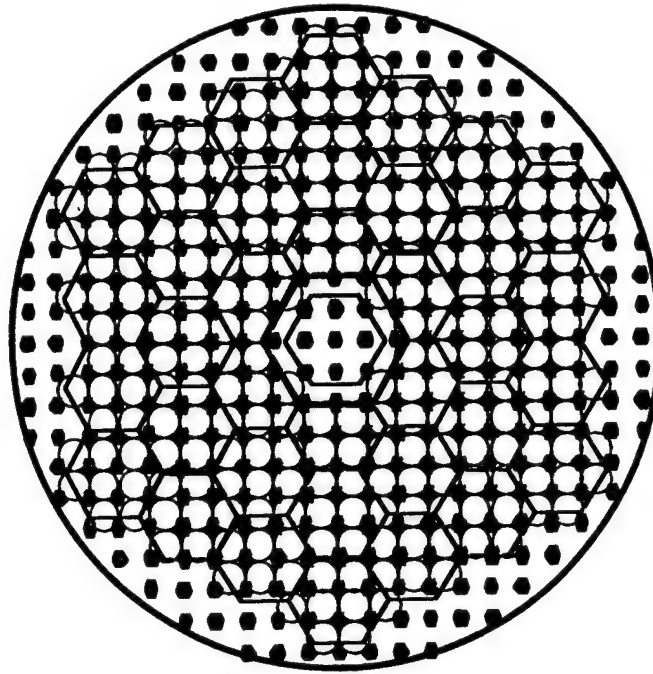


Figure 2. Relationship between the deformable mirror actuators (filled hexagons), wavefront sensor subapertures (open circles), and the segmented ten meter telescope aperture. There are 244 illuminated subapertures in this configuration.

The expected performance of the system was described in [2]. We expect to provide images with $\text{Strehl} > 0.3$ using a laser guide star reference and a natural guidestar tip-tilt reference with V magnitude > 18 . With a natural guidestar reference for the deformable mirror we should have a limiting magnitude of > 10 . We can optionally reduce the spatial frequency bandpass of the controller to allow operation with a dimmer reference.

Challenges of wavefront control on the Keck Telescope

The design and performance goals of the Keck adaptive optics system pose several particularly challenging problems. The diffraction limited image cores will range in size from 0.04 to 0.02 arcsec over the specified wavelength range of 1 to 2.2 microns. The small images must not move by more than 10% of their FWHM over exposure times of up to several hours. In addition we expect the tip-tilt sensor to have a limiting V magnitude of greater than 19 and to operate in bright time when the sensor is dominated by moonlit sky background. These performance goals impose severe precision and stability requirements on the tip-tilt sensing and control system.

Because the Keck telescope has an alt-azimuth mount, the pupil image will rotate on the fixed Nasmyth platform mounted wavefront sensor and deformable mirror. The main

effect is that wavefront sensor subapertures near the aperture edge will move on and off the illuminated pupil as it rotates. The wavefront controller must adapt for varying illumination in subapertures by updating the weights in the weighted leastsquares wavefront reconstructor as the pupil image rotates.

The goal of developing an astronomical laser guidestar adaptive optics system which is usable in a normal astronomical observing environment poses major challenges throughout the adaptive optics system design. In the wavefront control subsystem a major impact is the need for extensive telemetry and diagnostics. Essentially any signal in the deformable or tip-tilt mirror control processes can be saved and reported to the user interface or supervisory control subsystems. This information can be used to off-load control loops, to monitor the system's operation, or to optimize its performance during extended exposures.

Acknowledgements

We gratefully acknowledge funding from the W.M. Keck Foundation.

References

1. P. Wizinowich, S. Acton, A. Gleckler, T. Gregory, P. Stomski, K. Avicola, J. Brase, H. Friedman, D. Gavel, and C. Max. "W.M. Keck Observatory Adaptive Optics Facility", these proceedings.
2. C.E. Max, D.T. Gavel, and S.S. Olivier, "Near Infra-Red Astronomy with Adaptive Optics and Laser Guide Stars at the Keck Observatory", Proc. SPIE, San Diego, Ca., July 11-14, 1995.
3. J. Brase, J. An, K. Avicola, H. Bissinger, H. Friedman, D. Gavel, B. Johnston, C. Max, S. Olivier, R. Presta, D. Rapp, J. Salmon, and K. Waltjen. Adaptive optics at Lick Observatory: system architecture and operations", SPIE 2201, 468, 1994.
4. P. Stomski et al. "Keck Adaptive Optics: user interface and supervisory control", these proceedings.
5. T. Gregory et al. "Keck Adaptive Optics: optics bench", these proceedings.

Performance of Keck Adaptive Optics with Sodium Laser Guide Stars

Don Gavel, Scot Olivier, and Jim Brase
Lawrence Livermore National Laboratory
P. O. Box 808, Livermore, CA, 94550

The Keck telescope adaptive optics system is designed to optimize performance in the 1 to 3 micron region of observation wavelengths (J, H, and K astronomical bands). The system uses a 349 degree of freedom deformable mirror, so that the interactuator spacing is 56 cm as mapped onto the 10 meter aperture. 56 cm is roughly equal to r_0 at 1.4 microns, which implies the wavefront fitting error is $0.52 (\lambda/2\pi)(d/r_0)^{5/6} = 118$ nm rms. This is sufficient to produce a system Strehl of 0.74 at 1.4 microns if all other sources of error are negligible, which would be the case with a bright natural guidestar and very high control bandwidth. Other errors associated with the adaptive optics system will however contribute to Strehl degradation, namely, servo bandwidth error due to inability to reject all temporal frequencies of the aberrated wavefront, wavefront measurement error due to finite signal-to-noise ratio in the wavefront sensor, and, in the case of a laser guidestar, the so-called cone effect where rays from the guidestar beacon fail to sample some of the upper atmosphere turbulence. Cone effect is mitigated considerably by the use of the very high altitude sodium layer guidestar (90 km altitude), as opposed to Rayleigh beacons at 20 km. However, considering the Keck telescope's large aperture, this is still the dominating wavefront error contributor in the current adaptive optics system design.

The laser guidestar brightness and the servo bandwidth are specifically chosen so as to make them not the dominant sources of error. For example, with the 20 watt sodium laser beacon, the return signal is predicted to be greater than 0.3 photons/second/ms/cm² at the telescope aperture, which gives a signal-to-noise of 10 per subaperture per frame at 1000 Hz readout rate. Measurement error is less than 100 nm (Strehl \geq 0.78 at 1.2 microns) at this signal level, and less than 50 nm if a 500 Hz readout rate is used. Similarly, the computer system is sufficiently powerful to run the 349 channel control loop with disturbance rejection bandwidth up to 100 Hz. The servo error is 30 nm (Strehl = 0.97 at 1.2 microns) at 100 Hz bandwidth and 50 nm at 50 Hz bandwidth, assuming a typical Greenwood frequency of 20 Hz at $\lambda = 1.2 \mu\text{m}$.

Table 1 summarizes the current Keck error budget. Analysis is based on the formulas presented in reference [1], and follows the the work of Fried, Greenwood, Tyler, and others, [2-5]. The table assumes that the seeing is typical for Mauna Kea, $r_0 = 20$ cm, $f_g = 50$ Hz at $\lambda = 0.55 \mu\text{m}$, and that the servo bandwidth has been adjusted to minimize the total rms wavefront error. The optimum bandwidth, in this case 57 Hz, is the result of a trade between servo bandwidth and the signal-to-noise ratio. Incidentally, bandwidth optimization can occur on-line as the seeing conditions vary simply by changing parameters in the controller software. Also shown in Table 1 is the budget for a hypothetical 900 degree-of-freedom system with three 20 Watt laser guide stars, which is the next logical upgrade in the direction of visible wavelength correction. The graph in Figure 1 shows the Strehl performance versus wavelength in the current and upgrade designs.

Table 1. Performance error budget for Keck adaptive optics system

Error Source	1 LGS, 349 DOF	3 LGS, 900 DOF
DM Fitting	115 nm	69 nm
Cone Effect	127 nm	80 nm
WF Measurement SNR	50 nm	50 nm
Servo Bandwidth	46 nm	49 nm
Total rms	184 nm	126 nm

The servo system has been designed to be an insubstantial source of wavefront error relative to fitting error and cone effect. This is accomplished by providing enough compute power for the 349 channel controller to operate at high bandwidth, and by carefully designing the compensation algorithms so as to best mimic

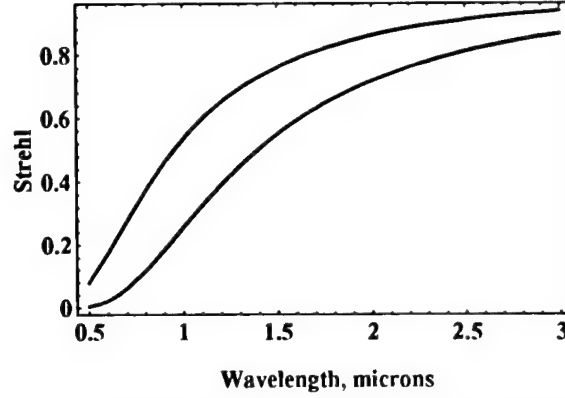


Figure 1. Strehl versus wavelength for the Keck laser guide star adaptive optics system. Bottom: current design with one laser guide star. Top: upgraded system with 3 laser guide stars.

the ideal servo assumed in the scaling law formula for rms servo error:

$$\sigma_{servo} = \frac{\lambda}{2\pi} \left(\frac{f_g}{f_c} \right)^{5/6} \quad (1)$$

Here f_c is the controller bandwidth and f_g is the Greenwood frequency. Greenwood frequency is specified at a given wavelength and this wavelength is substituted for λ in the formula above. Strehl contribution is given by $S = \exp[-(f_g/f_c)^{5/3}]$. The rms servo error is more fundamentally given by the integral over frequency of the controller's disturbance rejection function, $H(f)$, times the wavefront disturbance spectrum, $\Phi(f)$:

$$\sigma_{servo} = \int_0^\infty H(f) \Phi(f) df \quad (2)$$

Standard control law theory gives the disturbance rejection function as

$$H(f) = \|1 + L(f)\|^{-2} \quad (3)$$

where $L(f)$ is the cascade of all of the dynamics around the loop, including wavefront sensor stare time, sample and hold, compute delay, and hysteresis in the deformable mirror actuators. Disturbance rejection curves for the Keck system are shown in Figure 2. We have found that the unity gain crossover of $H(f)$ can be substituted for f_c in equation (1) to provide a reasonable approximation to the integral.

Figure 3 shows how the unity gain crossover of the disturbance rejection function (i. e. control bandwidth) varies as a function of compute delay and sample time. To obtain a bandwidth of greater than 100 Hz it is necessary to sample at 1000 Hz and have a compute delay of less than 800 μ s. This same compute delay and a sample rate of 500 Hz will give a control bandwidth of about 60 Hz.

This work was performed under the auspices of the U. S. Department of Energy by the Lawrence Livermore National Laboratory under contract number W-7405-eng-48 and under contract with the California Association for Research in Astronomy.

References

- 1 D. T. Gavel, J. R. Morris, and R. G. Vernon, *Systematic Design and Analysis of Laser Guide Star Adaptive Optics Systems for Large Telescopes*, *JOSA-A*, 11, 2, February, 1994, 914-924.

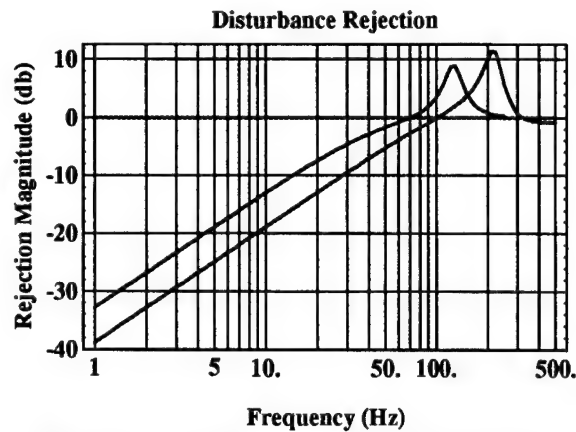


Figure 2. Wavefront controller disturbance rejection curves assuming compute delay is $\tau = 800 \mu\text{s}$ and sample periods of $T = 2 \text{ ms}$ (top) and $T = 1 \text{ ms}$ (bottom).

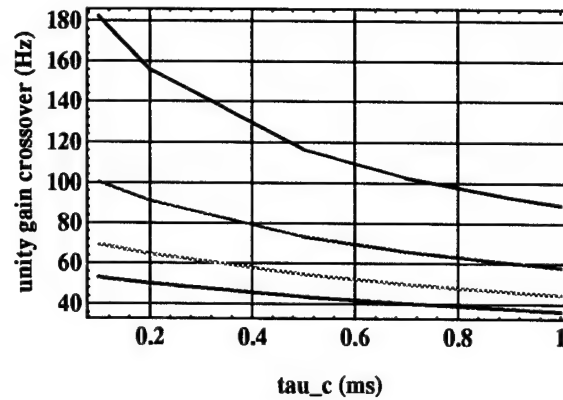


Figure 3. Crossover frequency vs compute delay for sample times (top to bottom) $T = 1, 2, 3,$ and 4 ms .

- 2 D. Fried, *Statistics of a Geometric Representation of Wavefront Distortion*, JOSA, 55, 11, November 1965, 1427-1435.
- 3 D. Greenwood, *Bandwidth Specification for Adaptive Optics Systems*, JOSA, 67, 3, March, 1977, 390-393.
- 4 G. Tyler, *Turbulence-induced Adaptive-optics Performance Degradation: Evaluation in the Time Domain*, JOSA-A, 1, 3, March, 1984, 251-262.
- 5 G. Tyler, *Rapid Evaluation of d_0 : the Effective Diameter of a Laser-Guide-Star Adaptive-Optics System*, JOSA-A, 11, 1, January, 1994, 325-338.

Adaptive Optics Specification for a 10m Telescope on the ORM

Nicholas Devaney, Instituto de Astrofísica de Canarias, Tenerife, Spain

The Spanish astronomical community has decided to build a 10m telescope employing a segmented primary mirror in the Observatorio del Roque de los Muchachos (ORM) on the island of La Palma in the Canary Islands. The telescope will incorporate an Adaptive Optics (AO) facility and work is underway to specify the requirements for this system. The AO requirements are being drawn up at this early stage so that they may be taken into account in the detailed optical and mechanical design of the telescope. In particular, the ability to carry out AO at the shortest wavelengths feasible should not be limited by errors in the phasing and tilting of the primary mirror segments. The form of the PSF and the Strehl ratio dependence on these errors is examined by Fourier transforming a simple simulation of the segmented mirror. The simulation includes inter-segment correlation of the piston errors.

Other considerations for the telescope design include the optical quality at scales smaller than the deformable-mirror actuator size, and of course the amplitude of aberrations should not limit the range of the atmospheric correction. An important issue is the possibility of carrying out the correction at an adaptive secondary, thus lowering emissivity. A Gregorian configuration allows the possibility of measurement of the mirror surface independently of the primary mirror. However the telescope tube (and dome) would need to be larger, thus significantly increasing the cost of the telescope. If the telescope is optimised for a fast focal ratio (e.g. for wide-field imaging in the visible) then the off-axis aberrations may limit performance even more severely than isoplanatic errors when the AO uses a small (slow) secondary.

The mechanical specifications of the telescope must minimise errors due to flexure or vibrations and measures will be taken to eliminate dome seeing.

Models of turbulence and data from radiosonde measurements are used together with the formulae of Sasiela (1994) to predict the various error variance terms arising in the AO system. These allow determination of AO performance, including limiting magnitude of guide stars and sky coverage (using the Galaxy models of Wainscoat et al.). It is clear that at least one laser guide star will be necessary to allow significant sky coverage. The likely focal anisoplanatism is being studied in order to determine how many guide stars a 10m telescope would require. Such a system requires a laser laboratory in the telescope building with provisions for beam transport and launching (probably from behind the secondary mirror).

References

- Sasiela, R.J., 1994, "Electromagnetic Wave Propagation in Turbulence -- Evaluation and Application of Mellin Transforms", Springer series on Wave phenomena, Springer-Verlag
- Wainscoat, R.J., Cohen, M., Volk, K., Walker, H.J., Schwartz, D.E., "A model of the 8-25 micron point source infrared sky", 1992, *Ap.J.*, **83**,111-146

SUBARU ADAPTIVE OPTICS PROGRAM

Hideki Takami, Masanori Iye, Naruhisa Takato

National Astronomical Observatory, 2-21-1 Osawa, Mitaka, Tokyo 181 Japan

Tel: 81-422-34-3856

Fax: 81-422-34-3864

Masashi Otsubo

The Graduate University for Advanced Studies, 2-21-1 Osawa, Mitaka, Tokyo 181, Japan

Koji Nakashima

Department of Astronomy, the University of Tokyo, 2-11-16 Yayoi, Bunkyo, Tokyo 113, Japan

1. Introduction

SUBARU telescope is being constructed atop Mauna Kea in the Hawaii island. It employs an 8.2 m thin-meniscus primary mirror that is supported by 261 actuators and 3 fixed points and will provide an almost perfect surface figure for the near infrared imaging. Under such circumstances, the atmospheric turbulence will become the dominant source of image degradation. Therefore, an adaptive optics (hereafter AO) system is essential in attaining the high resolution imaging capability for large ground-based telescopes.

We are building our first SUBARU AO system relying on natural guide stars, but will eventually be upgraded to a LGS based system. The LGS technology is still not mature, now not allowed to use at Mauna Kea, and we can do many scientific observations in several years even with a limited sky coverage. The system is optimized for near-infrared wavelength with relatively smaller number of control elements. Considering the fairly good seeing of Mauna Kea, 0.45 arcsec in average, it is possible to obtain the Strehl ratio greater than 0.6 at the K band, even by such a lower order compensation system. The scheduled completion date is early 1998, to be in time for the engineering first light of SUBARU. We are building a prototype system that is nearly identical with the real system, and will test it using the 1.6 m IR simulator telescope at Mitaka, Japan.

2. Overview of SUBARU Cassegrain AO system

The SUBARU Cassegrain AO unit will be set at about 500 mm above the telescope focus and will be mounted inside the peripheral optics tube with the inner diameter of 1.5 m. The

wavefront sensor unit will be attached directly to scientific instruments to reduce the mutual mechanical flexure (Fig. 1).

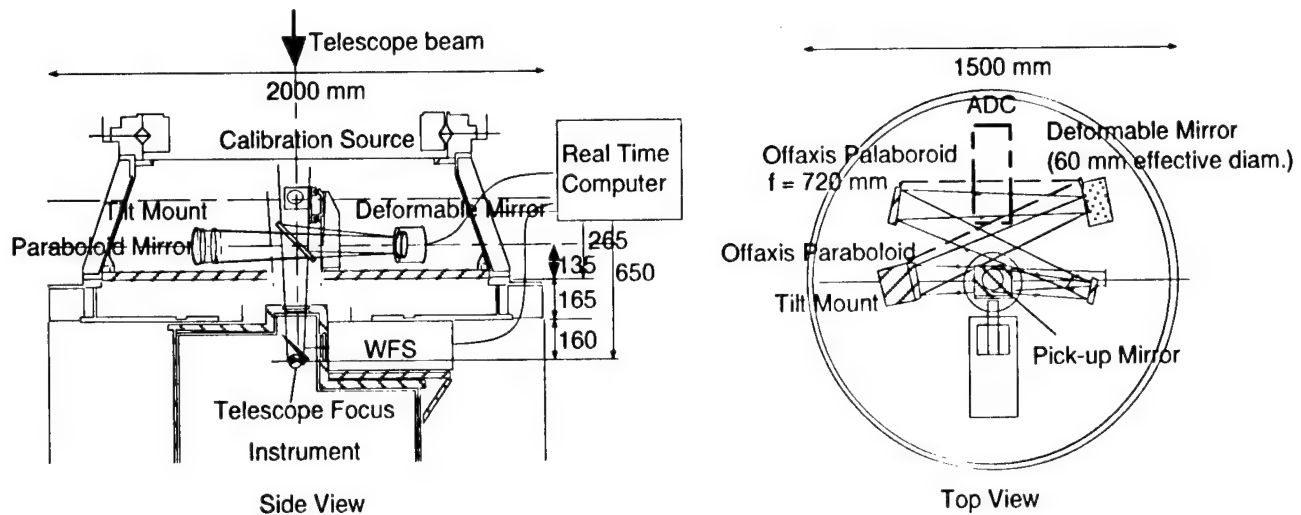


Fig. 1. Layout of SUBARU AO system. Left: Side view of the Cassegrain focus unit. The WFS is directly mounted with scientific instruments. Right: Top view of the AO optics. The optics is composed of a pair of offaxis paraboloids to cancel coma, astigmatism aberrations, and providing 2 arcmin wide field of view.

Table 1. Specification of SUBARU Cassegrain AO system

Spectral coverage:	1 - 5 μm (Optics covers from visible to mid-infrared)
WFS:	Curvature sensor with 36 photon counting APD modules
Deformable mirror:	Bimorph mirror with 36 control elements
Beam diameter:	60 mm
Focal length:	720 mm
F ratio:	12.4
FOV:	>2 arcmin. coverage of optics, tip/tilt correction 20 arcsec. higher order AO compensation
Control bandwidth:	> 100 Hz (1 k corrections / sec)

Specifications of the system are listed in table 1. The spectral coverage of the system is optimized for 1 to 5 μm , while the optics itself transmits from visible to mid-infrared light.

Combination of two off-axis paraboloids with identical focal length (720 mm) and off-axis angle (24 deg) cancels coma and astigmatism aberrations providing a field of view larger than 2 arcmin. A deformable mirror is placed between those two paraboloid. All the optical components are mounted

on a flat bench. The field of view for higher order compensation assumed to be about 20 arcsec, which corresponds to the typical isoplanatic angle and also the FOV of 1024 x 1024 IR array detector when adequate pixel sampling for diffraction limited imaging is made.

We employ a wavefront curvature sensor, with 36 avalanche photo-diode photon-counting modules having 80 % photon counting efficiency (table 2). The deformable mirror will be piezoelectrically driven by 36 bimorph control electrodes (table 3). The effective diameter of the bimorph mirror is 60 mm. The control closed loop matrices are nearly diagonal for this combination of the curvature sensor and bimorph mirror with matched electrodes geometry.

The maximum control bandwidth will be higher than 100 Hz, which corresponds to APD sampling speed of about 2 kHz. One of the paraboloid mirrors is mounted on a tilt control unit for tip/tilt correction. The secondary mirror of SUBARU telescope can also be used for tip/tilt correction.

Table 2. Specifications of the wavefront sensor

Type:	Curvature sensor
Number of elements:	36
Detector:	Photon counting avalanche photodiode modules SPCM-AQ produced by EG&G
Photon counting efficiency:	80 % at 0.63 mm
Saturating counting rate:	2×10^7 counts / sec
Dark counts:	< 150 counts / sec
Lens array:	37 (the central lenslet is not used) Subaperture diameter of 0.7 mm

Table 3. Specifications of deformable mirror.

Mirror type:	Bimorph
Electrodes:	36
Effective aperture size:	60 mm
Surface quality:	< $1/20 \lambda$ rms. at $0.632 \mu\text{m}$
Mirror curvature stroke:	> ± 0.05 / m
Response:	> 300 Hz at -3 dB

Progress Toward the 6.5-m MMT Infrared Adaptive Optics System

M. Lloyd-Hart, J.R.P. Angel, D.G. Sandler,
Center for Astronomical Adaptive Optics, University of Arizona, Tucson, AZ 85721
<http://athene.as.arizona.edu:8000/caao/>
Voice:(520) 621-8353 Fax:(520) 621-9843

P. Salinari,
Osservatorio Astrofisico di Arcetri, Largo Enrico Fermi 5, 50125, Firenze, Italy

D. Bruns, T.K. Barrett
ThermoTrex Corp. 9550 Distribution Av., San Diego, CA 92121

Introduction

In late 1996, the existing six mirrors of the Multiple Mirror Telescope (MMT) will be replaced by a single 6.5-m mirror, which is now being polished at the Steward Observatory Mirror Lab. Earlier work [1, 2] has shown that an adaptive optics system using a single sodium laser projected co-axially with the telescope can provide imaging at the diffraction limit in the H and K photometric bands over most of the sky. In the design of the system for the 6.5-m, we will project a 4-W beam from a continuous-wave dye laser from a refractive launch telescope [3] located behind the secondary mirror. Returning light will be corrected for the effects of atmospheric turbulence at the secondary mirror, which will be a 2-mm thick continuous facesheet whose shape can be modified at 1 kHz update rate by 300 voice-coil actuators. The major components of the system are shown in the schematic of Figure 1.

System design

Optics and detectors. To take advantage of the maximized optical throughput and reduced background emission offered by the adaptive secondary approach, corrected light is brought directly from the secondary to the science dewar. The entrance window is a dichroic beamsplitter which transmits infrared light to the imaging array (a 1024×1024 InSb detector), and reflects visible light to the wavefront sensor. Within the science dewar is a second, small-format, infrared array which is operated in the wavelength range 1.2 to $2.3 \mu\text{m}$ as a quadrant detector to provide global wavefront tilt information. The advantage of using infrared wavelengths to measure overall tilt has been previously discussed [1].

The wavefront sensor (WFS) is a Shack-Hartmann type with 150 subapertures feeding light to a 4-port CCD operated at 250 kHz per port pixel rate, giving updates to the secondary at 1 kHz. The whole WFS optical assembly is mounted on a precision translation table to accommodate changes in the distance to the sodium layer with zenith angle, and the distinct focal plane required when using a natural reference source.

Adaptive secondary mirror. The secondary mirror is a sandwich of three layers. Firstly, the deformable surface is made from a 2-mm thick Zerodur shell supported mechanically by a single bolt attached to a membrane in the center. On the back of the shell are 300 small magnets; the back surface is also aluminized to form a common plate for 300 capacitors which directly measure the mirror displacement at each actuator.

The second layer is a thick spherical reference surface, also of Zerodur, pierced by 300 holes

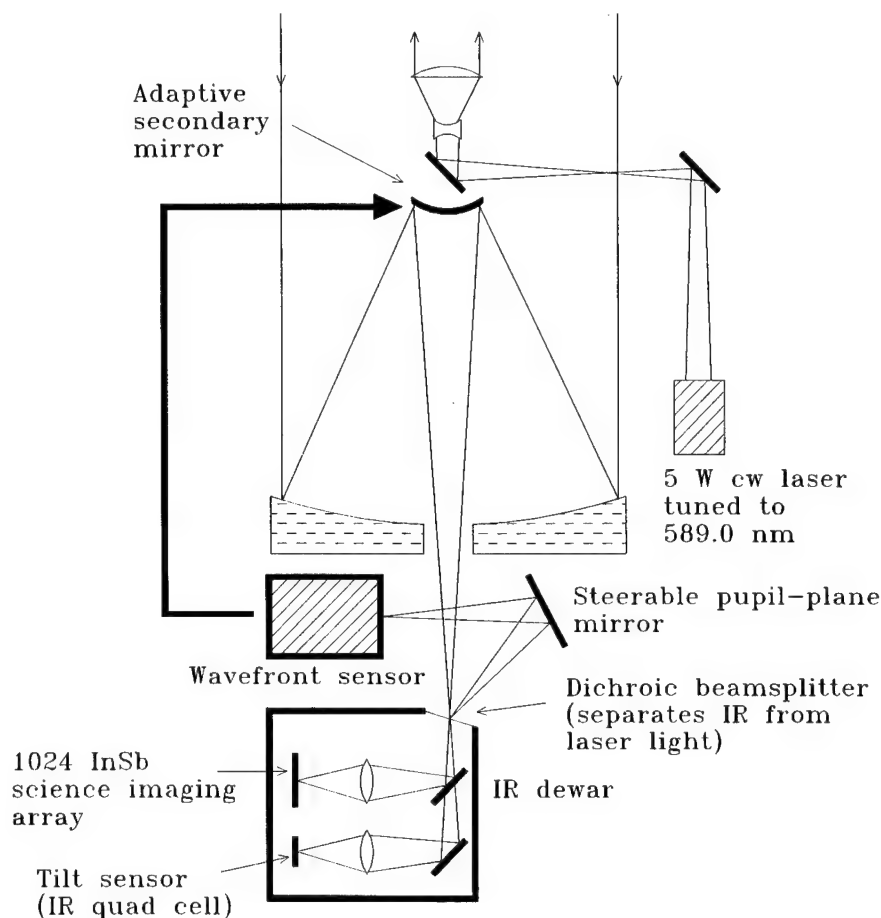


Figure 1. Schematic view of the 6.5-m adaptive optics system.

which accept the cold fingers supporting the voice coils which drive the mirror. Around each hole is a metallized ring which forms the second plate of the capacitive sensor. Heat from the coils is transported back up the cold fingers to the third layer, a thick aluminum plate to which the cold fingers are rigidly attached. The plate forms the heat sink for the actuators; glycol circulating through pipes hidden behind the arms of the secondary support spider removes the heat. Also attached to the aluminum are miniaturized electronic circuit boards carrying the voice-coil drivers and capacitive sensor electronics.

Digital control. Slope data from the WFS are reconstructed by a custom-built VME-based computer. The reconstructor matrix can accept a data vector containing up to five measurements from the WFS to allow for possible prediction based on spatial and temporal correlation of the wavefront. Once a set of actuator commands has been sent to the adaptive secondary, local feedback provided by the capacitive sensors ensures that the mirror surface responds in the shortest possible time. To defeat unwanted resonances in the thin facesheet, the local control will be implemented digitally. Each actuator has its own DSP built into the local circuitry, and communicates with the DSPs of neighboring actuators. The algorithm to filter the actuator signal can then readily be optimized.

Sodium laser. A new ring dye laser has been developed, pumped by a 25-W argon ion laser

operating in all-lines mode. Frequency stabilization and the optical diode required for ring laser operation are both provided by a sodium-vapor Faraday cell. The laser delivers about 4 W of power at the sodium D₂ line, sufficient to create an artificial beacon as bright as a star with V magnitude ~9. This laser is currently in use with the FASTTRAC II system for the MMT discussed below.

Prototype Systems

Two major efforts are underway to test components and system design strategies in prototype form. The first of these is a series of small-scale flat and curved mirrors, populated with up to 25 actuators, designed to test issues of force and power requirements and heat dissipation. Results are reported at this conference by Bruns et al.

The second effort is the operational adaptive optics system for the present MMT, FASTTRAC II, which is now producing results at moderate resolution on a routine basis. A summary of the science to come out of that system is presented by Groesbeck et al. at this conference. The adaptive beam combining mirror which FASTTRAC II uses to make corrections employs the same type of actuators, and the same capacitive feedback sensors to be used in the adaptive secondary. In addition, the optical layout was designed to duplicate as far as possible the layout of the 6.5-m system. The architecture of the computer software is designed to approach as closely as possible the ideal of one-touch operation, where almost all the decision-making about, for instance, the optical configuration of the system and the choice of guide star is left to the computer.

Acknowledgment

This work has been supported by the Air Force Office of Scientific Research under grant number F49620-94-1-00437.

References

- [1] D. G. Sandler, S. Stahl, J. R. P. Angel, M. Lloyd-Hart, D. W. McCarthy, 1994, "Adaptive optics for diffraction-limited infrared imaging with 8-m telescopes," *JOSA A* 11, 92
- [2] M. Lloyd-Hart et al., 1995, "Adaptive optics experiments at the MMT using sodium laser guide stars," *ApJ* 439, 455
- [3] B. P. Jacobsen et al., 1994, "Field evaluation of two new continuous-wave dye laser systems optimized for sodium beacon excitation," *Proc. SPIE conf. on Adaptive Optics in Astronomy*, ed. M. A. Ealey & F. Merkle, 2201, 342

Sodium Laser Guide Star Observations with FASTTRAC II

T. D. Groesbeck, M. Lloyd-Hart, J. R. P. Angel, D. W. McCarthy, Jr.,
G. Brusa, P. M. Gray, B. A. McLeod, S. Mohanty, T. Martinez,
B. Jacobsen, D. M. Wittman, & P. T. Ryan

Center for Astronomical Adaptive Optics, Steward Observatory
University of Arizona, Tucson, AZ, 85721
tel. 520-621-1539 *fax* 520-621-9843

D. G. Bruns & D. G. Sandler

ThermoTrex Corporation, 9550 Distribution Ave., San Diego, CA 92121

The Center for Astronomical Adaptive Optics (CAAO) at the University of Arizona is developing a diffraction-limited adaptive optics (AO) system at infrared wavelengths utilizing a sodium laser guide star. This system (Lloyd-Hart et al., this conference), based on an adaptive secondary mirror with 300 actuators, will be placed in operation following the installation of the 6.5 m mirror upgrade at the Multiple Mirror Telescope (MMT) mount. As an interim step, we have built an adaptive optics system which provides tip-tilt correction for each of the 6 individual beams of the current MMT. This instrument, called FASTTRAC II, will produce a combined image at the diffraction limit of the 1.8 m primary mirrors ($\lesssim 0.3''$ at $2.2 \mu\text{m}$) yielding moderately high resolution images in the near infrared. The current system incorporates the design philosophy of the 6.5 m system and provides a testbed for development of the system components in addition to serving as a significant scientific instrument in its own right.

A major goal of our development efforts has been to avoid the introduction of any additional optical surfaces, particularly at ambient temperature, into the beam path before the science detector. We therefore replace one of the existing elements in the telescope with an adaptive element, namely the adaptive secondary for the 6.5 m system or the adaptive beam combiner for FASTTRAC II. The six 1.8 m primary mirrors of the current MMT are arranged in a hexagonal configuration and the six beams are folded to the center by tertiary flat mirrors after reflecting off the secondaries. The beams are then directed downward to a common focus by the six facets of a beam combiner pyramid. For FASTTRAC II, the facets of the adaptive beam combiner are independently controllable in tip and tilt, and the infrared science instrument is located at the Cassegrain focus with no intervening optical surfaces. The entire AO system is mounted with the science camera on the telescope and has therefore been engineered so as to overcome such challenges as varying gravitational and wind loading and thermal variations. As FASTTRAC II displaces the normal MMT acquisition system when mounted, we have also included our own acquisition system as a part of the instrument.

A second part of our design philosophy has been to maximize the sky coverage available for observations by implementing a sodium laser guide star as part of our adaptive optics system. A CW dye laser tuned to the sodium D2 line at 589 nm is projected along the telescope axis to form a subarcsecond artificial beacon. The system has produced 3.2 W of tuned laser power in recent experiments at the MMT. The brightness of the laser return spot was equivalent to a natural star of magnitude 9.6 seen through an R band filter. This power level corresponds to the anticipated requirements for the future AO system for the 6.5 m telescope and is more than sufficient for the FASTTRAC II system with its lower bandwidth and larger subapertures.

The key elements of FASTTRAC II are 1) the beam combiner; 2) the steering mirror which allows the desired guide star to be selected; 3) the wavefront sensor; and 4) the global tilt sensor for operation in the laser guide star mode. As noted above, the beam combiner facets may be independently controlled in tip and tilt. Capacitive displacement sensors provide high resolution position information (± 10 nm rms) while voice coil actuators are used to drive the mirrors to their commanded position. A complete description of the beam combiner has been given elsewhere (Close et al., *Adaptive Optical Systems and Applications*, ed. R. K. Tyson & R. Q. Fugate, Proc. SPIE 2534, 105–115). The IR science camera, located immediately below the beam combiner, uses a tilted dichroic flat as its entrance window which transmits $\geq 95\%$ of the infrared light ($1.2\text{--}2.5\text{ }\mu\text{m}$) while reflecting $\geq 95\%$ of the visible light ($0.4\text{--}1.1\text{ }\mu\text{m}$). A relay lens (with a $3.9'$ field of view) then forms an image of the pupil at the location of the steering mirror. By tilting the steering mirror, any point within the field may be aligned with the optical axis of the Shack-Hartmann wavefront sensor. In this manner, any suitable point source within the field may be selected as the guide star while keeping the desired object centered in the science camera.

Because the primary mirrors of the MMT form the subapertures of our AO system, six images of the guide star are formed on the wavefront sensor CCD. A custom built lenslet array maps the hexagonal pupil geometry onto the square geometry of the CCD in such a way that the images of on-axis collimated light are located precisely at the intersections of pixel boundaries at the centers of separate quad cells. When the AO loop is closed, the beam combiner facets are driven so as to center the images of the guide star on the quad cells; this results in the six beams being well-stacked and focused on the IR science camera. The computer which controls the WFS CCD provides the input signals to the electronics controlling the beam combiner facets.

When FASTTRAC II is operated in its laser guide star mode, the above elements remain as integral parts of the system while a global tilt sensor and a combined science/acquisition camera for visible wavelengths are added. A dichroic flat which reflects a narrow range (<25 nm wide) of wavelengths centered on the sodium D2 line is inserted into the beam at the position of the steering mirror, thus bringing the artificial guide star into the WFS, while the remaining visible light is transmitted. The steering mirror itself is moved ~ 5 cm further along the transmitted light path, where it directs the beam into the tilt channel. A small prism is located at the center of an image plane in this channel, where it reflects the tilt guide star (as selected using the steering mirror) to the tilt sensor, which is a CCD operated as a single quad cell. The $3.9'$ field (minus a $\sim 5''$ patch obscured by the prism) is reimaged onto the science/acquisition CCD. When operating in the laser guide star mode, this camera is able to take advantage of the partial correction at optical wavelengths, allowing us to obtain simultaneous visible and IR images of an object.

A unified computer control system has been developed for FASTTRAC II, allowing a single user to control the various motions of the instrument, and adjust the AO loop parameters. A graphical user interface permits the operation of the system from an X terminal, or a series of commands may be entered into a text file as a script which is then read by the user interface. Independent subsystems which control the WFS CCD and the IR science camera share data with the system computer over network connections. The beam combiner receives its input directly from the WFS CCD computer, bypassing the network; this approach is used for all time-critical tasks. The system computer is also linked with the telescope mount computer. Because the MMT uses an altazimuth mount, the entire instrument assembly rotates as an object is tracked across the sky. However, the WFS is linked to the pupil geometry which does not rotate, so the WFS lenslet array and camera must be rotated to compensate for the instrument rotation. The WFS must also be translated axially in order to focus correctly on the laser beacon at an altitude of ~ 90 km. All of the tracking motions (WFS focus and rotation, steering adjustments compensating for gravitational deflections) are automatically maintained by the computer system during observations.

In several observing runs at the MMT during the past year, FASTTRAC II has performed well, producing a reduction in spot size from $0.8''$ to $0.5''$ FWHM and a corresponding increase in Strehl

ratio from 0.08 to 0.2 despite still being under development. During this time, we have utilized its capabilities in brown dwarf searches; we were easily able to detect Gliese 229 B in December 1995 with the adaptive loop turned on, while only the primary star was evident in uncorrected images. In April 1996, we will return to the MMT for a variety of astronomical observations utilizing the now complete system for both natural and artificial guide star operations. This will be the first test of FASTTRAC II as a facility instrument available to Steward Observatory astronomers. We will present further engineering and scientific results from these observations.

**Lick Observatory Laser Guide Star
Adaptive Optics System Commissioning**

Scot S. Olivier, Jong An, Kenneth Avicola, Horst D. Bissinger,
James M. Brase, Herbert W. Friedman, Donald T. Gavel,
Bruce Macintosh, Claire E. Max, Kenneth E. Waltjen

Imaging and Detection Program
Lawrence Livermore National Laboratory
L-437, P.O. Box 808
Livermore, CA 94551-9900
Phone: (510) 423-6483
Fax: (510) 422-3358

Introduction

A sodium-layer laser guide star adaptive optics system has been developed at Lawrence Livermore National Laboratory (LLNL) for use on the 3 meter Shane Telescope at Lick Observatory located on Mount Hamilton, near San Jose, California. The system is based on a 127-actuator continuous-surface deformable mirror, a Hartmann wavefront sensor equipped with a fast-framing low-noise CCD camera, and a pulsed solid-state-pumped dye laser tuned to the atomic sodium resonance line at 589 nm. Figure 1 shows a picture of the laser beam being projected from the dome of the Shane Telescope.

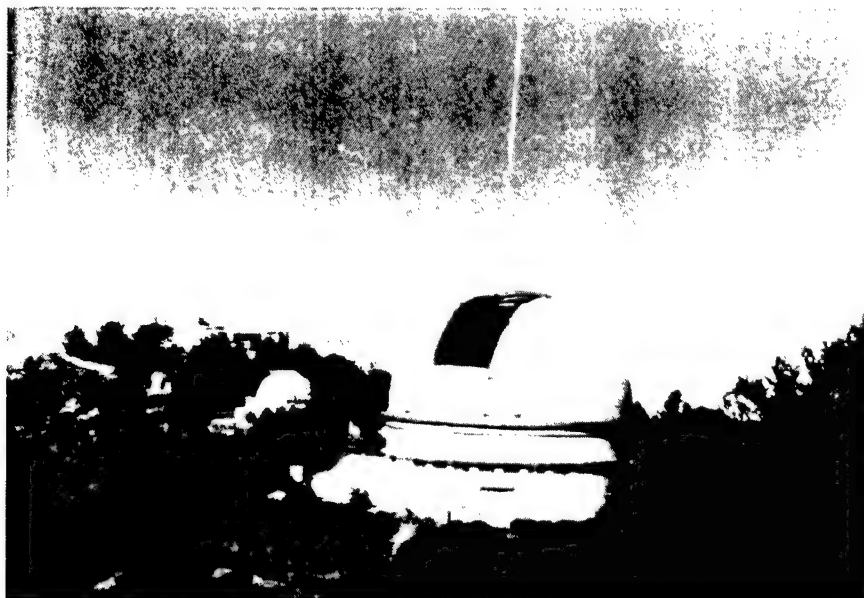


Figure 1 - Beam from LLNL laser guide star system projected out of the dome of the 3 meter Shane Telescope at the University of California's Lick Observatory located on Mt. Hamilton, California

Adaptive Optics System Description

The prototype Lick adaptive optics system^{1,2} is mounted at the f/17 Cassegrain focus of the 3 m telescope. The system can feed both an optical 1024x1024 CCD camera and a near-IR 256x256 NICMOS III camera.

The deformable mirror, built by LLNL, has 127 actuators arranged in a triangular pattern. In the current configuration, 61 of the actuators are actively controlled. A separate mirror, built by Physik Instrumente, is used to correct the overall wavefront tip-tilt.

The Shack-Hartmann wavefront sensor has 37 subapertures in the clear aperture of the telescope. The subapertures have a diameter of 44 cm mapped to the telescope primary mirror, and are also arranged in a triangular pattern to match the deformable mirror actuators. The wavefront sensor camera, built by Adaptive Optics Associates, has a 1.2 kHz maximum frame rate, and uses a 64x64 CCD, built by Lincoln Laboratory, with 12 electrons read noise.

The wavefront control computer is a 160 Mflop Mercury VME system with 4 I860 processors. The control system can be operated at a sample rate of up to 500 Hz and provides a control bandwidth of about 30 Hz including the effects of camera integration and readout time as well as the compute time and the transfer time to the deformable mirror drivers.

A separate tip-tilt sensor is necessary when the wavefront sensing is done using the laser guide star. The tip-tilt sensor uses four photon-counting avalanche photo-diodes operated as a quad cell.

Adaptive Optics Test Results

The prototype adaptive optics system has been tested on the Shane Telescope using natural reference stars yielding up to a factor of 12 increase in image peak intensity and a factor of 6.5 reduction in image full width at half maximum (FWHM)³.

Laser Guide Star System Description

The Lick laser guide star system^{4,5} uses a set of flash-lamp-pumped frequency-doubled solid-state (Nd-Yag) lasers to pump a dye laser. The pump lasers are located in a room below the floor of the Shane Telescope dome and are fiber-optically coupled to a dye laser that is mounted on the south side of the Shane Telescope. The dye laser produces light that can be tuned to the atomic sodium resonance line at 589 nm. The dye laser light is projected into the sky by a refractive launch telescope with a 30 cm primary lens that is also mounted on the south side of the Shane Telescope.

Laser Guide Star Test Results

The laser guide star system has been tested on the Shane Telescope⁶. The highest power achieved out of the dye power amplifier is 20 W. The pulse FWHM is 100 ns, and the pulse repetition rate is 11 kHz. The laser typically operates at about 15 W.

The size of the guide star produced in the mesospheric sodium layer by the laser guide star system has been measured to be 1.8 arc seconds for a 10 second exposure. The seeing during this measurement was 1.3 arc seconds, so the laser guide star size was consistent with the seeing given that the laser light must go through the atmosphere twice. The diffraction-limited size of the guide star in the sodium layer is 0.6 arc seconds, so the laser guide star should get as small as 1.0 arc seconds for long exposures in 0.5 arc second seeing.

The return signal from the laser guide star has been measured to be up to 0.26 photons per square cm per ms for an output power of 15 W. This corresponds to a V magnitude of 9.0.

Laser Guide Star Adaptive Optics Test Results

Using the laser guide star, the adaptive optics system has reduced the wavefront phase variance on scales above 44 cm by a factor of 4. These results represent the first high-order wavefront phase correction using a sodium-layer laser guide star⁷.

Assuming tip-tilt is removed using a natural guide star, the measured control loop performance should produce images with a Strehl ratio of about 0.4 at 2.2 microns in 1 arc second seeing. Additional

calibration procedures are now being implemented in order to achieve better imaging results with the prototype Lick adaptive optics system when using the sodium-layer laser guide star. Commissioning runs are currently scheduled for the Spring of 1996, and the results will be presented at this conference.

Acknowledgments

Work performed under the auspices of the U.S. Department of Energy by Lawrence Livermore National Laboratory under Contract W-7405-Eng-48.

References

1. "Performance of Adaptive Optics at Lick Observatory", S. S. Olivier, J. An, K. Avicola, H. D. Bissinger, J. M. Brase, H. W. Friedman, D. T. Gavel, E. M. Johansson, C. E. Max, K. E. Waltjen, W. Fisher, and W. Bradford, 1994, Proc. SPIE 2201, p. 1110.
2. "Adaptive Optics at Lick Observatory: System Architecture and Operations", J. M. Brase, J. An, K. Avicola, H. D. Bissinger, H. W. Friedman, D. T. Gavel, B. Johnston, C. E. Max, S. S. Olivier, R. Presta, D. A. Rapp, J. T. Salmon, K. E. Waltjen, and W. Fisher, 1994, Proc. SPIE 2201, p. 474.
3. "Performance of Laser Guide Star Adaptive Optics at Lick Observatory", S. S. Olivier, J. An, K. Avicola, H. D. Bissinger, J. M. Brase, H. W. Friedman, D. T. Gavel, C. E. Max, J. T. Salmon, and K. E. Waltjen, 1995, Proc. SPIE 2534, p. 26.
4. "Design of a Fieldable Laser System for a Sodium Laser Guide Star", H. Friedman, G. Erbert, T. Kuklo, T. Salmon, D. Smauley, G. Thompson, and N. Wong, 1994, Proc. SPIE 2201, p. 352.
5. "Sodium Beacon Laser System for the Lick Observatory", H. W. Friedman, G. V. Erbert, T. C. Kuklo, J. G. Malik, J. T. Salmon, D. A. Smauley, G. R. Thompson, and N. J. Wong, 1995, Proc. SPIE 2534, p. 150.
6. "A Sodium Guide Star Laser System for the Lick Observatory 3 meter Telescope", H. W. Friedman, G. V. Erbert, D. T. Gavel, T. C. Kuklo, J. G. Malik, J. T. Salmon, D. A. Smauley, G. R. Thompson, 1995, Proc. Optical Society America, in press.
7. "Initial Results from the Lick Observatory Laser Guide Star Adaptive Optics System", S. S. Olivier, J. An, K. Avicola, H. D. Bissinger, J. M. Brase, D. T. Gavel, B. Macintosh, C. E. Max, J. T. Salmon, and K. E. Waltjen, 1995, Proc. Optical Society America, in press.

Conceptual Design for a User-Friendly Adaptive Optics System at Lick Observatory

Horst D. Bissinger¹, Scot S. Olivier¹, Claire E. Max²

1 - Imaging and Detection Program
2 - Institute Geophysics & Planetary Physics
Lawrence Livermore National Laboratory
P.O. Box 808, M/S L-437
Livermore, CA 94551
Phone: (510) 422-6009
FAX: (510) 422-3358

Introduction

In this paper, we present a conceptual design for a general-purpose adaptive optics (AO) system, usable with all Cassegrain facility instruments on the 3 meter Shane telescope at the University of California's Lick Observatory located on Mt. Hamilton near San Jose, California. The overall design goal for this system is to take the sodium-layer laser guide star adaptive optics technology out of the demonstration stage and to build a user-friendly astronomical tool. The emphasis will be on ease of calibration, improved stability and operational simplicity in order to allow the system to be run routinely by observatory staff.

A prototype adaptive optics system^{1,2,3,4} and a 20 watt sodium-layer laser guide star system^{5,6,7} have already been built at Lawrence Livermore National Laboratory (LLNL) for use at Lick Observatory. The design presented in this paper is for a next-generation adaptive optics system that extends the capabilities of the prototype system into the visible with more degrees of freedom. When coupled with a laser guide star system that is upgraded to a power matching the new adaptive optics system, the combined system will produce diffraction-limited images for near-IR cameras. Atmospheric correction at wavelengths of 0.6 - 1 μm will significantly increase the throughput of the most heavily used facility instrument at Lick, the Kast Spectrograph, and will allow it to operate with smaller slit widths and deeper limiting magnitudes.

Description of existing prototype Lick AO system

The engineering tests of the prototype AO system using natural reference stars began at Lick Observatory on the 1 meter Nickel telescope in the Fall of 1993² and on the 3 meter Shane telescope in the Fall of 1994.³ The same prototype system also has served as the testbed for sodium-layer laser guide star adaptive optics experiments at Lick Observatory.⁴ The prototype AO system has provided us with valuable experience in design and engineering of the optical and control systems, specifically in alignment, calibration and operation of adaptive optics on astronomical telescopes.

The prototype AO system uses a Hartmann wavefront sensor, with a triangular array of 37 subapertures in the clear aperture of the 3 meter telescope. Subapertures have a diameter of 43.6 cm mapped onto the telescope primary. Images from the hex-shaped lenslets are recorded using a high-quantum-efficiency CCD camera built by Adaptive Optics Associates using a Lincoln Laboratory 64x64 chip with 27x27 μm pixels.

The deformable mirror is LLNL built with a triangular array of 127 electrostrictive lead magnesium niobate (PMN) actuators. Currently, 61 actuators are actively controlled and 66 are kept fixed since they lie outside the clear aperture of the telescope.

The tip-tilt system uses a set of four photon-counting avalanche photodiodes operated as a quad cell, and a small (2.5 cm) tip-tilt mirror.

The entire prototype AO system is taken apart for transportation to and from the LLNL for each observing run. Assembly, realignment and calibration requires almost 16 hours before initial observations can begin. The Lick laser guide star is based on the sodium resonance principle⁸ and generates the guide star at 589 nm. The laser guide star system, including the dye pump, diagnostic and control electronics, beam expanding telescope and FAA-certified safety system, is already mounted to the 3 meter telescope.

The laser was first propagated to the mesosphere in May 1995 and the first guide star characterized in July 1995. The photon return signal is ≈ 0.2 photons/cm²/msec at the top of the telescope which corresponds to a ninth magnitude visible star. This signal is adequate for the present prototype AO system but inadequate for the new proposed 349 actuator deformable mirror. For the latter, a laser power of roughly 50 W is needed to maintain a sufficient signal level.

Conceptual design of new adaptive optics user instrument

The new Lick adaptive optics user instrument is intended to be an evolutionary extension of the prototype AO system in the sense that many aspects of the optical design, calibration techniques, and control system design will be carried over. Significant upgrades will be made in several specific areas. Three of these areas are addressed in the conceptual design described in this paper:

- 1) the opto-mechanical structure will be larger and more robust and permanently mounted on the telescope;
- 2) the number of controlled degrees of freedom will be increased to 349;
- 3) a telescope simulator and turbulence generator (turbulator) will be installed in order to allow calibration and operational testing of the system during day time hours.

Additional upgrades will be made in the areas of supervisory control and user interface software.

The goal of these upgrades is to produce a robust user-friendly AO system able to provide significant image improvement down to optical wavelengths, and to be used with a wide variety of infra-red and visible cameras and spectrographs. In addition the astronomer will have the ability to refuse the AO capability and use the same interface as before. This can be done by removing the tertiary and the last AO turning mirror. Figure 1 shows the conceptual opto-mechanical layout of the new Lick adaptive optics user instrument.

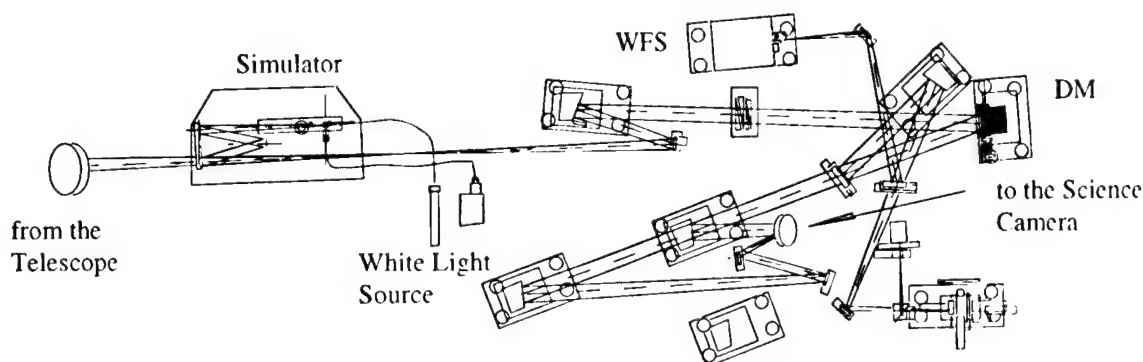
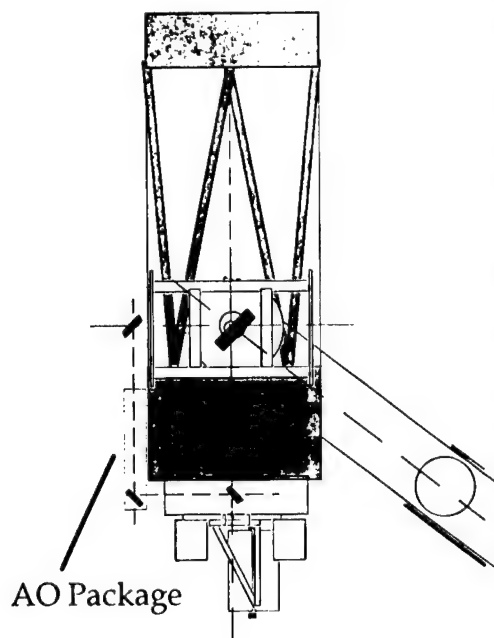


Figure 1 - preliminary layout of the Lick adaptive optics package

Light from the telescope tertiary mirror enters from the side and hits a turning mirror, the tip-tilt mirror, an off-axis parabolic collimating mirror, the 349-actuator deformable mirror, a broadband (450-600nm) dichroic beamsplitter, then an off-axis parabolic focusing mirror, to the science camera.

The reflected light from the dichroic beamsplitter is focused by an off-axis parabolic focusing mirror, a narrow band (589nm) dichroic beamsplitter reflects the sodium wavelengths to the wavefront sensor and transmits the rest of the light to the tip-tilt sensor and an image sharpening camera.



Wavelengths greater than $0.6 \mu\text{m}$ pass through the first dichroic beam splitter to the science camera leg. This consists of the focusing off-axis parabolic mirror and two turning mirrors which send the beam to the science instrument. The focusing off-axis mirror can be switched in order to change the f-number of the output beam from the nominal f/17 to any different f-number that is better suited to a specific science instrument. For instance the high-resolution IR camera currently being built by Prof. James Graham (UC Berkeley) currently requires an f/30 cone for optimal performance.

Figure 2 shows how the Lick adaptive optics user instrument will be mounted to the 3 meter Shane telescope. The AO system will be essentially transparent to the science instrument, in the sense that the f/17 output beam will have the same back focal length and output pupil position that the science instrument would see if it were mounted directly at the Cassegrain focus of the telescope.

The AO system will be based on a 349-actuator deformable mirror. The optical components (active and passive) will be increased in size in order to match the larger deformable mirror.

Figure 2 - Location of AO System and turning mirrors

To accomplish the transition to the routine use of adaptive optics laser guide stars systems in astronomical research, we will incorporate daytime alignment and calibration tools, and a user interface which will make it possible for the system to be calibrated and operated on a routine basis by only one or two people.

The Lick Observatory has important advantages as a development environment for this project. The laser (together with its FAA and environmental approvals) exists there today. The observatory is located within an hour and a half of UC Santa Cruz, UC Berkeley, and LLNL. It is easily accessible to astronomy faculty, engineering staff, and students.

Available astronomical instrumentation and performance enhancement.

Available instruments include the following. First, a near-infrared camera is being designed by Prof. James Graham of UC Berkeley, and will be built by Infrared Laboratories of Tucson. The camera will have a plate scale of 0.07 arc sec per pixel, matched to the diffraction limit of the 3 m telescope. The camera will be built around a 256x256 pixel NICMOS III array, sensitive from 1 to 2.5 μ m.

Second, Lick Observatory's LIRC-2 near-IR camera with a 0.13 arc sec pixel scale, is available for use in applications where slightly lower spatial resolution is optimum.

Third, the primary visible-light instrument will be the Kast Cassegrain spectrograph. The Kast is a two-channel device with a short-wavelength "blue" section and a longer-wavelength "red" section. Only the red section sensitive from 4000 to 11000 angstroms would be relevant to adaptive optics work. It uses gratings as dispersive elements, with resolution ranging from 4.6 to 1.2 Å per pixel with a 400x1200 pixel CCD and a plate scale of 0.78 arc sec per pixel.

Many scientific projects are not feasible under typical Lick Observatory seeing of 1 arc sec or greater, and will benefit from the routine availability of adaptive optics. Adaptive optics (AO) provides several advantages over normal seeing for optical and near infrared imaging and spectroscopy. The diffraction-limited core of the point spread function resulting from AO translates directly into an improved detection threshold for stellar objects, by increasing the contrast between object and background sky. AO provides a larger dynamic range for studies of faint objects near brighter neighbors. AO offers improved spatial resolution for detailed morphology studies, and even when there is only the beginning of a diffraction-limited core, AO can increase the signal to noise ratio for spectroscopy by allowing use of a smaller slit which admits less sky background.

Acknowledgements

Work performed under the auspices of the U.S. Department of Energy by Lawrence Livermore National Laboratory under Contract W-7405-Eng-48

References

1. "Adaptive Optics at Lick Observatory: System Architecture and Operations", J. M. Brase, J. An, K. Avicola, H. D. Bissinger, H. W. Friedman, D. T. Gavel, B. Johnston, C. E. Max, S. S. Olivier, R. Presta, D. A. Rapp, J. T. Salmon, K. E. Waltjen, and W. Fisher, 1994, Proc. SPIE 2201, p. 474.
2. "Performance of Adaptive Optics at Lick Observatory", S. S. Olivier, J. An, K. Avicola, H. D. Bissinger, J. M. Brase, H. W. Friedman, D. T. Gavel, E. M. Johansson, C. E. Max, K. E. Waltjen, W. Fisher, and W. Bradford, 1994, Proc. SPIE 2201, p. 1110.
3. "Performance of Laser Guide Star Adaptive Optics at Lick Observatory", S. S. Olivier, J. An, K. Avicola, H. D. Bissinger, J. M. Brase, H. W. Friedman, D. T. Gavel, C. E. Max, J. T. Salmon, and K. E. Waltjen, 1995, Proc. SPIE 2534, p. 26.
4. "Initial Results from the Lick Observatory Laser Guide Star Adaptive Optics System", S. S. Olivier, J. An, K. Avicola, H. D. Bissinger, J. M. Brase, D. T. Gavel, B. Macintosh, C. E. Max, J. T. Salmon, and K. E. Waltjen, 1995, Proc. Optical Society America, in press.
5. "Design of a Fieldable Laser System for a Sodium Laser Guide Star", H. Friedman, G. Erbert, T. Kuklo, J. T. Salmon, D. Smauley, G. Thompson, and N. Wong, 1994, Proc. SPIE 2201, p. 352.
6. "Sodium Beacon Laser System for the Lick Observatory", H. W. Friedman, G. V. Erbert, T. C. Kuklo, J. G. Malik, J. T. Salmon, D. A. Smauley, G. R. Thompson, and N. J. Wong, 1995, Proc. SPIE 2534, p. 150.
7. "A Sodium Guide Star Laser System for the Lick Observatory 3 meter Telescope", H. W. Friedman, G. V. Erbert, D. T. Gavel, T. C. Kuklo, J. G. Malik, J. T. Salmon, D. A. Smauley, G. R. Thompson, 1995, Proc. Optical Society America, in press.
8. "Atmospheric Turbulence Compensation by Resonant Optical Backscattering from the Sodium Layer in the Upper Atmosphere", W. Happer, G. J. MacDonald, C. E. Max, and F. J. Dyson, 1994, J. Optical Society of America A 11, p. 263.

The Palomar Adaptive Optics System

Richard G. Dekany

Jet Propulsion Laboratory, California Institute of Technology, 4800 Oak Grove Blvd., Pasadena, CA 91109

Abstract

Currently under construction at the Jet Propulsion Laboratory, the Palomar Adaptive Optics System (PALAO) is a Cassegrain-mounted system for infrared astronomy incorporating active laser metrology to minimize the effects of mechanical flexure.

System overview

The Jet Propulsion Laboratory began in January 1995 the design and construction of an adaptive optics system for the 5 meter Hale Telescope at Palomar Mountain. This instrument will be mounted at the Cassegrain focus of the telescope and optimized for scientific use in the infrared (K, H, and J-bands). The PALAO system has at its heart a Xinetics 349 actuator deformable mirror (DM) and utilizes JPL-developed skipper CCD technology for the Shack-Hartmann-based wavefront sensor camera. The wavefront sensor (WFS) is based upon a 16 x 16 subaperture lenslet array, within which is inscribed a reduced image of the 5 meter telescope pupil. Initially natural guide star based, the system is designed to accommodate the future installation of a laser guide star subsystem without modification to the optical design.

The user interface for the PALAO control subsystem is resident on a Sun workstation that communicates externally with the telescope control computer and the science camera computer via the Palomar LAN. Internally, this host workstation communicates with a real-time VME control system that consists of a 68060 servo computer and 10 Texas Instruments C40 DSPs on 3 VME boards. The 68060 processor, running VxWorks, coordinates motor control and system telemetry signals, including video, as well as the wavefront controller high level functions, including loading reconstruction matrices and control loop filters onto the DSPs. The 10 TI C40 DSPs flat-field the WFS pixel data, calculate the WFS subarray centroid values, reconstruct the wavefront, and generate DM actuator commands, with a closed loop bandwidth of 500 Hz.

Optical configuration

The optical system is fundamentally a 1:1 relay, as shown in the layout as shown in Fig. 1. The optics are located on a custom Newport RS4000 optical bench which attaches horizontally and can rotate upon the Cassegrain ring of the Hale Telescope. A 45-degree fold mirror (FM1) diverts the F/15.7 Cass beam after focus to a collimating off-axis parabolic mirror (OAP1). An independent fast steering mirror (FSM) corrects global tip and tilt, while the deformable mirror (DM), located conjugate to the primary, corrects higher order aberrations. Another fold mirror (FM2) reflects the light to meet packaging requirements, although this mirror is also used for system alignment and DM calibration. A second OAP relays an F/15.7 beam through an output fold mirror (FM3) to the science camera (not shown). An advantage of this optical configuration is that the two off-axis parabolic mirrors have parallel parent axes and are in proximity on the optical bench, which proves useful during alignment. Prior to FM3, an articulated dichroic mirror reflects the visible component of light through a second articulating mirror to the wavefront sensor field stop. Thus, science imagery is always on-axis, while the field steering mirror pair directs the guide star into the wavefront sensor (WFS). The WFS field stop is a reflective spot of nominally 2 arcsec diameter deposited upon an optical flat. After reflecting from the field stop, the guide star light is recollimated and then passes through an atmospheric dispersion corrector (ADC). The WFS light then forms a pupil, conjugate to both the DM and primary mirror, inscribed within a 16 x 16 lenslet portion of the lenslet array (LA). The lenslet foci are demagnified onto the WFS CCD. Each subaperture is assigned a 4 x 4 pixel area, from which a two-staged centroiding algorithm extracts subaperture tilt information with nearly quad-cell performance and increased dynamic range.

An acquisition camera resides beyond the WFS field stop, and views the stop and sky simultaneously, providing direct feedback during the guide star acquisition process. During operation, the field steering mirrors place the guide star onto the field stop. The guide star signal reaching the WFS CCD is used for fine adjustment before centroid offsets are recorded.

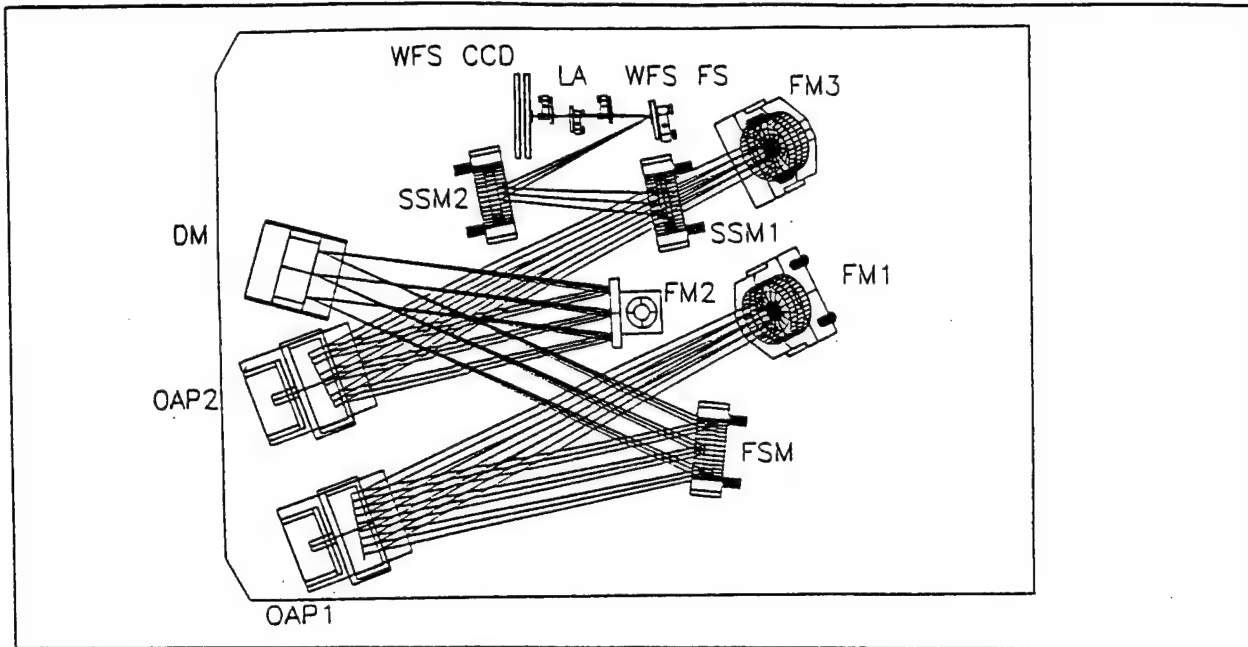


Figure 1. Optical layout of PALAO relay. A 45-degree fold mirror (FM1) diverts the F/15.7 Cass beam after focus to a collimating off-axis parabolic mirror (OAP1). Next come an independent fast steering mirror (FSM), followed by the deformable mirror itself (DM). A fold mirror (FM2), used for packaging the system in the existing cage which surrounds Cassegrain instrumentation, feeds a second OAP which relays an F/15.7 beam through an output fold mirror (FM3) to the science camera (not shown).

Control system electronics

In addition to the computers described above, the PALAO control system utilizes several custom electronics boards resident in two VME chassis. The data room chassis contains the computers, the DM electronics interface board, and the WFS CCD interface board. A separate chassis resides in the Cass cage and is connected to the data room chassis via a VME bus extension. The Cass cage chassis houses 21 JPL-built DM high voltage driver boards, the DM interface board, a C40 image processing module and IP module carrier boards that contain digital I/O, A/D, D/A, and serial (RS-232) IP modules used to control approximately 30 computer controlled elements, including automated positioners, shutters, sources, flip-in mirrors, and lens wheels. A depiction of this architecture is given in Fig. 2.

Real-time wavefront control

The real-time wavefront controller consists of a combination of hardware and software components, which shall provide up to 50 Hz closed-loop bandwidth control. The PALAO deformable mirror is a Xinetix continuous facesheet mirror utilizing poled PMN electrostrictive actuators. Of the 349 actuators, 241 are active controlled by PALAO, with the remainder slaved to the outermost active actuators. The Shack-Hartmann wavefront sensor is based upon a JPL-developed 64 x 64 pixel, 35 micron pitch, TEC-cooled CCD with 64 output amplifiers. Operated nominally at 500 Hz frame rates, this skipper technology chip and electronics allow multiple non-destructive reads in order to reduce centroid errors due to read noise. The goal of this detector development is $< 5e^-$ read noise from a single read and $< 1 e^-$ noise after multiple reads. Initial noise measurements of this chip are expected in April 1996. The DSPs can perform the reconstruction in 1.9 milliseconds. The average data age, from a 2 millisecond exposure, applied to the incident wavefront is 3.7 milliseconds.

Available to the operator as system telemetry are representations of the raw or flat-fielded pixels, the centroid values, the reconstructed wavefront, and the DM actuator motions. The control system allows loading of new reconstruction matrices during closed-loop operation, to account for changes in seeing conditions.

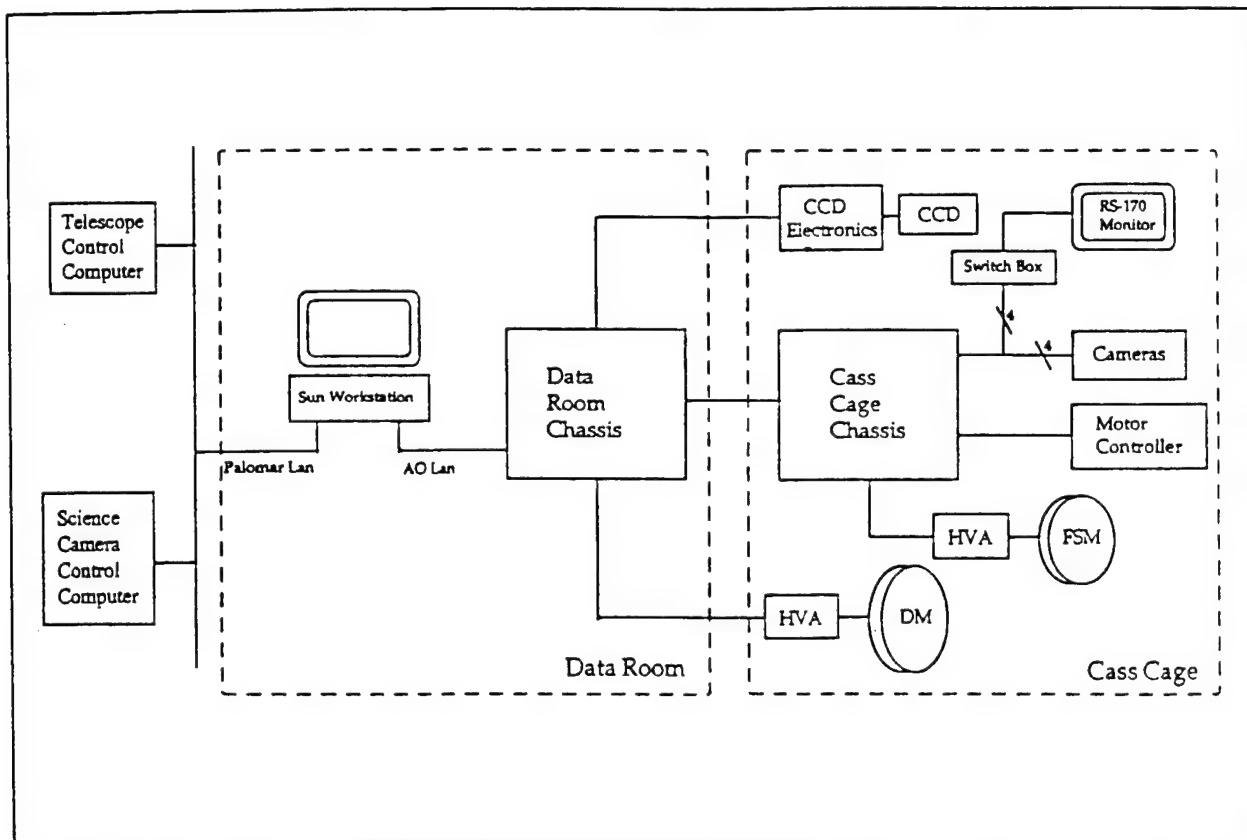


Figure 2. Hardware architecture for PALAO control system. A host workstation communicates with the telescope drive controller, the science camera controllers, and a VME chassis in the data room connected via bus extension to a second VME chassis in the Cass cage.

Active metrology

Two laser metrology systems monitor the optics of the PALAO relay and WFS. The first system is incorporated into an integrated stimulus, which additionally serves as a telescope and atmospheric seeing simulator. A phase-shifting interferometer within the stimulus will be used for initial system alignment and maintenance. Additionally, the stimulus laser source will allow sensing of the DM-to-WFS lenslet registration, as viewed by observing the WFS CCD signal in the presence of an applied DM actuator pattern. It is expected that this registration procedure will require less than 1 minute and is to be performed several times per night of observation. Physically, the stimulus occupies the volume within the spacer that attaches the AO instrument to the Cass ring.

The second metrology system, currently under design, will monitor non-common-path flexure between the WFS camera and the science camera. Non-common-path flexure has proven to be a significant problem in operational telescope-mounted AO systems. In order to maintain image stability at the 10 milliarcsecond level over integrations as long as an hour, active metrology must be incorporated. The principle sources of these non-common-path errors are mount and table gravity flexure. We are currently considering several possible arrangements including a slit-viewing camera and several forms of laser metrology. Our final metrology design will be presented at the July meeting.

Acknowledgments

This work is being performed at the Jet Propulsion Laboratory, California Institute of Technology, under a contract with the National Aeronautics and Space Administration.

**Results from the Cassegrain adaptive optics system of the
Mount Wilson 100-inch telescope**

J.C. Shelton
Mount Wilson Observatory
2416 Crest Dr., Manhattan Beach, CA 90266
310 812-0318 phone; 310 813-4873 fax; shelton@mtwilson.edu

T.G. Schneider
Schneider Engineering
1825 Helmet Trail, Topanga, California 90290

D. McKenna
Canada France Hawaii Telescope Company, Kamuela, Hawaii 96743

S.L. Baliunas
Mount Wilson Observatory, Mount Wilson, California 91023 and
Harvard-Smithsonian Center for Astrophysics, Cambridge, Massachusetts 02138

Since June of 1994 we have been operating and improving a natural-guide-star adaptive optics system on the Mount Wilson 100-inch telescope.^{1,3} The system is routinely operated by one person plus a telescope operator. First astronomical observations have achieved image profiles with a full-width-at-half-max (FWHM) of 0.068 arcsec, using a silicon CCD with no wavelength discrimination (Fig. 1).

The system resides on a 3 x 9 foot optical bench mounted on the north bent-Cassegrain focus of the 100-inch telescope, whose primary mirror has no hole. The south bent-Cass flange is free for non-adaptive observations.

The wavefront sensor has two modes of beam-splitting, object-plane and pupil-plane, alternatively called coronagraphic and conventional mode. In the pupil-plane splitting, or conventional, mode, a beamsplitter in collimated space right after the dispersion correction prisms sends the light to the science camera. In object-plane splitting, or coronagraphic, mode, the science camera sees reflected light from the wavefront sensor field stop, which is actually a mirror with precision holes in the mirror coating. In both cases, the field stop limits background light to the wavefront sensor and prevents optical cross-talk between subapertures. It may also allow compensation on a bright star during daytime similar to what was achieved on the ACE system on the 60-inch telescope, although this has not yet been attempted.^{2, 4}

The deformable mirror has 341 actuators, 241 of which are illuminated, and is on loan from the Air Force. A 0-600 Hz tip/tilt mirror guides the beam. The science camera uses a 1024 x 1024 CCD of CRAF-Cassini design (JPL). Remote focusing, offsetting and filter selection are also provided.

The wavefront sensor uses a high-frame-rate, small-format, low-noise CCD, the ADAPT I device designed by J. Janesick (Pixel Vision) and fabricated by Loral and Reticon. Its noise performance in lab measurements was 7.6 electrons rms at 3300 frames/sec.⁵

Communication with the science camera, wavefront sensor, deformable mirror, tip/tilt mirror and various remote-alignment actuators are all through fiber optic links. The reconstructor, or wavefront processor, uses eight Texas Instruments C40 digital signal processors running in parallel in a host 486 computer. Currently the update rate of the system is 330 per second. Most of the time delay is in processing, as the ADAPT I CCD reads out in 512 microseconds.

The system can be aligned and operated completely from the control room of the telescope. Windowing software, called 'Adoptics', shows real-time displays of wavefront sensor intensity, wavefront sensor x and y gradients, and actuator activity. The loop gain and damping of both the tip-tilt and deformable mirror loops can be changed on the fly with software sliders. A menu of seventeen alignment positioners can be pulled down and any number of positioners selected. A small control window appears for each of the selected positioners showing current position, a go-to position, jog left/right buttons, and so on.

Figure 1 shows the double star tau Cygni with the adaptive optics system functioning. This image was taken on 15 September 1995 when the system was still being assembled. No dispersion corrector or spectral filter was used, and the camera was a Pulnix video camera with an eight-bit acquisition system. The image shown was obtained when the star was transiting. The second object, while difficult to see in the reproduction, is quite widely separated from the primary object 0.755 arcsec away. The FWHM of the primary object is 0.068 arcsec and the strehl ratio obtained is about 0.25. The system-off image (not shown) had a FWHM of 0.95 arcsec. The strehl improvement was 46:1 and the FWHM improvement was 17.5:1.

Figure 2 show the combination Gliese 105 a.c. taken with the cooled science camera and with an atmospheric dispersion corrector. The image was obtained by Shri Kulkarni on 16 November 1995 using the cass AO system on the 100-inch. In an effort to see how well the system, particularly its dispersion corrector, performed at extreme zenith angles, we observed this object when it was 4:08 hr from zenith. The faint companion is clearly resolved, and has a profile width of about 0.3 arcsec. The image is taken in I-band, at which wavelength the companion is 10^4 times fainter than the primary. The dark spot to the left of the primary is a scratch on the inside of the dewar window; the dark vertical line is a serial trap in the science CCD; the bright streaks are diffraction spikes from the secondary and tertiary spiders and the coude flat drive shaft. Since this was taken, we have begun the practice of removing the coude shaft during cass observations, and have installed a Lyot stop on the deformable mirror, which is conjugate to the primary.

REFERENCES

1. Shelton, J.C., Schneider, T., McKenna, D. and Baliunas, S.L., "First tests of the Cassegrain Adaptive Optics System of the Mount Wilson 100-inch Telescope," SPIE, Vol. 2534, p 72, 1995.
2. Shelton, J.C., Baliunas, S.L., Russell, J. and Donahue, R.A., "Adaptive Optics at Mount Wilson Observatory," in *Active and Adaptive Optics*, Proc. ICO-16 Satellite Conf., ed. F. Merkle, ESO Conf. & Workshop Proc. No. 48, p. 53, 1994.
3. Shelton, J.C. and Baliunas, S.L., "Second Generation Adaptive Optics: Plans for the Mount Wilson 100-inch Telescope," in *Optical Astronomy from the Earth and on the Moon*, ed. R.J. Angione, PASP Conf. Ser., 55, 1994.
4. Shelton, J.C. and Baliunas, S.L., "Results of Adaptive Optics at Mount Wilson Observatory," in *Smart Structures and Materials 1993: Active and Adaptive Optical Components and Systems II*, ed. M.A. Ealey, Proc. SPIE, 1920, 371, 1993.
5. Levine, B.M., Janesick, J. and Shelton, J.C., "Development of a low noise high frame rate CCD for adaptive optics," in *Adaptive Optics in Astronomy*, ed. M.A. Ealey and F. Merkle, Proc. SPIE, 2201, 596, 1994.

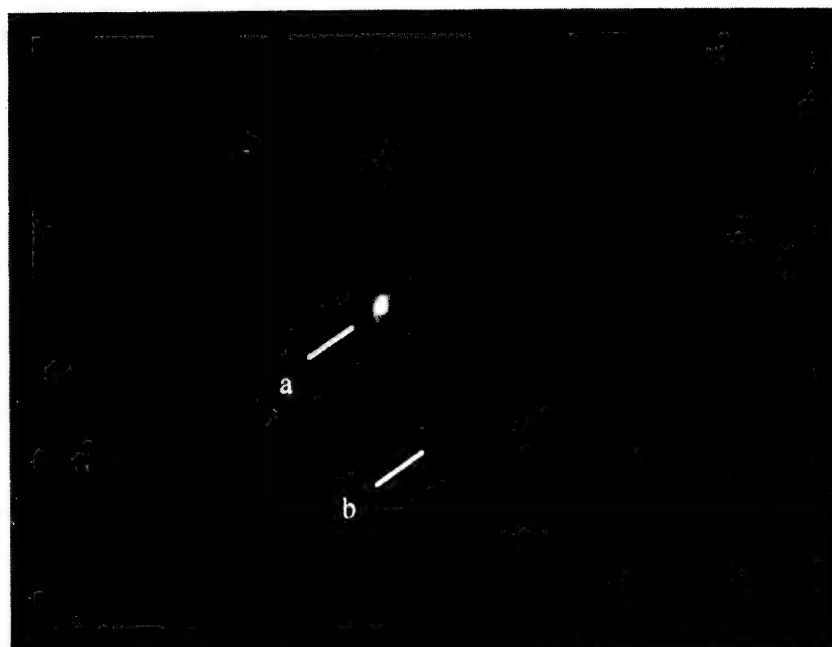


Fig. 1. Tau Cygni, 1/15 sec exposure, near zenith, no filter.
The separation of the stars is 0.755 arcsec.
The resolution (FWHM) is 0.068 arcsec.

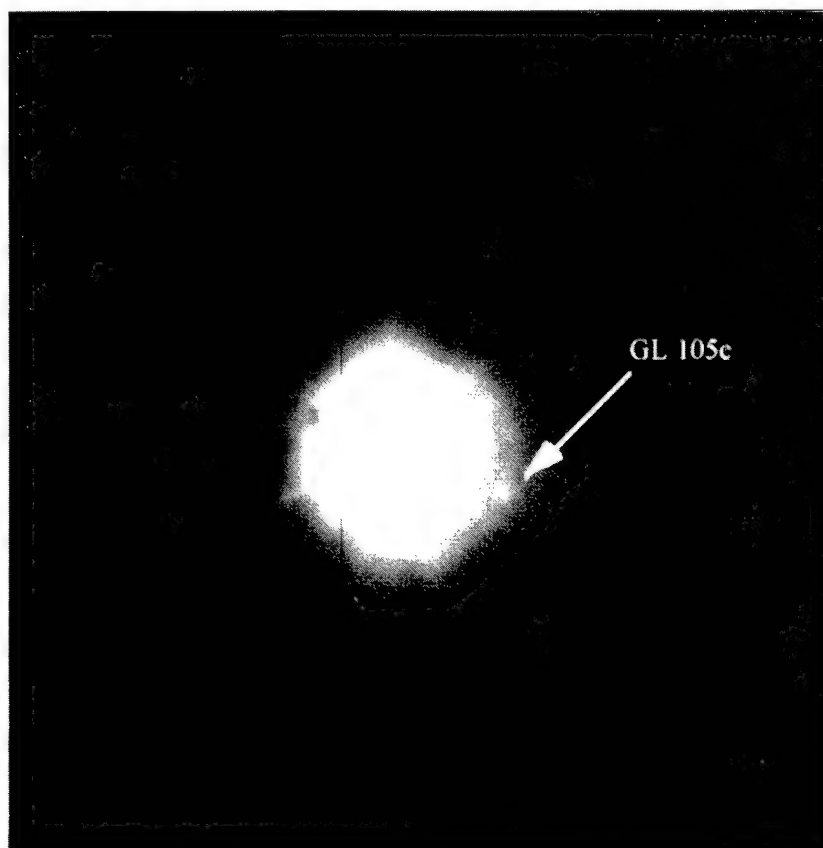


Fig. 2. GL 105a,c 40 s exposure, I-band, elevation angle 26 degrees.
The companion is approx. 10^4 fainter than the primary object.

First results of the CFHT Adaptive Optics Bonnette on the telescope

François Rigaut, Derrick Salmon, Robin Arsenault, Scot McArthur, Jim Thomas

Canada-France-Hawaii Telescope, 65-1238 Mamalahoa Hwy, Kamuela, HI-96743

Olivier Lai, Daniel Rouan, Pierre Gigan, Jean-Pierre Véran

Observatoire de Paris-Meudon, 12 Place Jules Janssen, 92195 Meudon Principal Cedex, France

David Crampton, Murray Fletcher, Jim Stilburn, Brian Leckie, Scot Roberts, Robert Woof

Dominion Astronomical Observatory, 5071 West Saanich Road, Victoria, B.C., V8X 4M6, Canada

Corinne Boyer, Pascal Jagourel, Jean-Paul Gaffard

CILAS, Route de Nozay, BP 27, 91460 Marcoussis, France

The CFHT adaptive optics bonnette is a general user instrument for astronomical applications. The results of the first technical and scientific runs at the telescope, not available at the summary due date, will be presented but are obviously not reported in this paper. A brief system description is given. We present the expected system performance and laboratory results.

Introduction

The Canada-France-Hawaii telescope (CFHT) Adaptive Optics Bonnette (AOB) has been integrated successfully in 1994-1995 at the Dominion Astronomical Observatory (Canada) and at the Observatoire de Paris Meudon (France). It is currently (Feb 96) at CFHT, awaiting its installation at the Cassegrain Focus on March 1996 for engineering and scientific commissioning. This first run will be followed by two others, in May and June. Given the deadline for the submission of this summary, results are not yet available. Therefore, although the presentation will be focused on actual results on the telescope, this summary will mostly serve as a general presentation of the CFHT system. We report briefly the system characteristics, and its most original features. We then present the expected performance, and the type of results that will be reported during the presentation.

1. System description

The system has been presented in detail in previous publications.^{1,2} It has been designed to be a general adapter, a "bonnette" on which various astronomical instruments can be mounted.

Operation with faint sources, leading to modest to good performance -in opposition to overwhelming performance on very bright guide star- was one of the main design parameter, together with the overall efficiency (minimum overhead, minimum calibration and set-up). User-friendliness was also highly ranked, as the system is to be operated largely by users unfamiliar with adaptive optics.

Wave-front curvature sensors, using shot noise limited avalanche photodiodes, offer good performance on faint guide stars. The CFHT AOB is inspired from the F.Roddi curvature concept³ and uses a 19-element curvature sensor, coupled with a 19 electrode bimorph mirror. Taking advantage of the site's intrinsic excellent seeing (median $r_0(0.55\mu\text{m}) = 25\text{ cm}$),⁴ this allows the instrument to reach its best performance in the red (see below). The system is to be installed at the F/8 Cassegrain focus. It delivers a corrected F/20 beam. A dedicated tip-tilt mirror is used to compensate tracking errors and low-frequency tip-tilt perturbations. The wave-front sensor can use on-axis and off-axis guide stars, over the entire field of view of the instrument (90 arcsec in diameter). A set of beamsplitters is used to optimize the transmission in a given observing mode. As in the UH AO system, a vibrating membrane is used to adjust the wave-front curvature sensor sensitivity. The system real-time computer, in addition to dedicated input/output boards, uses a Sparc 3 and a Sparc 5 board.

Some original features of this instrument are the optimization processes which take place in the background. These processes monitor in semi-real-time the system condition and are used for a variety of tasks. The command

matrix is regularly updated, as the system mode gains are optimized. The sensitivity of the wave-front sensor is also regularly updated to track the seeing fluctuations. During the course of an astronomical exposure, the average PSF is computed, using the WFS measurements and the deformable mirror commands.⁵ In general, these automatic optimizations relieve the user from laborious setup work and allowed us to significantly simplify the user interface. Our general user interface includes only a limited number of choices in order not to unnecessarily confuse the AO non-specialist.

Instrumentation available with the CFHT AOB include an infrared imager currently using a NicmosIII array (a 1Kx1K camera is being built) with adequate sampling down to $1.2 \mu\text{m}$, a visible imager with two sampling configurations (0.02 and 0.04 arcsec/pixel), and, soon to come, a visible integral field spectrograph (OASIS).

2. Performance and laboratory results

The system performance was evaluated using a numerical simulation code developed at CFHT.² Strehl and image full-width at half maximum (FWHM) under typical seeing condition ($r_0(0.5\mu\text{m}) = 20\text{cm}$) at CFHT are reported in the table below for several imaging wavelengths and guide star magnitudes.

$\lambda(\mu\text{m})$	Strehl			FWHM		
	$m_R=10$	$m_R=14$	$m_R=18$	$m_R=10$	$m_R=14$	$m_R=18$
0.5	0.02	0.015	0.005	0.10	0.17	0.41
0.9	0.24	0.15	0.025	0.06	0.07	0.31
1.6	0.62	0.52	0.13	0.09	0.10	0.18

Using a multi-layer model, we have also been able to include the anisoplanicity error. A multi-parameter model of the PSF (r_0 , guide star magnitude, imaging wavelength and distance to guide star) has been synthesized from the simulation results and is available at <http://www.cfht.hawaii.edu/manuals/aob/ao.html> and [psf.html](http://www.cfht.hawaii.edu/manuals/aob/psf.html). Among other things, it helps AOB users to prepare their observing programs prior to the run.

The AOB has been extensively tested in the laboratory during the second semester of 1995 at the Observatoire de Paris-Meudon. The test setup included a full telescope simulator (tip-tilt table and F/8 beam generator) and a simple turbulence generator. Figure 1 presents a corrected and uncorrected image for a $r_0(0.5\mu\text{m}) \approx 26\text{cm}$. The FWHM of the corrected image is 0.06 arcsec, slightly larger than predicted, due to a high frequency resonance in the mount for the telescope simulator optics (outside the AOB).

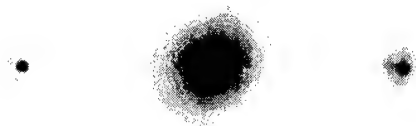


Fig.1. Laboratory $0.7 \mu\text{m}$ images obtained with a turbulence generator. Left : Image in absence of perturbation. Middle : Uncorrected image, ($D/r_0(0.5\mu\text{m}) = 14$), Strehl ratio = 3.5%. Right : Corrected image, same r_0 , Strehl ratio = 24%.

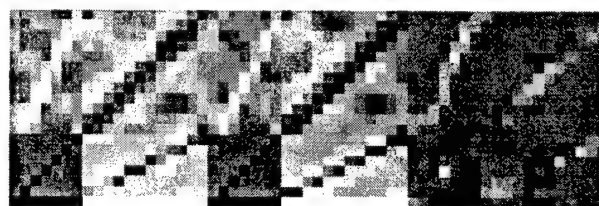


Fig.2. Interaction matrix for a typical sensor optical gain. Left : Experimental matrix. Middle : Matrix computed with the numerical simulation code. Right : Difference of the experimental and the simulated matrix, same grey scale.

Altogether, the results obtained during the laboratory tests are in very good agreement with the numerical simulations (including actual interaction matrices, see figure 2). This gives us confidence in the performance predicted with the numerical simulation code.

3. Tests on the telescope

The 3 runs to take place during the first semester 1996 will include both engineering and scientific tests. We plan to characterize the system performance for a number of operating conditions. We will put the emphasis on testing the optimization processes, and insure that they deliver the best possible set of working parameters. We also plan to get data on large fields, providing valuable inputs for statistical studies of the isoplanatic properties of the atmosphere at Mauna Kea. We might also characterize the PSF properties at short wavelength (0.4-0.6 μm). Finally, we plan to concentrate on 4 scientific programs, addressing various area of astrophysics, which should help to better define the frontier of application of this instrument.

Acknowledgements

We wish to thank F.Roddier, M.J.Northcott and J.E.Graves at University of Hawaii for their help during the early development stages of the AOB. We are also grateful to Daniel Nadeau and René Doyon (Université de Montréal) for making their infrared camera available for the AOB tests on the telescope.

-
1. "PUEO : The Canada-France-Hawaii telescope adaptive optics bonnette I: System description" , Arsenault R., Salmon D., Kerr J., Rigaut F., Crampton D., Grundman W., SPIE 2201 (1994)
 2. "The Canada-France-Hawaii adaptive optics bonnette II: simulations and control", Rigaut F., Arsenault R., Kerr J., Salmon D., Northcott M., Dutil Y., Boyer C., SPIE 2201 (1994)
 3. "The University of Hawaii adaptive optics system I : general approach", Roddier F., Graves J.E., Northcott M.J, SPIE 1542 (1991)
 4. "Mirror, dome and natural seeing at CFHT", Racine R., Salmon D., Cowley D., Sovka J., 1991, PASP 103, 1020-1032.
 5. "AO long exposure PSF retrieval from WFS measurements", Véran J.P., Rigaut F., Rouan D., Maitre H., this conference (1996)

Future Directions for the University of Hawaii Adaptive Optics Program

J. Elon Graves,
University of Hawaii
2680 Woodlawn Drive
Honolulu, Hawaii 96822

graves@ifa.hawaii.edu

Abstract

The highly successful AO program at the UH is now planning to expand the curvature technology into higher order correction systems with a unique Vis/IR WFS concept.. Computer simulation have been carried out scaling the current 13 element system now being used at the CFHT on Mauna Kea to a 36 element design. The Vis-IR WFS sensor is expected to increase the performance overall, all as it is used to study young stellar objects that are at many times deeply reddened. An example is HL Tau, in the visible it is around magnitude 14 and at the H band it magnitude 9 or 100 times brighter!

Science goals

There is indeed a lot of competition growing in the area of high resolution imaging between telescope facilities on the ground and with those in space. Facility AO systems will be coming on-line in increasing number in the next 5 years. It is a natural evolution that some AO systems will evolve toward more narrow and specific scientific goals just like spectrographs have evolved. Our adaptive optics program is moving in the direction that will modify our current instrument towards achieving better performance in the areas of observing early evolving stars, possibly in the process of forming other planets. In this research area, high angular resolution, low scattering optics, and having stable PSF's is vital. In the study of evolving stars, they are many times obscured and highly reddened by the dust envelope from which they were born. We plan to enhance our abilities to guide on these objects by build a curvature wavefront sensor which is sensitive in the infrared. The instrument we are designing will be optimized to work at the diffraction limit in the spectral region covered by the highly successful HgCdTe array technology, namely the 1024 x 1024 Hawaii array. It is in this spectral region where one can observe early star formation in both scattered light and thermal emission.. Presented in this paper is a higher order curvature AO system optimized for this research.

Design goals

The current low order 13 element AO system used routinely at the CFHT achieves Strehl's of the order of 0.2 to 0.4 @ H (1.6 microns), under average seeing conditions on Mauna Kea (0.5 to 0.7 arcsec.). Expanding the number of actuators to 36, will give improve the Strehl to about 0.7 to 0.8 @ H. This will also give reasonable performance down to the I band (850nm) in the neighborhood of 0.2 to 0.4 Strehl. Based on our experience with the 13 element system we are comfortable deconvolving images of this quality to enhance the resolution and detection of faint point sources. The importance of high Strehls in coronagraphic work are well know. The search for very faint objects close to very bright ones, as in the search for planets or brown dwarfs, places very demanding performance on both the AO system and the scattering properties of the optical components. Even the Space Telescope primary mirror which has been advertised as the smoothest mirror ever made could be improved with a very high order correction system arranged to remove the polishing grooves produced during fabrication.

Stability and quality of the PSF is very important in detecting faint point like objects around bright sources. The curvature or Laplacian deformable mirror technology has some distinct advantages over the more conventional stack piston mirror technologies. Stack mirrors and their control systems are prone to wafer mode events while correcting atmospheric turbulence. The periodic structure of the actuators spacing produces a diffraction pattern, of the bright source, in the image plane. The intensity distribution in this pattern depends on the wafer mode configuration and the duration of this pattern during the exposure. This makes post processing or deconvolutions extremely difficult if not impossible. This problem can be minimized if one can take short exposures and carefully frame select, but the extreme faintness of some objects pushes the limits of detection. Adding short exposures only accumulates the read noise in the camera. The curvature or Laplacian mirror on the our hand does not suffer from waffle mode problems because there is no need for a reconstructor in the control system or another way to put it is the system properly samples its modes. This is done naturally with the Laplacian mirror. Another advantage is the WFS calibration is automatic because the measurement is differential and does not rely on an external source. It has proven to be very robust in deriving a good wavefront signal from extended, diffuse sources like HL Tau, GG Tau, the Red Rectangle, and Frosty Leo to name a few.

Our new AO system will have 36 elements in both the WFS and the correcting mirror. Like our 13 element system the match between the WFS and the mirror is such that the control matrix is nearly diagonal. That is to say, for each correcting element there will be a single detector in the WFS for control. We plan to make good use of this by reducing the 36×36 matrix multiple to only those terms which are significantly not zero. By doing this, the delay between the measurement and control voltages sent to the mirror will be minimized. The design for the 36 element lenslet array can be found in figure 1.

Unique Vis/IR WFS

The WFS sensor in our new system will have a very unique feature that will allow the use of either visible light or IR light for wavefront sensing. Switching between the detectors will be remotely activated via a fiber switcher. The same lenslet will be used for both spectral regions. In the visible portion of the spectrum we will use the newly available avalanche photo diodes (APD's) from EG&G. Significant performance over the earlier model APD's are expected. The QE has increased from 40% to nearly 80% and the count range has been increase to from 1.5 megahz to 10 megahz. When using the IR WFS, the fibers will be optically coupled to either a single row of 36 pixels or be separated into 4 quads to be read out in parallel. Imaging directly onto the array from the lenslet is not very efficient in terms of a rapid readout. Mapping the circular geometry of our WFS design has always been a poor match to the rectangular geometry of array detectors. By coupling the light into a fiber with the lenslet array it gives us the flexibility to arrange them in any way we like. We hope to use one of the IR Hawaii array's with its very low read noise. Read noise performance on this device has been measured at 6 electrons at the frame rates we are expecting to use (2khz). At this level of performance we are expected to be sky background limited. See figure 2 for the details of the dual light WFS configuration.

Spectral region for the IR WFS will be limited to that defined by the fiber transmission which cuts off at around 1.8 microns on the red end and the detector response on the blue end. We are not expecting the fiber to transmit thermal radiation. At the blue end, we will allow the natural response of the detector to define the cut off. The HgCdTe detector is sensitive down to a little less than 800nm. Sharing the light between the IR camera and the IR WFS will take some careful planning. We plan to use all of the light not being used by the science camera for wavefront sensing. This require us to have a number a beamsplitters available in the optical train that are remotely selectable. A design which will need to be carried out carefully.

University of Hawaii
36 element Lenslet Array

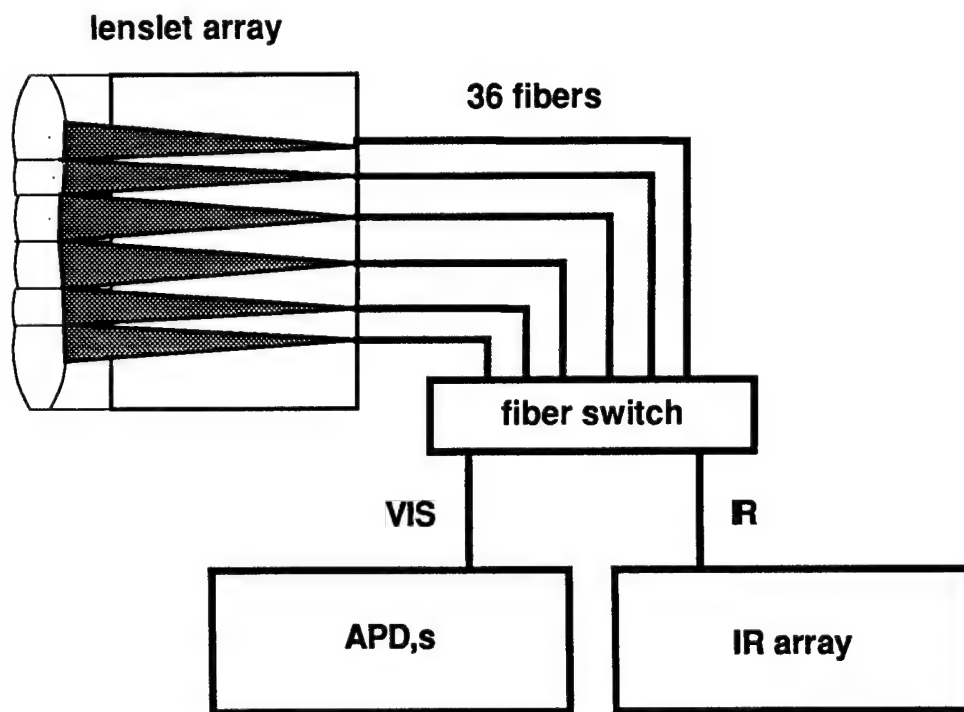
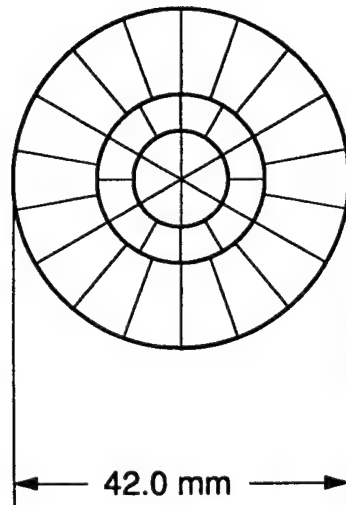


figure 1

Conclusions

The University of Hawaii adaptive optics team is moving forward with a 36 element higher order curvature adaptive optics system that will include a unique Vis/IR WFS package. The system is being optimized for astronomy on young stellar objects that on many occasions are highly reddened by dust envelopes surrounding the star.

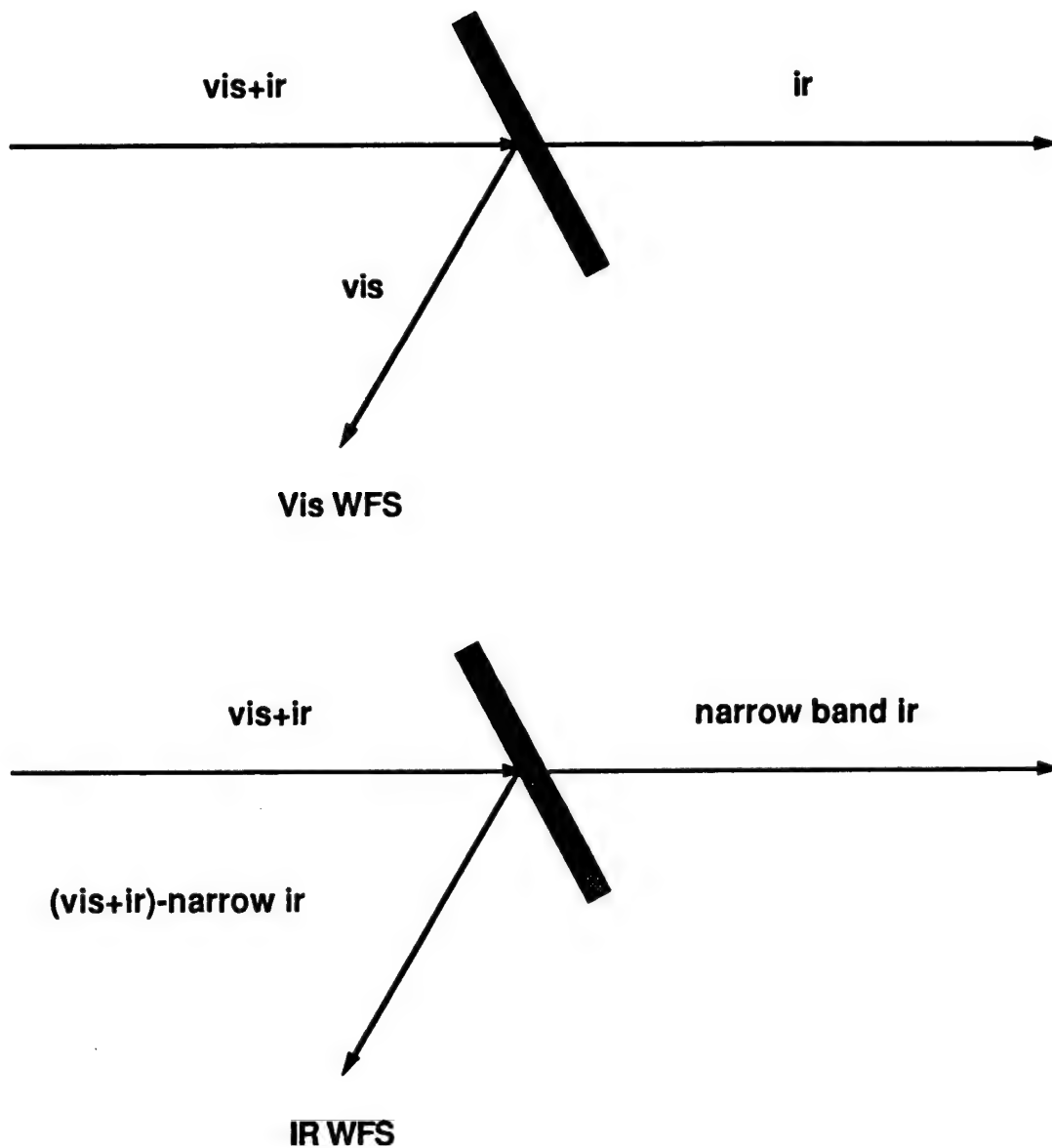
WFS/IR camera beamsplitter

figure 2

Adaptive Optics for a 70 cm Solar Telescope

D. Soltau¹, D.S. Acton², Th. Kentischer¹, M. Roser¹, W. Schmidt¹, and M. Stix¹

¹Kiepenheuer-Institut für Sonnenphysik, Schoneckstr. 6, D-79104, Freiburg, Germany
Tel: (49) 761 3198 0; Fax: (49) 761 3198 111; email: soltau@kis.uni-freiburg.de

²W. M. Keck Observatory, 65-1120 Mamalahoa Highway, Kamuela, HI 96743, U.S.A.
Tel: 808 885 7887; Fax: 808 885 4464; email: sacton@keck.hawaii.edu

The sun is a bright, low-contrast, extended object. One arcsecond corresponds to 725 km on the sun. In the solar atmosphere the density scale height and the photon mean-free-path are both ~ 100 km. Due to the large conductivity, the solar magnetic field has an extremely inhomogeneous structure with a typical scale of 100 km or even less. In order to resolve 50 km on the sun, a telescope should have an angular resolution of 0.07 arcsec. In the visible ($\lambda=500$ nm), this would require an aperture of about 2 m.

Currently, the presence of atmospheric turbulence or "seeing" limits the resolution of existing telescopes to values of about 0.5 arcseconds which correspond to the resolving power of 30 cm-telescopes. In our poster we want to point out what can be expected if one upgrades a medium sized telescope with an AO system.

The sun shows granulation with a rms-contrast of a few percent all over the disk. The lifetime of the granulation is in the order of minutes. In addition there are dark structures with high contrast (sunspots and pores) and lifetimes of hours to weeks. But they are rare. In order to have a reasonable "sun coverage," an AO system must be able to lock on granulation. This demand has consequences for the design of the wavefront sensor and the algorithms to calculate the corrections.

The Kiepenheuer-Institut operates a 70 cm solar telescope on the Canary Island Tenerife (Soltau, 1991). Wavefront and r_0 measurements made with this telescope have yielded isoplanatic patch sizes of larger than 10 arcsec and r_0 values in the order of 10 cm under seeing conditions which occur frequently enough to justify an AO system to start with (Acton, Soltau, and Schmidt, 1996).

A correlation tracker has been developed at the Kiepenheuer-Institut and its performance confirms the findings about the quality of the site (Rimmele, 1993).

In 1995 the 19-segment-mirror system developed by Lockheed (Acton, 1992) was brought to Tenerife and successfully tested on pores as targets. The system is able to determine the current

value of r_0 . It turned out that the system improves the image quality as soon as r_0 is larger than ~ 9 cm. Based on these experiences, we present a possible design for an AO system for our telescope which should be able to increase the time for diffraction limited observations significantly. The following design parameters are to be considered:

1. Type of wavefront sensor.

There are several ways of measuring a wavefront. We prefer the Shack Hartmann type where we can apply reliable techniques of fast image shift determination which have been successfully used in solar correlation trackers.

2. Number of subapertures.

For a given telescope the number of subapertures is determined by their diameter. Since the system must work on granulation, the subaperture must be large enough to image the granulation with reasonable contrast. On the other hand, the subaperture has to be small enough to allow for measurements of the wavefront with a sufficient resolution in the aperture plane. In the case of a mirror with hexagonal segments, the number of subapertures across the telescope aperture must be an odd integer. In our case this number can only be 5 or 7, corresponding to subapertures of 14 or 10 cm, resp. Based on the results of r_0 measurements (Acton, Soltau, and Schmidt, 1996) and experiences with the Lockheed system, we choose 10 cm as a reasonable size for a subaperture. This gives us 7 subapertures across the telescope and a resolution of 1.3 arcsec in the WFS image. We expect the granular rms contrast to be 1 to 2% under working conditions. This is probably the lower limit for the determination of image shifts.

3. Field of view.

The field of view of the wave front sensor has to be large enough to allow for precise image shift measurements (subpixel accuracy required!). On the other hand the isoplanatic patch limits the useful size of a field of view. We choose 15~arcsec as a compromise.

4. Sensor size.

A reasonable pixel size for the given subaperture would be 0.5 arcsec. This leads to a subfield of 30 x 30 pixels and a total sensor array of 210 x 210 pixels. A commercially available sensor with 256^2 pixel therefore seems suitable, where only a subfield may be used. In order to match a pixel size of 10 microns, a demagnification by a factor of 10 is necessary.

5. Bandwidth.

The desired bandwidth is several hundred Hertz in order to be able to compensate for seeing variations.

We are now in the process of evaluating the different alternatives for such a system. Related questions are:

- Segmented mirror vs. monolithic mirror. Does the choice of the mirror affect the expected photometric accuracy by producing "strange" pointspread functions?

- Choice of algorithms for determining the image shifts in the WFS.
- Optical setup in order to keep as much light as possible in the science beam.

We plan to begin tests at the telescope in the second half of 1996 using the 19 segment Lockheed system as a start.

References

- Acton, D.S., Soltau, D., Schmidt, W., 1996, Astron. Astrophys. (in press).
 Acton, D.S., Smithson, R.C., 1992, Appl. Opt. 31, 3161.
 Rimmele, Th., Kentischer, Th., Wiborg, P., 1993, in: Real Time and Post Facto Image Correction, Radick, R., (ed.), p. 24.
 Soltau, D., 1991, Adv. Space Res. Vol. 11, No. 5, p.(5)133.

Optimization of the Starfire Optical Range 3.5 M adaptive optics for astronomical imaging

Donald J. Link
Science Applications International Corporation
140 Intracoastal Pt. Dr.
Jupiter, FL 33477
(407) 575-5775
FAX (407) 575-4370
e-mail dmdon@aol.com

Russell G. Vernon
Science Applications International Corporation
140 Intracoastal Pt. Dr.
Jupiter, FL 33477
(407) 575-5775
FAX (407) 575-4370
e-mail russvernon@aol.com

SAIC has developed a wave-optics, time domain, engineering simulation of adaptive optics systems. The Atmospheric Compensation Simulation (ACS) includes both physics effects (e.g., inner and outer scale, various turbulence profiles, wind, anisoplanatism, time of flight, scattering, absorption, sodium layer saturation) and engineering effects (e.g. jitter, misregistration, latency, digital controls, control surface electro-mechanical response, gain variation, shot and detector noise, quantization, aberrations). The code includes the ability to model multiple three-dimensional laser guidestars, propagating the lasers up from the ground and imaging the irradiance from multiple atmospheric layers onto the detector plane using multiple optical transfer functions or speckle imaging. This simulation has been used to support engineering development on a number of programs and has been validated against theory, experiments, and other codes.

For this paper ACS was used to simulate the adaptive optics system for the Starfire Optical Range (SOR) 3.5 M telescope for astronomical imaging. Performance was investigated using a natural guidestar, a sodium guidestar, and a hybrid system which combines a sodium guidestar and a Rayleigh guidestar. For the laser guidestar systems performance was investigated as a function of beacon power, detector noise, control system bandwidth, wavefront sensor field of view, and beacon spot size. Sensitivity to Sodium layer saturation and changes in the scatter profile were also investigated. For the natural guidestar the effects of source strength, detector noise and control system bandwidth are investigated.

Simulations were also run to show how to reduce sensitivity to wfs misregistration by careful selection of actuator and wfs configuration, and of wavefront reconstructor generation.

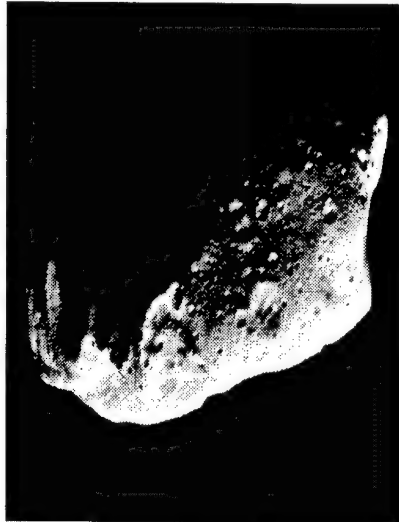
Predicted imaging performance for selected astronomical objects are presented (e.g., see Figure 1). Comparisons are made with actual images from the Hubble Space Telescope.

Figure 1. Image of an asteroid using a sodium laser guide star for adaptive optics wavefront sensing

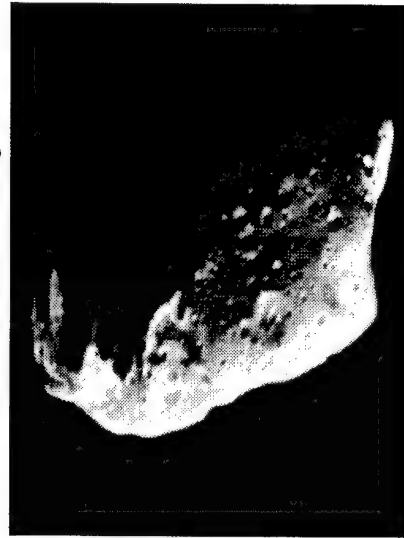
Parameters:

- 384 x 384 Focal plane, 38.4 μ rad total FOV, 30 ° Zenith, Hufnagel Valley 5/7 Turbulence, SOR spring wind, 200 Watt Sodium Laser, includes saturation effects, asteroid is 16th mv source which is used for tilt tracking, 0.7 μ m Imaging wavelength
- 476 Active DM actuators, 113 Slaved Actuators, 456 Wavefront Sensor Subapertures, 1 KHz WFS framerate, 128 x 128 CCD array, 4 pixels/subaperture, 8 noise electrons per pixel, 100 Hz Adaptive Optics Bandwidth
- 250 Hz tracker frame rate, 25 Hz Tilt Bandwidth, 8 x 8 Avalanche Photo Diode array used for tracking, QE = 0.8

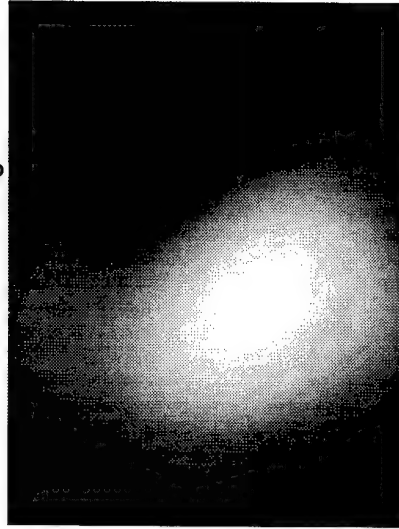
Pristine Scene



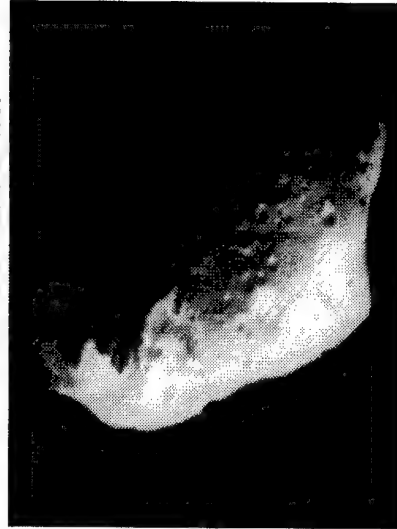
Diffraction Limited Image



Uncorrected Image



**Corrected Image Using Sodium Guide Star and
25 x 25 Deformable Mirror**



Status of the Advanced Electro-Optical System (AEOS) Adaptive Optics

John R. Kenemuth
Phillips Laboratory/LII
Kirtland AFB, NM 87117
(505) 846-4270 Phone
(505) 846-6197 FAX

James J. McNally
Phillips Laboratory/LII
Kirtland AFB, NM 87117
(505) 846-5044 Phone
(505) 846-6197 FAX

James R. Passaro
Phillips Laboratory/LII
Kirtland AFB, NM 87117
(505) 846-5045 Phone
(505) 846-6197 FAX

Paul J. Berger
MIT Lincoln Laboratory
Lexington, MA 02173
(617) 981-1946 Phone
(617) 981-5069 FAX

Carlo La Fiandra
Hughes Danbury Opt. Sys.
Danbury, CT 06810
(203) 797-5565 Phone
(203) 797-5919 FAX

Rene Abreu
Hughes Danbury Opt. Sys.
Danbury, CT 06810
(203) 797-6114 Phone
(203) 797-5919 FAX

The Advanced Electro-Optical System (AEOS) is being developed as an upgrade to the Air Force Maui Space Surveillance Site (MSSS) on Haleakala, Maui, Hawaii. It consists of a new 3.6-m diameter telescope in an azimuth-elevation configuration mounted atop a pier approximately 60 ft above the local ground level. A bent-Cassegrain configuration provides for selection between three (3) sensor locations on the telescope trunnion and access to a coudé path through the elevation and azimuth axes to ground level. The coudé optics in the telescope provide a ± 150 μ rad field of view over a 0.5 to 5.0 μ m spectral band to a 941-actuator adaptive optics system located in the coudé path directly beneath the telescope at ground level (coudé room) which will provide dynamic compensation for atmospheric turbulence effects so that a significantly improved image quality may be achieved. A switching mirror located at the output of the adaptive optics system will provide a capability to direct either a compensated beam, or a beam which bypasses the adaptive optics system, to any of seven (7) optics laboratories concentrically located around the room which contains the adaptive optics system.

The optical elements of the adaptive optics system are mounted on a thermally controlled optical bench in the coudé room. The coudé beam is first incident on a turning flat which directs the beam into the remainder of the adaptive optics system. When this turning flat is removed, the uncompensated beam bypasses the adaptive optics system and may be directed into any of the optics laboratories. When directed into the adaptive optics system, the beam is relayed first to the tilt control mirror, next to the deformable mirror, and then to a dichroic. The dichroic reflects the 0.5 to 0.7 μ m spectral band to the tracker and wavefront sensors and transmits the 0.7 to 5.0 μ m spectral band for detection by a 0.7 to 1.0 μ m imaging

sensor on the adaptive optics bench or a complement of sensors in the optics laboratories. An optical source simulator on the optical bench provides a capability for testing the adaptive optics system prior to a mission. For cost efficiency, the wavefront sensor, real-time reconstructor, and deformable mirror for the AEOS adaptive optics system share the same basic designs as those for the Starfire Optical Range 3.5-m telescope system.

The support equipment for the adaptive optics system is located in a room adjacent to the coudé room. The control console for the adaptive optics system is in the AEOS control room located on the second floor of the AEOS facility. The entire AEOS system, including the adaptive optics system, is being designed to be controlled and operated by a single operator. High data rate communications, both within the AEOS facility and between the AEOS facility and the rest of the MSSS, are through optical fibers.

The adaptive optics system is primarily designed to operate during the evening and morning terminator periods and during the night, on targets as dim as $M_v = 8$ and as large as $100 \mu\text{rad}$, for zenith angles from 0° to 70° and target crossing rates up to $2.5^\circ/\text{sec}$. Tilt corrections are applied by the tilt control mirror at 20 - 200 Hz. The Hartman wavefront sensor samples 900 subapertures over the telescope pupil at 2,520 frames/sec. Appropriate corrections are calculated in real time by the wavefront reconstructor and applied by the 941-actuator deformable mirror at up to 200 Hz. Computer simulations of this AEOS adaptive optics system predict significant improvement in target identification capabilities for the MSSS.

The operational requirements at MSSS impose ease of maintenance, high reliability, high availability, and a built-in test capability as important design criteria. The design has also provided for ready implementation of pre-planned product improvements to enable future enhancement of the adaptive optics system performance. Specific provisions have been made for additional wavefront sensors and a fast figure sensor for laser guidestar capability, the addition of a second tracker, wavefront sensor frame rates to 5000 frames/sec, and for the drop-in replacement of the 941-actuator deformable mirror with a 1500-actuator design.

The contract for the AEOS adaptive optics system was awarded to Hughes Danbury Optical Systems on August 22, 1994. The Preliminary Design Review was approved on March 24, 1995 and the Critical Design Review was approved on September 21, 1995. Development of the hardware and software is in progress. The current status of the AEOS adaptive optics system and the schedule for completion of the effort will be presented.

Mechanically-Induced Line-of-Sight Jitter in the Starfire Optical Range 1.5 Meter Telescope

James M. Brown II
Starfire Optical Range
US Air Force Phillips Laboratory/LIG
3550 Aberdeen Ave. SE
Albuquerque, NM 87117
Tel. 505-846-4712 ext. 365
Fax 505-846-2213
email brownjm@plk.af.mil

James C. Goodding
CSA Engineering, Inc.
2850 Bayshore Road
Palo Alto, CA 94303-3843
Tel. 415-494-7351
Fax 415-494-8749
email gooddinj@plk.af.mil

Introduction: Prior to the use of adaptive optics, many sources of line-of-sight jitter were masked by atmospheric effects. That is, we cannot observe small jitter in the optical data while wave-front distortions dominate the error in our images. However, we have seen that seemingly negligible error sources become significant as we conquer the atmospheric problems.

Problem Specifics: Figure 1 shows a power spectral density (PSD) plot for the centroid location of a star image taken with the SOR's 1.5 meter telescope with adaptive optics active. The dominant feature of this curve is the large hump near 80 Hz. The energy represented by this hump is significant in that the area under the curve between about 70 - 90 Hz is large due to the height and width of this bulge in the PSD. The SOR employs a tracking-control loop utilizing an optical sensor and a tip-tilt mirror. Unfortunately, the loop's bandwidth extends only to about 80 Hz. Thus, most of this disturbance is not handled by the tracker.

Disturbance Source and Alleviation: Since the currently-employed tracker cannot compensate for jitter above about 80 Hz, we set out to determine the root of the jitter with hopes of attenuating the problem at the source. Another approach would have been to completely redesign the tracker control loop; however this would require new hardware and a more complex control law, involving significant impact in both schedule and budget.

SOR personnel first conducted an experiment wherein the telescope was 'bolted down' while observing Polaris. Analysis of the data taken for this experiment showed no evidence of excessive jitter near 80 Hz, leading to the conclusion that the telescope was contributing to the jitter. Armed with this information, we used a combination of accelerometers, load-cell hammers, and modal-analysis software to track down the troublesome component(s). This investigation zeroed

in on the secondary mirror as the source of the 80 Hz vibration. Further examination yielded the invar rods which meter the secondary mirror (M2) to the primary. M2 is supported by four invar rods, each approximately eight feet long and 1 1/8 in. in diameter. Figure 2 shows a schematic of the support structure. Modal analysis conducted by we revealed the rods as the source of the vibration; each rod exhibits a primary mode near 80 Hz. Since the rods vibrate independently and are coupled to the M2's support structure, vibration in M2 is forced to tip and tilt along with the rods.

Contraves, the telescope's manufacturer, foresaw a possible problem with the rods. Their solution was to force a structural node by incorporating a jacking-block clamped to each of the rods which has screws designed to push against the telescope canister. We simply added more jacking-blocks to the rods in order to more tightly couple the rods to the canister. Figures 3 and 4 illustrate the success of this fix. Figure 3 clearly shows that the jitter contribution near 80-90 Hz is attenuated by the addition of jacking-blocks. Perhaps more illustrative, Figure 4 shows the cumulative integral of the curves given in Figure 3. The curve marked by circles (original jacking blocks only) includes a large jump in centroid location power from 80 to 100 Hz (about 40% of the total power). In contrast, the second curve, which includes the effect of extra jacking-blocks, jumps by a significantly smaller amount.

Conclusions and Comments: The jitter problem outlined in this paper was alleviated successfully by a simple structural modification. Even if the control loop had been modified to move the bandwidth beyond the problem area, significant control authority would be expended to combat a disturbance best addressed via other means. Our intent in presenting these results is to encourage other telescope facilities to search for mechanical disturbances which may be attenuated by simple modifications, thereby freeing the control system.

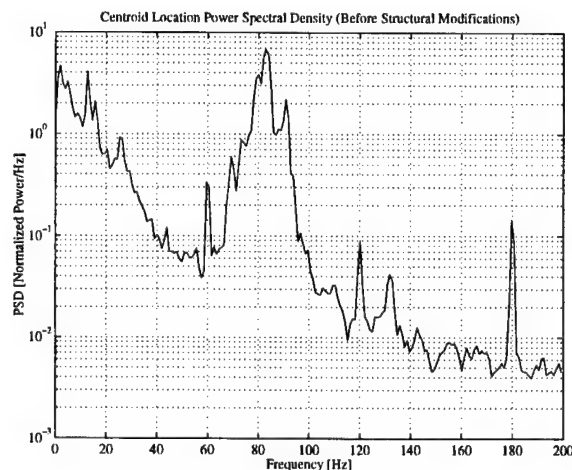


Figure 1: Centroid Location Power Spectral Density

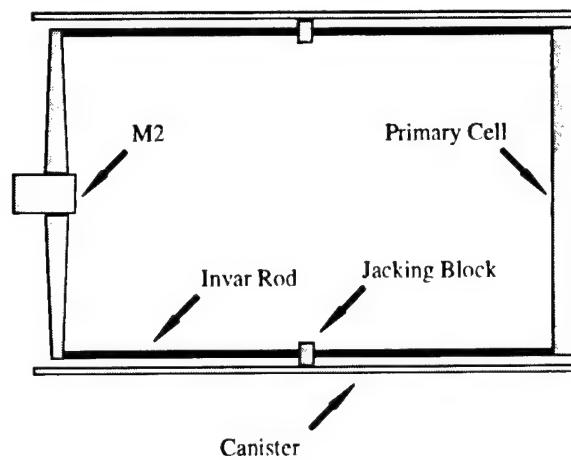


Figure 2: M2 Metering-Rod Schematic

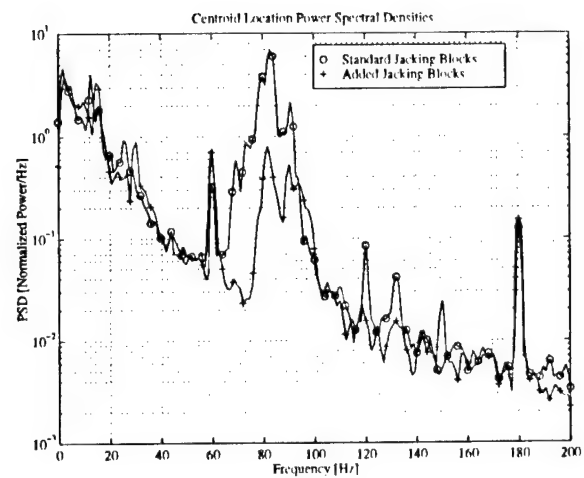


Figure 3: Centroid Location Power Spectral Densities

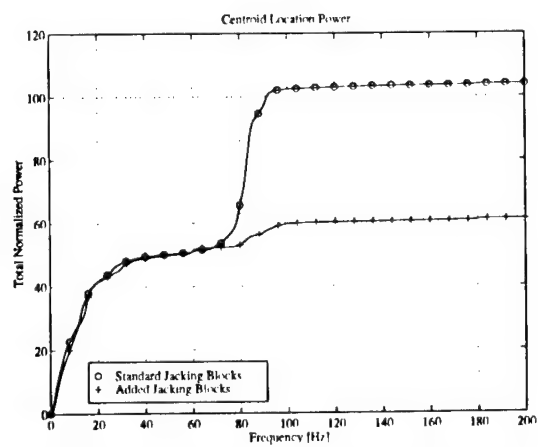


Figure 4: Centroid Location Total Power Integrals

Five-order adaptive optics for meter-class telescopes

Donald G. Bruns

Stellar Products, P.O. Box 720879, San Diego, CA 92172

(619)-538-8362

1. Introduction

A low order adaptive optics system for astronomical telescopes based on simple optics and commercially available key components can serve as more than an introduction to adaptive optics hardware and testing. For a one meter telescope, in the case of (D/r_0) between about five and eight, only five correction orders are required to produce significantly improved images. Such a low order system has been designed and built, using translating lenses to produce smooth aberration corrections. The system, called the AO-5, is meant to correct atmospheric turbulence in the visible and near infrared spectral regions. This paper reports on measurements of the corrections applied to synthesized atmospheric aberrations created by a turbulence generator. The AO-5 will be installed in the summer of 1996 on one of the Meyer Foundation's dual 0.72 m Ritchey-Cretien telescopes on the 4300 meter level of Mount Evans, Colorado.

2) Optical Design

The optical layout is shown schematically in Figure 1. The telescope focal ratio is F/21, but is relayed to F/48 at the science camera and F/6 at the wavefront sensor. At the prime focus is a

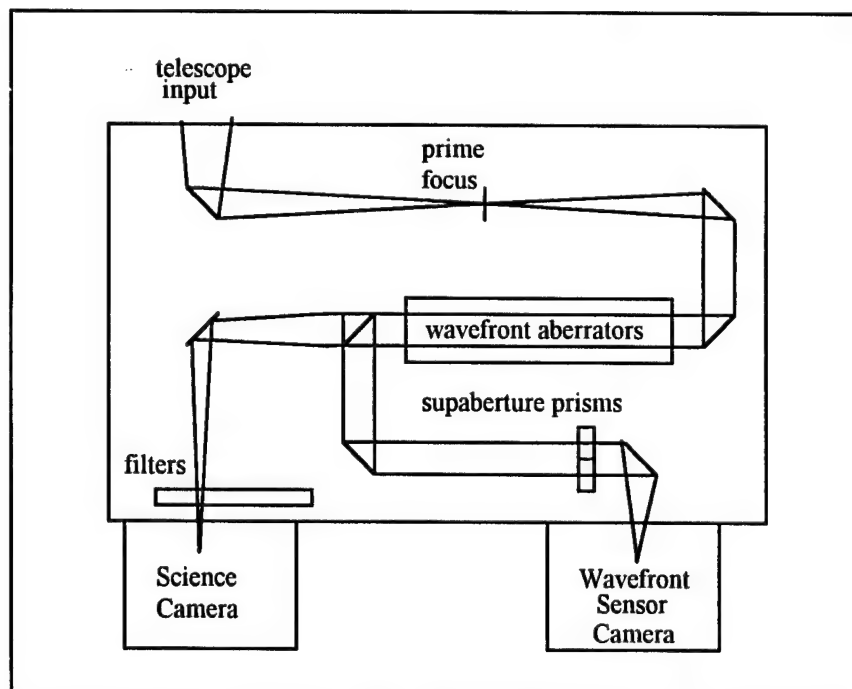


Figure 1. AO-5 Optical Schematic

movable pinhole and set of LEDs which are used to calibrate the wavefront sensor and wavefront aberrators. After collimating the light, the beam goes through a set of five individually actuated wavefront aberrators to remove defocus, then two cylinders, then tip and tilt. A beamsplitter passes some of the light to a lens which reimages the light to a silicon CCD science camera, while the rest of the light is diverted to four prisms which split the light into subapertures. The four resulting beams are focused onto another small CCD camera, where only the active pixels in the four quad cells are read out.

The wavefront aberrators are made with voice coil actuated lens pairs. The defocus aberrator consists of a nearly zero-power pair of simple lenses spaced about 1 mm apart. Changing the separation with the actuators changes the optical power very slightly, just enough to correct the defocus measured over the telescope aperture. The astigmatism correction is accomplished in the same way, but using matched cylindrical lenses. The astigmatic power at the actuator bias point of the cylinders is made zero by using different glass types in lenses with the same (but opposite) curvature. Tip and tilt are corrected by translating very weak lenses transverse to the optical beam.

While the system is not achromatic, science imaging with typical color filters is not impacted. This is primarily because all the lenses are either very weak, or used in nearly zero power combinations, all in collimated light. In future systems, color correction may be optimized by using custom designed achromats or triplets for the focusing lenses.

The wavefront sensor uses four weak prisms to create and divert the four subapertures to the wavefront sensor camera. The four spots are located near the readout register corner in a SpectraSource Lynxx CCD camera, which is based on the Texas Instruments TC211 CCD. This is one of several commercially available cooled CCD cameras designed for low cost astronomical use.

3) Mechanical and Electronic Design

The optical bench measures 18 cm x 31 cm x 60 cm, and bolts directly to the telescope. Without the science camera, it weighs about 18 kg. Cables 15 meters long connect the optics head to a 486DX computer, which contains the camera controller and the actuator digital-to-analog converter card. A small amount of electronics, such as the stepping motor drivers for the filter wheel and the calibration source, and the voice coil drivers, are located in the optical head.

4) Software Control

The computer software performs the functions of reading the wavefront sensor camera, calculating the wavefront errors, and sending the appropriate command signals to the aberrator actuators.

The software also does semi-automatic calibration as frequently as desired. The operator manually corrects the image of the calibration source into the perfect Airy pattern on the science camera by adjusting the aberrator actuators. When completed, the computer then stores those

offset voltages and the corresponding wavefront tilts on the wavefront sensor. This corrects any alignment drift in the actuators. The gain coefficients of the actuators is also automatically measured on demand, which can be used to generate a new reconstructor. Since only five actuators and eight wavefront tilts are measured, the software is fast and simple.

The operator can manually control the position of any actuator between observing runs. The software also gives manual control to a number of other features, such as the filter wheel, calibration source intensity, shutter operation, and wavefront sensor integration time.

5) Performance

The system has been assembled, and is undergoing preliminary calibration and testing starting in January 1996. The system design is limited by the wavefront sensor integration period, with a goal to operate on magnitude 12 stars with 10 millisecond integration time. Actuator response time to a step input is less than 5 millisecc, while the readout time of the wavefront sensor camera, including tilt calculations, matrix multiplication, and actuator output, is less than 3 milliseconds.

To test the system before it is installed, a heat generator will be placed in the calibration beam. The effective r_0 can be measured with the wavefront sensor. The data from this atmospheric simulator will be used in the presentation.

**Natural Guide Star Adaptive Optics
for the 4.2m William Herschel Telescope**

David Buscher

Peter Doel

Ron Humphreys

Richard Myers

University of Durham Department of Physics, Science Laboratories,

South Road, Durham DH1 3LE UK.

Tel: +44 191 374 7462, Fax: +44 191 374 3749

Martyn Wells

University of Edinburgh Institute of Astronomy, Royal Observatory ,

Blackford Hill, Edinburgh EH9 3HJ UK.

Tel: +44 131 668 8358, Fax: +44 131 668 8356

Andy Longmore

Royal Observatory Edinburgh, Blackford Hill, Edinburgh EH9 3HJ UK.

Tel: +44 131 668 8308, Fax: +44 131 662 1668

Bruce Gentles

Gareth Jones

Sue Worswick

Royal Greenwich Observatory, Madingley Road, Cambridge CB3 0EZ UK.

Tel.: +44 1223 374000, Fax: +44 1223 374700

The William Herschel Telescope (WHT) is a 4.2m telescope on La Palma, one of the Canary Islands. The University of Durham (UK) ELECTRA AO system and WHT Natural Guide Star (NGS) AO projects have entered a close collaboration to build a series of AO systems culminating in the WHT NGS system which is specified for common-user (facility) astronomical operation. The collaboration is intended to reduce technical risk through a staged development and to deliver various performance enhancements, based on the ELECTRA segmented mirror design, to the final system. The ELECTRA system, its performance and the project stages are described. The final NGS stage has an opto- mechanical design which permits AO correction to be performed at variable conjugate heights and to dither the science camera field without changing the science pupil. This system and its projected performance are described.

Paper Withdrawn

A Low Cost, High Performance, Self-Scanning Correlating White Light Fringe Tracker System

Jeffrey T. Baker
Rockwell Power Systems Co.
Rockwell International Corporation
P.O. Box 5670
Kirtland AFB, NM 87185
(505) 846-0563 phone (505) 846-7824 fax

Isabelle Percheron,
Darryl Sanchez
Air Force Phillips Laboratory
Kirtland AFB, NM
(505) 846-2711

The concept of using a phased array of small, inexpensive telescopes to achieve high angular resolution of faint, distant objects is nothing new, but the practical considerations of alignment and cophasing has always limited its implementation. To be effective, the coupling of white light from these telescopes must be done in such a way as to achieve zero optical path difference (OPD) between the object being studied, the telescopes, and the point of beam recombination. In practice, this has always been very difficult due to (1.) static and time varying OPD errors from mechanical sources, (2.) large but predictable OPD shifts due to geometrical aspects of the telescopic array, and, (3.) rapid atmospheric turbulence based OPD modulations. In addition to phase errors, one must also deal with time varying mechanical and turbulence based angular misalignments of the beams.

Our system (see figure 1) solves all of these problems simultaneously using a fast tip/tilt/piston mirror, a centroid tracker sensor, a correlating fringe position sensor, and dedicated servo control electronics. An extended quartz-halogen unfiltered white light source illuminates a two hole mask, simulating a dual telescope configuration. A mirrored cube and 4 broadband reflecting optics separate and recombine the two white light beams, making for two optical "trombones." A motorized translation stage on the top optical trombone adjusts course OPD, while the tip/tilt/piston mirror on the bottom trombone makes smaller but faster adjustments. Closed loop bandwidths have been measured to be 700Hz in each axis. A 988mm focal length lens then focuses the two beams down onto the centroid sensor, CCD camera, and fringe position sensor. The fringe position sensor uses a mask which is rotated in two axes to tune it to the fringe which is to be detected. An avalanche photodiode provides adequate sensitivity on detecting the light falling through the mask. Changes in fringe position, if present on the mask, cause changes in fringe sensor voltage output. Decode, scanning, and servo electronics do the work of centering the beams and scanning OPD ± 100 waves until the white light fringe has been locked in.

We discuss our fully functional laboratory demonstration model emphasizing the correlating fringe position sensor, and show a live video of white light fringe acquisition. We then discuss our plans for deployment in the field.

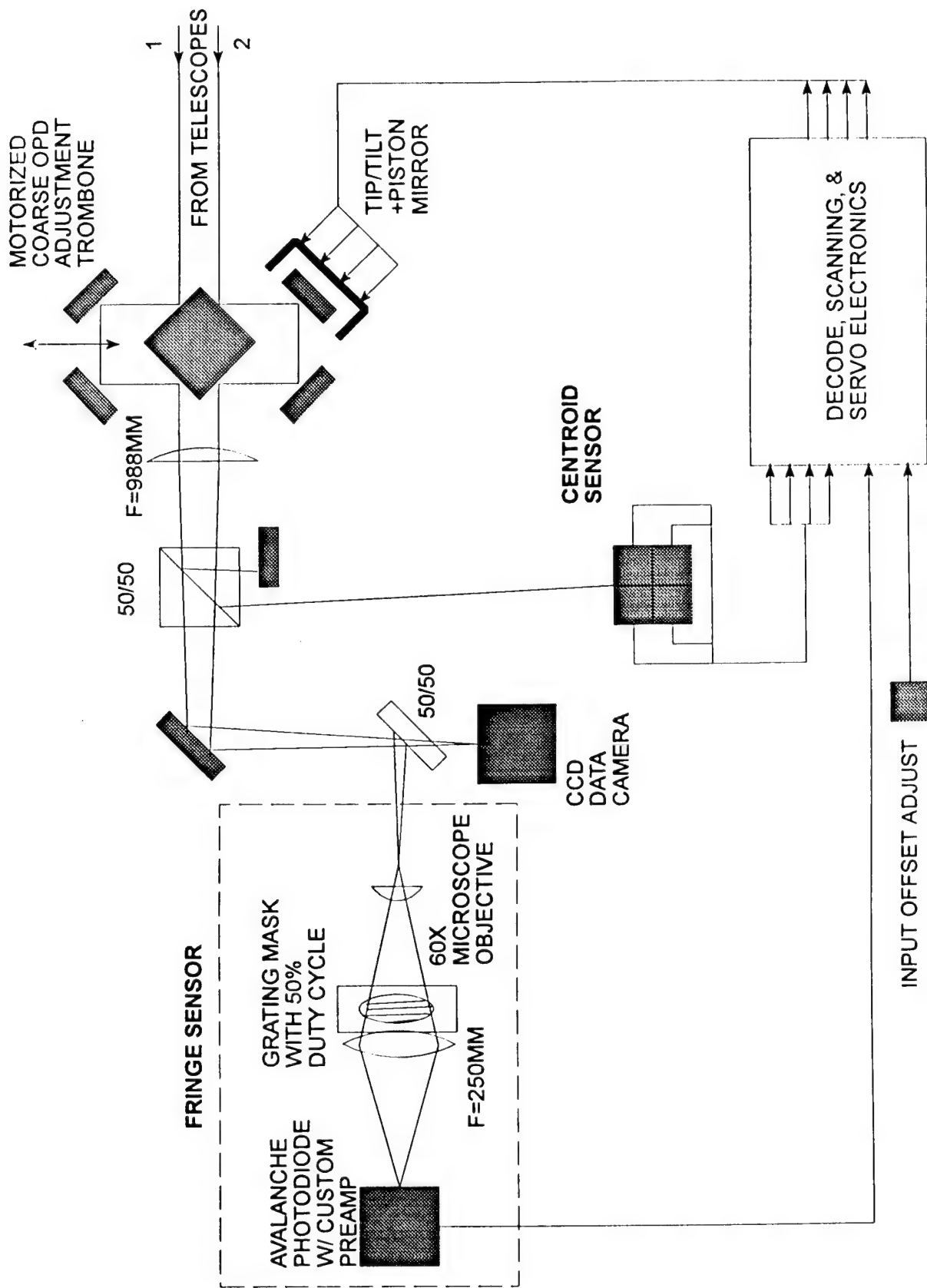


FIGURE 1 OPTICAL LAYOUT OF FRINGE SENSOR DEMONSTRATION

Current status of the Oxford Scalable Sodium Laser Guide Star System

G.P. Hogan, H. Booth, L. Montandon-Varoda and C.E. Webb

Laser Group, Clarendon Laboratory, Parks Road, Oxford OX1 3PU UK

Tel: +44 1865 272205 Fax: +44 1865 272400 Email: g.hogan@physics.ox.ac.uk

Introduction

Oxford is currently designing a scalable laser system to generate a sodium layer laser guide star (LGS) for astronomical adaptive optics. The emphasis in our design is upon an architecture that allows the average output power of the system to be increased arbitrarily without increasing peak power, and thus saturation level in the sodium layer. It is intended that in this way a system may be designed that, once installed, may be enlarged in the confidence that additional power launched will result in additional photons returned.

The architecture around which our system is designed employs a single, CW dye master oscillator (DMO) and an arbitrary number of pulsed dye amplifiers. The output wavelength of the DMO is accurately locked to the sodium D_2 transition in an atomic sodium cell, and is spectrally broadened to give an effective bandwidth of around 600 MHz. The output of the DMO is then routed to the first of a number of pulsed dye amplifier "sub-units". Each "sub-unit" consists of one or two dye cells, pumped by a high pulse repetition frequency (prf), short pulse pump laser. The amplified, pulsed output is then returned to a common output beam path to beam diagnostics and the launch telescope. The DMO beam is then re-routed to the next amplifier sub-unit, the output of which is returned to the same beam path as the first.

The output pulse format of our system, therefore, consists of a burst of short, relatively low energy pulses, followed by a delay, the number of pulses in the burst corresponding to the number of dye amplifier sub-units, as illustrated in Fig 1.

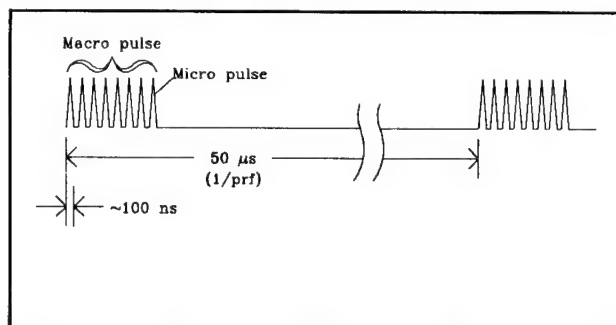


Figure 1

In this way the average output power of the system may be increased by the incorporation of additional amplifier sub-units, thus increasing the number of pulses in the burst, without increasing the peak power, which remains that of a single pulse. The peak power of the individual pulses may therefore be optimised to provide the highest conversion efficiency in the dye cell, whilst retaining an acceptable level of saturation of the mesospheric sodium.

We are currently using the copper vapour laser (CVL) as our chosen pump beam source for its combination of prf, pulse energy, pulse length and wavelength. We are, however, aware of the current generation of high prf, Q-switched Nd:YAG lasers. Commercial devices are approaching the pulse parameters desirable in this application. It is a characteristic of our design that power scaling by the incorporation of additional amplifier sub units may be accomplished using a variety of different pump sources for them.

There are a number of multiplexing schemes currently under consideration for the delivery of the DMO seed beam to the amplifier sub-units, and the recombination of the amplified beams into a single, high beam quality, output. These each offer different advantages and disadvantages, and the two most promising have been presented elsewhere (Hogan and Webb, 1995).

Current status

We are currently at the stage of studying a number of specific technical issues associated with our design in order to optimise the individual components of the system, and optimise each.

We have constructed a DMO consisting of a commercial argon ion laser pumping a commercial dye laser. A "universal" sodium cell has been constructed to allow the evaluation of a number of the potential frequency locking techniques, both Doppler limited and Doppler free, to allow the selection of the most suitable in this application. Electro-optic phase modulation techniques are also being studied to allow the output effective bandwidth to be tailored to make optimum use of the Doppler profile of the mesospheric sodium population. In this way the optimum spectral format may be imposed on the output of the DMO, and hence on the LGS as a whole.

Custom dye amplifier cells have been procured and experiments on the single and double pass, pulsed amplification of a cw seed beam have been commenced. Experiments with single and double sided pumping also are to be undertaken in order to minimise the

number of dye cells required whilst maximising the efficiency of conversion of pump laser power into the required wavelength.

The efficient fibre optic delivery of high power, pulsed pump laser light, and its efficient coupling into a dye cell is also being studied. This is a vital constituent of our system in order to allow the pump lasers to be sited remotely from the telescope, whilst the dye amplifiers are mounted on the telescope gantry itself. It is intended that the DMO, too, be sited with the pump lasers, its beam being conveyed to the amplifiers via single mode fibre. There are a number of reasons for keeping as much of the system away from the telescope as possible. It greatly simplifies access for maintenance and alignment, it simplifies the management of the waste heat generated in order to minimise the impact on dome seeing, and it minimises the number (and weight) of components that need to be mounted on the telescope gantry itself.

Conclusions

Experiments addressing various design issues relating to our design of scalable laser system for sodium laser guide star generation are well under way, and the current status will be presented.

References

Hogan G P and Webb C E (1995)

Proposed design for a scalable dye laser for use in sodium laser guide star generation

Adaptive Optics, Vol. 23, 1995 OSA Technical Digest 121-123

A Solid State Raman Laser for Sodium D₂ Line Resonant Excitation

E. C. Cheung, J. G. Ho, H. Injeyan, M. M. Valley, J. G. Berg

Laser Research Dept. TRW

R1-1184 One Space Park, Redondo Beach, CA 90278, Tel: (310) 812-2587, FAX (310) 813-4873

R. L. Byer, Y. Huang

Center for Nonlinear Optical Materials - Edward L. Ginzton Laboratory

Stanford University, Stanford, CA 94305-4085, Tel: (415)723-0228, FAX: (415) 723-2666

A reliable, cost-effective sodium resonance source is needed for mesospheric sodium excitation in adaptive optics applications [1-2]. Previous approaches include a dye laser pumped by a green source and systems with nonlinear frequency conversion [3,4]. This paper presents a new, all solid-state source [5], which can be scaled to over 100 W in average power at 589 nm. In this approach, a 1064 nm Nd:YAG laser pumps a CaWO₄ Raman laser with an intra-cavity doubler (Fig. 1). Alignment of the frequency conversion system is relatively simple because the Raman process requires no phase matching, and the doubling crystal is non-critically phase matched LBO.

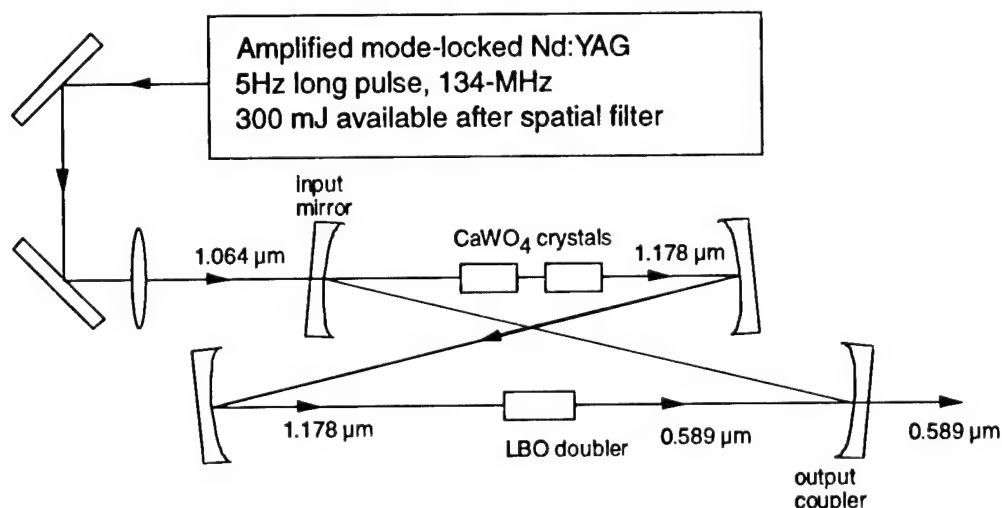


Figure 1. Schematic diagram of the experimental set-up.

The pump laser consists of a long-pulse, mode-locked Nd:YAG master oscillator and two power amplifiers operating at 1064 nm, all flash lamp pumped at 5 Hz. Output from the master oscillator is a 70 ms long train of 350 ps mode-locked pulses with a 7 ns repetition rate. After amplification and spatial filtering, the macro-pulse has a maximum energy of 300 mJ. An individual mode-locked pulse has a maximum energy of 30 mJ and peak power of 86 kW. The mode-locked pulsewidth remains close to 350 ps, measured by auto-correlation. The pump beam is mode matched into the bow-tie cavity.

The bow-tie resonator shown in Fig.1 has a temperature-tuned lithium triborate (LBO) crystal to frequency double the intracavity 1178-nm beam to 589 nm. As a result of good spatial mode matching and the bow-tie cavity design, TEM₀₀ mode output in the yellow is produced.

Temporal profiles of the macro-pulse envelopes are shown in Fig. 2(a) for the pump, transmitted pump, and the yellow output. These profiles are normalized to the measured pulse energy. The peak energy conversion efficiency from pump to yellow is 30%, and integrating over the entire pulse produces an overall conversion efficiency of 14.5% (Fig. 2(b)).

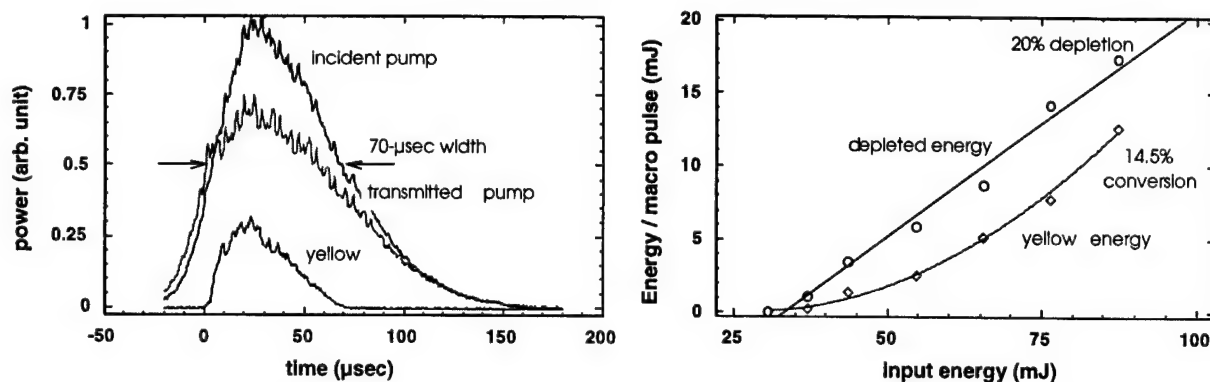


Figure 2. (a) Temporal profiles of macro-pulse envelopes normalized to measured pulse energy. (b) Overall energy conversion.

An etalon in the bow-tie cavity is used to tune the Raman wavelength so that the yellow output matches the D_2 sodium line (Fig. 3(a)). The 911 cm^{-1} Raman line of CaWO_4 [6] has sufficient bandwidth to tune the yellow output to the D_2 sodium absorption line at 988.995 nm. Figure 3(b) shows the Raman gain curve of CaWO_4 deduced from Raman fluorescence scans. At the D_2 sodium line, the gain drops to approximately 60% of the peak, but nonetheless it is sufficient for the Raman laser to reach threshold. To verify tuning around the D_2 line, the yellow output beam was sent through a heated sodium vapor lamp, and resonance fluorescence was observed.

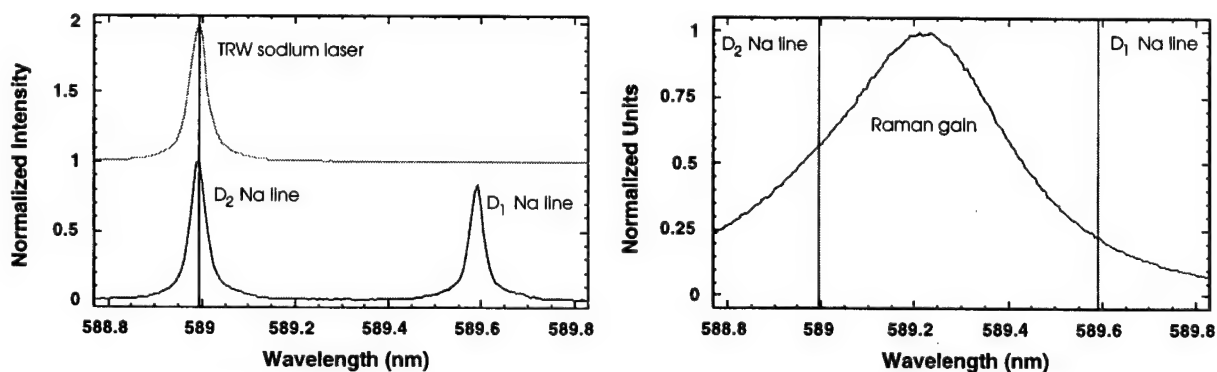


Figure 3. (a) Laser output and the sodium emission lines from a vapor lamp. (b) Raman gain profile after doubling to the yellow.

In conclusion, an all-solid-state sodium resonance excitation source, with good beam quality and high conversion efficiency, has been demonstrated. Tuning of the yellow output to resonance with the D_2 sodium line was demonstrated. By independently tuning both the Nd:YAG wavelength [3] and the Raman wavelength, 30% conversion from 1064 nm to 589 nm should be obtained, with the yellow output matching the D_2 sodium line.

This work is partially funded by the Air Force Phillips Laboratory. The authors wish to thank Bruce Chai for valuable discussions.

References

1. R. Q. Fugate, D. L. Fried, G. A. Ameer, B. R. Boeke, S. L. Browne, P. H. Roberts, R. E. Ruane, G. A. Tyler, and L. M. Wopat, *Nature (London)* 353, 144 (1991).
2. R. A. Humphries, C. A. Primmerman, L. C. Bradley, and J. Hermann, *Opt. Lett.* 16, 1367 (1991).
3. Thomas H. Jeys, A. A. Brailove, and Aram Mooradian, *Appl. Opt.* 28, 2588 (1989).
4. E. C. Cheung, Karl Koch, and Gerald T. Moore, *Opt. Lett.* 19, 1967 (1994).
5. Patents pending by Stanford and TRW.
6. J. P. Russel and R. Loudon, *Proc. Phys. Soc.* 85, 1029, (1965)

Nd:YAG Laser Beam Pointing Stability and Artificial Guide Star Generation

Vadim A. Parfenov and Sergei N. Rodin

Research Centre "S.I.Vavilov State Optical Institute"
 12, Birzhevaya liniya, St.Petersburg, 199034, Russia
 Fax: (812)218-3720

Laser beam pointing instability is one of the most actual problem at the artificial guide stars generation, because high angular stability ($\sim 1...2$ arcsec) of laser beacons is required for atmospheric compensation with adaptive optics. In our work we investigated the beam pointing stability of frequency-doubled Nd:YAG lasers generating at the wavelength of 532 nm. Such lasers may be used for guide stars generation by Rayleigh optical scattering by air molecules in the stratosphere [1].

We studied the angular position stability of beams of available cw, lamp-pumped, frequency-doubled Nd:YAG lasers. The purpose of our work was to reveal the basic reasons causing the instability of beams angular position of Nd:YAG lasers and to measure the values of beams angular displacements.

Our work enabled to obtain experimental data about reasons, character and values of angular displacements of the lamp-pumped Nd:YAG lasers' beams. In particular, the results analysis revealed both the slow drift of the laser beam axis and its fast oscillations in the range of 0.01...1.0 Hz. The maximum fast oscillations of the beam axis occurred during the first 5...10 minutes of laser action, when the generation steady-state was establishing (the maximum amplitudes of the fast oscillations for lasers operating at various power levels were 20...30 arcsec). Later the amplitude of the fast oscillations was gradually diminishing. As for the slow drift of the beam axis, during some period from the start of laser action its beam axis was continuously moving from an original position to another one; when movement finished, the axis revealed small oscillations with respect to this position. The total slow displacement of the radiation beams from an original position during 1 hour of laser action for lasers operating at various power levels were 10...15 arcsec. After that beam axis revealed slow oscillations with respect to this new position within the angle interval of ± 2 arcsec. The overlapped fast oscillations occurred with spread up to 3 arcsec.

The experiments carried out provided that the basic destabilizing factors influencing beam pointing stability of lamp-pumped, frequency-doubled Nd:YAG lasers are the thermal deformations of the active element, transient processes induced by the establishment of second harmonic generation regime, thermal deformations of the resonator construction and mirrors as well as the vibrations of the laser cavity elements (caused, in particular, by influence of a cooling agent onto the active element).

Moreover, our work can result in conclusion that because beams angular displacements are high, the use of Nd:YAG lasers for guide star generation needs stabilization of beams angular position.

1. R.Foy, M.Tallon, M.Sechaud and N.Hubin, "ATLAS experiment to test the laser probe technique for wavefront measurements" in *Proceedings of SPIE*, Vol. 1114, pp. 174-183 (1989).

First Results of a Polychromatic Artificial Sodium Star for the Correction of Tilt

Herbert Friedman*, Renaud Foy, Michel Tallon** and Arnold Migus*****

***Lawrence Livermore National Laboratory, Livermore, California**

****Centre de Recherche en Astronomie de Lyon, Lyon, France**

*****Laboratoire d'Optique Appliquée, Ecole Polytechnique-ENSTA, Palaiseau, France**

With the present state of technology, the tilt component of a aberrated stellar wavefront which has been distorted by atmospheric turbulence cannot be ascertained by an artificial guide star. The absolute position of the artificial guide star cannot be determined since it wanders on the uplink portion of its propagation and there is no way, at least with a single receiving telescope, to distinguish an undetermined position of a guide star from tilt in the wavefront. In conventional adaptive optics systems, a natural star is needed to supply the tilt information in addition to the higher order corrections supplied by an artificial guide star. The probability of finding a suitably bright natural guide star for tilt correction is not significantly higher than for higher order correction despite the fact that the entire telescope area is used and both the tilt anisoplanatic angle and integration time are considerably larger. Since the tilt contributes $\approx 90\%$ of the phase variance, the accuracy in the tilt measurement has to be much greater than for higher order corrections¹. In particular at galactic latitudes above the galactic plane, or at visible wavelengths, the sky coverage for a tilt star becomes unacceptable for most applications.

A new concept has been proposed² which uses two wavelengths to optically pump the mesospheric sodium atoms to a higher level from which several lines are emitted. The two pump wavelengths, 589 nm and 569 nm are sufficiently close for dispersion to be negligible so that the optically pumped region is essentially the same volume as in the standard monochromatic guide star. However, the shower of lines all emanating from a single spatial position do suffer atmospheric dispersion and this effect can be used to measure the tilt aberration. In particular, the dispersion from one emission line at 330 nm is compared to the dispersion from the sodium D₁ line, chosen to eliminate interference with the pumping D₂ line, forms the basis of the technique.

Although the measurement scheme is on solid theoretical grounds, the difficulty lies in the measurement accuracy which is required and the subsequent need for high power lasers. For the two wavelengths chosen, the dispersion is only a few percent. This means that the centroids of the guide star viewed with 330 nm and 590 nm filters must each be resolved to an accuracy of a few milliarcseconds in order to resolve the differential motion. This measurement accuracy imposes a minimum on the signal to noise ratio in the centroid detector which requires high laser power. There are several innovations which can reduce the laser power requirement including better UV detectors. For the present, however, estimates were that about a hundred watts of average power in each of the two pumping wavelength are needed for this measurement. Previous (monochromatic) laser guide experiments at LLNL³ propagated over 1200 W at 589 nm and the capability does exist to split that power between the two pumping wavelengths.

As a first feasibility experiment, a joint experiment was carried out at LLNL during the first two weeks in January of 1996. Despite the usually poor weather in northern California during the winter season, 4 acceptable nights were encountered and this paper presents the results of that preliminary experiment. An optical system was designed, built and installed at the Cassegrain focus of a 50 cm telescope adjacent to the Atomic Vapor Laser Isotope Separation (AVLIS) building at LLNL. The optical system displayed both 330 nm and 590 nm guide stars in addition to a natural guide star for reference. The laser system was developed by the AVLIS program and was modified to deliver the two pumping

wavelengths with about 400 W -500 W of average power at system repetition rates of 4.3 kHz and 12.9 kHz and with a pulse duration of about 40 ns. The power split between the two lines was variable but generally equal. The laser beam was expanded to a rectangle of 40 mm x 80 mm and was projected out of an "elevation over azimuth" beam director 5 meters from the receiving telescope.

A schematic diagram of the optical system is shown in Figure 1. Three spectral channels are separated using dichroic beam splitters (3) and (5), for the 330 nm line, the sodium D₁ line, and a broader bandwidth for a superimposed natural star. In the laser line bandwidths, dispersion components are used to make the number of photons from the natural star lower than the photon noise in each laser line (see Fig. 1).

The three spectral channels produce three separated images of the same field on a Photometrics (Model CH250) CCD camera which uses a Texas Instruments CCD chip (TK512 MPP).

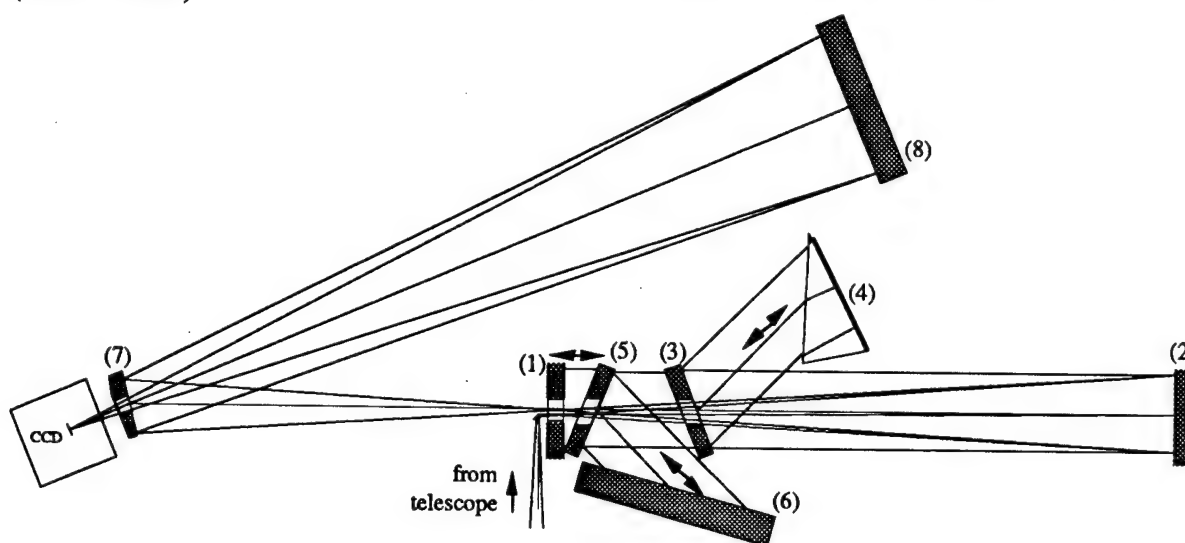


Figure 1. Simplified layout of the optics system. Two dichroic beam splitters isolate the UV (3) and the yellow (5) bandwidths. The broad band part is reflected on the flat (1). Dispersion elements are a prism (4) and an échelle grating (6).

The LLNL AVLIS laser system is a copper vapor laser pumped dye laser with full beam control including wavefront correction, wavelength stabilization and modulation, low bandwidth pointing and centering control and high bandwidth jitter control. A dye was chosen for the amplifiers which could provide gain for both wavelength in a co-propagation mode but the outputs of two separate dye oscillators were combined for this experiment. The modulation format for the 569 nm line was chosen to be single, 1 GHz wide format but two modulation formats were tried for the 589 nm line. The first was again a single, 1 GHz wide profile while the second was a double peaked, 3 GHz wide profile which was the format first used in the previous LLNL monochromatic guide star experiments³.

Observations of the radiative decay from the 4D5/2 energy level of mesospheric sodium atoms have been restricted to the 330nm and D₁ lines. The 569nm laser light was broadened to 1 GHz to fit with the Doppler profile in the mesosphere. The following laser parameters have been varied to attempt to maximize the returned flux in the D₁ line:

- the central wavelength of the D₂ line has been scanned from -2.1 to +1.8 GHz around the middle of the hyperfine structure with a 1 GHz FWHM profile. Fig. 2 shows the variation of the returned D₁ line. The curve peaks at -750 MHz. It is consistent with the convolution of the Doppler profile with the 1 GHz laser profile.

- the D₁ flux is roughly doubled when broadening D₂ from 1 to 3 GHz.
- the D₁ flux varies smoothly when tuning the central wavelength of the 569nm line.
- the balance between the D₂ and the 569nm lines has been varied from 30%-70% to 70%-30%, with little effect on the returned flux, as expected.
- the returned flux is slightly decreased when the repetition rate is increased from 4.3 to 12.9 kHz, which means that the sodium layer was not saturated.

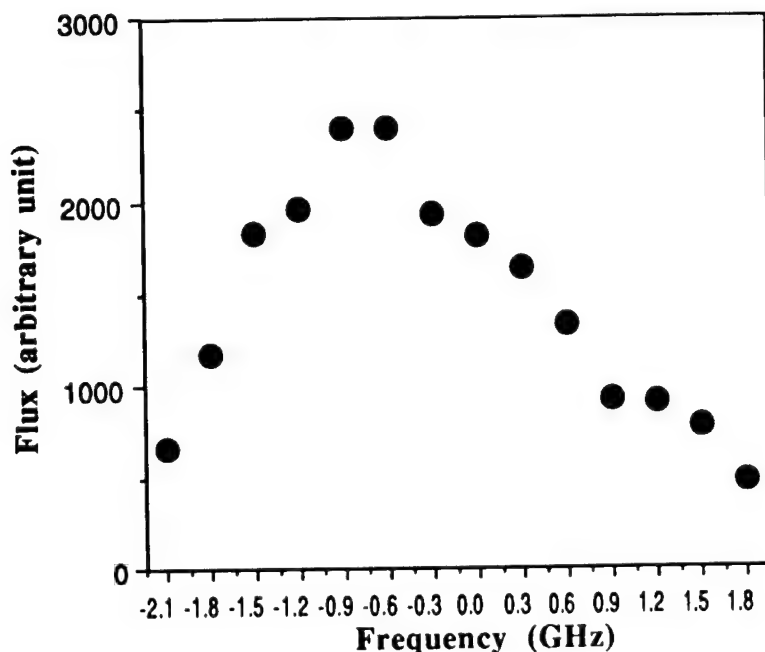


Figure 2. Returned flux in the D1 line versus shift of the central frequency of the D2 line beam.

With the optimized parameters (3 GHz wide D₂ line at -750MHz and a rep rate of 4.3 kHz), the returned flux in the 330nm line has been evaluated, using for the calibration the UV spectrum of the star SAO60855 observed simultaneously. Typically 16000 photons are detected per second with a seeing of $\approx 2.5\text{-}3''$, which is consistent with the flux requirement to sense the tilt at a good site.

The next step of the polychromatic artificial star concept will aim at tilt measurements. It will require to increase the sensitivity of the whole process, e.g.: by a factor of 3 using a CCD with a quantum efficiency of 70% in the UV, and by a factor of 1.3 using a polarized beam. In further steps, the polychromatic star should be observed through an adaptive optics to improve the accuracy in the tilt measurement and accordingly decrease the laser power.

Acknowledgements

CNRS (ULTIMATECH and INSU), GIE SYLAREC provided the funds for this experiment. We wish to thank the United States Enrichment Corporation for providing access to AVLIS laser and propagation facility.

- [1] Rigaut, F. and Gendron, E.: 1992, *Astron. Astrophys.* **261**, 677.
- [2] Foy, R., Migus, A., Biraben, F., et al.: 1995, *Astron. Astrophys. Supp.* **111**, 569.
- [3] Avicola, et al. *SPIE*, **2201**, 326, 1994

Design of an Infrared Camera Based Aircraft Detection System for Laser Guide Star Installations

**Herbert Friedman and Bruce Macintosh
Lawrence Livermore National Laboratory
Livermore, California**

For laser guide star installations above a few watts in average power, the irradiance of the beam exceeds the ANSI¹ standards for eye safety and an aircraft detection system is required to insure that pilots or passengers are not blinded. Even for powers lower than this level, numerous incidents of temporary flash blindness have been observed² and pose a threat to the safety of aircraft. LLNL has deployed two laser guide star systems^{3,4} and has obtained permits from the Federal Aviation Association which insure safe operation of these lasers. These aircraft detection systems use a combination of a rotating search radar, a narrow angle, boresight radar and visual observers to provide a triple layer of detection, each with its own access to the laser safety shutter.

For the installation of a 20 W for the generation of sodium-layer beacons at the 10 m Keck Observatory on Mauna Kea, the presence of active radars is not desirable. The reasons for this are possible interference with sensitive optical instruments at or near the Keck telescope and the presence of millimeter wave radio telescopes, also on the Mauna Kea site. An alternative for the active radar are passive near infrared cameras. Such cameras are commercially available using focal plane arrays of either Indium Antimonide (InSb) or Platinum Silicide (PtSi) which are sensitive in the 3-5 micron band.

There are many advantages to passive infrared cameras. These commercial cameras, operating at video frame rates, cannot detect stellar or planetary sources; this greatly reduces and in some applications eliminates altogether the signal processing required. The contrast between the cold night sky background and the hot exhaust emission of jet or piston aircraft engines is high so that the detection range of infrared equals or exceeds many small radars. The possibility of an aircraft not having lights as, for example, in the case of illegal or disabled aircraft, does not affect the detection scheme. Finally, infrared cameras can provide some penetration in haze and light cloud cover which can severely limit the detection capability of a visible camera.

Two infrared cameras have been tested at LLNL, one with a 256x256 pixel InSb array⁵, and the other with a 512x512 pixel PtSi array⁶. Tests were carried out in conjunction with a LLNL search radar to provide slant range information on detected aircraft. With both cameras, once the aircraft was resolved across more than one pixel it was easily visible, and even unresolved aircraft could be detected out to ranges of 10-12 miles. The InSb camera could in fact easily

detect large commercial aircraft out to ranges of 20 miles or more, and small single-engine aircraft at ranges of 12 miles. Aircraft were somewhat easier to detect from the rear than when approaching. Since air traffic was relatively low during these nighttime tests, and visibility somewhat limited by buildings at the LLNL sight, all possible combinations of aircraft size and distance were not tested. However, the IR cameras detected essentially every target within line of sight that could be detected by the radar. The PtSi camera did have some difficulty with very small aircraft seen from the front at ranges of greater than 6 miles. These tests were carried out with no signal processing whatsoever - aircraft were easily visible on the direct video output of the camera. More sophisticated target-detection algorithms operating on the digital output of the camera would provide even greater detection ranges. Both these cameras are extremely simple to operate, with self-contained closed-cycle coolers and both direct video and digital data readout.

With current technology a trade-off exists between InSb arrays, which are significantly more sensitive, and PtSi arrays, which are available in larger formats (512x512 pixels vs. 256x256.) Careful consideration must be given to selecting the best array for a particular purpose. For our application we prefer the InSb camera for the boresight sensor, to maximize sensitivity over a narrow field of view, and possibly the PtSi array for the wide-angle search application.

For the narrow angle, boresight application, a 7-10° field of view lens is sufficient and is readily available as a commercially supplied item. The camera would be located adjacent to the projection lens of the guide star laser system and would not be required to move. The camera would be enclosed in a box with heaters to prevent damage during cold nights. No software other than a threshold detector is required and the laser shutter would simply be closed if any aircraft entered the narrow angle field of view. The laser shutter system is sufficiently fast as to close the beam before an aircraft enters the center of the field of view where the laser beam is.

For the wide angle search function, there are several options. The camera should be located on top of the dome and would need to be shielded from the elements as well as heated when necessary. To cover the entire sky either the camera or a mirror/lens system could be scanned about the vertical axis. A better option in terms of low maintenance would be to use a hemispherical lens with full 180° coverage or a "panoramic" lens with has full azimuth coverage but has a hole centered about zenith. Most search radars also have this blind spot directly overhead. LLNL has designed both these lenses for other programs and designs at a commercial optical vendor presently exist⁷. Although these lenses are expensive, they may be the least expensive option when maintenance and software costs are folded in the estimate.

Even in a low-traffic area such as Mauna Kea the all-sky system could not simply shut down every time it detects an aircraft, since it will be sensitive to aircraft 10-20 miles away that may be in no danger from the laser. Either a human will have to monitor the all-sky display or a more sophisticated algorithm will have to be used, defining a cone or cylinder surrounding the laser beam. One disadvantage of passive infrared systems is that they provide no direct range information. However, once a target is close enough to be resolved (even if it spans only 2-3 pixels) its surface brightness per unit angle can be determined. Surface brightness is of course independent of range, and can be used to distinguish the hotter exhaust of jet aircraft from small propeller-driven aircraft. This classification can then be used together with the angular size of the target to provide an estimate of the range. For this reason we prefer the large-format PtSi array for wide-angle search application. For an all-sky application the PtSi array may be better, since it could resolve targets at a greater range.

The use of passive infrared cameras for aircraft detection has been discussed with officials at the FAA and has received a positive response; the burden of demonstrating the effectiveness of such systems remains, as always, with the laser group. A plan to purchase the InSb camera for the boresight camera and test the concept both at LLNL and the laser installation at the Lick Observatory has been formulated. Simulation of the wide-angle camera system to decide the optimal target detection and laser shutdown algorithms are being conducted. After detailed design, a camera and lens system will be purchased for the wide angle camera and tests will be repeated at the same locations. The FAA will be invited to witness both demonstrations prior to the filing of a formal permit for laser operation.

Acknowledgements

Funds for this investigation were provided by the W. M. Keck Observatory, California Association for Research in Astronomy.

References

1. American National Standards Institute, Inc. ANSI Z136.1-1986
2. Photonics Spectra, January 1966, p50
3. Avicola, K, et al, SPIE 2201, 326, 1994
4. Friedman, H., SPIE, 2537, 1995
5. Radiance 1 camera, manufactured by Amber, 5656 Thornwood Dr., Goleta, CA 93317. Phone: (800)-2322-6237
6. M-500 camera manufactured by Mitsubishi electronics. Contact: Mike Mays, 5665 Plaza Drive, Cypress CA 90630. Phone: (714)-236-6163.
7. Personal communication from Martin High, Applied Physics Specialty, Ltd, 17 Prince Andrew Place, Don Mills, Ontario, Canada, M3C 2H2.

**Focal Anisoplanatism Effect Affecting Techniques
for Laser Guide Star Absolute Tilt Measurements**

A. Riccardi, R. Ragazzoni, S. Esposito
Osservatorio Astrofisico di Arcetri, Italy

We present calculations aimed at establishing the error resulting from the anisoplanatism effect when two auxiliary telescopes are used to obtain the overall backward wave-front tilt from a laser guide star.

Analysis of Sodium Layer Scattering Physics

Peter W. Milonni
Atomic and Optical Theory Group (T-4)
Mail Stop B-212
Los Alamos National Laboratory
Los Alamos, New Mexico 87545
Tel. 505-667-7763
Facs. 505-665-6229

and

John M. Telle
Starfire Optical Range
Phillips Laboratory
3550 Aberdeen Ave. SE
Kirtland AFB, New Mexico 87117
Tel. 505-846-4712 ext. 332
Facs. 505-846-2213

We describe calculations of the photon return signals from mesospheric sodium fluorescence excited by laser pulse trains. The theory combines a full density-matrix treatment of the sodium D_2 line, including Doppler broadening and polarization-dependent optical pumping effects, with the Fried model of optical propagation through the turbulent atmosphere.

The photon return signal depends on the laser polarization, spectral distribution, beam quality, size and shape at launch, and temporal pulse format. We have focused our attention on two types of laser pulse trains: long, phase-modulated pulses whose spectra cover the roughly 3 GHz-wide sodium absorption profile, and short pulses producing coherent excita-

tion. "Long" and "short" pulses here are defined relative to the 16 ns radiative lifetime.

It is found that the spatial profile of the laser radiation in the mesosphere plays an important role in determining the return signal. In particular, as the laser pulse intensity is increased the spatial profile leads to a saturation of the return signal that can differ substantially in character from the saturation behavior of the sodium atoms themselves. Thus the evaluation of any particular laser pulse format must take into account not only the details of the temporal and spectral characteristics of the pulses, but also their propagation through the turbulent atmosphere. Consideration of these spatial effects is important also because, while the excitation of a larger area of sodium atoms in the mesosphere will lead to more backscattered photons, there can be a deleterious effect on the adaptive compensation for atmospheric turbulence.

Assuming typical values of the Fried coherence parameter r_0 , we have calculated variations of photon returns with peak pulse intensities in good agreement with long-pulse data measured by a group at Lawrence Livermore National Laboratory. Here we also describe computations that assume considerably larger pulse powers in order to assess the importance of saturation. These computations indicate that analytical fits to the photon backscatter versus peak pulse intensity are accurate over the entire range of intensities of interest, and in particular that there is no saturation effect above and beyond that computed over the range of smaller intensities. Depending on the laser polarization and pulse duration, the saturation behavior for long phase modulated pulses follows that expected for *homogeneous* line broadening, in spite of the strongly inhomogeneous (Doppler) broadening of the mesospheric sodium D₂ line. The effective saturation intensity $\sim 5 \text{ W/cm}^2$ deduced from the numerical simulations is consistent with an approximate analytical expression involving the spectral

overlap of the laser pulse spectrum with the sodium absorption profile.

The dependence of photon return signals on peak pulse intensities is considerably different in the case of short pulses, where coherent effects such as π -pulse excitation come into play. Our results show that the relative merits of long and short pulse trains depend strongly on achievable powers, duty cycles, and spatial field profiles.

Monday, July 8, 1996

Laser Technology and Laser Guide Stars

AMC 2:00 pm-4:10 pm
Pikake Room

Michael Lloyd-Hart, *Presider*
University of Arizona

Review of laser technology and status

Robert Q. Fugate

Starfire Optical Range, Phillips Laboratory

3550 Aberdeen Ave, SE, Kirtland AFB, New Mexico 87117-5776, USA

Phone (505) 846-4712 ext 314, Fax (505) 846-2213, Internet: fugate@plk.af.mil

This paper reviews the status of laser technology for the generation of artificial laser guide stars. The emphasis is on laser devices currently in use, under development, and planned. Lasers designed for resonant scattering in mesospheric sodium represent the major interest and area of greatest development. Mesospheric potassium and iron are metals of interest[1] since their wavelengths (769 and 372 nm, respectively) and nearly gaussian shaped absorption profiles are more easily reached by existing, solid-state laser materials such as Alexandrite and Ti:Sapphire. There is at least one example of lidar measurements using potassium as a mesospheric tracer[2]. Molecular oxygen and nitrogen are attractive since they are approximately 10 orders of magnitude more abundant than sodium but are problematic since conventional resonant excitation requires ultra-violet wavelengths. A few systems use or have used beacons generated by Rayleigh scattering.

Mesospheric sodium for laser guide star generation was first suggested by W. Happer in 1982[3]. The first atmospheric measurements using sodium beacons were made by Humphreys *et al.*[4], and Lloyd-Hart *et al.*[5] were the first to my knowledge to use a sodium laser guide star in a real time control loop. However, as this is being written (Feb, 1996) I have not seen a compensated image showing improved quality produced by a higher-order adaptive optics system operating from a mesospheric sodium beacon. In large part this seemingly slow progress is due to the difficulty in producing a practical laser having simultaneously sufficient power, beam quality, spectral properties, and a temporal format suitable for efficient excitation of mesospheric sodium.

Table 1 is a summary of sodium frequency laser devices actually fielded and used for measurements or adaptive optics. The fielded devices include installations during 1995 of a 15 watt pulsed dye laser at the 3m Lick telescope[6] and an 8 watt solid-state, sum-frequency laser at the 3.5m ARC telescope[7]. Table 2 lists mesospheric sodium lasers under development as well as conceptual ideas being demonstrated in the laboratory. There are at least two new concepts using CaWO_4 for intracavity Raman shifting Nd:YAG or configurational tuned ND:YAG to 1178nm and then frequency doubling to 589nm. Table 3 is a summary of Rayleigh beacon lasers and their current status.

The physics and engineering trade-offs of these lasers will be discussed.

References

- [1] G. Papen, "Mesospheric metals for guide star generation," in *Adaptive Optics, Technical Digest Vol 23*, Opt. Soc. Am., Garching, 247-249 (1995).
- [2] U. von Zahn, *Geophys. Res. Ltrs.*, **23**, 141-143 (1996).
- [3] W. Happer and G. J. MacDonald, MITRE Corporation reports JSR-82-106 and JSR 84-109 which are summarized in the first seven sections of the paper "Atmospheric-turbulence compensation by resonant optical backscattering from the sodium layer in the upper atmosphere," by W. Happer, G. J. MacDonald, C. E. Max and F. Y. Dyson, *J. Opt. Soc. Am. A* **11**, 263-276 (1994).
- [4] R. A. Humphreys, C. A. Primmerman, L. C. Bradley, and J. Hermann, "Atmospheric-turbulence measurements using a synthetic beacon in the mesospheric sodium layer," *Opt. Letters* **16**, 1367-1369 (1991).
- [5] M. Lloyd-Hart, R. Angel, B. Jacobsen, D. Wittman, D. McCarthy, E. Kibblewhite, B. Carter, and W. Wild "Preliminary closed-loop results from an adaptive optics system using a sodium resonance guide star," in *Adaptive Optics in Astronomy*, M. Ealey and F. Merkle, eds., Proc. SPIE **2201**, 364-372 (1994).
- [6] H. Friedman, *et al.*, "Sodium Beacon Laser System for the Lick Observatory," Proc. SPIE **2534**, 150-160 (1995).
- [7] E. Kibblewhite, "Status of ChAOS," Townes Workshop on Optical/Infrared Interferometry and Adaptive Optics, Berkeley (1996).

Concept	Temporal format	Duty cycle	Ener/pulse avg pwr	Spectral width	Beam quality	Status	Comments	Reference
Flashlamp pumped R6G dye	4μs pw, 20pps	0.012%	120 mJ/p 2.4 watts	3 GHz	4 x DL	Used at WSMR in SWAT I 1984	Built by AVCO for MIT/LL	LL Journal, 5(1), 45, 1992
Flash lamp pumped dye	2μs pw, 7.5pps	.0015%	20 mJ/p 0.15 watt	10.1 pm	0.4mrad div.	Used in 1987 Mauna Kea experiments	UIUC Lidar system	Nature, 328, 229-231, 1987
Flash lamp pumped 1.06 +1.32 Nd:YAG summed in LiIO ₃	100μs macro@ 10pps, each a 100MHz train of 0.7ns pulses	0.007%	0.5J 5 watts	3 GHz	2 x DL	Used in atmospheric measurements of optical pumping	Built by Tom Jeys MIT/LL	Optics Letters, 17, 1143-1145, 1992
Flash lamp pumped 1.06 + 1.32 Nd:YAG summed in LBO	60 μs macro@ 840pps each a 100MHz train of 0.4ns pulses	0.2%	24 mJ 20 watts	3 GHz	1.5 x DL	Signal return measurements at SOR, 1991	Built by Tom Jeys, MIT/LL	JOSA A, 11, 806-812, 1994
Copper vapor laser pumped dye laser	32ns pw @ 26Kpps	0.083%	42mJ 1100 W	3GHz	<1.5 x DL	Signal return measurements 1992	Built by LLNL	JOSA A, 11, 813-824, 1994
Light Age Alexandrite Raman shifted/ freq dbld	80ns pw @ 20pps	.00016 %	10 mJ 0.2 watt	100-150 MHz	un-known	Na lidar fielded in German	Potassium excited by fundamental at 769	Geophys Res Ltr, 23, 141, 1996
Argon pumpd Spectra-Physics 380C ring dye	CW	100%	1.2W	10 MHz	-DL	completed May 1993 UofA, UofC, MMT	Not optimized for stable freq operation	ESO Proc No. 48, 95, 1993
Argon pumped Coherent model 899-21 ring dye	CW	100%	2.7 watts	10 MHz	-DL	completed Dec 1993, MMT	filed experiments by UofC and UofA	SPIE, 2201, 342-351, 1994
Argon pumped standing wave dye	CW	100%	1.7 watts	10 MHz	-DL	completed Feb 1994, MMT	Built by LLNL	SPIE, 2201, 342-351, 1994
Argon pumped ring dye laser	CW	100%	0.8 watt	10 MHz	-DL	Wind and temp meas at SOR, 1995	Guide star expts SOR/U of Illinois	Chet Gardner, U of Illinois
Freq doubled Nd:YAG pumped dye laser	100ns pw @ 11Kpps	0.11%	1.55 mJ 17 watts	3 GHz	1.5 x DL	Installed on 3m Lick telescope	Built by LLNL	Herb Friedman, LLNL
Laser diode pumped 1.06+1.32 Nd:YAG lasers summed in LBO	150μs macro@ 400pps each a 100MHz train of 0.7ns pulses	0.42%	50 mJ 8 watts	3 GHz adjust-able	DL TEM00	Installed at ARC telescope Apache Pt, NM, 1995	Built by Tom Jeys, MIT/LL	Ed Kibblewhite, U of Chicago

Table 1. Mesospheric sodium lasers used in field experiments

End user or interested party	Developer	Laser concept	Temporal format	Duty cycle	Avg power	Status	Comments	Reference
SOR	Karl Koch, Phillips Lab	Combined intracavity OPO & Sum frequency pumped by Nd:YAG	CW ML at 76MHz chopped, 40Hz, 1ms	.015%	100 mW	Basic concept demonstrated	1.06µm limits NL materials, 1.03µm better	Opt. Lett., 19, 1967-1969, 1994
MPIA, Calar Alto, 3.5m	MPI-Garching	Ar pumped dye	CW	100%	2-3W		Commercial components	Andreas Quirrenbach
UK AO program, WHT	Oxford Lasers	CVL pumped dye	50ns at several Kpps	0.05%	~10W	Lab evaluation		Geoff Hogan
Keck II, Mauna Kea	LLNL	Freq doubled Nd:YAG pumped dye	100ns pw @ 30Kpps	0.3%	20 watts design	PDR +		Herb Friedman, LLNL
SOR	LLNL	Freq doubled Nd:YAG pumped dye	100ns pw @ 30Kpps	0.3%	~200W design	On-hold	Scale-up of existing technology	Herb Friedman, LLNL
SOR	Rocketdyne	Nd:YAG pumped OPO/OFA/SHG	1Kpps, 100 µs, ML	0.33%	10W design	Basic concept demonstrated		Chris Clayton, PL/LIDN
SOR	TRW	Intracavity Raman shifted Nd:YAG by CaWO ₄ and freq double to 589nm.	30µs macro pulses ML at 100MHz	0.11%	50-200W goal	Lasing on D2 line demonstrated	Concept by R. Byer at Stanford	Jackie Berg, TRW Paper this conference
Univ of Ariz, SOR	Univ of Arizona	Configurational tuned Nd:YAG intracavity Raman shifted by CaWO ₄ , freq doubled to 589nm.	300ns pw, 100Kpps, 1-10 GHz line width	3%	10W goal	Basic concept demonstrated with Nd:YAG		Dick Powell, Univ of Arizona, OSC

Table 2. Conceptual and developmental mesospheric sodium lasers

Laser	User	Temporal format energy/pulse	Beacon altitude	Aper diam	Status	Comments	Reference
Freq doubled Nd:YAG 532nm	SOR	10ns pw, 10pps, 300mJ/p	5-8km	40cm	completed 1984	Initial demo of laser beacon sensing	Nature, 353, 144, 1991
Flash lamp pumped dye 512 nm	MIT/LL	2µs pw, 5pps, 2J/pulse	6km	60cm	completed 1990	"go-to" AO system, two beacon stitching	LL Journ., 5(1), 67, 1992
Copper vapor 510 & 578 nm	SOR	50ns pw, 5000pps, 35mJ/p	10-14km	1.5m	Operational 1989	100 Hz control loop bandwidth AO	JOSA A, 11, 310, 1994
High energy excimer 353 nm	ThermoTrex	Single pulse, 10J/p	8km	1 m	completed 1991	"go-to" AO system	LGAO Proc, 2, 686, 1992
Freq doubled Nd:YAG 532 nm	ThermoTrex	10ns pw, 10pps, 0.8J/p	8km	1 m	completed 1993	"go-to" AO system	ESO Proc, 48, 503, 1993
Freq doubled Nd:YAG 532 nm	CERGA	10pps, 900mJ/pulse	8-17km	1.5m		Laser and natural guide star meas.	OSA Tech Digest 23, 1995
Pulsed excimer 351nm	U of Illinois	20ns pw, 300pps, 200mJ/p	18km	2.5m	Used at Laguna	Planned for Mt Wilson 100 inch	Peter McCullough

Table 3. Lasers used for Rayleigh beacons

Laser Systems for the Generation of Sodium Layer Guide Stars
H. Friedman, G. Erbert, T. Kuklo, T. Salmon,
G. Thompson, N. Wong, J. Malik
Lawrence Livermore National Laboratory
Mail Stop L-464, P.O. Box 808
Livermore CA, 94550

Laser generated guide stars in the mesosphere at 90 km provide an effective beacon for adaptive optics schemes which compensate the effects of atmospheric turbulence. Atomic sodium, the species with the highest product of integrated density and cross section, requires an exciting laser with a stable wavelength of 589 nm, a spectral bandwidth of ≈ 3 GHz and a peak power incident on the mesosphere of $\leq 5 \text{ W/cm}^2$ in order to reduce the effects of saturation. There are several other attributes of the laser which are desirable from a point of view of overall adaptive optics system performance and operation ease. These include the following: (1) near diffraction limited beam quality which is needed to make a small laser guide star, (2) pointing accuracy in the arcsecond range with resolution in the subarcsecond range, (3) the ability to detune the laser for background subtraction or retune to another wavelength for polychromatic guide stars¹, (4) a configuration which simplifies the laser projection optics and does not require beam paths through the telescope bearings and (5) an effective method of removing waste heat from the laser before it enters the dome volume. Finally, while lasers with average power in the ten watt range may be sufficient for observations in the near IR, extension to visible observations will require multiple guide stars with total powers in the hundred watt range. Therefore the ability to scale up in power by an order of magnitude in a straightforward manner is certainly desirable.

Liquid dye laser such as those developed for laser isotope separation² have been used at LLNL for several years and have produced sodium layer guide stars which are actually visible to the unaided eye³. These lasers use copper vapor lasers as the dye pump source and are large and bulky but for dye laser outputs in the several kilowatt range, are an obvious choice. For the lower power guide star application, copper vapor lasers which deliver their power in both a yellow and a green line of short pulses are not the obvious choice. The yellow line at 578 nm is too close to the sodium line for efficient pumping and the short pulses complicates the problem on sodium saturation.

Frequency doubled YAG lasers have proven to be an effective pump source for dye lasers with just green emission, high pulse repetition rates and longer pulses. These lasers are CW pumped by either flashlamps or diode arrays, Q switched to produce PRF's of tens of kilohertz and pulse duration of hundreds of nanoseconds and doubled by an intracavity KTP crystal. Even with inexpensive flashlamps, the beam quality of these lasers is adequate for coupling to a multimode fiber which is acceptable for dye laser pumping. The dye lasers can accept multiple fiber inputs either simultaneously to increase the peak power or sequentially to increase the average power. The YAG lasers are relatively inexpensive and can be packaged four to a standard electronics rack for efficient space utilization. The fiber optic delivery scheme allows the dye lasers to be mounted directly on the telescope itself while the less efficient YAG lasers are located remotely for easy removal of waste heat. In addition, the dye laser oscillator is also remotely located and coupled to the dye lasers on the telescope by single mode fiber. The fibers are routed through the telescope cable wraps in much the same manner as signal cables. The preamplifier and power amplifier dye lasers on the telescope are quite efficient and most of their waste heat is removed by the dye itself with little heat escaping to the dome volume.

A 20 W version of this YAG pumped dye laser has been built and installed on the 3 m Shane telescope at the Lick Observatory, Mt. Hamilton, CA. Photographs of the installation and the beam exiting the dome in are shown in Figures 1 and 2, respectively. The laser operates with a PRF of 11 kHz, pulse duration of 100 nsec (FWHM). With a beam projector telescope of 30 cm, the laser produced a 1.8 arcsec spot diameter when the seeing was 1.2 arcsec. The increased spot diameter is expected due to the spreading of the laser beam on the uplink path and is commensurate with a near diffraction beam quality. The return signal was ≈ 0.2 photons/cm²/ms which also agreed with model predictions. A significant correction in the dynamic atmospheric aberrations was observed but these results are preliminary and work is continuing in this area.



1.5.0296.0386#2pb02

Figure 1. Laser installation on the Lick Telescope



1.1.0395.0835Apb02

Figure 2. 20W Laser beam exiting the Lick Dome

A similar laser system is being designed for the 10 m Keck telescope. In this installation, the low turbulence requires a guide star spot of subarcsecond extent and the projection telescope has been increased to 50 cm accordingly. The laser system PRF has been increased to 30 kHz to keep the peak power at the sodium layer below the saturation value. This higher PRF is achieved by operating two sets of YAG lasers at 15 kHz and multiplexing the time sets in the dye. For simplicity, one YAG is operated at the full system PRF (at lower power) and is used to pump the oscillator and preamplifier. Other system parameters such as the average power and pulse duration are the same. A schematic diagram of the Keck laser system is shown in Figure 3. Several new control features will be tested at the Lick laser and added to the Keck system. These include a drift compensation circuit to maintain accurate YAG timing, an etalon control circuit to maintain the single mode output of the dye oscillator and a wavelength locking scheme based upon a spectroscopic sodium cell. These circuits together with the low bandwidth pointing and

centering beam control and high bandwidth uplink jitter control will reduce manpower requirements during observational runs.

For observations in the visible wavelength regime, models predict that more powerful multiple guide stars will be needed with lasers in the hundred watt regime. In order to upgrade the present 20 W laser system by an order of magnitude, another stage of dye laser amplification must be added. This second power amplifier is identical to the first with just the gap spacing increased; this amplifier configuration is capable of several hundred watts based upon thermal considerations. To pump the second dye amplifier, approximately 20 more YAG lasers are needed based upon previous estimates of the conversion efficiency. When added to the 5 YAG lasers needed for the Keck "front end" the total number of electronics racks is 6 which requires a floor area of 3' x 12'. Electrical power for the 25 YAG lasers is 200 kW for the flashlamp units and less for the diode pumped version but at present, substantially higher cost. The laser configuration is shown in Figure 4.

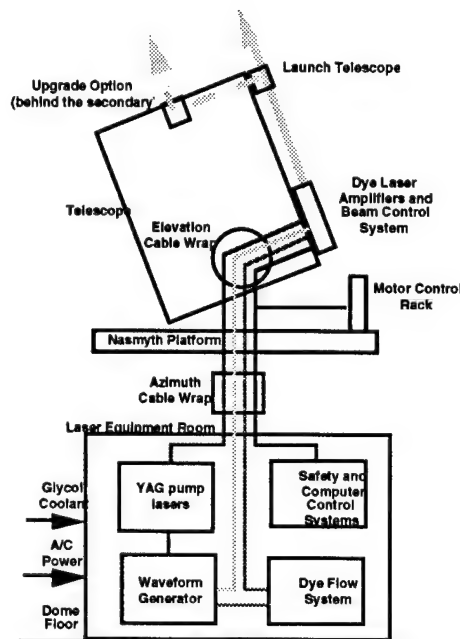


Figure 3. Keck laser installation

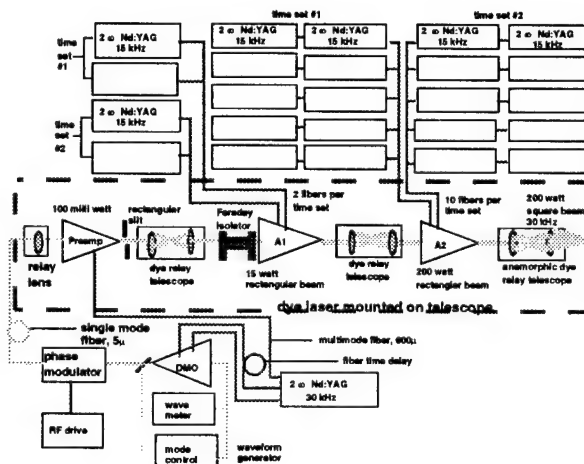


Figure 4. 200 W laser system concept

References

1. Foy, R., et.al., Astron. Astrophys. **42**(1994)
2. Hackel, R.P., and Warner, B., Proc. SPIE **1859** 120 (1993)
3. Avicola, K., et.al. Proc. SPIE **2201** 326 (1994)

Characterization of the Mesospheric Sodium Layer

GEORGE C. PAPEN, CHESTER S. GARDNER AND JIRONG YU

Department of Electrical and Computer Engineering, University of Illinois

1406 W. Green St., Urbana, Illinois 61801 USA

Ph. (217) 244-4115 Fax (217) 333-4303 e-mail: g-papen@uiuc.edu

Introduction

Several active adaptive optical systems using Na guide stars are currently in operation or under construction.¹ Optimization of these system requires a detailed knowledge of the temporal and spatial characteristics of the Na layer on both long term (seasonal) scales and short term scales (daily and hourly). Here we present recent results on the seasonal variations of the Na layer at 40° N and on temporal and spatial variations that occur at low latitudes using data collected at the AMOS observatory at Haleakala, Maui, and onboard an NCAR research aircraft.

Origin, Chemistry and Dynamics

There is strong evidence that the origin of the mesospheric Na layer is meteor ablation.² Once deposited in the upper mesosphere, the density of the neutral Na is controlled by various sink mechanisms several of which are strongly temperature dependent. The seasonal variations in density and temperature appear to be well correlated below about 95 km. This is confirmed by the correlation coefficient profile plotted in Figure 1. The correlation coefficient exceeds 0.7 at all altitudes below 96 km reaching a maximum of 0.93 at 92 km, very near the annual mean centroid height of the Na layer. Above 96 km the coefficient decreases rapidly with increasing altitude stabilizing near -0.2 above 100 km. The data suggest that below 96 km, temperature dependent chemistry plays an important role in determining the seasonal variations in Na density. This also implies that the mean Na density will have a latitude dependence because of the overall latitude dependent mesospheric temperature structure. Efforts are currently underway³ to develop models that can predict the mean Na density as a function of temperature (latitude) and should be useful for estimating Na densities at observational sites where no measured Na data exist (e.g. Cerro Pachon).

On daily and nightly time scales, atmospheric wave dynamics plays an important role. Gravity (density) waves, planetary waves, and tides can have substantial influences on the Na layer structure and are responsible for the night to night variability in the layer parameters.⁴ Furthermore, at low latitudes, large sporadic increases in the Na density can have a significant effect on the layer characteristics. Thus an

understanding of both the long term (seasonal) and short term (daily and hourly) characteristics of the Na layer are required to properly design Na guide star systems.

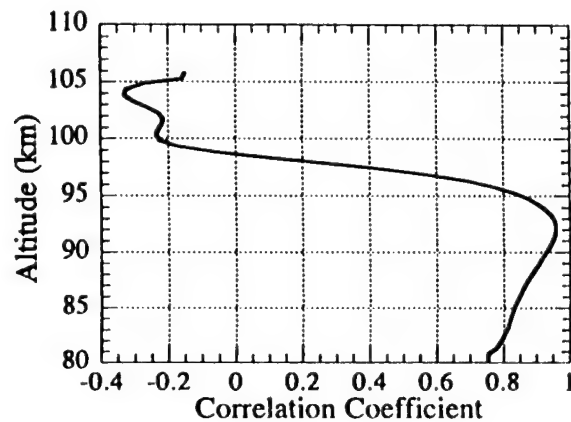


Figure 1. Profile of the correlation coefficient between the seasonal perturbations in Na density and temperature. (from Ref. 3).

Seasonal Variations

To determine the seasonal variations of the Na layer characteristics, an analysis of data collected from January 1991 until April 1994 on 147 nights at Ft. Collins, CO and 75 nights at Urbana, IL has recently been completed.³ The abundances, centroid heights, and root-mean-square (rms) widths of the nightly mean Na profiles are plotted in Figure 2. The mean density as a function of altitude and date is shown in Figure 3. The observation periods varied from 2 h to almost 10 h with a mean of approximately 6 h. The combined data sets include approximately 1285 h of observations on 222 nights distributed approximately uniformly throughout the year.

Because the annual and semiannual variations are the strongest harmonic components of the seasonal fluctuations of the Na layer parameters, a minimum-mean-square-error fit was used to determine the characteristics of these variations. The annual plus semiannual fits are plotted as thick curves in Figure 2, with the dashed curves lying one standard deviation

Table 1. Annual plus semiannual fit to the mesosphere parameters using Eq. (1). Parameters: A_0 is the mean, A_1 is the annual amplitude, A_2 is the semiannual amplitude, d_1 is the annual phase (days), d_2 is the semiannual phase (days). The fits using these parameters are shown in Figure 2.

$$x = A_0 + A_1 \cos\left[\frac{2\pi}{365}(d - d_1)\right] + A_2 \cos\left[\frac{4\pi}{365}(d - d_2)\right] \quad (1)$$

Quantity	A_0	A_1	A_2	d_1	d_2	RMS Residual
Na layer abundance ($10^9/\text{cm}^2$)	4.26	2.24	0.33	338	167	1.70
Na layer Centroid Height (km)	91.6	0.32	0.62	29	105	0.94
Na layer RMS width (km)	4.38	0.28	0.47	353	6	0.42
Mesopause temperature (K)	179.1	7.88	2.51	341	93	8.56
Mesopause altitude (km)	94.78	5.74	2.11	350	57	5.50

above and below the fits. The amplitudes and phases of the fits are summarized in Table 1. The Na abundance variations are primarily annual with a maximum in winter while both the centroid height and rms width variations are primarily semiannual but about 180 degrees or 90 days out of phase.

Gravity waves, planetary waves, and tides can have substantial influences on the Na layer structure and are responsible for the night to night variability in the layer parameters. Notice that the night to night variability of all three parameters is quite large. In fact, the rms residuals for the centroid height and rms width fits are comparable to the annual and semiannual amplitudes. Thus, on a night to night basis, we expect the variability of both the brightness (which is related to the abundance) and the focus of the guide star (which is related to the centroid height) to be comparable to the overall seasonal effects.

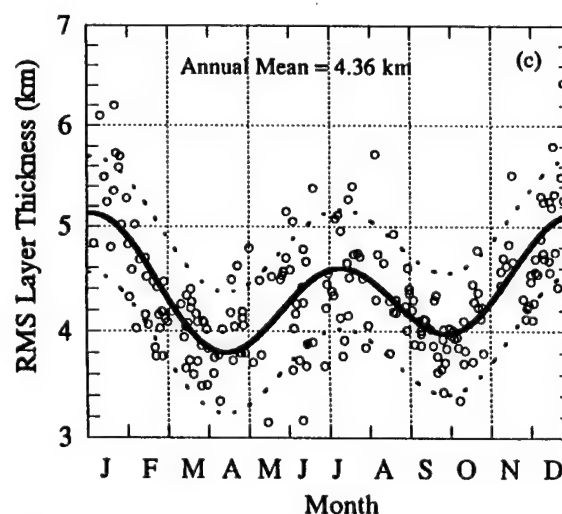
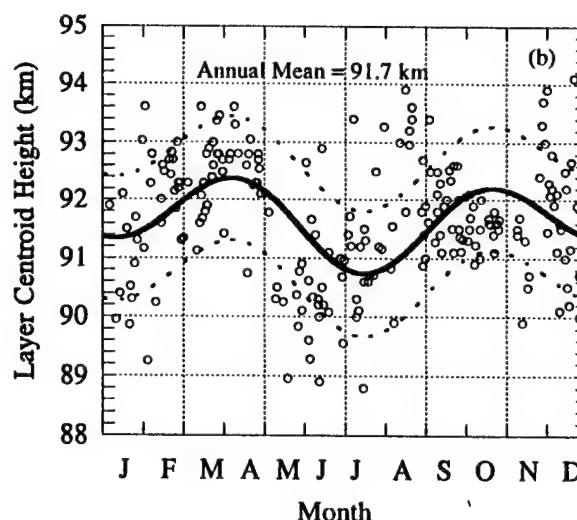
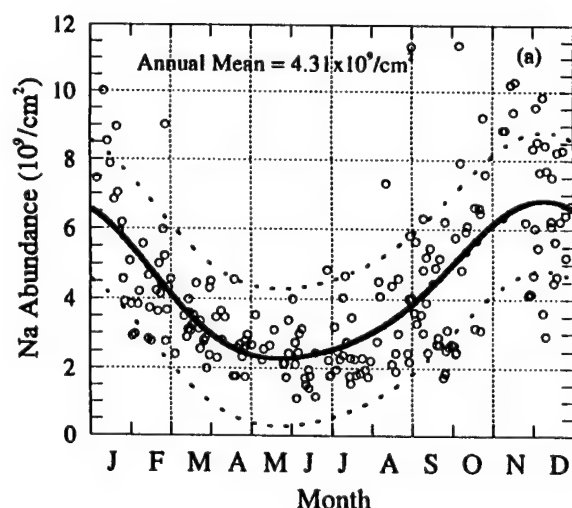


Figure 2. Plots of the Na layer (a) abundances, (b) centroid heights, and (c) rms widths versus date. The thick curves are least-squares fits to the data including annual plus semi-annual variations. The dashed curves are ± 1 standard deviation.

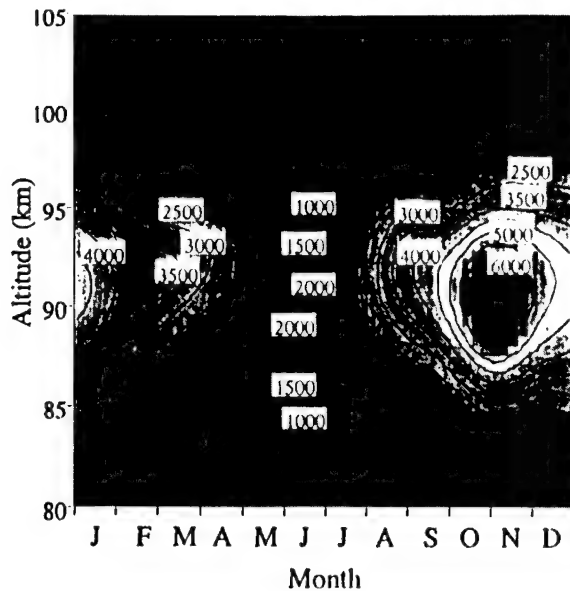


Figure 3. Contour plot of the seasonal Na density versus altitude and date.

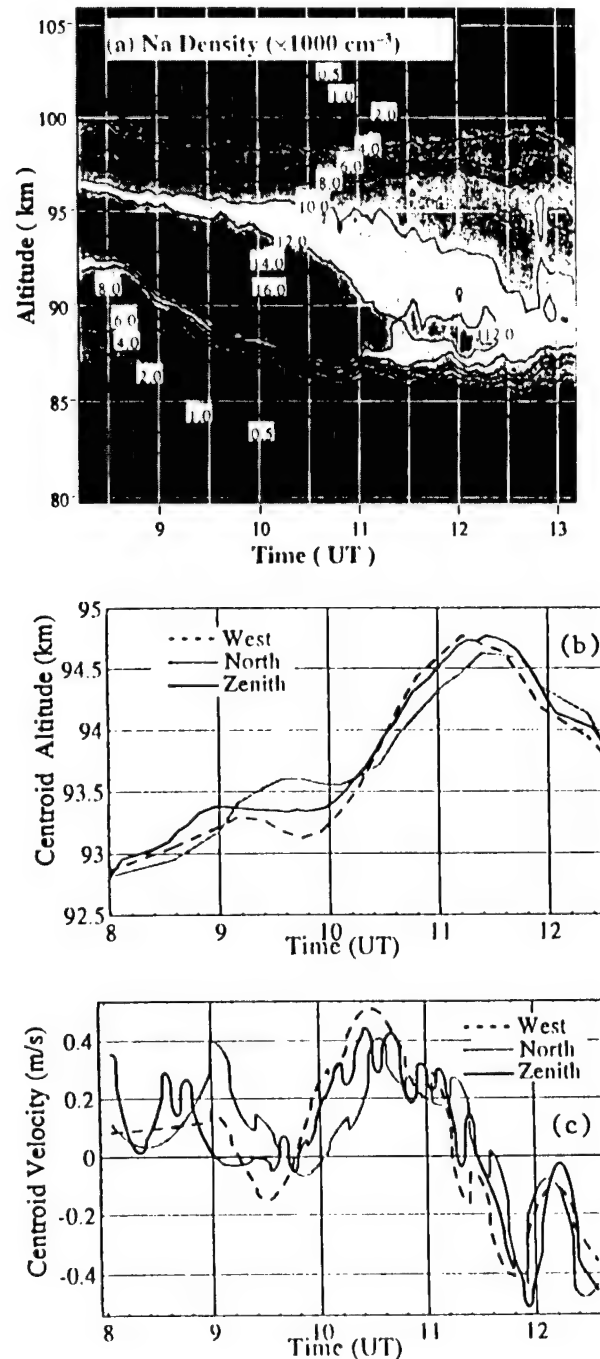
Short Term Temporal Variations

As mentioned earlier, the daily and nightly variations in the Na layer characteristics are predominately caused by gravity waves, planetary waves, and tides. In fact, the Na layer has been used for several years as a tracer for studies of this wave activity.⁴ However, at low latitudes,⁵ or at mid-latitudes where there is significant geomagnetic activity,⁶ sporadic Na layers can form within a short period of time (on the order of minutes) and generate a large influx of neutral Na confined within a small vertical region (~ 1 km). Depending on the magnitude of these events and where they occur in the layer, the deposition of large amounts of Na into the background layer can dominate the short term temporal variations of the centroid height and total column abundance and thus cause rapid changes in the layer characteristics relative to the changes from wave activity alone.

The mechanism for the formation of these layers is not completely understood and is an active research topic. However, it appears that these events are correlated with wind shears⁷ and auroral events⁸. Observationally, sporadic layers are rare at mid-latitudes, yet occur at high latitudes presumably from auroral activity and are a common feature of the Na layer above Hawaii with the frequency of occurrence peaking at roughly local midnight.

Analysis of several large sporadic events over Hawaii on two separate field campaigns^{5,7} indicate that the maximum velocity of the centroid height during large sporadic events is on the order of 0.5 m/s. Figure 4 shows one such event recorded on Oct. 21, 1993

over Haleakala Maui along with the centroid height and velocity.



Spatial Variations

The spatial variations of the Na are important to quantify if the telescope is tracking a object rapidly or for long exposures over an extended period of time. As the mount points off Zenith, the distance to the centroid increases with a $\sec(\theta)$ dependence assuming that the Na layer is spatially uniform. However, the same wave activity that causes temporal variations at a fixed location also cause spatial variations in the Na layer. In addition, because the formation mechanism for sporadic layers remains uncertain, all information about the spatial extent of sporadic layers is experimental⁹ and there are only a few data sets on the spatial distribution of sporadic layers.

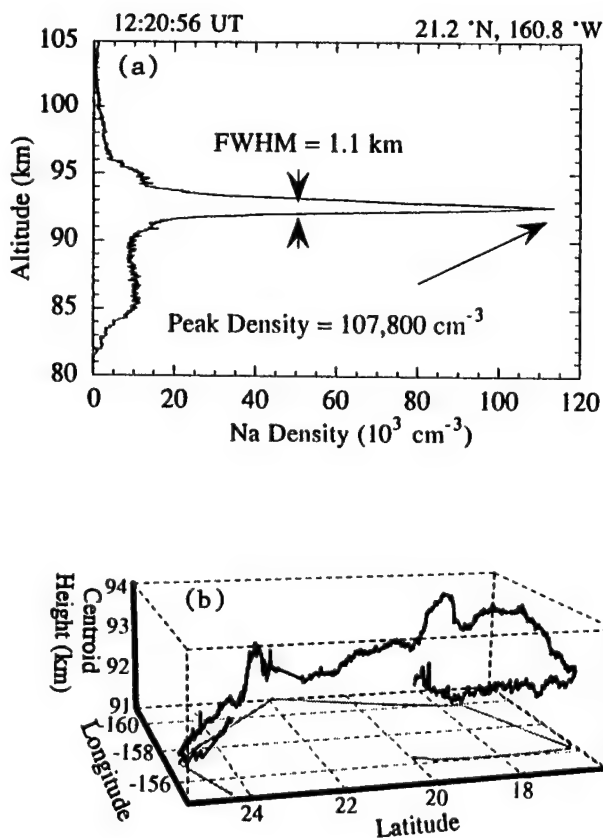


Figure 5. (a) Density profile of the largest (peak density) sporadic Na layer ever recorded. Data taken near the Hawaiian islands on Oct. 23, 1993. (b) Plot of the Na layer centroid height as a function of longitude and latitude for the entire flight. On two occasions, the centroid height changes by ~ 1 km over a spatial region of ~ 55 km (0.5 degrees).

Figure 5 shows one such data set where the largest Na sporadic event ever recorded was observed. The density at the peak of the sporadic layer was roughly $11\times$ the mean density. This caused a significant change in the centroid height as a function of longitude and latitude with the centroid height increasing roughly 1 km in 0.5 degrees (~ 55 km). At 30° off Zenith, this 1 km shift is roughly 7% of the ~ 14 km shift associated with the trigonometric dependence of the change in the centroid height. We note that because of the limited data available, all conclusions on the spatial extent of sporadic layers with respect to guide star generation are preliminary and require further study.

Conclusion

We have presented data on both the long term and short term temporal and spatial characterization of the Na layer at both mid-latitudes and over Hawaii. This data should be useful for initial design of guide star systems.

References

1. See for example "Adaptive Optics", *OSA 1995 Technical Digest Series*, **23** (1995).
2. T. Kane and C.S. Gardner "Lidar Observations of the Meteoric Deposition of Mesospheric Metals", *Science*, **259**, 1297-1300 (1993).
3. J.M.C. Plane *et. al.*, "The mesospheric Na Layer at 40° N: Modeling and Observations, *in press*.
4. D. C. Senft and C. S. Gardner, "Seasonal variability of gravity wave activity and spectra in the mesopause region at Urbana," *J. Geophys. Res.* **96**, 17229-17264 (1991).
5. K. H. Kwon, D. C. Senft and C. S. Gardner, "Lidar observations of sporadic sodium layers at Mauna Kea Observatory, Hawaii," *J. Geophys. Res.* **93**, 14199-14208 (1988).
6. C. Nagasawa, M. Abo, "Lidar Observations of a lot of sporadic Sodium layers in Mid-latitude", *Geo. Phys. Res. Lett.*, **22**, 263-266 (1995).
7. C. S. Gardner, X. Tao and G. C. Papen, "Observations of strong wind shears and temperature enhancements during several sporadic Na layer events above Haleakala," *Geophys. Res. Lett.* **22**, 2809-2812 (1995).
8. Y. Y. Gu, J. Qian and G. C. Papen, "Concurrent observations of auroral activity and a large sporadic sodium layer event during ANLC-93," *Geophys. Res. Lett.* **22**, 2805-2808 (1995).
9. C. A. Hostetler *et. al.*, "Spectra of gravity wave density and wind perturbations observed during ALOHA-90 on the 25 March flight from Maui to Christmas Island," *Geophys. Res. Lett.* **18**, 1325-1328 (1991).

Exploring High Altitude Beacon Concepts Other Than Sodium

John M. Telle
Starfire Optical Range
Phillips Laboratory
PL/LIG
3550 Aberdeen Ave. S.E.
Kirtland AFB, N.M. 87117-5776

phone: 505-846-4712 ext. 332
facs: 505-846-2213

Na and most other mesospheric species suffer from two major shortcomings, low density and low saturation intensity. The Na density in the mesosphere is typically $10^3 - 10^4$ atoms per cm^3 . Moreover this density is spread over about 100 velocity classes with a natural width of 10 MHz giving a total Doppler width of 1 GHz for each line. The D_2 line is split by 1.772 GHz into a doublet ignoring other hyperfine splittings of the order of 10 MHz. The doublet is often treated as a single line with 3 GHz FWHM. The Doppler-broadened Na cross section is about $2.7 (-12) \text{ cm}^2$ but the low density results in only about 1.5% unsaturated absorption across the entire mesosphere (depth $\approx 10 \text{ km}$).

Each velocity class is saturated by only about 10 mW/cm^2 , whereas the full Doppler profile requires about 4.5 Watts/cm^2 . A telescope subaperture size of 14.5 cm could conceivably resolve a mesospheric spot diameter of 39 cm or spot area of about 1700 cm^2 in conditions of good seeing. Thus the drive laser peak power should be kept well below 8 kW to avoid saturation which is not easy to achieve with lasers employing high average powers (200 Watts) and nonlinear optics (high peak powers) to produce the appropriate wavelength (589 nm).

In addition the resonance fluorescence approach is almost spatially isotropic resulting in an extremely small collection efficiency (1 part in 10^{10}).

Long wavelength transitions in Na do have sufficient gain to provide some degree of amplified spontaneous emission but the sensitivity of the Shack-Hartmann wave-front sensor varies inversely with wavelength. An upconversion cell on the ground processing an infrared beacon will reduce its wavefront distortion by the ratio of the upconverted wavelength to the infrared wavelength.

Oxygen (O_2) and nitrogen (N_2) on the other hand occur with densities of 10^{13} - 10^{14} molecules per cm^3 at about 100 km altitude. Moreover as long as the wavefront is not distorted gain from lower altitudes can be used.

A two-photon process can excite¹ species at high altitude while penetrating much higher densities of the same species at lower altitudes. Two pulse trains are established with different wavelengths. The initial pulses are delayed appropriately such that atmospheric dispersion causes the pulses to overlap at high altitude. Presumably the frequencies of the pulse trains can be adjusted so that the point of overlap sweeps towards the earth at the speed of light. It may turn out that the excitation and emission processes are sufficiently weak that excitation may proceed from the earth outward. In this case the emission process must be weak enough not to saturate the gain over the beacon path.

Modtran shows a rather abrupt cut off of atmospheric transmission at about 300 nm. This appears to be mostly due to Rayleigh scattering. Ozone absorption peaks at 255 nm with a FWHM of 40 nm.

The Edlen formula for atmospheric dispersion, accurate from 200 nm to 2 μm predicts a dispersion of 3.1 psec/nm at 350 nm for transmission through the entire atmosphere, straight up. This seems to impose reasonable constraints on the pulse lengths.

The strongest single-photon transitions in oxygen in the wavelength range of interest are the Schumann-Runge bands (B-X transitions). The electronic B-X absorption becomes continuous for wavelengths below about 175 nm corresponding to a two-photon transition at 350 nm. Absorption at these wavelengths leads to dissociation of the molecule into atoms with little potential for excitation. The discrete B-X transitions occur between 198 nm and 176 nm. These may pump stable B-state vibrational states which could emit to high vibrational states of the ground electronic state (X state). However many of the upper vibrational states are predissociated with linewidths on the order of 40 cm^{-1} . Also transitions from atomic states making up the B state to atomic states making up the X state are electric dipole forbidden. There are states intermediate to B and X which may enhance the two-photon cross section. Generally if a single-photon transition is allowed a two-photon transition is not. It is of concern that oxygen emission in nightglow is not commonly reported.

The peak B-X cross section in absorption reported by Hudson² is about $1.5(-17)$ cm², occurring near 143 nm. It is possible a long wavelength transition in emission could be found with similar cross section. They are not observed in absorption because the lower state is not thermally populated. If one could promote 10% of the mesospheric O₂ to the upper state of one of these presumed transitions and if the gain were spatially continuous across the mesosphere then it would be 10^{10} . Again gain at lower altitudes might be used as well.

Some of the questions to be answered are: (1) Are there any oxygen or nitrogen transitions with wavelengths between the atmospheric UV cutoff and 1 μ m whose upper states can be pumped with a two-photon transition? (2) What is the cross section and linewidth of the transition and lifetime of the upper state? (3) What are the properties of the two-photon absorption? (4) For a two-pulse-train excitation scheme what cross sections and lifetimes are required to beat the Na system? (5) Is it possible to achieve two-photon excitation and then stimulate Doppler-free two-photon emission and beat the Na system?

This work is being supported by the Air Force Office of Scientific Research.

References

1. private communications with Jean-Claude Diels of the University of New Mexico
2. R. D. Hudson, "Critical Review of Ultraviolet Photoabsorption Cross Sections for Molecules of Astrophysical and Aeronomic Interest," *Reviews of Geophysics and Space Physics* **9**, 305-406 (May 1971).

The sensing of tip-tilt in Laser Guide Star Adaptive Optical Systems

Domenico Bonaccini
European Southern Observatory
Karl-Schwarzschild Str. 2
D-85748 Garching bei Munchen - Germany
dbonaccini@eso.org

Second generation Adaptive Optical (AO) systems are being built or planned at many astronomical sites, which use Laser Guide Stars (LGS) as reference object in the wavefront sensor for the determination of wavefront aberrations. This is going to increase dramatically the sky coverage and the science throughput of AO systems used at astrophysical sites.

The determination of the tilt component or image motion from an LGS-AO system set-up is one of the problems which has to be addressed. A review of presently proposed solutions and current experimental results is presented at this meeting, based on published papers, current theories, and contributions from experiments.

The tip-tilt or image motion correction issue in AO systems should not be underestimated. Theory predicts that 87% of all the wavefront variance to correct lies in the tip-tilt component, responsible for the image motion. The rest lies in higher orders components, responsible for image blur. Hence the AO servo-system has to cancel the tip-tilt component down to a level of residual wavefront variance comparable or better than the rest of the aberrations. This means that the tilt loop gain has to be very effective, since it starts with a larger absolute error to correct.

Most of currently existing AO systems indeed smear their long-exposure Strehl ratio due to a residual jitter of the short-exposure diffraction limit corrected image. In the case of currently operating ESO Adonis system, for example, we have a single-loop approach, in which both tilts and high orders are sensed with the same Shack-Hartmann wavefront sensor (WFS). The propagation of WFS noise on the various Zernike modes is fixed and defined to a certain ratio, as given by the noise propagation coefficients (Rigaut and Gendron, 1992, *A&A* **261**, 678).

As an example, a measurement of the residual variance on the Noll's ordered Zernike polynomials is shown in Figure 1. It was obtained in one 20 sec J-band exposure at the last observing run at ESO 3.6m telescope equipped with the Adonis system, in May 1996.

Optimizing the tip-tilt loop separately from the higher order loop seems indeed effective for Natural Guide Star (NGS) systems. It is a must for LGS systems since at the moment the tilt signal cannot be derived directly, although some methods have been proposed and are being investigated.

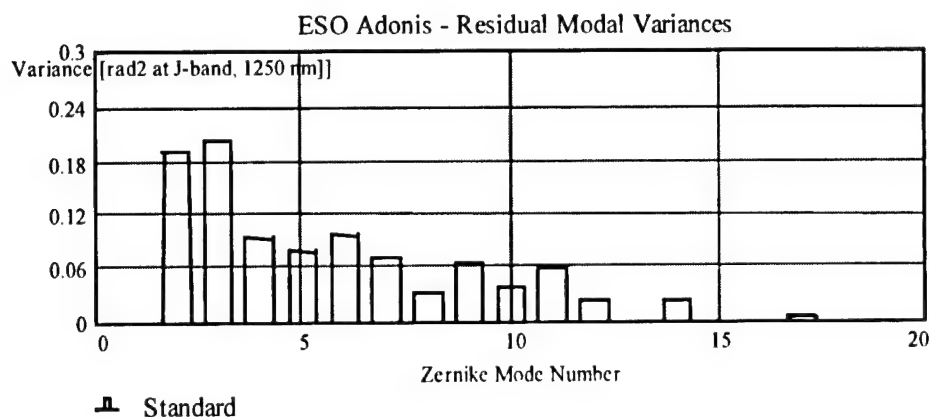


Figure 1: Distribution of residual variances on the Zernike modes on ESO Adonis, after correction. Results are experimental, of the May 7 night. Tip and Tilt are modes 2 and 3.

In order to cope with the separate optimization of tip-tilt correction, with respect to higher order modes, ESO has started a development jointly with EG&G Canada and Politecnico of Milan, to develop an optimized tip-tilt servo-loop which includes avalanche photo-diodes quad-cells and predictive algorithm for the centroid position. An update on this R&D activity and its expected results will be given.

Some authors are proposing the derivation of the tip-tilt signal from the LGS itself. Indeed ESO is also funding this year a collaborative research with Obs. de Lyon, where the R.Foy group is actively pursuing a method based on the polychromatic artificial star, using different lines of sodium excitation, to derive the tilt signal from differential effects (Foy et al., 1995, A&AS **111**, 569).

Other authors are proposing the use of differential tilt motions by spatial effects, e.g. observing a NGS close to the line of sight with side-by auxiliary telescopes, or monitoring the elongated strip of the LGS when the projector is consistently sideways of the observing telescope (Ragazzoni, R: 1996, A&A **305**, L13-L16).

The proposed solutions have to be carefully checked with practical implementation problems related to LGS-AO, i.e. amount of laser power required, complexity of the set-up, SNR considerations at different turbulence conditions, laser lifetimes, operability.

Nonetheless, the subject is interestingly open to new and clever solutions. The recent outburst of solutions indicate that the problem of LGS system tilt determination is very much felt. At stake is the ambitious goal of achieving the full sky coverage in astronomical AO systems.

This would extend enormously the astrophysical throughput of diffraction limited imaging from ground based telescopes.

Tuesday, July 9, 1996

Real Implementation Problems and Issues

ATuA 7:45 am-11:30 am
Pikake Room

Peter L. Wizinowich, *Presider*
W.M. Keck Observatory

Keck Adaptive Optics: Error Budget

Peter Wizinowich

W.M. Keck Observatory, 65-1120 Mamalahoa Highway, Kamuela, HI 96743, U.S.A.

Tel: 808 885-7887; Fax: 808 885-4464; email: peterw@keck.hawaii.edu

Introduction

The optics error budgets for the W.M. Keck Observatory natural guide star (NGS) and laser guide star (LGS) adaptive optics (AO) facilities¹ are presented. The purpose of generating this error budget² is three-fold: (1) to summarize the error sources which will contribute to the degradation of images on a science instrument fed by the AO facilities, (2) to compare the predicted performance with the requirements, and (3) to provide a tool for evaluating potential engineering, and observing, trade-offs.

Error sources

The residual wavefront error terms after AO correction can be divided into several categories: the uncorrected atmospheric turbulence and AO system errors, the uncorrected telescope errors, and the uncorrected science instrument aberrations. In addition, there are the field-dependent errors due to the atmosphere, telescope and science instrument. To first order these rms wavefront error terms, σ_i , can be summed in quadrature and the impact on the Strehl ratio can be given by the equation $SR = \exp[-(2\pi \sigma_{\text{total}}/\lambda)^2]$, where λ is the wavelength.

In addition, there are a number of error sources which affect the wavefront tilt. These rms tilt terms can also be summed in quadrature and their effect on the Strehl ratio is given by $SR = \sigma_D^2/(\sigma_{\text{tilt}}^2 + \sigma_D^2)$, where $\sigma_D = 0.45\lambda/D$ and D is the telescope diameter.

The uncorrected atmospheric and AO errors include the fitting error of matching the deformable mirror to the turbulence, the bandwidth or time delay error between sensing and correcting, the measurement error which can be broken into MTF and spot size terms, a calibration residual error due to non-perfect optimization on the science instrument, and some uncorrected internal errors in the AO system. In addition, when an LGS is used there is an additional measurement error due to the elongation of the LGS, a focal anisoplanatism term since the LGS is not at infinity, and an error in correcting for the focus of the LGS.

The telescope errors include surface errors in the telescope optics, referred to as warping harness residuals, noise in the primary mirror active control system, and differential phasing, vibration and stacking errors between the segments. The science instrument also will have internal uncorrectable aberrations. The field-dependent errors include the isoplanatic error term, field aberrations from the telescope and AO optics, and field aberrations from the science instrument.

The tilt errors include the bandwidth or time delay error, both MTF and spot size measurement errors, centroid anisoplanatism resulting from the tilt contributions of higher order coma terms, the

isokinetic angle term, and a term due to the misalignment of the science instrument with respect to the AO system.

Error budget and trade-offs

The error budgets for the NGS and LGS facilities are presented in Figure 1. The atmospheric parameters used in computing these terms are given in Table 1. The error terms are calculated for three sets of observing conditions: excellent seeing at zenith, average seeing at a zenith angle of 30°, and poor seeing at a zenith angle of 60°. Requirements for the Keck NGS and LGS facilities are defined in reference 3, along with most of the error terms. The AO system errors should be compared to the NGS requirements of 70, 140, and 400 nm for a bright on-axis NGS and the above three observing cases, respectively; and the corresponding LGS requirements of 110, 210, and 500 nm.

The equations for each error term have been used to create an Excel spreadsheet that helps in evaluating the trade-offs, both engineering and observing, between the various error terms. For example, laser power can be traded against such engineering choices as the increased measurement error due to putting the laser projector off the telescope axis, or against CCD read-noise.

References

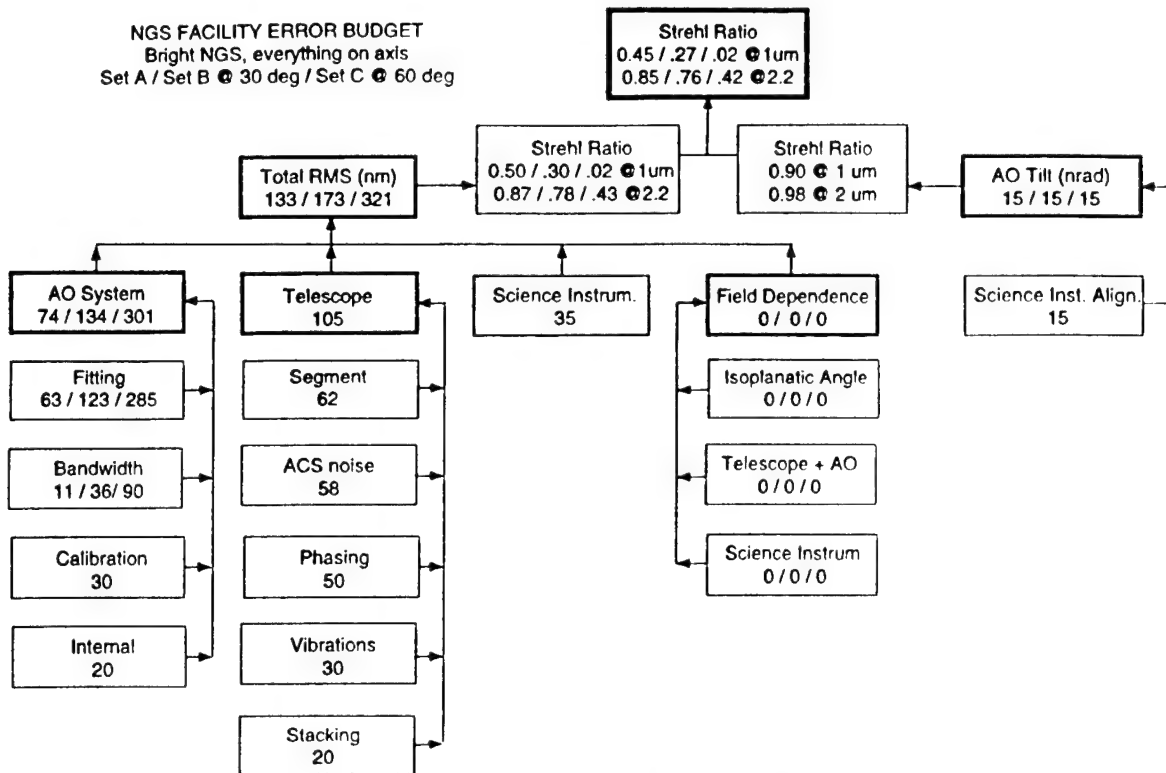
1. P. Wizinowich et al., "W.M. Keck Observatory Adaptive Optics Facilities," these proceedings.
2. P. Wizinowich, "Keck Adaptive Optics Error Budget," Keck Observatory Technical Note No. 422 (November 1995).
3. Keck Adaptive Optics Science Team, Adaptive Optics for the Keck Observatory, Keck Observatory Report No. 208 (revised January 1996).

Table 1. Atmosphere parameters at $\lambda_0 = 0.55 \mu$.

Wavelength and zenith angle dependence is $x_0(\lambda, \theta_z) = x_0(\lambda_0)(\lambda/\lambda_0)^{6/5} \sec^{-3/5} \theta_z$

	Set A at zenith	Set B at 30 degrees	Set C at 60 degrees
r_0 (m)	0.4	0.18	0.066
θ_0 (arcsec)	10	3.67	1.31
θ_k (arcsec)	300	147	52.8
τ_0 (ms)	10	2.75	0.99
τ_k (ms)	300	128	46.2
d_0 (m)	14	6.42	2.31
L_0 (m)	50	50	50

NGS FACILITY ERROR BUDGET
 Bright NGS, everything on axis
 Set A / Set B @ 30 deg / Set C @ 60 deg



LGS FACILITY ERROR BUDGET
 LGS flux = 0.2 photons/ms-cm², Bright NGS
 NGS&LGS on axis, off-axis laser projection
 Set A / Set B @ 30 deg / Set C @ 60 deg

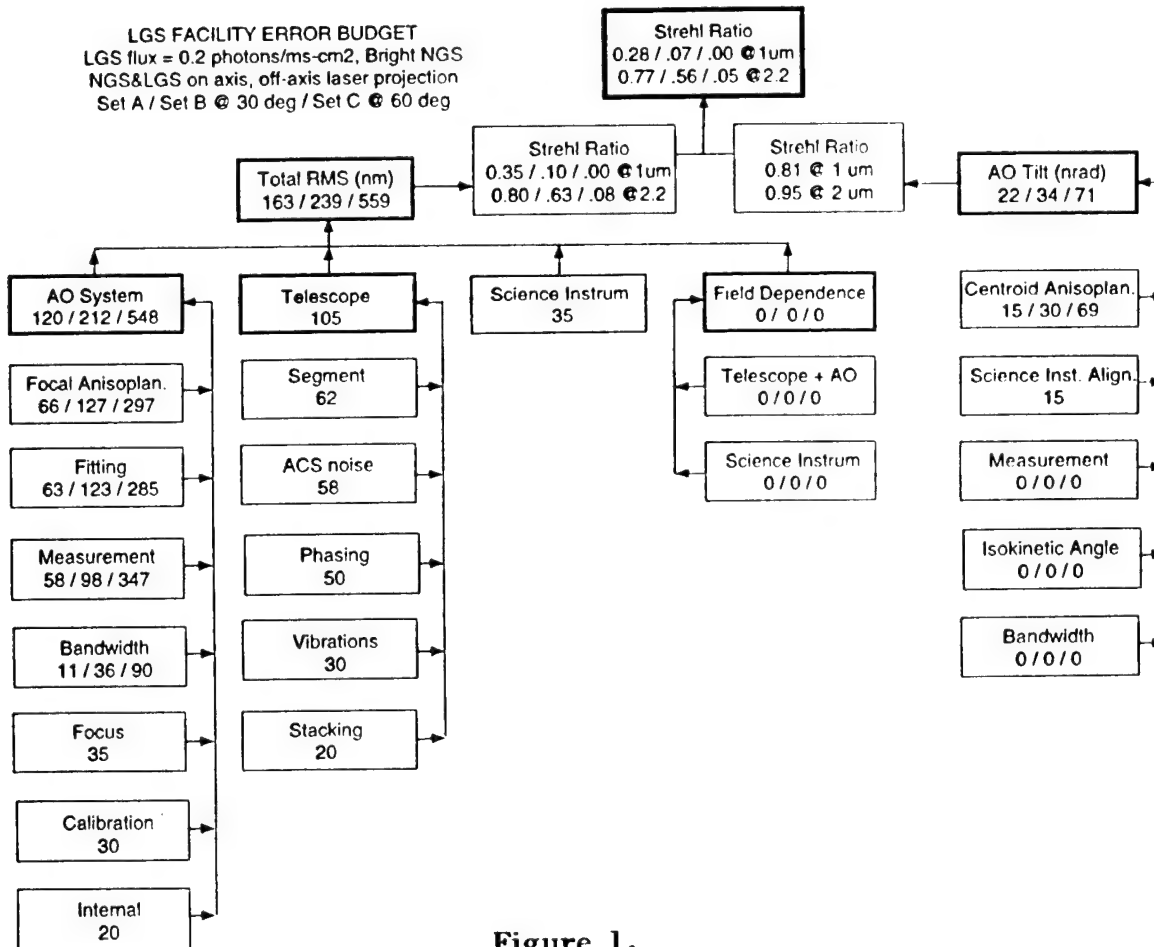


Figure 1.

Tuesday, July 9, 1996

Astronomical Science and Techniques

ATuB 1:00 pm-3:20 pm
Pikake Room

Gerard Lelievre, *Presider*
Observatoire de Paris, France

Bubbles, Disks, and Planets: Science with the University of Hawai'i AO System

Laird M. Close, Francois Roddier, Claude Roddier, Malcolm Northcott, &
J. Elon (Buzz) Graves

University of Hawai'i, Institute for Astronomy, 2860 Woodlawn Dr., Honolulu, HI 96722
VOICE: (808) 956 9842, FAX: (808) 956 4532
EMAIL: close@galileo.ifa.hawaii.edu WWW: <http://queequeg.ifa.hawaii.edu>

1. Introduction

The Adaptive Optics system, built at the Institute for Astronomy (University of Hawai'i), has been making unique scientific observations since 1993. During that period this versatile AO system has been mounted at both cassegrain and coude feeds at the 3.6m CFH telescope and the bent Cassegrain at the 3.8m UKIRT telescope. The instrument is now permanently a cassegrain instrument which has enjoyed 24 nights of 4m class observing at Manua Kea.

The scientific advantages of a cassegrain mounted instrument on an equatorial telescope are significant. In particular, such a mount maximizes optical throughput and minimizes thermal emissivity compared to more optically complex coude or nasmyth platforms. Moreover, since neither the field nor pupil rotates the PSF is independent of telescope position. This has proved important for obtaining usable calibration PSF's for post-detection processing such as deconvolution and PSF fitting photometry.

The AO instrument itself has proved remarkably reliable during these runs. In fact no telescope time has been lost due to any failure of the instrument itself. Much of this robustness can be attributed to the natural simplicity of the wavefront curvature approach to adaptive optics (F. Roddier et al. 1991). This instrumental simplicity also reduces closed-loop calibration time to a small fraction of the night (<5 min per new target on average).

The present instrument configuration is fully described in Graves et al. (1994) and references therein. The instrument consists of a 13 element wavefront curvature sensor consisting of 13 photon counting avalanche photodiodes. The resulting wavefront curvature signal is used to directly drive a deformable piezo-bimorph mirror which is updated at 1.3 khz. A real-time multi-tasking software environment controls the instrument and achieves a 120 hz closed-loop corrective -3dB bandwidth. The computer control system is more fully described in Northcott et al. (1996).

One of the outstanding features of the instrument is the science detector package utilized. Both a 1024x1024 CCD (0.024"/pixel) and a 1024x1024 HgCdTe (0.035"/pixel) near-infrared (~1-2.5 μ m) camera simultaneously image the AO corrected science fields from visible to the infrared. The newly upgraded 1024x1024 IR camera (HAWAII, c.f. Hodapp et al. 1995,1996) allows Nyquist sampling of the f/36 focus of the 3.6m aperture at J (1.2 μ m) with its fine platescale while still covering a reasonable 36x36" FOV. We have capitalized on this relatively large FOV to

implement object dithering which increases IR observing efficiency by ~100% through the elimination of costly off-object sky frames. In addition, the 36x36" FOV is often large enough to capture at least one field star bright enough to be used as a PSF star. This IR camera also provides increased sensitivity due to its low (~10 electron rms) read-noise, which is a factor of ~5 better than was commonly achieved in the smaller 256x256 IR arrays.

Typical system performance yields Strehls of ~0.2-0.4 at H (1.6 μ m) with a 13th mag guide star in average 0.5-0.7" seeing. These significant Strehl ratios imply enough S/N at the highest spatial frequencies to confidently restore these images back to the diffraction-limit of the telescope. Typically isoplanatic effects only reduce this Strehl by ~18% at the edge of the field (18" separation). This system can also correct static telescope aberrations and slow dome seeing while eliminating dynamic tip-tilt errors with fainter V~16 guide stars. Some image improvement is expected with guide stars out to V~19.

2. Data Reduction

A data reduction process has been developed to maximize the scientific potential of each image. This process starts with the traditional sky-subtraction and flat-fielding steps. Next the sharpest images are registered and averaged together into one final image. This resulting image is an optimization of both resolution and S/N.

This image typically has a Strehl of 0.2-0.4 and a resolution close to the diffraction-limited FWHM. Since such images have significant S/N inside a diffraction-limited core it is possible to restore the significant sections of such images to the diffraction-limit of the telescope by deconvolution techniques (cf. Christou 1996). Therefore all images were deconvolved to convergence. However, we have found this is only possible if a very good PSF is used in the deconvolution (at least this is true for the Lucy-Richardson algorithm which we utilized).

3. Examples of Recent Science Results

The best test of any AO system is the quality of science it can produce. Hence, we would like to briefly summarize a few highlights of the most recent scientific images and insights produced by the instrument.

Through diffraction-limited (~0.1") imaging of the planetary nebulae IRAS 09371+1212 (Frosty Leo) and AFGL915 (the Red Rectangle) it is apparent that many, if not all bipolar-nebulae, are produced by optically obscured edge-on binaries (F. Roddier et al. 1995).

The instrument has also, for the first time, directly observed a circumstellar ring around a young star in the infrared. In particular, diffraction-limited resolutions allowed the very faint (contrast ~10⁻⁴ at 1") dust ring around the 0.25" binary GG Tau to be directly imaged in the K, H, and J infrared bands (C. Roddier et al. 1996). This circumbinary ring is likely the remains of the initial dust cocoon out of which GG Tau formed. The ring is created as the binary ejects gas and dust through tidal clearing. The process of tidal clearing had been suspected to be active in these systems but until now it had never been directly studied. Moreover, the ability of the AO system to split the 0.25" binary has allowed accurate photometry to occur on each of the components. Roddier et al (1996) have found that each component has an infrared excess most likely caused by circumstellar disks still surrounding the individual stars.

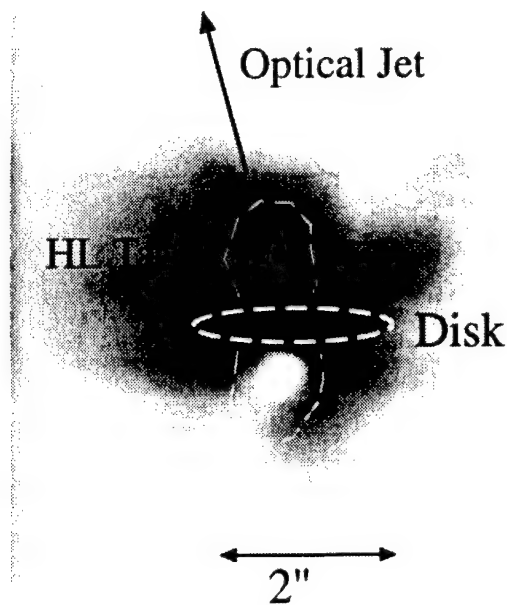


Figure 1: The young star HL Tau. Image is a negative (at $2.2 \mu\text{m}$). Exposure of 110s, LUCY restored to $0.15''$ FWHM. Image has been rotated 36° clockwise.

Such circumstellar disks are thought to be a critical mechanism for protostellar mass accretion, jet formation, and collimation. Perhaps most importantly such circumstellar disks allow for the formation of companions or planetary systems through fragmentation of the disk. Although the fragmentation of such disks is heavily utilized by theorists to explain binary and planetary formation, there has been very little direct evidence of such behavior.

However, the very young T Tauri star HL Tau (at ~ 140 pc) has shown signs of having a relatively massive circumstellar disk ($\sim 0.1 M_\odot$). We have monitored this disk around HL Tau over the last 2 years. Not only do we find direct evidence for a dense inner circumstellar disk around HL Tau, but it also appears that the nearly edge-on disk is fragmenting into 2 clumps (at 100AU and 110AU from the star) each of which may be forming com-

panions/planets around HL Tau ($M_{\text{clump}} < 0.05 M_\odot$). The observed density profiles along the accretion disk agree with that predicted by theoretical models of binary formation through fragmentation (Burkert 1996). Hence, these observations may be the first direct confirmation of the process responsible for binary and planetary system formation (Close et al. 1996).

The three epochs of observations of HL Tau over the last two years have provided the first images of bipolar bubbles of dust and gas being dynamically formed by ram pressure from the strong 180 km/s jet which is nearly perpendicular to the disk. For the first time we can see these bubbles expanding at ~ 30 km/s ($0.045''/\text{yr}$). Such observations show that these bubbles are probably very short lived ($t \sim 10000$ yr) but create significant density perturbations in the circumstellar disk. Hence these bubbles are likely to be important for the initiation and amplification of the disk fragmentation process (see figure 1).

Recently (in August 1995) Saturn's ring plane passed through the center of the Earth. This rare event (once every ~ 17 years) was studied at $0.1''$ resolutions by the AO instrument. The elimination of glare from the edge-on ring coupled with these IR resolutions allowed us to detect all the very faint satellites: Helena, Calypso, and Telesto (as well as Janus, Pandora, Epimetheus, and Prometheus). In addition, a new faint unexplained structure was detected extending just above and below the outer E ring.

Burkert, A. & Bodenheimer, P. 1996, preprint
 Close et al. 1996, ApJ submitted
 Christou J. 1996, these proceedings
 Graves, J.E. et al. 1994, SPIE 2201, 502

Roddier C. et al. 1996 ApJ in press
 Northcott M. et al. 1996, these proceedings
 Hodapp et al. 1995, SPIE 2475, 8
 Hodapp et al. 1996, in preparation
 Roddier F., Northcott, M., & Graves, J.E. 1991, PASP, 103, 131
 Roddier F. et al. 1995, ApJ, 443, 249

Observing with adaptive optics.

M.J. Northcott.

University of Hawaii
Institute of Astronomy
2680 Woodlawn Dr., Honolulu, HI 96822

Introduction

The University of Hawaii adaptive optics (AO) group is now been using their AO system at the CFHT Cassegrain focus to make astronomical observations. Having spent large amounts of time reducing that data from these observing runs, we have developed procedures at the telescope to ensure good quality data whilst also attempting to reduce the observing overhead. While the UH AO system is a low order natural guide star system, we feel that the lessons learned from this system should be broadly relevant to most AO systems.

I will describe the procedures we use to obtain good data and the software tools that we are developing to aid us. I will also discuss some options for increasing the observing efficiency of AO, which we are at present unable to implement.

Observation goals

As with all astronomical observations it helps to be aware ahead of time what sort of data reduction you wish to carry out on the observation data. The use of AO places an even heavier premium on advance preparation than does more traditional observation.

Goal	Calibrations
Morphology	PSF
Photometry	PSF, Standard
Spectroscopy	PSF, Standards

Required observational calibrations.

The above table shows the calibrations that will be needed for most types of AO observing. The requirement for more calibration than with standard observational programs leads to higher overhead with AO observing. We have no direct experience of doing spectroscopy, but we can infer observation requirements from imaging and photometry work, and from numerical simulations.

The art of the possible.

One of the unavoidable facts of life when AO observing, is that the quality of the data is very strong function of the seeing conditions. While it may be possible to build a high order laser guide star (LGS) AO system which is a little less dependent on seeing conditions, even a perfect LGS system will see the affects of isoplanatic angle variations. We therefore recommend that you have available a backup observation which can be carried out if the seeing is too bad for your primary observing goal. For our system, backup observations are just about anything that can be usefully observed in H and K. Obviously the backup will depend on the capability of your AO system.

The need for standards.

As shown in table , to get the best out of any AO observations, a reference PSF is needed. It could be argued that in the case of very high order LGS AO, a PSF would not be needed. However even if such a system can be realized, PSF references will probably still be needed to calibrate isoplanatic effects. In general this requires the SNR on the PSF to be higher than that on the object. To first order this implies that one must spend the same amount of time measuring the PSF, as measuring the object.

Obviously the same need exists for photometric and spectroscopic standards as exists with standard observing.

Taken together then, each AO observation may require the independent observation of a PSF and a photometric/spectroscopic calibration. Thus the overall observing efficiency drops to 30%. When one adds in time loss in beam switching and other overhead the efficiency can easily drop to 20% or less. AO observing thus places a high premium on maximizing the efficiency of all the individual observing steps.

Increasing efficiency.

It would be hoped that a single PSF measurement could serve for more than one object. However as shown in figure 1 the size of r_o can vary quite dramatically ($\times 2$) over fairly short time-scales (minutes). One would expect that the isoplanatic angle might show similar fluctuations. The variation of r_o during observations needs to be measured, to determine how frequently PSF measurements must be made.

An AO instrument is a complicated piece of observing equipment. The AO system itself is at least as complicated as a spectroscope. In addition one has also to run the observing instruments, which in our case consist of a CCD and an IR imager. Keeping track of all of this can become overwhelming. We have made an effort to integrate everything (telescope,AO,cameras) as much as possible, and are continuing to improve this aspect of our instrument. We use the Tcl scripting language to tie together the individual sub-systems. This provides a high level of integration, while maintaining a high degree of flexibility.

One can also save considerable time if the field of interest contains an object which can be used for a PSF. Since this PSF will be measured under exactly the same con-

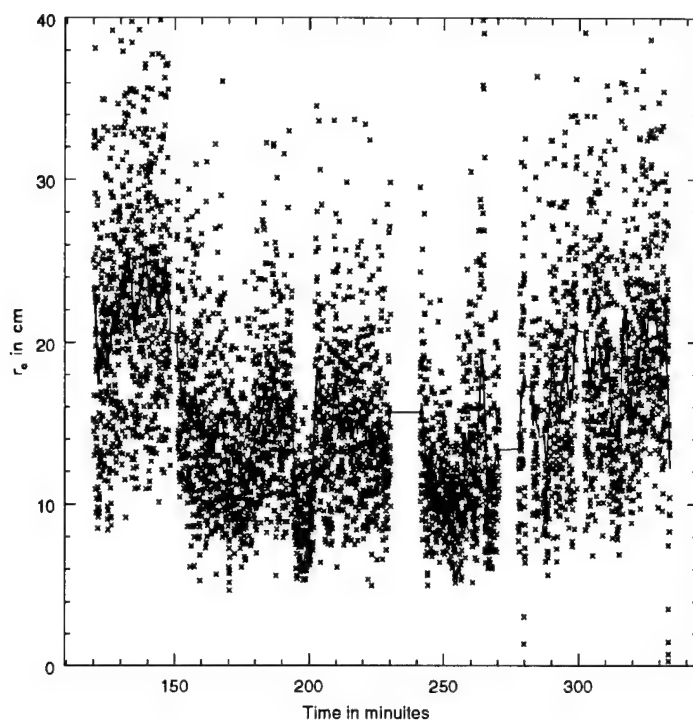


Figure 1: R_o as a function of time for one half night at the CFHT.

ditions as the program object, this is the preferred mode of operation. Unfortunately comparatively few objects fall into this category.

One can also increase observing efficiency by using photometric standard stars to measure the PSF. The problem here is that there are not enough faint standards available to make this option universally available. A program to measure of the order of 100 faint standards in the range of 14 to 16 magnitude would be very useful to the AO community. When available we use the UKIRT faint standards. Unfortunately as well as being too few, they turn out to be double stars with depressing regularity. The goal for a PSF measurement, is to run the system under the same wavefront sensor SNR conditions as with the program object. The HST catalogue appears to be the best source of stars to do this, but the lack of IR colours in the catalogue is problematical.

Halo Properties and Their Influence on Companion Searches at the Starfire Optical Range

P.T. Ryan, J.R.P. Angel, D.W. McCarthy, L.M. Close, S. Mohanty
Center for Astronomical Adaptive Optics (CAAO), University of Arizona
933 N. Cherry Ave., Tucson AZ 85721
phone: (520) 621-7866, fax: (520) 621-9843

R. Fugate
Starfire Optical Range
U.S. Air Force Phillips Lab Kirtland AFB, Albuquerque NM 87117
phone: (505) 846-4712 X314, fax: (505) 846-0439

D.G. Sandler
ThermoTrex Corp.
9550 Distribution Ave., San Diego, CA 92121
phone: (619) 578-5885, fax: (619) 536-8536

One of the questions which has endured for as long as man has looked at the heavens is "Are we alone?". Are there beings on other planets who are also looking into the heavens? The first requirement for alien life similar to our own is that there be planets orbiting other stars. The early stages of planet formation as dictated by theory appear to be robust and several large planets have recently been detected by indirect means[1][2]. Direct imaging is currently being used to search for less ambitious, yet still scientifically interesting faint objects called Brown Dwarfs. The most convincing evidence of a Brown Dwarf, a cross between a star and a planet, was discovered by direct imaging with the aid of a 7.7 arcsecond separation from a companion star[3].

The primary benefit in searching for faint companions on telescopes utilizing adaptive optics is the reduced signal at small radii. The character of the signal determines the largest magnitude companion which is detectable. While theoretical predictions have been made about the point spread function properties of adaptively corrected images, little experimental work has been done. Here the spatial and temporal halo properties of images taken at the Starfire Optical Range (SOR) 1.5 m telescope are explored. This telescope employs a 16 by 16 subaperture adaptive optics system. The halo is examined for its dependence on guide star magnitude, correction rate and atmospheric conditions.

The limiting magnitudes of companions which can be seen using the adaptive optics system at the SOR are given on both simulated and experimental bases. The factors limiting the detection levels achieved with a real world adaptive optics are examined and maximum detectable magnitudes without these errors are calculated.

Figure (1) shows the maximum magnitude difference which could be detected

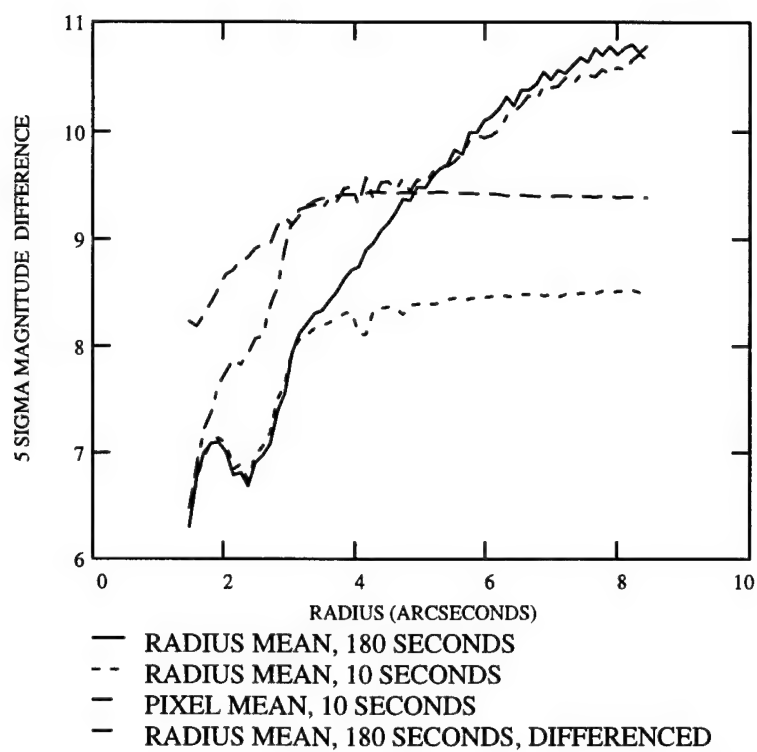


Figure 1: Maximum magnitude difference for a 5σ detection of a companion to HR1925. Calculated for 18 consecutive 10 s exposures of HR1925 in H band.

at the 5σ level for HR1925 in H band. This star was picked as an example of the performance on a typical night. The Greenwood frequency was 40 Hz and $\theta_0 = 2$ arcseconds at $0.5 \mu\text{m}$. The fluctuations were computed two different ways: the fluctuations from the mean at the radius and the fluctuations from the mean at the pixel. The data comes in three flavors: 18 consecutive 10 s frames, the mean of the same frames averaged together and the mean of the averaged frames subtracted from a similar average from a comparison star. A 2.5 arcsecond diameter chrome dot placed in a previous image plane attenuated the star's peak. This allowed longer exposure times without detector saturation.

The fluctuations from the mean at a radius are larger than the fluctuations from the mean at the pixel for the same exposure time at all radii. They must be when there is fixed pattern noise from either the point spread function or the detector. The fluctuations from the radial mean do not decrease significantly with time at radii smaller than 3 arcseconds. In this region fixed pattern noise is completely dominating despite photon noise being the greatest here. At larger radii the fluctuations from the mean at a radius do decrease with increasing exposure time. While there is still fixed pattern noise in this region, photon noise is not negligible.

The curve representing the differenced data has significant fluctuation reduction for radii up to 5 arcseconds. At larger radii there is no significant reduction nor increase. Differencing two independent signals results in an increase in the standard deviation by $\sqrt{2}$. This effect is evidently being compensated by cancellation of the fixed pattern noise. No companion to this star was found.

References

- [1] Marcy, G.W. and Butler, R.P., "A planetary companion to 70 Vir," *Astrophysical Letters*, submitted (1996).
- [2] Mayor, M. and Queloz, D., "A Jupiter-mass companion to a solar-type star," *Nature*, in prep.
- [3] Nakajima, T., Oppenheimer, B.R., Kulkarni, S.R., Golimowski, D.A., Matthews, K. and Durrance, S.T., "Discovery of a cool brown dwarf," *Letters to Nature*, **378**, 463-5 (1995).

AO Based Spectroscopy: Prospects and Pitfalls

Guy Monnet
European Southern Observatory, Germany

Summary not available.

An Optical Ultrahigh Resolution Spectrograph with the Adaptive Optics

J. Ge, B. Jacobsen, J.R.P. Angel, N. Woolf, J. H. Black, M. Lloyd-Hart, P. Gray

Center for Astronomical Adaptive Optics

Steward Observatory, University of Arizona, Tucson, AZ 85721

Phone:(520)621-1539 - Fax:(520)621-9843

R. Q. Fugate

Starfire Optical Range, U. S. Airforce Phillips Lab, Kirtland AFB, NM 87117

Phone:(505)846-4712 - Fax:(505)846-0439

A prototype optical wavelength ultrahigh resolution echelle cross-dispersed spectrograph has been tested at the Starfire Optical Range (SOR) 1.5 m telescope (Woolf et al. 1995; Ge et al. 1996). To our knowledge this is the first high resolution spectrograph to take advantage of the diffraction limited images produced by an adaptive optics system. Because of the sharpened images produced by the adaptive optics at visible wavelength, about $r_0/D \sim 1/15$ in the seeing-dominant domain, the narrow slits necessary for high resolution can be used without a large loss of light. This is a great advantage when compared with conventional high resolution spectrographs (e.g. Lambert et al. 1990; Diego et al. 1995). In addition, the smaller image widths inherent with the adaptive optics system allow the orders to be spaced closer together on the chip, allowing more orders to be observed simultaneously.

The main part of the spectrograph layout at the Coudé room of the SOR is shown in Figure 1. A $242 \times 116 \text{ mm}^2$ Milton Roy R2 echelle grating with 23.2 gr mm^{-1} and a blaze angle of 63.5° was used to provide the main dispersion. Theoretical resolution of this grating is 500,000 in the I band, 600,000 in the R band and 800,000 in the V band. Cross dispersion was provided by an 8° apex angle BK7 prism used in double pass configuration. The grating was illuminated in quasi-Littrow mode with a small ($\sim 0.25^\circ$) out-of-plane tilt. Collimation was provided by a large off-axis parabola with a focal length of 6 m. A large folding flat was used to reduce the overall length of the spectrograph. A Loral back-illuminated CCD with $15 \mu\text{m}$ pixels and antireflection (AR) coating in a 2048×2048 format was proposed. The pixel size was sufficient for Nyquist sampling. The spectral format for the spectrograph is shown in Figure 2. The central box is the CCD's physical size ($30 \times 30 \text{ mm}^2$), which can cover about 90 echelle orders, corresponding to a wavelength range of 0.47 to $1 \mu\text{m}$ (or from the 163rd to the 76th order), with a width of $\sim 8 \text{ \AA}$ per order. The 30 mm length of the CCD is such that 11 exposures are needed to obtain a complete coverage of all the orders.

We have conducted two observation runs at the SOR 1.5 m telescope, one in June and one in November of 1995. Here we briefly report the results.

At the SOR two different wavelength bands are available (but not simultaneously), the "Blue" leg (0.47-0.7 μm) and the "Red" leg (0.7-1.0 μm). Figure 3 and 4 show parts of spectra obtained for Vega for the Blue and Red legs respectively. They were taken in June 1995 with a 2048×2048 Kodak thermo-electrically cooled CCD with $9 \mu\text{m}$ pixels. Figure 5 is a reduced spectrum of a He-Ne laser obtained during the same run; the separate modes are clearly resolved indicating a resolving power of about 660,000 at 6328 \AA , which is very close to the predicted resolution of 680,000. However, stellar observations from Vega and other bright stars give a much lower resolution (approximately 250,000) due to the use of a larger slit (about $100 \mu\text{m}$)

(Figure 6). Due to the use of a smaller Kodak CCD (because of electronics problems with the prepared Loral CCD), the wavelength coverages for the Blue and Red legs are approximately 300 Å and 200 Å, respectively.

The spectrograph has 11 reflecting and 10 transmitting surfaces (including a relay system before the slit). This leads to large photon losses. Total efficiency for the June run, including sky and telescope transmission, spectrograph losses, and CCD quantum efficiency, was only about 0.3% near the peak of the blaze. Improvements in coatings, however, by November increased the total efficiency to approximately 0.8% (Figure 7).

Table 1 shows a comparison between different ultrahigh resolution spectrographs, and includes the proposed spectrograph for the SOR 3.5 m telescope. High resolution spectrographs mated with adaptive optics can make great gains in both throughput and wavelength coverage over conventional spectrographs.

Table 1. Comparison between Different Ultrahigh Spectrographs in the World

Name	McDonald (2.7 m) ^a	AAT (3.8 m) UHRF ^b	SOR 1.5 m	SOR 3.5 m (planned)
Resolution	$5\text{--}6 \times 10^5$	9.9×10^5	2.5×10^5 ^f	7.7×10^5
Total efficiency at V band	0.045%	0.32%	0.8%	4% ^g
CCD	TI-2 800 × 800	Thomson 1024 × 1024	Kodak 2048 × 2048	Loral 4096 × 2048
Pixel Size (μm)	15	19	9	15
Readout Noise (e ⁻)	15	3.9	12.2	5
Pixel Number/Res. Element	8	2.4	10.3	2
Wavelength Coverage (Å)	1.2	2.5	200,270,500 ^e	1300
Working Wavelength(Å)	3,300-8000 ^c	3,000-11,000	4,000-10,000	5,000-10,000
V Magnitude limit (mag) ^d	4.4	7.8	7.4	11.1

^a The information on McDonald Coudé Echelle is based on Hobbs & Welty (1991) and Tull et al. (1995).

^b The information on AAT UHRF is based on Diego et al. (1995).

^c From Cardelli (1995).

^d Based on the same readout noise, 5 e⁻/pixel, same pixel size, 15 μm, 30 mins exposure and S/N = 30 per pixel.

^e 200 Å for Red Leg spectrum coverage (7,000-10,000 Å) with Kodak 2kx2k CCD with 9 μm pixels, 270 Å for Blue Leg spectrum coverage (4,700-7,000 Å) with Kodak 2kx2k CCD. 500 Å for Blue Leg spectrum coverage with Lesser's 2048 × 2048 CCD with 15 μm pixels.

^f Due to the slitwidth of a temporary slit (~ 100 μm), we cannot narrow it down to the 40 μm width needed to reach more than half million resolution.

^g The efficiency has included the increase of the 3.5 m telescope/AO transmission, about 2.5 times 1.5 m telescope transmission (Fugate 1995, private communication), and the increase of the Loral CCD QE, about 2 times the Kodak CCD QE.

REFERENCES

- Cardelli, J. A., 1995, in Laboratory and Astronomical High Resolution Spectra, ASP Conf. Series, Vol. 81. 411.
 Diego, F., et al. 1995, MNRAS, 272, 323
 Ge, J., et al. 1996, in Preparation
 Hobbs, L. M., & Welty, D. E., 1991, ApJ, 368, 426
 Kurucz, R. L., Furenlid, I., Brault, J., & Testerman, L., 1984, Solar Flux Atlas from 296 to 1300 nm,
 Lambert, D. L., Sheffer, Y., & Crane, P., 1990, ApJ, 359, L19
 Tull, R. G., et al. 1995, PASP, 107, 251
 Woolf, N., et al. 1995, Proc. SPIE Conference on Adaptive Optical Systems and Applications, 2534, Eds. R. K. Tyson & R. Q. Fugate

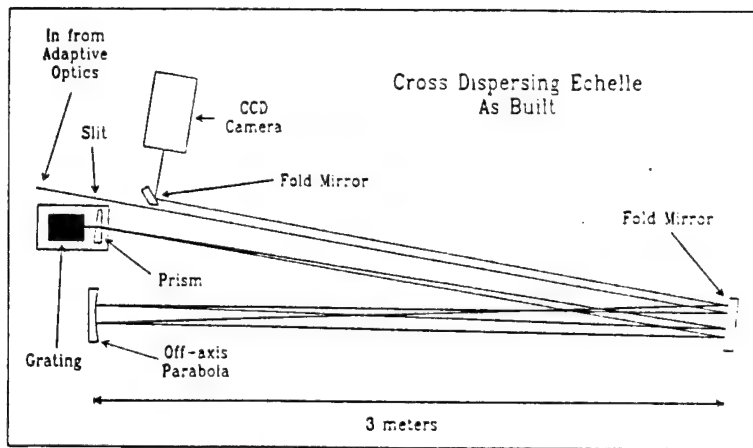


Figure 1 - Optical layout of the SOR cross-dispersed echelle spectrograph.

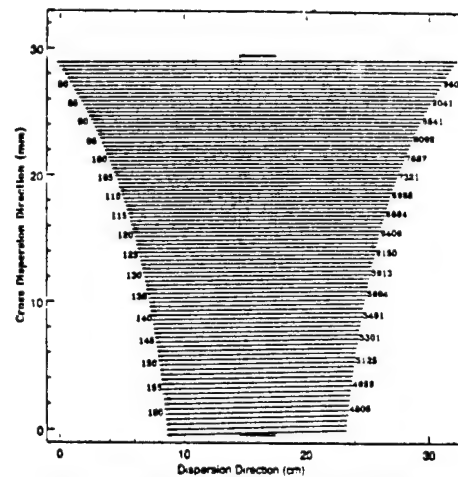


Figure 2 - Echelogram for the SOR cross-dispersed echelle spectrograph. Wavelength increases from left to right and from bottom to top. Several order numbers and central wavelengths are marked. The central line is the size for the Loral 2048 CCD with 15 μ m square pixels. The order separations and central wavelengths are measured from the observation data obtained at SOR in June and November 1995.

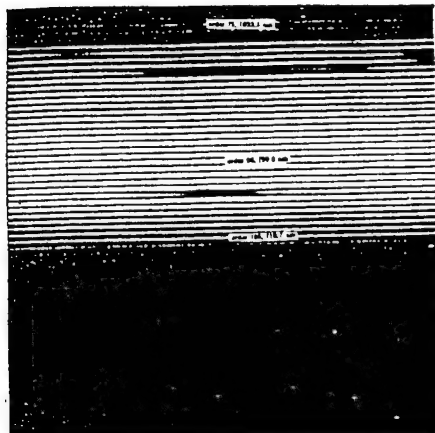


Figure 3 - Vega spectra from SOR 1.5 m telescope/AO "Red" leg with SOR Kodak 2048 CCD with 9 μ m square pixels. Several orders and wavelengths are marked.

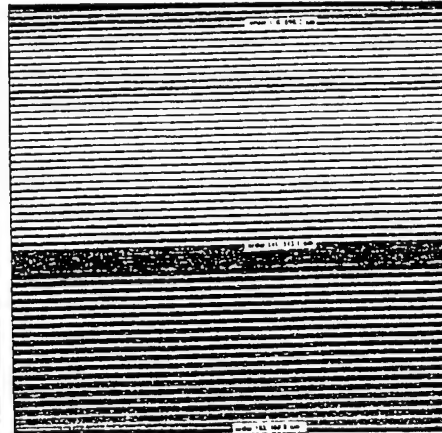


Figure 4 - Vega spectra from SOR 1.5 m telescope/AO "Blue" leg with the Kodak CCD.

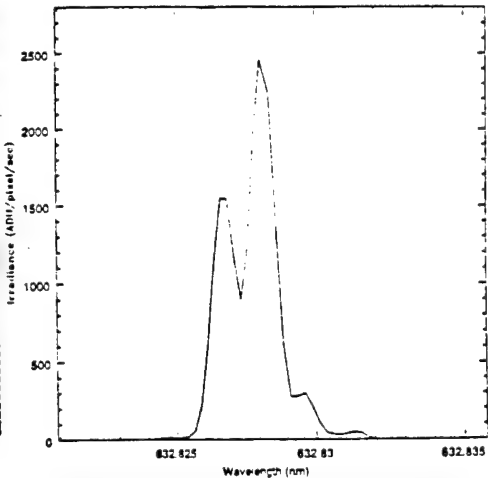


Figure 5 - The spectral profile of the He-Ne laser at 632.8 nm, where 4 adjacent laser modes separated by 0.00018 nm are clearly resolved. The FWHM resolution is 3.8 pixels or 36 μ m corresponding to a resolving power of 680,000.

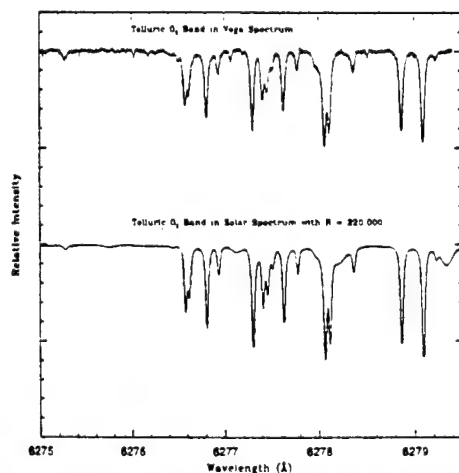


Figure 6 - Part of the telluric O_2 absorption lines in the Vega spectrum obtained with the SOR echelle spectrograph. It is compared to the Kurucz et al. (1984) solar spectrum which was smoothed to resolution of 260,000 via convolution with Gaussian function. Two sets of telluric lines show similar line profiles, indicating Vega spectral resolution of about 250,000.

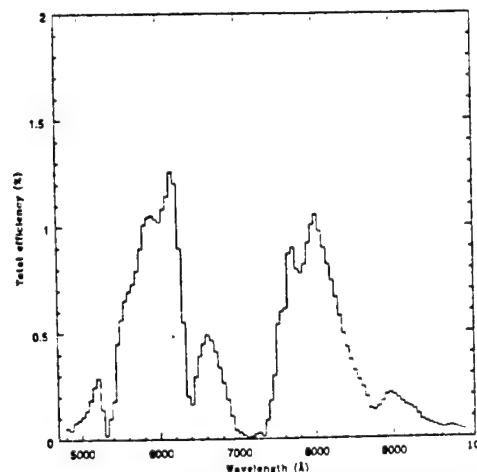


Figure 7 - Actually achieved total combined efficiency of the SOR echelle spectrograph as a function of wavelength, which includes the sky transmission, telescope/AO transmission. Several parts of the image are lost and the spectrograph is Kodak CCD. The quick fall-offs at wavelengths longer than 8500 Å and shorter than 5500 Å are mainly caused by the fall-offs of the Kodak CCD QE at these wavelength ranges.

Phase Diversity Imaging: Report of Experiments and Simulations

**Robert A. Gonsalves, Steven M. Ebstein, Peter Nisenson
Lexitek, Inc.
Woburn, MA 01801**

**Chris Shelton
Mount Wilson Institute
Pasadena, CA**

We report research results on phase diversity imaging, a technique for pre and post processing of atmospherically degraded images. The method uses an in-focus image and an out-of-focus image to deduce the aberrating wavefront introduced by the atmosphere and telescope; and deconvolves the measured images to produce a near-diffraction-limited estimate of the object.

The pre-processing mode would use the wavefront estimate to control an adaptive optic; the post-processing mode would sharpen the estimate in near-real time or off line. The method allows the designer to trade optical (pre-processing) hardware for computer (post-processing) hardware.

In the talk we will review the theory and describe:

Static lab experiments which demonstrate the theory.

Algorithms for white-light applications.

Simulations which estimate the performance vs. noise level and turbulence strength.

Measurements made at the Mt. Wilson Observatory, including an evaluation of the adaptive optic currently installed there.

An example of the laboratory experiments is shown in Figure 1. This illustrates the wavefront sensing capability. On the top are the data: the main and diversity images for a bar target imaged through a cylinder-like phase aberration. On the bottom is the estimated phase, an x-slice through the phase, in waves, and a corresponding slice through an interferometer's measurement of the aberration.

Figure 2 shows the image restoration capability. The data are on the left and in the middle; and the restoration is on the right.

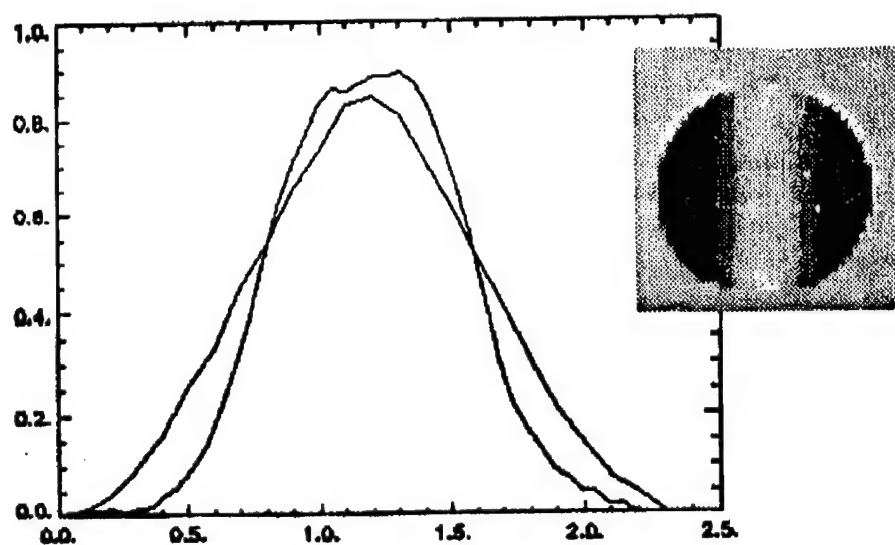
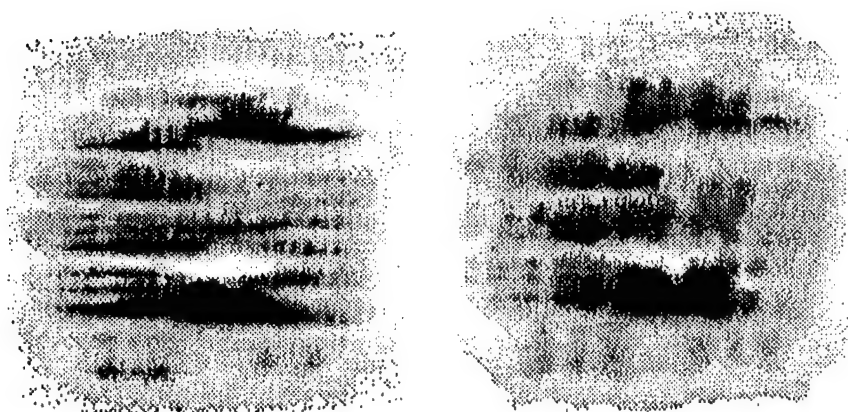


Figure 1. Lab demonstration of wavefront estimation.



Figure 2. Lab demonstration of image restoration.

Figure 3 is an example of the ability to characterize an optical system. The system is the adaptive and imaging optics currently installed on the 100 inch telescope at Mt. Wilson. With a base-line signal commanded from the control console the main and diversity data shown at the bottom were recorded. The algorithm's fits to the data are shown in the middle. And on the top are the main and diversity phases estimated by the phase diversity algorithm. The checker board pattern is a well-known artifact of some adaptive optics systems.

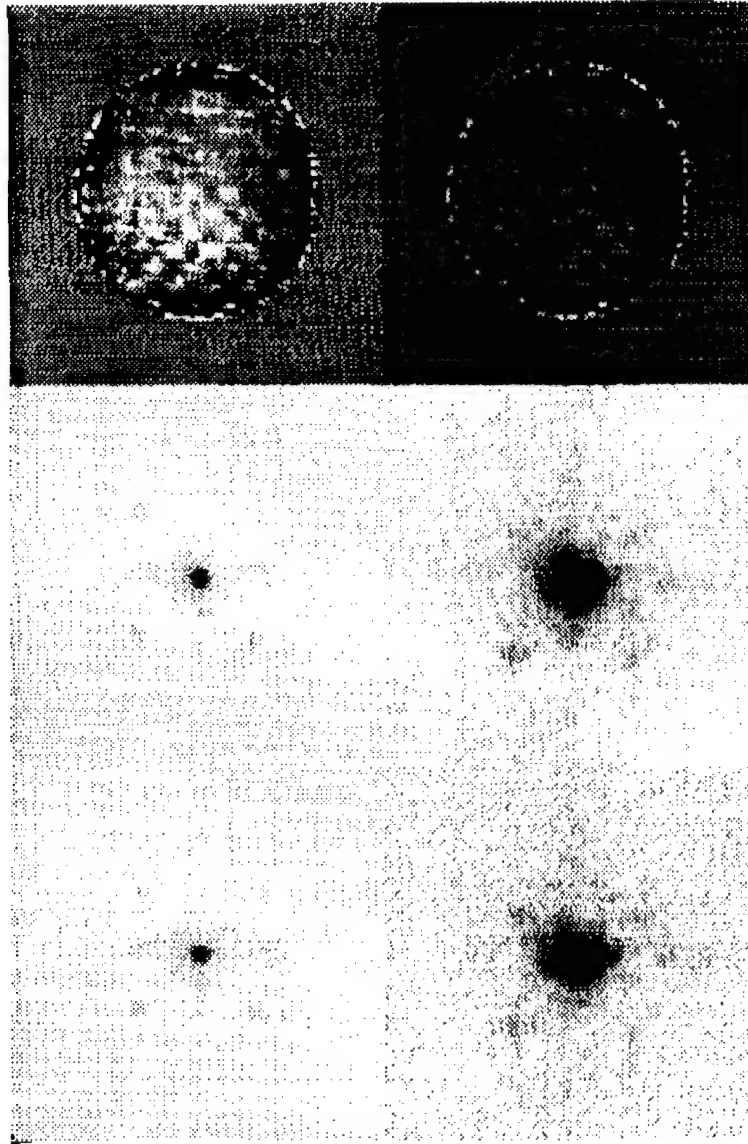


Figure 3. Phase diversity exercised on Mt. Wilson's adaptive optics

Wednesday, July 10, 1996

Post-Processing of Adaptive Optics Corrected Imagery

AWA 8:00 am-10:00 am
Pikake Room

Byron M. Welsh, *Presider*
Air Force Institute of Technology

Post-Processing of Adaptive Optics Images: Blind Deconvolution Analysis

Julian C. Christou¹, E. Keith Hege², & Stuart M. Jefferies³

1 - Starfire Optical Range, Phillips Laboratory PL/LIG, Kirtland Air Force Base,
NM 87117, USA, (505) 846-4712, (christoj@plk.af.mil)

2 - Steward Observatory, The University of Arizona,
Tucson, AZ 85721, USA, (520) 621-1049, (hege@as.arizona.edu)

3 - National Solar Observatory Tucson, AZ 85726, USA, (520) 318-8182
(stuartj@noao.edu)

1 Introduction

Adaptive Optics (AO) has the capability of providing diffraction-limited images from ground-based astronomical telescopes through the turbulent atmosphere. Because of limitations in the AO system, the point spread functions (PSF's) of the AO system suffers from incomplete compensation and variability. Depending on the observation wavelength (λ), the spatial coherence length of the atmosphere (r_0), the sub-aperture size (d), the correlation time of the atmosphere (τ_0), the sample time of the wavefront sensing (t_s), and the signal strength of the source, the Strehl ratios of the compensated images can vary considerably (between 2% - 90%). In addition, residual errors in tilt compensation due to the source signal strength can further degrade the image quality. Thus, AO compensated imaging generally requires some post-processing to extract the maximum possible information. As long as the PSF for the imaging process is stationary, then standard deconvolution algorithms can be applied. These algorithms have been recently developed and applied to Hubble Space Telescope imaging and include maximum-likelihood, maximum-entropy and pixon-based algorithms, etc.[1].

It is also possible to use an artificial beacon to close the high-order AO loop on an object which is too faint to track. The lack of tilt-tracking in these circumstances severely degrades the long-exposure images. In this case, the images can be analysed by standard speckle interferometry techniques, e.g. bispectrum analysis [2] as well as shift-and-add and centroiding [3].

However, both long- and short-exposure analysis discussed above require a stationary PSF. Experience with the Starfire Optical Range (SOR) AO system has found that the for 30s integrations, the Strehl ratio of the PSF can vary by $\sim 10\% - 20\%$ on a single source [3]. This effect is also seen when chopping between the target source and a reference source. Thus, conventional deconvolution al-

gorithms are no longer applicable and can lead to systematic errors in the reconstructed objects.

2 Blind Deconvolution

For isoplanatic imaging, the observed image is written as

$$g(\vec{r}) = f(\vec{r}) \odot h(\vec{r}) + n(\vec{r}) \quad (1)$$

where $f(\vec{r})$ is the object distribution and $h(\vec{r})$ is the PSF of the system. $n(\vec{r})$ is the noise contamination of the image and \odot denotes the convolution operator. When the PSF, $h(\vec{r})$, is either poorly known or unknown, then the problem of extracting the object distribution and the PSF from the observation is known as "blind deconvolution". Over the last few years there has been a strong interest in this technique [5 - 9] resulting in sophisticated algorithms for this analysis. The algorithm discussed here is based on that of Jefferies & Christou (JC) [7] and uses a conjugate gradient error-metric minimisation scheme. The error metric is written as

$$\mathcal{E} = \mathcal{E}_{\text{conv}} + \mathcal{E}_{\text{bp}} \quad (2)$$

where $\mathcal{E}_{\text{conv}}$ is the convolution error metric and \mathcal{E}_{bp} is the bandpass constraint error metric. In the Fourier domain, the convolution constraint is

$$\mathcal{E}_{\text{conv}} = \sum_k \sum_{\vec{f}} |G_k(\vec{f}) - \hat{F}(\vec{f}) \cdot \hat{H}_k(\vec{f})|^2 \cdot \Phi(\vec{f}) \quad (3)$$

where $G_k(\vec{f})$ is Fourier transform of the k^{th} convolution image of a set, i.e. $G_k(\vec{f}) = \mathcal{F}[g_k(\vec{r})]$, $\hat{F}(\vec{f})$ is the object estimate Fourier transform, i.e. $\hat{F}(\vec{f}) = \mathcal{F}[\hat{f}(\vec{r})]$, and $\hat{H}_k(\vec{f})$ is the k^{th} PSF estimate Fourier transform, i.e. $\hat{H}_k(\vec{f}) = \mathcal{F}[\hat{h}_k(\vec{r})]$. $\Phi(\vec{f})$ is a filter which permits the convolution error metric to be computed over a limited range of the Fourier domain and which also permits weighting according to the signal-to-noise (SNR) ratio of the observations.

When

$$\Phi(\vec{f}) = \frac{|G(\vec{f})|^2 - |N(\vec{f})|^2}{|G(\vec{f})|^2} \quad (4)$$

then the filter behaves as an optimal or Wiener filter weighting the Fourier domain by the SNR of the observations. When $\Phi(\vec{f})$ is unity for $|\vec{f}| \leq f_c$, where f_c is the cut-off frequency, then all spatial frequencies carry the same weight. If $\Phi(\vec{f}) = 1 \forall f$ then the noise contamination, i.e. for $|\vec{f}| > f_c$ will affect the error metric and therefore the convergence.

In the image domain, the convolution constraint is written as

$$\epsilon_{\text{conv}} = \sum_k \sum_{\vec{r}} \left[\frac{g_k(\vec{r}) - \hat{f}(\vec{r}) \odot \hat{h}_k(\vec{r})}{\sigma(\vec{r})} \right]^2 \cdot M(\vec{r}) \quad (5)$$

where $\sigma(\vec{r})$ is the error estimate for each pixel. This has advantages and disadvantages over the Fourier domain convolution constraint. The advantages are that it is now possible to apply a binary mask containing "bad" pixels, $M(\vec{r})$, and it also permits analysis of data extending beyond the range of the sampled image. The disadvantage, however, is that noise is affecting the convolution, and it is therefore equivalent to using (3) with $\Phi(\vec{f})$ equal to unity for the whole spatial frequency domain. Both versions of the the convolution constraint are currently implemented.

The band-pass constraint takes into account known information about the observation, i.e. that the PSF only contains spatial frequency information out to the diffraction-limit of the telescope used, i.e.

$$\epsilon_{\text{bp}} = \sum_k \sum_{\vec{f}} |\hat{H}_k(\vec{f})|^2 \cdot B_k(\vec{f}) \quad (6)$$

where $B_k(\vec{f})$ is unity for $|\vec{f}| > f_c$ and zero elsewhere. This constraint prevents the trivial solution of the convolution image and a δ -function.

In the original JC code we used a loose-loose constraint for the positivity of the object and PSF estimates. Negative valued pixels were penalized by contributing to an image error-metric which was part of the total error metric shown in (2). We have since investigated the strict-strict positivity constraint used by Thiébert & Conan [8] which defines both the object and PSF as the squares of two other variables, i.e. $f(\vec{f}) = \phi_f(\vec{f})^2$ and $h(\vec{f}) = \phi_h(\vec{f})^2$, which are then minimised. We found that the strict-strict algorithm produced significantly better photometric fidelity in the presence of noise than the loose-loose constraint. Thus the former is now implemented.

3 Imaging "The Trapezium"

Figure 1 shows a series of 4 out of 10 independent Rayleigh beacon compensated AO images of "The Trapezium", θ_1 Orionis obtained at the SOR 1.5m

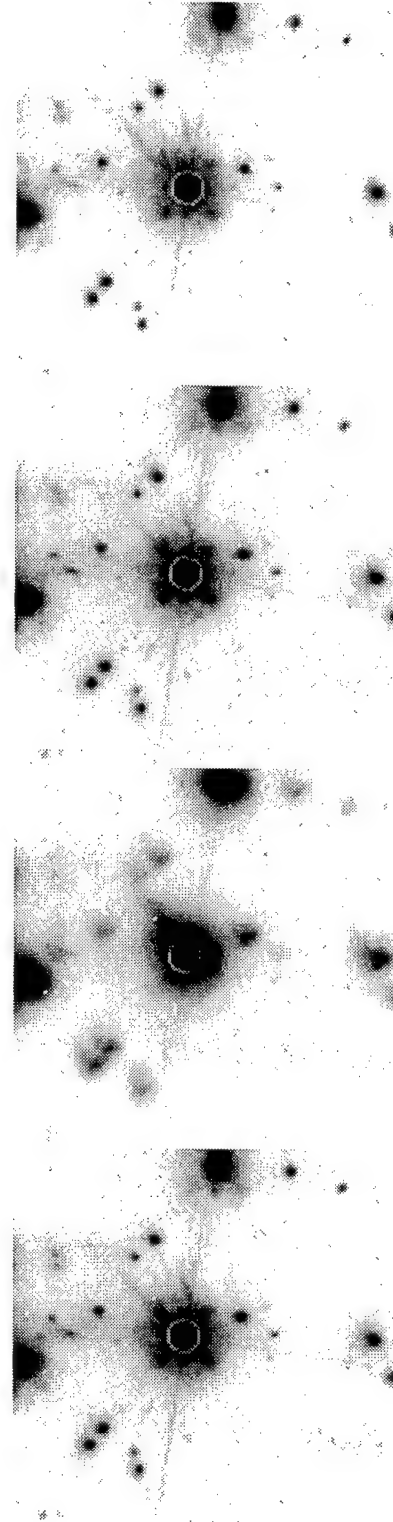


Figure 1: Four independent Rayleigh beacon AO images of "The Trapezium".

at H , $1.65 \mu\text{m}$. These images are centered on θ_{1c} Ori-
onis which is attenuated by ~ 5 magnitudes. This
permits investigation of the nearby surrounding re-
gion. The integration times were 30s. Comparison
of these images show the variability of the AO. The
attenuation mask is clearly visible.

Eight of these frames were reduced simultaneously
using the image domain constraint (5) with $\sigma(\vec{r})$ set
to unity. Initial estimates for the saturated sources
were obtained by appropriate scaling to 1s integra-
tions which were also taken. The central peak of θ_{1c}
Ori. was restored by multiplication by 108, the mea-
sured attenuation factor for a radius of 9 pixels. This
left the annulus between the regular and attenuated
signal as being poorly corrected. This was incorpo-
rated into the convolution domain mask, $M(\vec{r})$ in (5)
as well as including the "bad" pixels in the array.

The results of a preliminary analysis are shown in
figures 2 and 3. The reconstructed PSF's show a
similar variability as the convolution images in fig-
ure 1. Note that the source at ~ 2 o'clock to the
central component leaves a residual in the PSF in-
dicating that convergence is not yet achieved. The
reconstructed object shows the stellar sources to be
significantly sharpened although the fixed "quilting"
pattern around θ_{1c} Ori. has not been completely re-
moved. As the PSF's are not vastly different, the
multiple image constraint is compromised.

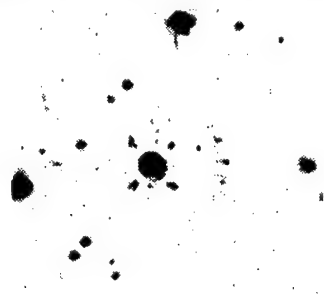


Figure 3: Preliminary object estimate for the convo-
lution images in figure 1.

4 References

- [1] "The Restoration of HST Images & Spectra - II",
ed. R.J. Hanisch & R.L. White, STScI, 1994.
- [2] A.W. Lohman, G.P. Weigelt, & B. Wirtitzer,
Appl. Opt., **22**, 4028, 1983.
- [3] J.C. Christou, *Pub. Astron. Soc. Pac.*, **103**, 369,
1995.
- [4] J.C. Christou, B.L. Ellerbroek, & R.Q. Fugate,
Astrophys. J., **450**, 369, 1995.
- [5] R.G. Lane, *J. Opt. Soc. Am. A*, **9**, 1508, 1992.
- [6] T.J. Schulz, *J. Opt. Soc. Am. A*, **10**, 1064, 1993.
- [7] S.M. Jefferies & J.C. Christou, *Astrophys. J.*,
415, 862, 1993.
- [8] E. Thiébaud & J.-M. Conan, *J. Opt. Soc. Am.*
A, **12**, 485, 1994.
- [9] Z. Mou-yan & R. Unbejauen, *Opt. Eng.*, **34**,
2945, 1995.



Figure 2: Preliminary estimates of the non-
stationary PSF for the four convolution images in
figure 1.

Fourier phase spectrum estimation using deconvolution from wavefront sensing and bispectrum reconstruction

Michael C. Roggemann, Cynthia A. Hyde,* Byron M. Welsh

USAF Institute of Technology
2950 P St.
Wright-Patterson AFB OH 45433

*University of Dayton

1 Introduction

Many techniques for overcoming the optical effects of turbulence have been studied. These correction techniques include post detection image processing, such as speckle imaging (SI) [1] and deconvolution from wavefront sensing (DWFS) [2]. The post detection image processing techniques of speckle imaging and DWFS are of interest because they avoid the investment in expensive and complicated hardware required for adaptive optics. A key factor distinguishing DWFS from SI is that no separate phase spectrum reconstruction step analogous to computing and processing the bispectrum is required in DWFS. We show here that for bright extended objects DWFS provides much better phase spectrum estimation than the bispectrum technique. The qualifier *bright* is used to describe the case where the object or beacon is bright enough to provide ample signal for low noise wave front estimation using a Hartmann sensor.

2 Models and Simulations

The DWFS method requires an estimate of the optical transfer function (OTF) $H(\vec{u})$, referred to here as $\tilde{H}(\vec{u})$. In DWFS the estimate, $\tilde{H}(\vec{u})$, is obtained in the following manner: (1) the WFS is exposed to a pupil image which contains the aberration $\theta(\vec{x}_p)$; (2) an estimate of $\theta(\vec{x}_p)$, called $\tilde{\theta}(\vec{x}_p)$, is computed from the WFS measurement; and (3) the estimate $\tilde{\theta}(\vec{x}_p)$ is used to compute $\tilde{H}(\vec{u})$ using standard Fourier optics methods [3]. A least squares wave front estimation scheme based on Hartmann sensor measurements as described in Ref. [4] was used to estimate $\tilde{\theta}(\vec{x}_p)$. For the work presented here the first 40 Zernike polynomials, excluding piston, were used for wave front phase reconstruction. An idealized Hartmann sensor was assumed here to provide an upper bound on performance. To accurately simulate the effects of an extended object on the Hartmann sensor output the noise model developed in Ref. [5] was used. The beacon width σ_b was set equal to the longest dimension of the object, which is 12 m in the present case. The Hartmann sensor modeled here had 12 subapertures spanning the 1 m diameter of the telescope pupil. Hence, the subapertures had side length of $d = 8.33$ cm. Only subapertures completely contained by the telescope pupil were used, providing a total of 88 subapertures in the Hartmann sensor.

The object spectrum estimate $\tilde{O}_D(\vec{f})$ is obtained from DWFS using

$$\tilde{O}_D(\vec{f}) = \frac{\langle D(\vec{f}) \tilde{H}^*(\vec{f}) \rangle}{\langle H_{\text{ref}}(\vec{f}) \tilde{H}_{\text{ref}}(\vec{f})^* \rangle} = |\tilde{O}_D(\vec{f})| \exp\{\tilde{\phi}_D(\vec{f})\}, \quad (1)$$

where $D(\vec{f})$ is the spectrum of the detected image, the $*$ indicates the complex conjugate, $\tilde{H}(\vec{f})$ is the associated estimate of the OTF obtained from the wave front sensor measurements of the object, $H_{\text{ref}}(\vec{f})$ is the OTF computed from reference

Table 1: K_W and K_I as a function of visual magnitude.

m_v	K_W	K_I
0	416,994	26,805,639
4	10,472	673,243
8	263	16,910

star measurements, $\hat{H}_{\text{ref}}(\vec{f})$ is the associated estimate of the OTF obtained from the wave front sensor measurements of the reference star, and $\langle \bullet \rangle$ is the time or ensemble average operator.

Speckle imaging was implemented using Labeyrie's speckle interferometry technique [6] to estimate the modulus of the object spectrum, and the bispectrum technique [1] to estimate the phase of the object spectrum. The estimated object spectrum for speckle imaging is defined as

$$\tilde{O}_S(\vec{u}) = |\tilde{O}_S(\vec{u})| \exp\{j\tilde{\phi}_S(\vec{u})\}. \quad (2)$$

The key metric for comparing DWFS and speckle imaging examined here is the squared error between the estimate of the object phase spectrum and the true object phase spectrum. To mathematically define this squared error, let the true object spectrum $O(\vec{u})$ be represented by a modulus $|O(\vec{u})|$ and phase $\phi(\vec{u})$ as

$$O(\vec{u}) = |O(\vec{u})| \exp\{j\phi(\vec{u})\}. \quad (3)$$

The phase error between the true object spectrum and the estimated object spectrum is then obtained using Eq. (3) in conjunction with either Eq. (1) or Eq. (2) to obtain the two dimensional square phase error $\epsilon_{D,S}^2(\vec{u})$ defined by

$$\epsilon_{D,S}^2(\vec{u}) = \left[\arg \left\{ O(\vec{u}) \tilde{O}_{D,S}^*(\vec{u}) \right\} \right]^2, \quad (4)$$

where the use of the subscripts D and S are used to indicate that this operation was applied to object spectrum estimates obtained with both DWFS and speckle imaging.

Simulations were used to compute object estimates using DWFS and SI. Simulations provide a convenient means of estimating performance for cases where the statistical estimators cannot be written in a form which permits easy analytic evaluation, such as is the case for phase spectrum estimation using DWFS and SI. These simulations also provide a tool for evaluating performance across a wide range of input parameters. Separate computer programs were used for the DWFS and SI results. These programs were derived from codes which have been carefully tested against theoretical performance [7].

3 Results

The phase spectrum error metrics $\epsilon_D(\vec{u})$ and $\epsilon_S(\vec{u})$, defined in Eq. (4), were evaluated as functions of r_0 , the visual magnitude m_v of the object, and the distance between the telescope and the object. For purposes of calculating photoevent rates from visual magnitude it was assumed that the objects simulated had the same spectrum as the sun. For the results presented here the mean wavelength of operation for the wave front sensor is 600 nm, and the spectral bandwidth was ± 60 nm. The mean wavelength of operation for the image plane is 700 nm, with the spectral bandwidth of ± 35 nm. The integration time for both the wave front sensor and the image plane is 10 ms. All losses from the top of the atmosphere to the output of the detector were assumed to provide an overall efficiency of 0.5. These assumptions yield the average number of photo events per integration time in both the wave front sensor K_W and the image plane K_I shown in Table 1.

The simulations were then run using the extended object at a distance of 500 km from the telescope for the same set of seeing and visual magnitude conditions studied for the point source. A computer rendering of a satellite was used as the extended object. The satellite object was placed in a 256×256 pixel array with physical side length of 12 m. To simulate the effects of varying distance, the object was scaled so that the spectral components of the Fourier transform of the sampled object and the spectral components of the sampled optical transfer function fell on the same grid in frequency space.

Phase error metric results for the extended object are presented in Fig. 1. In Fig. 1 the subfigure labeled (a) is for $r_0 = 7$ cm, and the subfigure labeled (b) is for $r_0 = 10$ cm. The horizontal axis in Fig. 1 is normalized to the diffraction limited cutoff frequency D/λ . The results presented in Fig. 1 can be discussed in terms of the noise effective cutoff frequency f_{eff} , defined as the normalized spatial frequency at which $\epsilon_D^2(u)$ and $\epsilon_S^2(u)$ exceed one radian squared. For the 500 km object case shown in Fig. 1 f_{eff} for speckle imaging is approximately 0.2 for all seeing and light level cases. However, for DWFS $f_{eff} \geq 0.85$ for the $m_v = 0$ and 4 cases, indicating that DWFS provides superior phase spectrum estimation compared to the bispectrum technique for extended objects when sufficient signal is available to the wave front sensor. We conclude from these results that when sufficient light levels exist in the wave front sensor to provide good wave front phase reconstruction, DWFS provides object phase spectrum estimates superior to the object phase spectrum estimates obtained from the bispectrum technique.

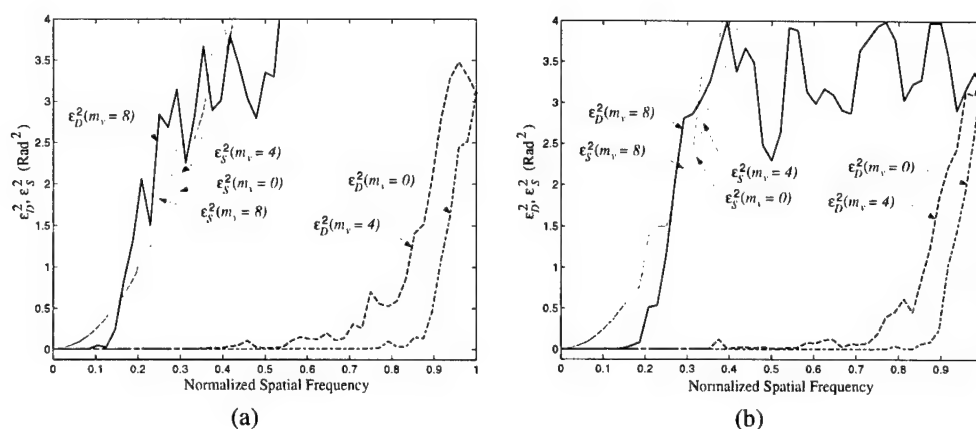


Figure 1: Phase error metrics $\epsilon_D^2(u)$ and $\epsilon_S^2(u)$ for the satellite object at a range of 500 km with visual magnitude $m_v = 0, 4, 8$: (a) $r_0 = 7$ cm; and (b) $r_0 = 10$ cm.

References

- [1] A. W. Lohmann, G. Weigelt, and B. Wirtzner, "Speckle masking in astronomy: triple correlation theory and applications," *Appl. Opt.*, vol. 22, pp. 4028–4037, 1983.
- [2] J. Primot, G. Rousset, and J. C. Fontanella, "Deconvolution from wave-front sensing: a new technique for compensating turbulence-degraded images," *J. Opt. Soc. Am. A*, vol. 7, pp. 1589–1608, 1990.
- [3] J. W. Goodman, *Introduction to Fourier Optics*. New York: McGraw-Hill Book Co., 1968.
- [4] M. C. Roggemann, B. M. Welsh, and J. Devey, "Biased estimators and object-spectrum estimation in the method of deconvolution from wavefront sensing," *Appl. Opt.*, vol. 33, pp. 5754–5763, 1994.
- [5] B. M. Welsh, B. L. Ellerbroek, M. C. Roggemann, and T. L. Pennington, "Fundamental performance limitations and comparison of the hartmann and shearing interferometer wavefront sensors," *Appl. Opt.*, vol. 34, pp. 4186–4195, 1995.
- [6] J. W. Goodman, *Statistical Optics*. New York: John Wiley & Sons, 1985.
- [7] M. C. Roggemann, "Optical performance of fully and partially compensated adaptive optics systems using least-squares and minimum variance phase reconstruction," *Comp. & Elec. Eng.*, vol. 18, pp. 451–466, 1992.

Roles for Phase Diversity in Compensated Imaging

Richard G. Paxman

Electro-Optics Laboratory
Environmental Research Institute of Michigan
P.O. Box 134001, Ann Arbor, Michigan 48113-4001
(313) 994-1200 ext. 2710; email: paxman@erim.org

1. Introduction

Astronomers have long known that the resolution in ground-based astronomy is almost always limited by aberrations introduced by the atmosphere. Over the years, researchers have developed a variety of clever pre- and post-detection approaches for correcting these effects. A strong argument can be made for pre-detection correction. It can be shown that the Modulation Transfer Function (MTF) will achieve a maximum at each spatial frequency when the system is unaberrated [1]. Aberrations can only modulate object spatial-frequency information to reduced levels. This modulation could be perfectly inverted in the absence of noise. However, detection of the imagery always introduces noise and inversion schemes result in noise amplification. Therefore, when it can be successfully accomplished, pre-detection correction is preferable to post-detection correction with regard to signal-to-noise ratio.

Although adaptive-optics (AO) technology has proven to be very powerful in combating turbulence-induced aberrations, residual (uncorrected) aberrations will always be present. Residual aberrations arise from wavefront-sensing errors, servo-lag errors, and deformable-mirror fitting errors. In many cases, these residual aberrations can be corrected with post-detection processing methods such as long-exposure deconvolution, multi-frame blind deconvolution, deconvolution with wavefront sensing, and *phase-diverse speckle*. Given the enormous expense of the development of and instrumentation for AO systems, the added value of relatively inexpensive post-detection processing methods is a bargain.

2. Phase-Diverse Speckle

As its name suggests, phase-diverse speckle [2,3] is a blend of phase diversity and speckle imaging concepts. The method of phase diversity [4,5], first proposed by Gonsalves, requires the collection of two or more images. One of these images is the conventional focal-plane image that has been degraded by the unknown aberrations. Additional images of the same object are formed by perturbing these unknown aberrations in some known fashion, thus creating *phase diversity*, and reimaging. This can be accomplished with simple optical hardware. For example, a beam splitter and a second detector array, translated along the optical axis, further degrades the imagery with a known amount of defocus. The goal is to identify a combination of object and aberrations that is consistent with the collected images, given the

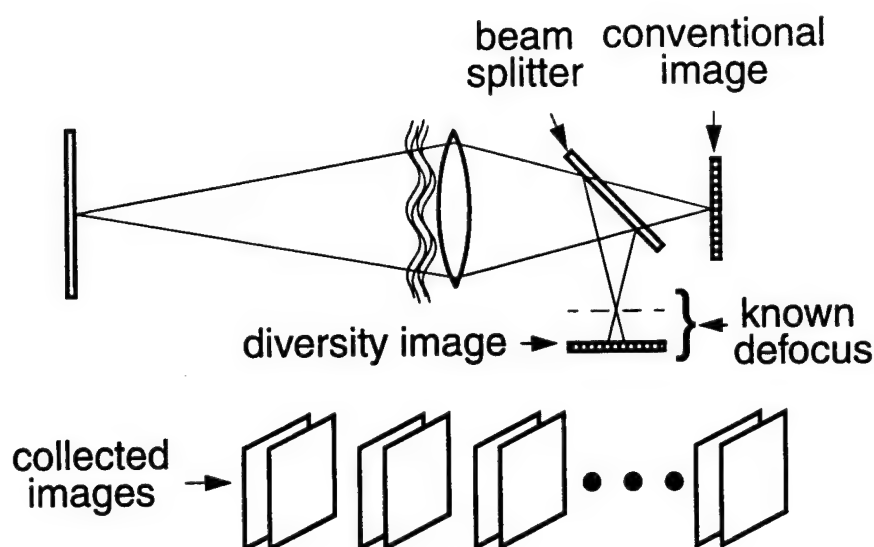


Figure 1: Optical layout for phase-diverse speckle imaging.

known phase-diversity functions. Note that phase diversity provides *system-identification* information by estimating aberrations.

Speckle imaging is a relatively mature technique for obtaining fine-resolution images in the presence of turbulence. This technique requires the collection of many short-exposure images of a static object. Phase-diverse speckle requires the simultaneous collection of one conventional image and at least one diversity image for each of multiple atmospheric realizations, as depicted in Figure 1. Fortunately, the primary strengths of the two constituent methods, namely the system identification provided by phase diversity and the added information content in a sequence of short-exposure images, persist. Post-detection correction of compensated binary-star images by using phase-diverse speckle was recently reported [6].

3. Additional Roles for Phase Diversity

The system-identification capability of phase diversity suggests that this technology can also be used in a wavefront-sensing role. Phase diversity can complement AO designs (that already employ a conventional wavefront sensor) by sensing fixed or slowly varying aberrations. For example, AO systems will compensate wavefront errors induced by both atmospheric turbulence and fixed aberrations in the host telescope. However, they are unable to sense errors introduced by their own internal optical components, which can be extensive [7]. Phase diversity can be used to sense wavefront errors arising from these internal sources because it relies on an external reference – the object being imaged. Once these internal phase errors are sensed, the deformable mirror can be adjusted accordingly. Another example is provided by telescopes with segmented primary mirrors, such as the Keck telescopes. AO systems that employ Hartmann-Shack wavefront sensors are being developed for these telescopes. Recall that a Hartmann-Shack sensor measures wavefront slope. It follows that slowly-varying piston misalignments among segments cannot be sensed and compensated under this design. The use of phase diversity to sense piston and tilt misalignments in segmented-aperture and

phased-array telescopes has been previously demonstrated [8,9]. Therefore, phase diversity is a strong candidate for the Keck application.

There are also applications for which phase diversity could be used as the primary wavefront sensor in a compensated-imaging system. For example, extended objects, such as the solar surface, pose problems for Hartmann-Shack or curvature-sensing wavefront sensors. However, phase diversity has been shown to work well in such applications [3,10,11]. Conventional wavefront sensors also have difficulty sensing space-variant (anisoplanatic) wavefronts arising from high-altitude turbulence. Preliminary work suggests that phase diversity could be used to sense these wavefronts as well [12]. The computational requirements for using phase diversity as a wavefront sensor in a closed-loop system are formidable, although closed-loop laboratory experiments have been reported [9].

REFERENCES

1. J.W. Goodman, *Introduction to Fourier Optics* (McGraw Hill, San Francisco, 1968).
2. R.G. Paxman, T.J. Schulz, and J.R. Fienup, "Phase-diverse speckle interferometry," in *Topical Meeting on Signal Recovery and Synthesis IV*, Technical Digest Series **11**, (Optical Society of America, Washington DC, 1992), New Orleans, LA, April 1992.
3. J.H. Seldin and R.G. Paxman, "Phase-diverse speckle reconstruction of solar data," in *Image Reconstruction and Restoration*, T.J. Schulz and D.L. Snyder, eds., Proc. SPIE **2302**, 268-280 (1994).
4. R.A. Gonsalves and R. Chidlaw, "Wavefront sensing by phase retrieval," in *Applications of Digital Image Processing III*, A.G. Tescher, ed., Proc. SPIE **207**, 32-39 (1979).
5. R.G. Paxman, T.J. Schulz, and J.R. Fienup, "Joint estimation of object and aberrations using phase diversity," J. Opt. Soc. Am. A **9**, 1072-1085 (1992).
6. J.H. Seldin, R.G. Paxman, and B.L. Ellerbroek, "Post-detection correction of compensated imagery using phase-diverse speckle," in Proc. ESO/OSA Topical Meeting on Adaptive Optics, ed. M. Cullum, ESO, Garching, Germany (1995).
7. D.S. Acton, "Correction of static optical errors in a segmented adaptive optical system," Appl. Opt. **34**, 7965-7968 (1995).
8. R.G. Paxman and J.R. Fienup, "Optical misalignment sensing and image reconstruction using phase diversity," J. Opt. Soc. Am. A **5**, 914-923 (1988).
9. R.L. Kendrick, D.S. Acton, and A.L. Duncan, "Phase-diversity wave-front sensor for imaging systems," Appl. Opt. **33**, 6533-6546 (1994).
10. M.G. Löfdahl, and G.B. Scharmer, "Wavefront sensing and image restoration from focused and defocused solar images," A&A supplement series, **107**, 243 (1994).
11. R.G. Paxman, J.H. Seldin, M.G. Löfdahl, G.B. Scharmer, and C.U. Keller, "Evaluation of phase-diversity techniques for solar-image restoration," accepted for publication in *Astrophysical Journal*, **467**, August 10, 1996.
12. R.G. Paxman, B.J. Thelen, and J.H. Seldin, "Phase-diversity correction of space-variant turbulence-induced blur," Optics Letters **19**, 1231-1233 (1994).

Speckle techniques for adaptive optics in the partial correction regime

E. Tessier

Royal Greenwich Observatory, Madingley Road, Cambridge, U.K. CB3 0EZ
E-mail: tessier@ast.cam.ac.uk, fax: +44 1223 374700, tel: +44 1223 374742

C. Perrier

Observatoire de Grenoble, BP 53X, 38041 Grenoble Cedex, France
E-mail: perrier@gag.observ-gr.fr, fax: +33 76448821, tel: +33 76635839

1) Adaptive optics correction, seeing and calibration

Adaptive optics (AO) works in many cases in the partial correction regime, i.e. with a Strehl ratio lower than 0.8. In this regime, seeing variations induce some variations in the correction (see Tessier 95), as shown on Fig. 1 which plots the Strehl ratio for continuous frames taken with the Come-On Plus instrument (see Beuzit et al. 94 for a description of this instrument).

Point spread function (PSF) calibration is needed for a-posteriori deconvolution of AO images. The current technique is to calibrate the PSF on a point source in conditions as similar as possible to the astronomical target source ones. This technique is referred to as the point source calibrator technique. In this technique, matching the noise level in the wavefront sensor is an important requirement which is possible to achieve by using neutral density filters for adjusting the photon flux. However, the shape and the color of the source could still induce some differences. When those precautions are taken, Tessier (1995) has shown on real data that the mismatch in the PSF calibration mainly comes from the seeing differences between the observations of the astronomical target and its point source calibrator.

The PSF calibration is similar to the calibration of the speckle transfer function. Some observing procedures are known to improve the calibration in speckle (Perrier 1988), e.g., selecting a calibrator close in the sky, observing both sources within a time as short as possible (a few minutes), and repeating this coming and going between the source and its calibrator a few times if possible. We have shown that this procedure identically improves the calibration efficiency in adaptive optics (see Tessier 1995).

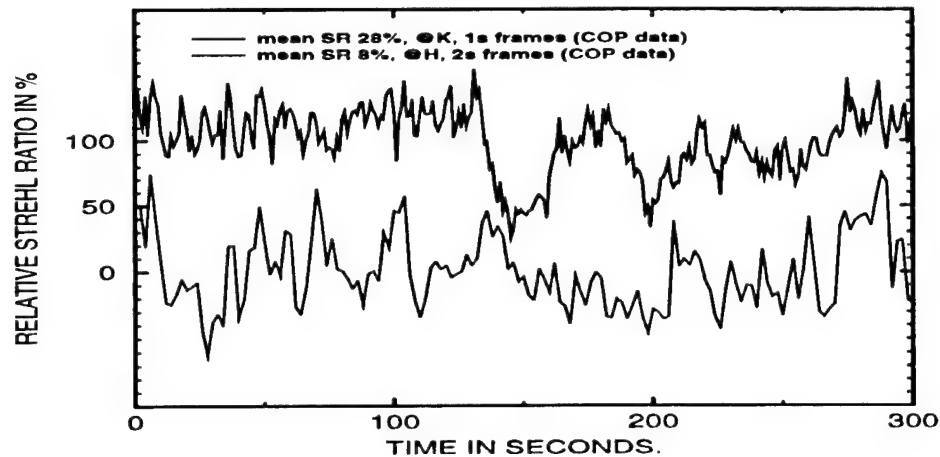


Figure 1: Strehl ratio in function of time from Come-On Plus data. SR is normalized to its mean value to highlight relative variations. SR is shifted by -100% for H data for visibility.

2) Speckle with Adaptive Optics

Rigaut et al. have observed (1991) an enhancement of the speckle transfer function by up to a factor 7 using the AO prototype Come-On. From AO simulations in the partial correction regime Conan (1995) showed that the speckle transfer function with AO yields a significant gain in signal and signal to noise compare to the ones obtained without AO.

We have carried out some Come-On Plus observations in speckle mode. A critical value for the Strehl ratio is observed for long exposure AO images. In the images with a SR lower than about 5%, the diffraction-limited coherent peak is lost as the optical transfer function (dashed line in Fig.2) does not show anymore high spatial frequencies. The use of short exposure times allows to recover the high spatial frequencies part in the modulation transfer function (solid line in Fig.2). In our case, the 250ms exposure time in J was quite long in comparison to the typical speckle coherence time estimated from the wavefront sensor data. This suggest that a speckle analysis improves the high frequencies even with exposure times larger than the speckle coherence time. By contrast, in case of good SR ($> 10\%$), this mode does not yield so much gain and is not relevant.

The behavior of the signal to noise depends more on the quality of the MTF calibration possibly achievable. We have completed the observation of a close

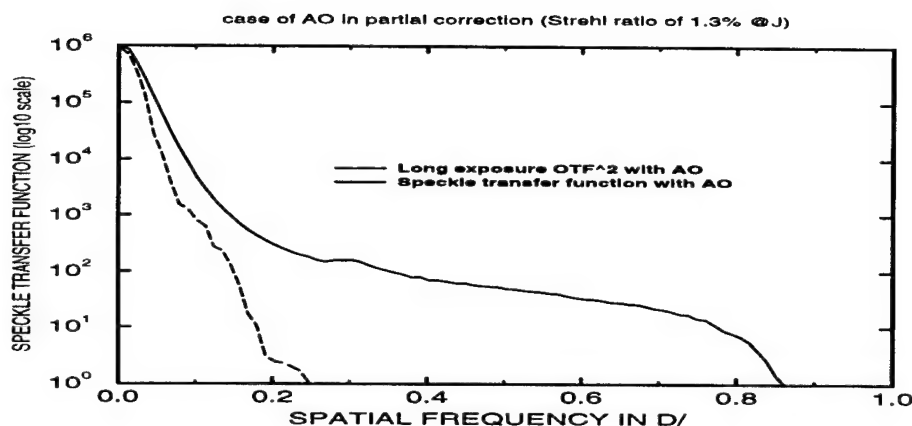


Figure 2: Speckle transfer function of short exposures AO images (exposure time is 0.25s in J band) under poor correction compared to the square optical transfer function of the long-exposure AO image. From COP data.

binary ($0''.2$) using this technique. From the rms residual of the reconstructed complex visibility, we can conclude that the phase is much less sensitive to seeing effects than the modulus is. The rms residual for the phase is about 0.03 radians from 500 frames. The rms residual for the visibility in modulus is 3% in the high spatial frequency range but some seeing effects affect up to 20 % the low spatial frequency region (r_0/λ).

To conclude, the field of application of speckle with AO applies essentially to low corrections (a few %). This occurs when, e.g., going shortward in wavelength for given conditions. We should be able to observe fainter sources with a higher resolution than in speckle without AO because of the gain in signal and the possibility to use longer exposure times.

References

1. Beuzit J.-L., Hubin N., Gendron E., Demailly L., Gigan P., Lacombe F., Chazallet F., Rabaud D., Rousset G. in Proc. SPIE 2201, p955 (1994)
2. Conan J.-M., Ph. D. Thesis, ONERA-Chatillon France (1995)
3. Perrier C. in Diffraction-Limited Imaging with Very Large Telescopes, Ed. D.M. Alloin and J.-M. Mariotti, NATO ASI Series, Series C, Vol. 274, p99-111 (1988)
4. Rigaut F., Kern P., Léna P., Rousset G., Fontanella J.C., Gaffard J.P., Merkle F., A&A, 250, p280 (1991)
5. Tessier E. in Adaptive Optical Systems and Applications, Robert K. Tyson, Robert Q. Fugate, Editors, Proc. SPIE 2534, p178-193 (1995)

Wednesday, July 10, 1996

Additional Adaptive Optics Applications

AWB 10:30 am-11:30 am
Pikake Room

Janet S. Fender, *Presider*
U.S. Air Force Phillips Laboratory

Review of Industrial Applications

Fritz Merkle
European Southern Observatory, Germany

Summary not available.

Adaptive Optics for the Human Eye

David R. Williams, Junzhong Liang, and Donald T. Miller
Center for Visual Science, University of Rochester, Rochester, NY 14627
Phone: 716 275-8672 FAX: 716 271-3043 email: david@cvs.rochester.edu

Aberrations limit the optical quality of the normal human eye, particularly when the pupil is large. These aberrations reduce the eye's contrast sensitivity to high spatial frequencies in the visual environment. They also limit the resolution of cameras designed to image the living human retina, a critical tool in the diagnosis and treatment of retinal disease. The eye's aberrations generally prohibit imaging structures in the living retina the size of single cells. Though it is possible to correct defocus and astigmatism with spectacle lenses, additional aberrations such as coma, spherical, and higher order aberrations remain. Moreover, the pattern of aberrations is highly variable from eye to eye, so that each eye must be independently corrected.

We have constructed an adaptive optics system that measures the wave aberration of the eye and compensates for it with a deformable mirror. A point source (632.8 nm) is imaged on the retina and the wavefront returning back through the pupil is evaluated by a Hartmann-Shack wavefront sensor. The wavefront sensor measures the wavefront slopes at 217 locations across the central 6.7 mm of the dilated pupil. The light budget is generous with $\sim 10^6$ photons/subaperture in a typical exposure, and is limited only by the standards for safe exposure of the retina. The wave aberration is calculated from the wavefront slopes with a least squares technique. We compensate for the wave aberration with a deformable mirror (Xinetics, Inc.) that has 37 actuators each with a stroke of 3 μm . The wave aberration of the eye changes rather little over time, particularly when accommodation is paralyzed with a cycloplegic drug, so that the temporal bandwidth required to achieve good compensation is close to zero.

In one subject with a 6 mm pupil and 632.8 nm light, adaptive compensation reduced the peak to peak phase error from 2.9 μm to less than 0.5 μm . Fig. 1a shows the wave aberration before adaptive correction; Fig. 1b shows the wave aberration following adaptive compensation. Fig. 1c and d

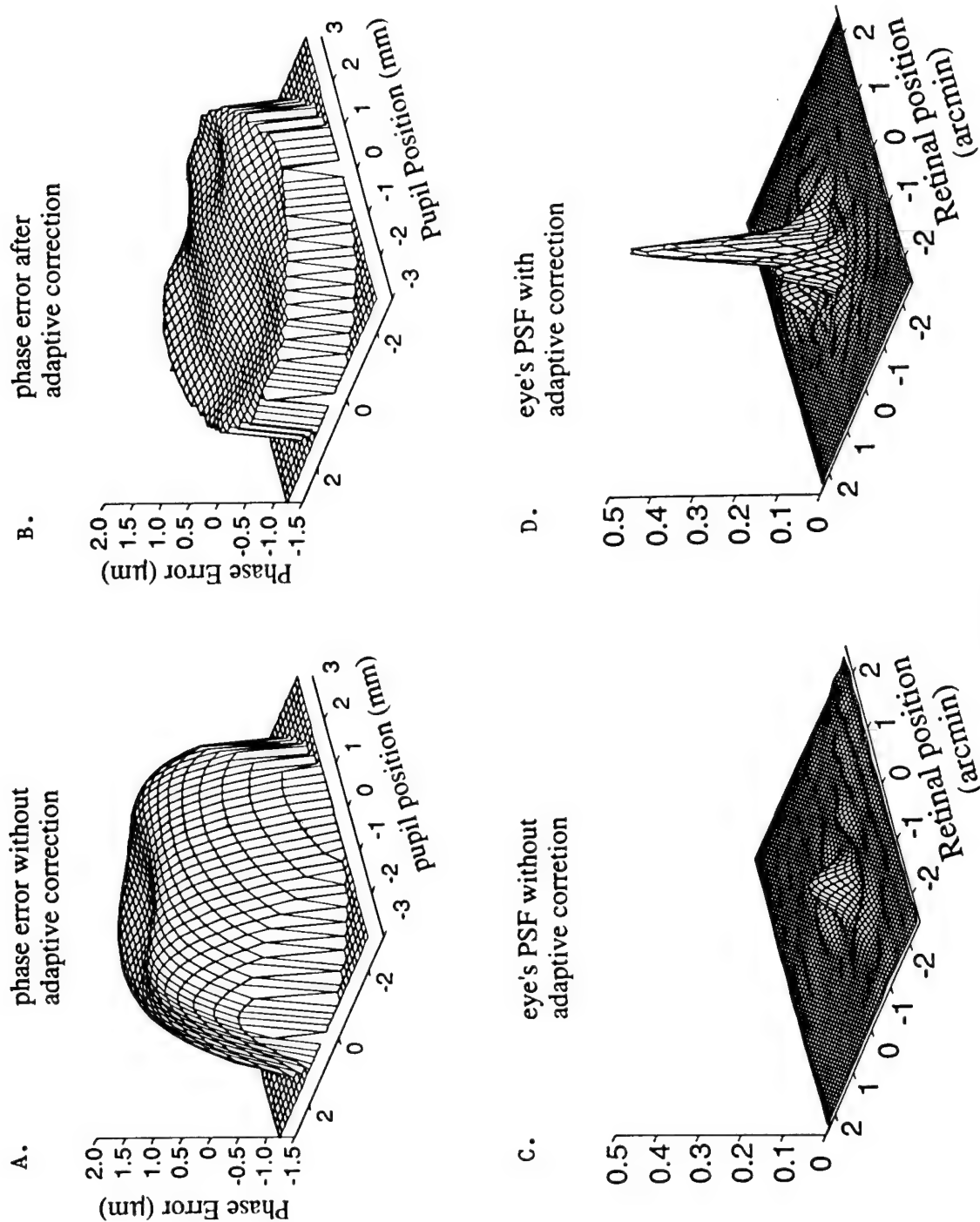


Figure 1.

show the corresponding point spread functions calculated from the wave aberration data. In Fig. 1a and c, defocus and astigmatism have been removed because they can be corrected with spectacle lenses. Adaptive correction increased the Strehl ratio by more than a factor of 5 from 0.09 to 0.47. The fullwidth at half height of the PSF after correction was about 2 μm which is close to the value of 1.7 μm expected from diffraction alone. The PSF after adaptive compensation represents the best optical quality ever produced in a human eye.

Subjects report that objects seen through the compensated deformable mirror look much sharper than when the mirror is flattened. Corroborative evidence comes from measurements of the contrast sensitivity of subjects to gratings viewed through the deformable mirror. The threshold contrast required to detect a 27 cycle/deg grating, viewed with a 6 mm pupil, is about 7 times lower when the mirror is compensating than when it is flat. The ability to expose the human retina to images of higher spatial bandwidth than it has ever experienced before provides a way to probe the neural limits of spatial vision relatively uncontaminated by optical blurring.

If the eye's aberrations were compensated across a fully dilated pupil (~8 mm), the transverse resolution will be about a factor of 3 higher than current cameras for retinal imaging. Our measurements with a 6.7 mm pupil suggest that the PSF after adaptive compensation is smaller than a single foveal cone photoreceptor (~2.4 μm). This should allow us for the first time to routinely image single cells such as photoreceptors or optic nerve fibers in their natural state inside the living eye. Such observations may clarify normal retinal function as well as aid in the diagnosis and treatment of retinal disease. We are currently incorporating a camera into the adaptive optics system to determine whether these potential benefits can be realized.

Wednesday, July 10, 1996

Atmospheric and Adaptive Optics Performance Characterization

AWC 1:15 pm-3:05 pm
Pikake Room

Vladimir Lukin, *Presider*
Institute of Atmospheric Optics, Russia

Models and measurements of atmospheric turbulence characteristics and their impact on AO design

Vladimir P. Lukin

Institute of Atmospheric Optics, Siberian Branch of RAS

av. Akademicheski, 1, 634055, Tomsk, Russia

tel. (382-2) 25-9606, fax: (382-2) 25-9086, E-mail: ZUEV@IAO.TOMSK.SU

1. DEVELOPMENT OF MODELS OF TURBULENCE SPECTRA

Using the experimental data we would suggested to investigate behavior of spectral density of atmospheric turbulence in the region of large spatial scales. Special efforts will be done to detect the variability of large optical inhomogeneities as manifestation of the influence of thermodynamic instability of the atmosphere.

In the practical calculations of fluctuations of the optical waves various models are used to describe the spectrum in the region of large scales: **von Karman**, **Greenwood-Tarazino**, and **Russian** model. These models have already had two parameters, one of which was the so called outer scale of turbulence.

Together with the dependence of the outer scale of turbulence on variations of meteorological parameters of the atmosphere, there exists anisotropy of the atmospheric turbulent spectra properties, in other words, inhomogeneities with dimensions exceeding several meters possess the properties that depend on direction. For example, random displacements of an image, which is formed by the optical radiation passed through atmospheric layers, exhibit such properties. The so-called coefficient of anisotropy K , being obtained immediately in the experiment, varied in the interval from 0.62 to 2.57 with the mean value $K_m = 1.57$, that indirectly indicated that the optical inhomogeneities, which produce the phase fluctuations, were anisotropic in the large-scale region. The relationship is quite obvious between the K value and the instability parameter.

Let us finally analyze the our data on the astroclimatic characteristics obtained in the region of the Elbrus mountain. In our analysis of the experimental data we assume that the atmosphere is stratified and its inhomogeneities have the shape of elongated ellipsoids of revolution. This implies that: (1) in the case of vertical propagation (precisely along the zenith direction) the image jitter must be practically isotropic, (2) the anisotropy of the jitter of an optical source image must be maximum for the case of horizontal propagation and will be determined by the atmospheric instability.

In the experiment we have used the measurer of fluctuations of the angles of arrival of the optical waves based on the telescope, which has a clockwork guide and a photoelectric adapter. This adapter was manufactured based on the soviet TV

tube. The parameters of the telescope and the measurer ensure the determination of angular position of the center of gravity of the focal spot with the accuracy about 0.08" and the measurements of its deviation in the frequency range from 0.01 to 100Hz. As a result we have obtained the values of the variance of an image jitter and of the orthogonal components. Under the near-surface conditions one can expect a strong anisotropy of the turbulence that leads to the anisotropy of the jittering process. Based on the experimental data it was revealed that: (1) in the ground atmospheric layer the outer scale of turbulence is comparable to the height above the underlying surface; (2) the value of this outer scale appears to be dependent on the atmospheric stability; (3) in the ground atmospheric layer the most large-scale inhomogeneities of the atmospheric turbulence are anisotropic; (4) from the standpoint vertical distribution of the atmospheric inhomogeneities one can introduce the average integral spectrum.

2. GROUND-BASED TELESCOPES, SPATIAL INTERFEROMETERS AND ATMOSPHERIC TURBULENCE

The asymptotic and numerical analysis of characteristics for telescopes and stellar interferometers has been performed based on the development of models of atmospheric turbulence. The influence of the outer scale of turbulence is under study. The results of the fields measurements, carried out using stellar interfereometers in different sites of the world, are analysed on the basis of the literature data available.

First of all, we shall consider the influence of atmospheric turbulence on the characteristics of stellar interferometers with large optical bases. We shall start from the possibility of description of atmospheric turbulence in the framework of models taking into account the vertical profiles of the structure parameters of the refractive index of the atmosphere, altitude variations on the wind velocity vector and values of the outer scale of turbulence. Moreover, since all these values depend not only on the running altitude but also on the altitude above the sea level, the possible variations of the model should be seriously discussed in this aspect depending on aerography of underlying surface.

At the same time the models of the atmospheric turbulence spectrum, taking into account the finiteness of the value of outer scale of turbulence, and, especially, the running value of this parameter for vertical path are rarely used for inhomogeneous surface paths. For particular purposes it is shown that the value, is fully finite (commensurable with the height above the underlying surface). At the same time, for astronomical observations a number of researchers consider this value to be equal to hundreds of meters up to some km. There are many observations when the results correspond to the values of outer scale of the order of one meter.

Undoubtedly, the outer scale of the turbulence undergoes serious altitude variations both in the surface layer and at large altitudes. Therefore we cannot speak about the value of outer scale as having the definite value for the entire atmosphere. We propose to consider a number of possible version of variations of the outer scale with altitude.

The created by the authors software makes it possible to use effectively the whole set of models of the outer scale, turbulence intensity, wind velocity. The calculations were conducted for the following interferometer bases: 3,1m, 12m, 36m, 128m, 437m, covering practically the entire range of operating and designed instruments. It turned out that for all the used models of altitude variation of outer scale one can select the averaged over the atmosphere, as a whole, value of outer scale, affecting strongly the given measured optical characteristics. In practice always this value does not exceed 2-5m.

In order for the results of measurements of phase difference fluctuations to become the basis for improving the model of turbulent atmosphere it is required to fix in measurements the following parameters: initial altitude, value and direction of wind velocity relative to orientation of the interferometer measuring base, the value of turbulence intensity at the initial altitude as well as the value of contrast of the interference pattern (for estimating the Fried radius value at the operation wavelength).

A new method for separating atmospheric layers using a Shack-Hartmann Curvature Sensor

Andreas Glindemann and Thomas Berkefeld

Max-Planck-Institut für Astronomie, Königstuhl 17, 69117 Heidelberg, Germany

Abstract

Using a Shack-Hartmann sensor for measuring the wavefront gradient and the wavefront curvature by integrating over the subapertures allows to separate the influence of atmospheric layers.

Introduction

The isoplanatic angle sets a principle limit to the performance of adaptive optics systems. For high order systems, this effect limits the field of view to a few arc seconds and, thus, it makes the point spread function vary enormously over the field of view.

The reason for this limitation is that the light from different stars travels through slightly different parts of the atmosphere. In adaptive optics systems usually the disturbance by the atmosphere is treated if it was caused by a single layer. The position of this virtual layer is in the plane conjugate to the plane of the Shack-Hartmann lenslet array or, in the case of a curvature sensor, in the conjugate plane of the position half way between the two planes of measurement. As the deformable mirror is placed in the pupil plane of the telescope, the same correction is applied to every object in the telescope field of view.

If several deformable mirrors are placed in conjugate planes of the dominant turbulent layers, a much larger field of view could be corrected. The optical design of a system with deformable mirrors in the proper positions is rather simple. The problem is to separate the aberrations of different layers.

In this paper we suggest a new method for the measurement of the turbulence in multiple atmospheric layers. The isoplanatic angle can then be increased by doing this measurement for several stars simultaneously.

Measurement principle

The problem of measuring the atmospheric turbulence can be reduced to imaging a phase object, *i.e.* an object affecting only the phase of the wavefront. This is a common problem in microscopy, and defocusing is an old cure. Then, the phase object that is invisible in the focused image shows up in the intensity distribution. If the phase varies only slightly, ($\phi(x) \ll 1$) the image intensity is proportional to the curvature of the phase distribution. In order to reconstruct the phase distribution completely, the intensity distribution has to be measured in two planes positioned symmetrically to the image plane of the phase object. The curvature sensor by Francois Roddier¹ is based on this idea.

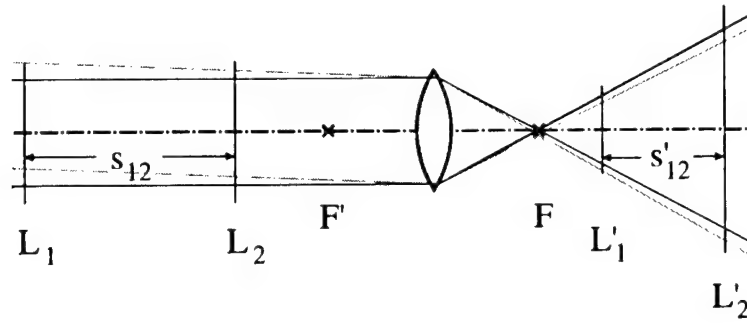


Figure 1: Illustration for the optical paths of two different stars.

To simplify the explanation, we start with two dominant layers that carry the bulk of the turbulence. Then, the intensity distribution $I_1(x_1)$ in the conjugate plane L'_1 of layer L_1 in Fig. 1 would be determined solely by the turbulence in layer L_2 . The turbulence in layer L_1 has no effect on the intensity distribution in its image plane, L'_1 . Vice versa, the intensity distribution in L'_2 is caused only by the turbulent layer in L_1 .

Assuming that the phase variation is weak, with $\phi(x) \ll 1$ (Eq.(7.2) in [2]), the complex amplitude immediately behind layer L_1 can then be written as

$$u_1(x_1) = 1 + i\phi_1(x_1).$$

The wavefront amplitude $u_2^-(x_2)$ immediately before L_2 is the Fresnel diffraction pattern of the turbulence in L_1 . Using an approximation for Fresnel diffraction for small angles³, it is

$$\begin{aligned} u_2^-(x_2) &= u_1(x_1) - i \frac{s_{12}}{2k} \frac{\partial^2 u_1(x_1)}{\partial x_2^2} \\ &= 1 + i\phi_1(x_2) + \frac{s_{12}}{2k} \frac{\partial^2 \phi_1(x_2)}{\partial x_2^2}, \end{aligned}$$

with $k = 2\pi/\lambda$. The turbulence in layer L_2 adds to the imaginary part of $u_2^-(x_2)$ yielding

$$u_2(x_2) = 1 + i(\phi_1(x_2) + \phi_2(x_2)) + \frac{s_{12}}{2k} \frac{\partial^2 \phi_1(x_2)}{\partial x_2^2}. \quad (1)$$

Calculating the wavefront in image space, one has to be careful to include the phase disturbances of both layers. Thus, the complex amplitude in L'_2 is, neglecting imperfections of the imaging optics, identical to $u_2(x_2)$ in L_2 . However, to calculate the wavefront in L'_1 the turbulence in L_2 has to be considered. This can be done by first calculating the complex amplitude in L'_1 as the defocused image of layer L_2 , and then calculating the distribution in L'_2 as the defocused image of L'_1 .

With $u'_2(x'_2) = u_2(x'_2)$, the complex amplitude in plane L'_1 is

$$\begin{aligned} u'_1(x'_1) &= u_2(x'_1) + i \frac{s'_{12}}{2k} \frac{\partial^2 u_2(x'_1)}{\partial x_1'^2} \\ &= 1 + i(\phi_1(x'_1) + \phi_2(x'_1)) - \frac{s'_{12}}{2k} \frac{\partial^2 \phi_2(x'_1)}{\partial x_1'^2}. \end{aligned} \quad (2)$$

The phase parts of both u'_1 (Eq.(1)) and u'_2 (Eq.(2)) are given by $\phi_1 + \phi_2$. Thus, the exact position of a Shack-Hartmann sensor measuring the wavefront tilts is not very critical.

The intensity distributions in L'_1 and L'_2 can be calculated as

$$I'_1(x'_1) = 1 - \frac{s'_{12}}{2k} \frac{\partial^2 \phi_2(x'_1)}{\partial x'^2_1} \quad \text{and}$$

$$I'_2(x'_2) = 1 + \frac{s'_{12}}{2k} \frac{\partial^2 \phi_1(x'_2)}{\partial x'^2_2}$$

The intensity distribution in L'_1 is unaffected by ϕ_1 and the intensity distribution in L'_2 is unaffected by ϕ_2 . Using the difference of the intensity distributions like a curvature sensor yields the second derivative of the sum of the phases. This is the result of a measurement with a curvature sensor neglecting the wavefront radial tilt.

Using Shack-Hartmann sensors in both planes L'_1 and L'_2 the resulting phase $\phi_1 + \phi_2$ of the wavefront is measured in each plane by determining the wavefront tilt in each subaperture. Additionally, the intensity distribution can be measured in both planes by integrating over each subaperture of the lenslet array. The normalised signal $I'_1 - I'_2 / I'_1 + I'_2$ is the quotient of the second derivative of the sum and of the difference of the phases. As the sum of the phases is measured directly, the difference of the second derivatives can be determined and, thus, the phase curvature in both layers.

The isoplanatic angle can now be enlarged by observing multiple stars with the Shack-Hartmann sensor. The phase as well as the intensity distribution can be measured for each star individually. Then, the information about the different layers can be stitched together to steer the deformable mirrors in the conjugate planes of L_1 and L_2 .

Practical considerations

Before placing the Shack-Hartmann curvature sensors in the conjugate planes of the turbulent layers their altitude has to be determined by *e.g.* using a method suggested by Vernin⁴.

So far, the discussion has been restricted to two layers. If the turbulence profile indicates multiple strong layers there has to be a Shack-Hartmann curvature sensor in each conjugate plane of those layers. The position of the deformable mirrors can be adjusted to correspond to the conjugate planes of the layers. The number of deformable mirrors in a real system is obviously fixed. However, the system could be designed with several deformable mirrors using only the required number.

The isoplanatic angle is limited by the separation of the stars used for the measurement of the turbulence. The practical limitation is given by the field of view of each subimage of the Shack-Hartmann sensor. With CCDs of 500×500 pixels it would be possible to correct a field of view of 30×30 arc seconds with 50 Zernike modes.

References

1. F. Roddier 1988, Appl. Opt. **27**, p. 1223.
2. F. Roddier 1981, Progress in Optics XIX, ed. E. Wolf, p. 281.
3. E. Menzel 1951, Optik **8**, p. 295.
4. J. Vernin and F. Roddier, J.Opt.Soc.Am. **63**, p. 270.

Focal anisoplanatism and conjugation of the correcting surface to turbulence

Martyn Wells
Institute for Astronomy
University of Edinburgh
Royal Observatory
Edinburgh, EH9 3HJ
Tel. (44) 131 668 8100 Fax. (44) 131 668 8356
email: M.Wells@roe.ac.uk

Vince Klückers and Miles Adcock
Blackett Laboratory
Imperial College
London, SW7 2BZ

When using a laser guide star (LGS) as the reference object in an adaptive optics system the accuracy of the correction is limited by the so-called 'cone-effect' or focal anisoplanatism (FA). There are two effects

- a) the footprint of the LGS wavefront at the turbulent layer is smaller than that for the wavefront from the science object and
- b) the LGS wavefront expands by a factor of $(1+h_{\text{turb}}/h_{\text{Na}})$ when it reaches the telescope pupil. For example - with the height of turbulence $h_{\text{turb}}=6.5$ km and the height of laser guide star $h_{\text{Na}}=90$ km at the edge of an 8m pupil there is a displacement of ≈ 30 cm between the actual and measured wavefront from a science object.

Several authors^{1,2,3,4,6} have analysed how these effects limit the Strehl of the corrected image but they usually assume that the correction is made at a pupil plane or that multiple LGS's are used. The former does not allow for the correction of FA while for the latter "the practical implementation of this scheme is far from trivial"². This paper describes an alternative approach which, in the case of a dominant turbulent layer, will remove most of the wavefront variance caused by FA but which requires a relatively small amount of additional complexity in the wavefront sensor (WFS). The scheme for conjugation of the deformable mirror to turbulence for a natural guide star system⁵ is used. However, because the LGS image and science focal planes are separated, extra optics are required in the WFS to accommodate the change in focus position and focal ratio of the laser light as the conjugate height is altered to match changing conditions and/or different zenith angles.

We give predictions for the gains in Strehl that can be obtained with this scheme, both on and off-axis, for real C_n^2 profiles.

References.

1. Gavel D.T. and Olivier S.S., SPIE 2201, 295, 1994
2. Greenwood D.P. and Parenti R.R., in Adaptive Optics for Astronomy ed. Alloin D.M. and Mariotti J.-M., NATO ASI Series 423, p185, 1993
3. Stahl S.M., SPIE 2201, 636, 1994
4. Tallon M., Foy R., Vernin J., in Laser Guide Star Adaptive Optics Workshop, p555, Phillips Laboratory, Albuquerque, 1992
5. Wells M., Conjugation of turbulent layers in AO systems, Proc. of OSA topical meeting on Adaptive Optics, Garching 1995.
6. Welsh B.M. and Chester C.S., JOSA, 8, 69, 1991

Second-Order Statistics of the Performance of the Starfire Optical Range Adaptive Optics System

Dustin C. Johnston, James M. Brown II, Julian C. Christou,
Brent L. Ellerbrock, Robert Q. Fugate

Starfire Optical Range
US Air Force Phillips Laboratory/LIG
3550 Aberdeen Ave. SE
Kirtland AFB NM 87117-5776
Tel. 505-846-4712 ext. 362
Fax 505-846-2213

Michael D. Olier
Adaptive Optics Associates
US Air Force Phillips Laboratory/LIG
3550 Aberdeen Ave. SE
Kirtland AFB NM 87117-5776
Tel. 505-846-4712 ext. 228
Fax 505-846-0439

James M. Spinhirne
Rockwell Power Systems
US Air Force Phillips Laboratory/LIG
3550 Aberdeen Ave. SE
Kirtland AFB NM 87117-5776
Tel. 505-846-4712 ext. 228
Fax 505-846-0439

Early in the development of adaptive optics technology, the goal was to obtain good instantaneous results, i.e., well-compensated short-exposure images. The next goal was expressed in terms of average results, for example, acquiring good long-exposure images. The next logical step in characterizing and improving adaptive optics (AO) system performance is to investigate the second-order statistics. For example, we are interested not only in the average point spread function (PSF), but also the variance of the PSF. Depending on the application, we may be interested in the second-order statistics of other widely used measures of AO system performance such as the optical transfer function (OTF), Strehl ratio, image width, and encircled energy. The variance of the PSF/OTF is of interest when post-processing AO-compensated images.¹ The variance of the OTF appears explicitly in the denominator of the image spectrum signal-to-noise ratio.² Some researchers have suggested that AO may be useful in the area of optical communications to deep space probes.³ In such an application, one is interested in the statistical variation of the coupling efficiency of the compensated beam to an optical receiver and the frequency, duration, and distribution of signal excursions below threshold levels.⁴

In 1995, we conducted an observing program to measure the second-order statistical performance of the Starfire Optical Range (SOR) AO system. Our measurements of compensated star images fell into three general categories: (1) images of a field large enough to encompass virtually the entire PSF, (2) images of the central portion of the PSF, and (3) measurements of the output of a photodiode having a field-of-view (FOV) equal to the diffraction-limited image width (λ/D radians where D equals 1.5 meters -- the diameter of our AO-equipped telescope).

We collected both types of image data using high-frame-rate solid state cameras. We used a 64x64 silicon charge-coupled device array, having selectable frame rates of up to 2 kilohertz (kHz), to collect

images at an average wavelength of approximately 0.9 microns (μm). We also collected images at about 1.3 μm using a 48x48 germanium focal plane array having two selectable frame rates: 2.5 and 4.0 kHz. The pixel FOV of each sensor was set to approximately $\lambda/2D$ to Nyquist sample the images. The full FOV of each array was then large enough to capture virtually all of the starlight in a compensated image. The full-frame images were useful for computing parameters that require the full PSF for their calculation such as OTFs, Strehl ratio, and encircled energy. However, finite computer memory limited these full-frame data sets to 5—10 seconds of contiguous images.

To collect image data over longer time periods, we made hardware and software modifications to both of our cameras to allow collection of 8x8-pixel subarrays. At the cost of less information in each image, we were able to save data sets up to 500 seconds long. These data were useful for evaluating the performance of the tracking and higher-order compensation loops over fairly long periods. We could evaluate track-loop performance by computing the variance in the spot centroid position, while the higher-order loop could be evaluated by computing the variance in the image width.

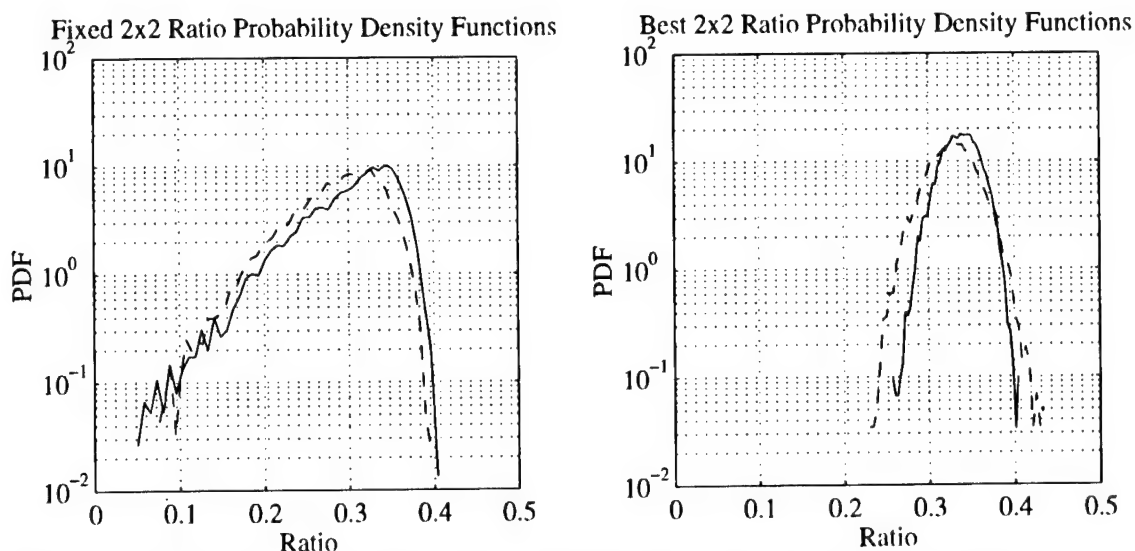
The third type of data was the photodiode signal. The voltage output of the photodiode was amplified, filtered to reduce aliasing, sampled at a 10-kHz rate, and digitized. These data were useful for computing threshold crossing statistics. Because each sample was only one digital number representing the amount of energy collected in a $\lambda/2D$ -radian bucket, available computer memory allowed collection of data sets up to 1000 seconds long.

The observing program took place in the Winter and Spring of 1995. We collected data during daytime, nighttime, and twilight periods. Observing sessions encompassed 16 days and nights. Data were collected at elevation angles ranging from as low as 15° to near zenith.

For comparison with the experimental data, one of us (Ellerbroek) has developed an AO system analysis and simulation program. This simulation accounts for the geometric description of the telescope aperture, including central obscuration; and the wavefront sensor (WFS) subapertures, including those which are partially illuminated. The atmospheric data is input in terms of wind speed and refractive index structure constant profiles, scaled to conform to the atmospheric coherence diameter (r_0) and Greenwood frequency measured during the experiment. The effects of shot noise, WFS read noise, scoring camera noise, chromatic aberration in the optics, and system latency are also included.

We have processed and analyzed most of the experimental data, allowing us to draw some conclusions. For example, the accompanying figure shows the results of some of our experimental encircled energy calculations (computed using the full star image data) compared to simulation results. We computed the curves labeled "Fixed 2x2 Ratio Probability Density Functions" using the fraction of the total energy contained in the *same* 2x2-pixel area in each of 14,000 star images in a single data set. The data were collected at a 2500-Hz frame rate, so the data set is composed of about 6 seconds of contiguous star images. On average, 29% of the light was contained in the 2x2-pixel area (the simulation average was 30%), which corresponds to a FOV of 1 microradian (μrad). The curves on the left in the figure show the probability density function (PDF) of these ratios, for both simulated and experimental data. We computed the curves on the right, labeled "Best 2x2 Probability Density Functions" using the fraction of total energy in the *brightest* 2x2-pixel area in each image. By using the brightest 2x2-pixel area, we removed most of the effects of residual image motion. Thus, the notable difference between the curves on the left and the curves on the right is due to tracking performance. This observation illustrates how high-frequency sampling of AO system performance helps identify areas to focus improvement efforts -- in this case the track loop.

A fortuitous byproduct of this experiment was the additional insight gained into systemic limitations to performance. For example, power spectral densities of both spot centroid position and the photodiode signal showed disturbances in the 80—90 Hz range. Through further investigation, we learned that the source of these disturbances was in the mechanical vibration of the secondary mirror support structure. We installed clamps to partially damp out this vibration.⁵ Similar studies led to the isolation of noise sources on the optical bench. Such noise sources included effects caused by chopper motors employed when using laser beacon AO, and jitter in one of the steering mirrors used in the track loop. We are investigating ways to reduce these noise sources.



Probability density functions of encircled energy. The dotted lines correspond to experimental measurements; the solid lines correspond to simulation results. The experimental data were collected using the star Betelgeuse at 12 minutes after sunset when the star was at 46° elevation. With the AO loop closed, we collected 14,000 star images at a 2500-Hz frame rate, with an average wavelength of about $1.3 \mu\text{m}$. For each star frame, we computed the ratio of the intensity in a 2×2 -pixel area ($\text{FOV} = 1 \mu\text{rad}$) to the total intensity in the image. We then computed the PDFs of these ratios. The simulation data were computed for the same atmospheric conditions as measured during the experimental data set, using 10,000 randomly generated wavefronts with Kolmogorov statistics. We computed the curves on the left using the same 2×2 -pixel area in each frame. The experimental mean ratio was 0.29, with a standard deviation of 0.052. The simulation mean ratio was 0.30 with a standard deviation of 0.054. To compute the curves on the right, we removed most of the effects of residual image motion by computing the ratios using the brightest 2×2 -pixel area in each frame. For this case, the experimental mean ratio was 0.33 with a standard deviation of 0.028. The simulation mean ratio was 0.34 with a standard deviation of 0.022. The differences between the "Fixed" and "Best" curves is due to tracking performance.

¹ J. C. Christou, B. Ellerbroek, R. Q. Fugate, D. Bonaccini, and R. Stanga, "Rayleigh beacon adaptive optics imaging of ADS 9731: measurements of the isoplanatic field of view," *Ap. J.* **450**, 369--379 (1995).

² M. C. Roggemann, D. W. Tyler, and M. F. Bilmont, "Linear reconstruction of compensated images: theory and experimental results," *Appl. Opt.* **31**, 7429--7441 (1992).

³ K. E. Wilson, "An overview of the Compensated Earth-Moon-Earth Laser Link (CEMERLL) experiment," in *Free-Space Laser Communication Technologies VI*, G. S. Mecherle, ed., *Proc. Soc. Photo. Opt. Instrum. Eng.* **2123**, 66--70 (1994).

⁴ H. T. Yura and W. G. McKinley, "Optical scintillation statistics for IR ground-to-space laser communication systems," *Appl. Opt.* **22**, 3353--3358 (1983).

⁵ J. M. Brown II and J. C. Goodding, "Mechanically-induced line-of-sight jitter in the Starfire Optical Range 1.5-meter telescope," this proceedings.

Temporal Characteristics and Modelling of Atmospherically-Distorted Wavefront Slopes

Donald McGaughey and George J. M. Aitken

Department of Electrical and Computer Engineering, Queen's University
Kingston, Ontario, Canada K7L3N6

Email: mcgaughd@ee.queensu.ca, aitkeng@post.queensu.ca
Tel. 613-545-2932, Fax 613-545-6615

Background.

The wavefronts distorted by a Kolmogorov turbulent atmosphere are fractal surfaces [1] and have the properties of fractional Brownian motion (FBM) with a self-similarity parameter of $5/6$. Such a FBM process is nonstationary and has a power-law spectrum with spectral index $-8/3$. In an adaptive optics system a Shack-Hartmann (SH) wavefront sensor (WFS) delivers the time series of wavefront (WF) slopes measured at each lenslet subaperture. While the FBM wavefront exhibits persistence, and consequently has predictability, the derivatives or slopes of this FBM process are antipersistent [2] with spectral index $-2/3$. This means that the WF slopes would have limited predictability at least by conventional mean-square prediction methods. Thus the adaptive optics (AO) control strategy that treats WF slopes as an unpredictable random walk process would seem justified. Within a closed loop system the difference between the incident wavefront and the correction by the deformable mirror is equivalent to a differentiation or increments process because of the loop delay, in which case the wavefront sensor gives essentially the second derivative. The second derivative process of FBM is also antipersistent.

Jorgenson and Aitken [3,4] have demonstrated that the slopes of stellar wavefronts are indeed predictable with both linear predictors and neural networks. This is contrary to the properties of FBM mentioned above. They have speculated that because the distortion process is due to turbulence, there might be some degree of deterministic chaos that would explain the predictability. In this paper we describe the application of rescaled-range (R/S) analysis [5] and correlation-dimension (CD) analysis [6] to ascertain the nature of the wavefront distortions. R/S analysis is a direct measure of persistence in a time series, while CD analysis can deduce the dimension of a chaotic attractor if one exists, and is effective at distinguishing stochastic and chaotic processes.

Results of RS and CD Analysis

Two-dimensional wavefront-slope data were obtained from the COME-ON A/O system operating open loop on the ESO 3.6 m telescope at La Silla, Chile [7]. The lenslet array of the SH WFS has 20 subapertures each of which is 72 cm when projected onto the telescope pupil. Wavefront sensing is done in the visible where D/r_0 is about 6 for the subapertures, while correction is made

for near infrared imaging. Data sets consist of from 1024 to 7168 samples of the x-y coordinates of the 20 image centroids. One group of data sets was taken at a sampling rate of 103 Hz on a night with moderate seeing, and the other was taken at 116 Hz in very good seeing. Also studied were six, 2000-sample time series of stellar centroids measured at visible wavelengths with one 1.84 m mirror of the Multiple Mirror Telescope (MMT), Mount Hopkins, AZ. Sampling was at the 30 Hz video rate in very good seeing.

The CD analysis estimates the dimension, or the number of degrees of freedom, of the attractor describing a dynamical process. When a low dimension is found in a seemingly random behaviour it often means that the process is due to deterministic chaos. A stochastic process will have an infinite dimension indicating an infinite number of degrees of freedom. However, filtered stochastic processes can also appear to have low correlation dimensions. To resolve whether or not a low-dimension process is stochastic, the data are randomized by uniformly randomizing the Fourier phases. The CD analysis is then applied to the randomized time series. If the original series is chaotic a higher dimension will be found after randomization. If there is no change the original process is stochastic. The CD analysis shows the ONERA WF-slope data to be stochastic, thus the predictability does not arise from deterministic chaos.

The R/S analysis applied to the ONERA data on the good seeing night showed a persistence time, T_p , of the order of 0.12 s, and for the poorer data less than 0.04 s. The power spectral densities (PSDs) show the characteristic knee frequency, f_k , where the slope of the PSD changes from $-2/3$ at low frequencies to $-11/3$ at high frequencies. This change of slope is due to the spatial filtering effect of the telescope aperture, in this case the subapertures defined by the SH lenslets of diameter D [8]. The velocity of a single-layer Kolmogorov atmosphere has been shown to be $v = \kappa D f_k$ where the constant κ is about 0.3 to 0.4 [8]. Thus the time for the disturbance to cross the aperture is D/v or $1/\kappa f_k$. This time is essentially the same as T_p found by the R/S analysis. In fact we observe that the product of T_p and f_k is typically 0.35. In the case of the MMT data the value of $T_p f_k$ is about 0.4. In both cases the speckle lifetime is almost an order of magnitude shorter than the T_p . Finally, the neural-network, time-series predictors [3,4] achieved best results on each of these quite different data sets with a 10-sample input vector. The input vectors spanned time windows comparable to the measured persistence time in each case. What this suggests is that the persistence, and hence the predictability, of the wavefront slopes is determined by the smoothing or filtering action of the lenslet aperture. In other words the time constant associated with f_k determines the maximum number of past samples that can be expected to contribute to the prediction of the next. This window is proportional to D and inversely proportional to v .

The predictability imposed by the aperture smoothing should be exploitable to improve AO performance. Lloyd-Hart [9] has reported results that support this idea as well. However, it must be noted that the increments process (derivative) of the aperture-filtered WF slopes remains antipersistent, suggesting that prediction within closed control loops must be done after reconstruction of the slopes.

Modelling of Wavefront-Slope Time Series.

The modelling of wavefront-slope data with the correct predictive properties and power spectrum requires filtering of the FBM process. First generate a FBM with $H=5/6$ by one of the standard methods such as mid-point displacement or Fourier-domain spectral weighting [10]. This will have a spectral index of $-8/3$. The WF must then be filtered with a flat transfer function up to the desired f_k then with a spectral index of -3 . The increments of the filtered process will have the correct persistence characteristics for WF slopes. Since the wavefront slopes are simply a filtered linear process, the order of taking increments and filtering can be interchanged. The filter should represent the effects of spatial filtering by the circular aperture, either by a simple impulse response that drops rapidly toward each end or the exact function given in [8]. Yule-Walker routines in Matlab have been used to create IID filters that give good models of the observed WF-slope data.

References

1. Schwartz, C., Baum, G., and Ribak, E. N., "Turbulence degraded wavefronts as fractal surfaces," J. Opt. Soc. Am. A, 11, 444 (1994)
2. Mandelbrot, B. B., and Van. Ness, J. W., "Fractional Brownian motions, fractional noises and applications," SIAM Review, 10, 422 (1968)
3. Jorgenson, M. B., and Aitken, G. J. M., "Prediction of atmospherically-induced wavefront degradations," Optics Letters, 17, 466 (1992)
4. Jorgenson, M. B., and Aitken, G. J. M., "Wavefront prediction for adaptive optics," in Active and Adaptive Optics, F. Merkle, ed. (Garching bei Munchen, Germany, European Southern Observatory) 143 (1994).
5. Mandelbrot, B. B., and Taqqu, M.S. , "Robust R/S analysis of long-run serial correlation," Proc. 42nd Session ISI, Book 2, 69 (1979)
6. Thieler, J., J., "Estimating fractal dimensions," J. Opt. Soc. Am. A, 7, 1055 (1990)
7. Rousset, G., Fontanella, J. C., Kern, P., Lena, P., Gigan, P., Rigaut, F., Gaffard, J. P., Boyer, C., Jagoureland, P., and Merkle, F., "Adaptive optics prototype system for infrared astronomy," Proc. SPIE, 1237, 336 (1990)
8. Conan, J-M., Rousset, G., and Madec, P-Y., J., "Wave-front temporal spectra in high resolution imaging through turbulence," J. Opt. Soc. Am. A, 12, 155 (1995)
9. Lloyd-Hart, M., and McGuire, P., "Spatio-temporal prediction for adaptive optics wavefront reconstructors," Proc. of Adaptive Optics, Garching, Germany, October 2-7, 1995, Cullum, M., ed. (Washington, OSA) to appear.
10. Peitgen, H.-O. and Saupe, D., eds., *The Science of Fractal Images* (Berlin, Springer Verlag, 1988)

Wednesday, July 10, 1996

Poster Previews: 2

AWD 3:15 pm-3:45 pm
Pikake Room

Byron M. Welsh, *Presider*
Air Force Institute of Technology

Adaptive Optics at MPE: Astronomical Results and Future Plans

A. QUIRRENBACH (Max-Planck-Institut für Extraterrestrische Physik, MPE)

We have used the Adaptive Optics system ADONIS at the ESO 3.6 m telescope on La Silla, Chile, to obtain high-resolution images of the R136 complex in the young massive cluster 30 Doradus in the Large Magellanic Cloud. Within our $12''.8 \times 12''.8$ field-of-view, we find more than 500 stars in our H and K near-infrared images. Combining these data with Hubble Space Telescope observations in the visual wavelength range, and comparing the brightness and colors with stellar models, we can determine the mass of each individual star. We have thus been able to construct the stellar mass function in the central crowded area down to ~ 5 solar masses. The inclusion of the infrared data obtained with Adaptive Optics in this analysis reduces the uncertainty due to varying amounts of extinction towards the individual stars. In addition, we find about 60 red sources that went undetected by the Hubble observations; these are probably young low or intermediate-mass pre-main-sequence stars, which are still embedded in dense circumstellar gas. We can constrain the age of the starburst in the center of 30 Doradus to about 3 to 5 Myrs. The mass function appears to vary between the innermost 0.4 pc and the outer region, indicating mass segregation on a time scale of only 10^5 to 10^6 years.

A similar set of data has been obtained for NGC 3603, the most massive optically visible star forming region in the Galaxy. Because of the relative proximity of NGC 3603 (~ 7 kpc compared to ~ 50 kpc for 30 Doradus), our star counts go down to much lower masses here; it is possible to determine the stellar mass function over the entire range from the most massive OB and Wolf-Rayet stars down to subsolar masses.

With a recent upgrade of the SHARP II camera – this is the focal plane instrument built by the Max-Planck-Institut für Extraterrestrische Physik (MPE) and used with ADONIS – it has become possible to carry out Adaptive Optics observations with spectral resolution $R \approx 2500$ using a scanning Fabry-Perot. We present the first results from this instrument, an observation of the prototypical pre-main-sequence star T Tauri in the light of the $2.12\mu\text{m}$ line of molecular hydrogen. A complex structure is seen in this image; several streaks of H_2 emission can probably be associated with jets emanating from the binary star.

ALFA (Adaptive Optics with Laser Guide Star for Astronomy) is a joint project of the Max-Planck-Institutes for Astronomy (Heidelberg) and Extraterrestrial Physics (Garching). The aim of ALFA is the development and installation of an Adaptive Optics system with a Laser Guide Star for the 3.5 m telescope on Calar Alto, Spain. With this system, it will be possible to obtain nearly diffraction-limited images in the H and K bands under median seeing conditions, and in the J band under favorable conditions. ALFA will use a 97-actuator deformable mirror with a continuous face sheet to correct the wavefront for the effects of atmospheric turbulence. The

wavefront will be measured with a Shack-Hartmann device; the wavefront sensor will be equipped with a fast CCD, which can be read at frame rates between 100 and 1200 Hz. Three different lenslet arrays mounted on a filter wheel provide additional flexibility; the number of Shack-Hartmann subapertures can be 32, 60, or 120. ALFA will be mounted at the Cassegrain focus of the 3.5 m telescope, between the telescope itself and the science instrument. The number of optical elements in the light path is as small as possible (namely 5), to avoid light loss and to keep the additional thermal background low. The input $f/10$ beam from the telescope is reflected by an active mirror, which also corrects the tip/tilt (image motion), onto an off-axis parabola, which produces an image of the pupil on the deformable mirror. Another off-axis parabola produces the $f/25$ output beam, which is split into visible (used for wavefront sensing) and IR (used by the scientific instrument) by a dichroic beam splitter.

For satisfactory operation, the wavefront sensor needs a fairly bright star ($m_V \lesssim 12$) within the isoplanatic field ($\sim 30''$ for the K band). Since such stars are frequently not available, an artificial guide star can be produced with a laser, which is integral part of ALFA. The laser will be tuned to the 589 nm line of sodium and focused into the mesospheric sodium layer at an altitude of ~ 90 km. It will thus create a small spot ($\sim 1''$ diameter, limited by "seeing" in the upwards propagation of the laser beam), which can be used for wavefront sensing. Since a laser guide star cannot be used to measure image motion, the tip/tilt component of the seeing must still be determined from a natural star; however, much fainter objects ($m_V \lesssim 17$) are suitable for this purpose. ALFA will use a continuous wave dye laser pumped by an argon ion laser to produce a 3 W beam at 589 nm; the laser system will be located in the coudé laboratory, and the beam will be transmitted through a modified coudé path. It will be expanded to 50 cm by a telescope attached to the main body of the 3.5 m telescope. The components of ALFA are currently being designed and constructed at MPIA, MPE and industry contractors (Adaptive Optics Associates and Xinetics); the necessary upgrades of the infrastructure on Calar Alto have been initiated. It is expected that first operations can start in mid-1996, with focal instruments such as the OMEGA IR camera currently under development at MPIA, and a modified version of the MPE imaging spectrometer 3D.

Coronagraphic Spectrometer

Masanori IYE, Kouji MURAKAWA, Youichi ITO,
Noboru EBIZUKA and Motohide TAMURA
National Astronomical Observatory, Mitaka, Tokyo 181 JAPAN

1. INTRODUCTION

Observations of faint diffuse and/or unresolved objects in the vicinity of bright objects are of importance in the studies of protoplanetary disks, circumstellar envelope of red supergiants, quasar host galaxies, emission line regions of AGNs, and gravitational lensed objects.

Recently reported in this concern are HST imaging studies of protostellar disk around a young stellar object, ground based observations of brown dwarf companion of a young star, planet of a nearby star, and reflection nebula around a pre-main-sequence star.

As for the quasar host galaxies, imaging studies have been carried out with ground based telescopes (e.g., Huchings and Neff 1992) and the HST WFPC2 (Hutchings and Morris 1995). However, recent HST imaging study of nearby luminous quasars raised a classical issue of calibration of the image and revealed the importance of removing the scattered light component of the central point source to study extended faint objects around a much brighter central object (Bahcall et al. 1995). Reliable observation to elucidate the properties, or even the existence, of host galaxies of quasars is a key issue to understand the evolution of quasars.

One obvious way to achieve such observations is to increase the spatial resolution by future large telescopes in orbit free from atmospheric seeing degradation, by ground based large telescopes with an adaptive optics system to obtain the diffraction limited image, or by optical or infrared interferometers. The calibration of the point spread function remains as a delicate problem especially for those observations from the ground.

Another way to probe the properties of diffuse light component around the bright central object is to perform a spectroscopic study. The scattered light component of a central bright quasar, which may contribute at least to some extent to the faint extended halos observed, would show the spectrum identical to the quasar itself. Whereas a faint extended halo consisting of stars and/or ionized gaseous component would show a distinctly different spectrum and may be easily discerned from the scattered light of the quasar, if the intrinsically extended component is bright enough as compared with the scattered component.

By analyzing the spectral features, one shall be able to obtain information on the stellar population and the internal dynamical properties of these host galaxies. As for the protostellar disks, spectra of protostellar disks will give information on the physical and kinematical properties of such gaseous disks that will serve as strong observational constraints to construct star formation scenarios.

What we propose here and are actually designing is an original instrument, coronagraphic spectrometer, that will have this capability to obtain low resolution spectra of spatially contracted images of extended object around a central bright source.

2. DESIGN CONCEPT OF A CORONAGRAPHIC SPECTROMETER FOR SUBARU

The coronagraphic spectrometer will take full advantages of the adaptive optics system (Takami et al. 1995) to realize the diffraction limited imaging of the region surrounding the central point source. The occulting mask removes most of the light from the central bright point source and leaves only the light from the faint extended halo and some residual scattered light component from the central bright source, if any. The light component diffracted by structural components in the light beam, e.g. the spider of the secondary mirror support etc., will be suppressed by an apodizing mask

placed at the pupil plane that is provided by the collimating optics behind the telescope focal plane. One can reduce the contribution from diffracted component by increasing the area to block in the apodizing mask at the expense of reducing the light collecting power. The actual fraction of the residual scattered light component will be dependent on the performance of the adaptive optics system and hence also on the brightness of the guide star, which is in most cases the central bright object.

In the most favourable case, only the light component from the faint extended halo around the bright point source is expected to path further along the optical path. By placing a dispersive element, e.g., a grism, and incorporating a focal reducing camera optics, one can have a low resolution spectrum of spatially contracted image of such a diffuse extended object. This is the backbone of the basic design concept.

The coronagraphic spectrometer is designed as one of the four modes of operation to be incorporated in the Coronagraphic Imager with Adaptive Optics (CIAO) (Tamura et al. 1995), that is planned as one of the F/12 Cassegrain instruments for the 8m Subaru telescope (Iye 1995). The four modes to be incorporated in the CIAO are the high resolution imaging mode (HRM), low resolution imaging mode (LRM), pupil imaging mode (PIM), and the spectrometric mode (SPM).

In order to suppress the scattered light and ghosts produced by optical elements, the optical trains are to be made with minimum number of lenses. An infrared detector array will be used commonly in all of these modes, and a mechanism ensuring easy and reliable switching among these four modes is required. The collimating optics common for all the modes consists of two achromatic lens pairs. The high and low resolution imaging modes are designed to have focal enlarging cameras to give fine pixel sampling at 0.012 and 0.024 arcsec, respectively for HRM and LRM. On the other hand, the camera for the spectrometric mode is designed to give a focal reduction to F/4 so as to provide spatial contraction of light. The resulting pixel sampling scale is 0.19 arcsec. In order to share the collimator and the detector with other modes, a relay lens system consisting of two achromatic pairs of lenses is used for the spectrometric mode of CIAO. One can remove this relay lenses for the spectroscopic mode with the focal extending optics. The camera lenses of the coronagraphic spectrometer for 1 to 2.5 μm comprise of 4 separate lenses. The entire optical layout of the coronagraphic spectrometer is shown in Figure 1.

A grism placed at the second pupil plane provided by the relay lenses will be used as a dispersive element. The spectral resolving power of 300 and 600 will be attained with a slit width of 1 arcsec and 0.5 arcsec, respectively. For example a CaF_2 grism with 87 grooves/mm and an apex angle of 50 degrees can be used. As an alternative, development of a LiNbO_3 grism with 123 grooves/mm and an apex angle of 24 degrees is under way.

The diameter of the occulting mask for the spectrometric mode should be equal or larger than the Airy disk. Compromizing the coexistence of a focal reducing optics for spectrometry and a focal extending optics for imaging makes the optical designing somewhat demanding. However, for the spectrometric mode, the requirement to reduce the number of reflecting surface is not as severe as in the case for imaging modes, although proper care should be taken to suppress the scattering light and ghost images. Table 1 shows the summary of specification for the spectrometric mode of CIAO.

Evaluation of expected performances of the spectrometric mode is under way.

Table 1. Specification of the Coronagraphic Spectrograph Mode for CIAO.

Spatial Scale	0".19/pixel
Spectral Resolution	R=300 @1".0 slit
Wavelength Coverage	1.0-2.5 μm
Spot diameter	$\leq 30\mu\text{m}$
Pupil diameter	20mm (10mm at Apodizer)
Field of View	≥ 600 pixels, one dimensional

References

- Bahcall, J.N., Kirhakos, S., and Schneider, D.P., 1994, 435, L11.
- Hutchings, J.B. and Neff, S.G. 1992, AJ, 104, 1.
- Hutchings, J.B. and Morris, S.C., 1995, preprint
- Iye, M., 1995, *Scientific and Engineering Frontiers for 8-10m Telescopes* ed.M.Iye and T.Nishimura, Universal Academy Press, Tokyo, pp.67-76.
- Takami, H., Iye, M., Takato, N., Hayano, Y., and Otsubo, M., 1995, *Scientific and Engineering Frontiers for 8-10m Telescopes* ed.M.Iye and T.Nishimura, Universal Academy Press, Tokyo, pp.327-332.
- Tamura, M., Takami, H., Kaifu, N., Hayashi, S., Takato, N., Nishimura, T., Murakawa, K., and Itoh, Y., 1995, *Scientific and Engineering Frontiers for 8-10m Telescopes* ed.M.Iye and T.Nishimura, Universal Academy Press, Tokyo, pp.339-345.

ADAPTIVE OPTICS LONG EXPOSURE POINT SPREAD FUNCTION RETRIEVAL FROM WAVEFRONT SENSOR MEASUREMENTS: TESTS ON REAL DATA

J.-P. Véran^{1,3}, F. Rigaut², D. Rouan¹, H. Maître³

¹ DESPA, Observatoire de Paris, 92195 Meudon Cedex, France

² Canada-France-Hawaii Telescope, P.O. Box 1597, Kamuela, HI, 96743, U.S.A.

³ Département Image, Télécom Paris, 46 Rue Barrault, 75634 Paris Cedex 13, France

Current astronomical adaptive optics (AO) systems are not able to fully correct the atmospheric turbulence. As a result, the quality of the AO long exposure images is degraded by a residual blur which significantly reduces the contrast of the fine details [1]. Removing this residual blur is the field of image restoration (deconvolution) and since this problem is general to many imaging applications, many different methods have already been developed. To achieve an accurate restoration however, an accurate estimation of the system Point Spread Function (PSF) is usually required. For adaptive optics imaging, the shape of the PSF depends on how well the deformable mirror is able to compensate for the wavefront distortions. This "degree of correction" in turn depends on the size and magnitude of the object used as a reference for wavefront sensing, but also on the characteristics of the turbulence, which is known to be a non-stationary process. As a results, the AO PSF is highly variable [2]. The usual way around this problem involves dedicating of significant portion of the observing time to the sole acquisition of a point source, from which the current PSF is estimated.

In a previous paper [3], we presented an alternative approach. Our method makes use of the AO wavefront sensor measurements and the commands applied to the deformable mirror during the acquisition of the science object. An off-line statistical processing of these data allows to retrieve the PSF related to this particular acquisition. The advantage of this approach is two-fold: first, no observing time has to be spent for the PSF; second, the PSF is estimated from data exactly synchronous with the object acquisition, which should insure the best accuracy.

In [3], an outline of the method was given, along with test results obtained from simulated data sets, generated by a full AO simulation package developed by one of us (FR). The simulation was for a Shack-Hartman type system.

We have now adapted the method to a curvature AO system, and more specifically to PUEO, the Canada-France-Hawaii Telescope (CFHT) AO system, scheduled to come on-line at the telescope this spring (96). Critical stages such as sensing noise variance and spatial aliasing estimations were re-designed to accomodate the particularities of curvature systems.

Late 1995, PUEO was integrated and tested at Observatoire de Paris. Closed loop

imaging tests were carried out using an artificial source and a seeing generator to mimic the atmospheric distortions. I band images of the artificial source were acquired using a CCD camera. Simultaneously, AO loop data (WFS measurements and mirror commands) were collected and stored in a file after each acquisition. Our PSF retrieval method was then run on these data and the result compared to the actual image of the point source obtained from the CCD camera. Figures 1 and 2 show that the quality of the reconstruction match the performance obtained on simulated data. The error on the Modulation Transfer Function is less than 10% at low frequencies. Larger errors do occur, but only at the highest frequencies, which is satisfactory.

PUEO is scheduled for several engineering and scientific nights at CFHT this spring (96) during which we will be able to acquire real observing data in order to validate our PSF retrieval method.

References

- [1] F. Rigaut, E. Gendron, P. Léna, P.Y. Madec, P. Couvée, and G. Rousset. Partial correction with the adaptive optics system come-on. In *High resolution imaging by interferometry II*, Garching, 1991.
- [2] E. Tessier. Natural guide star adaptive optics data. In *O.S.A. Topical meeting on Adaptive Optics*, Garching, October 1995.
- [3] J.-P. Véran, F. Rigaut, and H. Maître. Adaptive optics long exposure point spread function retrieval from wavefront sensor measurements. In *O.S.A. Topical meeting on Adaptive Optics*, Garching, October 1995.

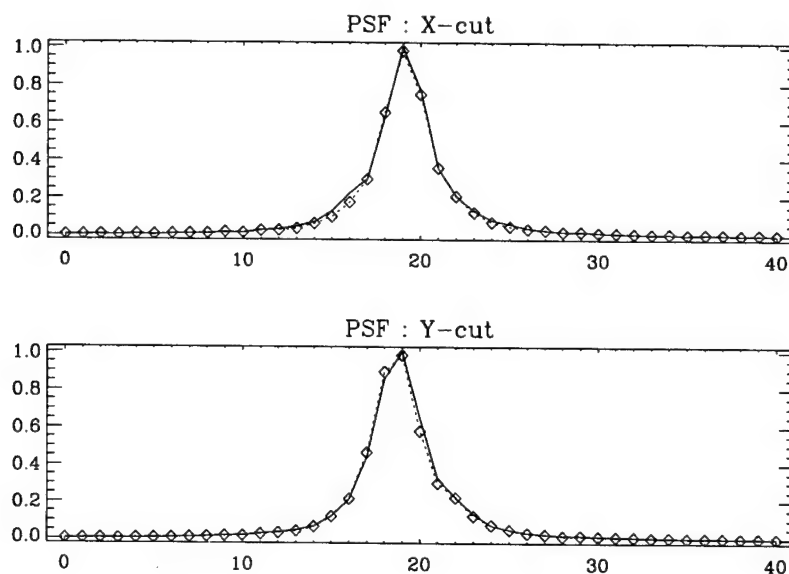


Figure 1: Example of estimation of a long exposure PSF (I Band): Solid line: CCD image of the "real" PSF (Strehl Ratio 26%). Dot line and diamond: Estimated PSF from the AO loop data, synchronous to the acquisition. X-axis units are in pixels.

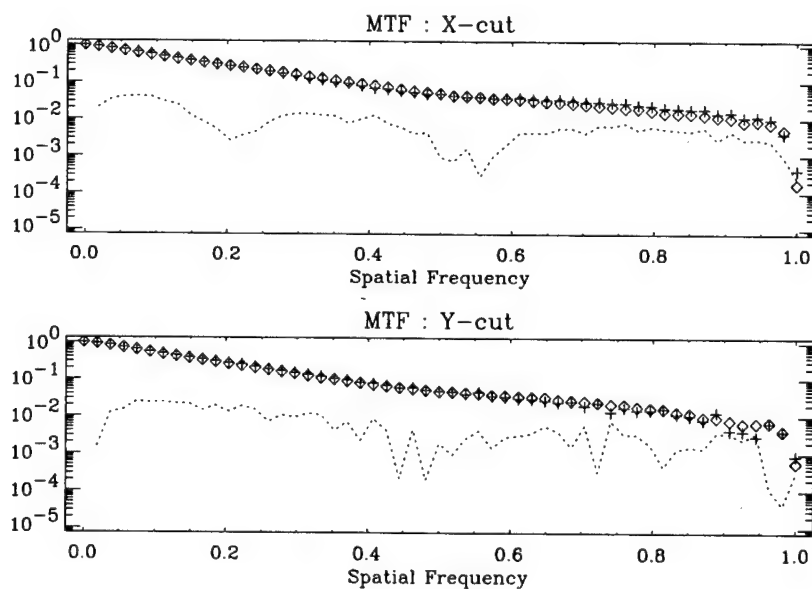


Figure 2: Corresponding Modulation Transfert Function: +: "real" MTF. Diamond: estimated MTF. Dash: Absolute difference (error). Spatial frequencies are normalized to the diffraction limit of the telescope.

Phase Diversity Wavefront Sensing and Image Reconstruction on the MDI instrument at L1

T. D. Tarbell¹, D.S. Acton², and Z. A. Frank¹

¹Stanford-Lockheed Institute for Space Research, Lockheed Martin Advanced Technology Center
3251 Hanover, B/252, O/91-30, Palo Alto, CA 94304
Tel: 415 424-4033; Fax: 415 424-3994; email ttarbell@solar.stanford.edu

²W. M. Keck Observatory, 65-1120 Mamalahoa Highway, Kamuela, HI 96743
Tel. 808 885-7887; Fax. 808 885-4464; email sacton@keck.hawaii.edu

Introduction

The Michelson Doppler Imager (MDI) is a spectral imaging experiment on the ESA-NASA Solar and Heliospheric Observatory spacecraft (SOHO--see Domingo et al., 1995). SOHO was launched in December, 1995, and reached its final orbit about the Earth-Sun Lagrangian point L1 in mid-February, 1996. This point, about 1.5×10^6 km towards the Sun, is where the Earth's and Sun's gravity balance, allowing a nearly stable orbit ideal for continuous observations of the Sun and solar wind. MDI is collecting the observational data for the Solar Oscillations Investigation (SOI), a study of the interior structure of the Sun as inferred from the normal modes of oscillation seen on its surface ("heliosismology"). Since launch, MDI has been collecting images showing the Doppler velocity, continuum intensity, and magnetic field on the solar surface with high spatial and temporal resolution. SOI/MDI were developed jointly by Stanford University and Lockheed Martin Advanced Technology Center, supported by NASA (see Scherrer et al., 1995). The Principal Investigator is Prof. P. Scherrer of Stanford.

MDI contains a refracting telescope and focal plane package for obtaining nearly diffraction-limited, monochromatic images. Since there is no atmospheric turbulence (and pointing jitter is removed by a fast tilt mirror), images of solar granulation at varying focus suitable for phase diversity analysis can be taken sequentially. The goals are to map the wavefront of MDI, confirm the best focus position, and to deconvolve the point spread function from the images. In this paper, we describe the successful application of phase diversity to accomplish these goals, using data taken during both normal observations and thermal transients of the instrument.

The Michelson Doppler Imager

The figure at the end of this summary shows a schematic of the MDI optical system. The 12.7 cm refracting telescope delivers images to the 1024x1024 CCD camera either in "full disk" mode (2 arcsecond pixels) or "high resolution" mode (0.61 arcsecond pixels). The operating wavelength is a 0.010 nm band in the vicinity of the Ni I line at 676.8 nm, isolated by the series of filters from the 5 nm front window to the dual tunable Michelson interferometers (0.02 and 0.01 nm). Image focus is changed by moving glass blocks into the beam, using the two calibration/focus wheels. With one blank and two different blocks in each wheel, nine evenly-spaced focus positions over a 3-wave range are available. Phase diversity data are high the resolution mode images with different focus positions. The filters are tuned to a continuum wavelength to show solar granulation, which changes slowly compared with the 3-second image cadence.

The initial focus tests after launch showed that best focus had shifted from the ground-based setting at the center of the available range to nearly the edge. Since temperature gradients in the front window were suspected, phase diversity data were collected each time the door was reopened (after closing for orbital maneuvers). Image sharpness and phase diversity clearly show the focus shift, along with initial growth and then decay of additional aberrations during the thermal transient. When thermal equilibrium is reached, the images are at best focus and of very good quality, though not perfect.

Phase Diversity

The term "Phase Diversity" refers to methods of measuring the optical wavefront errors by sampling the 3-D volume surrounding the focal plane. In principle, this could be implemented in many ways. In practice, however, this is accomplished by recording an image at the best focus and an additional image about 1 wave out of focus. Within reasonable limits, the two images will contain enough information to determine the optical wavefront errors present in the imaging system, and to reconstruct the original unaberrated object.

There are several algorithms available for determining the wavefront errors. The method of Lofdahl and Scharmer (1994) was chosen for the task at hand, mainly because of its ease of implementation in IDL (Interactive Data Language) and its proven effectiveness on images of solar granulation. A detailed discussion of the Lofdahl-Scharmer algorithm is beyond the scope of this summary. However, the essence of the algorithm is very straightforward. The optical wavefront errors are parameterized by a finite number of Zernike polynomials. An initial guess of the Zernike coefficients is made (usually assumed zero), and the Optical Transfer Functions (OTF's) associated with the focused and defocused imaging systems are calculated from these coefficients. Next, an object-independent metric is formed, combining the OTF's with the focused and defocused images. The Zernike coefficients are varied until the metric is minimized indicating that the optical wavefront errors are correctly represented. The Lofdahl-Scharmer algorithm makes use of a clever linearization technique that provides rapid convergence. The algorithm also estimates the unaberrated object from both the focused and defocused images combined.

Data and Results

The best focus was formed when all focusing blocks were removed from the beam. An 80 X 80 arcsecond subarray of this image was extracted to represent the focused image. The corresponding section of an image 1 wave out of focus was extracted to represent the defocused image. The extracted subimages are shown at the end of this summary. For clarity of display, only the central 40 X 40 arcsecond section of each image is shown.

The Lofdahl-Scharmer algorithm was applied to the images. A total of 10 Zernike coefficients were estimated: focus, 2 astigmatism terms, spherical aberration, 2 coma terms, and 4 additional terms. The resultant phase map was converted to an interferogram and is shown at the end of this summary. The focus term was very nearly zero, indicating that the instrument is nearly perfectly focused when no focus blocks are in the beam. There was about 0.5 waves PTV of aberration in the wavefront. The dominate term is coma. The unaberrated object was estimated and is shown below.

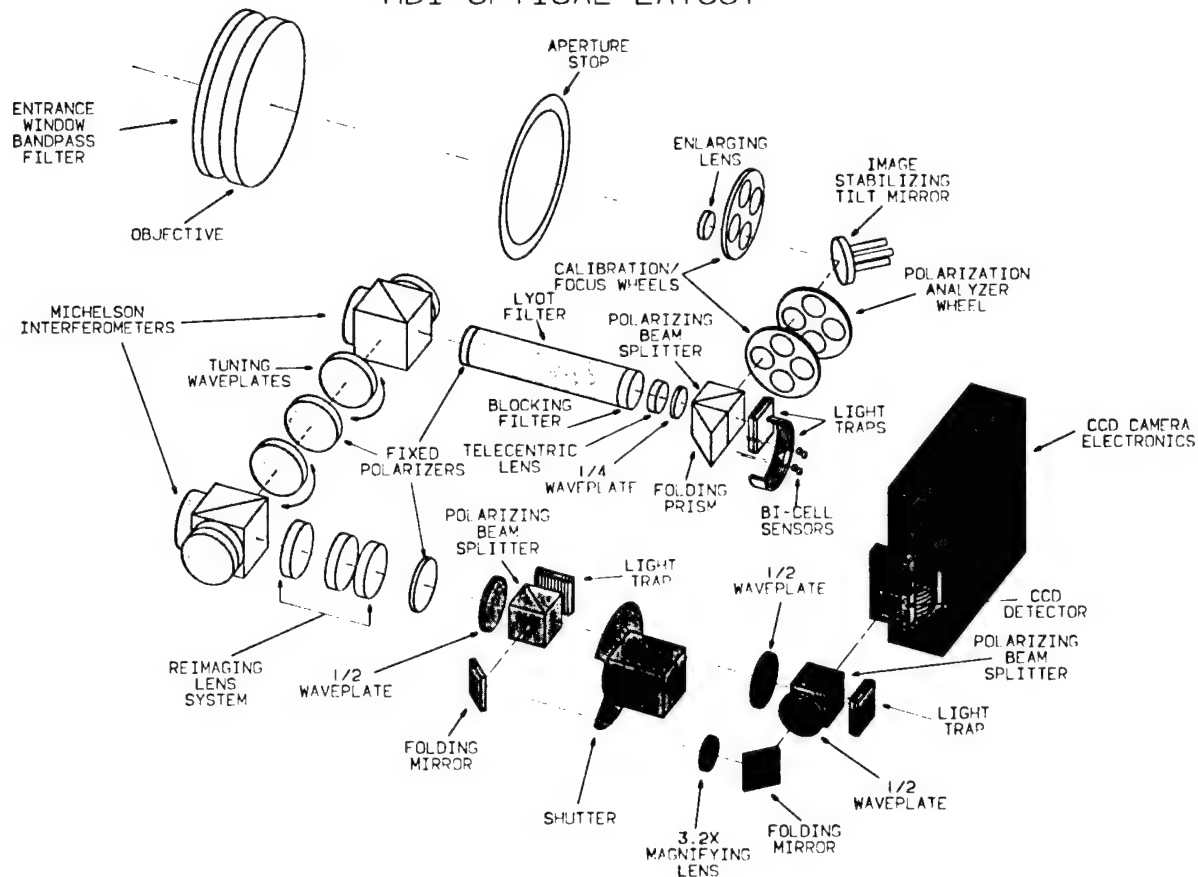
Conclusions and Comments

Phase diversity analysis has proven to be a valuable tool for two reasons. It provides insight into subtle instrumental effects first encountered in the space environment, without requiring special hardware or access to the instrument. Second, it permits reconstruction of images to diffraction-limited quality, which enhances their scientific value for studying the solar atmosphere and interior.

References:

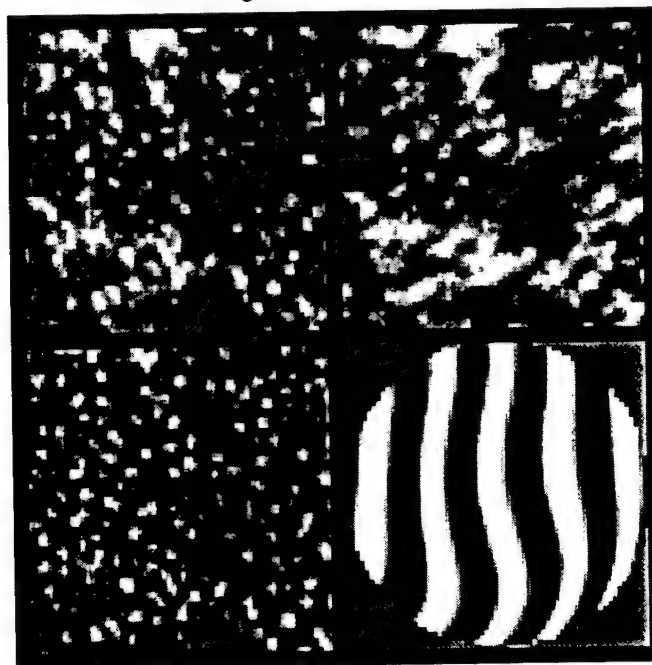
- P.H. Scherrer et al., "The Solar Oscillations Investigation--Michelson Doppler Imager," *Solar Physics*, vol. 162: 129-188, 1995.
- V. Domingo, B. Fleck and A.I. Poland, "The SOHO Mission: An Overview," *Solar Physics*, vol. 162: 1-37, 1995.
- M.G. Lofdahl & G.B. Scharmer, "Wavefront Sensing and image restoration from focused and defocused solar images," *Astron Astrophys. Suppl. Ser.* vol. 107: 243-264, 1994.

MDI OPTICAL LAYOUT



Focused image

Defocused image



Reconstructed Object

Wavefront

Intensity peak tracking in extended-object astronomical imaging

David W. Tyler
 W.J. Schafer Associates
 2000 Randolph Rd. SE, St. 205
 Albuquerque, New Mexico 87106 USA
phone: 505.846.1880, email: tyler@plk.af.mil

1. Introduction

Adaptive optics are becoming more common at astronomical facilities. At sites such as Mauna Kea, near-IR seeing can be good enough that aberration power is largely confined to tip-tilt, even with larger telescopes. Accordingly, many low-order systems are being planned and studied, with simple tilt compensation schemes being used at several observatories [1,2,3] for near-IR imaging. Image motion can also be removed in post-detection processing if an ensemble of short-exposure images is collected. For either real-time or post-detection processing, proper choice of a tilt removal scheme can improve resolution in long-exposure images.

With active tracking schemes, tilt is removed using inputs from a wavefront sensor or quad cell tracker to apply signals to a turning mirror in a closed feedback loop. The same effect can be accomplished in post-detection processing by collecting an ensemble of images with exposure times that are short relative to the atmospheric tilt time constant. These short exposure images can be added together after registering to form an average image with resolution equivalent to that obtained with active tilt tracking. Typically, the data is registered by calculating the intensity centroid of each image and shifting that point to a common reference, such as the center of the data array. The shift is easily applied to the image by adding an appropriately scaled linear phase to the image spectrum.

Computer simulations have been used with point-source objects to demonstrate improvements in Strehl ratio and spectral content by shifting the image intensity peak to the detector array origin rather than the centroid [4]. The following experimental results and analysis show these point-source results do not generalize to increased resolution when imaging extended objects except where the ratio of the pupil diameter D to the Fried parameter r_0 is small and a bright, compact source exists in the field. For large D/r_0 , however, tilt compensation alone does not significantly improve resolution, so the difference between peak and centroid tracking becomes academic. Further, for small D/r_0 , the peak tracking scheme has potential to increase long-exposure image resolution over that obtained with centroid tracking. Peak tracking could be implemented in an active tilt compensation system or in post-processing.

2. Observations and analysis

Both algorithms have been used to process ensembles of short-exposure data from the Air Force Maui Optical Station (AMOS) 1.6-m telescope on Mt Haleakala. Measured seeing gives $D/r_0 \approx 10$. Although a tracking/tilt-correction loop was running to keep the object centered, there was noticeable frame-to-frame residual motion due to the high telescope slew rate and very small field (6"). The signal-to-noise ratio (SNR) of the modulus spectrum of the average images was calculated, with the SNR defined as the sample mean divided by the square root of the variance. Where the SNR is significant, the value for the peak-registered image is clearly lower than the value of the centroid-registered image, providing a quantitative measure of the difference in blurring seen in the average images themselves.

The discrepancy between these results and the point-source results in [4] are accounted for as follows: Consider an image-plane intensity realization $i(x)$ consisting of a background $b(x)$ and a point significantly brighter than the background, representing a compact source. Diffraction and turbulence speckle from the compact source is included in b . Noise is assumed to be additive, uniform, and negligible in intensity with respect to the compact source. The intensity distribution is then written

$$i(x) = b(x - x_b) + A_p \delta(x - x_p), \quad (1)$$

where A_p is the amplitude of the compact source, δ denotes a spatial delta-function, x_p is the location of the bright point, and x_b is the intensity centroid of the background. The single spatial dimension x is used for notational clarity. The effect of atmospheric aberrations is modelled by random motion of the two components; it is assumed that aberrations do not significantly change the intensity centroid of either component. Since an arbitrary background could be decomposed into small subfields over which this assumption is true, the following analysis is easily extended. The coordinate x_c of the instantaneous image centroid is

$$x_c = [A_b(x_b + r_b) + A_p(x_p + r_p)] / (A_b + A_p), \quad (2)$$

where A_b is the integrated intensity of the background, and r_b and r_p are chosen to be zero-mean, Gaussian random variables with variances σ_b^2 and σ_p^2 , respectively, and correlation coefficient ρ_{bp} depending on the relative atmospheric tilt power. The Fourier spectrum $I_c(\omega)$ of the centroid-registered instantaneous image is then

$$\begin{aligned} I_c(\omega) &= B(\omega) e^{i\omega(x_b + r_b - x_c)} + A_p e^{i\omega(x_p + r_p - x_c)} \\ &= B(\omega) e^{i\omega[x_b(1-N_b) + r_b(1-N_b) - N_p(x_p + r_p)]} + A_p e^{i\omega[x_p(1-N_p) + r_p(1-N_p) - N_b(x_b + r_b)]} \end{aligned} \quad (3)$$

where N_p and N_b are the normalized intensities $A_p/(A_p + A_b)$ and $A_b/(A_p + A_b)$, respectively, and ω is the spatial frequency variable. The spectrum of the peak-registered image is

$$I_p(\omega) = B(\omega) e^{i\omega[(x_p - x_b) + (r_p - r_b)]} + A_p \quad (4)$$

Now we compute the expected values $\langle I_c \rangle$ and $\langle I_p \rangle$, the Fourier transforms of the averaged images formed by centroid and peak tracking, respectively. The expectation $\langle e^{ar} \rangle$, where a is a complex constant and r is a zero-mean Gaussian random variable with variance σ^2 , is $e^{a^2 \sigma^2 / 2}$, so these expectations yield

$$\begin{aligned} \langle I_c(\omega) \rangle &= B(\omega) e^{i\omega[x_b(1-N_b) - N_p x_p]} e^{-\sigma_b^2 \omega^2 (1-N_b)^2 / 2} e^{-(\omega \sigma_b N_p)^2 / 2} \\ &\quad + A_p e^{i\omega[x_p(1-N_p) - N_b x_b]} e^{-\sigma_p^2 \omega^2 (1-N_p)^2 / 2} e^{-(\omega \sigma_p N_b)^2 / 2} \end{aligned} \quad (5)$$

and

$$\langle I_p(\omega) \rangle = B(\omega) e^{i\omega(x_p - x_b)} e^{-(\omega \sigma_{bp})^2 / 2} + A_p, \quad (6)$$

where σ_{bp}^2 is the variance of the random variable $r_p - r_b$ and has a maximum value of $\sigma_b^2 + \sigma_p^2$ for $\rho_{bp} = 0$ and a minimum of zero for $\rho_{bp} = 1$.

These results account for the superior performance of peak tracking for compact objects, even when D/r_o is large: If the background $b(x)$ is a speckle distribution, peak tracking attenuates the speckle Fourier spectrum by the factor $e^{-(\omega \sigma_{bp})^2}$. However, if $b(x)$ contains the object itself, then the same spectral attenuation results in blurring and loss of contrast in the average image. Conversely, the form of (5) implies much less attenuation of $B(\omega)$ for a diffuse, extended object. This is because N_b for an diffuse object is likely to be near unity and N_p is likely to be relatively small.

Note that increasing wavelength at a constant telescope diameter tends to correlate all random motion in the image because of the increase in tilt power relative to higher-order aberration. This decreases the attenuation described above and equalizes the performance of the two algorithms. To test this notion, further satellite data was taken with a 162-actuator adaptive optics system running, since the AO also correlates motion of all components in the field. The orbital pass was chosen to be similar to the first, so residual image motion of about the same amplitude was evident. Again, both algorithms were used and the modulus spectrum SNR compared; for this case, the curves lie close enough to be considered identical.

Assuming the background component is part of the object scene, the conditions under which peak tracking performs as well or better than centroid tracking can be inferred by comparing (5) and (6). Using $1 - N_b = N_p$ and taking the log of the Gaussian attenuation factors multiplying $B(\omega)$, the condition

$$\sigma_{bp}^2 < \sigma_b^2 N_p^4 \quad (7)$$

is required for the background spectrum to have less attenuation with peak tracking. If D/r_o is large, then $\rho_{bp} \approx 0$. If we assume $\sigma_b^2 = \sigma_p^2$, then a slight manipulation of (7) yields,

$$2 < N_p^4, \quad (8)$$

a condition that is impossible to meet, given that N_p has an upper bound of 1. However, if D/r_o is small, then $\rho_{bp} \approx 1$ and σ_{bf}^2 assumes some small value ϵ . Then, (7) yields

$$\epsilon < \sigma_b^2 N_p^4. \quad (9)$$

This last result implies that if atmospheric aberrations are largely confined to tilt and a bright, compact source exists in the imaging field, peak tracking will provide lower attenuation of the average image background spectrum.

To summarize, 1.) peak tracking can indeed produce sharper images, relative to centroid tracking, of compact objects under arbitrary seeing conditions, and 2.) peak tracking can also yield higher resolution in the case where the object field has a bright, compact source, and D/r_o is small. Consideration should be given, therefore, to likely object morphology when planning tilt compensation systems or post-processing for observations where D/r_o is small.

- [1] J.W. O'Byrne, et al., Proc. OSA Conference on Adaptive Optics, paper TuA54, Garching (1995)
- [2] S. Esposito, et al., Proc. OSA Conference on Adaptive Optics, paper TuA32, Garching (1995)
- [3] L.M. Close, et al., Proc. OSA Conference on Adaptive Optics, paper TuA49, Garching (1995)
- [4] J. C. Christou, Pub. Astron. Soc. Pac. 103, p. 1040 (1991)

Simultaneous short exposure measurements of anisoplanatism using compensated images at optical and near infrared wavelengths

*Julian C. Christou, Brent L. Ellerbrock, Timothy L. Pennington,
James F. Riker, J. Timothy Roark, and Earl J. Spillar*

U.S. Air Force Phillips Laboratory
3550 Aberdeen Blvd. SE, Kirtland Air Force Base, NM 87117
(505) 846-4712 ext. 330; fax: (505) 846-2213

Work is in progress towards a series of observations to characterize the short- and long-exposure performance of an adaptive optics system as a function of wavelength and field-of-view. A principal goal of this effort will be to characterize the anisoplanatism observed in the infrared while using an off-axis visual guide star for tracking. More generally, we will investigate the effects of various methods for real-time and post-facto image tracking upon image quality in the presence of anisoplanatism. The instrumentation for the experiment is similar to that reported in [1], with the addition of an infrared sensor. Images are formed using the 1.5-meter telescope at the U. S. Air Force Phillips Laboratory Starfire Optical Range and its adaptive optics system [2]. A beamsplitter sends the visible portion of the spectrum to a high speed, 64 by 64 pixel MIT/Lincoln Laboratory CCD array with high quantum efficiency and low readout noise. Re-imaging optics enable both components of wide binaries to be formed on the same array with a plate scale of 289 nrad/pixel. The infrared portion of the spectrum is imaged onto a 256 by 256 pixel NICMOS III detector with Infrared Labs electronics yielding approximately 100e- read noise. We are able to obtain simultaneous wave front sensor, optical, and infrared data with integration times of from 1 to 50 milliseconds.

As of this writing, we have used simulated binary star data to investigate the the expected performance of two particular tracking algorithms. These data simulate observations obtained with Laser Guide Star (LGS) compensation at a wavelength of $0.875\mu\text{m}$ at the SOR 1.5-meter telescope. Nyquist sampling was used for the focal plane imaging, i.e. 289 nrad/pixel. The two components are separated by $\sim 15''$ with the on-axis source (i.e. the direction of the LGS) being dimmer than the off-axis source. The data was contaminated by additive gaussian noise. We have investigated both peak- and centroid-tracking for both on- and off-axis sources. We investigated the performance of the centroiding algorithm with different thresholds for the on-axis source and compared the performance to peak-tracking. This analysis is summarized in figure 1, which shows the rms difference of peak and centroid locations, their correlation, and their resulting Strehl ratios as a function of the applied threshold in units of the rms of the background noise. One thousand frames were used for each data point. The importance of thresholding is clearly evident in the Strehl ratios. Once a threshold of 3σ is reached the Strehls change very little with increasing threshold. We note that for the on-axis source, the individual frames are typically dominated by a single bright speckle so that the centroid and peak correlate strongly. However, for the frames which show multiple speckles this is no longer the case so that peak-tracking always gives better Strehl performance. We have decided to use a threshold limit of 3σ . A higher threshold risks ignoring the low-power speckles in a multiple speckle case (more common for the off-axis source) and a lower threshold shows the effect of noise contamination.

We next investigated the tilt-anisoplanatism between the two source using peak- and 3σ centroid-tracking. These results are shown in figures 2 & 3. The centroid motion between the two components is quite large with excursions as much as 3 pixels ($0.''18 \sim 1.5 \lambda/D$). Furthermore, there are very low correlations between the two sets of centroids with correlations of only 0.36 along the x-axis and 0.1 along the y-axis. There is also a preferred orientation to the confusion circle as illustrated in the top left. The time series plots clearly shows the "drift" between the two components as being very smooth. By comparison, the difference in peak locations is much more of a scatter plot. Comparison to the centroid shows there to be a similar trend, but there are much larger excursions, up to 6 pixels, ($0.''36 \sim 3 \lambda/D$) due to the increased speckle structure of the off-axis component. Thus tilt-anisoplanatism can yield significant image degradation as can be seen by the accumulated images in figure 3. Without post-processing the non-tracked component is extended with an orientation along the separation vector. With post-processing, i.e. either peak- or centroid- tracking, the

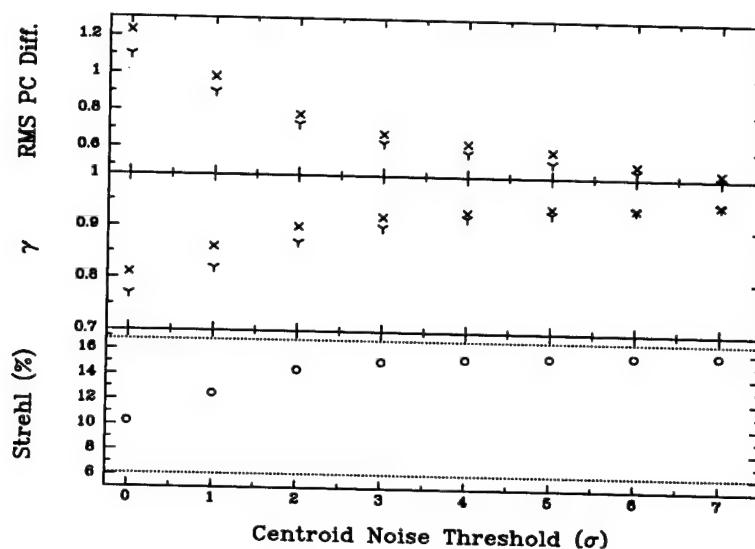


Figure 1: Variation of the Peak location - Centroid rms difference (top), the Peak location - Centroid correlation (center); and the Centroid image Strehls (bottom) as a function of the frame centering threshold. The two dotted lines on the bottom panel represent the Strehl ratios of the Peak-tracked (top) and pseudo long-exposure images (bottom).

non real-time tracked component becomes dominated by a bright symmetric speckle. The Strehl ratios of these images are given in table 1 and their ratios are given in table 2.

Tracking Algorithm	on-on	on-off	off-on	off-off
Peak	0.165	0.061	0.049	0.128
Centroid (3σ)	0.151	0.070	0.055	0.097

Table 1: Strehl ratios of the images shown in figure 3. (N.B. xx-yy refers to the xx-axis source with yy-axis tracking).

Tracking Algorithm		Tip-Tilt	High-Order	Combined
Peak	On-axis	0.37	0.78	0.30
	Off-axis	0.39		0.48
Centroid	On-axis	0.47	0.64	0.37
	Off-axis	0.57		0.72

Table 2: Ratios of the Strehls listed in table 1 for the accumulated peak- and centroid-tracked images shown in figure 3. Tip/Tilt: (on-off)/(on-on) and (off-on)/(off-off). Higher-Order: (off-off)/(on-on). Combined: (off-on)/(on-on) and (on-off)/(off-off)

As this is being written, we are preparing to take data with the combined optical/infrared system. Our results will be superior to our previous infrared results [3] since we will be able to freeze the seeing with our more sensitive camera.

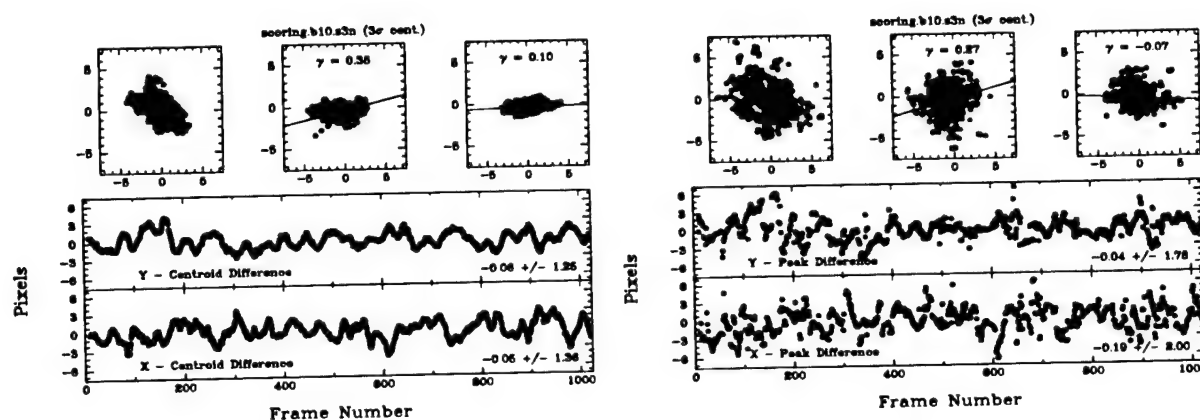


Figure 2: (Top Left) Scatter diagram of the centroid (with a threshold of 3σ) (left) and the peak-location (right) differences between the on-axis and off-axis sources and their (Top Center & Right) correlations; (Bottom) the Peak location and Centroid differences.

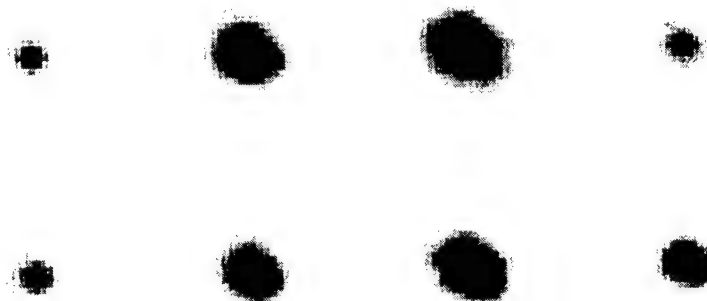


Figure 3: The effect of tilt-anisoplanatism on wide field AO imaging. Peak-tracking is shown on the top row and centroid-tracking on the bottom row: the on-axis source with on-axis tracking (left); the on-axis source with off-axis tracking (middle-left); off-axis source with on-axis tracking (middle-right); and off-axis source with off-axis tracking (right).

References

- [1] B.L. Ellerbroek, J.C. Christou, J.F. Riker, J.T. Roark, and T.L. Pennington, "Short-Exposure Anisoplanatism Measurements (SEAM)", presented at the OSA conference on adaptive optics in Garching, Germany, Oct. 1995,
- [2] R. Q. Fugate, B. L. Ellerbroek, C. H. Higgins, M. P. Jelonek, W. J. Lange, A. C. Slavin, W. J. Wild, D. M. Winker, J. M. Wynia, J. M. Spinhirne, B. R. Bocke, R. E. Ruane, J. F. Moroney, M. D. Olier, D. W. Swindle, and R. A. Cleis, "Two generations of laser guide star adaptive optics experiments at the Starfire Optical Range," *J. Opt. Soc. Am. A* **11**, 310-324 (1994).
- [3] J.C. Christou, B.L. Ellerbroek, R.Q. Fugate, D. Bonaccini, and R. Stanga, "Rayleigh Beacon Adaptive Optics Imaging of ADS 9731: Measurements of the Isoplanatic Field of View", *Astrophysical Journal*, **450**, 369, 1995.

Paper AWD7 has been changed to paper ATuB6.

Simulation Of Adaptive Optics Improvement On Laser Communication Link Performance

Brian Rosenberg
Laboratory for Physical Sciences
8050 Greenmead Drive
College Park MD 20740
(301) 935-6418 (tel.)

(301) 935-6723 (fax)

Pierre R. Barbier
Laboratory for Physical Sciences
and Electrical Engineering Dept., U. of Maryland
8050 Greenmead Drive – College Park MD 20740
(301) 935-6441 (tel.) (301) 935-6723 (fax)

Introduction

Terrestrial laser communication systems may be limited in their performance by atmospheric turbulence, which distorts the wavefront of a propagating laser beam [1]. At low turbulence levels a laser communication link is limited by atmospheric beam wander. This effect can be corrected by implementing an adaptive pointing system at the transmitter or by increasing the beam size at the receiver [2]. At higher turbulence levels the communication link is also limited by atmospheric scintillation, i.e., amplitude and phase distortions, at the receiver. These distortions induce power fading of the optical carrier detected by the receiver, resulting in an increased bit error rate (BER) of the system. The designer of a laser communication system will therefore seek to maximize the energy collected by the receiving photodetector while minimizing variations in this quantity. One approach to this problem is to implement an adaptive optic system to correct wavefront distortions and reduce power fadings. With an eye to astronomic applications, however, adaptive optics is usually designed to improve the Strehl ratio, resulting in greater image quality [3] but not necessarily in power fading improvement. Few comparisons of the Strehl ratio and collected energy (and hence BER) have been performed [4], making it difficult to assess the benefit of adaptive optics on a communication system. In this work we present the result of Monte Carlo simulations of a strongly turbulent atmosphere and compare the improvement on Strehl ratio and collected energy at the receiver of a laser communication link with and without adaptive optics.

Model and Simulation

To study the potential benefit of using adaptive optics in a laser communication link, we perform Monte Carlo computer simulations. From the results of these simulations, we compute the probability density functions of the Strehl ratio and of the energy collected by a photodetector placed in the focal plane of the link receiver. Note that the BER performance of a communication system can be calculated from the resulting power fading statistics, but this is not discussed here [2, 4, 5].

Our simulations parallel the design of a previously described low-intensity laser communication link [2]. This link comprises a 1.3 μm wavelength laser beam which is intensity modulated with an RF signal, collimated, and sent through the atmosphere onto a receiver. In the present work we assume near-ground operation of the link over 1 km of saturated atmospheric turbulence ($C_n^2 > 6 \times 10^{-14} \text{ m}^{-2/3}$). The transmitter and receiver apertures are both 7.5 cm in diameter. The receiver consists of a single 25 cm focal-length achromat which focuses the incoming laser beam onto a 100 μm diameter photodetector. We record the energy collected by the photodetector and the Strehl ratio in the focal plane of the achromat.

To maximize the number of Monte Carlo realizations computable in a reasonable time, we chose to implement a single-screen turbulence model [4, 5] based on the atmospheric statistics described in Ref. 6. We assume an inner scale of 1 mm and an outer scale of 2 m. Amplitude and phase spectra are created by multiplying a modified von Karman spectrum for the refractive index fluctuations by appropriate filter functions. In the saturation regime, we use an intensity variance proportional to $\sigma_{\chi_R}^{-2/5}$, where σ_{χ_R} is the standard Rytov variance. We assume stationarity of the turbulent statistics.

We form two 64-by-64 grids: the first covering a 10 cm square centered on the 7.5 cm receiver; the second (the Fourier transform of the first) covering a 200 μm square of the focal plane of the achromat, centered on the 100 μm photodetector. These grid dimensions allow the model to fully resolve turbulent features at the atmospheric coherence length without being limited by computational artifacts. For each set of parameters, we compute 10,000 realizations, from which we generate statistical distributions of the collected energy and of the Strehl ratio.

In the absence of atmospheric distortion, the arriving beam is modeled as a plane wave at the receiver. For each realization, two independent fields of pseudorandom normally-distributed complex numbers with zero mean and unit variance are created and combined with the amplitude and phase spectra described above [6] to produce the amplitude and phase screens. These screens are combined with a pseudorandom normally-distributed angle of arrival and applied to the arriving plane wave to simulate the atmospheric distortion. The field amplitude in the focal plane of the achromat is computed by a fast Fourier transform. We compute the collected energy as the ratio of the total energy on the photodetector to the energy collected from an undisturbed beam. Similarly, the Strehl ratio is computed as the ratio of the maximum intensities of disturbed and undisturbed beams. For consistency with the

conventional definition, the Strehl ratio is scaled by the total energy incident on the receiver. Instantaneous, i.e. single realization, and long-term or average values are reported for both quantities. It is important to note that the long-term Strehl ratio is the Strehl ratio of the long-term intensity field at the photodetector, not the average of the Strehl ratios from each realization.

We compute the collected energy and the Strehl ratio in three cases: 1) an uncompensated beam; 2) perfect phase compensation; 3) an adaptive optics model made up of a 6x6 segment deformable mirror with tilt compensation covering the whole receiver. The latter two models perform instantaneous phase detection and compensation of the incoming beam over the receiver area. The adaptive optics model subtracts the average phase over each mirror segment from the phase of the incoming beam.

Results

Typical performance of the three cases in strong turbulence ($C_n^2 = 7 \times 10^{-13} \text{ m}^{-2/3}$) is shown in Fig. 1. Probability density functions are plotted for the instantaneous collection efficiency (Fig. 1.a) and for the Strehl ratio (Fig. 1.b). As apparent in the figure, perfect phase compensation significantly improves both the Strehl ratio and the collected energy of the link. While the adaptive optics provides only a small improvement in the average values of these quantities, it nonetheless improves the performance of the communication system by narrowing the statistical distributions of those values, making deep power fades less likely. Note that collected energies greater than unity result from localized "hotspots" in the scintillation screens.

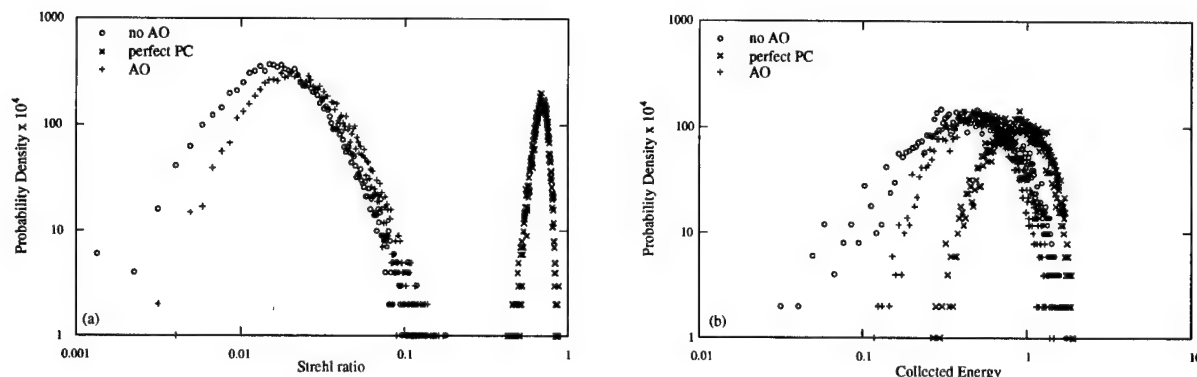


Figure 1: Probability densities of (a) Strehl ratio and (b) collected energy at $C_n^2 = 7 \times 10^{-13} \text{ m}^{-2/3}$ for the communication link without adaptive optics (no AO), with perfect phase compensation (perfect PC), and with an adaptive optics (AO) model.

This behavior can be observed more generally in Fig. 2, which shows average Strehl ratios and collected energies and their respective normalized standard deviations plotted against refractive index structure constant (C_n^2). Several observations can be made from this figure. The adaptive optics provides little improvement in the average collected energy, and the improvement in long-term Strehl ratio decreases with increasing C_n^2 . This decrease was noted by Primmerman [7] and attributed to an increasing number of phase discontinuities, which are absent in our model. As the turbulence grows in strength, the adaptive optics reduces the standard deviations of both quantities, particularly for the collected energy. But for $C_n^2 < 3 \times 10^{-13} \text{ m}^{-2/3}$, the standard deviations of all three cases converge to the limit imposed by the amplitude variations. Note that the uniform performance of the perfect phase compensation shown here indicates that our simulation resolves the relevant turbulent features.

Summary and Conclusions

We have modeled the effects of two phase-compensating adaptive optics systems placed at the receiver of a laser communication link operating in strong atmospheric turbulence, and we have generated the Strehl ratio and collected energy statistics of this link. The results of these simulations indicate that: 1) a deformable-mirror adaptive optics system has more effect on the long-term Strehl ratio than on the average energy collected by the receiver photodetector; 2) the standard deviation of the collected energy is improved by the incorporation of such an adaptive optics system; 3) below a refractive index structure constant of $3 \times 10^{-13} \text{ cm}^{-2/3}$, a perfect phase compensating system cannot improve the performance of such a communication link.

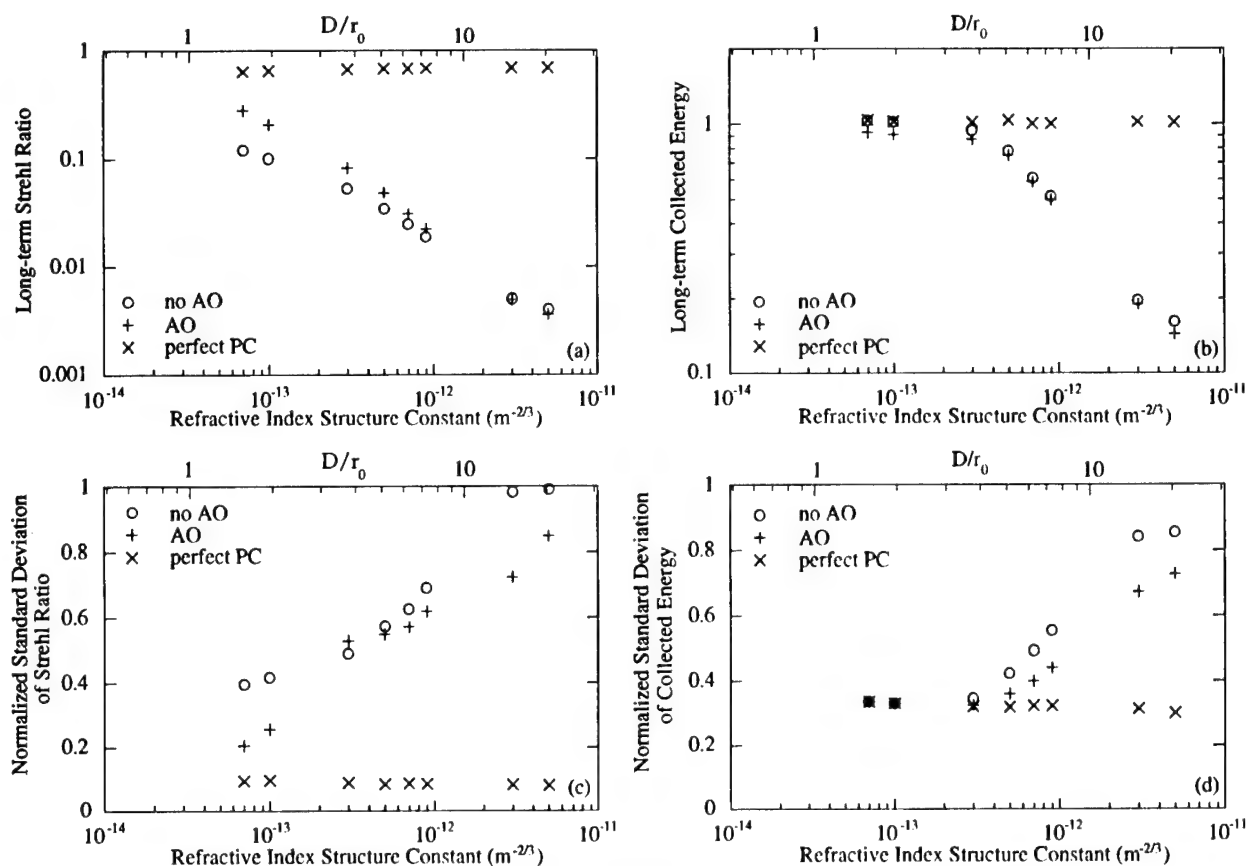


Figure 2: Long-term (a) Strehl ratios and (b) collected energies and their normalized standard deviations [(c) and (d)] versus the refractive index structure constant for the communication link without adaptive optics (no AO), with perfect phase compensation (perfect PC), and with the adaptive optics model (AO). The upper axes show values of D/r_0 , where D is the receiver diameter and r_0 is the Fried's coherence length.

The performance of a communication link equipped with adaptive optics may be further improved by using a continuous deformable mirror rather than a segmented mirror, as in our model. The use of adaptive optics at the transmitter may also increase the energy collected by the photodetector at the receiver. We intend to investigate these effects in upcoming field tests.

References

1. Lawrence, R.S., and J.W. Strohbehn, "A survey of clear-air propagation effects relevant to optical communications," *Proc. IEEE*, **58**(10), p. 1523-44, 1970.
2. Barbier, P.R., P. Polak-Dingels, D.W. Rush, D.W. Rosser, G.L. Burdge, *et al.*, "A terrestrial laser communication link at 1.3 μm with quadrature amplitude modulation," in *Free-Space Laser Communication Technologies VIII*, G.S. Mecherle, Ed., *Proc. SPIE*, Vol. 2699, p. in print.
3. Tyson, R.K., *Principles of Adaptive Optics*, Academic Press, San Diego, CA, 1991.
4. Kaufmann, J.E., "Performance limits of high-rate space-to-ground optical communications through the turbulent atmosphere," in *Free-Space Laser Communication Technologies VII*, G.S. Mecherle, Ed., *SPIE*, Vol. 2381, p. 171-82, 1995.
5. Belmonte, A., A. Comeron, J. Bara, J.A. Rubio, E. Fernandez, *et al.*, "The impact of the point-spread function distortion on the performance of a multiple-aperture optical ground station," in *Free-Space Laser Communication Technologies VII*, G.S. Mecherle, Ed., *Proc. SPIE*, Vol. 2381, p. 160-170, 1995.
6. Strohbehn, J.W., "Modern theories in the propagation of optical waves in a turbulent medium," in *Laser Beam Propagation in the Atmosphere*, J.W. Strohbehn, Ed., Springer-Verlag, New York, p. 70, 1978.
7. Primmerman, C.A., T.R. Price, R.A. Humphreys, B.G. Zollars, H.T. Barclay, *et al.*, "Atmospheric compensation experiments in strong scintillation conditions," *Appl. Opt.*, **34**(12), p. 2081-8, 1995.

COMBINED INTRACAVITY AND OUTER CAVITY ADAPTIVE CORRECTION OF ABERRATIONS IN A SOLID STATE LASER

Vladimir I. Polejaev

National Center for Design of Molecular Function,

Utah State University, Logan, UT 84322-4630

tel.: 801-797-3386, fax: 801-797-3328

E-mail: polejaev@sisna.com; vladimir@biocat.ncdmf.usu.edu,

Alexander V. Koryabin,

Victor I. Shmalhausen

Moscow State University, International Laser Center

Russian Federation, 119899, Moscow, Leninskie Gory, MSU ILC,

Non-linear Optics Laboratory

tel.: 7-095 939-3306, fax: 7-095-939-3113,

E-mail: avk@lado.phys.msu.su; shm@lado.phys.msu.su

Recent results of experimental investigations of the intracavity correction of the thermal aberrations (1-4) indicated that it may be possible to control parameters of the output radiation of solid state lasers with the help of an adaptive resonator, that contains one deformable mirror. This report presents the results of experimental investigations using pulsed YAG-laser with two intracavity 8-electrodes adjacent to adaptive mirrors (Fig. 1), and one similar external adaptive mirror to correct the phase profile of the output beam.

The mirror design shown in Fig. 2 enables one to correct the second order aberrations (focus and astigmatisms) and overall tip-tilts were also controlled by two separate piezoelectric actuators. To match the active apertures of intracavity mirrors (20 mm) and that of laser crystal (6 mm) the resonator contained two beam expanders, formed by the concave surfaces of the laser crystal and by focusing lenses at the mirrors. The control circuit included a personal computer, Camac interface and a set of high-voltage amplifiers.

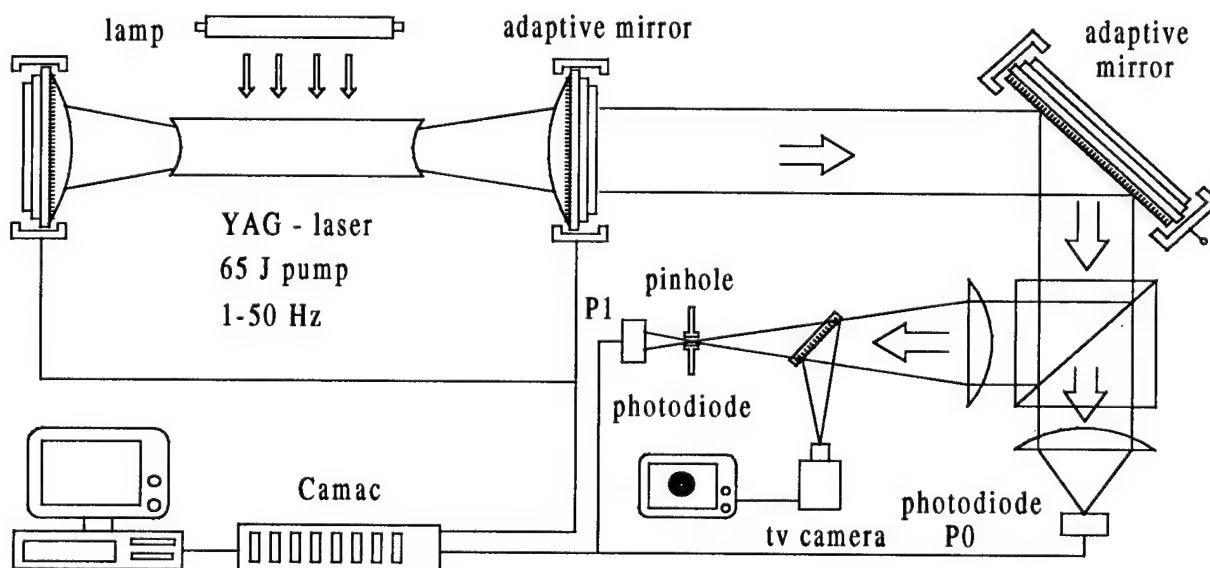


Fig. 1. Experimental Set-up

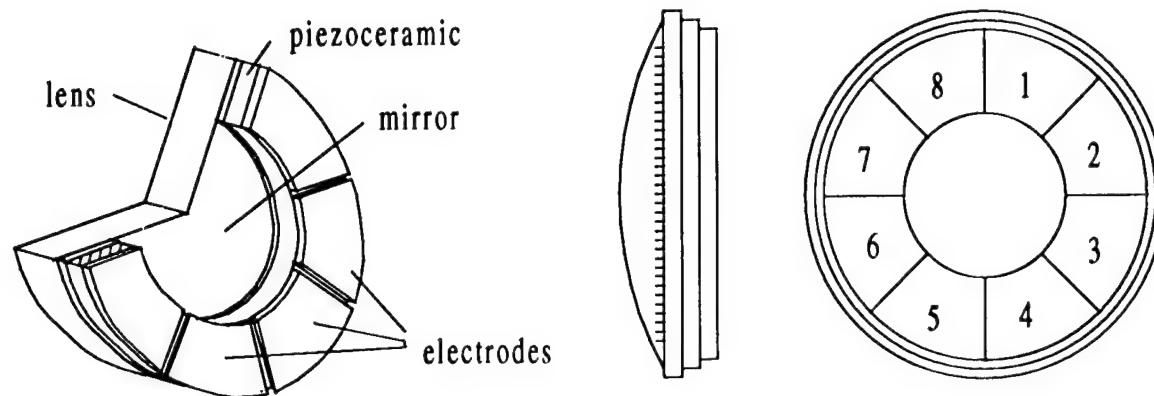
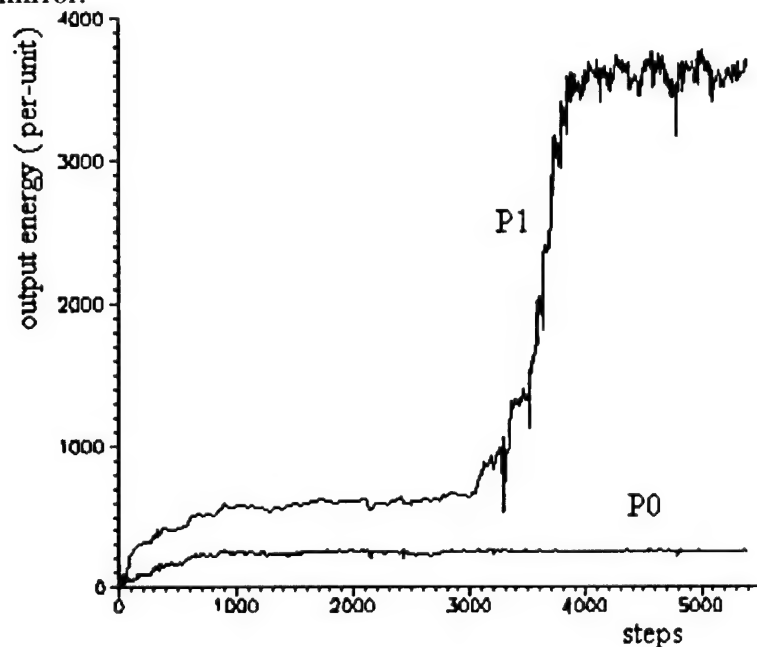


Fig. 2. Adaptive mirror design.

We used the total energy and/or on-axis intensity (energy after a pin-hole) of the output pulses as a criterion of the output beam quality. They were measured by photodiodes. To control the profiles of our mirrors we implemented a simple hill-climbing algorithm as a criterion maximization method. The laser operated in a free-running regime with a pulse repetition rate from 1 to 50 Hz. At 65 J pump we obtained about 30-50 mJ output per laser pulse.

Results obtained in these experiments revealed that both the output mirror and rear mirror had practically the same efficiency as an adaptive element to correct thermal aberrations in the laser cavity. In laser technology applications the output mirror is preferable to the rear mirror as an adaptive corrector since it enables one to obtain a wider output beam and hence stronger focusing. The total output energy P_0 of the laser pulses turned out to be the most suitable adaptation criterion to correct thermal distortions by the intracavity mirror, while the on-axis intensity P_1 was a suitable criterion to decrease the output beam divergence by the outer cavity mirror.

Fig. 3. Experimental curves of the total energy (P_0) and on-axis intensity (P_1) for cylinder control functions.

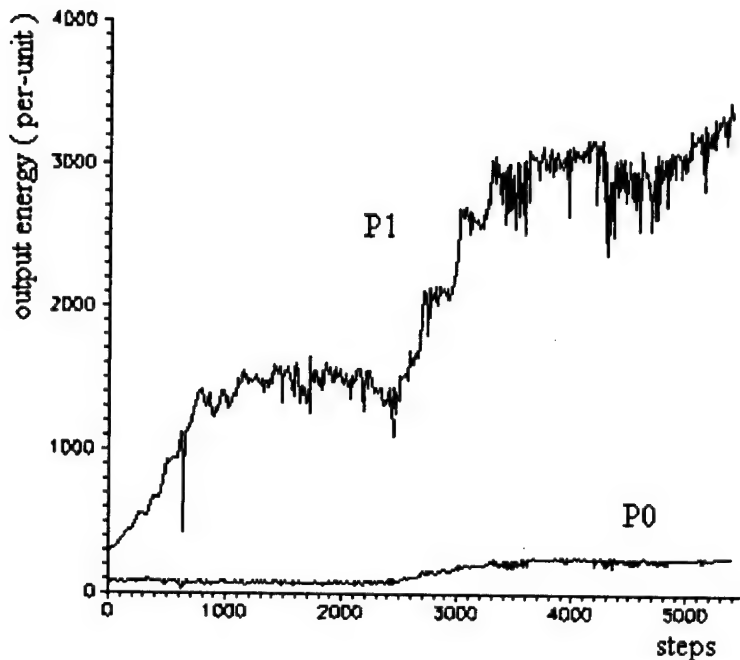


Fig. 4. Experimental curves of the total energy (P0) and on-axis intensity (P1) for defocus and astigmatism control functions.

Before turning on the feedback correction system all the optical elements of the laser set-up were aligned to get the maximize the criteria previously indicated. Then the adaptation process started. In a free-running regime, with a relatively small number of generated transverse modes we achieved a 3.6-fold increase in the output energy due to intracavity mirror performance and a 53-fold increase of the beam on-axis intensity due to external mirror performance.

We observed a strong dependence of adaptation efficiency on the number of generated transverse modes: when this number increased from 3 to 9, the adaptation efficiency fell by 2.5 times for the total energy and by 11 times for the on-axis intensity.

The theoretical investigations demonstrate that to obtain greater speed in the adaptation process the control algorithm has to implement the mirror profile representation as a sum of cylinders (X2 and Y2 functions, see Fig. 3) rather than a sum of the classic aberrations (defocus and astigmatism, see Fig. 4). Implementation of this method in the control procedure succeeded in increasing the speed of the adaptation process by a factor of 1.52.

References

1. M.A. Vorontsov, A.V. Koryabin, V.I. Polezhaev, V.I. Shmalhausen. Sov. J. Quantum Electron. Vol. 21, No 8, pp.818-819 (1991).
2. A.V. Koryabin, V.I. Polezhaev, V.I. Shmalhausen, M.A. Vorontsov. Proc.SPIE, Vol. 1839, pp.140-143 (1992).
3. V.V. Apollonov et al. Sov.J. Quantum Electron. Vol. 21, No 1, pp.116-118 (1991).
4. G.V. Vdovin, S.A. Chetkin. Sov.J. Quantum Electron. Vol. 23, No 2, pp.141-145 (1993).

Variances of Optical Transfer Functions of the Turbulent Atmosphere

Igor P. Lukin

Inst. of Atmospheric Optics, SB of the Russian Acad. of Sci.,
1 Akademicheskii Ave., 634055, Tomsk, Russian Federation.
Phone: (382-2) 25-96-82; Fax: (382-2) 25-90-86
E-mail: zuev.@iao.tomsk.su

The variances of optical transfer functions of the optical system "Turbulent Atmosphere - Telescope" are investigated theoretically by two methods of posterior processing (Labeyrie and Knox-Tompson) of the astronomical images. This characteristics are approximated the phase variances of intensity spectrum of the images.

Spatial Spikes of Intensity of the Atmospherically-distorted Images

Igor P. Lukin

Inst. of Atmospheric Optics, SB of the Russian Acad. of Sci.,

1 Akademicheskii Ave., 634055, Tomsk, Russian Federation.

Phone: (382-2) 25-96-82; Fax: (382-2) 25-90-86;

E-mail: zuev.@iao.tomsk.su

At registration of astronomical objects through the turbulent atmosphere for large telescopes conditions will be usually realized, when the astronomical image represents from self a chaotic picture interleaved light and dark spots (speckle-structure). In this connection, it is represented interesting to give an estimation of size of characteristic parameters of these areas. In given message the similar analysis will be carried out on the basis of treatment light spots of speckle-structure as the random spikes of intensity of the astronomical image.

In work [1] expressions for characteristics of the spikes of intensity of light radiation above level I_{sp} , in certain number of time exceeding the average value of intensity $\langle I_g \rangle$ are received: the average value of the area of one spikes; the average density of the spikes (the average number of spikes per unit of area); the average distance between the nearest spikes and the average volume of the spikes (the average complete flow of capacity in one spikes). For calculation of these characteristics it is necessary to know such value:

$$R_g''(0) = \frac{1}{2} \Re e \left\{ \frac{\partial^2}{\partial y_1 \partial y_2} \langle U_g(\rho_1) U_g^*(\rho_2) \rangle \right\} \Big|_{\rho_1 = \rho_2 = 0}$$

is the second derivative from

the second-order mutual-coherence function of a field of an optical wave $U_g(\rho)$ on cross coordinates at $\rho_1 = \rho_2 = 0$.

In conditions of well developed speckle-structure a field of an optical wave $U_g(\rho)$ to be distributed the according to the normal law. When the aperture radius of the optical system R is much greater of the coherence radius of an optical wave in the turbulent atmosphere ρ_0 ($R \gg \rho_0$), than the distribution of

average intensity of an optical wave at lens at developed speckle-structure has a form

$$\langle I_g(\rho) \rangle \cong I_i \exp \left\{ - \left(\frac{\rho}{\rho_i} \right)^2 \right\},$$

where $I_i = I_0 \frac{R^2}{\rho_i^2}$ is the intensity of the astronomical image on optical axis of

system; I_0 is the intensity of an optical wave, pass through a telescope; $\rho_i = \frac{2 F_t}{k \rho_0}$

is the linear size of the image of point object, observable through the turbulent atmosphere; $k = 2\pi/\lambda$, λ is the optical radiation wavelength in vacuum; F_t is the focal length of the optical system. In given situation the "turbulent" size of the average image is much greater than the diffraction size: $\rho_i \gg \rho_d$, where

$\rho_d = \frac{2 F_t}{k R}$ is the linear size of the image of point object, observable through

homogeneous medium (the diffraction size of the image). At $R \gg \rho_0$ the expression for the second derivative from the second-order mutual-coherence function has a form

$$R_g''(0) \cong I_i \frac{1}{\rho_d^2}.$$

Thus, the characteristics of spikes of intensity of the astronomical image can be represent in the following form: the average value of the area of one spikes is

$$\langle S(I_{sp}) \rangle \cong \frac{1}{2} \pi \rho_d^2 \frac{I_i}{I_{sp}},$$

the average density of the spikes is

$$\langle N(I_{sp}) \rangle \cong \frac{2}{\pi \rho_d^2} \frac{I_{sp}}{I_i} \exp \left(- \frac{I_{sp}}{I_i} \right),$$

the average distance between the nearest spikes is

$$\langle l(I_{sp}) \rangle \cong \sqrt{\frac{\pi}{8}} \rho_d \sqrt{\frac{I_i}{I_{sp}}} \exp \left(\frac{I_{sp}}{2 I_i} \right),$$

the average volume of the spikes is

$$\langle V(I_{sp}) \rangle \cong \frac{1}{2} \pi \rho_d^2 I_i.$$

The characteristics of spatial spikes of intensity of the astronomical image are determined by the diffraction size ρ_d and relation of a level I_{sp} to intensity of the astronomical image on optical axis of a telescope I_i . The astronomical image at developed speckle-structure represents from self system bright spots (speckles), the characteristic size of which coincides with by the diffraction size of the image ($\cong \rho_d$). Speckles the friend from friend on distance in some diffraction sizes of the image are removed and bear in self an average flow of capacity $\cong \pi \rho_d^2 I_i$, caused by intensity of the average image and by the diffraction size of the image. The speckle-structure of the astronomical image consists of randomly located diffraction images, the intensity of which is determined by intensity of the average image I_i , much more weak, than intensity of the diffraction image ($I_i \ll I_d = I_0 \frac{R^2}{\rho_d^2}$), the number of the diffraction images is thus increased

proportionally to easing of their average intensity (the number of speckles $\sim I_d/I_i$). The increase of the number of speckles in the astronomical image occurs at about constant meaning of their density, i.e. at expense of increase of area borrowed by them.

References

1. Aksenov V. P., Gochelashvily K. S., Shishov V. I. Spatial spikes of laser irradiance propagating over large distances in a turbulent medium. // Applied Optics. 1976. Vol.15. №5. P.1172-1177.

"1001" Correlations in Random Wave Fields

Isaac Freund

Department of Physics, Bar-Ilan University, Ramat-Gan 52900, Israel

Tel: +972-3-531-8428, Fax: +972-3-535-3298, email F67368@barilan

Introduction

The coherence length Λ_{coh} of a random wave field $E(x,y)$ is defined as the characteristic distance over which the whole field, ensemble averaged autocorrelation function $\mu(\Delta x) = \langle E^*(x,y)E(x+\Delta x,y) \rangle / \langle |E(x,y)|^2 \rangle$ decays to zero [1]. A natural, indeed universal interpretation is that on length scales larger than Λ_{coh} , different field structures such as maxima, minima, etc. are uncorrelated. Indeed, it is the apparently random distributions of positions, heights, and widths of these features that make the field appear "random". But as is often the case, appearances can be deceiving, and we have recently found that there are literally thousands of unexpected, often highly unusual, *local* correlations and anticorrelations present even in that apparently most random of all wave fields, the Gaussian field (i.e. a field whose fundamental field variables obey Gaussian statistics). These local correlations tend to be paired such that correlations with $\mu \sim +1$ in one region of the wave field are exactly canceled by anticorrelations with $\mu \sim -1$ in other regions, leading to a whole field average $\mu \sim 0$. Many of these correlations are topological in nature, and are thus universal features of all wave fields. Knowledge of these universal correlations may prove useful in the manipulation and reconstruction of a variety of aberrated fields.

Field Variables

We concentrate here on the maxima, minima, and saddle points of the intensity (U), phase (ϕ), real (R), and imaginary (I), parts of the field, and for the phase, also the singularities (vortices) that abound in these fields [2]. Collectively, these are called critical points, and as $U(x,y)$, for example, may be viewed as a surface, these critical points define the random field "landscape". There are six variables needed to provide a minimal description of each critical point. For maxima, minima, and saddle points, two variables describe the position (x,y) of the critical point and a third variable describes its height (field amplitude). All critical points lie on intersections of the zero crossings (the set of curves in the x,y -plane along which a function vanishes) of the first-order derivatives of the corresponding field variables. Maxima of U , for example, lie on zero crossing intersections where $U_x = \partial U / \partial x$ and $U_y = \partial U / \partial y$ both vanish, while phase singularities lie (by a limiting process) on intersections of the zero crossings of ϕ_x and ϕ_y , etc. Accordingly, first-order derivatives provide no additional information. In contrast, the second-order derivatives of the field evaluated at a critical point (e.g. $U_{xx} = \partial^2 U / \partial x^2$, $U_{yy} = \partial^2 U / \partial y^2$, and $U_{xy} = \partial^2 U / \partial x \partial y$

$= U_{yx}$), provide three additional, independent variables that describe the field curvature at this point, and that thus yield an estimate of the width of the corresponding field structure. The six variables that locally describe a phase singularity (vortex) are conveniently taken to be the two coordinates x, y of the vortex center, and the four first-order derivatives $R_x, R_y, I_x,$ and I_y at this point.

In the next section we apply the sampling theorem of information theory to the six critical point variables [3], and in the following section we review topological correlations between the different critical points. These very general considerations form the underlying theoretical basis for the universal nature of the "1001" correlations we have recently uncovered in random wave fields. Although space limitations prevent tabulating here the very large number of correlations measured *quantitatively* for Gaussian fields using highly accurate, large scale computer simulations [4], an overview of these correlations will be presented. We also note that a small part of these correlations have already appeared (or will soon appear) in print [3,5-7], while tabulations of the remaining bulk are being prepared for publication.

Sampling Theorem

The coherence length Λ_{coh} is not only the largest length scale above which global field correlations vanish, but it is also the smallest length scale below which significant variations in field structure are not expected to occur. The reason is that up to Λ_{coh} the field remains "coherent" because it hardly changes, while beyond Λ_{coh} when the field does change, it changes, on average, "randomly". In the far field of a distant random source, $E(x, y)$ is the Fourier transform (FT) of the source distribution. If this source is bounded, then so is $\text{FT}\{E(x, y)\}$, and $E(x, y)$ is band limited. Although a distant localized source (star) viewed through a thick aberrating medium (atmosphere) is not necessarily quantitatively modeled as a distant random source, the conclusion that the field is band limited with a shortest Fourier wavelength Λ_{coh} that may be identified with Fried's parameter r_0 is expected to hold.

When $E(x, y)$ is band limited the sampling theorem is applicable, and the double (one for R and one for I) number density of sampling points $2\eta(\text{samples})$ needed to completely specify the (complex) wave field obviously provides a good quantitative measure of the information content of the field. Now, the number density of critical points, $\eta(\text{critical points})$, multiplied by six, the minimum number of parameters per critical point, measures the number density of field parameters needed to locally specify the field structure. By comparing $6\eta(\text{critical points})$ with $2\eta(\text{samples})$, we obtain a quantitative estimate of the fractional information carried by the critical points. For the intensity U of a wave field obeying Gaussian statistics produced by a uniformly illuminated circular random scatterer, for example, we have the following number densities in units of $\Lambda_{\text{coh}}^{-2}$, where Λ_{coh}^2 ($\sim \Lambda_{\text{coh}}^2$) is the coherence area of the field: $\eta(U_{\text{Max}}) = 0.42$, $\eta(U_{\text{min}}) = 0.64$, and $\eta(U_{\text{Saddle}}) = \eta(U_{\text{Max}}) + \eta(U_{\text{min}}) = 1.06$, so that $6\eta(\text{critical points}) = 12.72$ [3]. But for this field we have $2\eta(\text{samples}) = 2[2(3)^{1/2}/\pi] = 2.205$ [3]. Surprisingly, perhaps, $6\eta(\text{critical points})$ actually *exceeds* the requirements of the sampling theorem, and does so by more than a factor of five! A similar degree of overspecification is found also for the critical points of ϕ , R , and I . It is thus evident that

most critical point parameters cannot be independent one of the other, and that there must exist an extensive network of correlations that connect together the various critical points. In the next section we show that many of these correlations are topological in nature, and are thus universal features of all wave fields.

Topological Correlations

As the wave field is everywhere continuous except possibly at isolated points (the vortices), the field structure is constrained by simple topological considerations. In one dimension these constraints may be summarized for continuous fields by the rule: "what goes up must come down", so that neighboring maxima must be separated by a minimum, and vice versa. For the two dimensional fields of interest here the corresponding rules are somewhat more complex. By using the well known laws of conservation of topological charge and topological index to relate the signs of the vortices (positive or negative) to the nature of the surrounding critical points, we have recently developed a set of four simple rules that explicitly constrain local and global configurations of extrema (maxima and minima), saddles, and vortices [8]. A review of these rules and their application will be presented. A striking consequence of the rules is that once the topology of the saddles is fixed, only a *single* degree of freedom remains, and if, for example, some arbitrarily located extremum is chosen to be a maximum, this choice automatically fixes the nature of *all other* extrema and the signs of *all* the vortices. Alternatively, fixing the sign of a *single* vortex anywhere in the wave field automatically fixes the signs of *all other* vortices and the nature (maximum or minimum) of *all* extrema. This drastic reduction in the number degrees of freedom of the wave field leads to extensive short and long range correlations between all critical points. These topologically mandated correlations are reflected in the sampling theorem results of the previous section, and are made manifest as the "1001" correlations recently measured explicitly for Gaussian random wave fields.

References

- [1] J. W. Goodman, *Statistical Optics* (Wiley, New York, 1985).
- [2] I. Freund, N. Shvartsman, and V. Freilikher, "Optical dislocation networks in highly random media," *Optics Commun.* **101**, 247 (1993).
- [3] I. Freund, "Amplitude topological singularities in random electromagnetic wavefields," *Phys. Lett. A* **198**, 139 (1994).
- [4] I. Freund, "Optical vortices in Gaussian random wave fields: Statistical probability densities," *J. Opt. Soc. Amer. A* **11**, 1644 (1994).
- [5] N. Shvartsman and I. Freund, "Vortices in random wave fields: Nearest neighbor anticorrelations," *Phys. Rev. Lett.* **72**, 1008 (1994); I. Freund and N. Shvartsman, "Wave field phase singularities: The sign principle," *Phys. Rev. A* **50**, 5164 (1994); N. Shvartsman and I. Freund, "Wave field phase singularities: Near neighbor correlations and anticorrelations," *J. Opt. Soc. Amer. A* **11**, 2710 (1994).
- [6] I. Freund and N. Shvartsman, "Structural correlations in Gaussian random wave fields," *Phys. Rev. E* **51**, 3770 (1995); N. Shvartsman and I. Freund, "Speckle spots ride phase saddles sidesaddle," *Optics Commun.* **117**, 228 (1995).
- [7] I. Freund, "Intensity critical point correlations in random wave fields," *Optics Commun.* (in press).
- [8] I. Freund, "Saddles, singularities, and extrema in random phase fields," *Phys. Rev. E* **52**, 2348 (1995).

Atmospheric Characterization for Adaptive Optics at the
Keck Telescope

Gary Chanan

Department of Physics and Astronomy
University of California, Irvine
Irvine, CA 92717
Phone: (714) 824-6619
Fax: (714) 824-2174

Romana Crnkovic

Department of Physics and Astronomy
University of California, Irvine
Irvine, CA 92717
Phone: (714) 824-2605
Fax: (714) 824-2174

Frank Dekens

Department of Physics and Astronomy
University of California, Irvine
Irvine, CA 92717
Phone: (714) 824-2605
Fax: (714) 824-2174

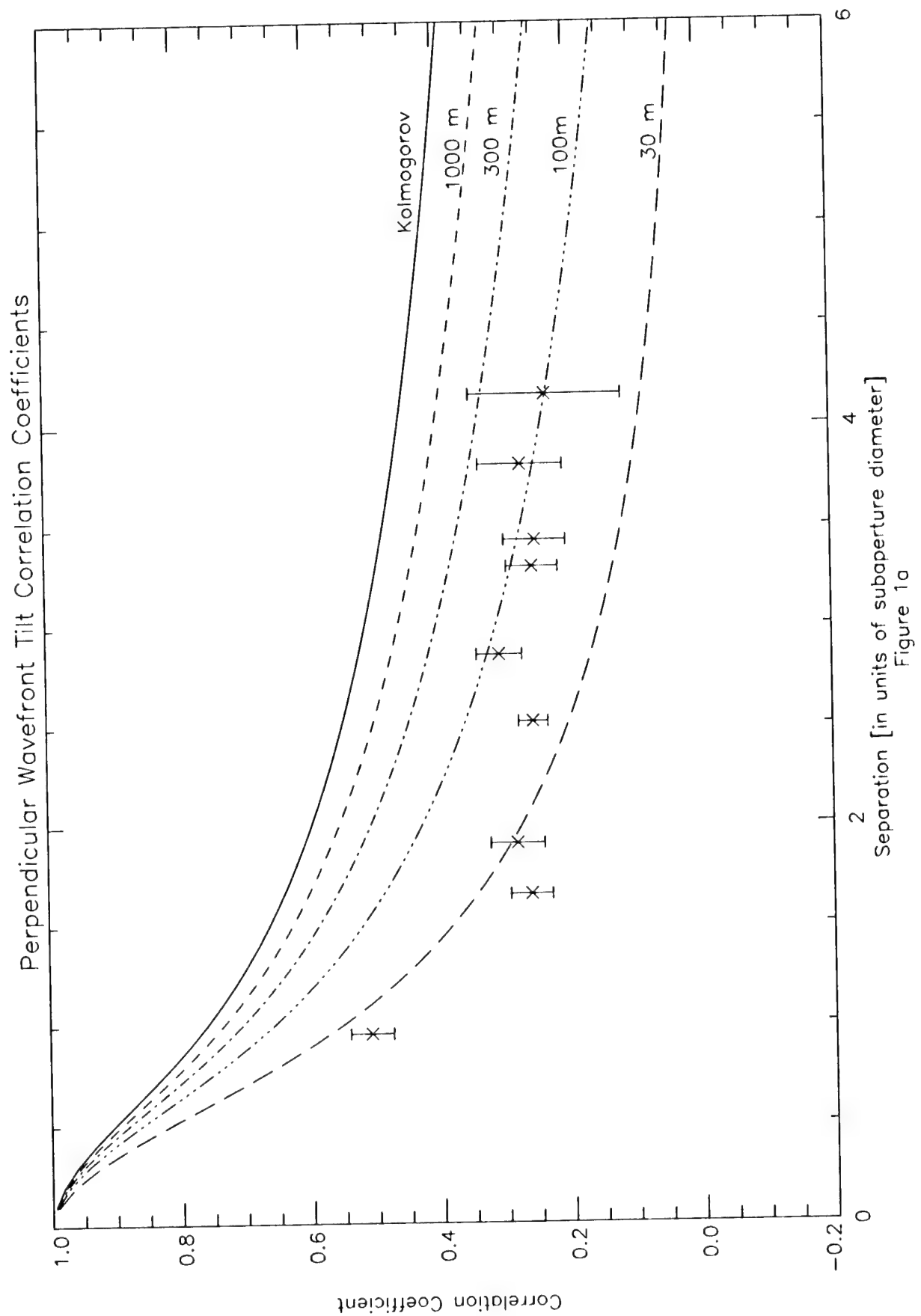
Figure Caption

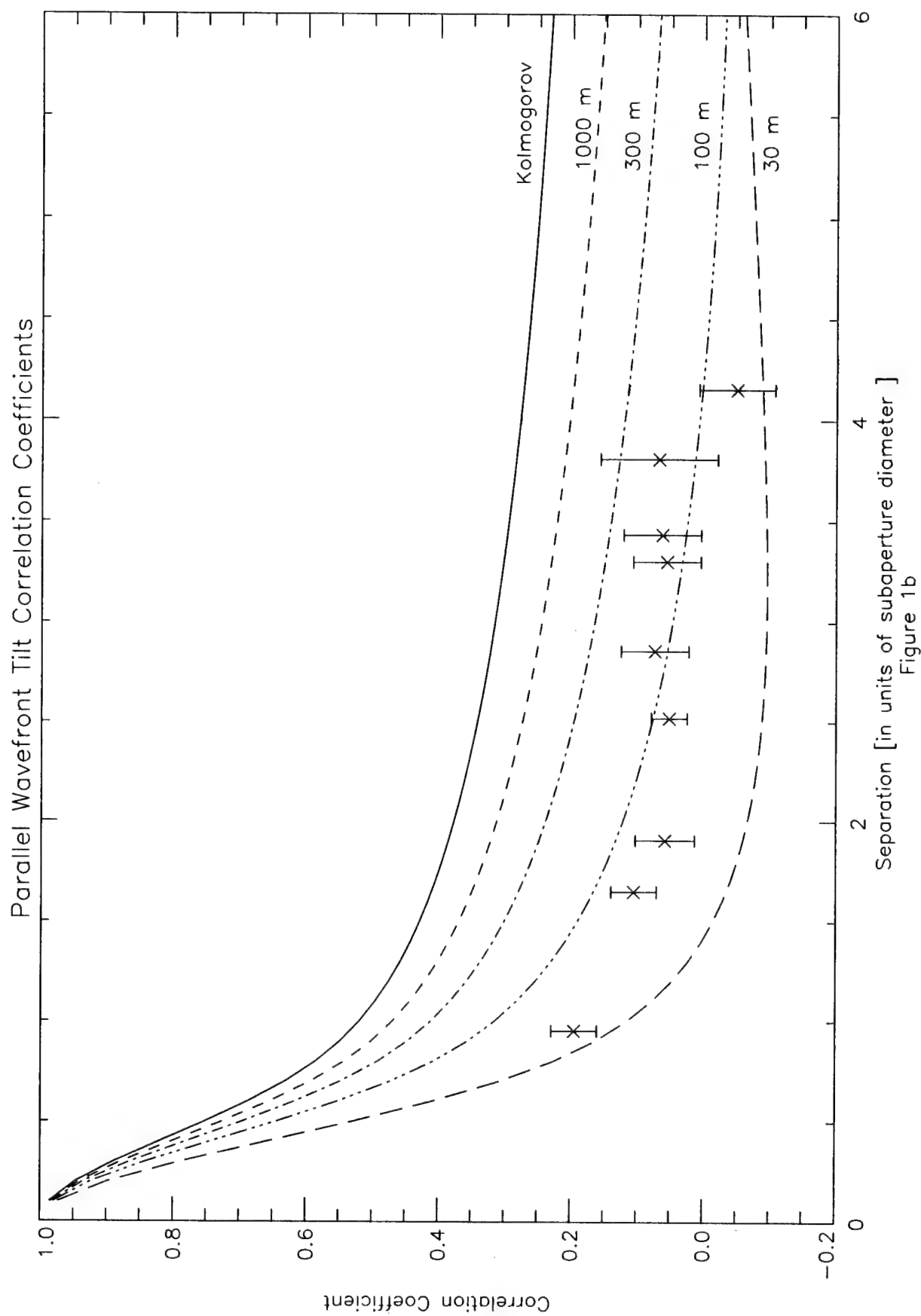
1a Perpendicular segment-to-segment tilt correlations for the Keck Telescope, caused by atmospheric turbulence. Here, "perpendicular" refers to that tilt component perpendicular to the line connecting the segment centers. Horizontal axis is separation in units of the segment diameter (1.64 m). The full 10 meter baseline was not reached because of limitations on the detector size. Sampling was at 91 Hz for 164 seconds. Tilts were corrected for telescope drift by removing global linear trend. Theoretical curves (after Takato and Yamaguchi 1995) are labeled with assumed outer scale; curve marked "Kolmogorov" is for infinite outer scale. Data points are from a representative run; a series of 28 runs from May 1994 and August 1995 shows similar results, with the average value of the outer scale less than 200 m.

1b Same as 1a but for tilt component parallel to the line connecting the segment centers.

References:

N. Takato and I. Yamaguchi (1995) *J. Opt Soc. Am. A.* **12**, 958-63.





Evaluation and development of SCIDAR with the aid of 3D propagation code.

Miles J. Adcock, Vincent A. Klückers, Nicholas J. Wooder and Christopher Dainty.
Imperial College of Science Technology and Medicine,
The Blackett Laboratory,
Prince Consort Road,
LONDON, SW7 2BZ.
Tel: + 44 171 5947712 Fax: + 44 171 5947714

SCIDAR (SCIntillation Distance And Ranging) is used to determine the height and strength of optically turbulent layers in the atmosphere. One use of this information is in adaptive optics, both in the design of a system and in its regular operation. The technique of was first proposed by Vernin and colleagues [1, 2, 3, 4], and further developed by Tyler [5]. This paper evaluates SCIDAR as a method for turbulence profiling, and describes algorithms which have been developed to make it viable. This has been aided by a simulation of the propagation of light through 3D random media.

If there is a layer of turbulence at height h above the ground then some fluctuation of intensity in the telescope pupil will be observed, the variance of which is a function of C_n^2 (the refractive index structure constant). In order to extract information about the height of a turbulent layer, consider a binary stellar object of angular separation θ . Light from each source that passes through the same point in a turbulent layer at height h will produce areas of intensity in the pupil which are partially correlated at separations $r = \theta h$.

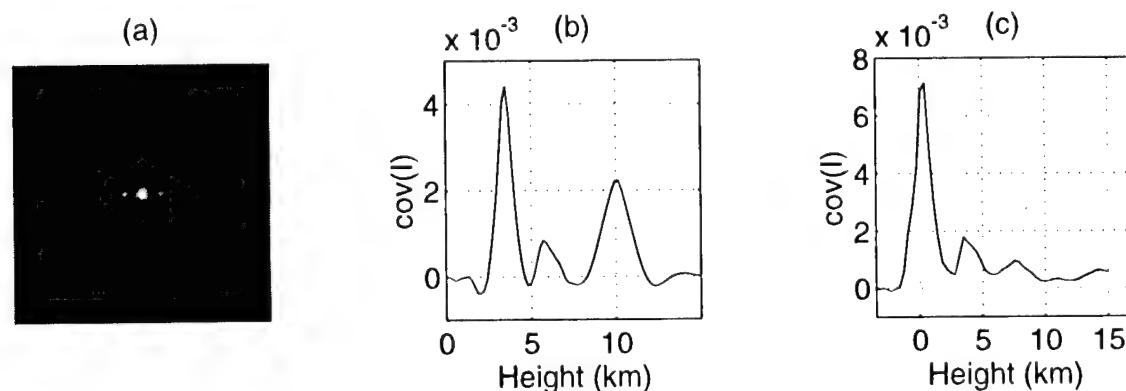


Figure 1: (a) The average covariance of 4000 frames of simulated pupil intensity for a binary source. (b) A slice of the covariance through the axis of the binary, and with the perpendicular slice subtracted in order to remove the central peak (because it is noise). Only one half of this slice is shown because it is symmetrical about the centre. The x-axis has been scaled to represent height. (c) The average of 40000 frames of real data. Note that the x-axis is shifted, this is an example of generalised SCIDAR; the optics on the telescope were defocused by 3.5km so that information about turbulence at ground level was not destroyed by the central covariance peak.

Figure 1(a) is the average covariance of 4000 frames of pupil intensities. The data was produced by simulating the 3D propagation of light through 3 layers of optical turbulence at 4km, 6km and 10km. The height of the turbulence is easily determined through simple geometry: $h = r/\theta$, where r is the distance in the pupil and θ is the angular separation of the binary. Determining the strength of the turbulence at a given height is less simple. Let the covariance of pupil intensity due to the binary nature of the source (i.e. with the central peak removed) be denoted $A(r)$ (see Fig 1 (b) and (c)).

$$A(r) = \int_h T(r, h) C_n^2(h) dh \quad (1)$$

where $C_n^2(h)$ is the required turbulence strength profile as a function of altitude, and $T(r, h)$ is a two-dimensional matrix containing the geometry and physics of the problem; Kolmogorov turbulence is assumed. If one assumes further that the atmosphere can be decomposed into a series of uniform slabs of thickness Δh then,

$$A(r_i) = \Delta h \sum_h T(r_i, h_j) C_n^2(h_j), \quad (2)$$

and so in matrix notation one has simply,

$$\mathbf{A} = \mathbf{T} \mathbf{c} + \mathbf{n}. \quad (3)$$

where \mathbf{n} is noise. This is a Fredholm equation of the first kind [6]; it is not a trivial exercise to extract C_n^2 (\mathbf{c} in matrix eqn 3) given the observed \mathbf{A} and the calculated \mathbf{T} in the presence of noise.

We have used three methods to solve Eq 3.

Least squares inversion

The least squares solution to Eq. 3 is

$$\mathbf{c} = (\mathbf{T}^T \mathbf{T})^{-1} \mathbf{T}^T \mathbf{A}. \quad (4)$$

It is possible to obtain results for \mathbf{c} close to the known values used in the simulation only if the vertical resolution of \mathbf{T} (and thus C_n^2) is reduced to approximately 2km (for $\theta \approx 8$ arc secs). Resolutions better than this resulted in highly unstable results. The advantage of this method is that it is very fast.

Maximum entropy

An iterative method of maximum entropy was developed. This provides a more robust solution to Eq 3, and resolutions of approximately 300m produce stable results.

Solution space search

The solution space is limited i.e. there is a finite range of values which C_n^2 can have. The approach is to make a 'first guess' of \mathbf{c} : either a random choice, or maybe a low resolution least squares solution as described above. This guess, \mathbf{c}_1 say, can be matrix multiplied by \mathbf{T} , resulting in \mathbf{A}_1 . \mathbf{c}_1 is then be modified in a pseudo random manner to \mathbf{c}_2 . If \mathbf{A}_2 ($= \mathbf{T} \mathbf{c}_2$) is closer (using a chi squared comparison for example) to the observed \mathbf{A} than \mathbf{A}_1 , then it replaces \mathbf{A}_1 as the 'best guess'. This approach of constantly modifying the last best guess solution in the hope that it produces a better match to \mathbf{A} , and thus a new best guess, can be repeated until $A_{N+1} \rightarrow A_N$.

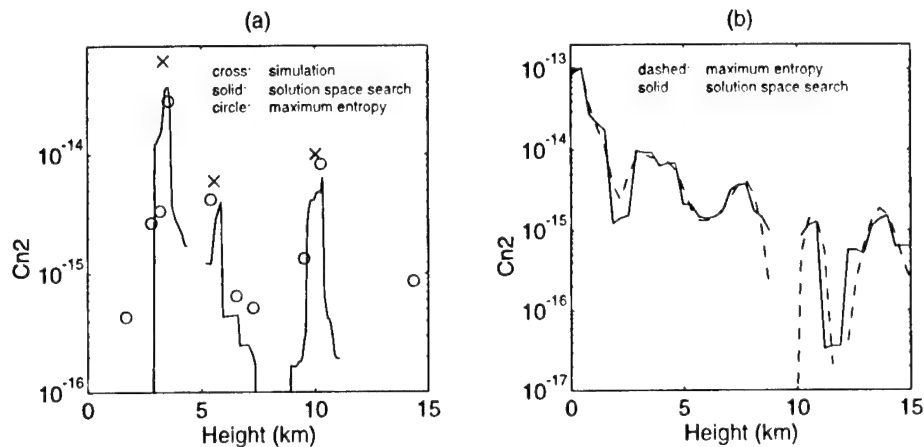


Figure 2: Comparison between techniques. (a) Maximum entropy and solution space search results for simulated data. The C_n^2 values used are also shown. (b) Maximum entropy and solution space search results for real data.

References

- [1] J Vernin and F Roddier. Experimental determination of two-dimensional spatiotemporal power spectra of stellar light scintillation. Evidence for a multilayer structure of the air turbulence in the upper troposphere. *J. Opt. Soc. Am.*, 63:270–273, 1973.
- [2] M Azouit and J Vernin. Remote investigation of tropospheric turbulence by two-dimensional analysis of stellar scintillation. *J. Atmos. Sci.*, 37:1550–1557, 1980.
- [3] J Vernin and C Muñoz-Tuñón. Optical seeing at La Palma Observatory: Intensive site testing campaign at the Nordic Optical Telescope. *Astron. Astrophys.*, 281:311–318, 1994.
- [4] A Fuchs, M Tallon, and J Vernin. Folding of the vertical atmospheric turbulence profile using an optical technique of movable observing plane. *Proc. SPIE*, 1994.
- [5] G A Tyler and K E Steinhoff. SCIDAR: Measurement characteristics and noise amplification properties. *The Optical Sciences Company*, TR-755R, 1987.
- [6] J M Wing. A primer on integral equations of the first kind. *Society for Industrial and Applied Mathematics Philadelphia*, 1991.

Acknowledgements

This work is supported by grants from the Particle Physics and Astronomy Research Council.

Measurement of a Non-Kolmogorov Structure Function

Tom Nicholls, Nicholas J. Wooder and Christopher Dainty.

Imperial College of Science, Technology and Medicine,

The Blackett Laboratory,

Prince Consort Road,

LONDON, SW7 2BZ.

Tel: + 44 171 5947712

Fax: + 44 171 5947714

The structure function of atmospheric phase fluctuations is defined as follows:

$$\mathcal{D}_\varphi(\Delta\mathbf{r}) = \langle |\varphi(\mathbf{r}) - \varphi(\mathbf{r} + \Delta\mathbf{r})|^2 \rangle. \quad (1)$$

A generalised model for the structure function of phase is:

$$\mathcal{D}_\varphi(\mathbf{r}) = \gamma_\beta \left(\frac{r}{\mathcal{R}_0} \right)^{\beta-2}. \quad (2)$$

\mathcal{R}_0 is related to the size of the long-exposure image formed by a large-aperture telescope, while γ_β is a parameter which depends on β and on the precise definition of \mathcal{R}_0 . The widely-used Kolmogorov model of refractive index fluctuations [1] predicts a value of 11/3 for β ; in this case, with the appropriate definition, \mathcal{R}_0 is equivalent to r_0 , the Fried parameter [2]. Under the Kolmogorov assumption, the parameter r_0 entirely describes the time-averaged statistics of the phase fluctuations. A knowledge of r_0 can be used, for example, to predict how the energy in the phase fluctuations is distributed between the Zernike modes.

Some observations [3] [4] [5] have, however, led to concern that β may, on occasion, take on values other than 11/3. Such behaviour would have implications for the modelling and specification of an adaptive optics system. Indeed, a recent analysis [6] has shown that the effect of a decrease in β is to shift some of the energy of the phase fluctuations from lower to higher order Zernike modes. Under these circumstances, a higher order of correction would be required in order to compensate for the phase fluctuations. It is therefore important to have a knowledge not only of the behaviour of \mathcal{R}_0 , but also of the range of values of β that can be expected.

The principle of the differential image motion monitor (or DIMM [7]) is to use the correlations between the motions of images formed from two apertures in different parts of the pupil to measure r_0 directly. Such a measurement requires that a relation between the statistics of the seeing and the statistics of the wavefront

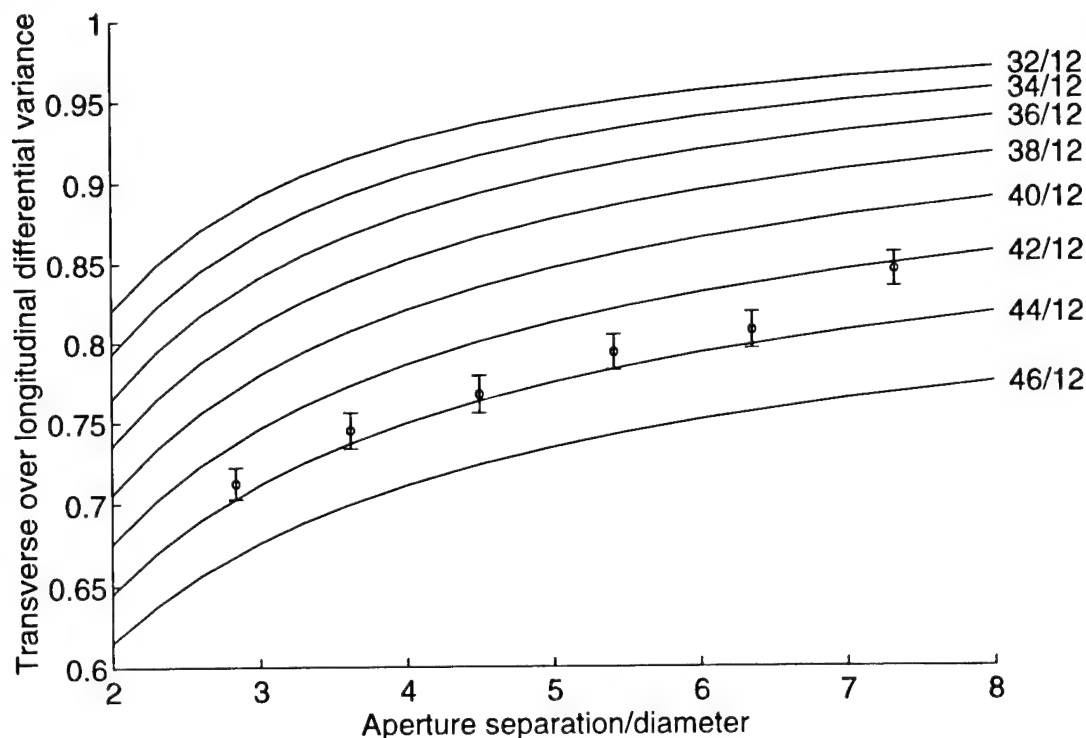


Figure 1: The predicted ratio between the differential angle-of-arrival variance measured in the transverse direction to that measured in the longitudinal direction, plotted against separation, for a range of values of β (solid lines). The plotted points are calculated from 20000 frames of data acquired at Calar Alto in July 1995.

angle-of-arrival be known. An earlier paper [8] shows how it is possible to predict the behaviour of a DIMM under the more general conditions governed by the non-Kolmogorov structure functions defined in Eq. 2. A numerical integration of an equation given by Fried [9] has allowed this information to be expressed in terms of the differential variances of the angle-of-arrival measured through a pair of apertures in the transverse and longitudinal directions (*i.e.* in the directions parallel and perpendicular to the axis joining their centres). Figure 1 shows the ratio of these two quantities plotted against the separation of the centres of the apertures for a range of values of β . Also shown are a number of points calculated from experimental data obtained at Calar Alto using a Shack-Hartmann wavefront sensor; this sensor provides a large number of DIMMs with a range of aperture separations. Each point represents the mean value of the ratios of the two variances using a group of aperture pairs with approximately equal separations. The data suggests a good fit with the Kolmogorov model at the time in question. Further results will be shown from data currently being obtained over an extended period by the UK Joint Observatory Site Evaluation project.

References

- [1] V.I. Tatarski. *Wave Propagation in a Turbulent Medium*. McGraw-Hill, 1961.
Translated from the Russian by R.A. Silverman.
- [2] D.L. Fried. Statistics of a geometric representation of wavefront distortion. *Journal of the Optical Society of America*, 55(11):1427–1435, November 1965.
- [3] R.G. Buser. Interferometric determination of the distance dependence of the phase structure function for near-ground horizontal propagation at 6328 angstroms. *Journal of the Optical Society of America*, 61(4):488–491, April 1971.
- [4] D. Dayton, B. Pierson, B. Spielbusch, and J. Gonglewski. Atmospheric structure function measurement with a Shack-Hartmann wave-front sensor. *Optics Letters*, 17(24):1737–1739, December 1992.
- [5] A.S. Gurvich and M.S. Belen'kii. Influence of stratospheric turbulence on infrared imaging. *Journal of the Optical Society of America, A.*, 12(11):2517–2522, November 1995.
- [6] G.D. Boreman and J.C. Dainty. Zernike expansions for non-Kolmogorov turbulence. *The Journal of the Optical Society of America, A*. Accepted for publication in March 1996.
- [7] M. Sarazin and F. Roddier. The ESO differential image motion monitor. *Astron. Astrophys.*, 227:294–300, 1990.
- [8] T.W. Nicholls, G.D. Boreman, and J.C. Dainty. Use of a Shack-Hartmann wavefront sensor to measure deviations from a Kolmogorov phase spectrum. *Optics Letters*, 20(24):2460–2462, December 1995.
- [9] D.L. Fried. Differential angle of arrival: Theory, evaluation, and measurement feasibility. *Radio Science*, 10(1):71–76, January 1975.

Acknowledgements

The data for the survey is being provided by the UK Joint Observatory Site Evaluation project.

Measurements of the Isoplanatic Angle of the Wavefront Tilt

Thomas Berkefeld and Andreas Glindemann

Max-Planck-Institut für Astronomie, Königstuhl 17, 69117 Heidelberg, Germany

e-mail: berkefeld@mpia-hd.mpg.de

Abstract

Investigating the tilt correlation as a function of separation angle, exposure time and aperture, the maximum angular distance between the object and the tip-tilt guide star is determined. This distance can be increased by multiple guide stars.

1. Introduction

The use of a laser guide star for correcting the image degradation induced by the atmosphere does not give any tip-tilt information. To answer the frequently asked questions about the necessary brightness and possible maximum angular distance between the object and the guide star, it is important to determine the minimum sample rate for a desired correlation and the resulting minimum brightness of the natural guide star. Two observing runs have been performed in July 1995 and Februar 1996 to obtain various important parameters for ALFA, the Adaptive Optics System for the 3.5 m telescope of the Max-Planck-Institute for Astronomy at Calar Alto, Spain. Of special interest was the maximum possible angular distance between the object and the natural guide star and possibilities of its increase, resulting in a better sky coverage. We will show that this can be done by using multiple guide stars.

2. Tip-Tilt correlation

In July 1995, the open cluster IC 4996 was observed at K ($2.2\ \mu\text{m}$) with our infrared camera MAGIC¹ at the Calar Alto 3.5-m telescope. The aim was to determine the correlation of the tilt as a function of the angular distance. The exposure time was varied between 65 ms and 200 ms and, using aperture stops, the telescope aperture was reduced from 3.5 m (full aperture) to 1.1 m (1/3 aperture) and to 35 cm (1/10 aperture). The corresponding correlation functions show that for the same value of the correlation the angular distance is about proportional to the aperture. Increasing the exposure time also increases the correlation, although this effect is not very large. The average movement between adjacent frames increases from very short exposure times to a maximum at about 100 ms, and then decreases as the movement is averaged out at long exposure times (see also [2]). The correlation for full aperture and an angular distance of 90 arc sec was about 0.8. It went down to 0.6 for 1/3 aperture and to 0.2 for 1/10 aperture. The strong correlation for full aperture and the weak correlation for 1/10 aperture can be interpreted as good dome seeing, apparently turbulent layers at altitudes higher than 500 m are dominant.

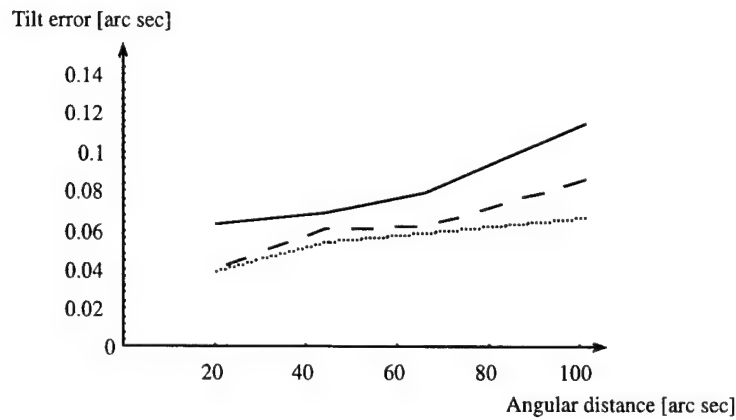


Figure 1: Tilt error as a function of angular distance and number of guide stars. The results for using one (solid line), two (dashed line) and four (dotted line) are displayed.

3. Tip-Tilt-correction with several guide-stars

Usually the star with the smallest angular distance to the object will be used as a tip-tilt reference. The idea of interpolating the tip-tilt from a star field is a logical step³. It is sufficient to interpolate directly, weighting the tilt of each guide star with the inverse of its angular distance to the object. The calculation is done for x- and y-direction separately.

$$\langle pos_{x,y}(obj) \rangle - pos_{x,y}(obj, i) = \sum_{n=1}^N \frac{(\langle pos_{x,y}(n) \rangle - pos_{x,y}(n, i)) w_{x,y}(n)}{\sum_{m=1}^N w_{x,y}(m)}$$

$$w_{x,y}(n) = | \langle pos_{x,y}(obj) \rangle - \langle pos_{x,y}(n) \rangle |$$

The left hand side of the upper equation are the coordinates of the tilt of i-th frame of the object. The weighting factor $w(n)$ depends on the angular distance (x and y separately) between object and guide star n . The power law k of the weighting factor was examined by using two guide stars, the object located between the two, one guide star being twice as far away from the object as the other. The interpolated tilt was compared to the true tilt. k was varied from -0.5 to -2, but the interpolated tilt changed only by a few percent. Furthermore, the power law seemed to depend on the exposure time. Since this effect is very small as well, additional measurements will be necessary to get an exact understanding of this effect. In our tilt corrections, $k = -1$ has been used as the power of the weighting factors.

The results of the comparison between true and interpolated tilts are shown in Fig. 1 and 2, using data of an observation of the Trapezium at $2.2 \mu\text{m}$ in Februar 1996 by H. Hippelein and M. McCaughrean with MAGIC. The observation parameters were $0.81 \text{ arc sec / pixel}$, giving a field of $207 \times 207 \text{ arc sec}$, 0.2 s exposure time and a seeing of 2 arc sec . Figure 1 shows the tilt error as a function of the angular distance and the number of guide stars used (solid line = one guide star, dashed line = two guide stars, dotted line = four guide stars). When using two guide stars, the object was between the guide stars. The four guide stars were chosen in a square configuration with the object in the center.

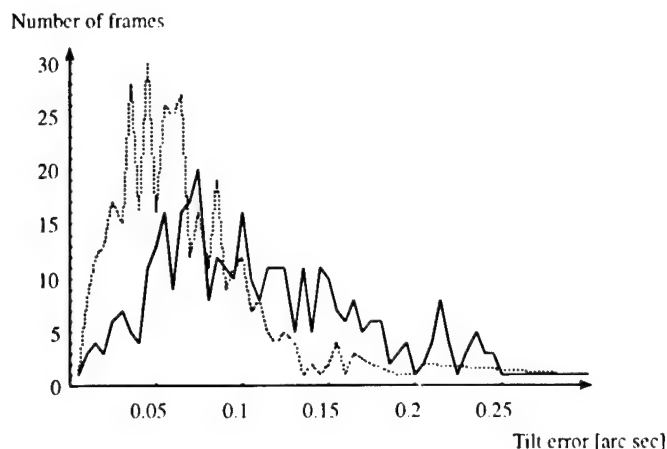


Figure 2: Histogramm of the tilt error.

Even at 100 arc sec angular distance between object and guiding stars the tilt error can be reduced to $< 0.7''$ by using four guide stars (see Fig.1). Compared to the limit of resolution (0.15 arc sec at $2.2 \mu\text{m}$) and to the rms-error of the tip-tilt-system CHARM⁴ of 0.03 arc sec when guiding on the object this result is remarkably good. The seeing of 2 arc sec can be regarded as a worst case. For better seeing the maximum angular distance between object and guide stars is expected to be larger. Observations with shorter exposure times are necessary to test this method on smaller time scales.

Figure 2 shows the histogram of the tilt error for one guide star (solid line) and four guide stars (dotted line) at an angular distance of 100 arc sec. Note that in the case of the single guide star not more than 50% of the tilt corrections fulfill the required accuracy of 0.08 arc sec, whereas in the case of four guide stars about 80% are within this limit.

4. Conclusion

We have shown that the sky coverage can be increased by using multiple guide stars for the tip-tilt correction. This method will be tested when ALFA will be commissioned in autumn of this year. Additional measurements have to be done to determine the power law of the weighting factor at small time scales. Another application of this method is the separation of lower and upper turbulent layers of the atmosphere⁵. By studying the tilt correlations for various apertures and angular distances the contribution of the single turbulent layers to the overall turbulence can be measured.

References

1. T.M. Herbst, S.V.W. Beckwith, Ch. Birk, S. Hippler, M.J. McCaughrean, F. Mannucci and J. Wolf 1993, Proc. SPIE **1946**, p. 605.
2. H.M. Martin 1987, Publications of the Astronomical Society of the Pacific, p. 1360
3. D. Fried 1995, Proc. Adaptive Optics, OSA Technical Digest Series 23, p. 188.
4. A. Glindemann, Mark J. McCaughrean, Stefan Hippler, Karl Wagner and Ralf-Rainer Rohloff 1996, these proceedings.
5. A. Glindemann and T. Berkefeld 1996, these proceedings.

Focal Spot in the Presence of Phase Dislocations

V. A. Tartakovski, N. N. Mayer

Institute of Atmospheric Optics of the Russian Academy of Sciences. Tomsk 634055 Russia

Fax: (3822) 25 90 86 E-mail: zuev@iao.tomsk.su

At present the Hartmann wavefront sensor design has not been sufficiently supported by necessary researches. The motion and structure of focal spots in the region of strong intensity fluctuations and in the presence of phase dislocations of wave function have not been adequately explored.

The Hartmann screen focal spot for the light wave propagating through a randomly inhomogeneous medium was studied in quasimonochromatic and parabolic approximations. To this end, a known numerical model was used¹. In this model, the method of splitting and FFT by the Singleton algorithm were used for solving the wave equation. The Gaussian beam and its angular spectrum were approximated by periodic functions entered in a computer in the form of two-dimensional matrices of their readings. The order of matrix of readings was equal to 90. Two phase-screen setting was used for modeling the turbulence with some Fried's coherence scale r_o for both weak and strong intensity fluctuations. The law of conservation of energy was secured in the model with the computer accuracy. Spectral density of phase fluctuations of the beam and other model parameters are:

$$F_s(\kappa) = 0,489 r_o^{-5/3} (\kappa^2 + \kappa_o^2)^{-11/6}, \kappa_o = 2\pi/L_o, L_o = 1\text{m}, L = 3\text{km}$$

$$r_o = \left[0,423 k^2 \int C_n^2(L) dL \right]^{-3/5} = 0,05\text{m}, k = 2\pi/\lambda, \lambda = 0,6328\mu\text{m}$$

As seen from Fig. 1 (1), the phase dislocations appear at the points where the intensity reaches its minimum. These points correspond to zeros of the wave function. In the vicinity of these points the phase varies spirally. Along the whole length of boundaries between white and black areas in Fig. 1 (2), between two points of dislocation formation, the phase surface undergoes discontinuity of $\pm 2\pi$. Such discontinuity cannot be removed with the use of translations of surface fragments. The focal spot from subaperture without dislocations, Fig. 1 (4), essentially differs from the spots connected with dislocations of the first order in subaperture, Fig. 1 (5, 6, 7, 8). This spots are doubled and the line of minimums between two parts of spot is directed along tangent toward the zero line of the field imaginary part.

The experiment was conducted in support of existence of the second order phase dislocations in a wave propagating in linear randomly inhomogeneous medium. These dislocations were discovered by the following signs. The focal spots from apertures with dislocations of the second order form the triplet. The zero lines of real and imaginary parts of the field are crossed twice at the points of dislocations. The phase addition along the path around the dislocation point reaches $\pm 4\pi$.

The focal spot width is estimated when dislocation points are lacking in subapertures, when dislocations only exist there, and for the both above cases together. Results are shown on Fig. 2.

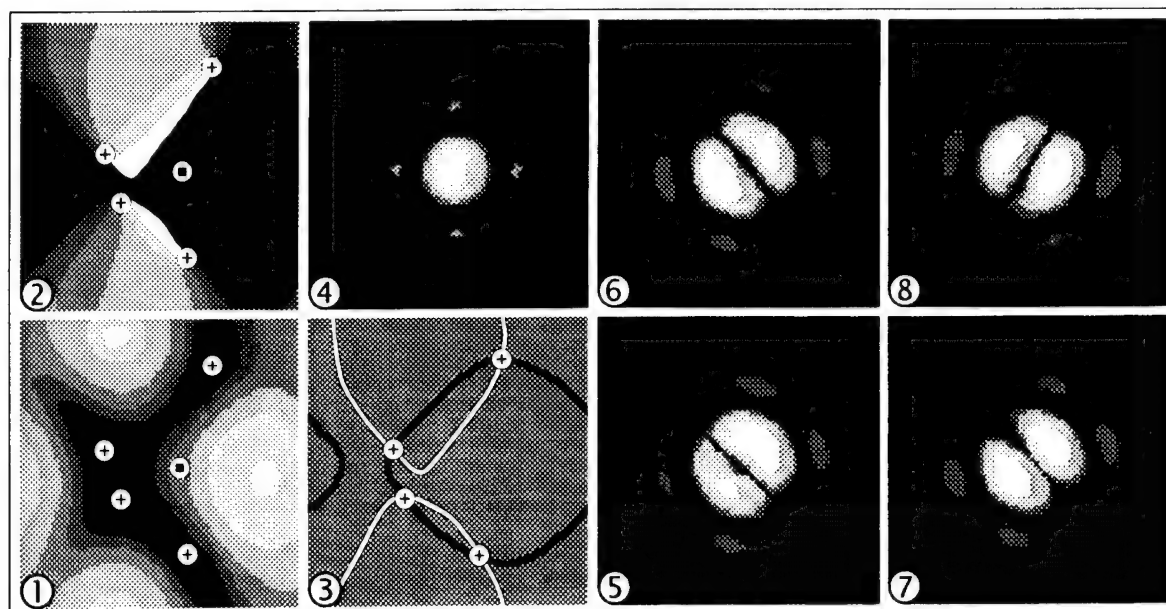


Fig. 1. First order phase dislocations and focal spots created by them. Crosses denote zeros of the intensity and corresponding points of phase dislocations. Focal spots in logarithmic scale. Wave intensity (1). Wave phase (2). Zero-lines of real part (black) and imaginary part (white) of wave function (3). Focal spot for subaperture (square) without dislocations in it (4). Focal spots when the dislocation points are at the following subapertures centers (crosses): down & left (5), down & right (7), up & left (6), up & right (8).

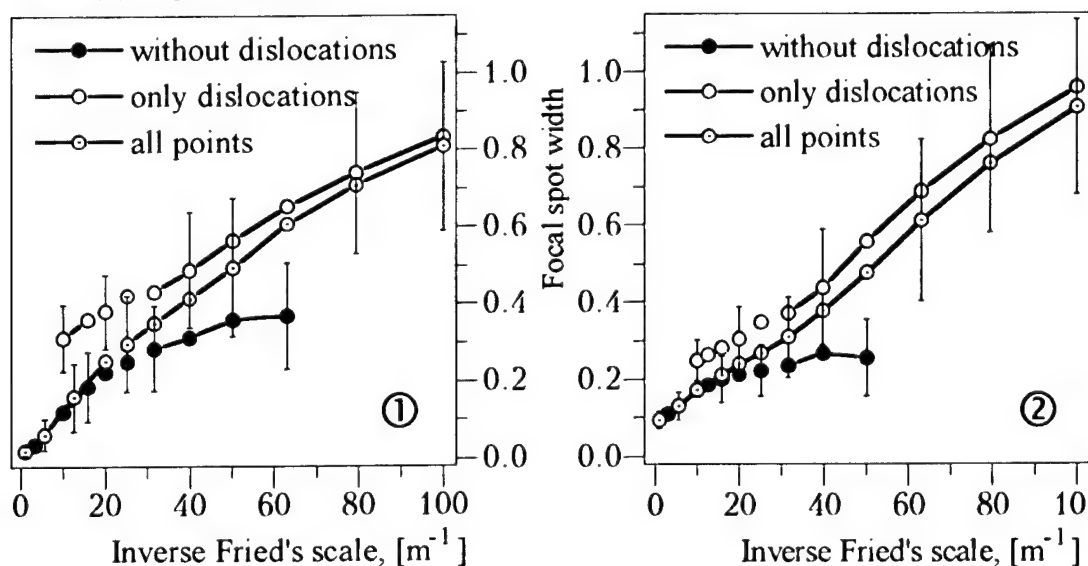


Fig. 2. Estimates of the focal spot normalized width versus turbulence intensification. Normalization is carried out by the subaperture diameter. Ratio of the Hartmann subapertures size to matrix order are: 0.05 for (1), 0.1 for (2). Standard deviation are indicated as confidence intervals. Number of experiments is varied from 20 to 300.

Reference

1. P. A. Konjaev, V. P. Lukin, *Izv. Vyssh. Uchebn. Zaved., Fizika*. №2, 79–89 (1983)

Phasing of Elements of a Primary Mirror of AST-10

V.Lukin, B.Fortes

Institute of Atmospheric Optics, Siberian Branch of RAS,

av.Academicheski, 1, Tomsk, 634055, Russia

tel.(382-2)25-9606, fax:(382-2)25-9086, e-mail: ZUEV@IAO.TOMSK.SU

It is pertinent to note that the applications of adaptive optics (AO) for implementation of the total potential of such a high-power telescope as AST-10 imposes heavy demands on the quality of production, adjustment and phasing of a primary mirror (PM). The atmospheric turbulence was a controlling factor of the image quality for previous generations of telescopes.

Therefore the image quality formed by PM is to be no worse than atmospheric limit. The application of AO enables one to come nearer to the diffraction quality of the image in the IR-range already at the current state of the art in the development of AO and in the future this is also true for the visible range.

The diffraction resolution of a completely phased telescope aperture is the order of $0,01''$ of magnitude for the visible range. Therefore the requirements for the quality of production, adjustment and phasing of PM are very rigid, especially relative to adjustment of separate elements and their phasing. The requirements for production of separate elements remain at the level of traditional for optical systems condition, and the value of errors is of the order of $\lambda / 8$. Practically the same requirement is imposed on the accuracy of the aperture phasing, and the accuracy of angular adjustment of the image is to be no worse than diffraction image diminution, i.e., $0,01''$.

The part of this work may be fulfilled by the AO system capable of compensating both the atmospheric distortions and the distortions occurring in the optical channel. As one of the versions one can suggest the placement of a small segmented adaptive mirror in the plane conjugated with the plane of entrance pupil of PM of AST-10 telescope, corresponding to PM in configuration and the number of elements. In this case the requirements to the accuracy of adjustment and phasing of separate PM elements may be reduced to the level, corresponding to that of turbulent distortions, i.e., of the order of $1''$ by the errors of adjustment and order of $1-2\lambda$ by the precision of aperture phasing. Such an approach decreases considerably the requirements for the precision to the elements of PM segments control, without solving the problem of measurement of disadjustment.

We shall consider some results of carried out calculations of the Point Spread Function (PSF) of the telescope-atmosphere system. To investigate the effect of AST-10 aperture dephasing we gave the optical wave phase within each PM segment accidentally with the use of a program data sensor unit of random

numbers with normal distribution. We shows in paper the PSF for different values of dephasing.

The results of these calculations indicate that the PSF effective width for a dephased aperture is about ten times larger than the width for a completely phased aperture, i.e., the AST-10 angular resolution is determined in this case by diffraction on a separate segment. A clear nucleus of 0,01" size (for $\lambda=0,5 \mu\text{m}$) occurred at $\sigma = \lambda / 6$. This value determines the level of requirements to the accuracy of the aperture phasing, necessary for consideration of the efficiency of the system of adaptive compensation of turbulent distortions.

The PSF peak intensity for the dephased aperture (normalized to the diffraction-limited maximum) is somewhat higher than it may be expected. However, this is dictate by speckled image structure. When blurring the speckle-structure of PSF due to the image jitter or other distortion sources, the normalized peak intensity (the Strehl parameter) is inversely proportional to the square of the PSF angular size and is about 0,01 for a completely dephased aperture.

Similar calculations were performed for investigating the PSF quality with the availability of the error of image tabulation from different segments of AST-10. The inclination of each segment in every of two directions was given as a random value with normal distribution. Here shows the examples of PSF for different values of rms deviation normalized to the angular dimension of the diffraction image λ / D . It is evident that the condition, when the Strehl ratio $\geq 0,5$, results in the requirement for the precision of reduction of $\sigma \leq 4(\lambda / D)$. It is should be noted that the sufficiently well-defined diffraction nucleus is retained in PSF at lesser values of the Strehl parameter up to the value 0,1 ($\sigma=9(\lambda / D)$). This effect has an analog also for partial correction of turbulent distortions.

Partial correction of turbulent distortions

Spatial distribution of turbulent distortions is rather extensive and although the major contribution to the variance of phase fluctuations is introduced by the most low-frequency aberrations (tilts and square-law aberrations) of wave front, at large dimensions of the telescope aperture the correction of these lower aberrations does not improve considerably by the image quality. Therefore for attaining a sufficiently high correction level we need to use the wave front correctors with large number of degrees of freedom.

It is necessary to select such configuration of the corrector, which, on the one hand, does not result in a considerable complication and increase in the cost of AO system, and, on the other hand, could provide a sufficient increase of the image quality. Besides, as far as the correction efficiency is determined by the other AO elements, it is essential that the characteristics of a correcting device (configuration, space resolution, frequency range) should be compatible with the

parameters of the other components of the system of adaptive optics, for example, a reference source and wave front sensor.

At present we know the three main types of wave front correctors, developed for adaptive telescopes, namely; modal, zonal and segmented correctors. We consider the requirements for the spatial resolution of these devices based on simple analytical estimation as applied to the AST-10 project.

Modal corrector

A modal corrector is such a hypothetical means for correction, whose response functions represent a certain analytical basis. The Zernike polynomials, orthonormalized on a circle, are commonly selected as the above basis. Such class of correctors as bimorph mirrors, the information on creation of which has been gathered in Russia, makes it possible to reproduce up to 20-30 Zernike aberrations to the required precision. It is well known that for attaining the level of residual distortion, corresponding to the $\lambda/6$, we obtain the following estimate for the number N of corrected aberrations

$$N = 0,244(D / r_o)^{1,92}.$$

With the number of degrees of freedom of the modal corrector the Strehl parameter is about 0,37. It is apparent that the existing bimorph mirror are incapable of providing such a level of correction in the visible range (when the most probable value of $D/r_o = 40-50$, and $N=400-500$), however, their application for correction in the IR-range (at $D/r_o=10-50$) is fully justified. Moreover, as will be shown below, at larger values of variance of residual error the angular resolution close to the diffraction one can be obtained (determined as PSF width by the 1/2 level from the maximum).

The PSF of the modal adaptive optical system (AOS), obtained by numerical simulation, are presented. The calculations were carried out for several values of the normalized aperture diameter $D/r_o=10, 20, 30$ at the values of $N=3, 10, 15, 21, 28$. The radial sections of the normalized PSF depending on the normalized telescope diameter and the correction parameter N and the dependence of the Strehl parameter on the variance of the phase residual distortions.

It is clear that the sufficiently contrast diffraction nucleus of a partially corrected image can be retained up to the value of the Strehl parameter of 0,01. Really, one can expect that the 10-fold decrease of the image axial intensity results in about its three-fold broadening, because the intensity is inversely proportional to the square of an effective size when the "shape" of intensity distribution in the image plane is invariant. However, while compensating lower aberrations the spatial range of wave front distortions varies greatly. Uncorrected small-scaled aberrations result in the energy redistributions of corrected PSF to the far "wings" (as compared to the turbulent PSF at the same variance of phase

distortions). In this case the effective size of the corrected image turns out to be larger than it would be expected, but the PSF width in the $1/2$ level is found to be slightly different from the diffraction one. This makes it possible to carry out astronomical measurements connected with measurements of angular positions of the objects with an accuracy approximate to a diffraction one even at a comparatively "poor" (by the Strehl parameter) correction.

We can draw the following practical conclusions as applied to AST-10. The use of bimorph mirror (whose characteristics correspond closely with those of modal corrector) can be recommended at first steps of development of adaptive optics for AST-10 as the most accessible now in Russia. In the visible range the correctors of bimorph ideology are unlikely to be relied on if only we do not manage to produce a sufficiently good mirror with the number of control channels about 100-200.

Zonal and segmented correctors

The effect of "near-diffraction" resolution at small values of the Strehl parameters is also possible when using the other classes of wave-front correctors.

Summing up the discussion of the problem of partial correction it should be noted that the effect of occurrence of the sharp diffraction nucleus against the background of the turbulent image manifests itself earlier (for large residual distortions) at higher level of initial turbulence aberrations. It is due to the fact that at lower intensity level of the turbulent component of partially designed PSF, its diffraction-limited part is characterized by a large contrast at the same value of Strehl parameter.

Thursday, July 11, 1996

Wavefront Sensing Techniques and Detectors

AThA 8:00 am-10:10 am
Pikake Room

Presiders:

Brent L. Ellerbroek, *U.S. Air Force Phillips Laboratory*
Robert Q. Fugate, *U.S. Air Force Phillips Laboratory*

Review of CCDs and Controllers: Status and Prospects

James W. Beletic
European Southern Observatory, Germany

Wavefront sensor CCDs and controller electronics are reviewed, including functional systems and those in development. All major programs and manufacturers are presented and compared.

Aluminum Gallium Arsenide/Gallium Arsenide Photon Counting Cameras for Very Low Light Level Wavefront Sensing

Gary C. Loos
USAF Phillips Laboratory
PL/LIMI
3550 Aberdeen Ave SE
Kirtland AFB, NM 87118-5776

Timothy W. Sinor
Developmental Engineering and Special Products
Litton Electron Devices-Garland Operations
3414 Hermann Drive
Garland, TX 75041

J. M. Abraham
Multi-Anode Microchannel Array Laboratory
Electro Optics/Cryogenics Division
Ball Aerospace
P.O. Box 1062
Boulder, Co 80306

Email: Loos@plk.af.mil Tel. 505-846-4410; Fax. 505-846-2045

The feasibility of using adaptive optics (AO) systems on large ground based optical telescopes for producing compensated images of both astronomical sources and artificial earth satellites has been demonstrated by a number of research groups. AO systems consist conceptually of a wavefront sensor (WFS) which measures atmospherically induced wavefront phase perturbations faster than the rate at which they occur and a wavefront phase compensation device, typically a deformable mirror, which takes the WFS data and produces a conjugate phase correction nulling the distortion. In the case of faint sources, the ability of an AO system to produce phase corrections is limited by the signal-to-noise ratio (SNR) in the WFS. In the case of the Shack Hartmann (SH) WFS this limit is a function of the SNR required to estimate with sufficient accuracy the centroid positions of unresolved images of the source formed by a lenslet array on an array of quadrant detectors composing the subapertures of the WFS. Although the use of laser guidestars may allow the substitution of faint source radiation with a bright artificial AO beacon, considerations of cost and complexity motivate a continuing interest in improving the detection sensitivity of a source referenced, low light level (LLL) WFS. This paper explores the promise of aluminum gallium arsenide/gallium arsenide (AlGaAs/GaAs) heterostructure photocathodes coupled to shot noise limited photon counting (PC) cameras and compares their performance with the read noise limited charge coupled device (CCD) cameras often used in this application. Figure (1) illustrates the quantum efficiency of the various detectors to be considered in the study, including two high performance AlGaAs/GaAs photocathodes recently obtained from Litton Electro-Optical Systems.

The subaperture LLL SNR of a SH WFS is given by Equation (1) where η is the detection quantum efficiency, P the number of incident photons, p the number of camera pixels per subaperture, and σ_e^2 the read noise variance, 0 for a PC camera. Figure (2) compares the performance of these photocathodes at low photon rates for the case of quadrant detection, or $p = 4$, with the additional assumption that quantum efficiency is taken to be the maximum value for each detector, independent of wavelength. In this example the two AlGaAs/GaAs photocathodes enjoy a significant SNR advantage

$$SNR = \frac{\eta \cdot P}{\sqrt{\eta \cdot P + p \cdot \sigma_e^2}} \quad (1)$$

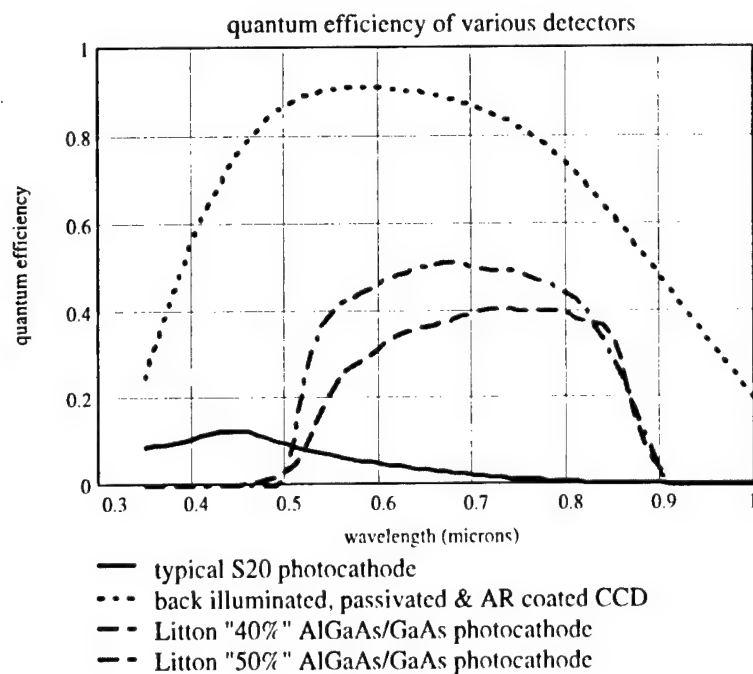


Figure 1

over the CCD based SH subaperture at the level of a few tens of incident photons or less due to the unique combination of high quantum efficiency and shot noise limited detection, i.e. no read noise.

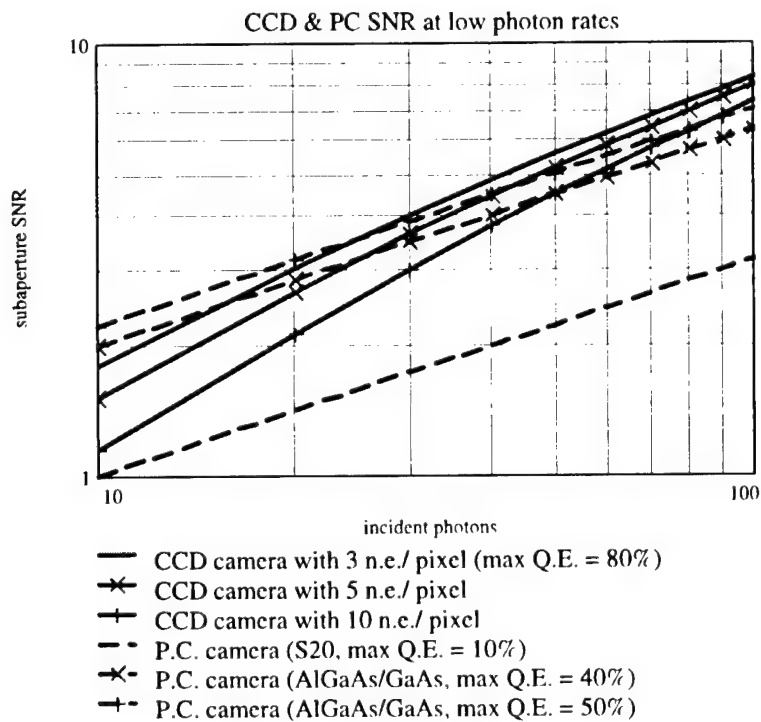


Figure 2

A more accurate description of the comparative performance of these detectors must take into account the spectral dependence of the photoresponse. Furthermore, for astronomical and space imaging applications it is useful to describe limiting detection sensitivity in terms of stellar visual magnitudes.

$$m_1 - m_2 = 2.5 \cdot \log \frac{K_2}{K_1} \quad (2)$$

The relationship between two stars of magnitudes m_1 and m_2 and their detected photocounts K_1 and K_2 is given by Equation (2). This expression may, in turn, be rearranged to yield Equation (3), where

$$K(m_v) = K_{sun} \cdot 10^{\frac{(m_{sun} - m_v)}{2.5}} \quad (3)$$

$m_{sun} = -26.78$ and K_{sun} is the photocount yield for each detector integrated over its photoresponse curve using the sun as a reference source. Inserting Equation (3) into Equation (1) allows the LLL subaperture SNR to be recalculated for this specific example with the subaperture SNR now a function of detectable

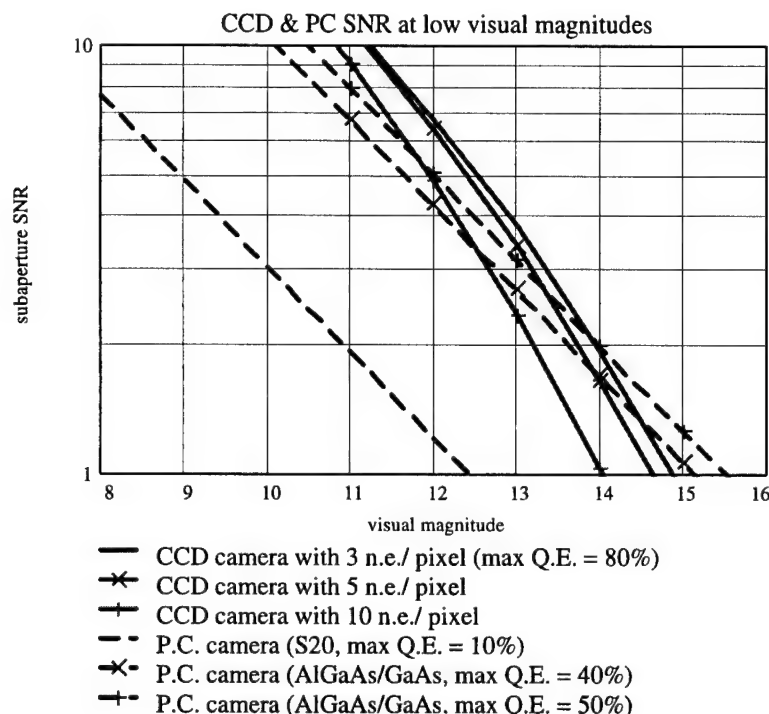


Figure 3

visual magnitude. These results are plotted in Figure (3). Once again, and despite their lower quantum efficiency, the AlGaAs/GaAs photocathodes enjoy a SNR advantage over all of the CCDs at the very lowest visual magnitudes by an amount which is a function only of the CCD read noise.

We have taken a preliminary look at the LLL performance of what may become a new generation WFS devices based upon the use of very high quantum efficiency AlGaAs/GaAs photocathodes. The risk, either financial or experimental, involved in successfully coupling this type of photocathode to the front end of a PC camera may well depend upon that camera's design, construction, and mode of operation. If successfully implemented as WFS devices these new AlGaAs/GaAs PC devices should significantly extend the sensitivity of existing astronomical adaptive optics systems.

Comparison of Adaptive-Optics Technologies for Large Astronomical Telescopes

Brent L. Ellerbrock

Starfire Optical Range, U.S. Air Force Phillips Laboratory
3550 Aberdeen Blvd. SE, Kirtland Air Force Base, NM 87117
(505) 846-4712 ext. 364; fax: (505) 846-2213

Malcolm J. Northcott

Institute for Astronomy, University of Hawaii
2680 Woodlawn Dr., Honolulu HI 96822
(808) 956-8758; fax: (808) 956-4532

François Rigaut

Canada-France-Hawaii Telescope
P.O. Box 1597, Kamuela HI 96743
(808) 885-3164; fax: (808) 885-7288

Doug Simons

International Gemini Project Office
950 N. Cherry Avenue, Tuscon, AZ 85726
(520) 318-8433; fax: (520) 318-8590

The emergence of new wavefront sensing techniques, such as wavefront curvature sensing, opens new pathways for astronomical adaptive optics. Even though the advantages and drawbacks of Shack-Hartmann and curvature wavefront sensing are known [1,2], no direct comparison of complete systems has yet been presented. The goal of this paper is to investigate and compare the performance of Shack-Hartmann and curvature based systems for an eight-meter telescope, evaluated at a $1.6\,\mu\text{m}$ wavelength under median Mauna Kea seeing conditions. This work was made at the request of the Gemini adaptive optics working group, who asked three independent parties to perform adaptive optics system simulations using both technologies. To make the comparison simple enough, a set of conditions was imposed on seeing, telescope size, and wavefront sensor detectors, as summarized in Table 1. Independent simulation codes were used. A common atmospheric turbulence generator provided constant inputs for all packages.

The Gemini adaptive optics working group requested that we consider AO system configurations including either a curvature sensor and a bimorph deformable mirror, or a Shack-Hartmann sensor and a piezostack mirror. The goal of the simulation effort was to develop

AO systems based upon near-term technology which minimized the guide star R magnitude required for an on-axis Strehl ratio of 0.5 at a wavelength of $1.6\ \mu\text{m}$. From here, the three of us were asked to design and carry out the system simulations independantly from each other, to prevent any bias in the results. The free design variables available to optimize system performance were the orders and geometries of the wavefront sensor (WFS) and deformable mirror (DM), the WFS sampling rate, the gain of the adaptive optics control loop, and the matrix coefficients of the wavefront reconstruction algorithm. In a second phase, the results were reviewed by the Gemini adaptive optics working group and additional simulations were performed to cross-check each of our results.

Fig. 1 summarizes the simulated performance of "medium-order" AO systems, in particular a curvature system with 56 subapertures and Shack-Hartmann systems with 9 by 9 and 10 by 10 subapertures. The overall agreement between two independant simulations of each the two technologies is very satisfactory. The performance of the curvature and Shack-Hartmann systems is very close up to $R=15.5$, even though the curvature system has significantly fewer actuators than the Shack-Hartmann system. This results from the fact that curvature systems have better overall efficiency because they correct curvatures, which are less correlated than slopes, therefore providing more information for a given number of subapertures. The fact that the two systems presented here have exactly (within 0.1 magnitude) the same limiting magnitude for an on-axis Strehl ratio of 0.5 at a $1.6\ \mu\text{m}$ wavelength is interesting. This represents an apparent crossover in the performance of the Shack-Hartmann and curvature based systems for the noise conditions adopted for this study, namely noise-free avalanche photo-diodes for the curvature system and five noise electron CCDs for the Shack-Hartmann. It is our feeling that higher order systems would have given the advantage to Shack-Hartmann based systems, whereas lower order systems would have favored curvature sensing, although this would deserve additional work.

REFERENCES

1. Roddier F., Roddier C., Roddier N., 1988, SPIE **976**, 203-209.
2. Rousset G., 1994, in *Adaptive Optics for Astronomy*, pp 115-138, D.M. Alloin and J.M. Mariotti (eds).
3. Racine R., Salmon D., Cowley D., Sovka J., 1991, PASP **103**, 1020-1032.

Telescope diameter	7.9 m
Central obstruction diameter	1.2 m
Sky brightness ⁽¹⁾ in R band	20.3/arcsec ²
R ⁽²⁾ = 0 star	8.2 10 ¹¹ photons/s
Total throughput ⁽³⁾	50%
CCD read-noise	5 e ⁻ rms
CCD read-out rate	max 1 Mpixel/s
APD read-noise	0 e ⁻
APD latency	0 s
Number of phase screens	1
Wind speed	20 m/s
r_0 @ 0.55 μm ⁽⁴⁾	0.25 m
Wavefront sensor wavelength	0.7 μm
Imaging wavelength	1.6 μm

Table 1: Basic parameters used for the simulations. ⁽¹⁾ value for Mauna Kea, dark sky, at zenith. ⁽²⁾ Astronomical R band is centered on 0.7 μm with a effective bandwidth of 0.22 μm . ⁽³⁾ includes optics and detector quantum efficiency (APD or CCD). ⁽⁴⁾ 50% probability at Mauna Kea [3].

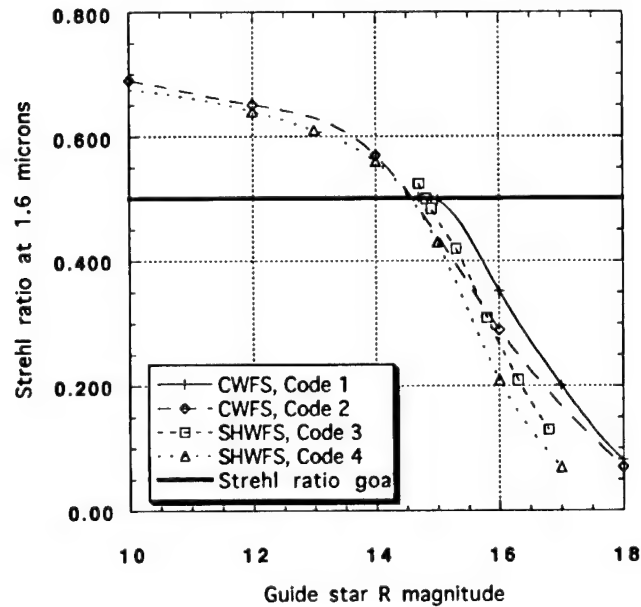


Figure 1: Summary of adaptive optics system performance versus guide star R magnitude for curvature- and Shack-Hartmann-based systems. $D/r_0 = 23.66$ at a wavelength of 0.7 μm , wind velocity = 20 m/s. Codes 1 and 2 simulate a 56 subaperture curvature system, code 3 a 10 by 10 subaperture Shack-Hartmann system, and code 4 a 9 by 9 subaperture Shack-Hartmann system.

Applications of Neural Networks in Adaptive Optics

George J. M. Aitken

Department of Electrical and Computer Engineering, Queen's University
Kingston, Ontario, Canada K7L3N6

Tel: 613-545-2932, Fax: 613-545-6615, Email: aitkeng@post.queensu.ca

1. Introduction

Artificial neural networks have been successfully applied to a wide variety of practical tasks ranging from the recognition of speech and handwriting to the prediction of future stock prices. Highly refined learning procedures allow these multilayer, nonlinear networks to construct internal representations from examples, thus removing the need for explicit programming. The power of neural networks (NN) derives from their ability to learn nonlinear relationships and to generalize from specific training situations. They are advantageous where a small number of decisions have to be made from a large amount of data, and where nonlinear or very complex mappings must be acquired.

The NN architecture suited to adaptive optics (AO) problems is the multilayer perceptron trained by supervised learning using the error backpropagation learning rule [1]. For good performance it is important that the training include the newer procedures developed in recent years to encourage generalization of the process, while discouraging the simple memorization of the training data.

This paper will present a number of AO situations to which NNs have been applied. The potential of NNs to improve AO performance in each case will be assessed, and problems or limitations discussed. An overview of the applications to be discussed is given below.

2. AO Applications of Neural Networks

Wavefront Sensing

Conventional slope-measuring wavefront sensors (WFS) such as the Shack-Hartmann (SH) lenslet array or a shearing interferometer require complicated optical trains that may introduce non-common aberrations between the sensor and science light paths, increase photon loss, and require specialized electronic hardware. Recovery of the wavefront (WF) from image-plane information avoids these problems, but requires a nonlinear inverse operation and additional constraints. In principle, the WF can be recovered from two images, one in focus and the other out of focus. Sandler et al [2] have demonstrated the use of a NN to achieve this nonlinear inverse operation on a single aperture. Angel et al [3] have shown that a NN can be used to co-phase an array of telescopes, and Lloyd-Hart et al [4] have implemented such a system on the Multiple Mirror Telescope (MMT). Sharples et al [5] have also investigated the use of NNs for co-phasing in the Martini AO system. In these applications the NN appears to treat phase recovery as a pattern recognition problem and, after training the weight pattern, shows sets of image features that are correlated in a non linear manner to the phase.

Wavefront Prediction

Short-term prediction of WF distortions could overcome to a large extent the time delay in the deformable-mirror control loop due to WFS integration, computation, and actuator response. Jorgenson and Aitken [6] have demonstrated that stellar centroids measured on one mirror of the MMT could be predicted by a 10-input, 10-hidden-node NN. They have predicted slopes 1 to 4 time samples ahead in WF-slope data taken by the COME-ON AO system operating open loop on the ESO 3.6 m at La Silla. Their spatio-temporal predictor employs 5 steps of past history at each of the 20 SH subapertures (a 100-element input vector) and two 30-node hidden layers to predict the 20 future slopes across the aperture [7]. The NN slope estimates have a mse 2 to 6 times lower than the conventional sample-and-hold (no-prediction) approach. Lloyd-Hart and McGuire [8] have developed a spatio-temporal predictor that uses 5 time steps back, a 160-element input vector, and a 100-node hidden layer to predict 16 x and 16 y slopes. Their tests on simulated data indicate that the NN is clearly superior to a linear predictor, especially at low SNR. Montera et al [9] have used 2 time steps back, a 100-element input vector, and an 200-node hidden layer to predict 25 x and 25 y slopes one step ahead. Their network was trained on data that includes r_0 values from 5 to 20 cm so that it will work over a wide range of seeing conditions. They have shown with simulated data that a single NN can approach the optimized statistical solution over a broad range of seeing conditions, while a single statistical solution can be optimum only for one specific condition. Their conclusion is that NN-prediction is an attractive means of improving AO performance even in the presence of noise. Armitage et al [10] have demonstrated successful temporal prediction of SH spot positions one sample ahead on WF data from the United Kingdom Infrared Telescope (UKIRT).

Prediction within the closed loop is the ultimate objective [11]. In the closed loop the WFS is looking at the difference between the incident and estimated WFs, and the dynamics of the loop must be taken into account. The spectral and temporal characteristics of the WF signal in the loop are quite different from those of the open-loop measurement. The use of NNs in this situation is currently the subject of separate investigations by Lloyd-Hart, Bonaccini and Aitken.

Centroiding

Armitage et al [10] have used NNs to determine the centroids of the lenslet images in the SH WF sensor. With simulated input data and a 4-pixel array, the estimator could achieve a position accuracy of 1%, but as the number of pixels increased the accuracy decreased. Montera et al [9] have found that NNs can perform better than conventional linear position estimators where the unaberrated spot size is comparable to, or smaller than, the pixels. While both methods show a nonlinear relationship between the estimated centroid position and the true position, the NNs provided more accurate estimates over a larger dynamic range and with less estimate variance. The superior performance of the NNs was maintained under noisy conditions. The mse of NN estimates was typically 5 times less than for the conventional centroid estimator used for comparison.

Atmospheric and System Parameters

A number of other NN uses have been investigated: Montera et al [9] have demonstrated that a NN can give better estimates of Fried's r_0 than variance-based methods where the information about the wavefront-slope statistics available to both processes is the same and a small number of WF-slope samples is available. If full statistical information about the wavefront slopes is available a priori, the variance based method is slightly better and on "a level playing

field" the variance-based method can do better than the NN if a sufficiently large number of WF-slope samples is used. NNs have also been used by Montera et al to estimate WF slope measurement error. This is of interest because they have found that the optimum Bayes estimator could outperform NNs for a specific D/r_0 and slope measurement error level. Perhaps the best performance could be obtained from a hybrid system in which the role of the NNs would be to provide accurate estimates of r_0 and measurement error for an optimized minimum-variance reconstructor. Armitage et al [10] have investigated the use of a NN to map the WFS output slopes into Zernicke polynomials. Up to 15 coefficients can be derived. The system, trained on a mixture of WF data from UKIRT and simulated data, could find the coefficients to within 1% on previously unseen test data.

3. Conclusion

While neural networks will not be applicable to every type of problem in adaptive optics, they offer some unique opportunities for system improvement, especially where there are nonlinear transfer relationships. Promising areas for achieving improved AO performance using neural networks appear to be in prediction, centroiding and the estimation of system parameters. In all applications it will be important to assess whether the additional complexity and computing overhead of NN's are justified by the improvements achieved in performance.

References

1. C. M. Bishop, *Neural Networks for Pattern Recognition* (New York, Oxford Univ. Press, 1995) (an excellent new book covering all issues about the backpropagation algorithm)
2. D. G. Sandler, T. K. Barrett, D.A. Palmer, R.Q. Fugate, W.J.Wild, *Nature* 351, 300-302 (1991)
3. J. Angel, P. Wizinowich, M. Lloyd-Hart, D. Sandler, *Nature* 348, 221-224 (1990)
4. M. Lloyd-Hart, P. Wizinowich, B. McLeod, D.Wittman, D. Colucci, R. Dekaney, D. McCarthy, J. Angel, G. D. Sandler, *Astrophys. J.* 390, L41 (1992)
5. R. M. Sharples, A. P. Doel, C. N. Dunlop, J. V. Myers, A. J. A. Vick, A. Glindemann, *Active and Adaptive Optics*, F. Merkle, ed.(ESO, Garching, Germany, 1994) pp 475-477
6. M. B. Jorgenson and G. J. M. Aitken, *Opt. Lett.* 17, 466-468 (1992)
7. M. B. Jorgenson and G. J. M. Aitken, *Active and Adaptive Optics*, F. Merkle, ed.(ESO, Garching, Germany, 1994) pp 143-148
8. M. Lloyd-Hart and P. McGuire, *Proc OSA Adaptive Optics*, Garching, Germany, October 1995, to appear.
9. D.A. Montera, B.M. Welsh, M. C. Roggermann, D. W. Ruck, papers to appear (1996)
10. A.F. Armitage, Y. Guillo and F. Meyer, in *Practical Applications of Neural Networks In Control*, IMC Symposium, London September 1994
11. D. Bonaccini, D. Gallieni, R. Giampieretti, *Proc OSA Adaptive Optics*, Garching, Germany, October 1995, to appear.

Prediction of Wavefront Sensor Slope Measurements Using Artificial Neural Networks

Dennis A. Montera[†], Byron M. Welsh[†], Michael C. Roggemann[†] and Dennis W. Ruck[†]

[†]Department of Electrical and Computer Engineering

[‡]Department of Engineering Physics

Air Force Institute of Technology

Wright-Patterson AFB, OH 45433-7765

(513)255-3636

The resolution of ground based telescopes is limited by the random wavefront aberrations caused by atmospheric turbulence. Adaptive optics systems, which compensate for atmospheric effects, have been shown to improve the resolution of these telescopes. The purpose of an adaptive optics system is to remove the atmospheric induced aberrations from an incident optical wavefront. This is accomplished by measuring the incident aberrations and removing them using a deformable mirror. Correction with a deformable mirror must take into account the effects of additive noise in the wavefront sensor, system time delays, and the possibility of a spatial separation between the object of interest and the beacon used to measure the incident wavefront. While an optimal wavefront reconstruction algorithm, such as the minimum variance reconstructor, can be derived based on statistical knowledge of the atmosphere, noise and other random effects in the adaptive optics system, the actual performance of this reconstructor may be limited by imperfect knowledge of several key parameters [1, 2, 3]. These parameters include both atmospheric and system parameters. The key atmospheric parameters include the Fried coherence length [4], r_0 , the C_n^2 profile, and the wind speed profile. The key system parameter is the wavefront sensor (WFS) mean square slope measurement error. One source of wavefront reconstruction error is the system time delay. While it would be impossible to build an adaptive optical system without delay, it may be possible to predict the wavefront at the time of reconstruction based on the measured slopes. A statistical technique exists for slope measurement prediction which relies on prior knowledge of the key atmospheric and system parameters. This technique is based on knowing the covariance of the measured WFS data. Artificial neural networks, which do not require knowledge of the key parameters or the covariance statistics of the data, are compared to the statistical techniques to see if a single neural network offers the adaptability to perform well over a broad range of parameter values, without prior knowledge of the statistical parameters.

When seeing conditions are set, and thus the statistics of the slope measurements are fixed, a simple linear transformation can be used to perform prediction [5]. If we predict slope measurements at the time of correction based on the previous two frames of measured slopes, then this linear transformation becomes

$$\hat{x}_t = \begin{bmatrix} A_1 & A_2 \end{bmatrix} \begin{bmatrix} x_{t-1} \\ x_{t-2} \end{bmatrix}, \quad (1)$$

where \hat{x}_t is the vector of estimated slopes at time t , and x_{t-1} and x_{t-2} are two previous vector frames of noisy slope measurements. The matrices A_1 and A_2 are found by solving [5]

$$\begin{bmatrix} R_{xx}(0) & R_{xx}(-1) \\ R_{xx}(1) & R_{xx}(0) \end{bmatrix} \begin{bmatrix} A_1^T \\ A_2^T \end{bmatrix} = \begin{bmatrix} R_{xx}(1) \\ R_{xx}(2) \end{bmatrix}, \quad (2)$$

where $R_{xx}(\hat{t})$ is the covariance matrix between two measurement frames separated by time \hat{t} .

This linear transformation is Bayes optimized in the mean square sense for data governed by Gaussian point statistics, and thus represents the best prediction possible for WFS slope data when the statistics of the signal are known. However, implementing such a transformation may not always be possible. Prior knowledge of the signal and

noise covariances are required to produce the matrix $R_{xx}(\hat{t})$. In real world applications, conditions are continually changing and thus these covariances are continually changing. Therefore, knowing which values of signal and noise covariance to use at any given time is a difficult task. Neural networks, which can be trained to operate over a wide range of conditions, offer the possibility of taking advantage of the covariances and correlations between wavefront measurements to implement a prediction scheme. While the best performance that a neural network can obtain is to equal the Bayes optimal solution given above, a network should be able to perform prediction without the need to know the current statistics of the signal and noise.

Before neural networks can be trained to perform prediction, random slope measurements with the proper spatial and temporal statistics are required. For this research, random slope measurements are generated based on turbulence statistics having a Kolmogorov power spectrum and the assumption that the atmosphere can be modeled as N independent turbulent layers, each with its own r_0 and wind speed velocity. An atmosphere with four independent layers based on the Submarine Laser Communication night (SLC-N) profile is used [6]. Also, we must set a limit on the maximum wind speed each layer may have in both the x and y directions before generating data. In an adaptive optics system which does not employ predictive techniques (that is correction after the system time delay is based solely on the measured slope values), wind speed conditions are limited by the correlation between a slope at the time of measurement and that same slope at the time of correction. Statistically, this implies that adaptive optics only improve image quality when the mean square difference of the current true slope measurement and the past noisy slope measurement is less than the mean square variation of the current true slope measurement:

$$E\{(s_t - s_{t-\tau})^2\} \leq E\{s_t^2\}, \quad (3)$$

where s_t represents the true slope at the time of wavefront correction and $s_{t-\tau}$ is the past measured slope, including noise. Simplifying Eqn. (3) into the form of a correlation coefficient yields

$$\frac{E\{s_t s_{t-\tau}\}}{\sqrt{E\{s_t^2\} E\{s_{t-\tau}^2\}}} \geq \frac{1}{2}. \quad (4)$$

Because s_t and $s_{t-\tau}$ are both proportional to $\frac{D}{r_0}$, the left-hand side of Eqn. (4) is independent of $\frac{D}{r_0}$. However, it does depend on the number of subapertures in the wavefront sensor, the mean square slope estimation error of the subapertures, and on the magnitude of the wind speed profile. For this research, when we use a 5×5 array of subapertures (yielding 50 slope measurements, 25 x -slopes and 25 y -slopes), global tilt removed data, and the worst case of slope measurement error 25% of the slope variance, we find that the maximum velocity each layer can have is $0.1D$ per frame. That is if all four layers have both x and y velocities exceeding $0.1D$ per frame, then the system time delay would be sufficiently large that correction using adaptive optics would hurt performance rather than improve it. Therefore, for this research, wind speeds are limited to a maximum of $0.1D$ per frame. This allows comparison of the prediction techniques to the performance of an adaptive optics system which does not implement predictive techniques.

Tests are conducted under varying conditions, and on data with and without global tilt. These tests represent how well neural networks will perform prediction under real world conditions. Because seeing conditions are continually changing, any viable prediction scheme must be able to operate over a useful range of conditions. This test shows the ability of neural networks to function in realistic conditions and still provide benefit. In our tests, a set of slope measurements is predicted based on the previous two frames of measured slope data. For these tests, neural networks are trained to take as input the 100 slope measurements from the previous two frames, and output the 50 slope measurements of the current frame. For each sequence of three frames (2 for inputs and 1 as output) random values for D/r_0 , wavefront sensor mean square slope measurement error, and the wind speed profile are chosen. The value of D/r_0 is chosen between 5-20 representing from 1 to 4 r_0 's per subaperture. Wavefront sensor mean square slope measurement error is modeled as an additive, zero mean, white Gaussian random variable with a variance randomly chosen in the range of 0-25% of the wavefront slope variance. The x and y wind speeds of each of the four layers are randomly chosen between $\pm 0.1D$ per frame. Sets of slope measurements representing three consecutive frames of data with the proper spatial and temporal statistics are generated to train the neural networks. Measurement error is only added to the first two frames (inputs to the neural network) while the third frame is error free. Independent sets of similar data are generated to test the neural networks and the statistical predictors. In the case of slopes with

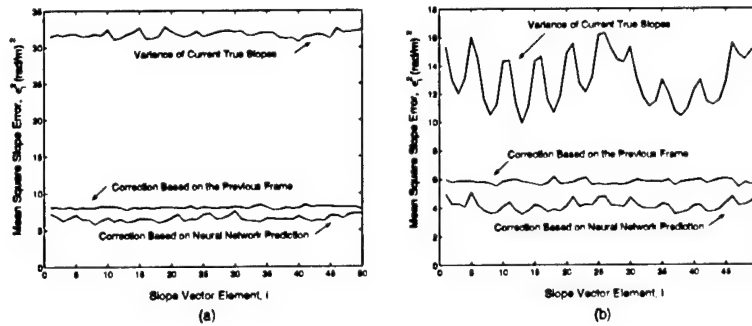


Figure 1: Mean square slope error plotted as a function of WFS slope index on data a) with global tilt, and b) with global tilt removed. Also shown are the variances of the current true slopes. Parameters varying with $\frac{D}{r_0}$ between 5-20, noise variance between 0-25% of slope signal variance, and x and y wind speeds between $\pm 0.1D$ per layer.

global tilt, a neural network with 200 hidden nodes is trained to perform prediction, while a network with 160 hidden nodes is used for data with global tilt removed. Figure 1 shows the result obtained for both cases. In both graphs, the MSE between the true current slope measurements and the predicted slope measurements is shown. Also shown in the figures are the variances of the current true slopes (representing no correction), and the MSE between the current true slopes and the previous frame of measured data (representing correction based solely on the previously measured slopes). The MSE is plotted as a function of the index of the 50 WFS slopes per frame. Figure 1 clearly shows that using a single neural network for prediction reduces the MSE between the true slopes and those that would be used for correction, even if the seeing conditions are allowed to vary over a broad range. In the case with global tilt, correction based on the previous frame reduces the variance of the true slopes by 75%, and correction based on neural network prediction reduces the variance of the true slopes by 79%. When global tilt is removed, correction based on the previous frame reduces the variance of the true slopes by 56%, and correction based on neural network prediction reduces the variance of the true slopes by 68%.

Overall, neural networks offer a viable solution for prediction of WFS slope measurements which helps compensate for system time delay. This reduction of time delay effects, especially in the presence of noise, makes the use of neural networks for WFS slope prediction attractive for improving the performance of adaptive optics systems.

1 REFERENCES

- [1] B. Welsh and M. Roggemann, "Evaluating the Performance of Adaptive Optical Telescopes," NATO Advanced Study Institute, Adaptive Optics for Astronomy, D. Alloin and J.-M. Mariotti editors, Kluwer Academic Publishers, 1993.
- [2] B. Welsh and C. Gardner, "Effects of turbulence-induced anisoplanatism on the imaging performance of adaptive-astronomical telescopes using laser guide stars," *Journal of the Optical Society of America A* pp. 69-80 (1991).
- [3] B. Welsh and C. Gardner, "Performance analysis of adaptive optics systems using laser guide stars and slope sensors," *Journal of the Optical Society of America A* pp. 1913-1923 (1989).
- [4] D. L. Fried, "Optical resolution through a randomly inhomogeneous medium for very long and very short exposures," *Journal of the Optical Society of America* **56**, 1372-1379 (1966).
- [5] S. M. Kay, *Modern Spectral Theory* (Englewood Cliffs, New Jersey: Prentice Hall, 1988).
- [6] S. Troxel, B. Welsh, and M. Roggemann, "Off-axis optical transfer function calculations in an adaptive-optics system by means of a diffraction calculation for weak index fluctuations," *Journal of the Optical Society of America A* **11**, 2100-2111 (1994).

Thursday, July 11, 1996

Adaptive Optics Control Optimization

AThB 10:30 am-11:40 am
Pikake Room

Presiders:

Brent L. Ellerbroek, *U.S. Air Force Phillips Laboratory*
Robert Q. Fugate, *U.S. Air Force Phillips Laboratory*

Optimal Estimators for Astronomical Adaptive Optics

Walter J. Wild

Department of Astronomy & Astrophysics

University of Chicago

5640 S. Ellis Ave.

Chicago, Illinois 60637

An adaptive optics system is a closed-loop servo control system that seeks to maximize PSF Strehl ratio performance by minimizing wavefront distortions. The wavefront is sampled over discrete subapertures and the local slopes are used to estimate the instantaneous wavefront shape which is then used to drive a deformable mirror with a discrete array of actuators. The temporal and spatial performance of the system is embodied in a single mathematical descriptor of the form

$$\Gamma = \langle [\boldsymbol{\varphi}(t_{i+1}) - \boldsymbol{\phi}_{dm}(t_i)][\boldsymbol{\varphi}(t_{i+1}) - \boldsymbol{\phi}_{dm}(t_i)]^T \rangle . \quad (1)$$

Γ is a covariance matrix of the error between the atmosphere phase $\boldsymbol{\varphi}(t_{i+1})$ at time t_{i+1} and the deformable mirror figure, $\boldsymbol{\phi}_{dm}(t_i)$, derived from measurements at the previous time t_i . Boldface quantities are vectors and matrices. The phase reflecting off the mirror is $\boldsymbol{\varphi}(t_{i+1}) - \boldsymbol{\phi}(t_i)$, presently assuming that $\boldsymbol{\phi}_{dm}(t_i) \approx \boldsymbol{\phi}(t_i)$, where $\boldsymbol{\phi}(t_i)$ is the estimated wavefront phase. Covariance matrices are a powerful mathematical tool because they contain information, in an ensemble average sense, about the sources of error and correlations present in the system. From Γ , the Strehl ratio, the MTF, time-delay, etc., can be computed. The Strehl ratio in the Marechal approximation is $S \sim \exp(-\sigma^2)$, where $\sigma^2 = \text{Tr}(\Gamma) / N_a$, for N_a actuators within the pupil.

There are two additional pieces of information and one constraint that enable the information contained in Γ to be used for generating optimal estimators for controlling the system. These estimators are matrices that can be used in existing hardware wavefront reconstructors that perform matrix-vector multiplications. The approach outlined here is for application to existing and many planned systems rather than for systems with reconstructor architectures yet to be built.

The first is the structure of the servo system. Many systems are first-order (or type I) servo loops wherein deformable mirror updates are a correction to the previous mirror shape. A first-order servo is described by the difference equation (Wild et al. 1995)

$$\boldsymbol{\phi}(t_{i+1}) = a_0 \boldsymbol{\phi}(t_i) + k \mathbf{M} [s(t_{i+1}) - \mathbf{A} \boldsymbol{\phi}(t_i)] , \quad (2)$$

where a_0 is approximately unity (a "lossy integrator" to bleed off unobserved modes on the mirror), k is the servo loop gain, and \mathbf{M} is the wavefront estimator. The matrix \mathbf{A} is the gradient or geometry matrix relating the measured slope vector $s(t_i)$ to the phases by the expression

$$s(t_i) = \mathbf{A} \boldsymbol{\phi}(t_i) + \mathbf{n}(t_i) , \quad (3)$$

where $\mathbf{n}(t_i)$ is measurement noise. Here \mathbf{A} specifies the formal mathematical rules governing how slopes are estimated from the phases. Most zonal adaptive optics systems use a digital matrix-vector multiplier to generate $\boldsymbol{\phi}(t_i)$ from the measured slopes using some \mathbf{M} . Equation (2) can be solved for $\boldsymbol{\phi}(t_i)$ in terms of the past history of the measured slope vector, k , \mathbf{M} and \mathbf{A}

$$\boldsymbol{\phi}(t_n) = k \sum_{i=0}^n (a_0 \mathbf{I} - k \mathbf{M} \mathbf{A})^{n-i} \mathbf{M} s(t_i) . \quad (4)$$

If future reconstructor architecture allows iterative use of the past slope data stream, Equation (2) can be generalized and the tools developed here can still be used to seek out optimal estimators which take advantage of these more powerful systems.

The second piece of information is the *a priori* knowledge of the first- and second-order statistics of the turbulence degraded wavefront phase, or Kolmogorov phase covariance matrix, which for times t_i and $t_{i'}$ is

$$\mathbf{X}_{\phi ii'} = \langle \phi(t_i) \phi(t_{i'})^T \rangle. \quad (5a)$$

For conditions where the Taylor frozen turbulence hypothesis holds, with wind velocity \mathbf{v} , the analytic form for the elements of (5a) becomes

$$[\mathbf{X}_{\phi ii'}]_{jj'} = -3.44 \frac{|\mathbf{x}_j - \mathbf{x}_{j'} - \mathbf{v}\tau(i-i')|^{5/3}}{r_0}, \quad (5b)$$

for vector locations \mathbf{x}_j of the actuators in the pupil and Fried parameter r_0 . An outer scale length can be accommodated in the forms of these phase covariance matrices.

Optimal estimators \mathbf{M} are found by imposition of a minimization constraint upon, for example, $\text{Tr}(\Gamma)$, which maximizes the system Strehl ratio. Setting the derivative of $\text{Tr}(\Gamma)$ with respect to \mathbf{M} to zero results in an equation for \mathbf{M} as a function of \mathbf{A} , D/r_0 for aperture diameter D , noise statistics, \mathbf{v} , the framerate, subaperture size, the phase covariance matrices (5b), and servo loop parameters. To demonstrate the process note that it is possible to rewrite Γ as follows

$$\begin{aligned} \sigma^2 = \text{Tr}(\Gamma) = & \text{Tr}[\langle \phi_{dm}(t_i) - \phi(t_i) \rangle \langle \phi_{dm}(t_i) - \phi(t_i) \rangle^T] + \text{Tr}[\langle \phi(t_{i+1}) - \phi(t_i) \rangle \langle \phi(t_{i+1}) - \phi(t_i) \rangle^T] \\ & + \text{Tr}[\langle \phi(t_i) - \phi(t_i) \rangle \langle \phi(t_i) - \phi(t_i) \rangle^T] + \text{cross terms}. \end{aligned} \quad (6)$$

The first term is the fitting error between the shape of the deformable mirror surface and that invoked from the reconstructed wavefront. The second term is the time-delay error and the third is computation error arising from the approximation of the wavefront estimate which depends on \mathbf{M} . An example of estimators for which the third term is important are the iterative estimators, though the increased computation error (per sample time) is balanced by a diminished error propagator (Wild et al. 1995). Equation (6) can be further cast to have terms for off-axis beacons and focal anisoplanatism. The cross terms designate the coupling between these effects, which, for the purposes of Strehl ratio maximization, can be ignored.

Finding an optimal \mathbf{M} entails minimizing any one or a combination of these terms and selecting some $n \geq 0$ in (4). For example, if only the computation-induced fitting error (the third) term is to be minimized, and $n=0$ (the present time step), then the minimization of this term leads to Wiener-Kolmogorov optimal estimator

$$\mathbf{M} = \tilde{\mathbf{X}}_{\phi ii} \mathbf{A}^T \{ \mathbf{A} \tilde{\mathbf{X}}_{\phi ii} \mathbf{A}^T + \alpha \mathbf{X}_{n ii} \}^{-1}, \quad \alpha = \frac{-\sigma_n^2}{\frac{3.44}{[2R_a]^{5/3}} \left(\frac{D}{r_0} \right)^{5/3}}, \quad (7)$$

where $\tilde{\mathbf{X}}_{\phi ii}$ designates that modes such as piston, and possibly tip/tilt, have been projected out of the phases in (5a), R_a is the pupil radius and σ_n^2 is the photon noise variance. When there are high noise levels, i.e., the beacon is dim, α is large whereby useful information resides in the lowest order or smoothest (global) wavefront modes. When σ_n^2 is small (7a) goes to the least-squares limiting form of \mathbf{M} , which is commonly used in most systems.

Since optimal estimators introduce spatial smoothing in the reconstructed wavefront, or a lower probability of occurrence associated with the highest order modes in the wavefront, the waffle mode that appears in systems using the Fried geometry is substantially reduced. This has been demonstrated in experiments. Our tests using optimal estimators were the first time these matrices were ever used in a closed-loop adaptive optics system.

If $n > 0$ is used in (4) in the minimized $\text{Tr}(\Gamma)$, more complex algebraic matrix equations will govern the structure of \mathbf{M} . This hierarchy of equations will be increasingly more complex as n increases. Estimators utilizing the past history of the servo loop via (5b) are referred to as predictive optimal estimators, though strictly speaking they minimize time-delay errors in an ensemble average sense rather than actually predicting future wavefronts.

The information contained in Γ can be used to analyze system performance. The time-delay formula often used is of the form

$$\sigma_{\text{td}}^2 = \left(\frac{\tau}{\tau_0} \right)^{5/2}, \quad (8a)$$

where $\tau_0 = 0.4r_0/v$, $r_0 \approx \lambda^{6/5}$, and $\tau = 1/\text{framerate}$. If $n=1$ in (4) the time delay error is

$$\sigma_{\text{td}}^2 = \text{Tr} \langle [\phi(t_{i+1}) - \phi(t_i)][\phi(t_{i+1}) - \phi(t_i)]^T \rangle = \frac{1}{N_a} \text{Tr} \{ 2\tilde{\mathbf{X}}_{\Phi_{ij}} - \tilde{\mathbf{X}}_{\Phi_{i,j-1}} - \tilde{\mathbf{X}}_{\Phi_{i-1,j}} \}, \quad (8b)$$

assuming a least-squares estimator which satisfies $\mathbf{MA} = \mathbf{I}$, and with servo gain $k=1$. Evaluation of (8b) shows little departure from using (8a) as N_a increases. However, (8b) can be generalized to include $\mathbf{MA} \neq \mathbf{I}$ estimators, arbitrary k , and by using $n > 1$ in (4). These formulae will enable one to quantify the Strehl performance of a low-order system operating with various levels of Zernike or Karhunen-Loeve mode correction by including ("projecting in") only those specific modes in \mathbf{M} .

Other quantities can be derived from Γ , an example being

$$\mathbf{B} = e^{-(1/2)\Gamma}, \quad (9)$$

which is the matrix exponential analog of the MTF of the Kolmogorov phase structure function generalized to include Γ . One example of where \mathbf{B} may be useful is to develop optimal estimators that, at the expense of peak on-axis Strehl ratio, will furnish compensated PSFs that are approximately space-invariant over a field of view that is on the order of several isoplanatic angles in extent. These are areas of continuing research using the tools outlined herein.

From basic mathematical considerations and the tools of matrix algebra a unified adaptive optics paradigm can be constructed enabling characterization of system performance and optimal wavefront estimation that can be parameterized with the closed-loop servo quantities and prevailing atmospheric conditions. Experiments for quantifying the Strehl performance, waffle reduction, and scintillation behavior of the many different forms of \mathbf{M} are either planned or are presently underway. Finally, a very powerful software package, known as \mathbf{A}^+ , and its successive generations, enables most of the estimators discussed herein to be generated with ease.

Wild, W.J., E.J. Kibblewhite, and R. Vuilleumier, "Sparse matrix wavefront estimators for adaptive-optics systems for large ground-based telescopes," *Opt. Lett.* **20**, 955 (1985).

Optimization of Closed-Loop Adaptive-Optics Control Algorithms Using Measured Performance Data: Experimental Results

Brent L. Ellerbroek

Starfire Optical Range, U.S. Air Force Phillips Laboratory
3550 Aberdeen Blvd. SE, Kirtland Air Force Base, NM 87117
(505) 846-4712 ext. 364; fax: (505) 846-2213

Troy A. Rhoadarmer

Center for Astronomical Adaptive Optics
Steward Observatory, University of Arizona, Tucson, AZ 85721
(520) 621-7864; fax: (520) 521-9843

Experiments have shown the reward adaptive-optics provides in improving the resolution of ground-based astronomical telescopes [1,2,3]. A critical contributor to adaptive-optics system performance is the control algorithm that converts wavefront sensor (WFS) measurements into the deformable mirror (DM) actuator commands. For the adaptive-optics systems in use today this control algorithm consists of a wavefront reconstruction step to estimate the instantaneous phase distortion to be compensated [4], followed by a servo control law to temporally filter this instantaneous estimate before it is applied to the deformable mirror [5]. So-called modal adaptive-optics systems can apply different temporal filters to separate spatial components, or modes, of the overall phase distortion [6]. Extensive analysis has been performed to evaluate and optimize the performance of these adaptive-optics control systems [7,8,9,10,11], but the results obtained depend on atmospheric parameters which are seldom known exactly and are constantly fluctuating. The uncertainty and variability of atmospheric conditions implies that an optimal degree of turbulence compensation cannot be achieved or maintained for long time intervals with a fixed control algorithm. A need exists for methods to update adaptive-optics control algorithms based upon actual system performance. Encouraging results have already been obtained demonstrating the value of empirically optimizing the control bandwidths for a modal adaptive-optics system [12]. In comparison, the subject of real-time adjustments to reconstruction matrices on the basis of measured system performance has received little attention.

Any method for empirically optimizing the performance of an adaptive-optics control system must account for the limited linear dynamic range of many WFS's actually in use today. Given sensors with sufficiently large dynamic range, measurements of open-loop phase distortions could be used to determine the spatial and temporal statistics of uncompensated atmospheric turbulence. Optimal control bandwidths and wavefront reconstruction matrices could then be computed from these statistics, using any of the approaches already developed for use with theoretical atmospheric turbulence models. Unfortunately, concerns regarding cost and detector noise effects often lead to Shack-Hartmann WFS designs which minimize the number of detector pixels per subaperture and limit the sensor's linear dynamic range [13]. In this case, accurate phase measurements are only possible for the residual phase distortions remaining after the adaptive-optics loop has been closed. Existing optimization methods developed for use with theoretical atmospheric models are not applicable to such closed-loop data.

This presentation presents a technique which uses experimentally measured performance data from a closed-loop adaptive-optics system to empirically optimize the system's control algorithm. This performance data is supplied by an auxiliary scoring WFS which provides high resolution, low noise closed-loop measurements of a bright star, recorded simultaneously with additional measurements obtained from the primary WFS used to close the adaptive-optics control loop. Empirical correlations between the scoring and primary WFS measurements are used to calculate adjustments to the control algorithm which will minimize the residual mean-square error for the reconstructed scoring WFS phase profile. Depending upon the par-

ticular parameters of the control algorithm which are adjusted, this general process specializes to one of four specific optimization problems:

- Optimizing the wavefront reconstruction matrix for a specified control loop bandwidth,
- Optimizing the control loop bandwidth for a fixed wavefront reconstruction matrix,
- Selecting optimal modal control bandwidths for a predefined modal algorithm with an *a priori* set of modes and wavefront reconstruction matrix, and
- Determining both the modes and associated control bandwidths for a fully optimized modal control algorithm.

The method is applicable to single-guidestar-single-deformable-mirror adaptive-optics systems as well as more complex systems incorporating multiple guidestars or multiple deformable mirrors. Because the scoring WFS requires a bright on-axis natural guidestar (NGS), the method as currently formulated is most applicable for optimizing the adaptive-optics control algorithm once before extended observation of an actual target field. It could also be used to iteratively update the control algorithm in the special case where the target field includes a bright NGS. The more difficult problem of iteratively updating the control algorithm for a laser guide star (LGS) adaptive-optics system while observing a field lacking a bright NGS is not addressed directly by the present technique.

The techniques described in this presentation have been used to empirically determine a wavefront reconstruction matrix for a "hybrid" adaptive optics configuration employing a Rayleigh LGS Shack-Hartmann WFS with 16 by 16 subapertures and a NGS WFS with 8 by 8 subapertures. This experiment was performed in August 1995 using the 1.5-meter telescope at the Phillips' Laboratory Starfire Optical Range (SOR), with the aim of investigating how the effects of focus anisoplanatism might be reduced by augmenting a bright laser beacon with a dim natural guide star. We first closed the adaptive optics control loop using only the Rayleigh WFS measurements and a standard least-squares wavefront reconstruction matrix, and collected 1024 frames of closed-loop LGS and NGS WFS data at a frame rate of approximately 55 Hz. A new reconstructor was computed from these measurements to drive the adaptive optics control loop using measurements from both WFS's, and the system's short-exposure Strehl ratio was increased from about 0.11 to 0.18 (See Fig. 1). We believe that this experiment represents the first stable closed-loop operation of a higher-order adaptive optics control system using multiple guidestars. This significantly improved Strehl ratio was still somewhat inferior to that achieved using only the 8 by 8 subaperture NGS WFS and a standard least-squares reconstruction matrix, indicating that the empirically derived reconstructor was not yet optimal for the given operating conditions. Potential explanations for this result include (i) the limited number of frames of data used to compute the reconstructor and (ii) possible drift in the effective range of the laser beacon over the course of the experiment.

REFERENCES

1. G. Rousset, J. C. Fontanella, P. Kern, P. Gigan, F. Rigaut, P. Lena, C. Boyer, P. Jagourel, J. P. Gaffard, F. Merkle, "First diffraction limited astronomical images with adaptive optics," *Astron. and Astrophys.* **230**, L29-L32 (1990).
2. F. Roddier, M. Northcott, and J. E. Graves, "A simple low-order adaptive optics system for near-infrared applications," *Pub. Astr. Soc. Pac.* **103**, 131-149 (1991).
3. R. Q. Fugate, B. L. Ellerbroek, C. H. Higgins, M. P. Jelonek, W. J. Lange, A. C. Slavin, W. J. Wild, D. M. Winker, J. M. Wynia, J. M. Spinhirne, B. R. Boeke, R. E. Ruane, J. F. Moroney, M. D. Olier, D. W. Swindle, and R. A. Cleis, "Two generations of laser guide star adaptive optics experiments at the Starfire Optical Range," *J. Opt. Soc. Am. A* **11**, 310-324 (1994).
4. R. H. Hudgin, "Wave-front reconstruction for compensated imaging," *J. Opt. Soc. Am.* **67**, 375-378 (1977).
5. G. A. Tyler, "Turbulence-induced adaptive-optics performance evaluation: degradation in the time domain," *J. Opt. Soc. Am. A* **1**, 251-262 (1984).
6. J. Y. Wang and J. K. Markey, "Modal compensation of atmospheric turbulence phase distortion," *J. Opt. Soc. Am.* **68**, 78-87 (1978).

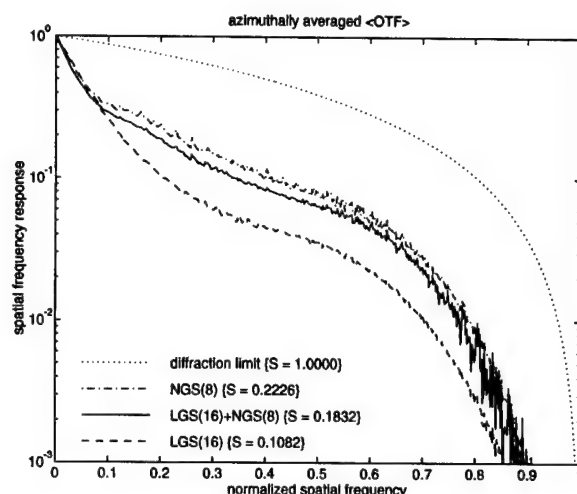


Figure 1: Results obtained from an experiment performed using the 1.5-meter telescope at the Phillips' Laboratory Starfire Optical Range. The purpose of the experiment was to investigate how the effects of focus anisoplanatism in a LGS AO system might be reduced by augmenting a bright laser beacon with a dim natural guide star. LGS (16): The short-exposure OTF achieved using a Rayleigh beacon, a 16 by 16 subaperture Shack-Hartmann WFS, and a standard least-squares wavefront reconstruction matrix. LGS (16) + NGS (8): The improvement achieved with a "hybrid" adaptive optics configuration consisting of a 16 by 16 subaperture LGS WFS, a 8 by 8 subaperture NGS WFS, and an empirically derived reconstruction matrix computed using the techniques described in this paper.

7. E. P. Wallner, "Optimal wave-front correction using slope measurements," *J. Opt. Soc. Am.* **73**, 1771-1776 (1983).
8. C. Boyer, E. Gendron, and P. Y. Madec, "Adaptive optics for high resolution imagery: control algorithms for optimized modal corrections," *SPIE Proc.* **1780**, 943-957 (1992).
9. F. Roddier, M. J. Northcott, J. E. Graves, D. L. McKenna, and D. Roddier, "One-dimensional spectra of turbulence-induced Zernike aberrations: time delay and isoplanicity errors in partial adaptive correction," *J. Opt. Soc. Am. A* **10**, 957-965 (1993).
10. B. L. Ellerbroek, "First-order performance evaluation of adaptive optics systems for atmospheric turbulence compensation in extended field-of-view astronomical telescopes," *J. Opt. Soc. Am. A* **11**, 783-805 (1994).
11. B. L. Ellerbroek, C. Van Loan, N. P. Pitsianis, and R. J. Plemmons, "Optimizing closed-loop adaptive-optics performance with use of multiple control bandwidths," *J. Opt. Soc. Am. A* **11**, 2871-2886 (1994).
12. G. Rousset, J. L. Beuzit, N. Hubin, E. Gendron, C. Boyer, P. Y. Madec, P. Gigan, J. C. Richard, M. Vittot, J. P. Gaffard, F. Rigaut, P. Lena, "The Come-On-Plus adaptive optics system: results and performance," *Proc. ICO-16 Satellite Conf.* 65-70 (1993).
13. T. L. Pennington, D. W. Swindle, M. D. Oliker, B. L. Ellerbroek, and J. M. Spinherne, "Performance measurements of generation III wavefront sensors at the Starfire Optical Range," *SPIE Proc.* **2534**, 327-337 (1995).

Adaptive Correction of Phase-Distorted Extended Source Images: Experimental Results

D.V. Pruidze,¹ J.C. Ricklin,² D.G. Voelz³ and M.A. Vorontsov¹⁻²

1. New Mexico State University, Mechanical Engineering Department
Las Cruces, New Mexico 88003 tel. 505/646-6533 fax 505/646-6111

2. Army Research Laboratory, Battlefield Environment Directorate
White Sands Missile Range, New Mexico 88002 tel. 505/678-1528 fax 505/678-2053

3. Air Force Phillips Laboratory, Optical Sensing Division
Kirtland AFB, New Mexico 87117 tel. 505/846-5162 fax 505/846-2045

We demonstrate a new type of adaptive imaging system capable of improving the quality of phase-distorted images of extended objects. The operational algorithm was based on optimization of the spectral image quality criteria suggested in [1]. For adaptive control of the nine-electrode semi-passive bimorph mirror we used gradient optimization algorithms. To introduce slowly varying large scale phase distortions into the imaging system a second deformable mirror with computer control was used. Small scale phase distortions were created using the nonlinear optics technique described in [2]. Image quality criteria were measured using the optical image quality analyzer described in [1].

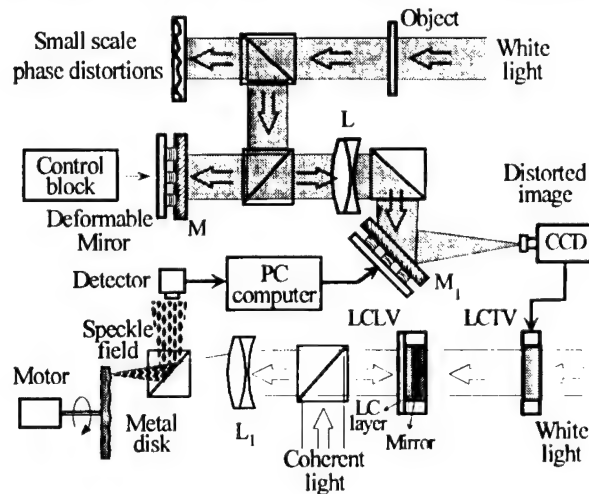


Fig. 1. Experimental setup

The experimental setup is shown in Fig. 1. The lens L images the extended object (a slide illuminated by a white light source) through two phase screens that introduce random dynamic phase distortions having different spatial scales. Using a liquid crystal television (LCTV) connected to a CCD camera and a liquid crystal light valve (LCLV) operating in the phase modulation regime the distorted image $I(\mathbf{r})$ was converted into a phase image having a coherent field complex amplitude of $A_{ph}(\mathbf{r}) = A_0 \exp[i\alpha I(\mathbf{r})]$, where α is the depth of phase modulation. The lens L_1 focuses this field onto a rotating metal disk with rough surface placed in the lens focal plane. As shown in [1], the speckle field

induced photocurrent $i(t)$ fluctuation variance $\sigma_i^2 = \langle (i - \langle i \rangle)^2 \rangle$ in the photodetector plane is determined by the intensity distribution $I_s(\mathbf{r}_F)$ of the coherent field in the focal plane of the lens L_1 , and is given by $J_\sigma \equiv \sigma_i^2 = \int I_s^2(\mathbf{r}_F) d^2 \mathbf{r}_F$. The value for J_σ can be used as an image quality criterion. Minimization of the criterion J_σ using the control voltages u_i ($i=1, \dots, 9$) applied to the imaging system's deformable mirror M_1 results in improved image quality.

For adaptive control we used the following iterative algorithm. Assume the control voltages at the n -th step of the iterative process are $u_i^{(n)}$. Small probe voltages $\delta u_i \cong 10$ -15 volts were then applied to all electrodes of the deformable mirror, and corresponding variations in the image quality criterion $\delta J_i^{(n)}$ were measured. After all variations $\delta J_i^{(n)}$ were determined control voltages were changed according to the algorithm

$$u_i^{(n+1)} = u_i^{(n)} + \gamma_i \text{sign}(\delta J_i^{(n)}), \quad (1)$$

where γ_i are constants. The time required for one-step wavefront control was on the order of 0.8 second. This time was primarily limited by the LCLV time response. Typical results for adaptive correction of an extended source phase distorted image are shown in Fig. 2 and Fig. 3. At the beginning of the adaptation process ($n=1$) a defocus-type static aberration was introduced into the system by applying 250 volts to all nine electrodes of the deformable mirror M in Fig. 1. The interferogram corresponding to this aberration and the distorted image are shown in Fig. 2a and Fig. 3a. The adaptation process continued through ten iterations with the resulting image shown in Fig. 3c. After $n_A=40$ iterations the feedback was disconnected by nulling the constants γ_i in (1), and an astigmatism type aberration was introduced into the imaging system. The interferogram of this aberration is shown in Fig. 2b, and the corresponding distorted image in Fig. 3b. After 20 steps without adaptation ($n_A < n < n_B$ in Fig. 2) the feedback was turned back

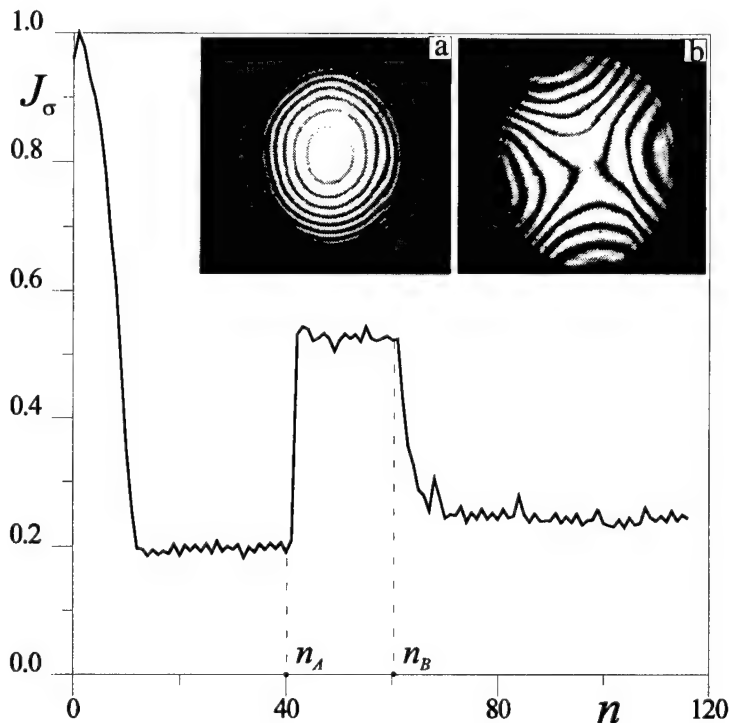


Fig. 2. Image quality criterion vs. the number of adaptation process iterations. The region $1 < n < n_A$ depicts spherical aberration alone; for $n > n_A$ both spherical and astigmatism type aberrations exist; for $n_A < n < n_B$ the feedback is off. Interferograms of aberrations: (a) spherical, (b) astigmatism.

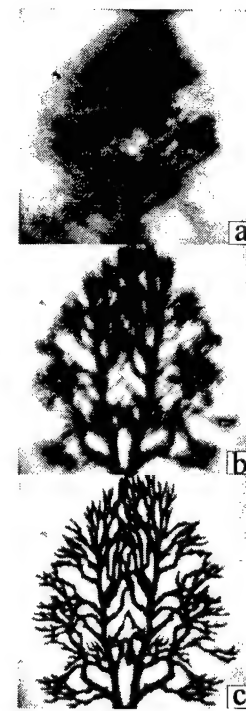


Fig. 3. Images during the adaptation process: (a) $n=1$; (b) $n=50$; (c) $n=100$.

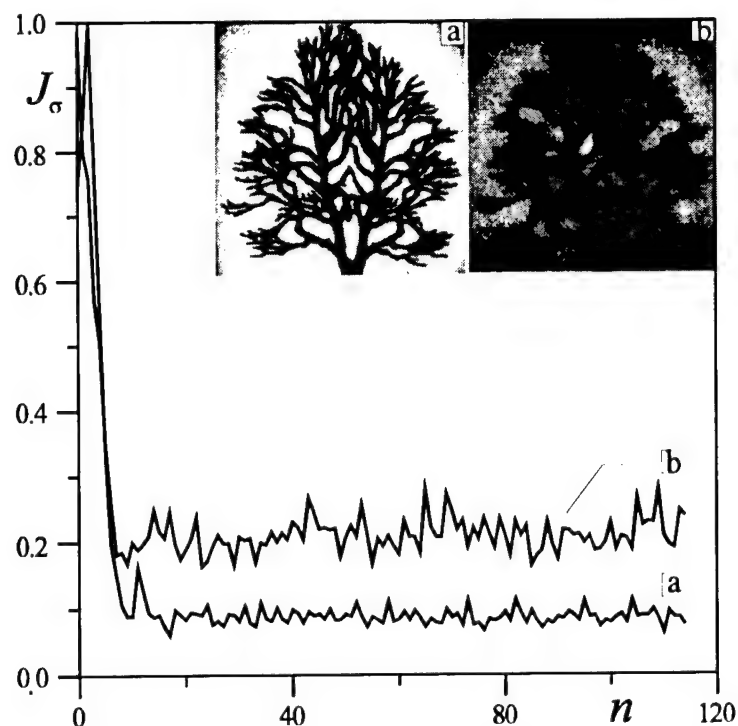


Fig. 4 Adaptation process curves with corresponding improved images: (a) large scale aberrations only; (b) large and small scale aberrations.

BIBLIOGRAPHY

1. M.A. Vorontsov, G.W. Carhart, D.V. Pruidze, J.C. Ricklin and D.G. Voelz, "Image quality criteria for an adaptive imaging system based on statistical analysis of the speckle field," J. Opt. Soc. Am. A (in press).
2. M.A. Vorontsov, J.C. Ricklin and G.W. Carhart, "Optical simulation of phase-distorted imaging systems: nonlinear and adaptive optics approach," Opt. Eng. 34(11), 3229-3238 (1995).

on. The improved image obtained by the adaptive system after this transition process ($n=100$) is shown in Fig. 3c.

Introducing small scale aberrations into the imaging system did not interfere with the efficiency of system operation. The adaptive system compensated only phase distortions resulting from large scale aberrations, which still resulted in improved image quality. The corresponding process is shown in Fig. 4. In the presence of small scale aberrations the stationary state value for the image quality criterion is larger, which corresponds to a decrease in image quality [compare curves and images (a) and (b) in Fig. 4].

Thursday, July 11, 1996

Poster Previews: 3

AthC 11:40 am-12:15 pm
Pikake Room

Peter L. Wizinowich, *Presider*
W.M. Keck Observatory

Fast CCD Imaging Systems for Tilt-Tip and Wavefront Sensing Applications

Craig D. Mackay

Institute of Astronomy, Madingley Road, Cambridge, CB3 0HA, England
and

AstroCam Ltd., Innovation Centre, Cambridge Science Park, Milton Road,
Cambridge, CB4 4GS, England

E-Mail: cdm@ast.cam.ac.uk Tel: +44-1223-337543 Fax: +44-1223-330804

New generations of fast, low-noise CCDs and their controllers are achieving the read-out noise and high frame rates that are critical to the successful completion of true adaptive optics systems. We describe the performance achieved for a variety of systems from those on COAST (Cambridge Optical Aperture Synthesis Telescope), the site evaluation program on the William Herschel Telescope on La Palma, and the results from the latest fast CCDs and new generation of CCD controllers.

Scan-Hartmann Wavefront Sensor

Valeri A. Tartakovski, Vladimir P. Lukin

Institute of Atmospheric Optics of the Russian Academy of Sciences. Tomsk 634055 Russia

Fax: (3822) 25 90 86 E-mail: zuev@iao.tomsk.su

Lomonosov and Descartes had known about the first principles of the Hartmann measurements. There are many references¹ to a classical version of this method concerning testing the telescope optics. At the modern stage the Shack-Hartmann sensor is used.

Some directions can be suggested to improve the method. A few of them were described in Refs. 2, 3. Here some other problems are formulated, the results of research and the sensor schematic are presented.

On the first place is the change of spatiotemporal resolution during measuring according to the light intensity fluctuations at the input aperture points. The areas with high intensity must be measured more precisely and inverted with less delay comparing with the low intensity areas.

Secondly, it is the removal of the boundary large ripples in signal and its filtering by FFT on closed lines on the aperture plane instead of least-square polynomial fitting. The latter case results in the linear set of equation which order is equal to the basic function number that is *a priori* essential for specific situations in the atmosphere but in practice it is hard to get this necessary number owing to noises. It must be noted that FFT-codes are very adaptable and have more operating speed than conventional codes solving the linear systems.

Third direction is the dynamic control of the subaperture size in accordance with a level of intensity fluctuations so as to change the focal spot size and its motion range. The Shack-Hartmann sensors with prisms solve this problem in statics, of course, but it is desirable to increase the spatial resolution.

The schematic in Fig. 1 could be called as the Scan-Hartmann sensor. This device has only one aperture on which the beams are scanned for measuring. There are two beams in this case: the first is called as an object beam and the second as a reference one, but the latter can be removed. The scanner or deflector is a plane mirror (4) with three actuators. From the aperture (6) the light going through Fourier-transformer (7) gets as focal spots to coordinator (8) which tracks total energy and displacement of spots. Usually the tracking parameter is time but another variable can also be used. There appear later the differences between abscissas and ordinates of the object and reference beams at the inputs of summators (9, 10). These differences as phase derivatives by tracking parameter are multiplied (11, 12) by trajectory derivative from generators (14, 15) and get to inputs of integrator (13). Later, at this integrator output the phase appears as a function of the tracking parameter $\varphi(t)$. Generators (14, 15) create at their outputs the trajectory derivatives by the tracking parameter. The trajectory form is first defined and then corrected during scanning by total energy of the focal spot through inputs connected with the coordinator (8). The influences of the above two actions on the trajectory form are programmed. The signals at outputs of generators (14, 15) are integrated, added, and actuate the deflector (4).

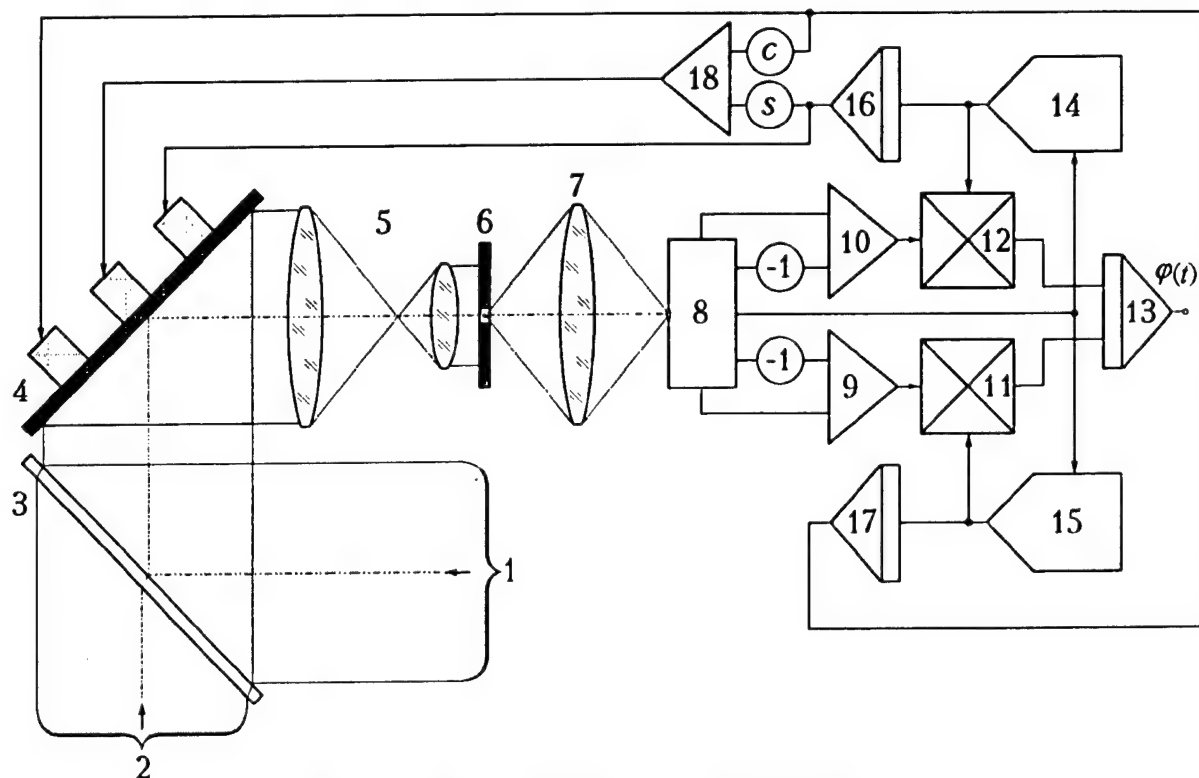


Fig. 1. Scan-Hartmann wavefront sensor.

Tracking parameter is time. Object beam 1. Reference beam 2. Optical summator 3. Deflector with actuators 4. Scale optical system 5. One subaperture Hartmann screen 6. Lens Fourier transformer 7. Coordinator to track total energy and displacement of two focal spots 8. Summator to calculate the object spot relative displacement 9, 10. Multiplier to form the phase derivative by tracking parameter 11, 12. Integrator to form the phase as a function of tracking parameter 13. Generator of derivative of trajectory by tracking parameter 14, 15. Integrator of trajectory to form the first and second actuator control 16, 17. Summator for control forming of the third deflector actuator 18.

The most interesting property of the Scan-Hartmann wavefront sensor operation is a possibility to estimate the restored phase error *a posteriori* using differing and orthogonal scanning in the same areas.

References

1. E. A. Vitrichenko, V. P. Lukin, L. A. Pushnoi, V. A. Tartakovski
Problems of Optical Testing. Novosibirsk. Nauka. 1990. 351 p.
2. V. E. Zuev, V. P. Lukin, V. L. Mironov, V. A. Tartakovski
Problems of Wavefront Sensor Design // Third All-union meeting on atmospheric optics & actinometry. Part II. Tomsk. IOA SO AN SSSR. 1983. P. 5-13.
3. L. V. Barabina, V. P. Lukin, V. A. Tartakovski
Numerical Model of the Hartmann Wavefront Sensor with FFT // Optical wave propagation in the randomly inhomogenous medium. Tomsk. IOA SO AN SSSR. 1988. P. 49-55.

Combined Wavefront Sensor with Internal Reference

Source: experimental study

Vladimir I. Podoba, Vadim A. Parfenov, Alexander G. Seregin

Research Center "S.I.Vavilov State Optical Institute"
12 Birzhevaya line, St.Petersburg, 19034, Russia
Fax: (812) 218-3720, E-mail: parfenov@soi.spb.su

A wavefront sensor (WFS) is the key element of ground and space-based adaptive telescopes that provides a high accuracy and reliability of the operation of an adaptive mirror control system. We developed a new WFS in the scope of the project of a 3.2 m adaptive astronomical telescope with a wide angular field of view [1]. It has two parts - channels: an autocollimation-point sensor and interferometric (or Hartmann) one. The WFS is to be installed at the autocollimation point of low efficiency hologram structure on the controllable surface of the adaptive mirror [2]. Such a WFS combines two useful features: a high accuracy of interferometers and a wide angular range of operation in comparison with ordinary interferometers. Therefore, it provides the necessary information for initial alignment of the mirror and allows to diminish requirements to the rigidity of a telescope construction.

We investigated a model of the WFS in the optical scheme including a mirror of 160 mm diameter with holographic structure on its surface and CW single-frequency Nd:YAG laser. The original holographic structure was made up by Dr.S.N.Koreshev. The mirror was considered as a segment of the telescope primary mirror. The construction of the laser allowed to get a generation either at 1064 nm or at 532 nm. Aberrations of the wavefront formed by the hologram structure were interferometrically measured at that wavelengths and found to be equal to 46 nm and 28 nm (rms) respectively. The operation of the WFS at 1064 nm is preferable, as it was shown earlier [3]. Also, we determined within what range of the segment inclinations (misalignments) the quality of the autocollimation point keeps to be acceptable. The limit angle appeared to be no more than 4 arcsec. It is in a good agreement with the calculations [4].

So, our experiments confirmed expected parameters and reliability of the WFS proposed for telescopic systems of different applications.

References

1. D.N.Yeskov, B.E.Bonshtedt, S.N.Koreshev et al. Adaptive astronomical telescope with two-stage wavefront correction: current status of a project in *Adaptive Optics*, Vol.23, 1995 OSA Technical Digest Series (Optical Society of America, Washington DC, 1995), pp.199-201.
2. M.A.Gan, B.A.Ermakov, D.N.Yes'kov et al. Problems of phasing a space telescope large segmented adaptive mirror for astronomy. *Transactions of S.I.Vavilov State Optical Institute*, 1989, Vol.74, N 208, pp.42-54 (in Russian).
3. V.V.Anistshenko, S.N.Koreshev, V.A.Parfenov, V.I.Podoba, A.G.Seregin, V.I.Sidorov. Laser interferometric control problems in adaptive astronomical telescope. *Proceedings of SPIE*, 1994, Vol.2200, pp.581-592.
4. A.G.Seregin, I.S.Potemin, V.I.Sidorov, T.N.Tul'eva. Autocollimation-point sensor in the control channel of an adaptive telescope. *Journal of Optical Technology*, 1995, Vol.62, N 10, pp.696-700.

Discrete-zonal method for widening field of view of adaptive telescope

V.I.Podoba, B.E.Bonshtedt, S.N.Koreshev, V.B.Lakhtikov, G.I. Lebedeva,
A.G.Seregin, D.N.Yeskov

Research Center "S.I.Vavilov State Optical Institute"
12, Birhevaya line, St.Petersburg, 199034, Russia
Fax: (812) 218-3720

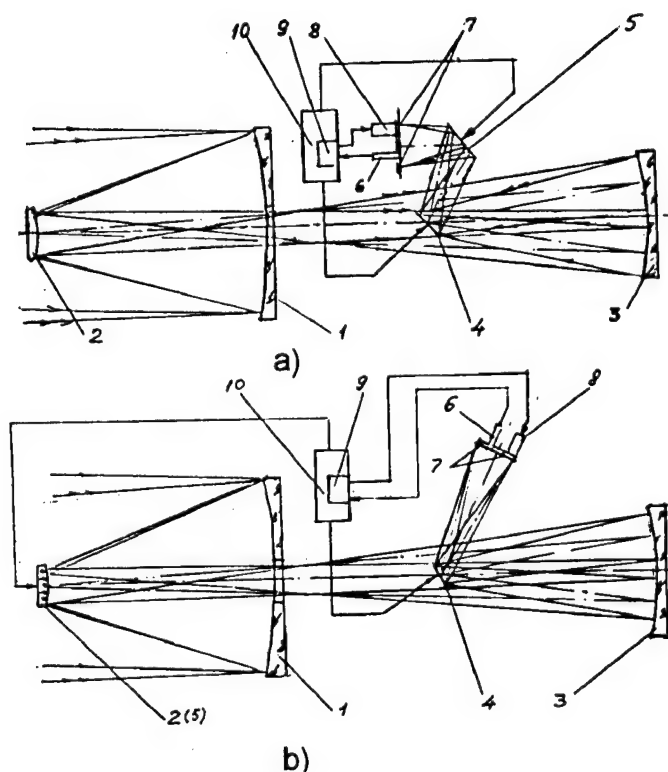


Fig 1. Telescope schematics. In the Figure: 1 - primary mirror, 2 - secondary mirror, 3 - field mirror, 4 - primary mirror corrector, 5 - secondary mirror corrector, 6 - wavefront sensor, 7 - photoreceiver, 8 - electronics, 9 - controller, 10 - control system

At present some large-scale programs are carried out in various countries that are aimed towards development of a new class of ground and space-based telescopes. Principal features required for modern telescopes are following: wide spectral range (from 0.2 up to 1000 mkm), high angular resolution of the order of 0.02 arcsec, large angular field of view (FOV) up to 1 degree, minimal dimensions and weights.

Several optical schemes are proposed to meet these requirements. Classical two-mirror systems provide a high spatial resolution only in the range of several arcmins with the presence of an image curvature. To make image wider and plainer telescope must have lens correctors. But such correctors can operate only in the visible part of spectrum. It is clear that such telescopes will not provide the desired width of spectrum range. D.Korsch suggested a three-mirror configuration where the third mirror corrects the image curvature and the real exit pupil exists [1]. It became a prototype for two-stage optics concept by A.Meinel and colleagues [2]. In the Meinel-Korsch configuration the first stage (primary and secondary mirrors) of the telescope forms an aberrated image while the second

stage eliminates field aberrations and corrects wavefront errors at the real exit pupil of the telescope by a small corrector.

Nevertheless, this configuration does not solve the task of the full compensation of primary mirror errors as pencils of light-rays fall on corrector at different angles for different fields of view. It was shown that correction may be reached with the desired accuracy only for some vicinity of the point on the optical axis or for enough narrow annular zones at the image plane [3].

We propose a new method to widen the FOV of the telescope. This method is based on using a system for direct and/or indirect control of asphericity of primary and secondary mirrors. A controller, a wavefront sensor and a photoreceiver of special construction are additionally introduced into the construction of the telescope to synchronously control the asphericity of the mirrors and read the information for each discrete zone under correction. The algorithm of the control consists in successive correction of the image quality for several overlapping annular zones of the image followed by synthesis of the total image of desired quality. Successive shift is performed from central to peripheral annular zone. Two versions of optical configuration for the proposed method realization are shown in the Fig.1a (with two small correctors in the second stage) and Fig.1b (first corrector at the exit pupil plane, second corrector is joint with the secondary).

A great challenge is the construction of the secondary mirror. The idea of controlling the secondary mirror to compensate atmosphere disturbances was suggested by V.Linnik in 1958 [4]. New techniques for optical fabrication of a 2-mm-thick adaptive secondary mirror were described in [5].

Our proposal discovers further perspectives for the development of telescopes with high quality of image and large field of view.

REFERENCES

1. Korsch D. USA Patent N 4101195, 18.07.1978.
2. Meinel A., et al. USA Patent N 4836666, 06.06.1989.
3. Yeskov D., Bonshtedt B., Lebedeva G., Rodionov S. *Journal of Optical Technology*, 1995, Vol.62, N 10, pp.13.
4. Linnik V.P. The proceedings of the conference on the study of star blink. Moscow, June 18-20, 1958, published AN SSSR, Moscow, 1959, p.228-232.
5. Martin H., Anderson D.S. in *Adaptive Optics*, Vol.23, 1995 OSA Technical Digest Series (Optical Society of America, Washington DC, 1995), pp.213-215.

Focault-like Wave-Front Sensor

A. Riccardi, S. Esposito, R. Ragazzoni, L. Fini, P. Ranfagni
Observatorio Astrofisico di Arcetri, Italy

We present first laboratory results for a focault-like wave-front sensor suitable for adaptive optics systems based on a squared-based refractive pyramid.

Experimental Comparison of Two Approaches for Solar Wavefront Sensing

Thomas R. Rimmele

National Solar Observatory

P.O. Box 62, Sunspot, New Mexico 88349

(505) 434-7000 FAX (505) 434-7029

Richard R. Radick

AF Phillips Laboratory, Solar Research Branch

P.O. Box 62, Sunspot, New Mexico 88349

(505) 434-7000 FAX (505) 434-7029

The Sun presents unusual problems for wavefront sensing. Unlike the nighttime sky, the Sun does not provide natural, high-contrast point sources, and creation of laser beacons bright enough to be visible against the solar disk poses major technical and operational problems. Small sunspots and pores can provide satisfactory substitutes for point sources, but these are available for only a tiny fraction of the solar disk. Wavefront sensing at arbitrary locations on the Sun requires a sensor capable of using the ubiquitous solar granulation as its target. Solar granulation is extended (its characteristic angular scale is about one arcsecond), unbounded (the angular extent of the composite granulation pattern greatly exceeds the isoplanatic angle), low contrast (a few percent), and both spatially and temporally variable (the typical evolution time scale is minutes). Conventional wavefront sensors such as shearing interferometers and simple Shack-Hartmann position sensors have difficulty dealing with targets having these characteristics, and therefore are not well-suited for general solar imaging.

Motivated by a desire to develop adaptive optics techniques for solar imaging, we have undertaken a series of experiments at the Sacramento Peak Vacuum Tower Solar Telescope to compare the performance and limitations of various wavefront sensor concepts for solar imaging. We have recently focussed our attention on two approaches: (a) a modified Shack-Hartmann sensor, and (b) an amplitude modulation or spatial filtering procedure, understandable in terms of the classic Foucault knife-edge test, and first proposed for solar wavefront sensing by von der Lühe(1).

The simple centroiding algorithms used by conventional Shack-Hartmann sensors do not work well with the complex and unbounded geometry of solar granulation, so we have adopted the more sophisticated cross-correlation technique as our tracking procedure. The availability of affordable high-speed digital hardware and the option of exploiting (if necessary) the intrinsic

parallelism of the Shack-Hartmann configuration persuade us that the increased computational burden of cross-correlation tracking need not fatally compromise the sensor's ability to meet the bandwidth requirements of real-time adaptive optics. In principle, the arcsecond size and the low contrast of the solar granulation could also handicap the performance of a Shack-Hartmann wavefront sensor (or any other wavefront sensor that performs aperture subdivision): as the seeing degrades, the need to use smaller subapertures could adversely affect the ability to resolve the target structure with sufficient contrast to track easily. Our experiments suggest that this may not be a serious concern in practice: we have found that subapertures as small as 6.5cm offer sufficient resolution to correlation-track solar granulation successfully.

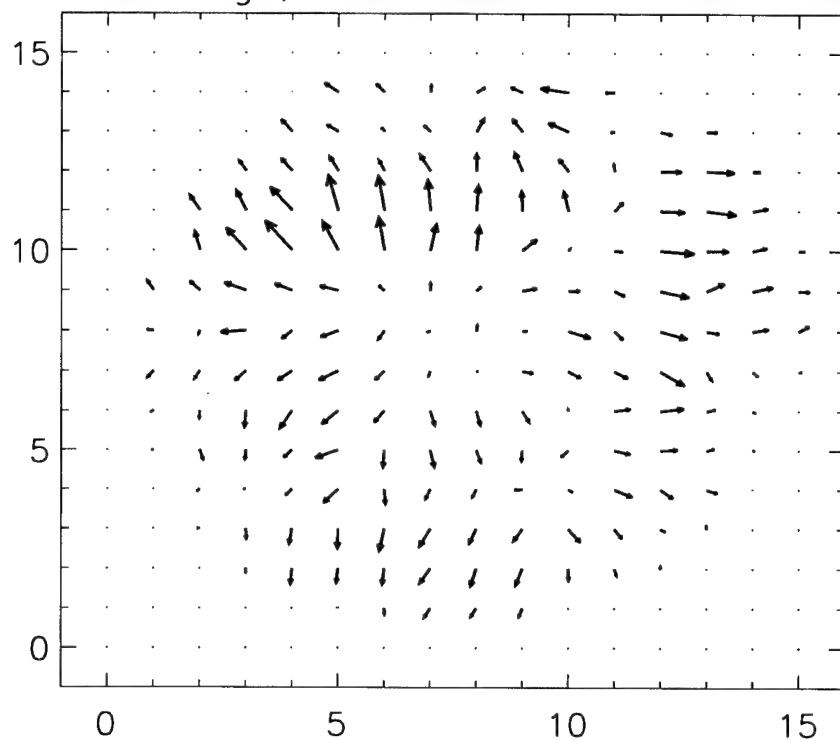
Considerable effort at the National Solar Observatory has also been directed toward developing the von der L  he concept as a real-time wavefront sensor. This sensor uses a programmable, transmissive screen (a liquid crystal display, for instance) to create an array of knife-edge equivalents that follows the intensity contours of the granulation pattern. It substantially substitutes optical processing for digital computation, which makes it attractive from the standpoint of bandwidth. Furthermore, its avoidance of subapertures suggests that its performance should not react strongly to seeing changes. However, its realization also raises worrisome engineering issues that remain to be solved.

Because it is new technology, we are studying von der L  he sensor through extensive mathematical analyses, computer simulations, and experimental measurements. We recently completed an experimental comparison its performance with respect to our modified Shack-Hartmann sensor through simultaneous measurements. For these comparisons we used extended, high-contrast targets (Venus and sunspots), and a fixed mask of two complementary knife-edge pairs (which will eventually be replaced by the LCD). Each of the two knife-edge pairs creates an intensity map of one Cartesian component of the local wavefront gradient. These data have been used to synthesize vector maps of the wavefront gradient, which may be directly compared to the corresponding Shack-Hartmann vector displacement maps. One of these synthetic vector maps is shown in one panel of the figure below. The other panel shows the Shack-Hartmann displacement map, computed for an 12x12 subaperture array covering the 76cm pupil of the telescope. Clearly, the wavefronts are virtually indistinguishable, demonstrating the essential equivalence of the two approaches.

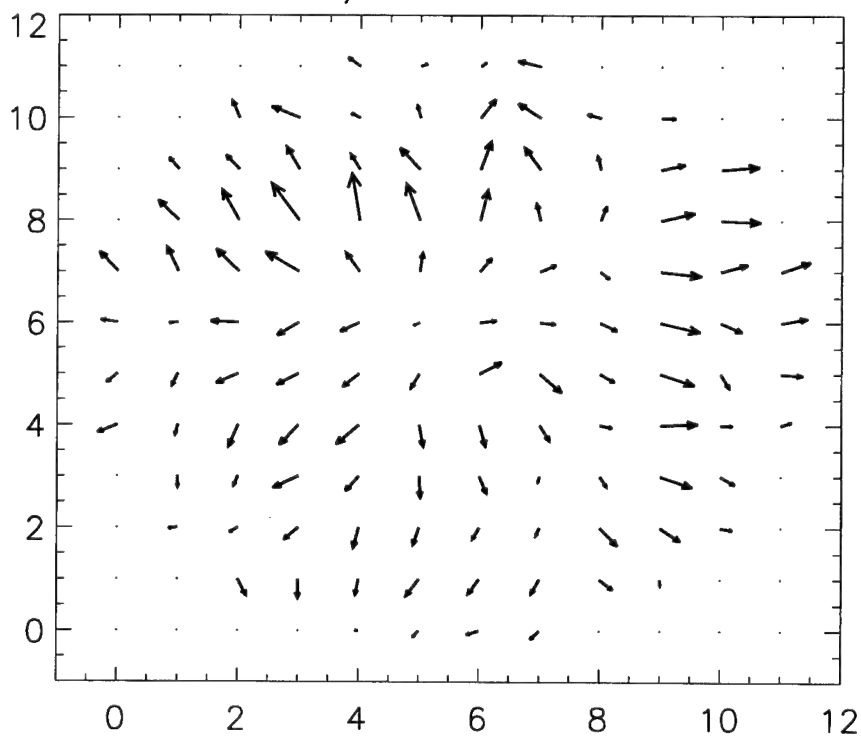
Reference

- (1) O. von der L  he, "Wavefront error measurement technique using extended, incoherent light sources," *Opt. Eng.* **27**, 1078-1087 (1988).

knife-edge, fixed aberrations removed



Shack-Hartmann, fixed aberrations removed



Use of Artificial Neural Networks for Hartman Sensor Lenslet Centroid Estimation

Dennis A. Montera[†], Byron M. Welsh[†], Michael C. Roggemann[‡] and Dennis W. Ruck[†]

[†]Department of Electrical and Computer Engineering

[‡]Department of Engineering Physics

Air Force Institute of Technology

Wright-Patterson AFB, OH 45433-7765

(513)255-3636

The resolution of ground based telescopes is limited by the random wavefront aberrations caused by atmospheric turbulence [1]. Adaptive optics systems, which compensate for atmospheric effects, have been shown to improve the resolution of these telescopes [2]. The purpose of an adaptive optics system is to remove the atmospheric induced aberrations from an incident optical wavefront. This removal is accomplished by measuring the incident aberrations and removing them using a deformable mirror. The compensation is degraded by the effects of additive noise in the wavefront sensor (WFS), system time delays, and the possibility of a spatial separation between the object of interest and the beacon used to measure the incident wavefront. While an optimal wavefront reconstruction algorithm, such as the minimum variance reconstructor, can be derived based on statistical knowledge of the atmosphere, noise and other random effects in the adaptive optics system cause the actual performance of this reconstructor to be limited by imperfect knowledge of several key parameters [3, 4, 5]. These parameters include both atmospheric and system parameters. The key atmospheric parameters include the Fried coherence length [6], r_0 , the C_n^2 profile, and the wind speed profile. The key system parameter is the WFS mean square slope measurement error. The most common form of WFS used in adaptive optics is the Hartmann WFS. In this paper we look at reducing the slope measurement error in a Hartmann WFS by improving the subaperture centroid estimation. In particular, neural networks are trained to estimate the subaperture centroid location, and the results are compared to those obtained using a conventional centroid estimator.

The error introduced into the wavefront measurements by the wavefront sensor is random. This error arises from such sources as charge-coupled device (CCD) read noise, shot noise, and spatial quantization of the lenslet array plane. The effect of these sources of noise is a WFS slope measurement error. Many adaptive optics systems use a quad-cell, or a 2×2 array of detectors for centroid estimation within a subaperture. However, many operators of adaptive optics systems would like to use larger arrays of detectors per subaperture for one of two reasons. One reason is to improve the dynamic range of slope estimation, the other is to improve the resolution in centroid estimation. In either case, the increase in detector array size makes the effects of read noise more significant. In this research we choose to investigate estimating the centroid location within a WFS subaperture for 4×4 detector arrays. Both read noise and shot noise are factored into data generation. Artificial neural networks are trained to take as input the values from each detector within a subaperture and estimate both the x and y centroid locations. The results obtained using the neural network are then compared to a standard centroid estimation algorithm. The standard centroid estimation technique uses the following expression to estimate the x centroid location within a subaperture [7] (the expression for a y centroid location is similar):

$$x_c = \frac{\sum_{i=1}^N \sum_{j=1}^M x_{ij} p_{ij}}{\sum_{i=1}^N \sum_{j=1}^M p_{ij}}, \quad (1)$$

where x_c is the x centroid location, N is the number of detectors in the x direction, M is the number of detectors in the y direction, x_{ij} is the x direction center location of the ij th detector, and p_{ij} is the signal count of the ij th detector. In this research, the performance of neural networks is compared to the conventional centroid estimator for noise free data, as well as with data which takes into account both read and shot noise. In the tests, noise conditions consistent with both natural guide stars and artificial beacons are considered. Tests are conducted on

lenslets where the main lobe of the speckle image is both a full, and half of a detector pixel's width. In all cases, the neural network performs better than the conventional centroid estimator. While the neural networks still produce a nonlinear response, the mean square error (MSE) in estimating both the x and y centroid locations is reduced between 36-82%.

In order to generate random subaperture phase data, random phase screens are generated for a 41×41 array of points. Then the image of a point source within the WFS subaperture is simulated and superimposed on a 4×4 detector array. In order to model read and shot noise under realistic conditions, an expression is developed for the signal to noise ratio (SNR) at the detector array. The expression for the SNR is

$$\text{SNR} = \frac{K}{\sqrt{0.0346K + 2.5\sigma_e^2}}, \quad (2)$$

when the image main lobe is half the width of a detector, and

$$\text{SNR} = \frac{K}{\sqrt{0.0378K + 2.5\sigma_e^2}}, \quad (3)$$

when the image main lobe is the full width of a detector. In these expressions, K is the average count detected per measurement per subaperture, and σ_e is the root mean square read noise count of a single detector element. While this expression does not represent a SNR in the traditional sense, it is widely used in the adaptive optics community. With this expression in mind, appropriate ranges of SNR must be determined to represent both natural guide stars and artificial beacons. We find that a typical natural guide star provides a SNR between 4.0 and 7.5 (low SNR case), while a typical artificial beacon provides a SNR between 7.5 and 11.0 (high SNR case). These SNR ranges are based on $\sigma_e = 12$ electrons and $K = 100$ photo events per lenslet for a natural guide star and 180 photo events per lenslet for an artificial beacon [8]. To keep this work independent of the system specifications, a SNR is randomly chosen in the proper range for each simulated image. The photo electron generation rate, K , is kept constant at 150 photo events per lenslet, and the value of the read noise, σ_e , is calculated using either Eqn. (2) or Eqn. (3). Detector shot noise is modeled as a Poisson random variable with arrival rate dependent on K , and detector read noise is modeled as an additive, independent, Gaussian random variable with variance σ_e^2 .

To properly account for noise, the percent of the subaperture irradiance on each detector pixel in the array is determined. This percentage of K is the assumed average count detected for that pixel, and is used as the arrival rate for a Poisson number generator. Then read noise with the appropriate variance is added to each detector pixel. Once noise is accounted for, a signal count for each detector in the array is calculated for each image of data. The detector counts for each image are then normalized by the largest detector value for that image. This makes the data independent of the value chosen for K , and thus all neural network solutions derived are dependent only on the SNR of the data.

Now that realistic WFS data can be generated, tests are conducted to compare the performance of neural networks with the standard centroid estimation technique. Sets of training images are generated for a 4×4 array of detectors with diffraction limited spot sizes of one half and one full pixel width, and for which the SNR is low, high, and infinite. Tests are conducted on the six cases shown in Table 1. In all cases phase screens of 41×41 points are used. Values for l/r_0 , where l is the dimension of a square subaperture are randomly chosen between 0.5 and 3.0, representing 0.5 to 3.0 r_0 's per subaperture. This makes any network solution capable of operating over a realistic range of atmospheric conditions. For each case, a neural network consisting of 20 hidden layer nodes and 2 output nodes is trained to take as input the 16 normalized detector counts, and output an estimate of both the x and y centroid locations. For this research, the detector array is assumed to be of unit dimension and centered about the origin. Once the networks are trained, new sets of data are generated for each case to compare the performance of the neural network with the conventional centroid estimator. Figure 1 shows the results obtained for estimating the x centroid location for the case when the spot size is half a pixel width, and under low SNR conditions. The 'x' and 'o' marks represent the mean estimate for each centroid location, while the error bars represent one standard deviation about the mean. Results for estimating the y centroid location are similar.

While both methods show a nonlinear response in estimation, the neural networks provide more accurate estimates, over a larger dynamic range, and with less estimate variance. This improved performance over the conventional

Table 1: Hartmann sensor subaperture centroid estimation test parameters: spot size and subaperture SNR.

Case	1	2	3	4	5	6
Spot Width	Full Pixel	Full Pixel	Full Pixel	Half Pixel	Half Pixel	Half Pixel
SNR	∞	High, 7.5-11.0	Low, 4.0-7.5	∞	High, 7.5-11.0	Low, 4.0-7.5

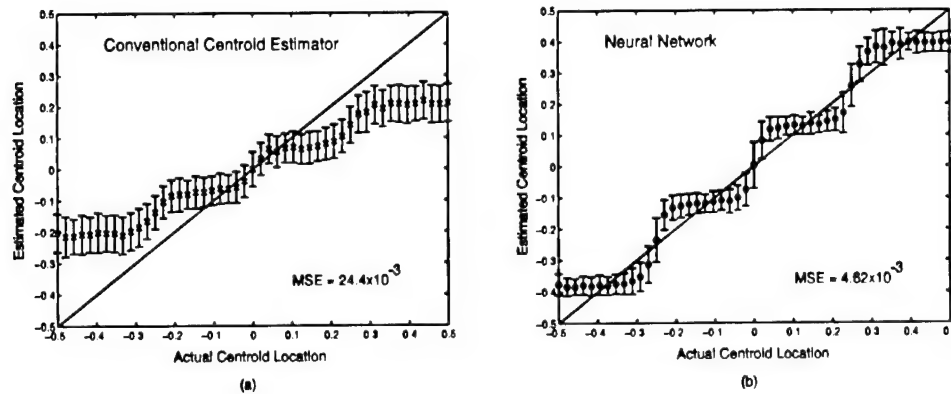


Figure 1: Comparison of WFS lenslet centroid estimation on images with main lobe half the width of a single detector and SNR between 4.0 and 7.5. Results shown for a) conventional centroid estimator, and b) neural network. Marks represent mean estimate value for true centroid location, and error bars represent one standard deviation about the mean. The MSE for the conventional centroid estimator is 24.4×10^{-3} , while the MSE for the neural network is 4.62×10^{-3} .

centroid estimator, especially in the presence of noise, makes the use of neural networks for WFS image centroid estimation attractive for improving the performance of adaptive optics systems.

1 REFERENCES

- [1] J. H. Hardy, "Active optics: a new technology for the control of light," *Proc. IEEE* **66**, 651-697 (1978).
- [2] R. Q. Fugate *et al.*, "Two generations of laser-guide-star adaptive-optics experiments at the Starfire Optical Range," *Journal of the Optical Society of America* **11**, 310-324 (1994).
- [3] B. Welsh and M. Roggemann, "Evaluating the Performance of Adaptive Optical Telescopes," NATO Advanced Study Institute, Adaptive Optics for Astronomy, D. Alloin and J.-M. Mariotti editors, Kluwer Academic Publishers, 1993.
- [4] B. Welsh and C. Gardner, "Effects of turbulence-induced anisoplanatism on the imaging performance of adaptive-astronomical telescopes using laser guide stars," *Journal of the Optical Society of America A* pp. 69-80 (1991).
- [5] B. Welsh and C. Gardner, "Performance analysis of adaptive optics systems using laser guide stars and slope sensors," *Journal of the Optical Society of America A* pp. 1913-1923 (1989).
- [6] D. L. Fried, "Optical resolution through a randomly inhomogeneous medium for very long and very short exposures," *Journal of the Optical Society of America* **56**, 1372-1379 (1966).
- [7] K. A. Winnick, "Cramer-Rao lower bounds on the performance of charge-coupled-device optical position estimators," *Journal of the Optical Society of America A* **3**, 1809-1815 (1986).
- [8] Telephone interview with the Staff of the Starfire Optical Range, Phillips Laboratory, Kirtland Air Force Base, New Mexico, 1995.

Simple Neural Networks as Wavefront Slope Predictors: Training and Performance Issues

Peter J. Gallant and George J.M. Aitken

Department of Electrical and Computer Engineering, Queen's University

Kingston, Ontario, Canada K7L 3N6

Tel: 613-545-2932, Fax: 613-545-6615

Introduction

Artificial neural networks have gained significant popularity over the past several years in a wide variety of engineering applications. This popularity is due in part to the ability of a neural network that is trained using a supervised training rule such as error backpropagation to acquire a non-parametric representation of the mapping between a set of inputs and outputs without any specific knowledge of the application domain. Given a sufficient number of nonlinear terms, represented by a number of hidden-layer neurons, a multilayer neural network can model any mathematical function that is continuous and differentiable (Hecht-Nielsen, 1990). Difficulties can arise however when a network is trained with a limited amount of noisy "real" data and is then expected to operate as part of a system for a specific application. The network must acquire an internal representation, as stored in its weights, during the training phase that subsequently generalizes well to unseen data. In the case of a prediction application, generalization capability becomes the paramount design criteria. The generalization performance of a trained network is a strong function of several factors, including: the architecture and complexity of the network, the type of supervised training rule employed, and the manner in which data is preprocessed and presented to the network.

In this paper, we focus on the problem of training a very simple, three-layer neural network to predict wavefront slopes for an adaptive optics application. Previous studies by our group and others have shown that a neural network trained with the error backpropagation training rule can predict the wavefront tip and tilt of a subsequent frame with an accuracy that exceeds the traditional random walk model (Jorgenson and Aitken, 1992). We extend this work by exploring the application of an accelerated backpropagation learning rule suggested by Vogl *et al.* (1988) to decrease the time required to train the network. We assess the performance of the resultant predictors on real data acquired under good seeing conditions. We also investigate the use of an additional data point in the output target vector of the predictor that appears to result in a smoother descent of the error gradient with no degradation in generalization performance. This work is motivated by the desire to gain a better understanding of the function of a simple neural-network model as a precursor to investigating a broad range of alternative neural-network architectures, training algorithms, and optimization techniques.

Using a Neural Network as a Wavefront Slope Predictor

In an adaptive-optics application such as the closed-loop control of an adaptive telescope, the incoming atmospherically distorted wavefront can be imaged through a Shack-Hartmann lenslet array to obtain the resultant tip-tilt values of the wavefront. For a time series of wavefront slopes $x(t_0, t_1, \dots, t_T)$ sampled in discrete intervals over time T , the problem of wavefront slope prediction resembles the general time series prediction problem of estimating the n future data points $x(t, \dots, t+n)$ from m previous points in the input vector $x(t-m, \dots, t-1)$. We

refer to the use of a single point ahead training target as the *point method* and the multi-point target as the *vector method*. We restrict our vector method experiments in this study to the case where $n = 1$, resulting in a two-element vector consisting of $x(t)$ and $x(t+1)$ being presented to the network as a target during training.

Accelerated Backpropagation

Error backpropagation refers to a family of techniques used to train a neural network in a supervised mode where historical or other exemplar data exists. The technique performs gradient descent to search for the set of network weights that optimizes the value of a defined objective function, usually mean-square error (MSE) with respect to the network weights. While simple error backpropagation is a robust technique for acquiring non-parametric representations, several alternative techniques have been suggested such as using a momentum term in the gradient descent to avoid “false” local optima and to decrease training time. The accelerated backpropagation technique used was originally suggested by Vogl *et al.* and increased backpropagation training efficiency in three ways: using a batch training approach to update the network weights after each *epoch* instead of after each training pattern, dynamically varying the learning rate of the gradient descent in response to local performance considerations, and keeping the momentum term set at zero until a gradient descent step reduces total error.

Experimental Results

Experiments were conducted on wavefront-slope data from the COME-ON wavefront sensor on the ESO 4-m telescope at La Silla, provided by G. Rousset. A set of 2000 samples taken under good seeing were used as training data, while a holdout set of 500 samples were used to validate the trained network. The network architecture was selected empirically and consisted of 10 input neurons, 10 hidden neurons, and either a single output neuron in the case of the point predictor or two output neurons when the vector method was used. Initial learning rate for the accelerated backpropagation algorithm was set at 0.1, and momentum at 0.6. A series of experiments comparing the training characteristics and holdout performance of the point and vector methods were conducted using up to 100,000 training epochs. The large number of training epochs was used to compensate for any training advantage the point method network might have because contains fewer weights need to be determined by the training process.

Our results indicate that the accelerated backpropagation algorithm encountered, then quickly overcame difficulties in performing gradient descent during the training of the point method network as is shown in Figure 1. The training characteristic for the vector network (dashed line) is quite smooth with no large peaks. It appears that the performance of the point method network (solid line) is more sensitive to changes in weight values in the network. The large increases in error that occurred several times during the training suggest that the gradient descent procedure was employing momentum to move out of potentially false (local) optima. An implication of this is that the gradient descent problem is simplified - containing fewer local optima - when a second frame ahead is added to the training target. This procedure also provides for a small improvement in the observed generalization capability of the network. Table 1 summarizes the relative performance of the point and vector training methods on a 500-point holdout set compared to the random walk hypothesis which assumes that the best

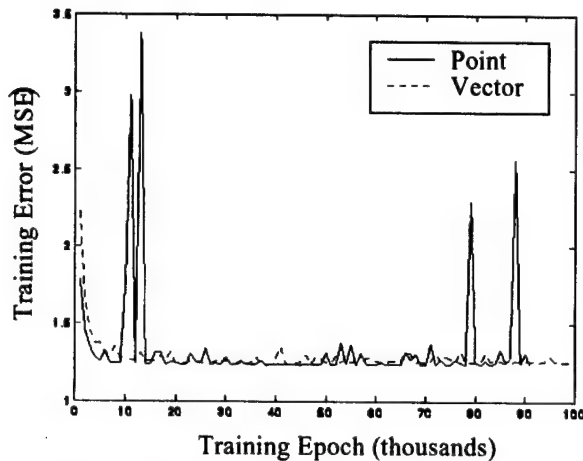


Figure 1 (left): Training characteristics for point and vector method networks.

	Point	Vector	RW
Sum Sq. Err.	1.24	1.23	1.52
Std. Dev.	0.050	0.050	0.056
Skewness	-0.019	0.02	0.019
Kurtosis	0.293	0.241	0.082

Table 1: Statistical summary of holdout errors for point, vector, random walk (RW).

estimate of the slope of the next frame is simply the slope of the current frame. These statistics suggest that both the point method and the vector method can outperform somewhat better than the traditional random walk hypothesis. Performance of the vector method is consistent with the point method, despite the greater complexity of the vector network. It is interesting to note that the effect of the predictor is to reduce overall sum-squared error by reducing the lower-order error statistic, standard deviation, at the expense of higher error kurtosis. The cause of higher error kurtosis is a more frequent occurrence of outlier errors at the tails of the distribution.

Conclusions

A smoother error surface results from the provision of an additional frame as a training target for the network. Improvement in error performance is at the expense of increased kurtosis in the error distribution, suggesting that predictions could be further improved possibly by augmenting the supervised network training algorithms that emphasize invariant structure with objective functions that more severely penalize outliers or with unsupervised learning algorithms that can acquire invariant features in the input patterns (Schraudolph, 1995). Several other alternatives are currently being considered, including use of real-valued genetic algorithms as a search methodology to address the trade-off between network complexity and generalization capability, and a broader study of alternatives to error backpropagation and multilayer networks.

References

- Hecht-Nielsen R., *Neurocomputing*, (Addison-Wesley, 1990).
- Jorgenson, M.J., Aitken G.J.M., "Prediction of atmospherically-induced wavefront degradations," *Opt. Lett.* 17, 466-468 (1992).
- Rumelhart D.E., Hinton G.E., Williams R.J., *Parallel Distributed Processing*, (MIT Press, 1986) vol. 1, chap. 8.
- Schraudolph, N.N., *Optimization of Entropy with Neural Networks*, Ph.D. Thesis, University of California at San Diego (1995).
- Vogl T.P., Mangis J.K., Rigler A.K., Zink W.T., Alkon D.L., "Accelerating the Convergence of the Back-Propagation Method," *Biol. Cybern.* 59, 257-263 (1988).

Sparse aperture phasing with phase diversity: Experimental Results

Rick Kendrick
Lockheed-Martin Advanced Technology Center
Department 97-20, Building 254 G
3251 Hanover Street
Palo Alto, CA 94304-1191
415-424-3974 fax 415-354-5002

Ray Bell
Lockheed-Martin Advanced Technology Center
Department 97-06, Building 202
3251 Hanover Street
Palo Alto, CA 94304-1191
415-354-5407 fax 415-354-5400

Alan Duncan
Lockheed-Martin Advanced Technology Center
Department 97-20, Building 254 G
3251 Hanover Street
Palo Alto, CA 94304-1191
415-354-5657 fax 415-354-5002

Phasing the sub apertures of a multiple aperture telescope is a difficult problem that has been addressed in various ways. Hartmann sensors and knife edge tests are techniques that work well for point source objects such as stars. Null fringe tracking is also suitable for point sources. However, none of these techniques are adequate for extended object imaging. Radial shearing white-light interferometers have been proposed and tested but are complicated to implement and have a strong object dependence. Laser metrology systems are extremely accurate but do not give a direct measurement of the phase errors and can be difficult to implement. Phase diversity is a very simple phasing technique that is suitable for extended objects and has developed into a mature technology over the past five years.

Phase diversity is a technique that derives the wavefront aberrations of an optical system using a focused and defocused image of the same object. The technique is essentially object independent and is extremely simple to implement. Previously, we have demonstrated the applicability of this technique to multiple aperture systems by phasing a seven segment mirror in closed loop. We have now shown that a twelve aperture multiple telescope system can be phased using phase diversity.

The experimental setup is shown in figure 1. A scene generator projects an image into a multiple aperture telescope that consists of an imaging lens and a segmented mirror that is positioned close to the entrance aperture of the lens.

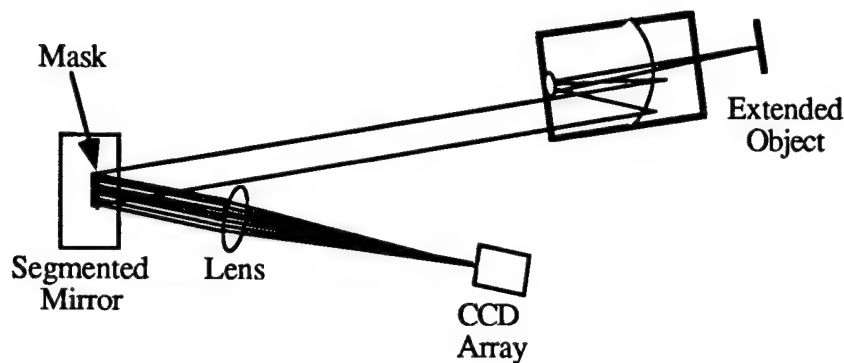


Figure 1. Experiment layout.

A twelve aperture mask is positioned over the segmented mirror to give 12 separate apertures. The piston and tilt of each aperture is controlled by moving the segments of the mirror. Each aperture is controllable in 2 axes of tilt and piston. The aperture mask is shown in figure 2.

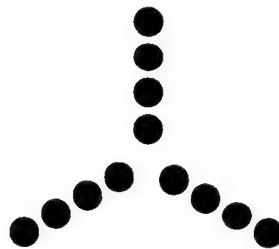


Figure 2. Aperture mask showing the multiple aperture arrangement.

The lens comes to a focus on a Kodak CCD array. A beamsplitter and prism assembly are positioned on the CCD array to give a simultaneous focused and defocused image. The beamsplitter and prism arrangement is shown in figure 3.

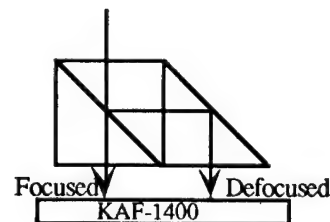


Figure 3. Method of acquiring a simultaneous focused and defocused image.

The simultaneous images are acquired with a frame grabber and analyzed to determine the piston and tilt errors present on the twelve aperture array. The error signals are fed back to the segmented mirror to phase the separate apertures. Measurements have been performed to determine the accuracy and resolution of the phase diversity technique when used to estimate piston and tilt errors on a 12 aperture sparse array.

Optimization of Adaptive Optics Digital Imagery Systems by Design of Experiments

Robert T. Brigantic, Michael C. Roggemann, Kenneth W. Bauer, Byron M. Welsh

Air Force Institute of Technology, AFIT/ENS, 2950 P Street, Wright-Patterson AFB OH 45433

Phone: 513-255-2549, Fax: 513-476-4943

Introduction: Adaptive optics systems are still a relatively new technology. As such, characterization of their performance under a given set of conditions still has many uncertainties. For instance, even though many variables for a particular imaging scenario are uncontrollable, such as seeing conditions, object brightness (visual magnitude), and object size/distance, many other Adaptive Optics System (AOS) parameters can be controlled by the system operator. These include system integration time, imaging and Wavefront Sensor (WFS) wavelengths, closed loop bandwidth, image exposure time, and others. Selecting parameter settings for these variables to yield the "best quality" image is far from obvious. Further, what does the "best quality" image mean?

The best looking image to a casual observer might not be the best to an image interpreter. The best image to an interpreter might not be the best for computer automated recognition, and so forth. Many different metrics have been suggested to characterize the quality of an image. Hence, it might be possible to optimize AOS settings to yield the "best" image for a particular set of conditions and imaging requirements by maximizing/minimizing a particular image quality metric. Alternatively, different image quality metrics may give rise to different AOS configurations. Adaptive optics system optimization is the major goal of this research effort.

Methodology: Given the potential number of variables involved, an exhaustive search for optimal AOS parameters for a given set of conditions is impractical. Consider three AOS input settings and two seeing condition variables and say each of these can take on six different levels. This means that more than 15,000 different possible scenarios would need to be tested. As the number of variables and levels increases, the number of possible combinations becomes hopelessly overwhelming. However, a methodology exists to overcome such a dilemma -- design of experiments [1].

A subset of Response Surface Methodology (RSM), design of experiments employs statistical techniques to construct empirical models of scientific phenomena when analytic models are unknown or their use is impractical. In design of experiments, one seeks to relate a system response to the levels of the input variables that affect it. In this manner, by careful design and analysis of experiments, it is possible to obtain empirical models without having to resort to an exhaustive search. Once obtained, these empirical models can be used decide on input settings to achieve desirable system results [1].

Experimental Setup: Initial work was accomplished using an adaptive optics systems simulation called the Hybrid Imaging Simulator (HYSIM). Developed by Michael Roggemann, HYSIM is a Fortran based program that allows different atmospheric conditions and AOS configurations to be specified. For provided input parameters, HYSIM models and computes the Optical Transfer Function (OTF), image spectrum statistics, and resulting image for either a point source or an extended object [2].

Controllable input variables to HYSIM are the number WFS subapertures, primary and secondary mirror diameters, imaging and WFS wavelengths, deformable mirror actuator separation, closed loop bandwidth (f_c), and image exposure time. Uncontrollable input variables are object distance (if an extended object), object brightness (visual magnitude), the Fried parameter (r_o), and wind velocity (v). Of these, the following variables were initially examined: f_c , short frame exposure time, visual magnitude, r_o , and v . A telescope with primary and secondary mirror diameters of 1.0 and 0.2 respectively was modeled. Initial work concentrated on imaging a computer generated rendition of a satellite which orbits the earth at an altitude of about 650 kilometers (Figure 1).

Utilizing the above HYSIM input variables, the following four variables were incorporated for the design of experiments methodology: $X_1 =: D/r_o$, $X_2 =: f_g/f_c$ where f_g is the Greenwood frequency, $X_3 =:$ visual magnitude, and $X_4 =:$ short frame exposure time (frmtime). A total average image exposure time of 5 seconds was used in all cases. High and low levels for each variable were selected, a design matrix was constructed, and the simulations run. This particular setup represents a full factorial design, where each variable has two levels so that there are a total of $2^4 = 16$ different runs. This design permits estimation of the affect of each variable and all of their possible interactions on AOS performance. Table 1 contains a sample design matrix used in this study. This table also contains the corresponding AOS output using three different metrics. Y_1 is the modulus of the average OTF of the combined AOS and atmosphere integrated to the cutoff frequency of the telescope. Y_2 is the same as Y_1 except the OTF is integrated to the frequency where the average Signal to Noise Ratio (SNR) of the resulting image is equal to five. And Y_3 is a normalized form of Y_1 .

Run	Uncoded Variables				Coded Variables				Response Variables		
	X_1 , D/r_o	X_2 , f_g/f_c	X_3 , vis mag	X_4 , firtime	x_1	x_2	x_3	x_4	Y_1 , MTF integrated to cutoff	Y_2 , MTF integrated to SNR = 5	Y_3 , Strahl Ratio
1	4.00	0.53	4.25	0.01	-1	-1	-1	-1	3683.4	3683.4	0.532
2	11.11	0.49	4.25	0.01	1	-1	-1	-1	3052.1	3052.1	0.441
3	4.00	1.07	4.25	0.01	-1	1	-1	-1	1977.6	1972.2	0.286
4	11.11	0.99	4.25	0.01	1	1	-1	-1	2154.5	2153.6	0.311
5	4.00	0.53	6.00	0.01	-1	-1	1	-1	3624.9	3616.0	0.524
6	11.11	0.49	6.00	0.01	1	-1	1	-1	2878.9	2866.4	0.416
7	4.00	1.07	6.00	0.01	-1	1	1	-1	1849.7	1699.9	0.267
8	11.11	0.99	6.00	0.01	1	1	1	-1	2072.6	2018.4	0.300
9	4.00	0.53	4.25	0.10	-1	-1	-1	1	3709.6	3709.6	0.536
10	11.11	0.49	4.25	0.10	1	-1	-1	1	3025.1	3025.1	0.437
11	4.00	1.07	4.25	0.10	-1	1	-1	1	1955.3	1949.9	0.283
12	11.11	0.99	4.25	0.10	1	1	-1	1	2185.4	2184.6	0.316
13	4.00	0.53	6.00	0.10	-1	-1	1	1	3518.8	3510.4	0.509
14	11.11	0.49	6.00	0.10	1	-1	1	1	2701.8	2690.6	0.390
15	4.00	1.07	6.00	0.10	-1	1	1	1	1732.6	1447.6	0.250
16	11.11	0.99	6.00	0.10	1	1	1	1	2130.1	2073.3	0.308
								AVE:	2640.8	2603.3	0.382

Table 1 - Design Matrix

Summary of Results: For the three mentioned AOS metrics, the larger the output, the better the resulting image should be. Figures 2 through 6 contain a sample of the resulting images of the Okean satellite in descending Y_2 rank order for design points 9, 2, 14, 4, and 7 respectively. These images tend to show decreasing clarity and detail as the corresponding value of Y_2 decreases.

Figure 1 – Okean Satellite



Figure 2 – Run 9



Figure 3 – Run 2



Figure 4 – Run 14



Figure 5 – Run 4



Figure 6 – Run 7



[Images are displayed as negatives for clarity.]

Figures 7 through 10 contain a sample of graphical results for the design matrix given in the table. Figure 7 shows the affect of each variable on the AOS response. Of the variables considered, it is evident that x_2 has the most influence on AOS performance. The next most influential variables are x_1 and x_3 . Figure 8 shows Y_2 in descending rank order for each run. These rankings can be used to objectively rank the resulting satellite images.

Figures 9 and 10 show two way interactions between x_1 - x_2 and x_2 - x_4 respectively. Figure 9 shows a significant interaction between x_1 and x_2 . That is, as x_1 is decreased (r_o increases for fixed D), one would like to decrease x_2 as well (i.e., increase f_c). However, as x_1 is increased (r_o decreases for fixed D), the interaction plot indicates that there might be a point where one would eventually like to also increase x_2 (i.e., decrease f_c). Figure 10 indicates that there is essentially no interaction between x_2 and x_4 . Similar types of insights can be ascertained from interaction plots of the other variables as well.

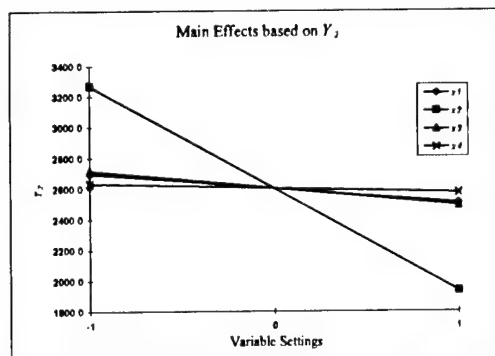


Figure 7

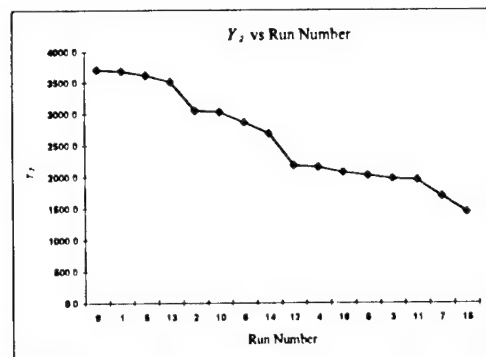


Figure 8

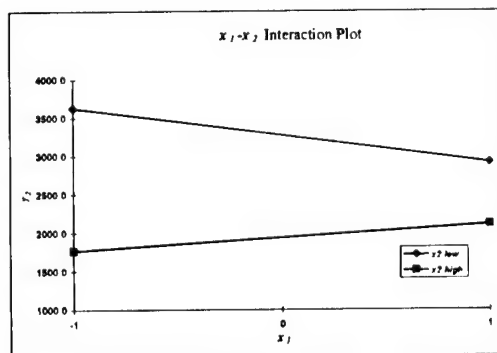


Figure 9

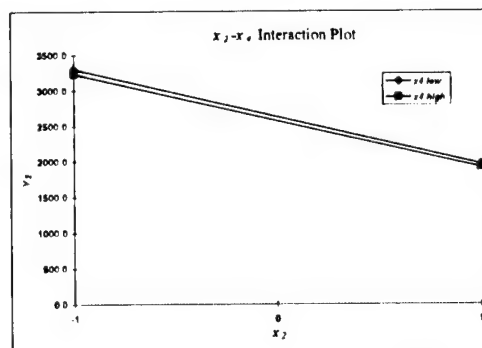


Figure 10

Conclusions: Design of experiments methodology is well suited for optimization of adaptive optics systems, especially with the huge number of variables to be considered. The following inferences are made. First, the ratio of Greenwood frequency to closed loop bandwidth has a very significant affect on AOS performance. Atmospheric conditions, as expressed through the Fried parameter, and object visual magnitude also influence performance, but to a much lesser degree. Short frame image exposure time had very little affect on performance.

Initial results reveal insights that might not be readily apparent. For instance, one might think that increasing f_c will always improve AOS performance. However, as seen by the interaction plot of x_1 and x_2 , this may not be the case. The physical origin of this result lies in the fact that as f_c increases, fewer photoevents are available to estimate wavefront tilts. Eventually, this leads to large errors that a rapidly updating AOS cannot overcome.

REFERENCES

1. Box, George E. and Norman R. Draper. Empirical Model-Building and Response Surfaces. New York: John Wiley & Sons, 1994.
2. M.C. Roggemann and C.L. Matson, "Power spectrum and Fourier phase spectrum estimation by using fully and partially compensating adaptive optics and bispectrum postprocessing." JOSA-A, vol. 9, 1525-1535 (1992).

Tip-Tilt Control Loop Optimization

L. Fini, S. Esposito
Osservatorio Astrofisico di Arcetri, Italy

We address problems of control loop parameters optimization for tip-tilt correction system based on the approach followed for the T.N.G. tracking system.

Optimized adaptive optics design for low light level, optical-wavelength imaging interferometer arrays

David W. Tyler
W.J. Schafer Associates
2000 Randolph Rd. SE, St. 205
Albuquerque, New Mexico 87106 USA
phone: 505.846.1880; email tyler@plk.af.mil

1. Introduction

Although there have been recent advances in the design and manufacture of large, single-aperture telescopes, the problems and costs involved are formidable enough that imaging interferometer arrays are being developed for such demanding missions as direct detection of extrasolar planets¹. Studies of AO-compensated interferometry have been accomplished both with computer simulations² and approximate analysis³. These studies have shown that even partial wavefront compensation can dramatically improve the limiting magnitude observable by the array. Here, an analysis of AO design for partially-compensating systems is presented. The method here is identical to that used by Angel¹, but 1.) more detail is provided, such as treatment of read noise and allowance for different AO and imaging wavelengths, and 2.) the dependence of control-loop bandwidth requirements on degree of AO compensation is accounted for.

2. Analysis

Finding an optimal AO configuration can be accomplished using computer simulations that accurately mimic the behavior of propagating light, feedback controls, and the spatial response of a deformable mirror (DM). To guide and understand numerical computations, however, it is important to formulate approximate analytical models. A global minimization approach can be used to find the number of actuators and closed-loop bandwidth minimizing the total residual phase variance. Since the problem of selecting an optimal imaging wavelength for a compensated telescope⁴ involves discrete atmospheric transmission windows and, for astronomy, wavelengths of scientific interest, both WFS and imaging wavelengths are assumed fixed for this problem.

Assume the major error sources (WFS noise, DM fitting, and finite bandwidth) are independent random processes. The total error power σ_t^2 may then be written as the sum of the individual variances. The total differential of σ_t^2 is given by

$$d\sigma_t^2 = \frac{\partial}{\partial N} \sigma_t^2 dN + \frac{\partial}{\partial f_c} \sigma_t^2 df_c, \quad (1)$$

where N is the number of DM actuators and f_c is the AO bandwidth. The critical point, where the minimum σ_t^2 occurs, is given by simultaneous solution of the two conditions

$$\frac{\partial}{\partial N} \sigma_t^2 = 0 \quad (2)$$

and

$$\frac{\partial}{\partial f_c} \sigma_t^2 = 0 \quad (3)$$

Note that WFS sensor error is coupled to both fitting and finite-bandwidth errors.

The condition (2) can be solved to find an optimum number of actuators N_o by defining the residual error $\sigma_{res,N}^2$ as the sum of the two variances dependent on N :

$$\sigma_{res,N}^2 = \left(D/\sqrt{Nr_o} \right)^{5/3} + \left(\frac{\pi}{\text{SNR}} \right)^2 \frac{\pi}{10} \Lambda^2, \quad (4)$$

where D is the pupil diameter, N is again the number of actuators, r_o is the Fried coherence diameter at the interferometry wavelength, SNR is the WFS signal-to-noise ratio, and Λ is the ratio of the WFS and interferometry wavelengths. Note the $\partial/\partial N$ operator gives the same result with either $\sigma_{res,N}^2$ or σ_i^2 , allowing consideration of the AO configuration problem as though the control-loop bandwidth f_c were fixed.

Substitution of (4) into (2) yields a nonlinear solution for N_o if read noise is accounted for in the SNR; however, in the limit of very low signal a straightforward solution is obtained:

$$N_o \approx 0.49 \left[\frac{K^2}{\Lambda^2 p \sigma_e^2} \left(\frac{D}{r_o} \right)^{5/3} \right]^{6/17}, \quad (5)$$

where K is the number of photodetection events in the telescope pupil, p is the number of detector pixels in a single WFS subaperture and σ_e^2 is the per-pixel read noise power in a subaperture. Note that use of Noll's results⁵ in (4) implies the assumption that N actuators will correct N turbulence modes (an assumption that will be used again). Also, this treatment disregards the fact that WFS and DM elements are not space-filling in the pupil; in practice, it is useful to use N_o to calculate the required subaperture diameter d using $d^2 = D^2/N_o$. The subaperture size is then used in a computer program to position WFS subapertures and mirror actuators so that a reconstruction matrix can be formed in a well-conditioned way.

Similarly, condition (3) can be solved for an optimum control bandwidth f_{co} by defining the mean-square residual phase error σ_{res,f_c}^2 as the sum of the two variances dependent on f_c :

$$\sigma_{res,f_c}^2 = (f_G/f_c)^{5/3} + \left(\frac{\pi}{\text{SNR}} \right)^2 \frac{\pi}{10} \Lambda^2, \quad (6)$$

where f_G is the Greenwood frequency. Again using the low-signal limit,

$$f_{co} \approx 0.2 f_G^{5/11} \left[\frac{(\phi/N)^2}{\Lambda^2 p \sigma_e^2} \right]^{3/11}, \quad (7)$$

where ϕ is the telescope pupil signal flux in PDEs per second. This result can be used with (5) to simultaneously solve the minimum-variance conditions (2) and (3), giving

$$f_{co} \approx 0.5 \frac{f_G^{5/7} \phi^{2/7}}{(D/r_o)^{1/2} (\Lambda^2 p \sigma_e^2)^{1/7}} \quad (8)$$

as the optimum control bandwidth for the case where the number of actuators is N_o .

Any real AO system responds over a finite spatial frequency band, effectively filtering the atmospheric disturbance in space as well as time. Recently, Roddier pointed out that this spatial filtering results in a reduced sensitivity to finite-bandwidth effects on the part of the AO system⁶. This may be understood by considering that if the only spatial modes observed by the wavefront sensor vary at, for example, 10 Hz, there will be little improvement observed if the AO bandwidth is increased from 20 Hz to 100 Hz.

To treat this effect, the turbulence modes not observed by the WFS are excluded from finite-bandwidth error calculations. This can be easily accomplished by again using Noll's calculations for the residual power σ_{bw}^2 after N turbulence modes are corrected. The residual error finite-bandwidth error becomes

$$\tilde{\sigma}_{bw}^2 = \sigma_{bw}^2 - \sigma_N^2, \quad (9)$$

where σ_N^2 is the first term on the right side of (4).

This change means an effective Greenwood frequency, $f_G(N)$, is defined as the frequency where $\tilde{\sigma}_{bw}^2 = 1$. The resulting expression for $f_G(N)$ compares favorably with data given in Roddier's work and a theoretical treatment by ten Brummelaar⁷. The resulting adjustment in required bandwidth allows a longer integration time for the AO wavefront sensor, increasing the number of photons collected and reducing measurement error. However, σ_{bw}^2 is now a function of N , forcing the optimization problem to be solved iteratively. In previous work using these results, the unfiltered Greenwood frequency was used to calculate an initial estimate for N_o .

3. Sample simulation results

The above expressions were used with computer simulations to predict available fringe visibility in a two-telescope interferometer. The first simulation is a Hartmann WFS model, which accounts for WFS detector noise, a user-selected number of detector pixels, and the effect of WFS subaperture size relative to r_o . The output of this simulation is an estimated WFS measurement error, which is used as an input to the second simulation, a full adaptive optics model. The procedures used for this work are identical to those described elsewhere^{8,9}.

An AO system was designed and simulated for a visual magnitude 12 object, $r_o = 12$ cm at an interferometry wavelength of $0.7 \mu\text{m}$, a wind speed of 5 m/sec (10 miles/hr), and a WFS wavelength of $0.46 \mu\text{m}$. The initial Greenwood frequency of 17 Hz was used to specify $N = 21$, leading to $f_G(N) = 10$ Hz and $f_{co} = 21$. For this system, a fringe visibility of 0.71 was obtained. Note this figure does not account for noise in the fringe detection process; only physics up to the formation of the interference pattern is modelled. Again using the 21-actuator system with a loop bandwidth of 8 Hz, a visibility of 0.66 was obtained for $m_v = 14$. Finally, visibilities of 0.44 and 0.02 were obtained for $m_v = 14$ with $N = 9$ and tilt-only AO, respectively.

-
1. J.R.P. Angel, *Nature* **368** (1994)
 2. G.Rousset, P.Y. Madec, D. Rabaud, *Proc. ESO Symposium on High Resolution Imaging* (1991)
 3. G.C. Loos, *Appl. Optics* **31** (1992)
 4. D.W. Tyler and J.S. Fender, *Proc. SPIE* **2204** (1994)
 5. R.J. Noll, *J. Opt. Soc. Am.* **66** (1976)
 6. F. Roddier, *et al.*, *J. Opt. Soc. Am A* **10** (1993)
 7. T. ten Brummelaar, *Proc. SPIE* **2200**
 8. D.W. Tyler and G.C. Loos, *Proc. IAU Symposium 158 on Very High Angular Resolution Imaging* (1993)
 9. D.W. Tyler, *et al.* *Proc SPIE* **2029** (1993)

Optimization of Bimorph Mirror Electrode Pattern for SUBARU AO System

Masashi Otsubo¹, Hideki Takami², Masanori Iye²

¹The Graduate University for Advanced Studies

²National Astronomical Observatory Japan

^{1,2}Osawa 2-21-1, Mitaka, Tokyo 181 Japan

NAOJ has been developing an adaptive optics(AO) system for SUBARU 8.2m telescope. The AO system is composed of a curvature wavefront sensor and a bimorph mirror with 36 elements.

It has larger flexibility for arrangement of the electrodes than stacked actuator deformable mirror, therefore we are able to maximize the performance by optimizing the geometry of the electrodes. Important characteristics to determine the performance of a bimorph mirror are the curvature stroke and the fitting error. Therefore we need to design the bimorph mirror electrode pattern to minimize the fitting error after compensating wavefront error without increasing the required curvature stroke. Suppressing the required stroke is necessary from the reason that the fabricating a thin bimorph mirror to increase the stroke, produces following drawbacks : 1) slow down of the temporal response because of the decrease of resonance frequency, 2) the degradation of the surface accuracy due to the decrease of the stiffness.

This kind of optimization has been discussed for 19 element bimorph mirror for CFHT AO system (Rigaut et al. 1994). They designed that outer ring electrodes should be out side of the pupil area and provided a gap between outer ring and inner ring to reduce fitting error for tilt correction.

We have performed optimization of the 36 elements bimorph mirror taking into account atmospheric turbulence(Kolmogorov turbulence), wavefront tilt from telescope tracking error as the error source. The detail conditions are listed below.

- 1) RMS fitting error after correcting atmospheric turbulence (seeing = 0.45") when putting together with a curvature sensor.
- 2) RMS fitting error for pure tilt wavefront (1" tilt)
- 3) Required stroke to compensate atmospheric turbulence (1" tilt)
- 4) Required stroke to compensate pure tilt (1" tilt)

The system requirements that were already determined were: the lens array pattern of wavefront sensor (Figure 1a); the external diameter of the outer ring, 108 mm; the effective area (a pupil of the optical path), 60 mm in diameter; and the maximum curvature stroke, 0.05 / m. Other dimensions of the mirror are shown in Fig.1-b. Here, R_n shows the electrodes of the n -th ring from the center and D_{nint} and D_{next} are internal and external diameter of the n -th ring respectively.

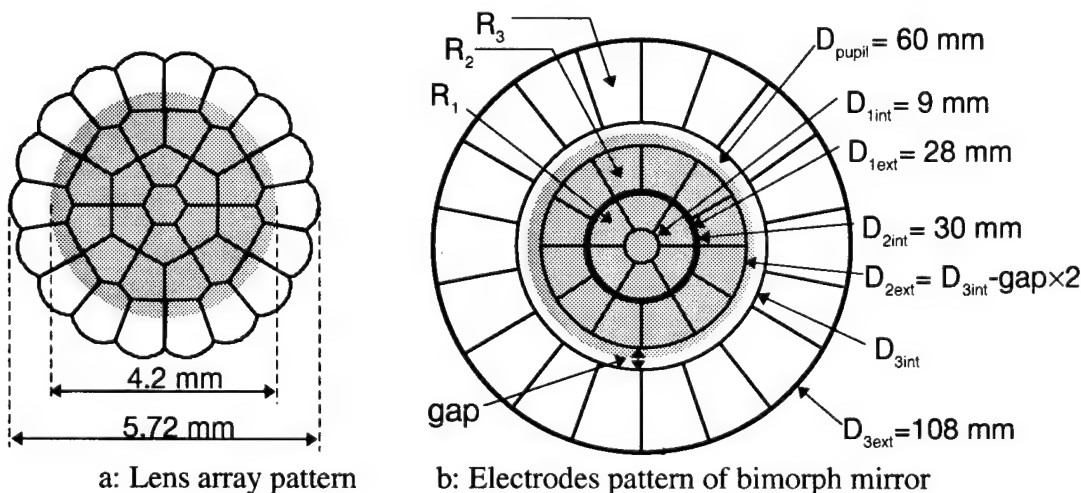


Fig.1-a. Lens array pattern of wavefront sensor and Fig.1-b. electrodes pattern of bimorph mirror which is used to calculate the performance. The effective areas are shown as gray circle.

Table 1-a. RMS fitting error after correcting atmospheric turbulence (seeing = 0.45'')

gap width (mm)	D_{3int}							
	48 mm	54 mm	60 mm	66 mm	72 mm	78 mm	84 mm	90 mm
0	0.184 μ m	0.185	0.187	0.187	0.187			
3		0.184	0.186	0.187	0.187	0.192		
6			0.185	0.186	0.187	0.192	0.196	
9				0.185	0.186	0.191	0.196	0.198

Table 1-b. RMS fitting error after correcting pure wavefront tilt (1'')

gap width (mm)	D_{3int}							
	48 mm	54 mm	60 mm	66 mm	72 mm	78 mm	84 mm	90 mm
0	0.651 μ m	0.193	0.014	0.005	0.004			
3		0.205	0.014	0.005	0.004	0.005		
6			0.015	0.005	0.004	0.005	0.008	
9				0.007	0.005	0.005	0.009	0.016

Table 1-c. Required stroke for 3rd ring electrodes to compensate atmospheric turbulence (seeing = 1'', 3 σ)

gap width (mm)	D_{3int}							
	48 mm	54 mm	60 mm	66 mm	72 mm	78 mm	84 mm	90 mm
0	0.029 1/m	0.036	0.053	0.090	0.152			
3		0.035	0.051	0.086	0.147	0.250		
6			0.050	0.083	0.142	0.244	0.427	
9				0.082	0.138	0.236	0.418	0.752

Table 1-d. Required stroke for 3rd ring electrodes to compensate pure tilt (1'')

gap width (mm)	D_{3int}							
	48 mm	54 mm	60 mm	66 mm	72 mm	78 mm	84 mm	90 mm
0	0.026 1/m	0.030	0.036	0.047	0.063			
3		0.030	0.036	0.047	0.063	0.089		
6			0.036	0.047	0.063	0.089	0.138	
9				0.047	0.063	0.089	0.138	0.239

The calculated fitting errors and required strokes are shown in Table 1a, 1b, 1c and 1d. We have shown only D_{3int} and gap width because the performances does not seriously depend on D_{1int} , D_{1ext} , D_{2int} in these tables. The required stroke for R_1 and R_2 were omitted because these values were smaller than that of R_3 .

We have obtained the following results from the above tables.

- 1) The RMS fitting error after the turbulence correction are not sensitive to the electrode diameters (Table 1-a).
- 2) RMS fitting error for the tilt suddenly increase when D_{3int} becomes smaller than 60 mm (Table 1-b).
- 3) D_{3int} should be smaller than 60 mm (Table 1-c).
- 4) D_{2int} should be smaller than 66 mm (Table 1-d).

We have adopted $D_{3int} = 60$ mm and gap width = 3 mm ($D_{2ext} = 54$ mm) from these results. After this calculations, we have added 18 square holes (3 \times 3 mm) on R3 for introducing the R1 and R2 electrode lead lines to the back side of the mirror (Fig. 2). The performance of the mirror is shown in Table 2. Fig. 3 shows the performance of suppressing wavefront error from atmospheric turbulence for each Zernike mode that was derived from the mean square residual fitting error after reflected by the designed bimorph mirror.

The authors wish to thank for Mr. P. Jagourel (CILAS) for his important comments about the deign of the mirror.

References

R. Arsenault, D. Salmon, J. Kerr, F. Regaut, D. Crampton, W. Grundman, "The Canada-France-Hawaii adaptive optics bonnette I: System Description ", SPIE proceeding vol.2201 (1994) p.833 - 842

F. Rigaut, R. Arsenault, J. Keer, D. Salmon, M. Northcott, Y. Dutil, C. Boyer, , "The Canada-France-Hawaii adaptive optics bonnette II: simulation and control", SPIE proceeding vol.2201 (1994) p.149 - 160

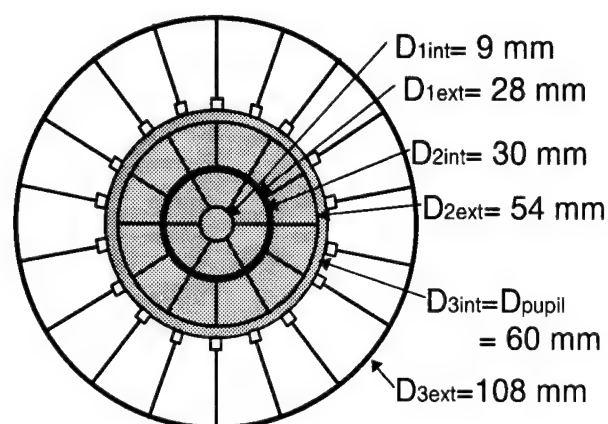


Fig.2. Final design of a bimorph mirror for SUBARU AO system. 18 Small square gaps on the outer ring are set for holes to lead lines from the internal electrodes to the back surface of the mirror.

Table 2. Performance of designed bimorph mirror

RMS fitting error (seeing = 0.45")	0.186 μm
Strehl ratio (K-band, seeing = 0.45")	0.754
RMS fitting error of tilt (1")	0.0121 μm
Required stroke of R3 for atmospheric turbulence (seeing = 1", 3σ)	0.0546 1/m
Required stroke of R3 for pure tilt (1")	0.0386 1/m

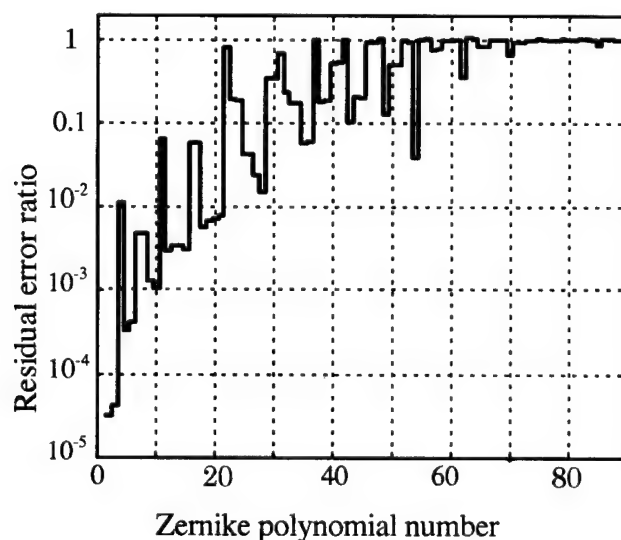


Fig. 3. Residual error ratio of each Zernike mode of the designed deformable mirror.

Wavefront Control Optimization using Adaptive Filters

M. Lloyd-Hart and T. Rhoadarmer

Center for Astronomical Adaptive Optics, University of Arizona, Tucson, AZ 85721

<http://athene.as.arizona.edu:8000/caao/>

Voice: (520) 621-8353

Fax: (520) 621-9843

Introduction

A key component in any close-loop adaptive optics (AO) system is the algorithm which converts signals from the wavefront sensor into commands to the correcting element. Much work has recently been devoted to the study of the optimal implementation of this algorithm, both in the theoretical [1, 2] and practical [3] domains. Typically, AO systems in operation at telescopes around the world measure a vector \mathbf{d} of local wavefront slopes, and rely on a linear transformation to obtain the phase vector ϕ applied to the correcting element:

$$\phi = \mathbf{M}\mathbf{d}. \quad (1)$$

The usual reconstructor matrix \mathbf{M} is a straightforward least-squares inversion of the so-called geometry matrix \mathbf{A} which relates ϕ to \mathbf{d} in the noise-free case:

$$\mathbf{d} = \mathbf{A}\phi. \quad (2)$$

There is much more information available in the wavefront sensor signal however, which is simply thrown away in this approach. In particular, correlations between elements of ϕ in both space and time can be measured, even as the AO system is in closed loop, and used to derive a reconstructor matrix which is optimized for the atmospheric conditions prevailing at the time.

In this paper, we report the results of an investigation using data taken at the Starfire Optical Range, Kirtland AFB, New Mexico. Long sequences of Shack-Hartmann wavefront sensor data in both open and closed loop have been taken using the 1.5-m telescope, whose pupil is divided into 256 subapertures. Of these, 204 are illuminated, providing slope vectors of 408 elements. Each data set consists of 10,000 frames collected at 1000 frames per second.

Approach to the analysis

In a dynamical system, equation 1 can be extended such that \mathbf{M} operates on a number of slope vectors drawn from the immediate past. This incorporates time history into the control loop, which allows short time-scale prediction of the behaviour of \mathbf{d} , and hence an improvement in the loop's performance by mitigation of the effect of processing delay. The reconstructor matrix \mathbf{M} can then conceptually be separated into two linear operators \mathbf{P} and \mathbf{S} . \mathbf{S} is the matrix normally thought of as the reconstructor, mapping the slope vector to the pupil-plane phase. \mathbf{P} on the other hand is a matrix containing knowledge of the spatial and temporal correlations between individual slopes. It operates on the series of slope vectors, and derives an estimate \mathbf{d}' of the vector in the near future. The corrected phase ϕ_c at time t is given in this model by

$$\phi_c = \phi_u - \mathbf{F}\mathbf{S}\mathbf{d}'_t, \quad (3)$$

where

$$= \mathbf{P}\Sigma_t, \quad (4)$$

and

$$\Sigma_t = \begin{bmatrix} \mathbf{d}_{t-1} \\ \mathbf{d}_{t-2} \\ \vdots \\ \mathbf{d}_{t-N} \end{bmatrix}. \quad (5)$$

Here, ϕ_u is the uncorrected phase, \mathbf{F} is the deformable mirror's influence function, and Σ_t is a column vector composed of the elements of \mathbf{d} from N immediately preceding wavefront sensor measurements.

The system model is shown in figure 1. It is fairly standard, with the exception of an additional loop on the right of the figure, which accumulates statistics of the closed-loop slope vector. After some period of time, a new predictor matrix \mathbf{P} is computed and plugged into the main, fast control loop. This operation could be performed by a separate computer which communicates directly with the wavefront reconstructor machine. In this paper, we will report the results of a number of algorithms used to derive \mathbf{P} from the SOR data, including global least squares minimisation, and simple machine learning using the delta rule.

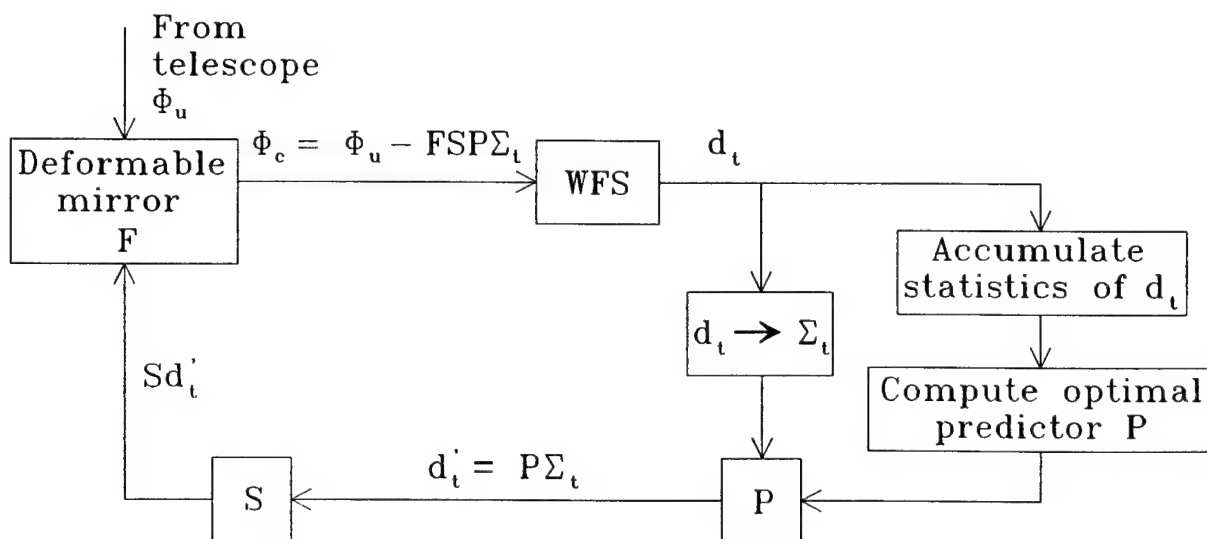


Figure 1. The adaptive optics servo loop envisioned in this paper. The loop is similar to the standard servo, with an additional slow loop which periodically updates the predictor matrix to keep track of changing atmospheric conditions.

Acknowledgment

This work has been supported by the Air Force Office of Scientific Research under grant number F49620-94-1-00437. We are very grateful to Maj. Dustin Johnston, Mike Olier, Bruce Boeke, and Bob Fugate of SOR for collecting the data used in this paper, and making them available to us.

References

- [1] Ellerbroek, B. L., "First-order performance evaluation of adaptive-optics systems for atmospheric-turbulence compensation in extended-field-of-view astronomical telescopes," 1994, JOSA A, **11**, 783
- [2] Wild, W. J. et al., "Investigation of wavefront estimators using the wavefront control experiment at Yerkes Observatory," 1995, Proc. SPIE Conf. on Adaptive Optical Systems and Applications, ed. R. K. Tyson & R. Q. Fugate, **2534**, 194
- [3] Rhoadarmer, T. A. and Ellerbroek, B. L., "A method for optimizing closed-loop adaptive optics wavefront reconstruction algorithms on the basis of experimentally measured performance data," 1995, Proc. SPIE Conf. on Adaptive Optical Systems and Applications, ed. R. K. Tyson & R. Q. Fugate, **2534**, 213

PRINCIPLES OF ACTION OF SEGMENTED CORRECTOR

Alexander P. Smirnov, Vladimir V. Reznichenko

Research Center "S.I. Vavilov State Optical Institute" St. Petersburg, Russia.

Determination of misalignment contributions of the optical system induced by individual elements errors and optimisation of "coarse" and "fine" corrections are the main purposes of the present paper. Function of the system performance dependability is investigated by means of a model of the adaptive segmented mirror telescope. The problem solution is found based on wave aberrations minimization in accordance with the corrector displacements. Position displacements of the secondary mirror in relation to the primary one as well as these of peripheral in relation to the central one seem to be parameters of this dependence. A correlation between these parameters and temperature fluctuation range is found for this optical module. Maximization of the said parameters weighted sum within the minimization problem solutions domain provides necessary conditions for correction process optimisation and determination of optimal alignment of the system main elements.

Fast Steering Mirror Performance

D. Bruns, ThermoTrex Corporation,

9550 Distribution Avenue, San Diego, CA 92121, USA, Phone (619)-536-8549 FAX (619)-536-8538,

S. Esposito, Astrophysical Observatory of Florence,

Largo E. Fermi 5, 50125 Firenze, Italy, Phone +55 2752290, FAX +55 2752292

J. Farinato, Department of Engineering, University of Padova, Italy

R. Ragazzoni, Astronomical Observatory of Padova, Italy

A fast steering mirror actuated with electromagnetic voice coils has been designed and built, shown in Figure 1. The mirror diameter is 100 mm, and made with 19 mm thick fused silica. Since only 1 milliradian angular deflections are required in typical astronomical applications, the mirror is held in place with a stiff, two-dimensional flexural pivot. Voice coil actuators are arranged in push-pull pairs about two orthogonal axes, resulting in a high torque against the mirror, but negligible piston excitation. To further control the system performance, a reaction mass inside the optical head cancels most of the external vibration.

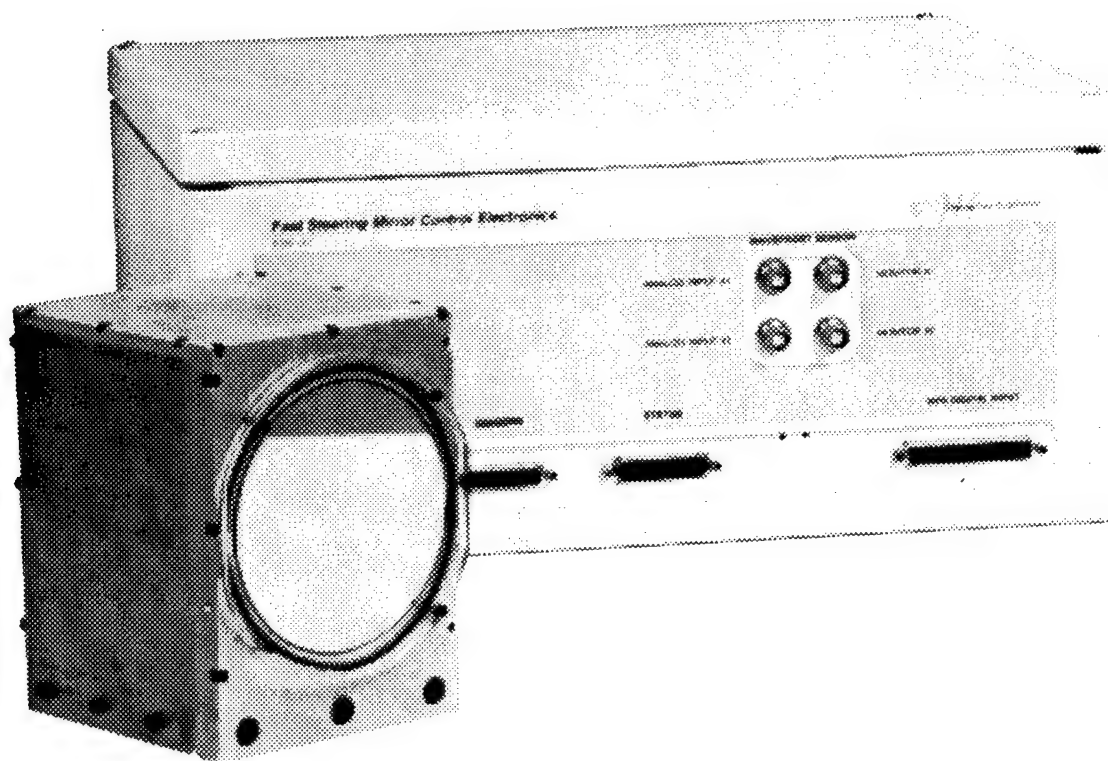


Figure 1. Fast steering mirror optical head and electronics unit.

Differential capacitance-based position sensors on the mirror back side measure the angular position of the mirror in an internal closed loop feedback system. The optical head contains the capacitance sensor electronics, but the voice coil drivers are located in the electronics unit, separated by 3 meter cables. Also contained in the electronics unit are the controls for the feedback loop, controls to electronically rotate the driving axes, and the input board. The mirror position can be driven from analog ± 10 volt signals, or a 24 bit wide parallel digital word can be used, 12 bits for each axis.

The mirror response to a square wave was measured to have a rise time of 1.3 msec. This value can be modified, depending on the amount of overshoot. The angular noise is less than 10 nanoradians/ $\sqrt{\text{Hz}}$ from DC to 200 Hz. Nonlinearity is less than 1%, due to the differential signal processing which cancels most error sources.

Status of the Design of an Adaptive Secondary for the 6.5m conversion of the MMT telescope

Guido Brusa and Peter Gray

Steward Observatory, 933 N Cherry Ave. Tucson, AZ 85721, USA
Phone (520)621-8515, Fax (520)621-9843, e-mail gbrusa@as.arizona.edu

Ciro Del Vecchio and Piero Salinari

Osservatorio Astrofisico di Arcetri, Largo Enrico Fermi 5, 50125 Firenze, Italy

Walter Gallieni

ADS Italia S.r.L. Sistemi Avanzati, Corso Promessi Sposi 23/d, 22053 Lecco, Italy

The advantages of using an adaptive secondary mirror for astronomical high resolution observations are very attractive. The drastic reduction of optical surfaces along the optical train of the adaptive system will allow a very compact system with high transmission and low emissivity. Also such a system has the potentiality of a very high actuator density.

Following the guidelines given in a first paper on an adaptive secondary based on electromagnetic force actuators and capacitive position sensors [1], various groups in collaboration have carried on both designing and prototype testing for an adaptive secondary to be installed at 6.5m conversion of the Multiple Mirror Telescope (MMT). In the last two years many progresses have been done, addressing: capacitive position sensor performances [2], general mechanical layout and thermal aspects [3]. Much work has been also done with a reduced scale flat prototype (25 actuators) in order to validate simulations and for debugging purposes [4] (see also D.Bruns et al., presented at this conference).

This paper will present the current status of the mechanical and thermal design of the entire unit.

The choice of the spectral band of operation of the adaptive optics system sets the specifications for the actuator design, this then sets the requirements of the overall structure. Since the operational band is the near infrared (NIR), a 30 cm equivalent spacing between neighbouring actuators projected on the pupil has been chosen. This is equivalent to a 30 mm spacing between actuators. Also for NIR operation a maximum settling time of 1 msec has been chosen. With these specifications the actuator has been designed in order to maximize the efficiency in terms of force applied per dissipated power and to minimize the heat exchange to the thin shell.

The overall structure has been designed in three layer: thin deformable shell (glass), thick ref-

erence plate (glass), heat sink plate (metal). The third layer has also the function of supporting the actuators that become decoupled from a thermal and mechanical point of view from the thick reference plate. Also the design of a new 36 actuators convex shape prototype that include the temperature control of the unit will be presented.

References

- [1] Salinari P., Del Vecchio C., Biliotti V., "A study of an adaptive secondary mirror", Proc. of ESO Conference on Active and Adaptive Optics, 1993
- [2] Biliotti V., Biasi R., Brusa G., Gallieni D., Spairani R. and Aiello R., "High accuracy capacitive displacement transducer for position local control loops at the adaptive secondary", Proc. of ESO/OSA Topical Meeting on Adaptive Optics, 1995
- [3] Biasi R. , Gallieni D. and Mantegazza P., "Simulation of adaptive secondary mirror dynamic response", Proc. of ESO/OSA Topical Meeting on Adaptive Optics, 1995
- [4] Bruns D., Barrett T., Sandler D., Martin H., Brusa G., Angel R., Biasi R., Gallieni D. and Salinari P., "Force-actuated adaptive secondary mirror prototype", Proc. of ESO/OSA Topical Meeting on Adaptive Optics, 1995

CHARM - A tip-tilt tertiary system for the Calar Alto 3.5m telescope

Andreas Glindemann, Mark J. McCaughrean, Stefan Hippler,
Karl Wagner and Ralf-Rainer Rohloff

Max-Planck-Institut für Astronomie, Königstuhl 17, 69117 Heidelberg, Germany

Abstract

We present a tip-tilt tertiary mirror system for the Calar Alto 3.5m telescope that reduces the rapid image motion from typically $0''.2$ to $<0''.03$ rms.

Introduction

The lowest-order adaptive optics systems are tip-tilt systems that remove the slope of the wavefront by stabilising the image motion. A number of systems have been built in the past, some of them using a tip-tilt tertiary mirror^{1,2,3} others a tip-tilt secondary⁴. The peak intensity of the corrected image is improved by up to a factor of 2–3 compared to the uncorrected image. By the end of 1996, UKIRT, the 3.8m infrared telescope on Mauna Kea, will be equipped with a tip-tilt secondary mirror that will not only correct for the image motion but also for focus⁵.

In this paper, we describe a tip-tilt tertiary system, called CHARM (Camera High Angular Resolution Module) where the emphasis is put on simplicity and on low cost without compromising the performance. An infrared camera, MAGIC⁶, is used for the first time both as a tip-tilt sensor and as a science camera⁷. For tip-tilt sensing in the visible the system is equipped with a CCD camera. CHARM was first used in September 1993 producing high resolution images of the Trapezium⁸. Then, the FWHM was reduced from $0''.7$ to $0''.35$ in the K band ($2.2\ \mu\text{m}$).

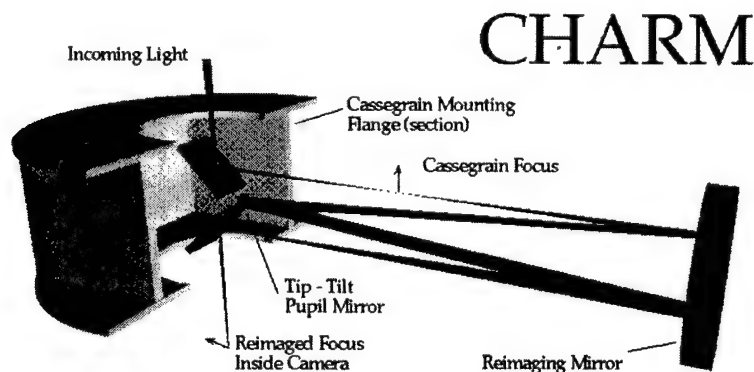


Figure 1: The optical setup of CHARM.

System Design

CHARM was built between March and September 1993. One of the design goals was to modify as little as possible MAGIC's optics and mechanics. Thus, we designed CHARM to fit into MAGIC's flange, and to leave the reimaged telescope focus in the same position as without CHARM. The reimaging optics can be removed remotely making CHARM available for MAGIC at a mouse click. Figure 1 displays the flange and the optics of CHARM.

The instrument has two wavefront sensors: MAGIC in subarray mode and an Astrocams CCD camera. The tip-tilt mirror is mounted on a Physik-Instrumente (PI) piezo unit PI-S330. A VME bus system under VxWorks is used to run the instrument and EPICS is used as a data handling system. A graphical user interface (GUI) makes it very simple to run the system. As there is an ethernet connection to the VME system, CHARM can be controlled from any computer with an ethernet connection. The same control system will be used for the UKIRT tip-tilt/defocus system⁹.

Inspired by the design of the MMT tip-tilt system³, a single parabola is used to reimage both the telescope pupil on the tip-tilt mirror, and the telescope focus into MAGIC's focal plane (see Figure 1). However, in order to keep the telescope focus in the same position with and without CHARM, the telescope focus is closer to the parabola. Consequently, the reimaged focus moves further away from the parabola into the same position as without CHARM.

The lower folding mirror, just before the infrared camera has a dichroic coating that reflects the infrared and transmits the visible to the CCD camera. The CCD camera optics reimages the f/45 telescope focus to an f/8 focus on the CCD producing a pixel scale of 0".11.

As a visible wavefront sensor, an Astrocams 4201 controller and an EEV CCD02 chip with 5 electrons read noise are used. At a pixel rate of 40 kHz the chip has to be read out in subarray mode in order to be fast enough to track the image motion. Reading out a 32 by 32 pixel, *i.e.* 3 by 3 arcseconds, subarray takes about 5 msec when 8 by 8 pixels are binned. Binning 4 by 4 pixels increases the readout time to 8 msec. As the binning is done before the A/D conversion it does not add to the read noise of the chip. Using exposure times between 5 and 30 msec, the loop frequency is between 30 and 100 Hz.

Results

Since the commissioning run in September 1993, CHARM has been used several times for astronomical observations with MAGIC⁸ and with 3D, an imaging spectrometer¹⁰. The image motion is usually reduced from about 0".2 rms motion to <0".03. Under good seeing conditions the improvement of the full width half maximum (FWHM) of the corrected star image is about a factor of two, reducing the FWHM from 0".7 to 0".35 at a wavelength of 2.2 μ m.

Fig. 2 displays the power spectra of the uncorrected and the corrected images for a loop frequency of 50Hz and three different settings for the gain. The system allows to modify the gain and to display the centroid position on-line, *i.e.* while the loop is closed. Thus, it is possible to fine tune the system while the correction is on.

The curves in Fig. 2 show that the system bandwidth is decreasing when reducing the gain. At 100% gain the bandwidth is about 6Hz, *i.e.* 1/8 of the loop frequency, at 60% it is 4Hz and at 30% it is 2 Hz. For 100% gain the power at frequencies higher than the bandwidth are amplified. However, as the power at these frequencies is about 10^3 lower than at low frequencies this effect

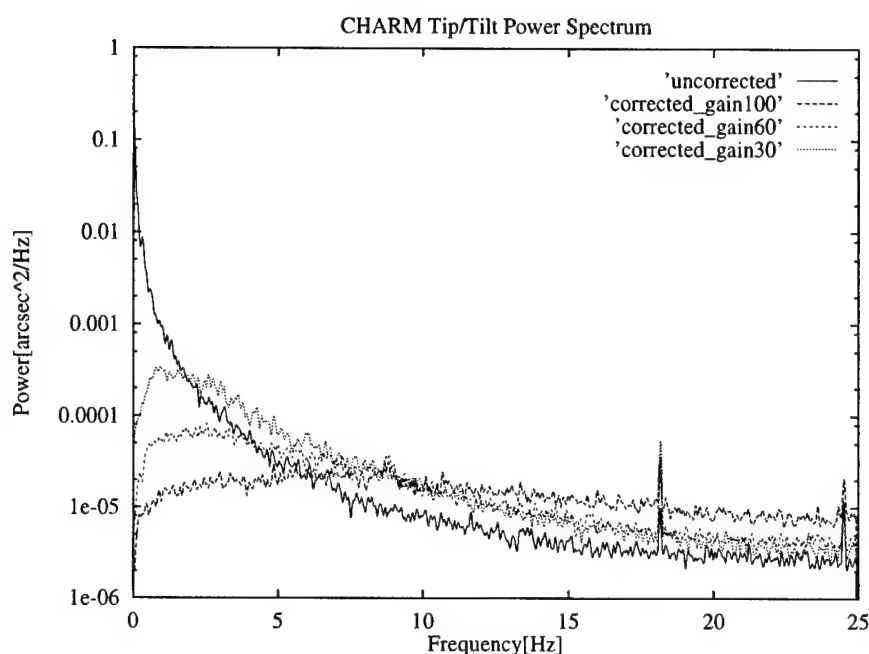


Figure 2: Power spectra of the uncorrected and the corrected image motion for gains between 30 and 100%.

is negligible. We found that a gain of 80–100% gave the best results without encountering any problems caused by the amplification at high frequencies.

More results will be given in Glindemann et al.¹¹.

References

1. A.P. Doel, C.N. Dunlop, J.V. Major, R.M. Myers. A. Purvis and M.G. Thompson 1990, Proc. SPIE, **1236**, p. 179.
2. D.A. Golimowski, M. Clampin and S.T. Durrance 1992, Appl. Opt., **31**, p. 4405.
3. D. Wittman, R. Angel, M. Lloyd-Hart, D. Colucci and D. McCarthy 1992, in Proc. ESO Conf. No. 42 on *Progress in Telescope and Instrumentation Technologies*, p. 453.
4. L.M. Close and D.W. McCarthy 1994, PASP, **106**, 77
5. T.G. Hawarden, C.P. Cavedoni, N.P. Rees, T.C. Chuter, D.G. Pettie, C.M. Humphries, R.J. Bennett, E. Atad, J.W. Harris, B. Mack, E. Pitz, A. Glindemann and R.-R. Rohloff 1994, Proc. SPIE **2199**, p. 494.
6. T.M. Herbst, S.V.W. Beckwith, Ch. Birk, S. Hippler, M.J. McCaughrean, F. Mannucci and J. Wolf 1993, Proc. SPIE **1946**, p. 605.
7. M. J. McCaughrean, A. Glindemann, C. Birk, T. M. Herbst, R.-R. Rohloff and S. V. W. Beckwith 1994, in *Infrared astronomy with arrays: the next generation*, p. 297.
8. M. J. McCaughrean and J. R. Stauffer 1994, Astron. J., **108**, p. 1382.
9. N. Rees and S. Hippler 1995, Proc. SPIE **2479**, p. 2.
10. T.M. Herbst, S.V.W. Beckwith, A. Glindemann, L.E. Tacconi-Garman, H. Kroker and A. Krabbe 1996, submitted to Astron. J.
11. A. Glindemann et al. 1996, in preparation for PASP

ACTIVE AND ADAPTIVE BIMORPH OPTICS: MIRRORS, TECHNOLOGY AND DESIGN PRINCIPLES

Andrey G. Safronov

TURN Ltd., P.O.Box 19, Moscow, 103104 Russia

Tel/Fax: (095) 299-8122, Fax: (095) 292-6511 Box 17581

Simplicity and low cost of a so-called "small" adaptive optics or the adaptive optics for low order correction make it more preferable for use than a traditional techniques. Adaptive bimorph mirrors appear to be the optimum wavefront corrector for such systems. The existing bimorph mirrors have some disadvantages, namely, a limited size of the aperture under control and low sensitivity.

Let us turn to one of the methods providing improvement of sensitivity of such mirrors as well as increase of the size of controlled aperture. The method is as follows. First, the piezoelectric ceramics on the rear side of a reflective plate is made not as a one-piece disk but as mosaic layer consisting of separate piezoelectric elements. Second, the elements, are made as a multilayer piezoelectric structure.

It is obvious that the simplest version of given technology is the use of just a single multilayer piezoelement. This is the version which was realised in practice when developing industrial one-channel molybdenum bimorph mirrors for laser optics. Response function of the mirrors correspond to defocusing. For the industrial samples of the mirrors values of sensitivity ranges from 48 to 79 $\mu\text{m/kV}$.

So, due to the use of multilayer piezoelectric plate in the construction of one-channel mirrors their sensitivity increased by 2.5 to 3 times compared to known mirrors.

Another simplest version of the above considered technology is to create a mosaic monolayer of standard piezoplates on the rear side of the mirror plate. Let us consider this version taking the development of a large-aperture bimorph mirrors as an example. As a basic model let us take a spherical mirror of 3.3 meters in a diameter with 54 electromechanical actuators and a pneumatic off-loading system. The main mirror characteristics are as following: a diameter of the central hole is 500 mm; thickness 78 mm; material - glass ceramic.

Let us use the mirror for construction a large-aperture bimorph mirror. Let all the characteristics of the mirror plate and the pneumatic off-loading system be the same. Let a mosaic monolayer of piezoelectric hexagons be formed on the rear side of a mirror plate. Thickness of piezoceramic layer is 1 mm.

3-meter bimorph mirror was studied by means of a computer simulation. For computer simulation it was assumed for simplicity that the shape of control electrode matches the final element of a computational model. Total number of control electrodes is 288. The mirror sensitivity for separate electrodes ranges from 0.95 to 4.6 mm/kV . The low value is explained by the very non-optimum relationship between the thicknesses of the mirror and the piezoceramic layer (78:1).

Efficiency of the 3-meter bimorph mirror was estimated according to its ability to compensate large-scale wavefront distortions. Maximum control voltage applied during the computer simulation was ± 300 V. The results of the correction for the 3-meter bimorph mirror and its basic model correlate only for astigmatism and coma. At compensation of defocusing and spherical aberration the advantage of the bimorph mirror is quite significant.

Therefore, the above considered technology of forming bimorph structures opens up the possibility to create large-aperture mirrors for optical telescopes. In addition to this, the investigation of the 3-meter bimorph mirror showed that it is more effective when compensating large-scale distortions than the basic model (even with its quite non-optimum construction).

High Resolution Adaptive System with a Phase Knife in the Optical Feedback Loop

A.V.Larichev

International Laser Center, Moscow State University,

Vorob'evy Gory, 119899 Moscow, Russia

tel: +7 095 939 3306; fax: +7 095 939 3113; e-mail: andrey@lado.phys.msu.su

I.P.Nikolaev

International Laser Center, Moscow State University,

Vorob'evy Gory, 119899 Moscow, Russia

tel: +7 095 939 3306; fax: +7 095 939 3113; e-mail: ilia@lado.phys.msu.su

P.Violino

Department of Experimental Physics, University of Turin, Via Giuria 1, 10125 Torino, Italy

tel: +39-11-670-7377; fax: +39 11 669 1104, e-mail: violino@ph.unito.it

Conventional adaptive systems, whose key elements are wavefront sensor and electro-mechanical wavefront corrector, face considerable difficulties, when high-order aberrations' correction is required [1]. The increase of number of adaptive mirror's control elements (up to several hundreds, recently [2]) inevitably leads to the sophistication of the sensor for measuring the wavefront "fine structure" and to intensive computations at the stage of wavefront reconstruction. Therefore, new techniques controlling light with light, which do not violate the distributed nature of light wave, attract attention of researchers [3, 4, 5]. There are a number of optically controllable hybrid devices (microchannel modulator [3], liquid crystal light valve (LCLV) [4], and membrane mirror [5]) that may be used for distributed wave front correction. However, the adequate control methods for such correctors should be developed.

We present experimental and theoretical investigation of phase distortions' suppression in a nonlinear LCLV-based optical system with distributed feedback. The feedback loop is a Fourier-filtering scheme with a phase knife, displaced in transverse direction. This spatial filter has the appropriate features: high sensitivity to phase modulation and controllable threshold of visualization in spatial frequency domain [6].

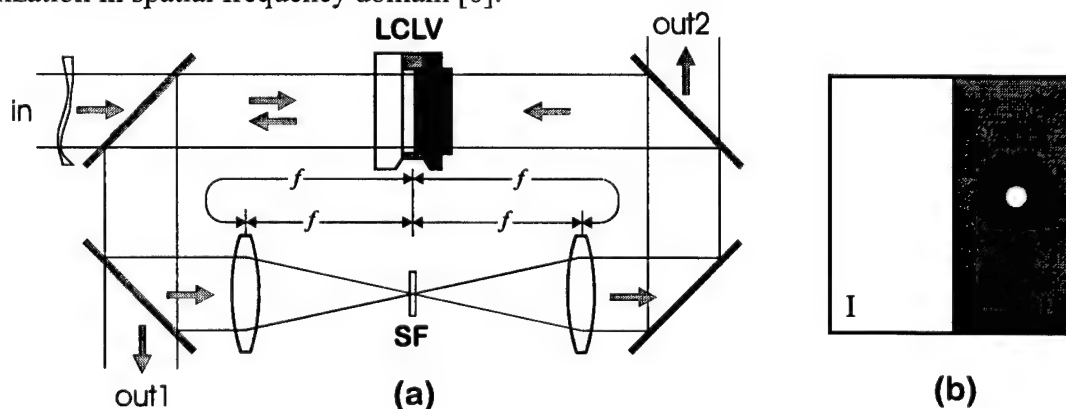


Fig.1

A schematic picture of the considered system is presented in Fig.1a. An input wave with uniform intensity and stationary phase modulation is incident on LCLV, being a hybrid wavefront corrector [4]. The beam, double-passed the liquid crystal (LC) layer and reflected from the internal mirror of LCLV, passes through the feedback loop and falls upon the photoconductor layer of LCLV. The feedback intensity distribution controls the additional phase modulation acquired by the input wave after the reflection. In the feedback loop the necessary intensity distribution is formed, dependent on the total (input plus obtained in the LC layer) phase modulation of the reflected wave, to perform an effective wavefront control. The light wave labeled as out1 is one having the corrected wavefront. The other output (out2) is made to check the residual phase distortions by monitoring the feedback intensity distribution.

Spatial filter SF, that transforms the phase modulation into the amplitude one, is a key element of the system. Fig.1b shows a schematic picture of the phase knife we used. It consists of two parts, one of them introducing an additional phase shift of $\pm \pi$ into the transmitted radiation. The phase knife is displaced in the Fourier-plane in such a way that the aperture spectrum (the Airy disc depicted schematically) lies wholly within part II of the phase-shifting plate.

The described system was implemented experimentally, with Ar^+ laser ($\lambda=514 \text{ nm}$) as a light source. Different types of stationary phase distortions were tested to be suppressed. Photographs of visualized phase distribution, for the phase profile being a 2D rectangular grating, are shown in Fig.2. Feedback is off for Fig.2a and on for Fig.2b. The phase modulation depth is considerably reduced by the system. The Strehl ratio was measured as well: it was equal to 0.13 (a) and 0.85 (b). Feasible range of suppressed spatial frequencies is from $\sim 0.2 \text{ lines/mm}$ (this value depends on knife displacement δ) up to $\sim 20 \text{ lines/mm}$ (limited by LCLV resolution). Dynamic phase distortions, having the characteristic variation time higher than the system response time, may be considered as quasistationary. Consequently, all the results are applicable in that case.

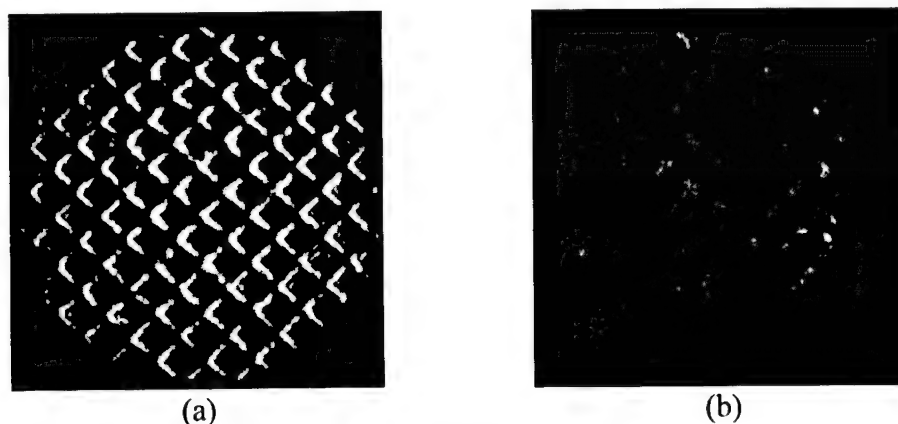


Fig.2

The linear analysis of the system mathematical model allowed us to derive the analytical dependence of the relative variance $S = \sigma_{out} / \sigma_m$ of output and input beams phase from system parameters:

$$S = \frac{1}{\sqrt{1 + (2K/(1 + v^2 l_d^2))^2}} ,$$

where K is a gain of open loop system, ν is a spatial frequency of the input phase modulation and l_d is a diffusion length, that characterizes a finite spatial resolution of the LCLV. The novelty of the considered system from the theoretical point of view is the possibility of wavefront correction in the case of nonlocal feedback (quarter-period shift of the feedback intensity, with respect to the phase grating) [6].

Absolute stability of the system, confirmed theoretically, permits to work at high feedback gain (to reduce the residual error of correction) without a risk of self-excitation. Another advantage of the suggested configuration is that a reference plane wave is not required for feedback signal generation. The developed Fourier-optical technique may be applied as well for the control of optically addressed membrane mirrors [5], that makes feedback systems with the phase knife promising for high-order wavefront distortions correction.

References

1. R.K.Tyson, Principles of Adaptive Optics, Academic, Boston, 1991
2. J.R.Kenemuth, J.S.Fender, B.L.Ellerbroek *et al.*, "Advanced Electro-Optical System with Starfire Optical Range Adaptive Optics", in *Adaptive Optics*, Vol.23, 1995 OSA Technical Digest Series (Optical Society of America, Washington DC, 1995), p.40
3. A.D.Fisher and C.Warde, *Optics Lett.* **4** (1979) p.131
4. M.A.Vorontsov, M.E.Kirakosyan, and A.V.Larichev, *Sov.J.Quantum.Electron.*, **21** (1991) p.105
5. C.J.Gaeta, T.R.O'Meara, W.P.Brown *et. al.*, *J. Opt. Soc. Am. A*, **11** (1994) p.880
6. A.V.Larichev, I.P.Nikolaev, S.Costamagna, and P.Violino, *Optics Comm.* **121** (1995) p.95

Liquid Crystal Spatial Modulators with Segmented Mirror for Adaptive Optics.

Vladimir V. Reznichenko, Vladislav V. Nicitin
Peterlab, 194214, Yaroslavsky, 40, 6, St.Petersburg, RUSSIA

Arkadi P. Onokhov, Michail V. Isaev, Natalia L.Ivanova,
Research Center S.I.Vavilov State Optical Institute
199034, St.Petersburg RUSSIA

Leonid A. Beresnev
and
Wolfgang Haase

Tecynische Hochsyble, Petersentstr 20, Darmstadt, 64287 GERMANY

We have developed efficient optically controlled liquid-crystal optically addressed spatial light modulators that possess modulation parameters for reflected light.

The recording speed of the OASLM was estimated from the rise and fall of the light intensity in the first diffraction order during frame-by-frame registration of a sinusoidal signal on the light valve. We have that, in order to ensure maximum diffraction efficiency, the duration of the writing pulses must be somewhat greater than the duration of the illumination pulse of the CRT screen (40 and 20 ms, respectively), which is apparently explained by a delay of the LC electrooptic response in the transitory control action. The minimum time of the light modulation cycle ($t = 40$ ms, $t = 70$ ms) is secured at the registration pulse amplitude of the order of 20V and amplitude of the erase pulse being equal about 5 V.

The signal-to-noise ratio in the spectral plane for an input signal frequency of 10 MHz in the maximum response speed regime was equal to 6, which for an image size of 20X20 mm corresponds to a limiting resolution of the CRT-OASLM system of 30 mm.

Specific means are available of increasing the response speed by using thin films of zinc selenide with improved properties. A decrease of the optical nonuniformity can be achieved by improving the orientation of the LC molecules and by suitably processing the layers of the structure.

Design of optical wavefront corrector based on liquid crystal concept

Vladimir V.Reznichenko, Vladislav V. Nicitin
Peterlab, 194214, Yaroslavsky, 40, 6 , St.Petersburg, RUSSIA

Arkadi P. Onokhov, Michail V.Isaev, Natalia L.Ivanova,

Research Center S.I. Vavilov State Optical Institute
199034, St.Petersburg, RUSSIA

A mack-up of a nematic liquid crystal (LC) phase corrector has developed for application in adaptive optical systems. Both design features of the optical addressed spatial light modulators and requirements to its are concedered. Optical surface processing technology is investigated for preperation of the modulator individual components. The modulator electro-optical responses obtained show the wider potentialities of the device application as a phase corrector.

The liquid crystal glassess with local modulation

Maxim G. Tomilin, Arkadi P. Onokhov, Michail V. Isaev,

Research Center S.I. Vavilov State Optical Institute
199034, St.Petersburg, RUSSIA,

Vladimir V. Reznichenko,
Peterlab, 194214, Yaroslavsky, 40, 6, St.Petersburg, RUSSIA,

Vladimir I. Kogan
Industry Constraction Bank, 191038 St. Petersburg, RUSSIA

A mack-up of a nematic liquid crystal (LC) glassess with local modulation has developed for wide application. Both design features of the LC sell and requirements to its are concedered. The processing technology is investigated for preperation new princple of local modulation. The modulator electro-optical responses obtained show the wider potentialities of the device application.

Liquid crystal displays as programmable adaptive optical elements

Don A. Gregory, John L. McClain Jr.

University of Alabama in Huntsville
Department of Physics
Huntsville, Alabama 35899
(205) 895-6276 ext. 314
(205) 895-6873 fax

Tracy D. Hudson
U. S. Army Missile Command
AMSMI-RD-WS-PO
Redstone Arsenal, Alabama 35898-5248
(205) 876-6242
(205) 876-7360 fax

Most common optical elements employ some sort of phase delay in order to manipulate wavefronts. These optical elements (lenses, prisms, etc.) are well known and have fixed phase delays. Using a pixelated, phase modulating device, such as a liquid crystal television (LCTV), it is possible to design tunable lenses, prisms, and gratings.

A phase ramp written to an LCTV, shown in Figure 1 (displayed in gray scale), would act like a wedge prism. This type of prism is commonly used for beam steering. Figure 2 shows the geometry for a wedge prism. The phase delay for such an optical element is given by:¹

$$\phi(x) = kn\Delta(x) + k[\Delta_0 - \Delta(x)] \quad (1)$$

where $\Delta(x)$ is the thickness of the prism at x , Δ_0 the maximum thickness, and n the refractive index. Inserting $\Delta(x) = L\tan\theta$ into Eq. 1 yields:

$$\phi(x) = kL\tan\theta + k(n-1)x\tan\theta \quad (2)$$

So, the transmission function of the wedge prism, $t(x) = \exp(i\phi(x))$, is of the form:

$$t(x) = e^{ikL\tan\theta} \times e^{ik(n-1)x\tan\theta} \quad (3)$$

The leading exponential in $t(x)$ is constant in x and goes to unity when the field is detected in the far field. The second exponential is in the form of a tilted plane wave. The shift theorem of Fourier optics states that this sort of phase delay in the object plane results in a physical shift in the far field.² Therefore, a wedge prism can be used to steer a beam provided that θ is large enough.

Since the maximum phase delay of an LCTV is on

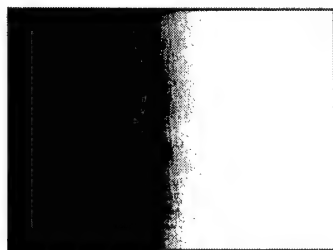


Figure 1. A phase ramp written to an LCTV

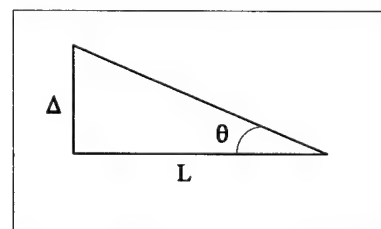


Figure 2. Geometry of a wedge prism

the order of a wavelength, the maximum angle of deflection for such a phase ramp would be approximately λ radians. Such a small angle of deflection would not be very useful. However, a blazed grating is essentially an array of small wedge prisms.³ The maximum phase modulation provided by an LCTV is comparable to the maximum phase delay employed by a blazed grating. Furthermore, when the LCTV's limited phase delay is considered, the obvious choice of lens design is a Fresnel type lens, which again is essentially an angular blazed grating.

The radii of the zones of a classical Fresnel zone plate are given by:⁴

$$R_m^2 = mf_0\lambda, \quad m = 0, 1, 2, \dots \quad (4)$$

where m is the order of the zone, f_0 the primary focal length, and λ the wavelength. The phase difference between the centers of successive zones, at a point $P = f_0$, is π . Therefore, light passing through successive zones will destructively interfere at P . Blocking alternate zones will let all of the light that passes through the zone plate to constructively interfere at P . This is what allows the zone plate to focus light at P .

Another type of zone plate is called the phase-reversal zone plate. This design introduces a phase delay of π at alternate zones rather than blocking them. In this manner, light passing through all of the zones should constructively interfere at P . However, this zone plate does not perform well in practice because the phase difference at the edge of each zone is not exactly π . This means that all of the light will not constructively interfere. In order to attain maximum performance, the phase delay should vary sinusoidally over the zone.⁵

In summary, even with phase modulation of less than 2π , a lens may be designed by allowing the phase modulation to vary sinusoidally with the phase delay given by:⁶

$$\Phi(x,y) = \cos\left(\pi \frac{x^2 + y^2}{\lambda f}\right) \quad (5)$$

Since the Fresnel lens has been shown to be closely related to the blazed grating, the experimental results summarized here are based on the study of LCTV-based Fresnel lenses. The basic procedure for writing a lensing element to the LCTV is (1) computing the necessary gray scale scene representation of the appropriate phase delay and (2) displaying the scene on an

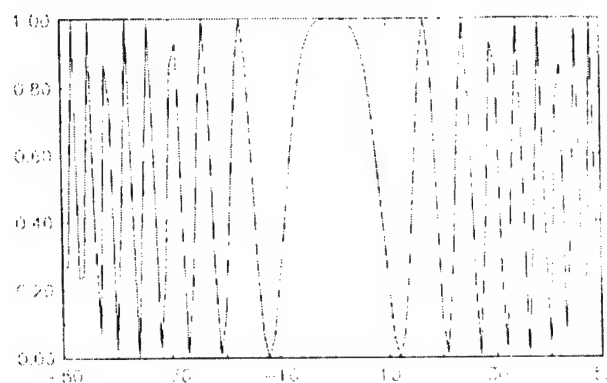


Figure 3. Phase profile of the Fresnel lens

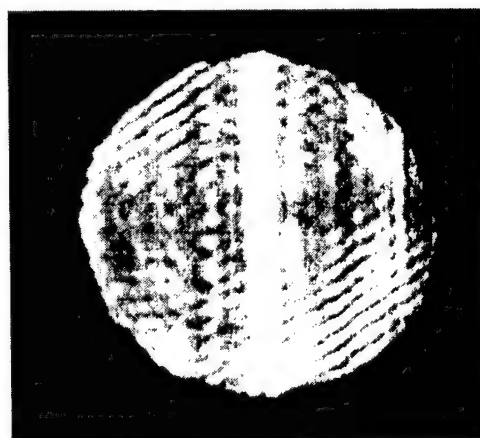


Figure 4. The far-field pattern with the cylindrical lens written to the LCTV.

LCTV operated in phase mode. Figure 3 shows the computed phase profile of a cylindrical Fresnel lens. The focusing power of this cylindrical lens was observed by viewing the far-field pattern (as shown in Figure 4). The diffraction efficiency of this lens was determined to be approximately 38%.

References:

1. J. W. Goodman, Introduction to Fourier Optics, McGraw-Hill Publishing Co., New York, 1968, p. 77.
2. Goodman, p. 9.
3. E. Hecht, Optics, Addison-Wesley Publishing Co., Reading, Mass., 1989, p. 426.
4. Hecht, p. 446.
5. Hecht, p. 446.
6. B. E. A. Saleh and M. C. Teich, Fundamentals of Photonics, John Wiley and Sons, Inc., New York, 1991, p. 116.

Polarization Insensitive 127-Segment Liquid Crystal Wavefront Corrector.

Gordon D. Love, Sergio R. Restaino,

USAF Phillips Laboratory, PL/LIM, 3550 Aberdeen SE.

KAFB, NM 87117, USA and also

Dept. of Physics and Astronomy, University of New Mexico,

Albuquerque, NM 87113, USA.

Richard C. Carreras, Gary C. Loos,

USAF Phillips Laboratory, PL/LIM, 3550 Aberdeen SE.

KAFB, NM 87117, USA

Rob. V. Morrison, Tom Baur, & Greg Kopp.

Meadowlark Optics Inc. 7560 Weld County Road 1,

Longmont, CO 80504, USA.

Email: loveg@plk.af.mil. Tel. +505-846-2711. Fax. +505-856-2711

In the past we have presented work on using nematic liquid crystal spatial light modulators (LC-SLMs) as wavefront correctors for adaptive optics (a summary of which is described in ref. 1 and references therein). For example, at the last OSA/ESO meeting on adaptive optics in Garching (1995) we described a high-quality LC-SLM which had 69-direct driven pixels which was custom designed for adaptive optics applications². One of the fundamental problems of this device, and of nematic LC-SLMs in general, is that they are inherently polarization sensitive, i.e. they can only phase modulate linearly polarized light. The use of a polarizer, and the associated wastage of light, is unacceptable for many applications, especially astronomy. In this paper we describe an LC-SLM which has been custom designed for adaptive optics and which can phase modulate unpolarized light.

There have been two main suggestions for making a device which is polarization insensitive. The first, and in some ways the simplest, technique is to use the LC-SLM in reflection mode with a quarter-wave plate (QWP) in between the device and the mirror³. The QWP-mirror combination rotates the two incident incoherent orthogonal linear polarization states through 90° with the net effect that device acts like a single-pass device for unpolarized light. This simple arrangement works effectively, however care must be taken to ensure near-normal incidence of the light.

otherwise on the return pass the beams pass through different areas of the LC-SLM to the first pass. The second technique, which is utilized in the device described here, is to construct a device having two orthogonal liquid crystal layers. Although, in principle, this is an extremely simple idea, it is significant to have actually demonstrated a high quality device because of the many associated technological hurdles which had to be overcome.

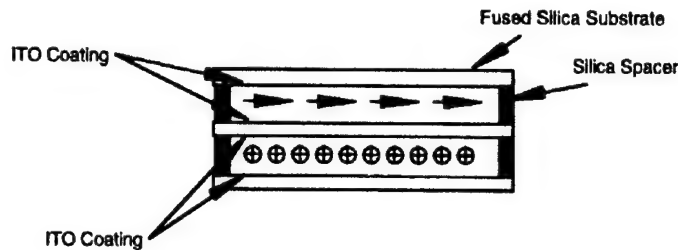


Figure 1. LC-SLM cross section showing the two liquid crystal layers and their respective optical axes.

The principle of operation of the LC-SLM is shown in figure 1. The two LC layers are shown sandwiched between the three pieces of high quality fused silica glass. The LC director (optical axis) is indicated by the arrow in the top layer, and the director is orthogonal to the plane of the paper in the bottom layer. The extraordinary refractive index of each orthogonal layer can be controlled by the application of an electric field. Thus the two mutually incoherent orthogonal linear polarization states of unpolarized light are both phase modulated. The ITO (indium tin oxide) electrodes are etched to produce the pixelated structure (fig. 2) on the central glass, and the outer glasses are coated with a continuous ITO ground plane.

Number of pixels	127	LC layer thickness	20 μ m
Active area diameter	14.2mm	LC material	Merck E44
Pixel size (max. diameter)	1.15mm	Total throw	4 μ m
Inter-pixel gap	36 μ m	Transmittance	>90%
Inter-pixel electrode width	5 μ m	Optical quality	< λ /5 P-V (HeNe)
Fill factor	~94%	Speed	~25Hz for 1 λ of total throw.
Glass thickness	1.52mm		

Table 1. LC-SLM specifications.

The device specifications are shown in table 1. The fitting error associated with such a piston-only pixelated structure yields a Strehl ratio of 75% for a D/r_0 of 6 (i.e. a 1m class telescope), according to the equations given by Hudgin⁴.

In summary: we have constructed a device which has overcome one of the two main problems facing the use of LC-SLMs in adaptive optics. The second problem is nematic LC response times. Work is in progress on improving liquid crystalline materials in order to increase the achievable temporal bandwidth.

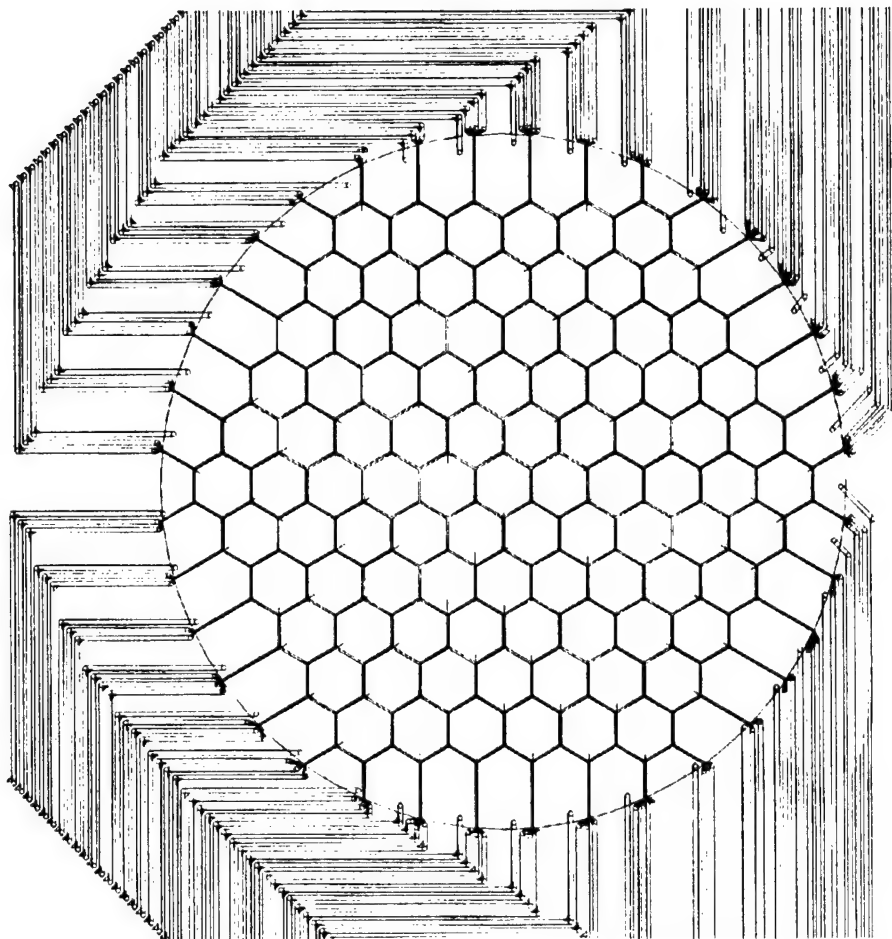


Figure 2. LC-SLM pixel map. The ITO electrodes can be seen leading into the hexagonal pixels.

References

- ¹Gordon D. Love, Janet S. Fender, and Sergio R. Restaino. "Adaptive Wavefront Shaping with liquid crystals." *Optics and Photonics News*. 6(10):16-21. Optical Society of America October (1995)
- ²Gordon D. Love, Sergio R. Restaino, Richard A. Carreras, Gary C. Loos, Ray M. Sharples, Rob V. Morrison. "High quality wavefront control with a liquid crystal spatial light modulator." in ESO/OSA Topical Meeting on Adaptive Optics. p.223-224, Optical Society of America (1995)
- ³Gordon D Love. "Liquid crystal phase modulator for unpolarized light." *Applied Optics* :p.2222-3 (1993).
- ⁴Richard Hudgin. "Wave-front compensation due to finite corrector-element size". *JOSA* 67(3): pp.393-395 (1977).

DIGITAL FILTERING TECHNIQUES AND CENTROID PREDICTORS IN AO SERVO-SYSTEMS

D. Gallieni, D. Bonaccini
European Southern Observatory
Garching bei München - Germany

1. ADAPTIVE OPTICS SERVO-SYSTEM BOTTLENECKS

Adaptive Optics systems need a wavefront sensor (WFS) for the servo-loop. The WFS integration time has to be selected considering SNR requirements. This requires to extend the integration period as much as possible, especially when dealing with faint sources. On the other hand, WFS sampling period imposes the discretization time-step to the entire servo-system, thus influencing its close loop bandwidth. The latter is also affected by additional time delays caused by WFS readout/reconstructor computing time.

To tackle both these aspects without affecting system performances, two different strategies are pursued. Both are intended to extend servo-system bandwidth and to reduce bandwidth contribution to the total residual error.

The first method has the aim to avoid that WFS sampling time imposes the servo-system considerably lower bandwidth than that given by subsystems ones. For example the reconstructor computer and the adaptive mirror itself, have usually bandwidths which can be up to one order of magnitude higher than the WFS sampling frequency with NGS. Two possible solutions are hereafter introduced, namely the Avalanche PhotoDiode based WFS and the prediction of WFS output signal when CCD devices are used.

The second method is to compensate for the other time delays that reduce servo-system bandwidth. This can be mainly achieved by a proper design of the mirror command filters. Their parameters can be adapted according to the variations of some statistics of the residual error, thus assuring constant performances in presence of time varying working conditions. Moreover, a different implementation of the WFS predictor can be implemented to compensate for these time delays.

The effects of the implementation of these strategies are evaluated by means of close loop simulations of a single mode control loop in the modal wavefront polynomial expansion. These are performed by using measured data of the Adonis AO system taken at the ESO 3.6m telescope.

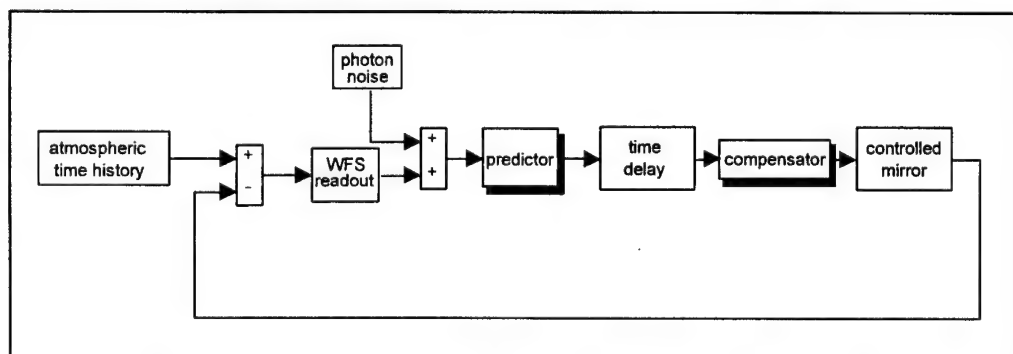


Figure 1: Adaptive Optics servo-system flow chart

2. WFS STRATEGIES

2.1 APD SENSOR

The advantages achievable by using an Avalanche Photo Diode as image motion sensors have already been described [Bonaccini et al., in SPIE Proc. Vol 2201, pp 650-654]. In this context this sensor is analyzed from the servo-system dynamics point of view.

The APD is used as a photon counting device that can be read at a quite high frequency, 1 kHz in the case here analysed. This device has no readout noise, thus it can be read at the desired rate without introducing additional noise. We use a high frequency sampled signal, filtered through a digital Running Window averager, whose width is determined as function of WFS SNR.

In this way the WFS does not introduce into the servo-system a low sampling frequency, hence allowing the adaptive element to correct with a large bandwidth. The number of retained samples, N , times the filter sampling period, τ , gives the Running Window amplitude $T = N \tau$ that can be related to an equivalent CCD integration period T .

2.2 CCD OUTPUT PREDICTION

When using a CCD based WFS, a feasible way to address the controller in a bandwidth larger than CCD sampling frequency consists in predicting WFS output one integration period ahead. This can be done by modelling the signal with an AutoRegressive linear model

$$y(t) = \sum_{k=1:m} a_k * y(t-k) + e(t)$$

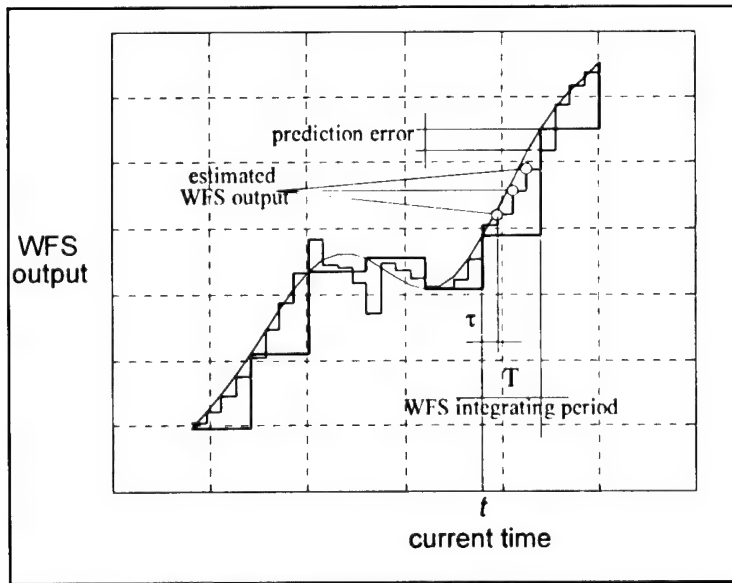


Figure 2: CCD output prediction scheme

Model parameters $\{a_k\}$ are trained by means of a Recursive Least Square (RLS) algorithm in order to minimize the prediction error. At a given time t , WFS output at time $t+T$ is computed based on the present model and estimates of WFS measures are fitted in the coming integrating period at a desired frequency $1/\tau$. With this technique, the WFS block of the AO servo-system (Figure 1) can be considered as a sampler working at the frequency $1/\tau$ instead of the CCD integrating one $1/T$ (Figure 2).

3. CONTROL DESIGN

STRATEGIES

3.1 HIGH ORDER MIRROR COMMANDS FILTERING

In order to shape the system transient response, mirror commands high order recursive filters have to be implemented. The compensator coefficients are derived analytically as a function of relevant system parameters.

$$H(T, T_{\text{DEL}}, CL_{\text{poles}}) = \frac{A + Bz^{-1} + Cz^{-2}}{1 + Bz^{-1} + Cz^{-2}}$$

A , B , C , D and E can be computed as explicit function of the equivalent WFS integration time T , the additional time delay T_{DEL} and the positions of the close loop poles, which are available as design parameters to shape the transient response. An optimal value of WFS integration time is computed based on system performance estimators, thus allowing to adapt system response to changing observing conditions (e.g. changes in the seeing during operation).

An estimate of a second order compensator effect can be obtained by comparing it with a pure integrator controller, the latter being the current case for Adonis. The gain of these control strategies appear either in terms of reduction of the wavefront mode residual rms error, σ , for a fixed WFS integration time, T , or as an extension of the allowed WFS integration time, for a constant wavefront mode residual rms error.

For example in the case of one-axis angular tilt and the Adonis readout noise free EBCCD, given an integration time $T=10$ ms, an overall time delay $T_{\text{DEL}}=5$ ms and a tilt Power Spectral Density cut off frequency of 2 Hz, the achievable results are summarized in Table 1 and Table 2.

Table 1: fixed $T=10$ ms

	Open Loop σ [arcsec]	Close Loop σ [arcsec]	Attenuation
integrator	1.25	0.26	4.8
2 nd order compensator	1.25	0.18	6.7

Table 2: constant σ

	Open Loop σ [arcsec]	Close Loop σ [arcsec]	WFS integration time [ms]
integrator	1.25	0.26	10
2 nd order compensator	1.25	0.27	20

3.2 APD OUTPUT PREDICTORS

The same centroid prediction algorithm used for CCDs may be applied to the APD WFS, in order to compensate time delays present in the servo-system.

When sensing centroid motion via APD WFS, the Running Window digital filter introduces a time delay of $(N\tau)/2$, where $T = N\tau$ is the Running Window width. This delay sums with other servo-system delays ($T_M=1.45$ ms for the tilt-mirror currently on Adonis) and can be compensated predicting the time sequence of the WFS outputs n steps ahead, where $n=(T/2+T_M)/\tau$, with τ the APD sampling period (we set $\tau=1$ ms). In Table 3 results achievable by implementing this kind of predictor are summarized with the same gains evaluation criteria used for the compensator analysis. In this case the tilt cut-off frequency is 1.3 Hz and the open loop residue is 0.28 arcsec.

T [ms]	σ_{pred} [masec]	σ_{nopred} [masec]	σ [masec]	τ_{pred} [ms]	$\tau_{\text{no_pred}}$ [ms]
16	9	12	12	28	16
20	10	14	14	34	20

Table 3: Multistep predictor effects

3. FINAL REMARKS

We have reported on the sensible gains achievable in adaptive servo-systems via an adaptive digital filtering strategy, as well as via centroid prediction algorithms embedded in the servo-system filter design. The major gains may be achieved with faint reference stars or long WFS integration times, which is the most common case in astronomical adaptive optics.

REPORT ON THE OPTICAL QUALITY OF ADONIS' DM AND RELAY OPTICS: IS THE MIRROR AGING ?

R.Tighe, E.Prieto
European Southern Observatory, La Silla
Casilla 19001, STGO.19, Santiago, Chile.
 (email: rtighe@eso.org)

November 1992 the Deformable Mirror (DM) for ESO's Near Infrared Adaptive Optics System (ADONIS), was delivered with a measured specification of surface flatness better than $\lambda/2$ without voltage applied on the actuators, and better than $\lambda/4$ when offset voltages are applied such that the first 8 Zernike terms are removed(1).

Subsequent surface quality checks have been performed since then. Fringe interferometry in 1993 and 1994, and phase shift interferometry in 1995 and 1996. The measurements have been performed with a *Tinsley Laboratories, Inc.* laser (632.8nm) interferometer in Twyman-Green configuration, upgraded for phase-shift interferometry with hardware and software from Phase Shift Technology, Inc(2). Results are summarized in Table 1.

Table 1

Date	Offset Voltages	Aberrations Remove	PTV (wavelength)	RMS (wavelength)
1992	No	None	0.36	0.06
1992	Yes	8 First Zernicke	0.18	0.02
1993*	Yes	8 First Zernicke	0.6	
1994*	Yes	8 First Zernicke	0.6	
1994	No	None	1.2	
1995	No	None	1.6	0.3
1996	No	None	1.6	0.3
1996	Yes	"Flattening" out	1.6	0.2

* DM covered by telescope pupil image simulating mask (i.e. the central part of the mirror is covered by the pupil central obstruction).

Apparently the mirror suffered a surface quality degradation with respect to the delivery specs, soon after installation and/or first operation, due principally to a strong dip in the center of the mirror. After that, the overall surface figure has remained fairly stable during these last three years. By applying adequate offset voltages to each actuator, the mirror can be "flattened" out gaining more than 10% in Strehl ratio by doing so (compare Figures 1 and 2).

Still, there remains around 0.2 waves P-V of "bumpiness" residuals that cannot be removed by this procedure and correspond to the location of the actuators (Figure 3). We wonder if the actuators (8x8 array separated 9.5mm from each other), push-pulling against the metallic base and silica substrate of the mirror, are producing permanent bumps in the surface.

We are now preparing for an experiment to do interferometry of the DM making the surface as flat as possible, as well as applying the highest spherical aberration possible to

check if stresses effects are present as well. With the instrument operating in open loop with offset voltages, we'll measure the surface error induced wavefront residuals and their influence on the overall AO image correction. We will present results of the overall analysis review.

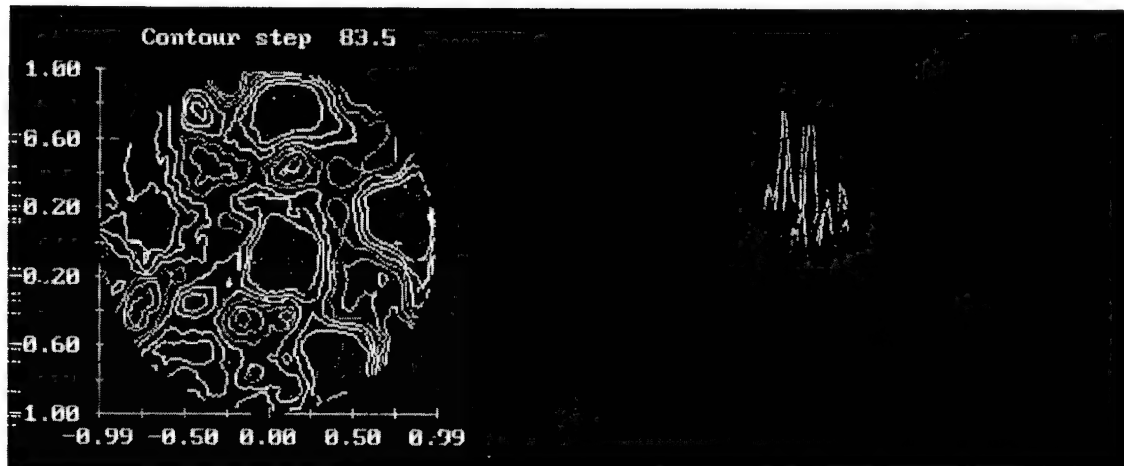


Figure1: Contour of phase map of DM without offset voltages applied. The P-V is 1046nm and the RMS is 162nm. The Strehl ratio is 0.08.

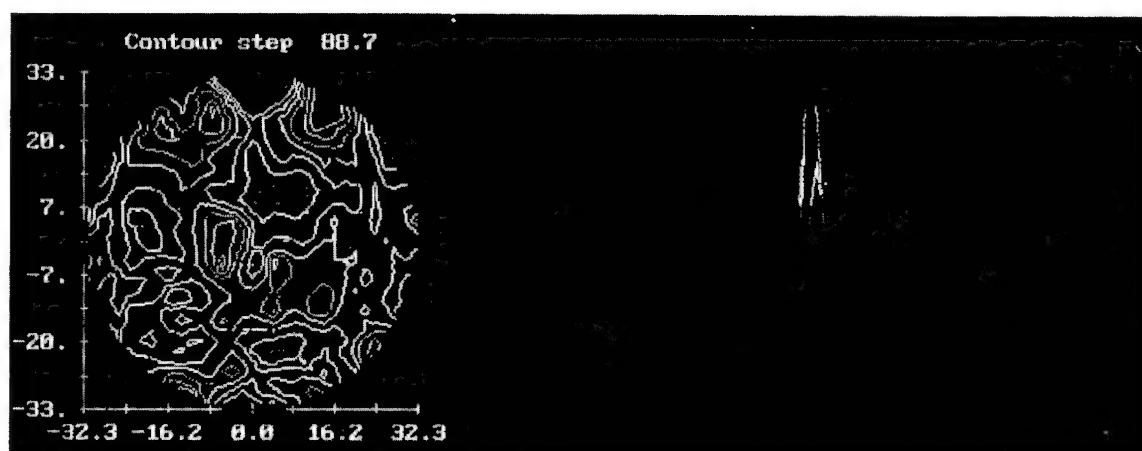


Figure2: Contour of phase of DM with offset voltages applied to some actuators so as to "flatten out" the surface. The P-V is 1066nm. The RMS is 136nm. The Strehl ratio is 0.17.

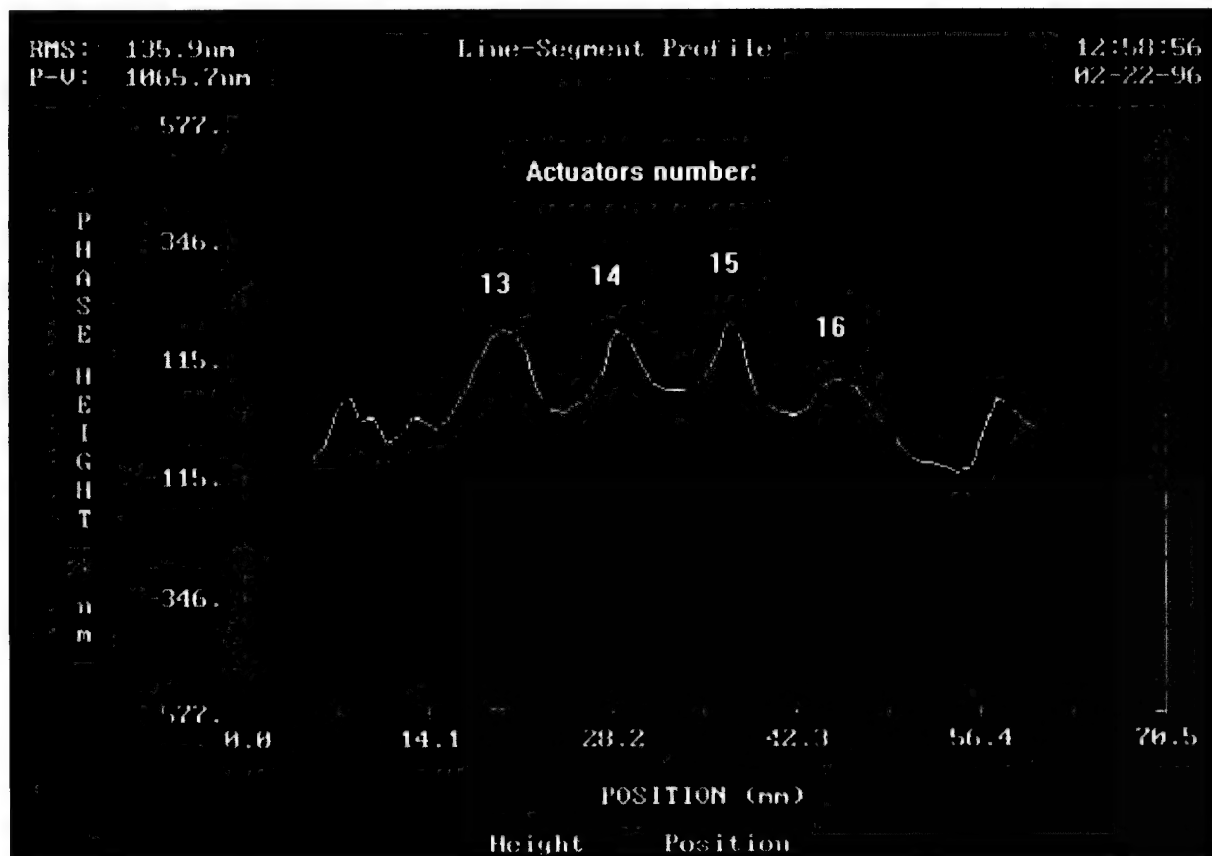


Figure3: Phase profile of a line segment traced across the pupil over the row of actuators number 11 through 18.

References:

- (1) ONERA, Rapport Final #24/3693 PY, Juin 1993, Come On Plus: Description et Performances du Systeme. G.Rousset, P.Y.Madec, J.L.Beuzit, S.Wang.
- (2) Phase Measuring Analysis Software Manual, February 1993, Phase Shift Technology Inc, 1430 E.Fort Lowell,Tucson AZ 85719.

Adaptive Optics Servo-system Performance Estimator: practical implementation

E. Prieto¹, D. Bonaccini¹, H. Geoffray¹, P. Prado¹, L. Demailly²

¹ European Southern Observatory Garching bei München - Germany

² Observatoire de Paris-Meudon - France

The evaluation of the quality parameters of the adaptive correction and their evolution with time is important while your adaptive optics system is running. It allows to give an observer a precise feeling of what he will get in the integrated image, it allows the operator to keep an eye on the system performance, and it allows the implementation of adaptive filtering techniques to the servo control laws. These reason have driven us to implement such a tool on the ESO Adonis system. To know the image quality parameters the only possibilities are to directly look at the science image or from the wavefront sensor residuals. Our purpose is to report on our attempts to evaluate the long exposure Strehl ratio and FWHM of the corrected PSF, by using the residual slopes given by the Wave Front Sensor (for us a Shark-Hartmann). We have used the following relation to compute the long exposure strehl¹:

$$SR = \frac{e^{-\sigma_{ho}^2}}{1 + \sigma_t^2} + \frac{1 - e^{-\sigma_{ho}^2}}{1 + \left(\frac{D}{r_0}\right)^2}$$

r_0 : Fried parameter without adaptive optics

σ_t^2 : wavefront variance from tip-tilt residuals

σ_{ho}^2 : High Order residuals wavefront variance

D: telescope diameter

With the subapertures slopes, using the differential image motion expression we can compute r_0 by²:

$$\sigma_{\tau}^2 \approx 2 \left(0.18 D_{sub}^{-1/3} - 0.145 d^{-1/3} \right)^2 r_0^{-5/3}$$

$$\sigma_{\parallel}^2 \approx 2 \left(0.18 D_{sub}^{-1/3} - 0.097 d^{-1/3} \right)^2 r_0^{-5/3}$$

where σ_{τ}^2 is the variance of the lateral motion, σ_{\parallel}^2 is the variance of the longitudinal motion, D_{sub} is the diameter of the sub-apertures, and d is the distance between the sub-apertures centers.

We can use σ^2 coming either from data taken in open loop, or else rebuild the wavefront by using the WFS residuals plus the DM commands. We have tested this method provides a reasonable approximation.

Due to the noise in real data, the simple computation of the variances is not efficient. We can use an algorithm which is able to give a better approximation of the variance. If we consider the noise as white in the frequency domain, its time autocorrelation should be null except in zero, i.e. a Dirac delta function. Looking at the time autocorrelation of a set of WFS centroid data (wavefront slopes), in zero we will have the variance plus the noise. But in other points we have only the variance, so if we fit a curve with a parabola extrapolating toward the

origin, we will find a good approximation of the variance (see fig 1) and an estimate of the sensor noise contribution.

Paradoxically this method works in cases of large wavefront slope (or centroids) residuals. In the case of very good correction, the residuals are very low, so the variance signal to noise ratio given by this method is poor, and it's difficult to find the precise residual slope variance value. As it can be seen on fig 2, the signal is of the same order as the noise.

This variance calculation method has been proposed by G.Rousset and implemented by E.Gendron³ and L.Demilly at ESO 3.6m telescope Adonis adaptive optics system.

We will present the experimental comparison between the image quality performance parameters obtained from the Wavefront sensor slopes and those obtained directly from the analysis of the Infrared camera data.

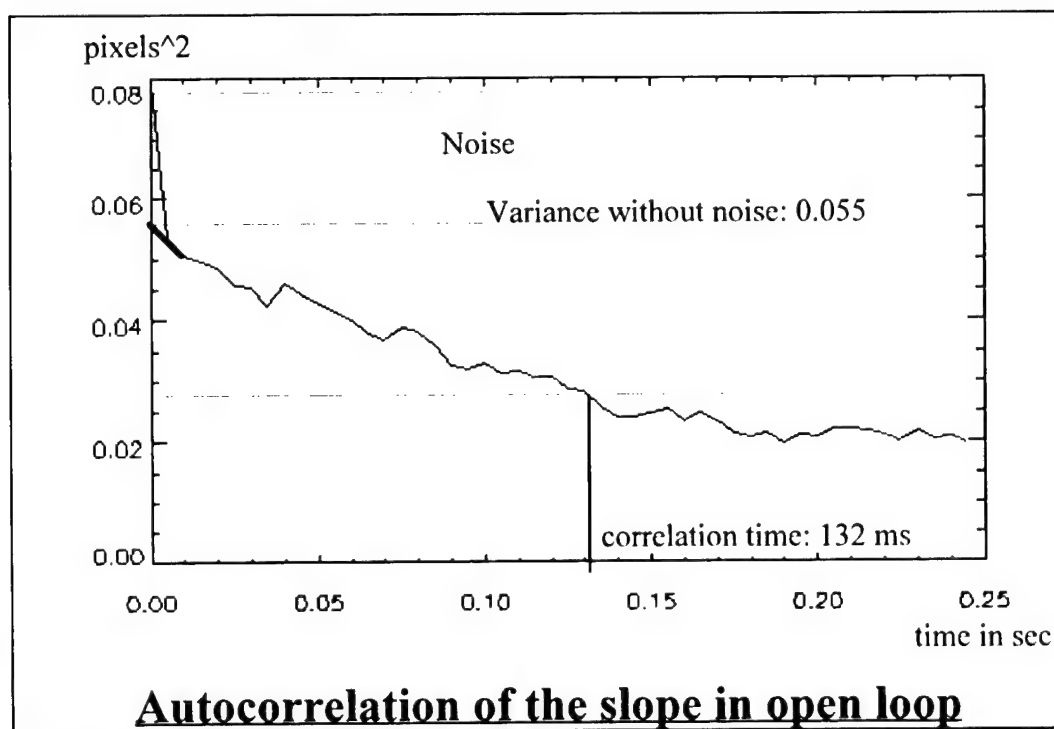


Figure 1

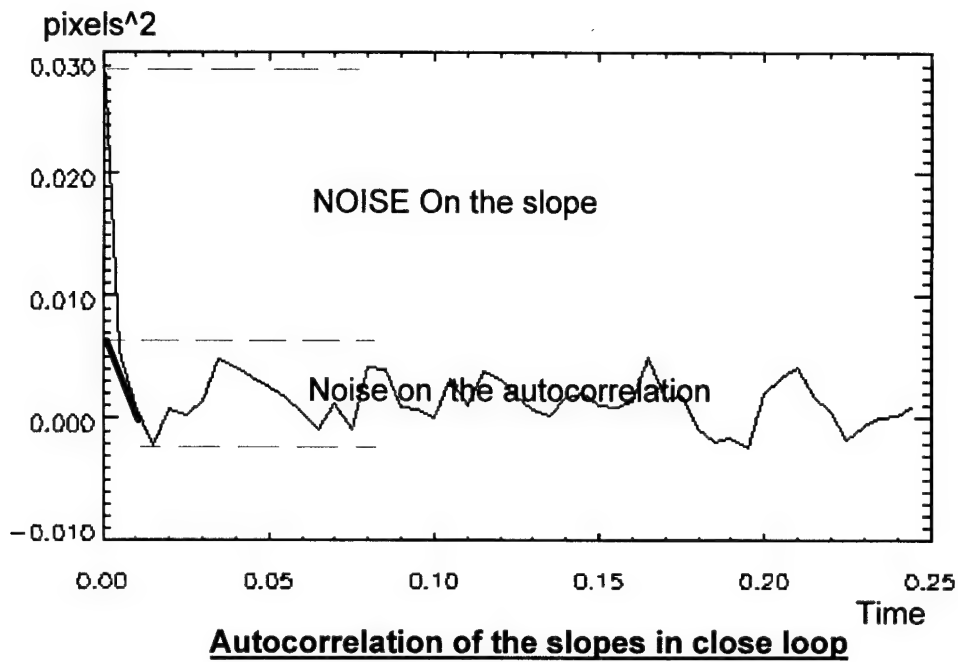


Fig 2

References:

- 1: Parenti, R.R, and Sasiela, R.J: JOSA A, Vol 11, 288-309, January 1994
- 2: M. Sarazin, F. Roddier: "*The ESO Differential Image Motion Monitor*", Astron. Astrophys. 227, 294-300 (1990)
- 3: E. Gendron thesis at " L'universite D. Diderot" (13 mars 1995): "optimisation de la commande modale en optique adaptative: application a l'astronomie"

**Searching for Brown Dwarfs and Extra-Solar Planets
from the Ground Using Adaptive Optics**

David Sandler
University of Arizona and ThermoTrex Corp.

Steven Stahl
ThermoTrex Corp.

Roger Angel
University of Arizona

The adaptive optics system under development for the new 6.5 m MMT, using an adaptive secondary mirror, will allow direct detection of cool brown dwarfs much closer in than Gliese 229B. An advanced system with 10,000 actuators will allow direct detection of Jupiter-like planets around bright stars within 10 pc. Requirements and detection limits will be discussed.

Friday, July 12, 1996

Wave-front Correctors

AFA 8:00 am-9:20 am
Pikake Room

Robert K. Tyson, *Presider*
W.J. Schafer Associates Inc.

Adaptive Secondary Development

Donald Bruns and Todd Barrett, ThermoTrex Corporation.

9550 Distribution Avenue, San Diego, CA 92121, USA. Phone (619)-578-5885, FAX (619)-536-8538,

Guido Brusa, Steward Observatory, University of Arizona.

Tucson, AZ 85721, USA, Phone (520)-621-8515, FAX (520)-621-9843

Roberto Biasi and Daniele Gallieni, Dipartimento di Ingegneria Aerospaziale.

Politecnico di Milano, via Golgi, 40 20133 Milano, Italy Phone +39 2 2399 4049, FAX +39 2 2399 4034

1. Introduction

The MMT will be converted to a single 6.5 m primary mirror in 1997. The new telescope will be equipped with adaptive optics for high-resolution infrared astronomy at wavelengths between 1.6 microns and 5 microns. Atmospheric distortions will be corrected using an adaptive secondary mirror which directly feeds a high-resolution infrared detector. The use of an adaptive secondary maximizes emissivity, which provides high throughput to the imaging detector and efficient wavefront sensing by eliminating many optical elements normally needed in Coudé systems.

The purpose of this prototype was to debug the components and allow comparisons with theoretical predictions. We have studied actuator-position sensor interactions and report on performance characteristics. Manufacturing techniques and reliability have also been tested, to reduce risks when building the final adaptive secondary.

2. Adaptive Secondary Design

Figure 1 shows the adaptive secondary design in schematic form. More realistic mechanical details are shown in another paper in this conference. A total of 300 electromagnetic (voice coil) force actuators, approximately 32 mm apart, will push on a 2 mm thick, 640 mm diameter glass mirror. The thin mirror's figure will be referenced about 60 microns from a thicker, relatively stable glass surface. A 10 kHz feedback loop using capacitance-based position sensors located at each actuator will maintain the distances commanded by a wavefront sensor or open-loop look-up tables. The capacitive sensors control the complex dynamics of the thin shell with a time constant at least ten times shorter than the wavefront sensor, and allow use of the adaptive secondary when adaptive optics is not operational (active mode).

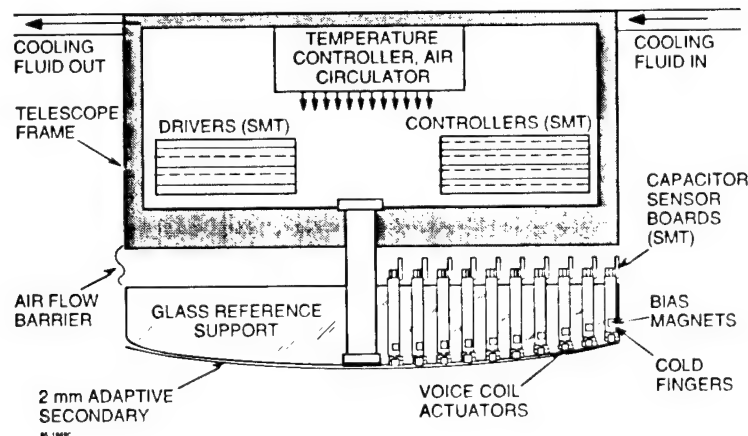


Figure 1. Adaptive secondary configuration.

3. Twenty-five Actuator Prototype Design

To test the concept on a smaller scale, we built the twenty-five actuator prototype shown in Figure 2. This prototype used a 200 mm diameter, 38 mm thick reference surface with 25 holes bored on a 5 x 5 square grid. A 150 mm square, 2.3 mm thick glass mirror was suspended by thin brass springs at each corner. These supports constrained motion transverse to the reference surface, but allowed essentially free motion in the normal direction. The front

surface of the mirror was not yet metallized in this view, so the actuators and magnets can be seen. The capacitance sensor circuit boards are attached to each actuator, and the voice coil pigtails lead to the voice coil driver electronics.

A digital feedback loop controlled the actuators. We implemented the digital control loop with commercially available DSP hardware on VME boards. The electronics digitized the capacitor sensor output voltages, processed the control loop, and output the analog control signals for each actuator at a 10 kHz rate. Simple current driver electronics boosted the signals from the computer to the voice coils.

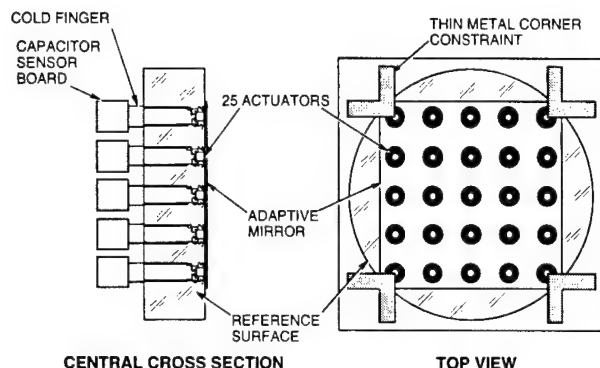


Figure 2a. 25 actuator assembly schematic.

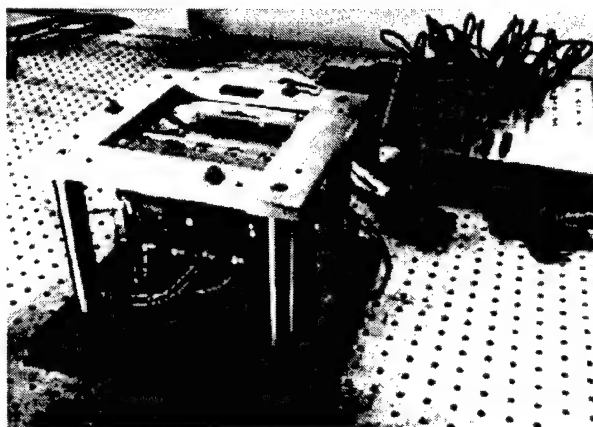


Figure 2b. 25 actuator assembly.

4. Twenty-five Actuator Prototype Measurements

We performed both static and dynamic tests on the completed prototype. Static tests were done to measure the ability to flatten the mirror, while dynamic tests were done to quantify the mirror's response time for different types of aberrations. A time series of surface shapes generated using Kolmogorov statistics were also used to determine realistic force requirements.

The 2.3 mm thick glass used in the prototype was not polished flat out to the edges, where the outer actuator rows have no influence. The static interferograms shown in Figure 3 shows the mirror before and after manually adjusting the actuator forces for a nominally flat figure. These images are made looking through the glass, so errors in the glass thickness also added to the figure. The image on the left was taken with no power to the actuators, and shows such a poor figure that some of the mirror surface was beyond the interferometer range. Approximately 1 watt per actuator was required to bend the mirror flat, 90% of which was used to control the small amplitude, high frequency spatial distortions that will not be present in the final system. Generating low spatial frequency modes, like defocus or astigmatism, requires very little power.

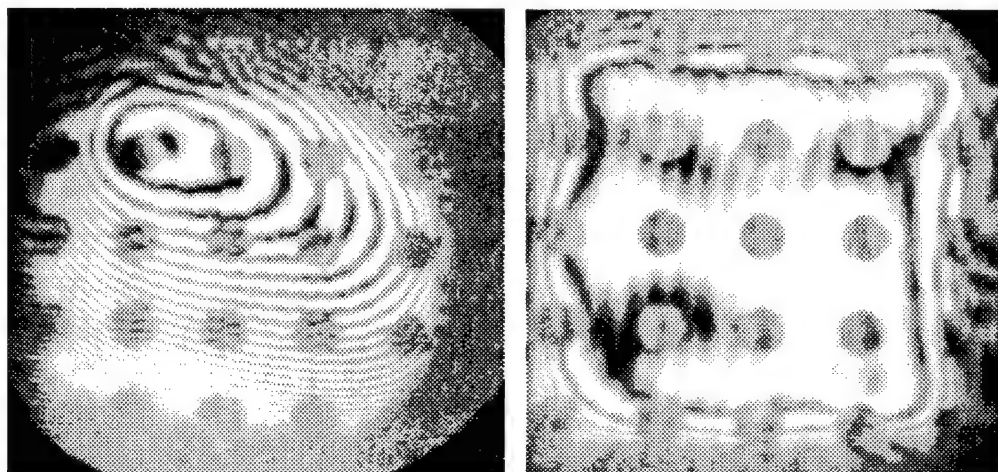


Figure 3. Mirror figures; before and after manual flattening

The temporal response for the center actuator in the mirror Zernike defocus mode is shown in Figure 4. The command step size was 0.75 microns at the mirror center, much bigger than would ordinarily be required to compensate for atmospheric turbulence. The large amplitude, high frequency modulation on top of the square wave is primarily periodic digitizer noise with some uncontrolled mirror vibration. The signal, near 700 Hz, has an rms amplitude of only 15 nm. The small overshoot and 3 msec rise time is a function of the parameters used in the digital control loop. Adjusting the parameters for optimum response is now in progress.

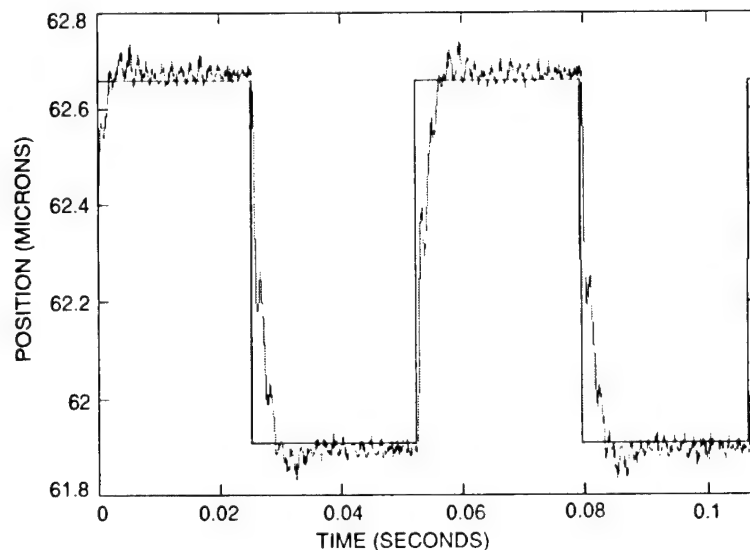


Figure 4. Mirror dynamic response

Measurements with a 10 kHz frame rate, high resolution interferometer (Barrett, 1994) at the Starfire Optical Range in New Mexico were undertaken to verify the precision and reliability of the capacitor sensors. Results confirmed that the capacitor sensors were accurate and operate with low noise. In addition, no uncontrolled high order spatial modes were generated in the mirror, even under a wide range of commanded positions at various temporal frequencies. This simplified additional tests, since only electronic measurements were required to evaluate different control loops.

Temporal Kolmogorov distributions, corresponding to an r_0 of 50 cm at 2.2 microns and a 15 m/sec ground wind speed were applied to the prototype with the mirror nearly flattened. Data analysis is still being performed, but preliminary results show that the average and peak powers are in agreement with mechanical modeling calculations reported by Salinari. (Salinari, 1993).

5. References

- Barrett, et al, "High-bandwidth interferometer for real-time measurement of deformable mirrors", Adaptive Optics and Astronomy, Proceedings of the SPIE, Vol. 2201, 1994.
- P. Salinari, C. Del Vecchio, V. Biliotti, "A study of an adaptive secondary mirror", Proceedings of the ICO-16 Conference on Active and Adaptive Optics, 1993.

Keck Adaptive Optics: Test of a Deformable Mirror in a Freezing Environment

D. S. Acton, P. Stomski, P. Wizinowich, J. Maute, T. Gregory
W. M. Keck Observatory, 65-1120 Mamalahoa Highway, Kamuela, HI 96743, U.S.A.
Tel: 808 885-7887; Fax 808 885-4464; email sacton@keck.hawaii.edu

M. Ealey, T. Price
Xinetics Inc., 410 Great Road #A6, Littleton, MA 01460
Tel. 508/486-0181, Fax. 508/486-0281

Introduction

The W. M. Keck Observatory and Lawrence Livermore National Labs are currently developing an adaptive optics system for use on Keck II--a 10.8-meter segmented telescope. This AO system will make use of a 349-actuator deformable mirror (DM). The Keck II telescope sits atop Hawaii's Mauna Kea, where the ambient nighttime temperature varies between -5 and 5 degrees C. In order to reduce dome seeing, and to minimize the thermal emissivity, the AO system (and hence the DM) will be cooled to the ambient temperature of the outside air. Therefore, we are motivated to use actuators in the DM that are optimized for operation at 0 degrees C.

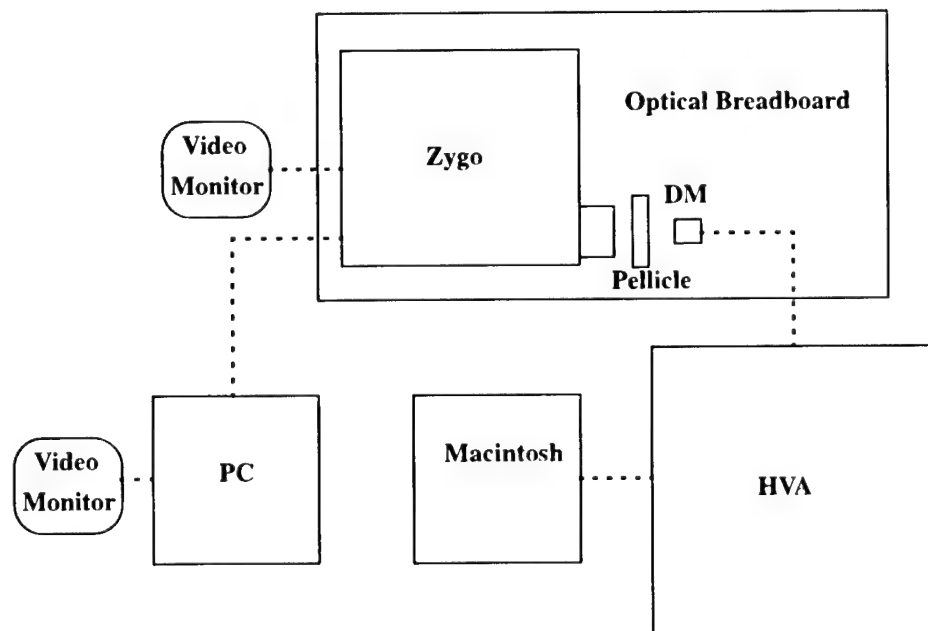
There are currently four different actuator materials available to us that we can use in the DM: PZT:5H (standard PZT), PMN:RP (a new type of PMN actuator manufactured by Xinetics Inc.), PMN:RZ (just now being developed by Xinetics), and PMN:RE (standard PMN material). Although some data is available on the behavior of these actuators at 0 degrees C, virtually no tests have been performed on integrated DM's at this temperature (to the authors' knowledge). We feel that such tests are essential before an informed decision can be made with regards to the best actuators for our AO system.

The table on the next page summarizes the issues associated with the various choices of actuators and our current understanding of them. The goal of our evaluation program is to verify (and quantify where possible) our expectations about the behavior of each actuator type, and fill in the blanks where they exist. This evaluation project is currently in progress. It is our hope that it will be completed in time to present all of the results at the conference. In this summary, however, we will only present results for tests performed on the PMN DM at 1 and 21 degrees C.

Experiment

Our goal is to measure the gain and hysteresis of the actuators, measure the drift (and creep) as a function of time, and check for failures of actuators. In order to accomplish this, we set up the experiment shown on the next page, using a 37-actuator Xinetics PMN:RP deformable mirror. The DM is mounted on an optical breadboard where it is monitored by a Zygo interferometer. The interferometer produces an RS-170 video image of the interference fringes, which can be viewed on a video monitor, and digitized by a frame-grabber board in a PC. The DM is powered by a rack of high-voltage amplifiers (HVA) which in turn are controlled by a Macintosh computer. The gain and hysteresis curves of all 37 actuators can be measured simultaneously. This is done by slowly pistoning all 37 actuators in unison, up and down, throughout their full dynamic range. During this process, the interferogram is digitized at a rate of 8 frames per seconds, and

	PZT:5H	PMN:RP	PMN:RZ	PMN:RE
Hysteresis at 0 degrees C	15-20% (at 4 μ m travel)	15-20% (4 μ m) 10% (1 μ m)	Expect 5-10% 4 μ m 3% (1 μ m)	20-30% (4 μ m) 15% (1 μ m)
Hysteresis at 23 degrees C	10-15% (at 4 μ m travel)	2-3% (at 4 μ m travel)	Expect 1-2% (at 4 μ m travel)	< 1% (at 4 μ m travel)
Temperature sensitivity	0.2% per degree C	2% per degree C	0.2% per degree C	2% per degree C
Drift and creep (at 0 C)	large	small	Expect moderate	Expect none
Actuator Failure	Expect several failures out of 349; 1 X 10 ⁵ cycles	Expect no failures ever; > 10 ¹¹ cycles	Expect no failures ever; > 10 ¹¹ cycles	Expect no failures ever; > 10 ¹¹ cycles
Optical Figure (unpowered)	$\lambda/2$ rms	$\lambda/20$ rms	$\lambda/10$ rms	$\lambda/5$ rms
Aging factor (% change per time decade)	-4.2	-0.3	-0.15	None



stored on the PC. Pixels in the digitized video images corresponding to each actuator are extracted, yielding the fringe intensity as a function of input voltage. This gives sinusoidal functions that can be unwrapped by locating the peaks and valleys, as well as the turn-around points. The result is a curve showing the hysteresis and gain for each actuator.

The phase map of the DM can be determined by analyzing the video fringed image with the WYKO "WISP" fringe analysis program. By analyzing frames taken over an extended period of time, drift in the mirror figure can be determined.

In order to test the lifetime of the actuators, we have written a "turbulence simulation" program on the Macintosh. The user inputs the value of r_0 and the τ_0 (the atmospheric coherence diameter and the mean life-time of a turbulence cell), and the program then generates a "movie" of atmospheric turbulence which is "played" on the DM for an indefinite period. Our current plan is to run the turbulence simulation program for several months, using realistic values of r_0 and τ_0 .

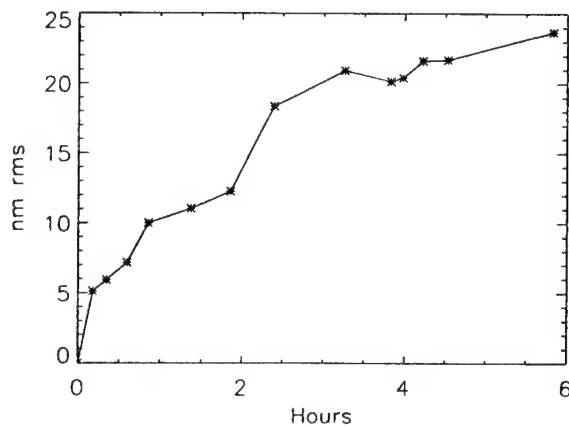
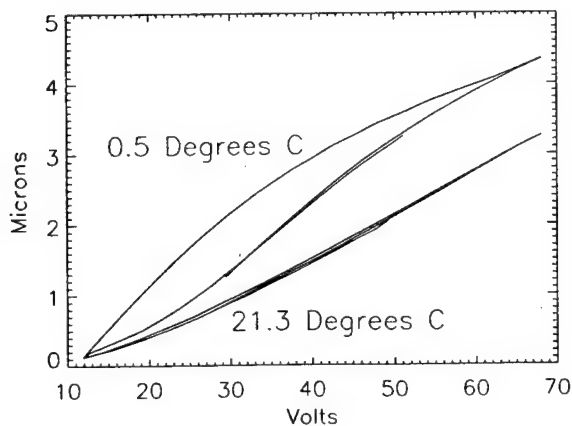
Results

The gain and Hysteresis curves were measured at 21.3 degrees C in the optics lab at Keck headquarters. Curves were also measured at about 0.5 degrees C at the Keck I telescope dome. The results for a single actuator are shown in the figure below on the left. On the average, the hysteresis increased from approximately 2.5% at 21.3 degrees C to approximately 15% at 0.5 degrees C. When using excursions of only 1 micron, the hysteresis at 0.5 degrees C reduced to about 10%. At 0.5 degrees C, the average gain increase by about 40% compared to its gain at 21.3 degrees C.

The drift of the DM was measured at approximately 2 degrees C over a 6 hour period. The results are shown in the figure below on the right, in terms of the rms change in the DM surface.

Future Plans

It is our intention to continue these tests with the PMN:RP DM, quantifying drift as a function of temperature change as well. We will continue to run the turbulence simulation, checking for hard failures of the actuators, as well as any degradation in their performance. If all goes as planned, we will perform the same tests on a 37 actuator DM made with the new PMN:RZ Xinetics actuators. It is hoped that the RZ actuators will demonstrate the good characteristics of both the PMN and the PZT actuators. We are also considering performing tests on a PZT DM.



Wavefront estimation by phase diversity and compensation with a liquid crystal wavefront corrector.

Gordon D. Love,

USAF Phillips Laboratory, PL/LIM, 3550 Aberdeen SE.

KAFB, NM 87117, USA. and also

Dept. of Physics and Astronomy, University of New Mexico,

Albuquerque, NM 87113, USA.

•

Steven M. Ebstein, Robert A. Gonsalves, Peter Nisenson,

Lexitek, Inc., 100-F Tower Office Park

Woburn, MA 01801, USA.

Sergio R. Restaino, Richard C. Carreras,

USAF Phillips Laboratory, PL/LIM, 3550 Aberdeen SE.

KAFB, NM 87117, USA.

William Junor.

Rockwell Power Systems,

KAFB, NM 87117, USA.

Email: ebstein@lexitek.com. Tel. +617-933-0613. Fax. +617-933-1887.

Nematic liquid crystal spatial light modulators (LC-SLMs) have been proposed as wavefront correctors for adaptive optics (a summary of which is described in ref. 1 and references therein). For example, at the last OSA/ESO meeting on adaptive optics in Garching (1995) we described a high-quality LC-SLM which had 69-direct driven pixels which was custom designed for adaptive optics applications². Additional work has been done with the goal of producing a polarization insensitive LC-SLM which does not suffer the reduced efficiency of a device which only works with a single polarization³. This paper demonstrates successful application of an LC-SLM to wavefront compensation and the first successful application of phase diversity sensing⁴ to wavefront compensation, to the best of our knowledge.

The experimental arrangement is shown in Figure 1. An imaging system includes an unknown aberration and an LC-SLM in the pupil. The image is recorded with a phase diversity camera which measures two focal plane images. One of the images is recorded in best focus and the other is recorded with a known amount of defocus introduced.

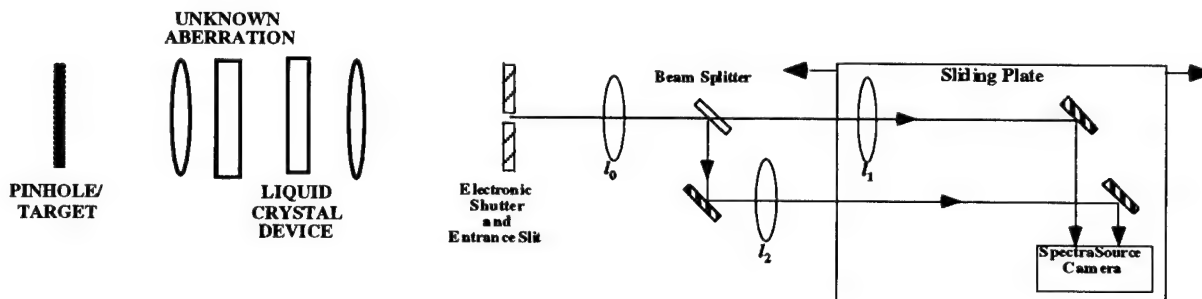


Figure 1. Schematic of the experimental setup. An optical system including an unknown aberration and an LC-SLM for phase compensation images a target onto a phase diversity camera which records two focal plane images.

The initial data was recorded with the LC-SLM off so it introduces no phase in the imaging system. The unknown phase was estimated with data from an unresolved pinhole which was input to an iterative phase diversity algorithm. The estimated phase was conjugated and a best fit was applied to the LC-SLM device. An example of the phase estimation is shown in Figure 2 where the LC-SLM device was used to introduce the aberration. The compensation was not done in real-time. The experiment used a static aberration and relied on the stability of the apparatus from when the distortion was recorded until it was compensated.

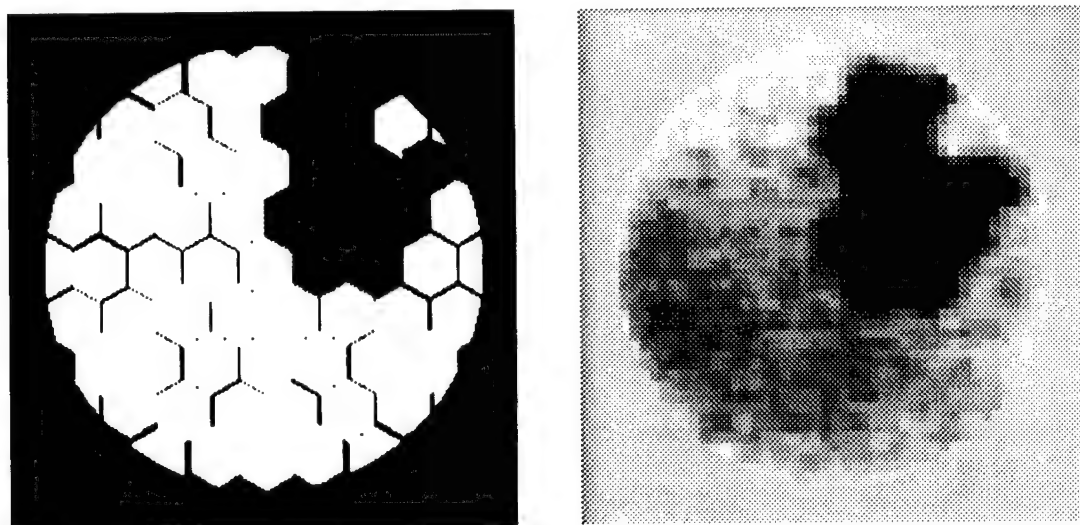


Figure 2. Demonstration of phase diversity wavefront sensing. An aberration shown at the left was introduced with the LC-SLM device. The estimated phase, shown at the right, matches the input to 0.05 waves rms.

Figure 3 shows the compensation of a point source (pinhole) using the experimental apparatus. The square root of the intensity is displayed to enhance the faint portions of the images. The results show a nearly 3X improvement in the Strehl of the point source, from 0.23 to 0.62. Figure 4 shows the compensation of an extended target, using the phase estimated from the pinhole data.

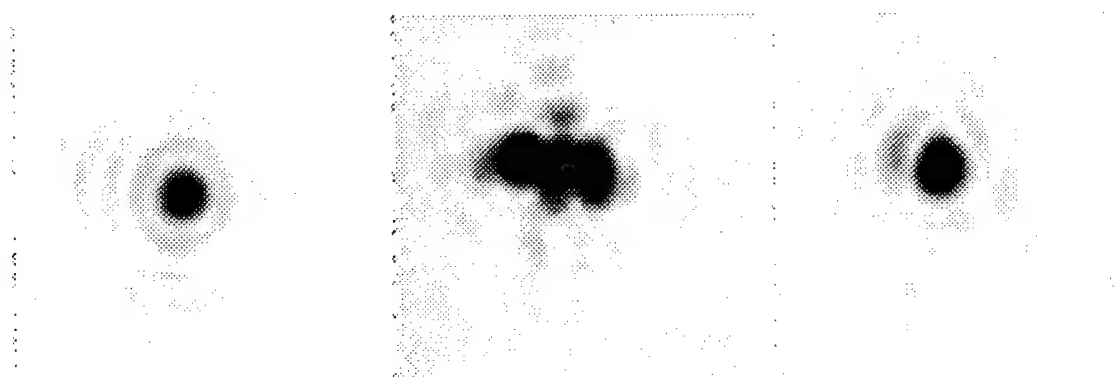


Figure 3. Pinhole images recorded (from left to right) with no aberration, with an unknown aberration, and with the aberration compensated by the LC-SLM. Square root of the intensity is displayed.

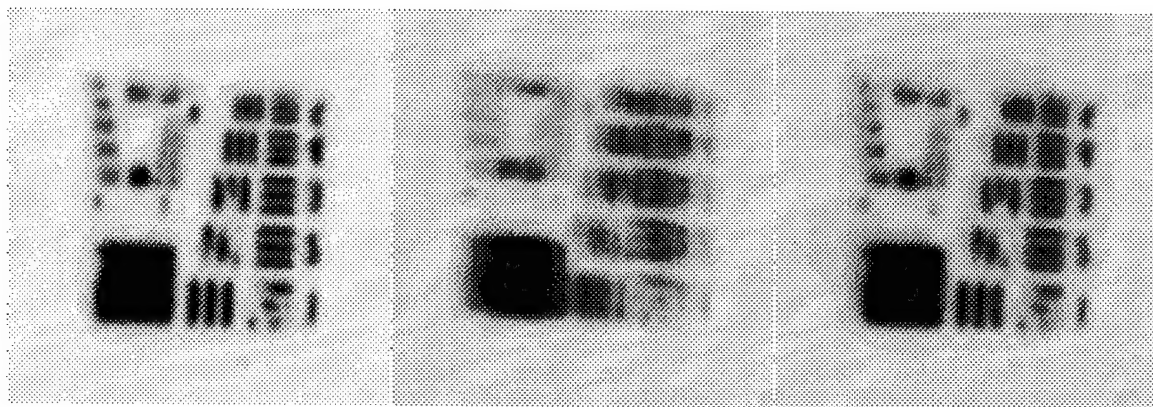


Figure 4. USAF resolution target images recorded (from left to right) with no aberration, with an unknown aberration, and with the aberration compensated by the LC-SLM. Square root of the intensity is displayed.

This demonstrates successful application of an LC-SLM to wavefront compensation and the first successful application of phase diversity sensing to wavefront compensation, to the best of our knowledge.. Work is in progress to quantify the accuracy of the phase estimation and compensation relative to expected values.

References

-
- ¹Gordon D. Love, Janet S. Fender, and Sergio R. Restaino. "Adaptive Wavefront Shaping with liquid crystals." *Optics and Photonics News*. 6(10):16-21. Optical Society of America October (1995)
 - ²Gordon D. Love, Sergio R. Restaino, Richard A. Carreras, Gary C. Loos, Ray M. Sharples, Rob V. Morrison. "High quality wavefront control with a liquid crystal spatial light modulator." in ESO/OSA Topical Meeting on Adaptive Optics. p.223-224, Optical Society of America (1995).
 - ³Gordon D Love. "Liquid crystal phase modulator for unpolarized light." *Applied Optics* :p.2222-3 (1993) and Gordon D. Love et al, "Polarization Insensitive 127-Segment Liquid Crystal Wavefront Corrector," this conference.
 - ⁴R.A. Gonsalves, "Phase retrieval and diversity in adaptive optics," *Opt. Eng.* 21, 829-832 (1982); R. A. Gonsalves, "Phase Retrieval by Differential Intensity Measurements," *J. Opt. Soc. of Am.*, January 1987; R.G. Paxman and J.R. Fienup, "Optical misalignment sensing and image reconstruction using phase diversity," *J. Opt. Soc. Am. A* 5, 914-923 (1988); R. A. Gonsalves, "Non-isoplanatic imaging by phase diversity," *Opt. Lett.* 19 (7), 493-495 (1994).

All-Optical Adaptive Systems: Nonlinear Optics Approach for Phase Distortion Suppression

M.A. Vorontsov

Army Research Laboratory, Battlefield Environment Directorate
White Sands Missile Range, New Mexico 88002
and
New Mexico State University
Las Cruces, New Mexico 88003

Recent studies of nonlinear optical systems with two-dimensional (2D) feedback have led to the possibility of a new type of adaptive optical system having extremely high spatial resolution for wavefront distortion suppression - the All-Optical Adaptive (AOA) system [1-3]. Presently, dynamic phase distortion suppression is achieved through one of three basic techniques:

- Conventional adaptive optics (AO) based on electronically driven deformable mirrors [4,5,6].
- Nonlinear optical methods including phase conjugation (PC) [7,8] and beam clean-up [9,10].
- All-optical adaptive 2D feedback systems [1-3].

The structure of conventional AO systems and their operating algorithms strongly depend on the technical characteristics and capabilities of two key elements: the adaptive mirror and the wavefront sensor. This hardware dependence creates an artificial functional structure for modern AO systems, as seen in Fig. 1. Both the input and output optical fields are 2D signals of the transverse coordinates $\{x,y\}$, while internal system operation consists of the one-dimensional (1D) electronic signals $b_l(t)$ ($l=1,..., M$) and $a_j(t)$, ($j=1,..., N$), where M is the number of wavefront sensor output signals and N is the number of the control channels.

Because of the use of deformable mirrors in this type of adaptive system, we must transform a 2D optical signal to 1D electronic signals; after data processing, these signals are inversely transformed back to the output 2D optical signal. The entire adaptive system becomes unnecessarily complicated, expensive, and require numerous (>100) control channels and electronic components to achieve even a modest level of wavefront distortion correction. This is perhaps the principle reason AO is not widely used, and has not been considered for many potential applications that might significantly benefit from the use of AO.

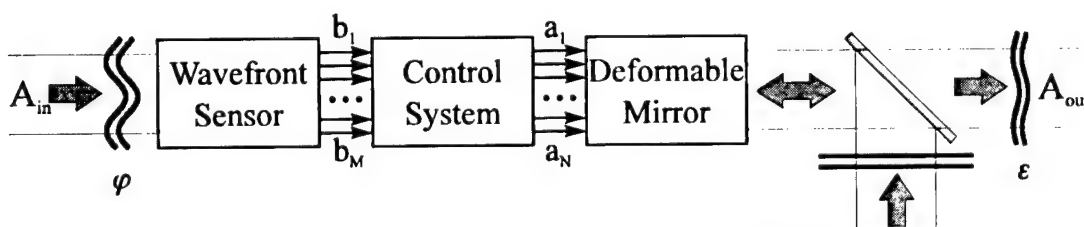


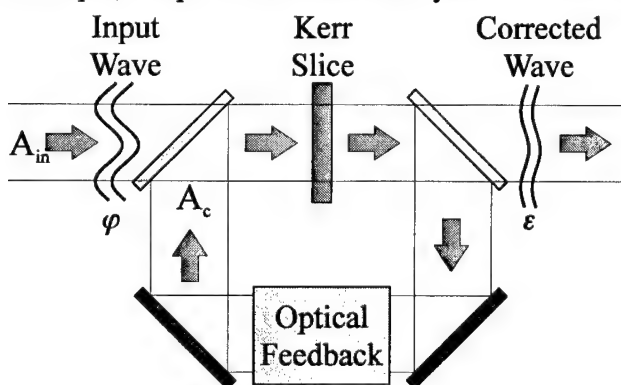
Fig. 1. Schematic diagram of a conventional adaptive system with deformable mirror.

The obvious advantage of phase distortion suppression using nonlinear phase conjunction (PC) is that the entire system is purely optical: no deformable mirror, wavefront sensor, or electronic components. However, there are some important applications where it is not possible to use PC adaptive systems. One limitation derives from the geometry of the PC approach: the source of the phase distortions must be located in the optical paths of both outgoing and reflected waves, so that the laser beam encounters these distortions twice. The disadvantage in this is that frequently the requirement is to suppress phase distortions having a source either unknown or inaccessible. Another disadvantage of the PC approach relates to limitations on the target type; this method assumes the target is either a point source, or can be considered to have a single bright glint.

In beam clean-up systems, instead of deformable or PC mirrors a nonlinear element such as a photorefractive (PR) crystal or spatial phase modulator is used [9,10]. To suppress the incident wavefront phase distortion an additional reference beam with undistorted wavefront is required. With PR crystals, due to two wave mixing in the crystal the energy transfers to the reference beam, which becomes the output beam with undistorted wavefront. The reference beam can be obtained directly from the incident beam using a low pass spatial filter. However, this results in a significant decrease of reference beam energy and requires extremely high signal amplification in the PR crystal. Reference beam amplification is also accompanied by noise amplification as a result of scattering on crystal inhomogeneities, yielding a poor quality output beam. An additional drawback is the requirement for small beam sizes due to the small PR crystal size (typically 3-6 mm).

Here we discuss AOA systems using nonlinear Kerr-type elements incorporated into a 2D optical feedback loop. A schematic diagram of this type of adaptive system is shown in Fig. 2.

A Kerr-type element introduces an additional phase modulation $u(r,t)$ into the passing wave, with the phase modulation proportional to the wave's intensity distribution inside the Kerr slice $I(r,t)$. The outgoing wave's corrected phase becomes $\epsilon(r,t) = \varphi(r,t) + u(r,t)$. The intensity distribution $I(r,t)$ is formed by the input wave $A_{in}(r,t)$ and by an additional controlling wave $A_c(r,t)$ entering from the 2D feedback loop: $I(r,t) = |A_{in}(r,t) + A_c(r,t)|^2$. In contrast with the PC technique, adaptive 2D feedback systems do not require back propagation through the distorting



medium. The controlling wave $A_c(r,t)$ is formed directly from a small portion of the output wave. The purpose of the optical feedback loop is to convert the residual wavefront error $\epsilon(r,t)$ into its corresponding intensity modulation; that is, to visualize the wavefront $\epsilon(r,t)$.

Fig. 2. Block diagram of an adaptive system with optical feedback.

The following issues relating to AOA systems will be discussed:

- Basic types of AOA systems and operational principles.
- Wavefront control efficiency and wave spatial coherence transformation.
- Stability of 2D feedback control and basic type of spatio-temporal instabilities.
- Experimental results using an AOA system.

REFERENCES

1. W.J. Firth and M.A. Vorontsov, *J. Mod. Opt.* **40**, 1841-6 (1993).
2. E.V. Degtiarev and M.A. Vorontsov, *J. Opt. Soc. Am. B* **12**(7), 1238-1248 (1995).
3. M.A. Vorontsov and K.V. Shishakov, *J. Opt. Soc. Am. B* **9**(1), 71-78 (1992).
4. R.K. Tyson, *Principles of Adaptive Optics* (Academic, Boston, 1991).
5. Special Issue: Atmospheric-Compensation Technology, *J. Opt. Soc. Am. A* **11** (1994).
6. J.W. Hardy, *SPIE Proc.* 1542, 2-17 (1991).
7. B.Ya. Zel'dovich et al., *Principles of Phase Conjugation* (Springer-Verlag, Berlin, 1985).
8. Jun-ichi Sakai, *Phase Conjugate Optics* (McGraw-Hill, New York, 1992).
9. A.E.T. Chiou and Pochi Yeh, *Opt. Lett.* **10**(12), 621-624 (1985).
10. A.E.T. Chiou and Pochi Yeh, *Opt. Lett.* **11**(7), 461-463 (1986).

- Abraham, J. M. — ATHA2
 Abreu, Rene — AMB18
 Acton, D.S. — AMB1, AMB2, AMB3, AMB16, AWD4, AFA2
 Acton, S. — AMB4
 Adcock, Miles J. — AWC3, AWD14
 Aitken, George J. M. — AWC5, ATHA4, ATHC8
 An, Jong — AMB4, AMB10
 Angel, J. R. P. — AMB8, AMB9, ATuB3, ATuB5
 Angel, Roger — ATHC29
 Arsenaault, Robin — AMB14
 Avicola, Kenneth — AMB1, AMB4, AMB10

 Baker, Jeffrey T. — AMB23
 Baliunas, S. L. — AMB13
 Barbier, Pierre R. — AWD8
 Barrett, T. K. — AMB8, AFA1
 Bauer, Kenneth W. — ATHC10
 Baur, Tom — ATHC25
 Beletic, James W. — ATHA1
 Bell, Ray — ATHC9
 Bely, Pierre — AMB22
 Beresnev, Leonid A. — ATHC21
 Berg, J. G. — AMB25
 Berger, Paul J. — AMB18
 Berkefeld, Thomas — AWC2, AWD16
 Bilbro, James W. — AMB22
 Bissinger, Horst D. — AMB10, AMB11
 Black, J. H. — ATuB5
 Bonaccini, Domenico — AMC5, ATHC26, ATHC28
 Bonshtedt, B. E. — ATHC4
 Booth, H. — AMB24
 Boyer, Corinne — AMB14
 Brase, James M. — AMB1, AMB4, AMB5, AMB10
 Brigantic, Robert T. — ATHC10
 Brown II, James M. — AMB19, AWC4
 Bruns, Donald G. — AMB8, AMB9, AMB20, AFA1
 Brusa, Guido — AMB9, ATHC17, AFA1
 Buscher, David — AMB21
 Butts, Russell R. — AMA3
 Byer, R. L. — AMB25

 Campbell, John — AMB22
 Carreras, Richard C. — ATHC25, AFA3

 Chanan, Gary A. — AWD13
 Cheung, E. C. — AMB25
 Christou, Julian C. — AWA1, AWC4, AWD6
 Close, Laird M. — ATuB1, ATuB3
 Conrad, A. — AMB3
 Crampton, David — AMB14
 Crnkovic, Romana — AWD13

 Dainty, Christopher — AWD14, AWD15
 Dekany, Richard G. — AMB12
 Dekens, Frank — AWD13
 Del Vecchio, Ciro — ATHC17
 Demailly, L. — ATHC28
 Devaney, Nicholas — AMB6
 Doel, Peter — AMB21
 Duncan, Alan — ATHC9

 Ealey, M. — AFA2
 Ebizuka, Noboru — AWD2
 Ebstein, Steven M. — ATuB6, AFA3
 Ellerbroek, Brent L. — AWC4, AWD6, ATHA, ATHA3, ATHB, ATHB2
 Erbert, G. — AMC2
 Esposito, S. — AMB29, ATHC5, ATHC11, ATHC16

 Farinato, J. — ATHC16
 Fender, Janet S. — AMA3, AWB
 Fini, L. — ATHC5, ATHC11
 Fletcher, Murray — AMB14
 Fortes, B. — AWD18
 Foy, Renaud — AMB27
 Frank, Z. A. — AWD4
 Freund, Isaac — AWD12
 Friedman, Herbert W. — AMB1, AMB10, AMB27, AMB28, AMC2
 Fugate, Robert Q. — AMC1, ATuB3, ATuB5, AWC4, ATHA, ATHB

 Gaffard, Jean-Paul — AMB14
 Gallant, Peter J. — ATHC8
 Gallieni, Daniele — ATHC26, AFA1
 Gallieni, Walter — ATHC17
 Gardner, Chester S. — AMC3
 Gathright, J. — AMB3
 Gavel, Donald — AMB1, AMB4, AMB5, AMB10
 Ge, J. — ATuB5
 Gentles, Bruce — AMB21

 Geoffray, H. — ATHC28
 Gigan, Pierre — AMB14
 Gleckler, A. — AMB1, AMB2, AMB4
 Glindemann, Andreas — AWC2, AWD16, ATHC18
 Gonsalves, Robert A. — ATuB6, AFA3
 Goodding, James C. — AMB19
 Graves, J. Elon — AMB15, ATuB1
 Gray, Peter M. — AMB9, ATuB5, ATHC17
 Gregory, Don A. — ATHC24
 Gregory, T. — AMB1, AMB2, AMB3, AMB4, AFA2
 Groesbeck, T. D. — AMB9

 Haase, Wolfgang — ATHC21
 Hege, E. Keith — AWA1
 Hippler, Stefan — ATHC18
 Ho, J. G. — AMB25
 Hogan, G. P. — AMB24
 Huang, Y. — AMB25
 Hudson, Tracy D. — ATHC24
 Humphreys, Ron — AMB21
 Hyde, Cynthia A. — AWA2

 Injevan, H. — AMB25
 Isaev, Michail V. — ATHC21, ATHC22, ATHC23
 Ito, Youichi — AWD2
 Ivanova, Natalia L. — ATHC21, ATHC22
 Iye, Masanori — AMA, AMB, AMB7, AWD2, ATHC13

 Jacobsen, B. — AMB9, ATuB5
 Jagourel, Pascal — AMB14
 Jefferies, Stuart M. — AWA1
 Johnston, Dustin C. — AWC4
 Jones, Gareth — AMB21
 Junor, William — AFA3

 Kalinowski, Keith — AMB22
 Kendrick, Rick — ATHC9
 Kenemuth, John R. — AMB18
 Kentischer, Th. — AMB16
 Kluckers, Vincent A. — AWC3, AWD14
 Kogan, Vladimir I. — ATHC23
 Kopp, Greg — ATHC25
 Koreshev, S. N. — ATHC4
 Koryabin, Alexander V. — AWD9
 Kuklo, T. — AMC2

- La Fiandra, Carlo — AMB18
 Lai, Olivier — AMB14
 Lakhtikov, V. B. — ATHC4
 Larichev, A. — ATHC20
 Lebedeva, G. I. — ATHC4
 Leckie, Brian — AMB14
 Lelievre, Gerard — ATuB
 Lewis, H. — AMB3
 Liang, Junzhong — AWB2
 Link, Donald J. — AMB17
 Lloyd-Hart, M. — AMB8, AMB9, AMC, ATuB5, ATHC14
 Longmore, Andy — AMB21
 Loos, Gary C. — ATHA2, ATHC25
 Love, Gordon D. — ATHC25, AFA3
 Lukin, I. P. — AWD10, AWD11
 Lukin, Vladimir P. — AWC, AWC1, AWD18, ATHC2
 Lupton, W. — AMB3
- Macintosh, Bruce — AMB10, AMB28
 Mackay, Craig D. — ATHC1
 Maitre, H. — AWD3
 Malik, J. — AMC2
 Martinez, T. — AMB9
 Mather, John C. — AMB22
 Maute, J. — AMB2, AFA2
 Max, Claire E. — AMB1, AMB4, AMB10
 Mayer, N. N. — AWD17
 McArthur, Scot — AMB14
 McCarthy, Jr., D. W. — AMB9, ATuB3
 McCaughrean, Mark J. — ATHC18
 McClain, Jr., John L. — ATHC24
 McGaughey, Donald — AWC5
 McKenna, D. — AMB13
 McLeod, B. A. — AMB9
 McNally, James J. — AMB18
 Merkle, Fritz — AWB1
 Migus, Arnold — AMB27
 Miller, Donald T. — AWB2
 Milonni, Peter W. — AMB30
 Mohanty, S. — AMB9, ATuB3
 Monnet, Guy — ATuB4
 Montandon-Varoda, L. — AMB24
 Montera, Dennis A. — ATHA5, ATHC7
 Morrison, Rob. V. — ATHC25
 Murakawa, Kouji — AWD2
 Myers, Richard M. — AMA, AMB, AMB21
- Nakashima, Koji — AMB7
 Nicholls, Tom — AWD15
 Nicitin, Vladislav V. — ATHC21, ATHC22
 Nikolaev, I. P. — ATHC20
 Nisenson, Peter — ATuB6, AFA3
 Northcott, Malcolm J. — ATuB1, ATuB2, ATHA3
- Oliker, Michael D. — AWC4
 Olivier, Scot S. — AMB4, AMB5, AMB10, AMB11
 Onokhov, Arkadi P. — ATHC21, ATHC22, ATHC23
 Otsubo, Masashi — AMB7, ATHC13
- Papen, George C. — AMC3
 Parfenov, Vadim A. — AMB26, ATHC3
 Passaro, James R. — AMB18
 Paxman, Richard G. — AWA3
 Pennington, Timothy L. — AWD6
 Percheron, Isabelle — AMB23
 Perrier, C. — AWA4
 Podoba, Vladimir I. — ATHC3, ATHC4
 Polejaev, Vladimir I. — AWD9
 Prado, P. — ThC28
 Price, T. — AFA2
 Prieto, E. — ATHC27, ATHC28
 Pruidze, D. V. — ATHB3
- Quirrenbach, A. — AWD1
- Radau, S. — AMB2
 Radick, Richard R. — ATHC6
 Ragazzoni, R. — AMB29, ATHC5, ATHC16
 Ranfagni, P. — ATHC5
 Restaino, Sergio R. — ATHC25, AFA3
 Reznichenko, Vladimir V. — ATHC15, ATHC21, ATHC22, ATHC23
 Rhoadarmer, Troy A. — ATHB2, ATHC14
 Riccardi, A. — AMB29, ATHC5
 Ricklin, J. C. — ATHB3
 Rigaut, Francois — AMA2, AMB14, AWD3, ATHA3
 Riker, James F. — AWD6
 Rimmele, Thomas R. — ATHC6
 Roark, J. Timothy — AWD6
 Roberts, Scot — AMB14
- Roddier, Claude — ATuB1
 Roddier, Francois — ATuB1
 Rodin, Sergei N. — AMB26
 Roggemann, Michael C. — AWA2, ATHA5, ATHC7, ATHC10
 Rohloff, Ralf-Rainer — ATHC18
 Rosenberg, Brian — AWD8
 Roser, M. — AMB16
 Rouan, Daniel — AMB14, AWD3
 Ruck, Dennis W. — ATHA5, ATHC7
 Ryan, P. T. — AMB9, ATuB3
- Safronov, Andrey G. — ATHC19
 Salinari, Piero — AMB8, ATHC17
 Salmon, Derrick — AMB14
 Salmon, T. — AMC2
 Sanchez, Darryl — AMB23
 Sandler, David G. — AMA1, AMB8, AMB9, ATuB3, ATHC29
 Schmidt, W. — AMB16
 Schneider, T. G. — AMB13
 Seery, Bernard D. — AMB22
 Seregin, Alexander G. — ATHC3, ATHC4
 Shelton, Chris — ATuB6
 Shelton, J. C. — AMB13
 Shmalhausen, Victor I. — AWD9
 Simons, Doug — ATHA3
 Sinor, Timothy W. — ATHA2
 Sirota, M. — AMB2
 Smirnov, Alexander P. — ATHC15
 Soltau, D. — AMB16
 Spillar, Earl J. — AWD6
 Spinhirne, James M. — AWC4
 Stahl, Steven — ATHC29
 Stilburn, Jim — AMB14
 Stix, M. — AMB16
 Stockman, Peter — AMB22
 Stomski, P. — AMB1, AMB2, AMB3, AMB4, AFA2
- Takami, Hideki — AMB7, ATHC13
 Takato, Naruhisa — AMB7
 Tallon, Michel — AMB27
 Tamura, Motohide — AWD2
 Tarbell, T. D. — AWD4
 Tartakovski, Valeri A. — AWD17, ATHC2
 Telle, John M. — AMB30, AMC4
 Tessier, E. — AWA4

- Thomas, Jim — AMB14
 Thompson, G. — AMC2
 Tighe, R. — AThC27
 Tomilin, Maxim G. — AThC23
 Tyler, David W. — AWD5, AThC12
 Tyson, Robert K. — AFA

 Valley, M. M. — AMB25
 Veran, Jean-Pierre — AMB14, AWD3
 Vernon, Russell G. — AMB17
 Violino, P. — AThC20
 Voelz, D. G. — AThB3
 Vorontsov, M. A. — AThB3, AFA4

 Wagner, Karl — AThC18
 Waltjen, Kenneth E. — AMB4, AMB10
 Watson, J. — AMB4
 Webb, C. E. — AMB24
 Wells, Martyn — AMB21, AWC3
 Welsh, Byron M. — AWA, AWA2,
 AWD, AThA5, AThC7, AThC10
 Wild, Walter J. — AThB1
 Williams, David R. — AWB2
 Wittman, D. M. — AMB9
 Wizinowich, Peter L. — AMB1, AMB2,
 AMB3, AMB4, ATuA, ATuA1, AThC,
 AFA2

 Wong, N. — AMC2
 Wooder, Nicholas J. — AWD14,
 AWD15
 Woof, Robert — AMB14
 Woolf, N. — ATuB5
 Worswick, Sue — AMB21

 Yeskov, D. N. — AThC4
 Yu, Jirong — AMC3